ENVIRONMENTAL CONDITIONS, LOADS AND INDUCED RESPONSES OF MARINE UNITS

NI691 - DECEMBER 2022

GUIDANCE NOTE

BUREAU VERITAS

BUREAU VERITAS
RULES, RULE NOTES AND GUIDANCE NOTES

The PDF electronic version of this document available at the Bureau Veritas Marine & Offshore website https://marine-offshore.bureauveritas.com/ is the official version and shall prevail if there are any inconsistencies between the PDF version and any other available version.

These rules are provided within the scope of the Bureau Veritas Marine & Offshore General Conditions, enclosed at the end of Part A of NR467, Rules for the Classification of Steel Ships. The current version of these General Conditions is available at the Bureau Veritas Marine & Offshore website.

BUREAU VERITAS MARINE & OFFSHORE

8 cours du triangle
92937 Paris La Défense Cedex - France
+33 (0)1 55 24 70 00

marine-offshore.bureauveritas.com/rules-guidelines

NI691

ENVIRONMENTAL CONDITIONS, LOADS AND INDUCED RESPONSES OF MARINE UNITS

December 2022

Table of Content

Section 1 General Considerations

Section 2 Environmental conditions

Section 3 Loads on Slender bodies

Section 4 Loads on Large Bodies

Section 5 Seakeeping response

Section 6 Global performance analysis

Section 7 Structural response

Table of Content

Section 8 Use of CFD

Section 9 Model testing

Appendix 1 Outline of the theories

Appendix 2 Illustrative Numerical Results

Section 1 General Considerations

1. General

1.1. Introduction

1.1.1 Purpose and scope

There exist large variety of offshore systems installed all over the world. They are either fixed to the sea floor or they are floating as shown in Figure 1. Once installed the structural components are exposed to the environmental loads to which they should resist during their operational lifetime. The purpose of the present document is to give guidance for modelling of environmental conditions and for evaluating the corresponding loads and the structural responses of the offshore systems.

Figure 1: Offshore installations (oilstate.com)

1.1.2 Environmental conditions and loads

The environmental conditions cover all the natural phenomena which can induce the structural or operational failure of the offshore system. In the context of marine structures, the most important environmental phenomena are wind, waves and current.

1.2. Types of offshore units

1.2.1 Introduction

Many different concepts for offshore platforms were proposed by the industry. The water depth appears to be a determining factor when choosing between fixed and floating structures. At the same time the environmental conditions together with the operational requirements drive the choice of the final design for a particular offshore site. Typical technical solutions, which are usually employed in practice are shown in Figure 1.

1.2.2 Fixed platforms

A fixed offshore platform is a platform extending above the sea level and is supported at the seabed by certain means. Two main types of fixed platform exist: jackets and gravity based platforms (GBS). In the case of jackets, the platform is supported by a piling system while in the case of GBS the platform is supported by its own weight. The jacket platforms are usually composed of set of steel cylindrical components with relatively small diameter while the GBS usually have components of larger dimensions and are made of concrete.

1.2.3 Floating platforms

When the depth becomes too large, or for prospection purposes, fixed structures are no longer practically possible and floating platforms are used. Many different concepts of the floating platform are in use today, either for prospection or production: Semi-submersible platforms, Spars, Tension leg platforms (TLP), FPSO's … An important aspect of the floating platform is that, in order to keep it at a required mean position, it needs to be moored to the seabed or alternatively a complex dynamic positioning system should be used. The design of the mooring system represents one of the major challenges in the offshore industry, both in shallow and deep waters which can exceed $3000\ m$ in practice.

1.2.4 Hybrid fixed-floating platforms

There exist offshore platforms which can operate in both floating and fixed conditions. A typical example is the jack-up platform. In transit conditions the jack-up platform is floating with its legs pulled out of the water and once installed the hull structure is pulled out of water. In the onsite operating conditions, the stability of the platform is ensured by its legs which penetrates the seafloor under the weight of the hull structure.

1.2.5 Compliant towers

A compliant platform is a bottom founded structure which has important flexibility so that part of the external loading is resisted by the inertial forces. These platforms are attached to the seabed by a piling system but can also be guyed. They are usually employed in intermediate water depth between 450 and 900 meters.

1.2.6 Very Large Floating Structures

A Very Large Floating Structures (VLFS) represent the artificial islands which may be used for various purposes: floating airports, floating landing platforms, bridges, docks, storage facilities, wind or solar power plants, military mobile offshore bases, huge living complexes and others. The dimensions of VLFS largely exceeds those of the classical offshore platforms used for oil exploration. Horizontally large floating structures can go from roughly 500 to 5000 meters in length, 100 to 1000 meters in width with the draught going from 2 to 10 meters. The particular feature of the VLFS is their significant flexibility which usually leads to the structural natural frequencies close to the frequencies of the most energetic water waves. For that reason, the full hydroelastic analysis (see Section 7, [3]) needs to be used when evaluating the behavior of VLFS in waves.

1.3. Classification of the loads and responses

1.3.1 Introduction

Since the geometry of the different offshore platforms is very different, the characteristics of the fluid flow which results from the interaction of the body with the environment (wind, wave, current), will be different too. Both the viscous effects as well as the potential flow effects may become important. The critical parameter for the choice of the particular analysis method is the ratio between the characteristics of the incoming flow (typically flow velocities) and the body dimensions. In practice the bodies are classified in two categories based on their dimensions with respect to the characteristics of the incoming flow: large bodies and the slender bodies.

1.3.2 Assessment of the loads

When operating in a particular environment, offshore structures are subjected to all sorts of environmental loads which need to be properly evaluated in the design process. The loads are usually evaluated either by model tests or by numerical simulations. Model tests being rather expensive, numerical simulations are usually preferred whenever that is possible.

Various numerical tools are available to evaluate the environmental loads. They include very complex CFD simulation tools, potential flow models (diffraction – radiation models) but also more pragmatic empirical models such as the famous Morison formula (see Section 5, [2.7.5]). Due to their relative simplicity and reasonable computational time, the potential flow models are preferred in practice. The CFD simulations are usually reserved to phenomena with strong influence of viscosity and vorticity (friction, flow separation…) and to the phenomena where the potential flow methods fail due to their physical limitations and assumptions, and due to various numerical difficulties (sloshing, green water, large body motions …).

The applicability of a particular simulation model depends on the flow conditions which can be of various types. It is common to separate the loads int two main categories: loads on slender bodies and the loads on large bodies. The body is considered to be slender when the ratio of the wave length over the characteristic dimension is large enough, usually $\lambda/D > 6$, with the additional condition that there is no end effect i.e., the length of the body is much larger than its characteristic diameter. For slender bodies the loading is usually dominated by the drag component so that the potential flow methods cannot be used and either CFD or empirical formulations (Morison formula) are employed in practice. For large bodies, the loads are dominated by the diffraction – radiation effects which can be accurately modelled by potential flow models. Very often a single offshore platform can be composed of both "large body" and "slender body" elements, a typical example being the semi-submersible platform. In those cases, the potential flow-based diffraction-radiation model for the "large body" needs to be combined with the Morison model for the "slender bodies"

1.3.3 Assessment of the responses

When analyzing the body response in waves there are two important types of periods which matter: the wave periods and the natural periods of the floating system. In reality the energetic water wave periods cover the range from roughly 3 to 20 seconds and at these periods' waves exert large loads on floating structures inducing responses at the same periods and more or less proportional to the wave amplitude. In case of resonance, a catastrophic response can occur.

In practice, when designing the floating system for a specific site it is common to try to shift the natural periods in order to avoid the resonant conditions at least in the linear sense. However, even if the natural periods of the system are far from the energetic wave periods, the resonance conditions still might occur. This is due to the nonlinearities of the loading. The nonlinear loading can be of various sources: viscosity, mechanical nonlinearities (parametric instabilities), nonlinear potential flow component of the wave loading and others. In the analysis of the global behavior of the floating systems, the nonlinear potential flow component of the wave loading is usually the most important. Typical examples are the second order wave loads which are obtained by extending the wave loading theory to second order with respect to wave steepness. The second order loads are smaller than the linear (first order) loads but they cover a much wider frequency range increasing the risk of resonance in the low and high frequency range. Accounting for these loads is fundamental in the analysis of the slow drift motion of softly moored systems which has a period of the order of minutes. Another example where the second order loads are fundamental is the so called springing phenomena which occurs for very stiff systems such as a TLP where the vertical natural periods are usually between 2 and 4 seconds (see Section 5, [3.2.3]).

Other nonlinear phenomena can also induce response at frequencies different from the wave frequencies. A typical example is parametric roll that may occur when the wave encounter frequency is twice the roll natural frequency. Another example is the high frequency ringing response of cylindrical structures which seems to be induced by the nonlinear effects above the second order i.e., third, fourth or even higher (see Section 4, [6.2]).

In any case, the determination, or at least the estimate, of the natural frequencies of the floating system, is an important prerequisite to the hydrodynamic analysis. It is also useful to have a proper estimate of the associated damping ratios.

1.3.4 Stochastic aspects

The environmental conditions (wind, waves, current) are highly unsteady and stochastic in nature, and it is fundamental to take into account these aspects when designing the offshore structures. The statistical description of the environment should cover both its short term and the long-term variations in order to properly assess the response in terms of extremes as well as in terms of the accumulated fatigue. Once the design environment is defined, the determination of the design responses for extreme and fatigue conditions needs to be performed following the dedicated methodology. The basic principles of the design methodologies recommended by Bureau Veritas are discussed in NI638 “Guidance for Long-term Hydro-structure Calculations”.

1.4. Relation to other BV documents

1.4.1 Introduction

The present document provides the general technical background for the evaluation of the environmental loads and responses of offshore structures. The methods discussed here are applicable to various BV Rule notes (NR’s) as well as the Guidance notes (NI’s) which covers specific marine structures. At the same time the large part of the theories discussed here are included in the dedicated BV software.

1.4.2 Offshore rules and guidance

The following NR’s and NI’s are concerned:

NR445	Rules for the Classification of Offshore Units
NR493	Classification of Mooring Systems for Permanent Offshore Units
NR494	Rules for the Classification of Offshore Loading and Offloading Buoys
NR534	Rules for the Classification of Self-elevating Units – Jack-ups and Liftboats
NR542	Classification of Floating Gas Units
NR569	Classification of Drilling Ships
NR571	Classification of Column Stabilized Units
NR578	Rules for the Classification of Tension Leg Platforms
NI572	Classification and Certification of Floating Wind Turbines
NI611	Guidelines for Fatigue Assessment of Steel Ships and Offshore Units
NI621	Guidelines for Moonpool Assessment

1.4.3 Software

The following software is of concern:

HYDROSTAR	First and second order diffraction – radiation
ARIANE	Mooring analysis
HOMER	Hydro-structure interactions
OPERA	Marine operations
FOAMSTAR	CFD in waves

The theories implemented in the above tools closely follows the theories described here so that the present document can be used as a basic theory manual for those tools.

1.5. List of references

Present document was written in close cooperation with Professor Bernard Molin, whose help and critical comments are greatly acknowledged.

The following references are the general ones valid for several Sections, and there are many others listed in separate sections that are more specific to those sections.

[1] Chakrabarti S.K., 1987.: “Hydrodynamics of offshore structures.”, Springer
[2] Chakrabarti S.K., 2005.: “Handbook of offshore engineering.”, Elsevier
[3] Faltinsen O.M. & Timokha A.N., 2009.: “Sloshing.”, Cambridge University Press
[4] Faltinsen O.M., 1990.: “Sea loads on ships and offshore structures.”, Cambridge University Press
[5] https://oilstates.com/
[6] Journée J.M.J & Massie W.W., 2001.: “Offshore hydromechanics”, Delft University of Technology.
[7] Lamb H., 1975.: “Hydrodynamics.”, Cambridge University Press
[8] Mei C.C, Stiassnie M. & Yue D.K.P., 2005.: “Theory and applications of ocean surface waves.”, Advanced series on ocean engineering, Vol.23, World Scientific
[9] Molin B., 2002.: “Hydrodynamique des structures offshore.”, Editions Technip
[10] Newman J.N., 1977.: “Marine hydrodynamics.”, MIT Press
[11] Sarpkaya T., 2010.: “Wave forces on offshore structures”, Cambridge University Press
[12] Wehausen J.V. & Laitone E.V., 1960.: “Surface waves.”, >> https://surfacewaves.berkeley.edu/ <<

Section 2 Environmental conditions

1. General

1.1. Introduction

1.1.1 Definitions

The environmental conditions describe the natural phenomena which exist at a specific site without the presence of the floating systems. In the present context the following phenomena are the most important:

- Wind
- Waves
- Current

Depending on the type of the floating units and the specificities of the site conditions, other phenomena can also become important and need to be taken into account, namely: tides, internal waves, tsunamis, earthquake, soil conditions, ice and snow, seiches, marine growth and others …

1.1.2 Environmental data

Most often, the environmental conditions are described by the quantities of probabilistic nature, and their influence on the design should be analyzed using statistics and probabilities. This requires a sufficiently large amount of measured data, from which the short term and the long term variations of the different quantities can be deduced. The necessary duration of the measurements depends on the targeted level of probability.

1.2. Water depth, tides and storm surges

1.2.1 General

The mean water depth and its variations should be defined prior to any other environmental effects. The water depth affects several design parameters among which the following ones are particularly important:

- the relative position of the different structural parts (decks…) and of the equipment
- mean mooring forces for taut or vertically moored floating structures (e.g. TLP)
- environmental forces in general

The instantaneous water depth consists of the mean value which is constant in time and the variations in time relative to this level. The mean value is the water depth at reference datum and is usually defined in terms of the Mean Surface Level (MSL). The variations of the water depth in time are mainly due to the astronomical tides and the storm-induced surges. Relevant definitions are shown in Figure 2.

Figure 2: Water depth, tide and storm surges

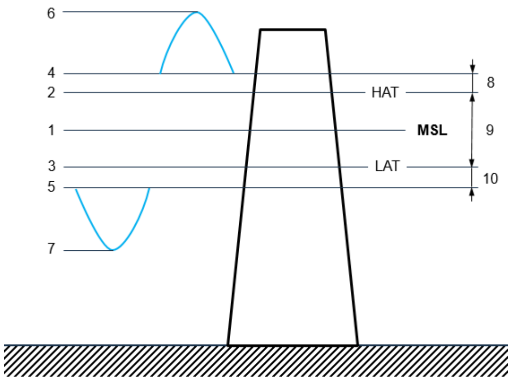

1 - Mean Sea Level
2 - Highest Astronomical Tide
3 - Lowest Astronomical Tide
4 - Highest still water level
5 - Lowest still water level
6 - Maximum crest elevation
7 - Minimum trough elevation
8 - Positive storm surge
9 - Tidal range
10 - Negative storm surge

1.2.2 Tides

Tidal variations of water level result from the interaction of the gravitational and rotational interaction between the sun, moon and earth. They happen regularly and are largely predictable. The maximum tidal variations are bounded by the Highest Astronomical Tide (HAT) and the Lowest Astronomic Tide (LAT)

1.2.3 Storm surge

A storm surge denotes the rising of water level due to the storm conditions such as cyclones (high atmospherical depressure). It is measured as the rise in water level above the normal tidal level and does not include waves. The main factor contributing to a storm surge is high-speed wind pushing water towards the coast over a long fetch. Because of their meteorological nature, the storm surges have essentially random character.

2. Waves

2.1. Regular wave theories

2.1.1 General

There exist many different regular wave theories and here we limit ourselves to the wave theories which are usually applied for the design of marine structures. In reality, water waves are generated by the wind, which creates a shear at the free surface which means that they have some vorticity. These effects are usually ignored in practice and the irrotationality of the flow is assumed which allows the use of the powerful frame of potential flow theory. This applies to waves propagating away from their generation areas, or to waves produced in a wave tank.

2.1.2 Definitions

When describing the regular water waves, the following quantities are usually employed (see Figure 3):

-	h	mean water depth $[m]$
-	A^+	crest height $[m]$
-	A^-	crest trough depth $[m]$
-	H	trough to crest height $[m]$, $H = A^+ + A^-$
-	A	linear amplitude $[m]$, $A = H/2$
-	λ	wave length (distance between two consecutive crests or troughs) $[m]$
-	k_0	wave number $[m^{-1}]$, $k_0 = 2\pi/\lambda$
-	T	wave period (time laps between two consecutive crests or troughs) $[s]$
-	ω	wave frequency $[rad/s]$, $\omega = 2\pi/T$
-	V_P	phase velocity $[m/s]$, $V_P = \lambda/T = \omega/k_0$
-	V_G	group velocity $[m/s]$, $V_G = \partial\omega/\partial k_0$

Figure 3: Definition of wave

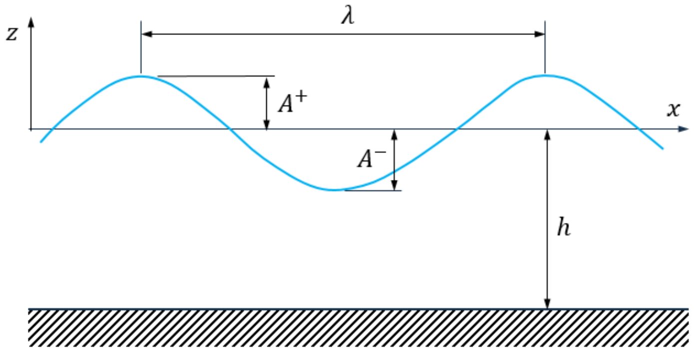

2.1.3 Dimensionless numbers

The following dimensionless numbers are relevant:

-	ε	wave steepness	$\varepsilon = \dfrac{H}{\lambda} = \dfrac{k_0 H}{2\pi}$
-	$\tilde{h}$	relative depth	$\tilde{h} = \dfrac{h}{\lambda} = \dfrac{k_0 h}{2\pi}$
-	U_R	Ursell number	$U_R = \dfrac{\varepsilon}{\tilde{h}^3} = \dfrac{H}{h}\left(\dfrac{\lambda}{h}\right)^2 = 4\pi^2 \dfrac{k_0 H}{(k_0 h)^3}$

2.1.4 Applicability of the wave theories

Wave models can be classified in many different ways, one of them being deep water and shallow water theories. When U_R is high, the shallow water theory needs to be applied (Korteweg-de Vries or Boussinesq). These types of models allow reducing the 3D problems to 2D problems in the horizontal plane, which is done by assuming a polynomial vertical distribution of the flow field, (e.g. see Bingham et al. (2009)). Typical applications are tidal waves or tsunamis but also wind waves in shallow areas. When U_R is not too high (less than 26 according to Holthuijsen (2007)), Stokes's theories, based on the assumption that the wave steepness is small, may be applied. A more complete decomposition of the different wave theories is presented in Figure 4 in the form of the so-called Le Méhauté's diagram.

Figure 4: Le Méhauté's diagram (Kraaiennest (2009))

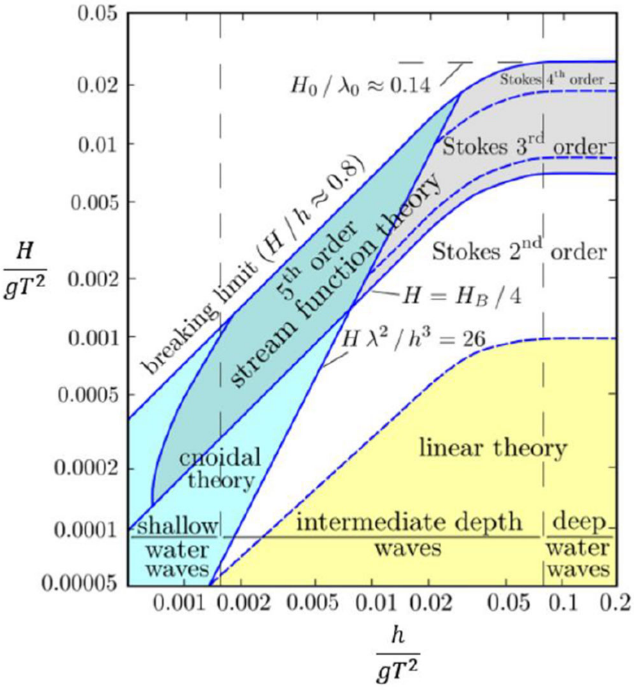

2.2. First order (linear) wave theory

2.2.1 Introduction

The basic description of the nonlinear potential flow model and its linearization in the context of water wave problems is presented in Appendix 1. By introducing the notation

$$\theta = k_0 x + \omega t \tag{1}$$

the linear velocity potential $\Phi_I^{(1)}(\boldsymbol{x}, t)$ of the incident wave (also known under the name of Airy wave) propagating in negative x direction is given by:

Shallow water	Intermediate depth	Deep water
$-\frac{gA}{\omega}\sin\theta$	$-\frac{gA}{\omega}\frac{\cosh k_0(z+h)}{\cosh k_0 h}\sin\theta$	$-\frac{gA}{\omega}e^{k_0 z}\sin\theta$

(2)

The wavenumber k_0 and the wave frequency ω are linked through the dispersion relation:

Shallow water	Intermediate depth	Deep water
$\omega = k_0\sqrt{gh}$	$\omega^2 = gk_0 \tanh k_0 h$	$\omega^2 = gk_0$

(3)

The velocity potential (2) (140)completely defines the flow induced by the linear incident wave and all the other characteristics of the flow can be easily deduced from it. Some of them are presented in Table 1 for the shallow, intermediate and deep water.

Table 1 : Characteristics of the flow induced by the linear propagating wave

		Shallow water	Intermediate depth	Deep water
Free surface elevation	$\eta^{(1)} = -\frac{1}{g}\frac{\partial \Phi_I^{(1)}}{\partial t}$	$A\cos\theta$	$A\cos\theta$	$A\cos\theta$
Hydrodynamic pressure	$p^{hd(1)} = -\varrho\frac{\partial \Phi_I^{(1)}}{\partial t}$	$\varrho g A\cos\theta$	$\varrho g A\frac{\cosh k_0(z+h)}{\cosh k_0 h}\cos\theta$	$\varrho g A\exp k_0 z\cos\theta$
Horizontal particle velocity	$u^{(1)} = \frac{\partial \Phi_I^{(1)}}{\partial x}$	$-\frac{A\omega}{k_0 h}\cos\theta$	$-A\omega\frac{\cosh k_0(z+h)}{\sinh k_0 h}\cos\theta$	$-A\omega\exp k_0 z\cos\theta$
Vertical particle velocity	$w^{(1)} = \frac{\partial \Phi_I^{(1)}}{\partial z}$	$-A\omega\left(1+\frac{z}{h}\right)\sin\theta$	$-A\omega\frac{\sinh k_0(z+h)}{\sinh k_0 h}\sin\theta$	$-A\omega\exp k_0 z\sin\theta$
Horizontal particle acceleration	$a_x^{(1)} = \frac{\partial u^{(1)}}{\partial t}$	$\frac{A\omega^2}{k_0 h}\sin\theta$	$A\omega^2\frac{\cosh k_0(z+h)}{\sinh k_0 h}\sin\theta$	$A\omega^2\exp k_0 z\sin\theta$
Vertical particle acceleration	$a_z^{(1)} = \frac{\partial w^{(1)}}{\partial t}$	$-A\omega^2\left(1+\frac{z}{h}\right)\cos\theta$	$-A\omega^2\frac{\sinh k_0(z+h)}{\sinh k_0 h}\cos\theta$	$-A\omega^2\exp k_0 z\cos\theta$
Horizontal particle trajectory	$x^{(1)} = \int_0^t u^{(1)} dt$	$x-\frac{A}{k_0 h}\sin\theta$	$x-A\frac{\cosh k_0(z+h)}{\sinh k_0 h}\sin\theta$	$x-A\exp k_0 z\sin\theta$
Vertical particle trajectory	$z^{(1)} = \int_0^t w^{(1)} dt$	$z+A\left(1+\frac{z}{h}\right)\cos\theta$	$z+A\frac{\sinh k_0(z+h)}{\sinh k_0 h}\cos\theta$	$z+A\exp k_0 z\cos\theta$

2.2.2 Particle trajectories

Depending on the water depth, the particle trajectories and the corresponding velocities evolve as shown in Figure 5. It can be seen that the particle trajectories are ellipses, which become flatter and flatter by the sea floor. In deep water the trajectories are circular.

Figure 5: Variation of the particle trajectories, horizontal (u) and vertical (w) velocities, and amplitudes with depth

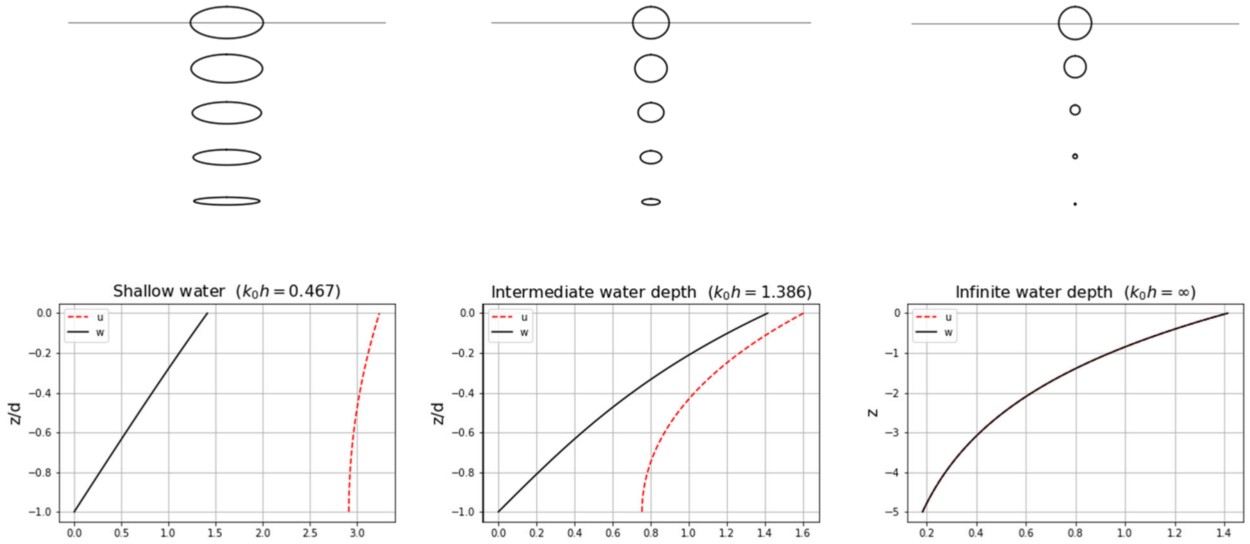

2.2.3 Phase velocity and group velocity

The phase velocity V_P represents the velocity of the wave profile while the group velocity V_G represents at the same time the velocity at which the group of waves is propagating and the velocity at which the wave energy propagates. The group velocity can be determined from dynamic analysis of the wave energy flux or from the purely kinematic study of a group of waves formed by two nearly equal plane waves. The group velocity of gravity waves is always lower than the phase velocity and it approaches one half of the phase velocity when depth goes to infinity as shown in Figure 6 – left, where the phase and group velocities, normalized by the infinite depth phase velocity $V_P^\infty = g/\omega$, are plotted vs k_0h. This implies that, in a wave system with a front, propagating into otherwise calm water, individual waves will overtake the front and vanish. This can be observed in Figure 6 – right where a sequence of photographs of a plane progressive wave system advancing in calm water is shown. The wave energy is contained within the two parallel diagonal lines making an angle α_G with the vertical axis and the wave crests are progressing along the diagonal line making an angle α_P with the vertical axis. The cotangent of the angles α_G and α_P defines the group and the phase velocities respectively and it can be clearly seen that $\alpha_G < \alpha_P$. In shallow water $\sinh 2k_0h \simeq 2k_0h$ and the group and phase velocities are equal meaning that all the wave components travel at the same velocity $\sqrt{gh}$. This means that the medium is no longer dispersive according to the linear theory. The expressions for the phase and group wave velocities at different water depth regimes are given by:

Shallow water	Intermediate depth	Deep water
$V_P = \sqrt{gh}$	$V_P = \sqrt{\frac{g}{k_0}\tanh k_0h}$	$V_P = \sqrt{\frac{g}{k_0}}$
$V_G = V_P$	$V_G = \left(\frac{1}{2} + \frac{k_0h}{\sinh 2k_0h}\right)V_P$	$V_G = \frac{1}{2}V_P$

(4)

Figure 6: Left – Normalized phase and group velocity vs $k_0 h$.
Right – Plane progressive wave system advancing in otherwise calm water

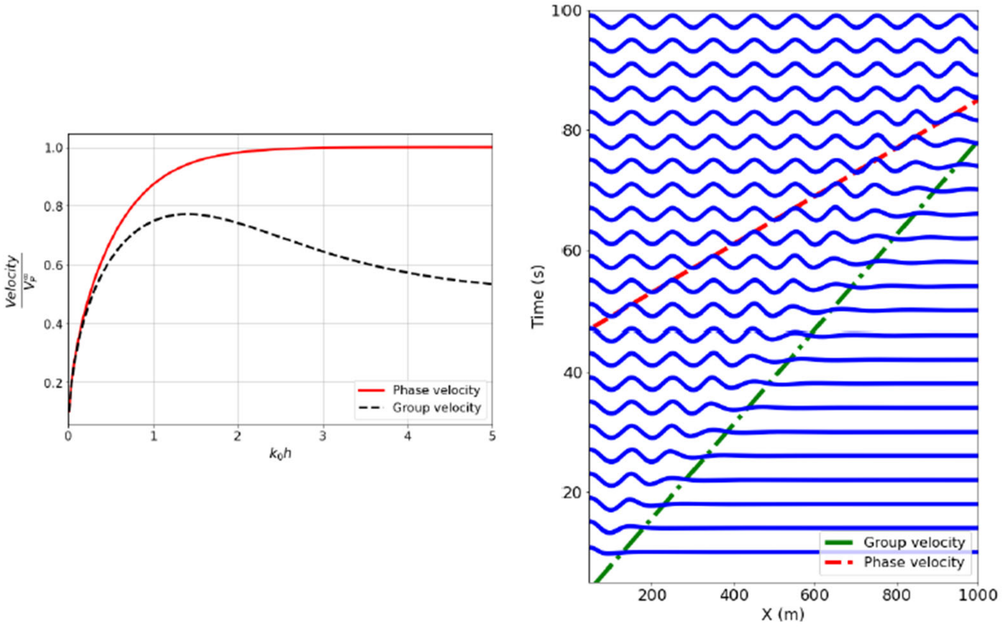

2.2.4 Wave energy and energy flux

The total wave energy E, of unit width, in a closed fluid domain Ω bounded by the free surface, sea-bottom and the two vertical lines, one wavelength apart from each other, is the sum of the potential energy E_P and the kinetic energy E_K . It can be deduced as:

$$E = E_P + E_K = \iint_{\Omega} \varrho g z dS + \frac{1}{2}\iint_{\Omega} (\nabla\Phi)^2 dS = \frac{1}{4}\varrho g A^2 \lambda + \frac{1}{4}\varrho g A^2 \lambda = \frac{1}{2}\varrho g A^2 \lambda \qquad (5)$$

Therefore, in a regular wave system, the averaged energy density per unit area is $0.5\varrho g A^2$.

The energy flux P_E is defined as the quantity of energy that enters the domain by unit time and can be written as:

$$P_E = -\varrho \int_{-h}^{\eta} \frac{\partial\Phi}{\partial t}\frac{\partial\Phi}{\partial x} dz \qquad (6)$$

Keeping the leading order term and after averaging in time over the one wave period, the mean energy flux $\bar{P}$ is obtained as:

$$\bar{P}_E = \frac{1}{2}\varrho g A^2 V_G \qquad (7)$$

meaning that the energy travels at the group velocity.

The mean energy flux represents the allowable power per unit width that can be potentially recovered by a wave energy converter.

2.3. Second order wave theory

2.3.1 General

The potential flow theory up to 2nd order is discussed in Appendix 1, where the corresponding kinematic and the dynamic free surface conditions are presented in detail. Those boundary conditions remain valid whatever the wave system: regular, bichromatic, or irregular.

2.3.2 Regular waves

A particular solution for the second order velocity potential of the regular wave propagating in the positive x direction, in water depth *h,* can be obtained in the following form:

$$\Phi_I^{(2)}(\boldsymbol{x},t) = \frac{3}{8}\frac{A^2\omega}{\sinh^4 k_0h}\cosh 2k_0(z+h)\sin 2\theta - g\delta^{(2)}t \tag{8}$$

where θ is given by (1).

The corresponding second order contribution to the free surface elevation is:

$$\eta^{(2)}(\boldsymbol{x},t) = \frac{k_0A^2}{4}(3\coth^3 k_0h - \coth k_0h)\cos 2\theta - \frac{k_0A^2}{2\sinh 2k_0h} + \delta^{(2)} \tag{9}$$

When $\delta^{(2)} = k_0A^2/(2\sinh 2k_0h)$ the mean water level becomes zero and this correspond to waves generated in the tank of constant volume.

In deep water the second order velocity potential $\Phi_I^{(2)}$ and the second order free surface correction $\eta^{(2)}$ are given by:

$$\Phi_I^{(2)} = 0 \quad , \quad \eta^{(2)} = \frac{k_0A^2}{2}\cos 2\theta \tag{10}$$

The Stokes theory is not applicable for shallow water, where the second order potential (8) is undefined ($\sinh k_0h \to 0$ for $k_0h \to 0$).

It is important to realize that the double frequency 2ω and the double wave number $2k_0$ are not linked by the dispersion relation:

$$(2\omega)^2 \neq g(2k_0)\tanh(2k_0h) \tag{11}$$

This means that the wave system described by $\Phi_I^{(2)}$ cannot exist independently from the first-order wave system. Such accompanying wave systems are known as locked or bound waves. It is only when the wave system interacts with a structure, or a change in bathymetry, that second-order free waves i.e. those with wave number linked to 2ω through the linear dispersion equation, can be released.

Figure 7: Free surface profiles of a regular wave at first (Airy) and second orders of approximation

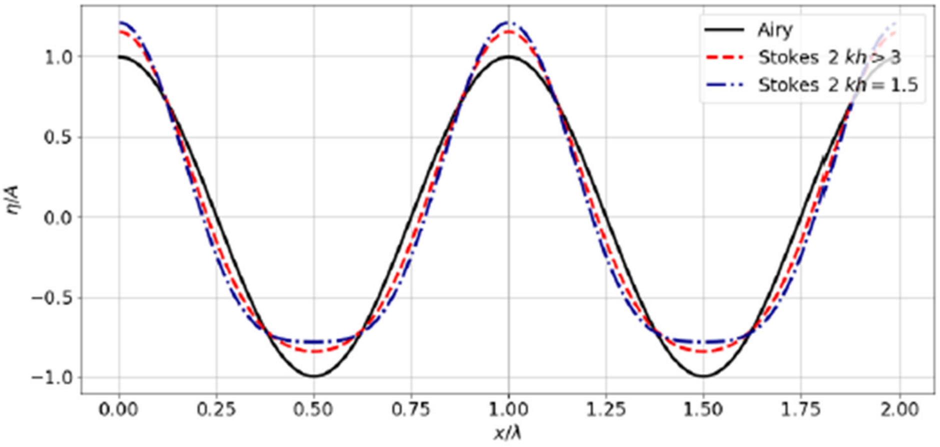

Figure 7 shows the free surface profiles obtained at orders 1 and 2, for a steepness $\varepsilon = 0.1$ and for two k_0h values. The main effect of the second-order correction is that the crests have become higher and steeper, while the troughs have become flatter and shallower. The values of the wave crest and the wave trough in intermediate and the deep water are given by:

Shallow water	Intermediate depth	Deep water
$A^{\pm} = A\left[1 \pm \frac{3}{4}\frac{k_0A}{(k_0h)^3}\right]$	$A^{\pm} = A\left[1 \pm \frac{k_0A}{4}(3\coth^3 k_0h - \coth k_0h)\right]$	$A^{\pm} = A\left(1 \pm \frac{k_0A}{2}\right)$

(12)

2.3.3 Mass transport – Stokes drift

The particle trajectories in Table 1 were derived under the linear assumptions which are valid for infinitesimally small wave motion. It was observed in practice that the particles are not moving around the fixed point in space but they are drifting at the same time. This drift is due to nonlinear effects and can be well explained by the second order theory (e.g. Molin (2002)). The mean time averaged second order horizontal velocity of the particle is given by:

$$\frac{\overline{dx^{(2)}}}{dt} = \frac{1}{2}A^2 k_0 \omega \frac{\cosh 2k_0(z+h)}{\sinh^2 k_0 h} \tag{13}$$

This phenomenon is known under the name of Stokes drift and one of the practical consequences is that the particle trajectories are not strictly closed and they are drifting in the direction of wave propagation as shown in Figure 8.

Figure 8: Particle trajectories with Stokes drift effects included

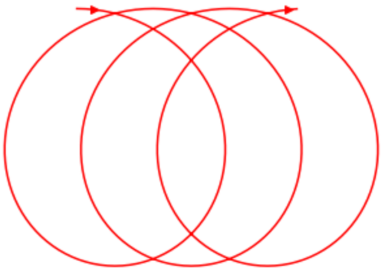

The flow rate Q, associated with the Stokes drift, is obtained by integrating the mean horizontal displacement over the water depth:

$$Q = \frac{1}{2}A^2 \omega \coth k_0 h \tag{14}$$

When waves are generated in a tank of finite length, mass transport is necessarily compensated by a return current which can be appreciable in practice.

2.3.4 Bichromatic waves

A bichromatic wave system consists of the superposition of two regular waves of different amplitudes (A_1, A_2), frequencies (ω_1, ω_2) and directions of propagation (β_1, β_2). The basic principles of the second order theory are described in Appendix 1. Without loss of generality, we assume that the first wave component propagates along the x axis, while the second component travels at an angle β relative to x axis. In that case the first order free surface elevation is given by:

$$\eta^{(1)}(\boldsymbol{x}, t) = A_1 \cos(k_1 x + \omega_1 t) + A_2 \cos(k_2 x \cos\beta + k_2 y \sin\beta + \omega_2 t) \tag{15}$$

The total solution for the second order velocity potential decomposes into 5 different components with the corresponding frequencies: 0 , $2\omega_1$, $2\omega_2$, $\omega_1 - \omega_2$ and $\omega_1 + \omega_2$. The first three components correspond to the regular wave case which was discussed in [2.3.2] and here we concentrate on the last two components at the sum $(\omega_1 + \omega_2)$ and the difference $(\omega_1 - \omega_2)$ frequencies. The corresponding second order velocity potentials can be found in a way similar to the regular wave case and the final expressions for the sum and the difference frequencies are:

$$\Phi_{I\pm}^{(2)}(\boldsymbol{x}, t) = \frac{q_\pm}{-(\omega_1 \pm \omega_2) + g k_\pm \tanh k_\pm h} \frac{\cosh k_\pm (z+h)}{\cosh k_\pm h} \sin[(k_1 \pm k_2 \cos\beta)x \pm k_2 y \sin\beta + (\omega_1 \pm \omega_2)t] \tag{16}$$

where the forcing terms $q_\pm$ are given by:

$$q_\pm = -\frac{1}{2}A_1 A_2 \left(\frac{\omega_1^3}{\sinh^2 k_1 h} \pm \frac{\omega_2^3}{\sinh^2 k_2 h}\right) - A_1 A_2 \omega_1 \omega_2 (\omega_1 \pm \omega_2)\left(\frac{\cos\beta}{\tanh k_1 h \, \tanh k_2 h} \mp 1\right) \tag{17}$$

and the interaction wave numbers $k_\pm$ are:

$$k_\pm = |\boldsymbol{k}_1 \pm \boldsymbol{k}_2| = \sqrt{k_1^2 + k_2^2 \pm 2k_1 k_2 \cos\beta} \tag{18}$$

It follows that the wave systems associated with $\Phi_{I+}^{(2)}$ and $\Phi_{I-}^{(2)}$ are bound (or locked) to the first-order waves and two wave systems propagate in different directions as shown in Figure 9.

Special phenomenon happen when the frequencies ω_1 and ω_1 are close to each other and the relative angle β is close to π. In that situation the wave number k_+ is very small which leads to very slow decay of $\Phi_{I+}^{(2)}$ with the vertical coordinate. Similarly, when $\omega_1 = \omega_2$ and $\beta = 0$ the $\Phi_{I+}^{(2)}$ does not depend any more on the space variable, consequently, the second order pressure is felt in the whole water column. Finally, for $\beta \sim 0$ an analogous situation occurs for the second order difference frequency potential $\Phi_{I-}^{(2)}$ which also decays slowly with the vertical coordinate.

Figure 9: Wave number vectors $k_1 + k_2$ and $k_1 - k_2$ of the second-order wave system

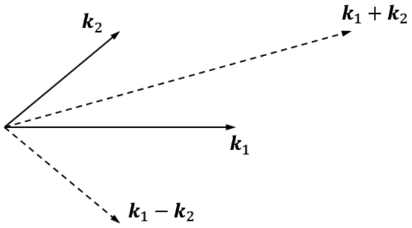

In the case of wave body interactions, a similar effect occurs in the second order diffraction problem due to the interaction between the incident and the diffracted wave systems. All this leads to an important conclusion that, from second-order, wave effects can be felt at much greater depths.

2.4. Higher order regular wave theories

2.4.1 Introduction

The maximum steepness of the regular waves in infinite water depth is $H/\lambda = 0.1412$. After this limit the wave starts to break and the potential flow theory cannot be applied anymore. However up to that limit the nonlinearities in the wave profile and wave kinematics can be significant and needs to be taken into account. There exist a large number of nonlinear wave theories each with its strength and limitations. Detailed discussions of the wave theories are given by: Sarpkaya (2010) Cokelet (1977), Dean (1974), Fenton (1985), Le Méhauté (1976), Skjelbreia and Hendrickson (1961), and Holthuijsen (2007), among many others. The wave theories which are used most often in practice are: higher order Stokes theory, stream function theory, and cnoidal wave theory.

2.4.2 Third order Stokes theory

The extension of the Stokes development up to third order leads to the modification of the wave number which becomes dependent on the wave amplitude. To third order included the free surface elevation of monochromatic wave in infinite depth becomes:

$$\eta(x,t) = \left(1 - \frac{3}{8}A^2k_0^2\right)A\cos\tilde{\theta} + \frac{1}{2}A^2k_0\cos 2\tilde{\theta} + \frac{3}{8}A^3k_0^2\cos 3\tilde{\theta} \qquad (19)$$

where $\tilde{\theta} = (k_0 - k_0^3A^2)x + \omega t$.

Compared to the linear solution, the crest to trough value is unchanged but the amplitude of the first-harmonic component has been modified as shown in Figure 10.

Figure 10: Regular wave in infinite depth. Free surface profiles at orders 1, 2 and 3 vs x/λ. Steepness is $2A/L = 0.1$

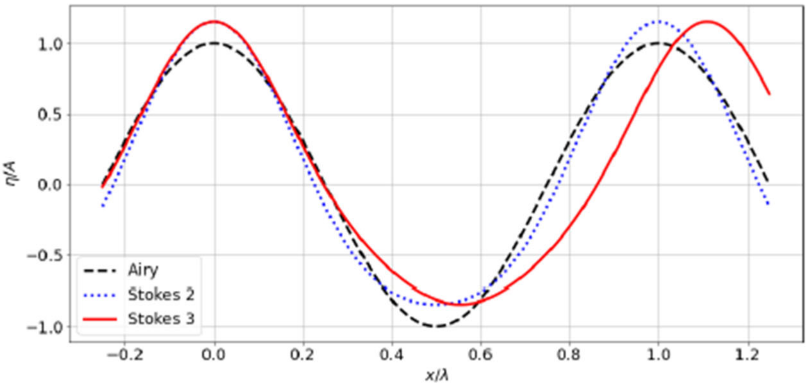

2.4.3 Fifth order Stokes theory

Extending the Stokes procedure to orders higher than 3 quickly becomes tedious and unpractical especially in finite water depth. For regular steep waves in deep waters the Stokes waves can be evaluated to any order as shown by Schwartz (1974) but the application to finite depth has important limitations. Different solutions in finite depth can be found in the literature. Among them, the one proposed by Fenton (1985) appears to be used most often. The solution is usually presented in the following form:

$$\Phi_I(\boldsymbol{x},t) = \quad -V_P x + \frac{C_0}{k_0}\sqrt{\frac{g}{k_0}}\sum_{i=1}^{5}(\pi\varepsilon)^i\sum_{j=1}^{i}A_{ij}\cosh jk_0(z+h)\sin jk_0x$$

$$k_0\eta_I(x) = \quad \pi\varepsilon\cos k_0x + (\pi\varepsilon)^2B_{22}\cos 2k_0x + (\pi\varepsilon)^3B_{31}(\cos k_0x - \cos 3k_0x)$$

$$(\pi\varepsilon)^4(B_{42}\cos 2k_0x + B_{44}\cos 4k_0x)$$

$$(\pi\varepsilon)^5[-(B_{53}+B_{55})\cos k_0x + B_{53}\cos 3k_0x + B_{55}\cos 5k_0x] \qquad (20)$$

where the exact analytical expressions for the coefficients C_0, A_{ij}, B_{ij} can be found in Fenton (1990).

When the wave height H, the water depth h and the wave length λ are given, the application of the expressions given above is straight-forward, and the wave period and phase velocity can easily be obtained. The Stokes theory cannot be used in very shallow waters where the stream function or cnoidal wave theories needs to be applied.

Most recent work on fifth order Stokes wave theory is discussed in Zhao et al (2022) where some differences with the Fenton's model have been pointed out.

2.4.4 Stream function method

This method was originally proposed by Dean (1965) and the method is known under many different names: stream function method, Dean's model, Fourier model, Rienecker & Fenton model, etc. The method is based on the evaluation of the stream function Ψ instead of the velocity potential Φ. Knowing that the two quantities are related by:

$$\frac{\partial\Phi}{\partial x} = \frac{\partial\Psi}{\partial z} \quad , \quad \frac{\partial\Phi}{\partial z} = -\frac{\partial\Psi}{\partial x} \qquad (21)$$

all the physical quantities of interest such as the wave elevation, pressure can be easily obtained once the stream function is known.

The input data for evaluation of the stream function are the water depth h the wave height H and the wave length λ, and the problem is formulated in the coordinate system attached to the wave crest where the flow is steady and the free surface is a streamline. The solution for the stream function $\Psi(x,z)$ is usually presented in the form of the Fourier series:

$$\frac{k_0\Psi(x,z)}{V_P} = -k_0(z+h) + \sum_{j=1}^{N}a_j\frac{\sinh jk_0(z+h)}{\cosh jk_0h}\cos jk_0x \qquad (22)$$

where $k_0 = 2\pi/\lambda$ and the unknown coefficients a_j are found numerically, after satisfying the kinematic and the dynamic free surface condition at a certain number of points in the interval $[0-\lambda/2]$.

It is important to note that the phase velocity V_P (and consequently the wave period) is also unknown and should be determined together with the coefficients a_j. The truncation order N in the Fourier series (22) must be chosen according to the steepness: the steeper is the wave, the higher is the truncation order. Figure 11 shows normalized wave profiles computed with the stream function model, in deep water, at wave steepnesses H/λ from 0.01 up to 0.14, the last value being very close to the limiting steepness 0.1412 where the crest becomes angular.

The advantage of the stream function model is that it applies to shallow as well as deep water, whatever the value of the Ursell number. It bridges the gap between the Stokes model and shallow water wave theories such as cnoidal waves.

Figure 11: Normalized free surface profiles, in infinite depth, for H/λ = 0.01, 0.05, 0.10, 0.12, 0.13, 0.14 (from Molin (2022))

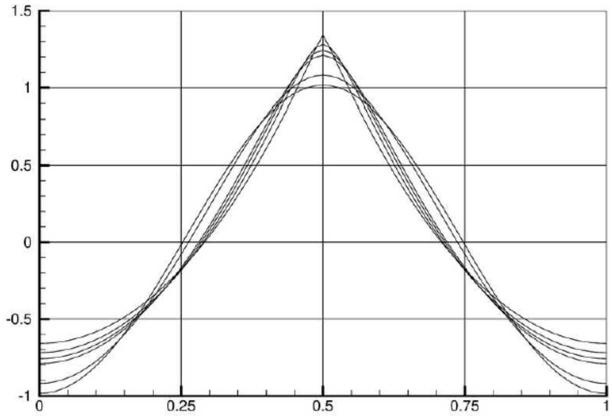

2.4.5 Cnoidal waves

From a mathematical point of view cnoidal wave is the exact nonlinear periodic solution of the Korteweg-de Vries wave equation (Korteweg & De Vries (1895)). It is suitable to describe the surface gravity waves in shallow water and it is characterized by sharp crests and wide troughs as shown in Figure 12. The cnoidal wave theory is suited when Ursell number is above 30 and for $h/\lambda < 0.125$.

Figure 12: Cnoidal wave

2.5. Wave kinematics

2.5.1 Introduction

Knowledge of the wave kinematics under the wave crest of an irregular sea is necessary for the evaluation of the loading on the elements above the mean free surface $z = 0$. The intuitive solution which would consist in applying the same formula from Table 1 for $z > 0$ leads to unrealistically high horizontal velocities and the resulting kinematics are highly exaggerated. As a result, the drag loads on structures such as jackets or compliant towers can be significantly overestimated. Empirical methods have been proposed to correct the wave kinematics and the most common models are presented in Figure 13.

Figure 13: Comparison of extrapolation models. Horizontal velocity profile below a wave crest

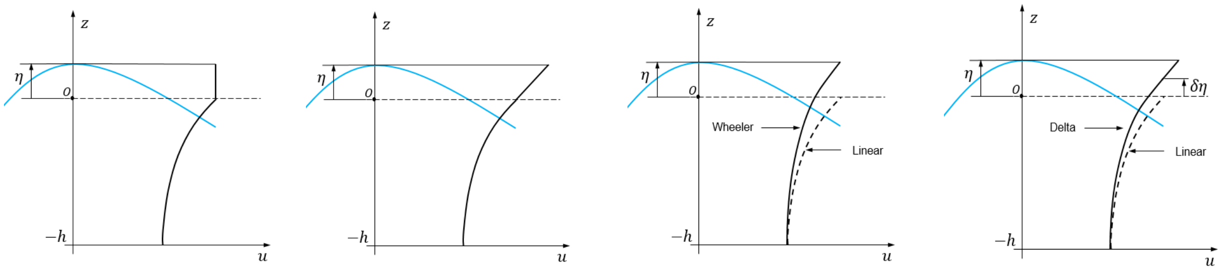

(a) Constant (b) Linear (c) Wheeler (d) Delta

2.5.2 Constant extrapolation

Within the purely linear model, the horizontal velocity is defined below $z = 0$ and is given by:

$$u(x,z,t) = -\sum_i A_i \omega_i \frac{\cosh k_{0i}(z+h)}{\sinh k_{0i} h} \cos(k_{0i}x + \omega_i t + \theta_i) \tag{23}$$

The constant interpolation model consists in assuming the velocity between $z = 0$ and $z = \eta$ to be constant and equal to $u(x, 0, t)$. This model is shown in Figure 13(a).

2.5.3 Linear extrapolation

Within this model the horizontal velocity under the crest is linearly extrapolated from $z = 0$ to $= \eta$:

$$u(x,z,t) \simeq u(x,0,t) + z\frac{\partial u}{\partial z}(x,0,t) \tag{24}$$

The model is shown in Figure 13(b).

2.5.4 Wheeler stretching

The Wheeler model (Wheeler (1970)) stretches the vertical coordinate in such a way that, at $z = \eta$, the same kinematics as given by the direct summation in $z = 0$ be retrieved. To the true vertical coordinate z is associated a fictitious one z_S given by:

$$z_S = h\frac{z-\eta}{h+\eta} \quad , \quad \eta = \sum_i A_i \cos(k_{0i}x + \omega_i t) \tag{25}$$

As a result, the horizontal velocity profile becomes:

$$u(x,z,t) = -\sum_i A_i\omega_i \frac{\cosh[k_{0i}h(z+h)/(h+\eta)]}{\sinh k_{0i}h}\cos(k_{0i}x+\omega_i t+\theta_i) \tag{26}$$

for $-h \le z \le \eta$.

The Wheeler stretching model is shown in Figure 13(c).

2.5.5 Delta stretching

There have been numerous experimental campaigns performed to check the adequacy of the different models usually concluding that the crest velocities are underestimated by the Wheeler stretching model and overestimated by the linear extrapolation model. The Delta-stretching, proposed by Rodenbusch et Forristall (1986), allows the achievement of velocity profiles intermediate between the Wheeler profile and linear extrapolation. The principle is the same as in the Wheeler model, i.e. to the true coordinate z one associates a fictitious coordinate z_S from which the kinematics are derived:

$$z_S = (z+h)\frac{h+\delta\eta}{h+\eta} - h \tag{27}$$

where z_S varies from $-h$ up to $\delta\eta$ when z goes from $-h$ to η.

When z_S is larger than zero, the kinematics is obtained through linear extrapolation; when $\delta = 0$ the Wheeler stretching model is recovered; when $\delta = 1$ the linear extrapolation is obtained. Rodenbusch and Forristall (1986) suggest a δ value of 0.3.

2.5.6 Second order model of wave kinematics

Wave kinematics under the wave crest can also be modelled by direct application of the second order theory. This leads to the following formal expressions (Stansberg (2008)):

$$u(x,z,t) \simeq \begin{cases} u^{(1)}(x,z,t) + u_+^{(2)}(x,z,t) + u_-^{(2)}(x,z,t) & ; \quad z \le 0 \\ u^{(1)}(x,0,t) + z\dfrac{\partial u^{(1)}}{\partial z}(x,0,t) + u_+^{(2)}(x,0,t) + u_-^{(2)}(x,0,t) & ; \quad z > 0 \end{cases} \tag{28}$$

where $u_+^{(2)}$ and $u_-^{(2)}$ are the sum and difference frequency second order components respectively.

Good comparisons of the above expressions with the experiments are reported by Stansberg et al. (2008).

2.6. Stochastic description of water waves

2.6.1 Introduction

By taking a simple look at the real wave surface (e.g. Figure 14), the complexity of the mathematical description of the waves becomes obvious. In reality waves are irregular in shape, vary in height, length, speed, and direction of propagation. Those features are most realistically described as a random process in which the sea is represented as a superposition of many individual regular wave components each of which is represented by its amplitude, frequency, phase and direction of propagation.

Figure 14: Water waves

2.6.2 Concept of wave spectrum

When the sea conditions are stationary over a certain period, the sea state can be accurately described by a wave spectrum i.e. power spectral density of the free surface elevation. Wave spectrum is defined with the help of the autocorrelation function $R(\tau)$ which is assigned to the random process $\eta(t)$:

$$R(\tau) = E[\eta(t)\eta(t+\tau)] \tag{29}$$

Strictly speaking, the E means the ensemble averaging, however because of the assumption of ergodicity (temporal statistics equal to ensemble statistics) the autocorrelation function $R(\tau)$ can be estimated by calculating the time averaged value of $\eta(t)\eta(t+\tau)$, and that is what is usually done in practice.

Once the autocorrelation function $R(\tau)$ is known the spectral density function is given by:

$$S(\omega) = \frac{2}{\pi}\int_0^\infty R(\tau)\cos\omega\tau\, d\tau \tag{30}$$

In practice it is useful to define the different spectral moments as:

$$m_n = \int_0^\infty \omega^n S(\omega) d\omega \tag{31}$$

Several characteristic periods associated with the wave spectrum are usually identified. Among them the mean period T_M, the zero up-crossing period T_Z and the peak period T_P are used most often:

$$T_M = 2\pi\frac{m_0}{m_1} \quad , \quad T_Z = 2\pi\sqrt{\frac{m_0}{m_2}} \quad , \quad T_P = \frac{2\pi}{\omega_P} \tag{32}$$

where ω_P is the frequency of the peak of the spectral density function $S(\omega)$.

The mean period T_M is sometimes denoted as T_1 and the zero up crossing period T_Z as T_2. Other characteristic periods can also be defined based on other spectral moments and the period T_{0m1} is sometimes used (Tolman (2014)):

$$T_{0m1} = 2\pi\frac{m_{-1}}{m_0} \tag{33}$$

Under the form $S(\omega)$ wave spectrum gives information on the free surface elevation at one point. To reconstruct the free surface elevation in time and space, additional information must be given on the angular distribution. Directional spectra are usually denoted as $S(\omega,\beta)$ and written in the following form:

$$S(\omega,\beta) = S(\omega)G(\omega,\beta) \tag{34}$$

where the function $G(\omega,\beta)$ must verify:

$$\int_0^{2\pi} G(\omega,\beta)d\beta = 1 \tag{35}$$

One typical wave spectrum is shown in Figure 15.

Figure 15: Typical wave spectra.
Left – energy distribution, right – directional spreading

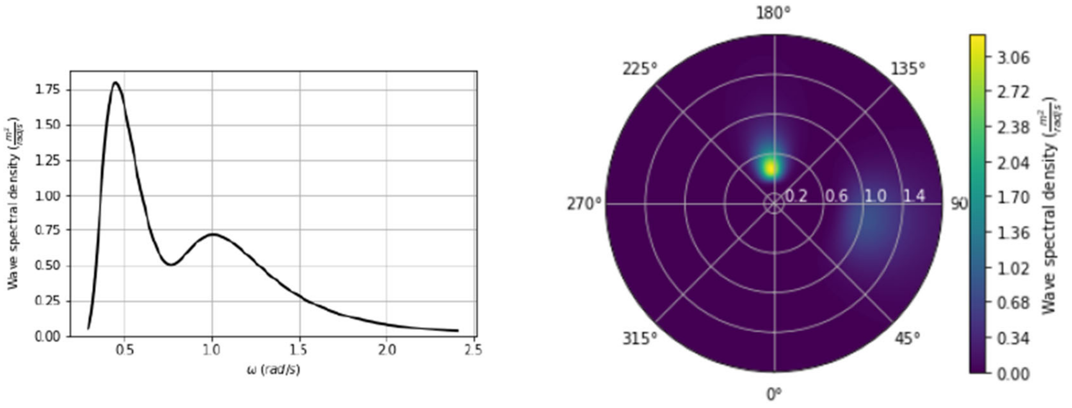

2.6.3 Short term statistics

The notion short term is used to describe the period during which the sea state is stationary, usually 3 hours. The practical question which needs to be answered is: What are the maximum waves which occur during that period of time? This can be evaluated by assuming the wave elevation to be Gaussian process, which appears to be a reasonable assumption in practice. For a Gaussian random variable X the probability density function (pdf) is given by:

$$p(x) = \frac{1}{\sigma\sqrt{2\pi}}e^{-x^2/2\sigma^2} \tag{36}$$

where σ is the standard deviation $\sigma^2 = E(X^2) = m_0$ and it was assumed that the mean value is zero.

With this assumption the following expression for the probability density function of the normalized maxima $y = \eta_{max}/\sqrt{m_0}$ can be written (e.g. Molin (2022):

$$p(y) = \frac{1}{\sqrt{2\pi}}\left[\epsilon e^{-y^2/2\epsilon^2} + \sqrt{1-\epsilon^2}\, y e^{-y^2/2}\int_{-\infty}^{y\sqrt{1-\epsilon^2}/\epsilon} e^{-u^2} du\right] \quad , \quad \epsilon = \sqrt{1 - \frac{m_2^2}{m_0 m_4}} \qquad (37)$$

where ϵ is called the narrowness parameter.

For $\epsilon = 1$ the pdf follows the same Gaussian law as the process η itself, while for $\epsilon = 0$ the pdf becomes the Rayleigh law. In Figure 16 the probability density function given by (37) for different values of the narrowness parameter ϵ is presented. The typical signals of the wave elevation for two particular values of ϵ are shown in Figure 17. It can be seen that, for low values of ϵ there exist almost no local maxima between the two zero up-crossings while for larger ϵ many local maxima occur. From Figure 16 it can also be observed that the pdfs obtained for ϵ less than 0.4 are very close to the Rayleigh law.

Figure 16: Probability density function of the maxima $\eta_{max}/\sqrt{m_0}$ for ϵ from 0 to 1 with steps equal to 0.2

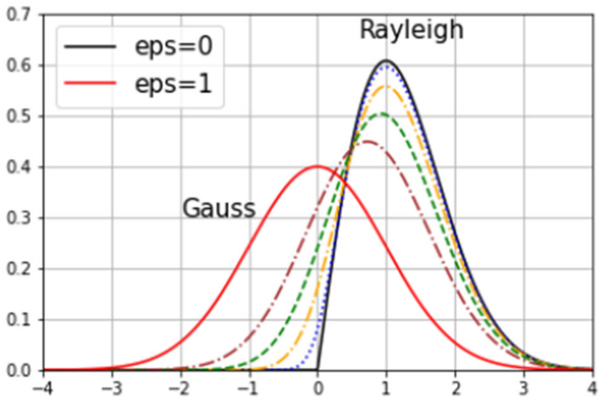

Figure 17: Wave elevation for different narrowness parameter

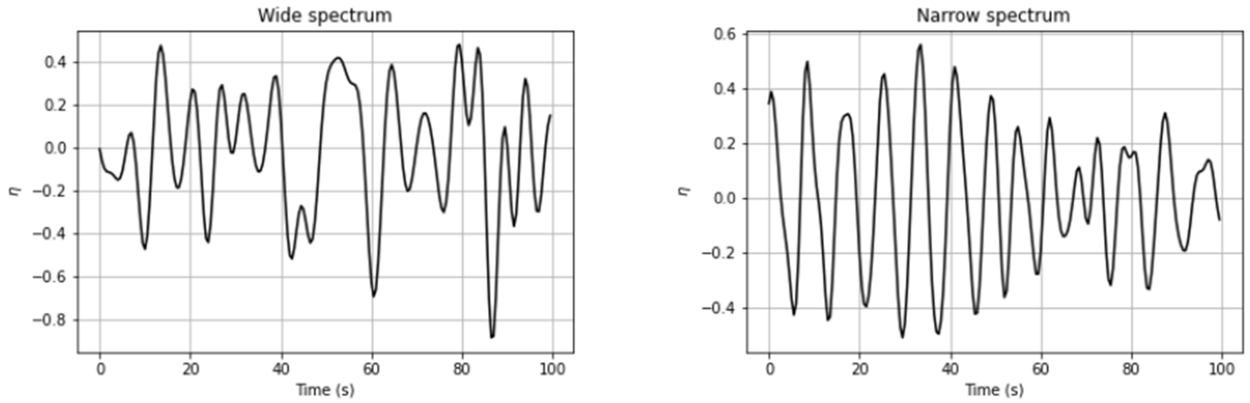

Many seastates in practice are consistent with this narrowness criterion so that the Rayleigh law can be assumed which leads to the following pdf for maximum wave elevation A (crest or trough):

$$p(A) = \frac{A}{2m_0} e^{-A^2/2m_0} \qquad (38)$$

From this pdf, the mean value of the maximum wave elevation A greater than a certain value can be deduced. In practice, it is common to introduce the quantity $A_{1/N}$ which describes the mean of the $1/N$ greatest waves. The value $A_{1/3}$ is particularly interesting because this value appears to be in the best agreement with the visual estimates. This value is usually given in terms of the wave height:

$$A_{1/3} = 2.002\sqrt{m_0} = 0.5005\, H_S \approx H_S/2 \qquad (39)$$

This expression is valid under the assumption of a narrow-banded Gaussian process. To make clear this restriction, the significant wave height H_S is defined as $4\sqrt{m_0}$. It is common in practice, to parametrize the seastates with the significant wave height H_S and the mean up-crossing period T_Z.

2.6.4 Maximum wave height

For a stationary sea state with a large number N of the independent local maxima, the expected value of the highest wave is given by:

$$E(H_N) = 2\left[\sqrt{2\ln N} + \frac{\gamma}{\sqrt{2\ln N}}\right]\sqrt{m_0} \qquad (40)$$

where γ is Euler constant $\gamma = 0.5772$.

For narrow banded sea spectra, the number of the local maxima can be obtained by dividing the duration of the sea state by the zero up crossing period. In the typical case of 3 hours duration and for the zero up crossing period of 10 seconds this gives $N = 1080$ and the

$$H_{max} = E(1080) = 7.78\sqrt{m_0} = 1.94H_{1/3} \qquad (41)$$

The value of H_{max} does not increase much when the duration of the sea state is increased and, for example when the duration is increased to 6 hours the H_{max} becomes $2.04H_{1/3}$.

2.6.5 Short term statistics for wave crests

In practice, the nonlinear nature of the wave propagation makes the wave crests higher than the wave troughs so that the extreme values of the wave crests cannot be taken as the half of the extreme wave height. Based on the second order wave theory (Forristal 2000) the cumulative probability distribution of the wave crests $P(\eta)$, was proposed in the Weibull form:

$$P(\eta) = 1 - e^{-\left(\frac{\eta}{\alpha H_S}\right)^{\beta}} \qquad (42)$$

where the parameters α and β were obtained by fitting the second order results.

The following expressions were proposed for the long crested (α_2, β_2) and the short crested (α_3, β_3) conditions:

$$\alpha_2 = 0.3536 + 0.2892S_1 + 0.1060\mathrm{Ur} \qquad (43)$$

$$\beta_2 = 2 - 2.1597S_1 + 0.0968\mathrm{Ur}^2 \qquad (44)$$

$$\alpha_3 = 0.3536 + 0.2568S_1 + 0.0800\mathrm{Ur} \qquad (45)$$

$$\beta_3 = 2 - 1.7912S_1 - 0.5302\mathrm{Ur} + 0.284\mathrm{Ur}^2 \qquad (46)$$

where S_1 and Ur are the steepness parameters and Ursell number respectively (see also [2.1.3]) which are redefined here as follows:

$$S_1 = \frac{2\pi}{g}\frac{H_S}{T_M^2} \quad , \quad \mathrm{Ur} = \frac{H_S}{k_M^2 h^3} \qquad (47)$$

with T_M being the mean period (32) and k_M being the associated first order wave number.

2.6.6 Long term statistics

From wave measurements over a long period, it is common to derive the so-called scatter diagram valid for a given geographical position. A wave scatter diagram is a description of the joint probabilities of the significant wave heights and wave periods (T_Z or T_P). A typical example is shown in Table 2 for the North Atlantic region. In each cell of the table, the number of occurrences of a particular pair (H_S, T_Z) is given. The scatter diagrams are derived based on visual observations and hindcast data, which are merged and extrapolated, using some analytical functions.

One of the practical problems which need to be solved is the determination of the significant wave height which has a certain probability to be exceeded within the certain period. This is usually done by building, based on the scatter diagram, an empirical cumulative distribution $P(H_S)$ and fit that distribution with a given asymptotic law. Among the different statistical laws representative of the tails of cumulative distributions, the most commonly used in offshore engineering is the Weibull law, expressed by:

$$P(H_S) = 1 - e^{-\left(\frac{H_S}{K}\right)^{\beta}} \qquad (48)$$

where β and K are the Weibull parameters.

Once the Weibull parameters are determined, the maximum significant wave height for any given return period can be easily determined.

The direction of wave propagation has also the associated probability of occurrence which needs to be taken into account in the analyses. In practice, most often, the scatter diagram is given for each direction separately, with the associated probability of occurrence. Those data need to be combined within the design process when evaluating the extreme responses and the fatigue life.

Table 2 : Probability of sea-states in the North Atlantic described as occurrence per 100000 observations

Hs/Tz	1,5	2,5	3,5	4,5	5,5	6,5	7,5	8,5	9,5	10,5	11,5	12,5	13,5	14,5	15,5	16,5	17,5	18,5	SUM:
0,5	0,0	0,0	1,3	133,7	865,6	1186,0	634,2	186,3	36,9	5,6	0,7	0,1	0,0	0,0	0,0	0,0	0,0	0,0	3050
1,5	0,0	0,0	0,0	29,3	986,0	4976,0	7738,0	5569,7	2375,7	703,5	160,7	30,5	5,1	0,8	0,1	0,0	0,0	0,0	22575
2,5	0,0	0,0	0,0	2,2	197,5	2158,8	6230,0	7449,5	4860,4	2066,0	644,5	160,2	33,7	6,3	1,1	0,2	0,0	0,0	23810
3,5	0,0	0,0	0,0	0,2	34,9	695,5	3226,5	5675,0	5099,1	2838,0	1114,1	337,7	84,3	18,2	3,5	0,6	0,1	0,0	19128
4,5	0,0	0,0	0,0	0,0	6,0	196,1	1354,3	3288,5	3857,5	2685,5	1275,2	455,1	130,9	31,9	6,9	1,3	0,2	0,0	13289
5,5	0,0	0,0	0,0	0,0	1,0	51,0	498,4	1602,9	2372,7	2008,3	1126,0	463,6	150,9	41,0	9,7	2,1	0,4	0,1	8328
6,5	0,0	0,0	0,0	0,0	0,2	12,6	167,0	690,3	1257,9	1268,6	825,9	386,8	140,8	42,2	10,9	2,5	0,5	0,1	4806
7,5	0,0	0,0	0,0	0,0	0,0	3,0	52,1	270,1	594,4	703,2	524,9	276,7	111,7	36,7	10,2	2,5	0,6	0,1	2586
8,5	0,0	0,0	0,0	0,0	0,0	0,7	15,4	97,9	255,9	350,6	296,9	174,6	77,6	27,7	8,4	2,2	0,5	0,1	1309
9,5	0,0	0,0	0,0	0,0	0,0	0,2	4,3	33,2	101,9	159,9	152,2	99,2	48,3	18,7	6,1	1,7	0,4	0,1	626
10,5	0,0	0,0	0,0	0,0	0,0	0,0	1,2	10,7	37,9	67,5	71,7	51,5	27,3	11,4	4,0	1,2	0,3	0,1	285
11,5	0,0	0,0	0,0	0,0	0,0	0,0	0,3	3,3	13,3	26,6	31,4	24,7	14,2	6,4	2,4	0,7	0,2	0,1	124
12,5	0,0	0,0	0,0	0,0	0,0	0,0	0,1	1,0	4,4	9,9	12,8	11,0	6,8	3,3	1,3	0,4	0,1	0,0	51
13,5	0,0	0,0	0,0	0,0	0,0	0,0	0,0	0,3	1,4	3,5	5,0	4,6	3,1	1,6	0,7	0,2	0,1	0,0	21
14,5	0,0	0,0	0,0	0,0	0,0	0,0	0,0	0,1	0,4	1,2	1,8	1,8	1,3	0,7	0,3	0,1	0,0	0,0	8
15,5	0,0	0,0	0,0	0,0	0,0	0,0	0,0	0,0	0,1	0,4	0,6	0,7	0,5	0,3	0,1	0,1	0,0	0,0	3
16,5	0,0	0,0	0,0	0,0	0,0	0,0	0,0	0,0	0,0	0,1	0,2	0,2	0,2	0,1	0,1	0,0	0,0	0,0	1
SUM:	0	0	1	165	2091	9280	19922	24879	20870	12898	6245	2479	837	247	66	16	3	1	100000

2.7. Commonly used wave spectra

Theoretical considerations and empirical adjustments have led to analytical expressions of wave spectra. Many different spectrum formulations were proposed in the literature and the most common ones are discussed below.

2.7.1 Pierson Moskowitz spectrum

This spectral shape results from observations in the North Atlantic Ocean. A fully developed seastate is assumed meaning that the fetch is infinite and the wind has been blowing long enough for a stationary seastate to have been established. When parametrized with H_S and ω_P the Pierson Moskowitz spectrum takes the following form:

$$S_{PM}(\omega) = \frac{5}{16} H_S^2 \omega_P^4 \omega^{-5} e^{-\frac{5}{4}\left(\frac{\omega}{\omega_P}\right)^{-4}} \tag{49}$$

Different characteristic periods of the Pierson Moskowitz spectrum are related to each other by

$$T_P = \left(\frac{5\pi}{4}\right)^{1/4} T_Z \approx 1.408\, T_Z \quad , \quad T_M \approx 1.086\, T_Z \tag{50}$$

The Pierson-Moskowitz spectrum is also known as ITTC or ISSC or Bretschneider spectrum.

2.7.2 JONSWAP spectrum

JONSWAP is an acronym for JOint North Sea WAve Project, a measurement campaign carried out in the early 1970's that resulted in a form more general than the Pierson-Moskowitz spectrum (see Hasselmann et al., 1973). The JONSWAP spectrum has the form:

$$S_J(\omega) = \alpha S_{PM}(\omega) \gamma^r \tag{51}$$

where γ is the peak enhancement factor taken in practice between 1 and 10, and r is given by:

$$r = e^{-\frac{(\omega-\omega_P)^2}{2\sigma^2\omega_P^2}} \tag{52}$$

with $\sigma = 0.07$ for $\omega < \omega_P$ and $\sigma = 0.09$ for $\omega > \omega_P$ and the coefficient α adjusted to have $H_S = 4\sqrt{m_0}$.

For $\gamma = 1$ the Pierson Moskowitz spectrum is recovered. For γ greater than one, the peak of the JONSWAP spectrum becomes narrower and higher as shown in Figure 18.

The measurement campaign in the North Sea resulted in an average value of γ equal to 3.3. For the values of γ being between 1 and 10, the following regression formula can be used:

$$
\begin{aligned}
\alpha &= \frac{487.045}{0.325\gamma^{0.803} + 0.675} \\
\frac{T_Z}{T_P} &= 0.6063 + 0.1164\sqrt{\gamma} - 0.01224\gamma \\
\frac{T_{0m1}}{T_P} &= 0.849 + \frac{0.0099}{\gamma} + 0.0477\log\gamma - 0.0017\gamma \\
\frac{T_M}{T_P} &= 0.6687 + 0.1182\sqrt{\gamma} - 0.01489\gamma
\end{aligned}
\tag{53}
$$

Figure 18: JONSWAP spectrum for different values of γ and for the same peak period

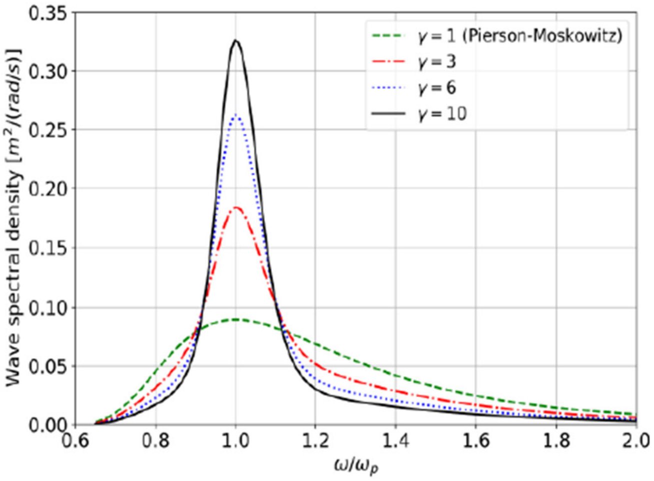

2.7.3 Ochi-Hubble spectrum

Ochi-Hubble spectrum allows describing seas that consist of a combination of two different wave systems. This is in particular useful for the geographical positions where the wind sea and swells coexist. Wind seas are generated by the local wind in the area, while swells have no relationship with the local wind and they consist of wind-driven waves that have travelled out of the area in which they were generated.

Ochi Hubble spectrum is defined as a sum of two wave spectra each of which is described by a generalization of the Pierson-Moskowitz spectrum including three instead of two parameters. Ochi-Hubble spectra thus have six parameters in total. The following expression is usually employed (ISO19901-1 (2005)):

$$
S_{OH}(\omega) = \sum_{j=1,2} \frac{H_{S,j}^4}{4\Gamma(\lambda_j)} \left(\frac{4\lambda_j + 1}{4} \omega_{P,j}^4 \right)^{\lambda_j} \frac{1}{\omega^{4\lambda_j+1}} e^{-\frac{4\lambda_j+1}{4}\left(\frac{\omega_{P,j}}{\omega}\right)^4}
\tag{54}
$$

where Γ denotes the Gamma function.

As it can be seen, in addition to the two classical spectral parameters H_S and ω_P , one additional parameter λ occurs for each spectrum. It is easily verified that for $\lambda_j = 1$, the *j*-th spectrum component reduces to the Pierson-Moskowitz spectrum. Typical shape of Ochi – Hubble spectrum is shown in Figure 19.

From (54) it follows that the spectral moments of the Ochi Hubble spectrum are the sum of the moment of each component, which means that the following relation can be used to define the total significant wave height:

$$
H_S^2 = H_{S,1}^2 + H_{S,2}^2
\tag{55}
$$

Ochi-Hubble spectrum has historically been used to describe multi-modal sea states in one direction. However, multi-modal sea-state can also be described by a simple superposition of several mono-modal spectra (JONSWAP, Pierson Moskowitz ...) which, at the same time, allows introducing the different directions for each of the spectra.

Figure 19: Ochi Hubble spectrum

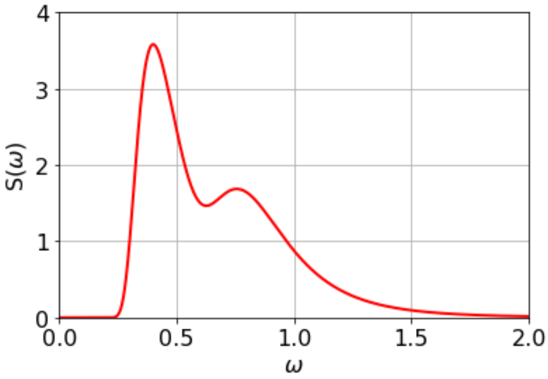

2.7.4 High frequency behavior of the spectra

At high frequency most of the spectra (including JONSWAP) behave asymptotically as ω^{-5} which means that the fourth spectral moment m_4 becomes infinite. This implies that the narrowness parameter ϵ is equal to 1 which is apparently contradicting the idea that the wave heights follow Rayleigh distribution. In practice, the wave spectra are always truncated at some upper limit so that the spectral moment m_4 will always have finite value and the narrowness parameter will be much lower than one. It should also be noted that in practice, even if the spectrum becomes wide banded (large ϵ) and the local maxima do not follow the Rayleigh law, the distribution of the zero up-crossing maxima can always be accurately represented by Rayleigh law.

2.7.5 Directional spreading functions

In practice, in the absence of further information, one usually assumes that the spreading function $G(\omega,\beta)$ depends only on β. By denoting β_0 as a main wave direction, the following three spreading functions are used most often:

$$G_1(\beta) = \begin{cases} C_1(n)\cos^n(\beta-\beta_0) & , \quad |\beta-\beta_0| \le \pi/2 \\ 0 & , \quad |\beta-\beta_0| \ge \pi/2 \end{cases} \quad ; \quad C_1(n) = \frac{\Gamma(n/2+1)}{\sqrt{\pi}\Gamma(n/2+1/2)} \tag{56}$$

$$G_2(\beta) = C_2(s)\cos^{2s}(\beta-\beta_0)/2 \quad , \quad -\pi \le \beta-\beta_0 \le \pi \quad ; \quad C_2(s) = \frac{\Gamma(s+1)}{2\sqrt{\pi}\Gamma(s+1/2)} \tag{57}$$

$$G_3(\beta) = \frac{1}{\sigma\sqrt{2\pi}} \sum_{k=-\infty}^{k=\infty} e^{-\frac{(\beta-\beta_0-2k\pi)^2}{2\sigma^2}} \tag{58}$$

The formulations are usually named *cosn*, *cos2n* and *wrapped normal* respectively, and their shapes are very similar for the following relationship between the different coefficients (σ in radians):

$$\sigma^2 \simeq \frac{1}{n+1} \simeq \frac{4}{2s+1} \tag{59}$$

2.8. Time domain representation of the sea state

2.8.1 Linear decomposition

Wave spectrum describes the distribution of wave energy among the different frequencies. Many wave realizations lead to the same energy content and the phasing between the different wave components becomes of no importance. Consequently the phases of the different wave components can be chosen randomly and the only condition for the wave description is that the energy of each wave component is consistent with the energy distribution defined by the wave spectrum. In practice the wave spectrum is subdivided into a certain number of wave components, with random phases associated with each of them (see Figure 20).

The wave amplitudes A_i follow by equating the individual wave energy (5) with the energy contained in the considered frequency interval $\Delta\omega_i$ of the spectrum. This leads to:

$$\frac{1}{2}A_i^2 = S(\omega_i)\Delta\omega_i \tag{60}$$

The resulting time signal of the wave elevation becomes:

$$\eta(x,t) = \sum_{i=1}^{N_w} A_i \cos(k_{0i}x + \omega_i t + \theta_i) \tag{61}$$

The number of wave components N_w is usually of the order of hundreds. To avoid the repeatability of the time signal after some time, several techniques can be used. Most often, the constant frequency interval $\Delta\omega$ is chosen and the wave frequency associated to each interval is chosen randomly. Another technique consists in putting the randomness on the interval $\Delta\omega$ and choosing the frequency at the half of the interval. Directional spreading can also be introduced in the definition of the time domain signal, which might lead to significant increase of the computational time.

Another method to define the time domain signal of the wave elevation is known under the name of random amplitude method. Within this method the wave elevation is written in the form:

$$\eta(x,t) = \sum_{i=1}^{N_w} [A_i \sigma_i \cos(k_{0i}x + \omega_i t + \theta_i) - B_i \sigma_i \sin(k_{0i}x + \omega_i t + \theta_i)] \tag{62}$$

where $\sigma_i^2 = S(\omega_i)\Delta\omega_i$ and A_i and B_i are the uncorrelated random variables following a standard normal distribution. The random amplitude method is used often to derive irregular design waves (see NI638)

Figure 20: Wave record analysis and regeneration. (from Journée (2001))

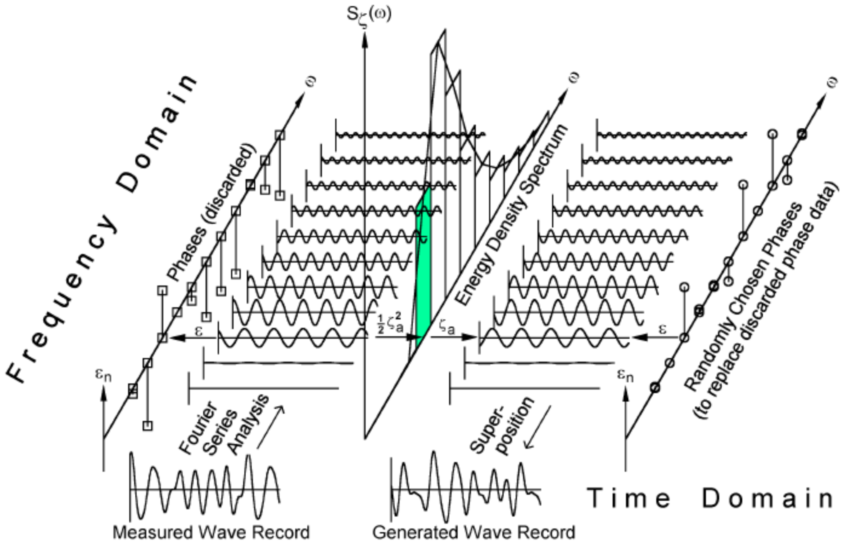

2.8.2 Representation up to second order

The time history of the second order wave elevation can be obtained following the general principles of the second order theory from Section 4, [5.2.2] and the expressions for the bichromatic waves from [2.3.4]

2.8.3 Higher Order Spectral method

The evolution in time of the nonlinear waves can be efficiently modelled using the Higher Order Spectral methods (HOS). These methods were first introduced by West et al (1987) and Dommermuth & Yue (1987) and it was popularized by ECN (Ducrozet et al. (2007, 2012, 2016)) Within this approach the fully nonlinear solution is first expanded into a series with respect to the steepness parameter:

$$\phi(x,y,z,t) = \sum_{m=1}^{M} \phi^{(m)}(x,y,z,t) \tag{63}$$

where M is the order of nonlinearity and $\phi^{(m)}$ of order $O(\varepsilon^m)$.

The nonlinear free surface condition is then developed up to order M using the Taylor series expansion which allows formulating the BVP for $\phi^{(m)}$ in a fixed domain. The BVP's at each order are successively solved using a spectral method using the spectral basis functions. In principle the method can be solved at an arbitrary order M and highly nonlinear waves can be simulated. One example of simulation is shown in Figure 21. However, once the wave breaks the original method fails and the artificial dissipation need to be added to the model (Seiffert et al (2017)).

Both the open sea and wave tank formulations of the HOS method exist (Ducrozet (2012, 2016)) and are used more and more in practice either for simulating the extreme events in open sea or to prepare the experimental campaigns in highly nonlinear waves.

Figure 21: Highly nonlinear wave propagation leading to freak wave
The directional JONSWAP spectrum is used for wave focusing (Ducrozet (2007))

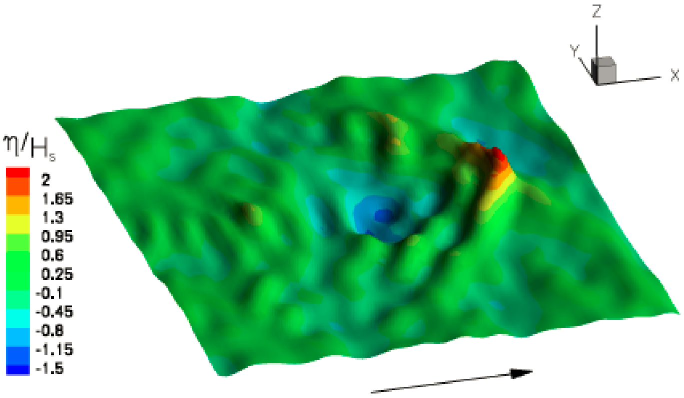

3. Wind

3.1. Introduction

3.1.1 General

Offshore floating systems usually have large superstructures directly exposed to the wind so that very large wind loads can be induced. These loads should be included in the global performance analysis of the system and in particular when analyzing the adequacy of the mooring system design. In the particular case of offshore wind turbines the wind loads play a special role in producing the energy. In that case the wind loads should be controlled in such a way that the extraction of the energy is maximized and that, at the same time, the supporting structure is not damaged by the wind-induced loads.

3.1.2 Wind flow features

The physical features of the wind flow vary significantly in time and space. Most often, they are considered stationary over approximately 10 minutes duration and the flow variations within this period are denoted as a turbulence. In space, the wind flow features over the sea surface are comparable to the turbulent flow over the rough flat plate, with the wave surface playing the role of the roughness. The physical scale being large, the thickness of the boundary layer becomes several tens (or hundreds) of meters. In the situations where the mean wind speed at a given height is approximately constant and unidirectional for a given period, the wind conditions are denoted as the sustained or stationary wind conditions. On the contrary, when the wind speed may change rapidly in time and in space the conditions are denoted as the transient wind conditions.

3.2. Sustained wind conditions

3.2.1 Introduction

The sustained wind conditions are those with the stationary character in terms of direction, intensity and duration.

3.2.2 Mean wind speed

The wind intensity is usually described by the different averaged (mean) velocities denoted by $U_{Wm}(z,T)$ with z denoting the height above the Mean Sea Level (MSL) and T denoting the duration over which the averaged value is derived. The wind direction is supposed to remain constant. The most common reference is $U_{Wm}(10,600)$ which means the wind velocity at $10m$ above the MSL and averaged over 600 seconds i.e. 10 minutes.

3.2.3 Mean wind vertical velocity profile

The wind speed profile is the variation of the mean wind speed with height above the MSL. The most commonly applied wind profile models are the logarithmic model (64) and the power law model (65). For the neutral atmospheric conditions it is commonly assumed that the mean wind profile follows the logarithmic law of turbulent boundary layers:

$$U_{Wm}(z) = U_{Wm}(H)\frac{\ln\frac{z}{z_0}}{\ln\frac{H}{z_0}} = U_{Wm}(H)\left(1 - \frac{\ln\frac{z}{H}}{\ln\frac{z_0}{H}}\right) \quad (64)$$

where the duration was fixed to 10 minutes, H is the reference height, and z_0 is the roughness height whose typical values varies over a very wide range, from less than a millimeter in the case of calm water conditions, to one centimeter in presence of waves.

An alternative to the logarithmic wind profile is the profile based on power law:

$$U_{Wm}(z) = U_{Wm}(H)\left(\frac{z}{H}\right)^{\alpha} \quad (65)$$

where the exponent coefficient α depends on the surface roughness and for the open sea varies from 0.08 to 0.13, depending on the free surface roughness. Note that the logarithmic model and the power law model gives very similar results provided that α is taken as:

$$\alpha = \frac{\ln\left(\frac{\ln\frac{H'}{z_0}}{\ln\frac{H}{z_0}}\right)}{\ln\left(\frac{H'}{H}\right)} \quad (66)$$

where H and H' are two heights where the two models give the same wind speed (for instance $H = 10m$ and $H' = 50m$). Typical value of roughness parameter and the power law exponent for few different surfaces are given in Table 3.

Table 3 : Typical roughness parameters and power law exponent

	Roughness parameter z_0 (m)	Power law exponent α
Plane ice	0.00001 – 0.0001	0.07 – 0.08
Open sea	0.0001 – 0.01	0.08 – 0.13
Ground	0.01 – 0.3	0.13 – 0.23

For offshore locations, the roughness parameter z_0 depends on the sea surface, which is itself highly influenced by the wind speed: the higher the wind speed, the higher the roughness parameter. Knowing the wind speed at height H, the roughness parameter may be solved implicitly from the following equation proposed in Foristal (1988):

$$z_0 = 0.0144\frac{1}{g}\left(\frac{K\,U_{Wm}(H)}{\ln\frac{H}{z_0}}\right)^2 \quad (67)$$

where K is the von Karman constant ($K \simeq 0.4$).

Another relationship is proposed in API 2INT-MET (2007), where the vertical velocity profile $U_{Wm}(z,T)$ is expressed as a function of the mean reference speed $U_{Wm}(10,T_0)$:

$$U_{Wm}(z,T) = U_{Wm}(10,T_0)\left[1 + C\ln\left(\frac{z}{10}\right)\right]\left[1 - 0.41I_v(z)\ln\frac{T}{T_0}\right] \quad (68)$$

where T_0 is 1 hour, $T \leq T_0$, and the constant C and the turbulence intensity I_v are given by:

$$C = 0.0573\sqrt{1 + 0.15U_{Wm}(10,T_0)} \quad , \quad I_v = 0.06[1 + 0.043U_{Wm}(10,T_0)]\left(\frac{z}{10}\right)^{-0.22} \quad (69)$$

This corresponds to a logarithmic profile, where the roughness parameter is taken as:

$$z_0 = 10\exp\left(-\frac{1}{0.0573\sqrt{1 + 0.15U_{10}}}\right) \quad (70)$$

Two typical examples of the logarithmic and power-based velocity profiles are shown in Figure 22.

Figure 22: Comparison for $U_{Wm}(10, 3600) = 10\ m/s$ and $40\ m/s$ of the logarithmic profile with the roughness parameter from (67) or (70) and the power law with α computed from (66)

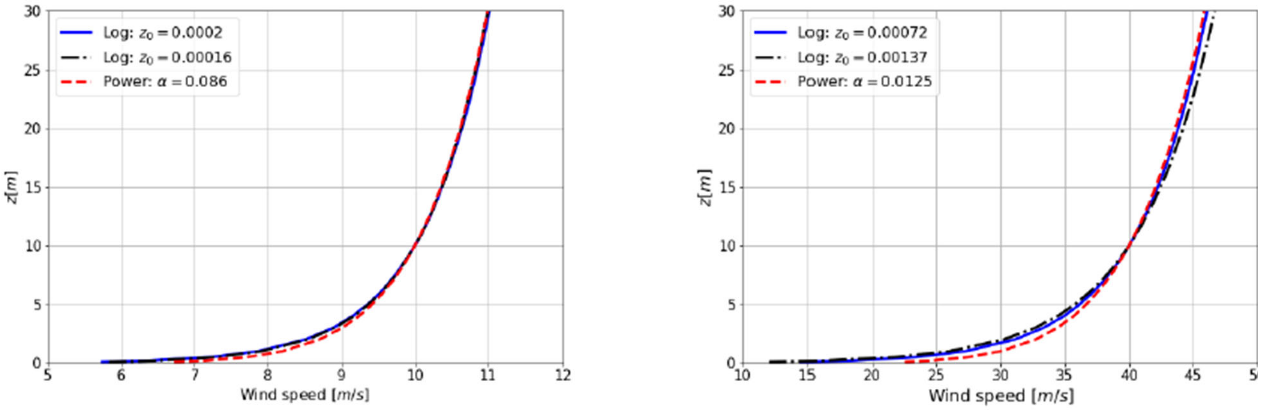

3.2.4 Turbulence

The instantaneous wind induced velocity at a given point in space is composed of its 10 minutes mean component and the time varying fluctuations also called turbulence:

$$U_W(z,t) = U_{Wm}(z,600) + U'_W(z,t) \tag{71}$$

The turbulent wind is characterized by its standard deviation σ. The ratio between the standard deviation of the turbulence and the 10 minutes wind speed is called the Turbulence Intensity I_v:

$$I_v = \frac{\sigma}{U_{Wm}(z,600)} \tag{72}$$

For a given value of $U_{Wm}(z,600)$ the I_v is itself a random variable, meaning that in different 10 minutes periods, the value of I_v can be different. The variability of I_v can usually be described by a lognormal distribution which parameters depend on $U_{Wm}(z,600)$. Other probability distribution functions such as Weibull distribution or Frechet distribution may also be used. The parameters of these distributions shall be fitted for each mean wind speed (and each wind direction) from site measurement of the turbulent intensity.

3.2.5 Wind spectra

Similar to the water wave elevation, the short term stationary wind conditions can be described by the wind spectra which can be deduced from the measured data. There exists a large number of different wind spectra formulations which were proposed in the literature (ISO, API, IEC …). Most of them can be written in the following generic form:

$$S(f) = \frac{\sigma^2}{f_P} \frac{a}{\left[1 + 1.5\left(\frac{f}{f_P}\right)^n\right]^{\frac{5}{3n}}} \tag{73}$$

σ is the standard deviation, the coefficient a is defined in such a way that $\int S(f)df = \sigma^2$ and the frequency f_P is the frequency for which the product of f and $S(f)$ reaches its maximum. In practice, the peak frequency f_P is related to the mean wind velocity and to the characteristic length L, which vary from one spectral formulation to the other. The coefficient a depends exclusively on the parameter n for which, three different values were usually proposed:

Table 4 : Parameters n and the associated coefficients a

n	0.468	1.0	2.0
a	4.19	1.0	0.582

The different parameters for the most common wind spectral formulations based on (73) are summarized in Table 5 where the notation U_{10} was used to denote the 10 minute mean wind speed at corresponding level.

The standard deviation σ characterize the severity of the particular wind condition and it is equivalent to the significant wave height H_S which is used for the description of the wave spectra (39). In principle its value should be deduced from the measurements at specific site, but some approximate expressions are also sometimes proposed (API 2INT-MET (2007), Orcina (2020), Bureau Veritas (2005))

Table 5 : Spectral parameters for most common wind spectra

	n	f_p	L
API	1	$\frac{U_{10}}{L}$	400
Kareem	1	$\frac{U_{10}}{L}\frac{ln\left(\frac{z}{z_0}\right)}{ln\left(\frac{10}{z_0}\right)}$	$47.3z$
Kaimal_IEC	1	$\frac{U_{10}}{L}$	$\begin{cases}22.7z & \text{for} \quad z < 60\,m \\ 1361 & \text{for} \quad z > 60\,m\end{cases}$
Harris	2	$\frac{U_{10}}{L}$	1237
Froya (NPD)	0.468	$\frac{U_{10}}{L}$	$723\left(\frac{U_{10}}{10}\right)^{0.25}\left(\frac{z}{10}\right)^{2/3}$

The exception to the formulation (73) is the Davenport spectrum which particularity is that it reaches the zero value for $f \to 0$. The Davenport spectrum is given by:

$$S_D(f) = \frac{2}{3}\frac{\sigma^2}{f_P}\frac{\left(\frac{f}{f_P}\right)}{\left[1+\left(\frac{f}{f_P}\right)^2\right]^{\frac{4}{3}}} \tag{74}$$

with $f_P = U_{10}/L$ and $L = 1200$.

The typical shape of the different wind spectra formulations is compared in Figure 23.

Figure 23: Spectral shape for different wind spectra

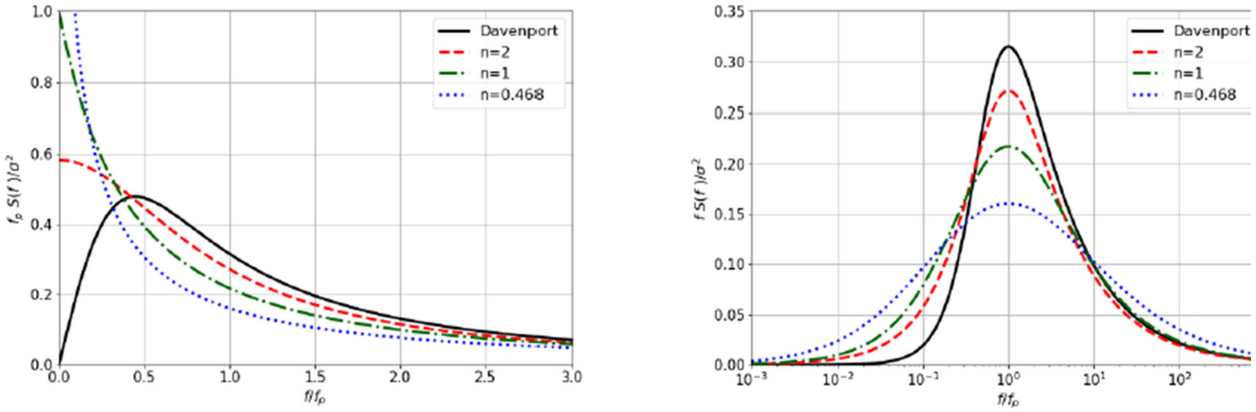

3.2.6 Spatial coherence of the wind velocity

For many practical applications the wind speed can be assumed constant over the part of the surface exposed to the wind, but for some applications a more detailed description of the wind speed spatial distribution might be needed. For that purpose the spatial coherence spectrum $Coh(r,f)$ is usually introduced. The coherence spectrum is the frequency-dependent measure of the correlation between the spectral densities at frequency f in two points separated by a distance r in space. Different coherence models are used in practice and, as an example, the IEC exponential coherence spectrum is recalled here in the form:

$$Coh(r,f) = e^{\left[-12\left(\frac{fr}{U_{Wm}}\right)^2+\left(0.12\frac{r}{L_c}\right)^2\right]} \tag{75}$$

where L_c is the coherence scale parameter which for the Kaimal wind spectrum model is given by:

$$L_c = 8.1\begin{cases}0.7z & \text{for} \quad z < 60\,m \\ 42 & \text{for} \quad z > 60\,m\end{cases} \tag{76}$$

3.2.7 Three dimensional wind spectra

The three dimensional wind turbulence modelling might also be needed for some applications and the typical example is the simulation of the wind turbine energy generation. In those cases a more complex description of the wind spectra and the associated spatial coherence is needed. One of the most widely used models is the Mann model which is also recommended by IEC. The detailed description of this model can be found in IEC 61400-1 (2019).

3.3. Transient wind conditions

3.3.1 Introduction

When the wind speed changes significantly, or the wind direction changes, transient wind conditions occur. Typical examples are the gust and squall phenomena.

3.3.2 Gusts

Gust is defined as a sudden and brief increase in wind speed. It is of shorter duration than a squall and is followed by a lull or slackening in the wind speed. Depending on the wind speed increase, different terms are usually employed. When the maximum wind speed exceeds the average speed by 10 to 15 knots, the term gusts is used while “strong gusts” is used for the exceedance of 15 to 25 knots, and violent gusts when it exceeds 25 knots. The duration of the gust is usually less than 20 seconds and the wind direction remains approximately constant. Gusts effects are not included in the definition of wind spectra and should be considered separately.

3.3.3 Squalls

In equatorial and tropical areas sudden storms frequently occur where the wind velocity increases rapidly and dies out. Contrary to the gusts the duration of the squalls can be much longer going from several minutes up to one hour. The wind direction usually changes at the same time.

A typical record is shown in Figure 24 where the wind velocity goes from 10 m/s up to nearly 30 m/s in less than 5 minutes. In this particular case, the abrupt rise in velocity is accompanied by a change in direction of more than 90 degrees. The squalls are of big concern for the mooring systems of the floating systems which may respond dynamically and undergo large excursions.

Figure 24: Typical squall in West Africa. Time series of wind velocity (left) and direction (right)

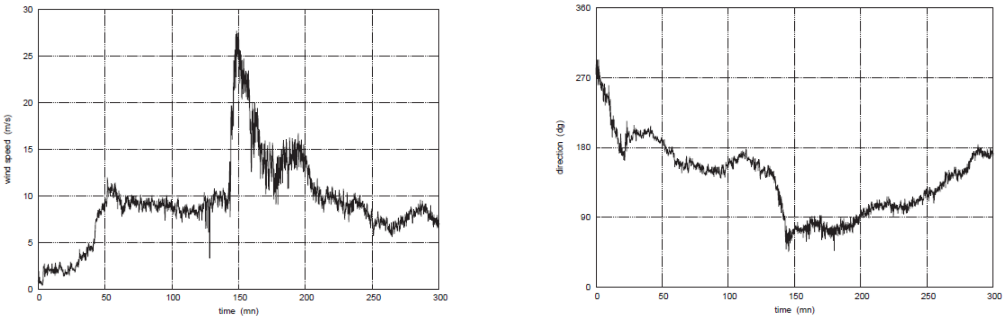

4. Current

4.1. Introduction

4.1.1 General

Current can affect the design and operation of the floating systems in many different ways. In addition to the increase of the loads on the floater, mooring lines and risers the presence of current usually has a detrimental effect on marine operations due to the changes in the position and the orientation of the floaters. In many situations a current causes the vortex shedding phenomena (see Section 3) which can sometimes lead to Vortex Induced Vibrations (VIV) of the risers or to Vortex Induced Motions (VIM) of the column stabilized floating units (TLP, Semi submersibles…). Finally, a current can also create the sea floor scouring which can influence the design of the subsea equipment.

4.1.2 Types of current

Current can be induced by different natural phenomena which combine at a specific offshore site. Three main types of current are usually identified (ISO 19901-1):

- Tidal current
- Oceanic circulation current
- Storm generated current

Tidal currents are regular and predictable because they follow the highest and lowest astronomical tides. The tidal currents can be modified by shoreline or sea floor configuration. They are generally weak in deep waters and are stronger in coastal regions where the surface velocities are in the range of a few meters per second (approximately $3\ m/s$ in Alaska's Cook Inlet).

The oceanic circulation currents are defined by the large-scale features of the general oceanic circulation. Typical examples are the Gulf stream in the Atlantic Ocean and the loop current in the Gulf of Mexico, where the surface velocities can be in the range of 1 to $2\ m/s$.

Storm-generated currents result from the wind stresses and the atmospheric gradient throughout a storm. The storm current velocities depend on many physical parameters: storm strength and meteorological characteristics, bathymetry and shoreline configuration, water density profile … In deep water, the storm-induced surface velocity can be roughly estimated to be up to 3% of the 1 hour sustained wind speed during storms.

4.2. Modelling of current

4.2.1 Introduction

In principle, the current intensity varies in space and in time. However, when compared to the waves, these changes happen at a much lower rate so that the current is usually considered as steady flow field in which the velocity is the function of the depth only.

4.2.2 Current velocity

The total current velocity at a given location is the vectorial sum of all the current components which were discussed in [4.1.2]. The information about the statistical distribution of currents and their variation with depth is generally poor in most areas of the world and dedicated measurement campaigns are recommended whenever that is practically possible.

4.2.3 Current profile

For situations (e.g. tidal current) in which the direction of the current velocities over the full water column can be considered constant and simple velocity profiles are appropriate, the simplified formulations can be used. The most widely used formulation assumes the power-law current profile in the form (ISO 19901-1):

$$U_C(z) = U_{C0}\left(\frac{z+h}{h}\right)^{\alpha} \tag{77}$$

where:

$U_C(z)$	current velocity at depth z (≤ 0)
U_{C0}	surface current speed at $z = 0$
z	vertical coordinate (positive upward of the still water)
h	water depth
α	the power law exponent (typically $\alpha = 1/7$)

Other current profiles which are commonly applied are:

- linear distribution between the surface current velocity U_{C0} and a bottom current equal to $0.5U_{C0}$
- multilinear distribution with parameters determined at several locations along the water column
- slab profile (uniform profile over certain depth and zero velocity in the lower part)

In the absence of more precise field data, these profiles can be used to approximately model any type of current.

4.2.4 Stretching of the current profile

In practice, the current profile is first determined for the still water conditions. The presence of waves modifies the vertical distribution of the flow velocity and the current profile needs to be modified and specified up to the exact instantaneous free surface position. To do that, the different stretching methods, similar to those used for extrapolation of the wave kinematics (See [2.5]), are introduced. Stretching means that the current velocity at particular vertical position z is obtained from the original current profile, by replacing z with its stretched value z_S. The linear and the nonlinear stretching methods are usually employed.

In the case of linear stretching the relationship between z_S and z, is the same as for the Wheeler stretching method in waves (25) while, in the case of the nonlinear stretching the relationship between z_S and z becomes:

$$z_S = z + \eta\frac{\sinh[k_0(z+h)]}{\sinh(k_0 h)} \tag{78}$$

where k_0 is the wave number.

The expression (78) is valid for the regular Airy wave and for irregular waves stretching applies to each wave component.

In both the linear and the nonlinear stretching methods z extends from $-h$ to η and the differences between the two approaches are shown in Figure 13. In practice, nonlinear stretching is recommended.

Figure 25: Stretching of current velocity up to the instantaneous free surface

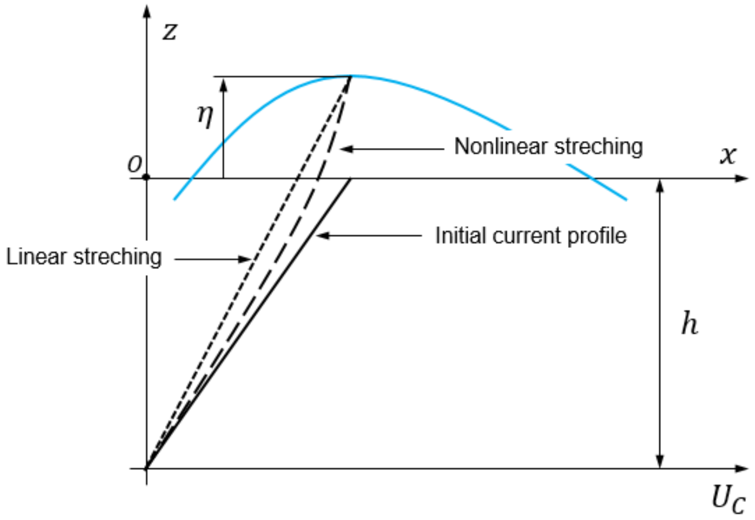

5. Other environmental factors

5.1. General

In most of the cases in practice, wind, waves and current give the main contribution to the environmental loads on floating systems. In some particular situations, some other environmental effects might also become important and need to be taken into account when necessary. Some of them are discussed below.

5.1.1 Internal waves

The density of seawater is not strictly constant and it varies with salinity and temperature. In particular, there can exist a significant jump or rapid change in density between the warmer surface waters and the colder deep waters. This phenomenon is particularly marked in the tropical and the equatorial zones, where the differences in temperatures between the upper and lower layers can reach twenty degrees. Their interface is typically at depths of the order of fifty meters. Stratification can also be related to a difference in salinity, for example near an estuary, or in Norwegian fjords (or in the vicinity of melting pack ice).

Because of the stratification the internal waves can occur at the interface of the different layers of water. The situation is similar to air-water interface except that the difference in density between two fluids is much smaller. In deep ocean the phase velocity C_P of the internal waves is approximately given by:

$$C_P = \sqrt{gh\frac{\Delta\varrho}{\varrho}} \qquad (79)$$

where h is the thickness of the upper layer and $\Delta\varrho/\varrho$ is the relative difference in density, typically in the order of 10^{-4} to 10^{-3}.

Internal waves propagate slowly but the horizontal components of the associated orbital velocities can reach notable values. To an observer, they appear as a time-varying current, strongly sheared, with a change in direction through the interface. For internal waves to be generated, the body of water must already be in motion, under the effect of tidal or oceanic currents, and it must encounter a change in bathymetry, for example the continental slope, or an underwater ridge. When the required conditions (stratification, strong currents, variable bathymetry) are satisfied, the currents associated with the internal waves can reach appreciable values, of the order of $1\ m/s$ or $2\ m/s$.

5.1.2 Tsunamis

Tsunamis are water waves generated by sudden displacement of large volume of water. Typical physical phenomena which can initiate tsunamis are earthquakes, seabed subsidence, landslides, underwater volcanoes, explosions … Tsunami waves are much different from the classical sea waves and their wave length is much longer (several tens of kilometres) with periods ranging from minutes to hours. The speed of propagation across the ocean is a function primarily of water depth; in the deepest oceans the tsunami waves can travel at speeds of several hundred kilometres per hour. In deep water, tsunamis have a low height and very long period and pose little hazard to floating or fixed offshore structures. The greatest hazard to offshore structures from tsunamis results from the inflow and outflow of water in the form of waves and currents. These waves can be significant in shallow water, causing substantial actions on structures. Currents caused by the inflow and outflow of water can also cause excessive scour problems.

5.1.3 Ice and icebergs

Sea ice and icebergs occur in the different parts of the world's oceans. The important parameters which characterize the importance of the ice and iceberg effects are:

- seasonal distribution and probability of sea ice, ice floes, pressure ridges and icebergs
- probability and effects of ice induced seabed gouging
- type, thickness, strength and other mechanical properties of ice
- drifting speed, direction, shape and mass of ice floes, pressure ridges and icebergs

Before starting the design process of the floating systems in areas that are likely to be affected by sea ice and icebergs the above data needs to be collected and accounted for in the design.

5.1.4 Snow and ice accretion

In cold region, snow accumulation and ice accretion can occur and should be taken into account in the design process. These effects can significantly increase the size and weight of the structural components. Consequently the environmental loading (wind, waves, current …) will be modified and the response of the floating system and its components will change. This is particularly true for long slender structures such as flares.

5.1.5 Seiches

A seiche defines the standing wave occurring in enclosed (e.g. lakes) or partially enclosed (e.g. harbour) bodies of water. Their amplitude is usually quite low (few centimetres) and the associated periods are of the order of a few minutes. Generally, the effects of seiches are rather small at offshore locations and can be ignored but, if a platform is located in shallow and partly enclosed seas this effect should be taken into account. The main practical effects of seiches in a harbour, are the large horizontal wave forces on ships, which can induce large horizontal ship motions and possibly lead to failure of the mooring system.

5.1.6 Marine growth

Marine growth quickly occurs on any submerged or occasionally submerged object in the sea. The thickness and type of marine growth depend on location, water depth, the age of the structure and the maintenance regime. It may consist of relatively soft material (algae, seaweeds, barnacles) or quasi-solid appurtenances (mussels, oysters, corals).

Marine growth adds to the size and to the weight of marine structures. In design it is accounted for as an extra thickness given to all members, typically 50 to $100\ mm$. The density is usually taken as about $1300\ kg/m3$. In addition, marine growth can significantly affect the drag coefficients.

5.1.7 Miscellaneous

Some other effects which were not explicitly considered above might also affect the design of the floating system depending on the location. Some of those are: temperature effects (air and sea), humidity, fog, wind chill, salinity, guano accumulation, wildlife preservation...

6. List of references

[1] API 2INT-MET, 2007.: “Interim Guidance on Hurricane Conditions in the Gulf of Mexico.”

[2] Bingham H.B., Madsen P.A., Fuhrman D.R. 2009.: “Velocity potential formulations of highly accurate Boussinesq-type models”, Coastal Engineering, 56, 467-478.

[3] Cokelet, E. D. 1977.: “Steep gravity waves in water of arbitrary uniform depth.” Philos. Trans. R. Soc. London Ser. A 286, 183–230.

[4] Dean R.G. 1965.: “Stream function representation of nonlinear ocean waves.”, Journal of Geophysical Research, 70(18):4561–4572,

[5] Dean, R. G. 1974.: “Evolution and development of water wave theories for engineering application”, I and II. U.S. Army Coastal Engineering Research Center, Special Rep. 1, Fort Belvoir, VA.

[6] Dommermuth, D. G. and Yue, D. K. P. 1987.: “A high-order spectral method for the study of nonlinear gravity waves.”, J . Fluid Mech, 184

[7] Ducrozet G., Bonnefoy F., Le Touzé D. & Ferrant P., 2007.: ” 3D HOS simulations of extreme waves in open seas”, Natural Hazards Earth System Sciences, Vol 7

[8] Ducrozet G., Bonnefoy F., Le Touzé D. & Ferrant P., 2012.: ” A modified High-Order Spectral method for wavemaker modeling in a numerical wave tank”, European Journal of Mechanics B, Fluids, Vol. 34

[9] Ducrozet G., Bonnefoy F., Le Touzé D. & Ferrant P., 2016.: ”HOS-ocean: Open-source solver for nonlinear waves in open ocean based on High-Order Spectral method”, Computer Physics Communications, Vol. 203

[10] Fenton J.D. 1990 “Nonlinear wave theories”, in The Sea, Vol.9: Ocean Engineering Science, Wiley, New York

[11] Fenton, J. D. 1985.: “A fifth-order Stokes theory for steady waves.” J. Waterway, Port, Coastal Ocean Eng. 111, pt. 2, 216–234.

[12] Forristall G.Z. 1988.: “Wind spectra and gust factors over water”, Proc. 20th Offshore Techn. Conf., paper No 5735

[13] Forristall, G.Z., 2000, “Wave Crest Distributions: Observations and Second-Order Theory,” Journal of Physical Oceanography, Vol. 30.

[14] Hasselmann K. et al. 1973.: “Measurements of wind-wave growth and swell decay during the Joint North Sea Wave Project (JONSWAP)”, Deutsche Hydr. Zeit, Reihe A8, 7-95.

[15] Holthuijsen L.H. 2007.: “Waves in oceanic and coastal waters.” Cambridge University Press

[16] IEC 61400-1, 2019.: “Wind energy generation systems.”, International standard

[17] ISO 19901-1, 2005.: “Petroleum and natural gas industries - Specific requirements for offshore structures - Part 1: Metocean design and operating considerations.”

[18] Korteweg, D. J.; De Vries, G. 1895. : “On the Change of Form of Long Waves Advancing in a Rectangular Canal, and on a New Type of Long Stationary Waves”, Philosophical Magazine, 39 (240): 422–443

[19] Kraaiennest 2009. : https://commons.wikimedia.org/wiki/File:Water_wave_theories.svg.

[20] Le Mehaute, B. 1976. : “An Introduction to Hydrodynamics and Water Waves.” Springer-Verlag, Dusseldorf.

[21] Rodenbusch G. & Forristall G.Z. 1986.: “An empirical model for random wave kinematics near the free surface”, Proc. Offshore Technology Conf., paper 5098.

[22] Schwartz L.W. 1974.: “Computer extension and analytic continuation of Stokes’ expansion for gravity waves”, J. Fluid Mechanics, 62, 553-578.

[23] Seiffert B.R., Ducrozet G. & Bonnefoy F.,2017.: “Simulation of breaking waves using the high-order spectral method with laboratory experiments: Wave-breaking onset”, Ocean Modelling, vol 119, pp 94-104.

[24] Skjelbreia L. & Hendrickson J. 1961.: “Fifth order gravity wave theory”, Proc. 7th Conf. on Coastal Engineering, 184-196.

[25] Stansberg C.T., Gudmestad O.T. & Haver S.K., 2008.: “Kinematic under extreme waves.”, Journal of Offshore Mechanics and Arctic Engineering.

[26] Tolman H.L., 2014.: “User manual and system documentation of WAVEWATCH III version 4.18”US Department of Commerce, National Centers for Environmental Prediction.

[27] West B.J., Brueckner K.A., Janda R.S., Milder M. & Milton R.L., 1987.: “A new numerical method for surface hydrodynamics”, J. Geophys. Res. 92.

[28] Wheeler J.D. 1970.: “Method for prediction of forces produced by irregular waves”, J. Petrol. Techn., 359-367.

[29] Wheeler, J. D. E., 1970.: “Method for Calculating Forces Produced by Irregular Waves,” JPT, J. Pet. Technol., pp. 359–367

[30] Zhao K & Liu P.L.F, 2022.: "On Stokes wave solutions" Proceedings of The Royal Society A Mathematical Physical and Engineering, 478(2258).

Section 3 Loads on Slender bodies

1. General

1.1. Definitions

1.1.1 Slender body

The denomination cylindrical section is used for any form of sectional geometry and not exclusively circular. The characteristic dimension, which can be defined in different ways, of the cylindrical section is denoted by D. Reference is made to Figure 26 where the body of length L with cross sectional area S is exposed to the uniform incoming flow of intensity $\boldsymbol{\mathcal{U}}(t)$.

Figure 26: Inclined tubular structure vs incoming flow

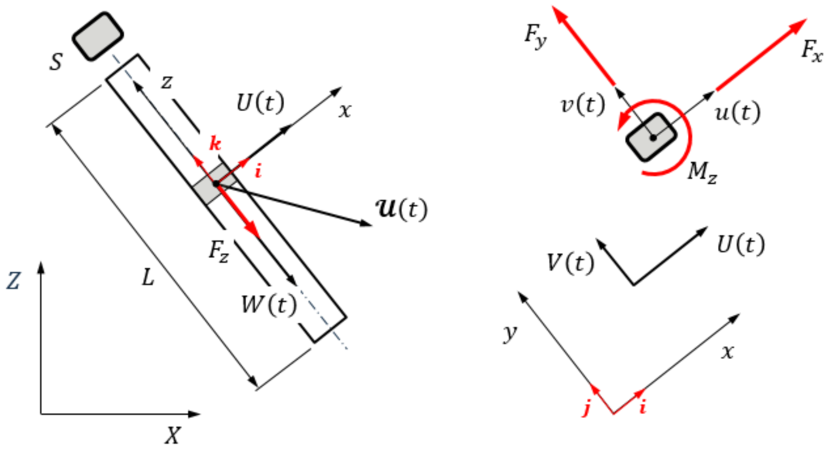

By denoting the wave length by λ, the body is assumed to be slender when the following conditions are met:

$$D \ll L \quad , \quad \lambda > 6D \tag{80}$$

For slender body the incoming flow is assumed uniform (constant over the section) and the perturbation effects are neglected. Furthermore the loads can be computed in each section independently, and then integrated over the length of the body.

1.1.2 Coordinate systems

The slender cylindrical section moves together with the body and two coordinate systems are defined (see Figure 26):

- Global earth fixed coordinate system (X, Y, Z)
- Local body fixed coordinate system (x, y, z) with the unit vectors $(\boldsymbol{i}, \boldsymbol{j}, \boldsymbol{k})$,located in the plane of the section with the z axis coinciding with the axis of the cylindrical structure

The incoming flow is defined by the flow velocity which is written in the local coordinate system as:

$$\boldsymbol{\mathcal{U}}(t) = U(t)\boldsymbol{i} + V(t)\boldsymbol{j} + W(t)\boldsymbol{k} \tag{81}$$

The time dependence of the flow is arbitrary and both the steady (typically current) and the oscillatory (typically wave) effects are of concern.

The motion of the section is defined by the translational velocity of its center and the instantaneous rotational velocity around it:

$$\boldsymbol{u}(t) = u(t)\boldsymbol{i} + v(t)\boldsymbol{j} + w(t)\boldsymbol{k} \quad , \quad \boldsymbol{\Omega}(t) = p(t)\boldsymbol{i} + q(t)\boldsymbol{j} + r(t)\boldsymbol{k} \tag{82}$$

The following quantities are also introduced:

$\boldsymbol{a_f} = a_{f_x}\boldsymbol{i} + a_{f_y}\boldsymbol{j} + a_{f_z}\boldsymbol{k}$	fluid acceleration relative to earth
$\boldsymbol{a} = a_x\boldsymbol{i} + a_y\boldsymbol{j} + a_z\boldsymbol{k}$	acceleration of the sectional center

$\boldsymbol{a}_R = \boldsymbol{a} - \boldsymbol{a}_f = a_{R_x}\boldsymbol{i} + a_{R_y}\boldsymbol{j} + a_{R_z}\boldsymbol{k}$	fluid acceleration relative to the body
$\boldsymbol{u}_R = \boldsymbol{u} - \boldsymbol{\mathcal{U}} = u_R\boldsymbol{i} + v_R\boldsymbol{j} + w_R\boldsymbol{k}$	relative fluid velocity

1.1.3 Non-dimensional numbers

The importance of certain physical effects is driven by the different non-dimensional numbers. In the present context, the most important non-dimensional numbers are the Reynolds number Re, Strouhal number S_t , the Keulegan – Carpenter number $\mathrm{K_C}$ and the Stokes parameter β which are defined as follow:

$$\mathrm{Re} = \frac{\mathrm{U}D}{\nu} \quad , \quad S_t = \frac{f_0 D}{\mathrm{U}} \quad , \quad \mathrm{K_C} = \frac{\mathrm{u}T}{D} \quad , \quad \beta = \frac{\mathrm{Re}}{\mathrm{K_C}} \tag{83}$$

where:

D	Characteristic width of the section $[m]$
U	Characteristic flow velocity $[m/s]$
ν	Kinematic viscosity $[m^2/s]$
f_0	Characteristic frequency $[Hz]$
u	Amplitude of the oscillatory flow velocity $[m/s]$
T	Period of the oscillation $[s]$

The exact definition of the velocities, the frequency and the oscillation period, which have to be used in the above expressions, depends on the flow conditions in consideration.

An additional important nondimensional number, which will be introduced later (see Figure 29,) is the roughness parameter which is defined as the ratio of the typical dimension of the surface irregularities and the characteristic width of the section.

1.2. Sectional loads

1.2.1 Decomposition of the loads

The hydrodynamic sectional loads are defined in the local coordinate system as:

F_n	Normal force – collinear with the normal velocity
F_l	Lift force – perpendicular to the normal force
F_t	Tangential force – collinear with the axis of the slender body
M_z	Torsional moment (around the axis of the slender body)

The two remaining moments M_x and M_y are not relevant in the context of sectional loads.

1.2.2 Flow features

Due to the assumption of slenderness, the $\mathrm{K_C}$ number can be quite large so that the flow separates massively prohibiting the use of the potential flow theory. The alternative is then to use the Computational Fluid Dynamics (CFD) which became quite mature but still a long way to being applicable to a structure composed of hundreds of tubular elements which should be analyzed for various environmental conditions. Semi-empirical methods remain the only practical way and they are commonly combined with the strip theory approach where the global loads are calculated as the sum of the individual loads at each section. The elementary physical problem to solve becomes the evaluation of the hydrodynamic forces on a 2D section in different flow conditions: steady, oscillatory and combined steady + oscillatory.

1.2.3 Potential flow considerations

The normal sectional force includes both the potential flow and the viscous contributions. Even though the potential flow theory is not directly applicable for slender bodies, it is useful to discuss it for better understanding of the force decomposition. For a symmetric cylindrical section of area S, such that the axis x and y are the axis of symmetry, the sectional hydrodynamic loads of potential flow can be written a:

$$\begin{aligned}
F_x(t) &= \varrho S\left[a_{f_x} - a_{R_x}C_{a11} + r v_R (C_{a22} - C_{a11})\right] \\
F_y(t) &= \varrho S\left[a_{f_y} - a_{R_y}C_{a22} + r u_R (C_{a22} - C_{a11})\right] \\
F_z(t) &= 0 \\
M_z(t) &= -a_{66}\dot{r} + \varrho S u_R v_R (C_{a22} - C_{a11})
\end{aligned} \tag{84}$$

where $C_{aii} = a_{ii}/\varrho S$ is the added mass coefficient of the section in the body fixed coordinate system and a_{66} is its added mass moment of inertia around the local z axis

It follows that the hydrodynamic forces vanish for fixed cylinder in steady flow which is known as D'Alembert paradox. It should be noted that the d'Alembert paradox applies to translation loads only and the potential theory predicts a moment, known as Munk's moment given by the last term in (84).

The inertial sectional loads can be written in alternative forms and the different expressions can be found in the literature but all of them should lead to the same values of the loads, as discussed in Appendix 1. In the absence of the rotational velocity ($\mathbf{\Omega} = 0$) , which is the case most often in practice, the expressions for the sectional loads reduce to the well-known form:

$$\begin{aligned} F_x(t) &= \varrho S[(1 + C_{a11})a_{f_x} - C_{a11}a_x] \\ F_y(t) &= \varrho S\left[(1 + C_{a22})a_{f_y} - C_{a22}a_y\right] \\ M_z(t) &= \varrho S(U - u)(V - v)(C_{a22} - C_{a11}) \end{aligned} \tag{85}$$

The added mass and moment of inertia a_{ij} can be easily evaluated by the potential flow theory. Their typical values for some sectional shapes are shown in Table 1 and Figure 27.

Table 1: Added mass coefficients for typical sectional shapes

Section shape		Sectional area S	$C_{a11} = \frac{a_{11}}{\varrho S}$	$C_{a22} = \frac{a_{22}}{\varrho S}$	$\frac{a_{66}}{\varrho S^2}$
Circle	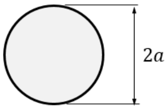	πa^2	1.0	1.0	0.0
Ellipse	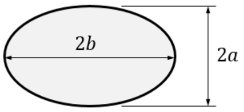	πab	$\frac{a}{b}$	$\frac{b}{a}$	$\frac{1}{128\pi}\left(\frac{a}{b} - \frac{b}{a}\right)^2$
Square		a^2	1.19	1.19	0.046
Rectangle	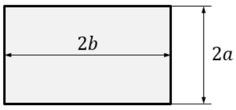	$4ab$	See Figure 27.		

Figure 27: Added mass coefficients for rectangular cylinder

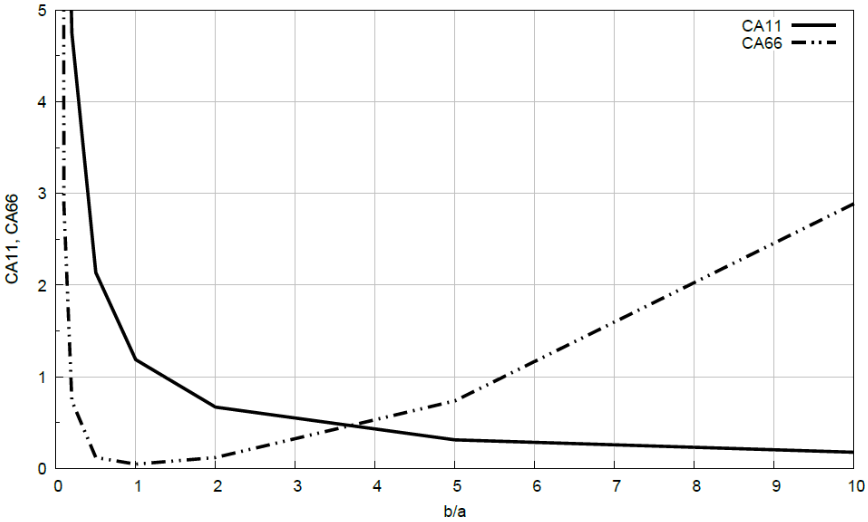

b/a	C_{a11}	C_{a66}
0.01	78.54	245.44
0.10	8.95	2.89
0.20	4.75	0.74
0.50	2.14	0.12
1.00	1.19	0.05
2.00	0.67	0.12
5.00	0.31	0.74
10.00	0.18	2.89

1.2.4 Effects of viscosity

In reality, the viscous effects will modify the potential flow forces by modifying the added mass coefficients, and by adding the drag forces. The normal force acting on the section of slender body, is usually decomposed into the inertial and the drag components:

$$F_n = F_{inertia} + F_{drag} \tag{86}$$

Furthermore the drag force component is usually written in the following form:

$$F_{drag} = \frac{1}{2}\varrho C_D D U|U| \tag{87}$$

where C_D denotes the drag coefficient and U is the characteristic flow velocity.

2. Sectional loads in normal direction

2.1. Generalized Morison equation

2.1.1 Definition

The Morison equation (Morison et al. [1950]) represents the sectional forces as a function of the unperturbed incoming flow velocity (U, V) and acceleration $\left(a_{f_x}, a_{f_y}\right)$, and the body velocity (u, v) and acceleration $\left(a_x, a_y\right)$:

$$\begin{pmatrix} F_x \\ F_y \end{pmatrix} = \varrho S(1 + C_a)\begin{pmatrix} a_{f_x} \\ a_{f_y} \end{pmatrix} - \varrho S C_a \begin{pmatrix} a_x \\ a_y \end{pmatrix} + \frac{1}{2}\varrho C_D D \begin{pmatrix} U - u \\ V - v \end{pmatrix}\sqrt{(U-u)^2 + (V-v)^2} \tag{88}$$

where the first two terms represent the inertial forces and the last term is the drag force component.

For the inertial part of the loads, it is common to regroup the incident and the perturbed flow contributions by defining the global inertia coefficient C_M as:

$$C_M = 1 + C_a \tag{89}$$

When using the generalized Morison equation, the viscous damping effects are completely included in the drag forces and no additional damping should be added.

It should be noted that the Morison formula is based on the flow independence or cross-flow principle which means that the normal loads at the section (i.e. inertia and drag coefficients) are independent of the tangential flow conditions. It can be shown that, in the pure potential flow case (inertia component only), this assumption is fully correct but, in the viscous case, its validity depends on the Reynolds number. In general the cross flow principle is reasonably valid in all regimes except the unstable critical Reynolds number regime (see Figure 29).

2.2. Specific flow conditions

2.2.1 Steady flow

The constant incoming velocity U_0 is assumed in x direction meaning that the normal force will be directed along x axis. The Reynolds number is defined accordingly and we can write:

$$U(t) = U_0 \quad , \quad \mathrm{Re} = \frac{U_0 D}{\nu} \tag{90}$$

The inertial component of the normal force in steady flow conditions is zero and the viscous drag force exists only. It is convenient to define the space dependent pressure coefficient as:

$$C_p = \frac{p - p_\infty}{\frac{1}{2}\varrho U^2} \tag{91}$$

where p_∞ is the reference pressure at infinity.

In the case of the potential flow assumptions the local pressure coefficient for circular cylinder becomes equal to $C_p = 1 - 4\sin^2\theta$, with θ denoting the local angle. In practice, this distribution is modified by the non-potential flow effects and the final distribution is shown in Figure 28 for different Reynolds numbers.

The potential flow value of the pressure coefficient becomes quickly invalid as we approach the lee side of the cylinder surface. This is due to flow separation which is driven by the Reynolds number (83) and the consequence is the occurrence of the mean drag load which is given by (87).

Figure 28: Pressure coefficients along the cylinder surface (from Molin (2002))

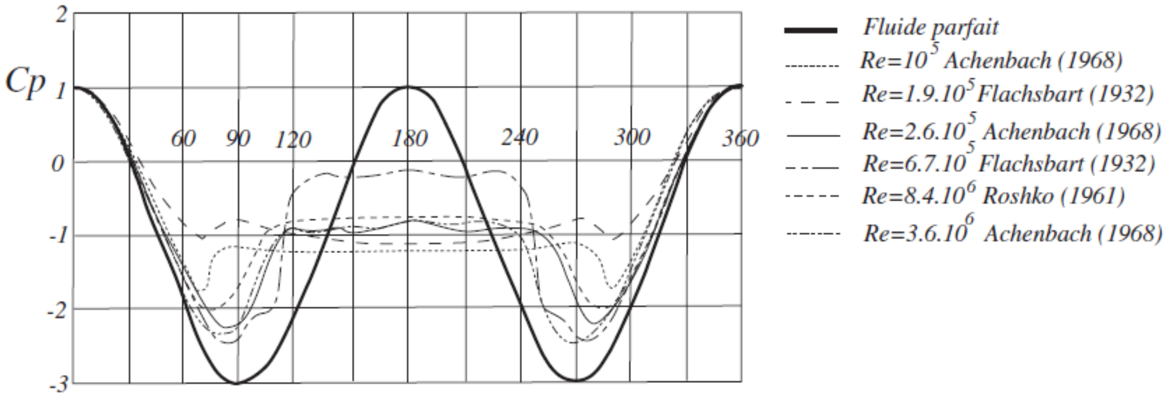

2.2.2 Oscillatory flow

When the harmonic flow at frequency ω and with amplitude A is assumed, the incoming velocity becomes:

$$U(t) = A\omega \sin \omega t \qquad (92)$$

This case corresponds to the practical case of a vertical cylinder in long regular waves where, in each horizontal strip, the flow is of this kind when the vertical component of the flow is neglected. The obvious difference with the steady flow is that during one wave period the cylinder is passing back through his wake. This has important consequences on the values of drag and added mass coefficients.

Here the non – dimensional Reynolds and the Keulegan Carpenter numbers (83), are defined with respect to the amplitude of the incoming velocity field $A\omega$:

$$\mathrm{Re} = \frac{A\omega D}{\nu} \quad , \quad \mathrm{K_C} = \frac{A\omega T}{D} = 2\pi \frac{A}{D} \qquad (93)$$

where T denotes the wave period $T = 2\pi/\omega$.

In this case, the inertial force component exists and the Morison equation becomes:

$$F_n = \varrho C_M S a_{f_x} + \frac{1}{2} \varrho C_D D U|U| \qquad (94)$$

The inertia coefficient C_M and the drag coefficient C_D depend only on $\mathrm{K_C}$ and Re and can be derived through harmonic analysis of the experimental measurements. The inertia term evolves in time as $\cos \omega t$ and the drag term as $\sin \omega t\, |\sin \omega t|$. By approximating $\sin \omega t\, |\sin \omega t|$ by $8/3\pi \sin \omega t$ it is interesting to consider the ratio of the inertia and drag loads which, for $C_D = 1$ and $C_M = 2$ gives:

$$\frac{F_{drag}}{F_{inertia}} \approx \frac{8}{3\pi^3} \frac{C_D}{C_M} \mathrm{K_C} \approx 0.043 \mathrm{K_C} \qquad (95)$$

The relative importance of drag and inertia components depends on $\mathrm{K_C}$ number. When $\mathrm{K_C}$ is small the inertia is dominant and when $\mathrm{K_C}$ is large the drag is dominant. For $\mathrm{K_C} \rightarrow 0$, and for the sections without sharp corners, the boundary layer remains attached and the potential flow theory is applicable, while the case $\mathrm{K_C} \rightarrow \infty$ corresponds asymptotically to the case of a cylinder in steady flow.

2.2.3 Combined steady and oscillatory flow

The incoming velocity is assumed as:

$$U(t) = U_0 + A\omega \sin \omega t \qquad (96)$$

where U_0 denotes the steady current velocity.

An additional parameter, which measures the relative importance of the current and the oscillatory velocity is also usually introduced:

$$\mathcal{R} = \frac{U_0}{A\omega} \qquad (97)$$

When $\mathcal{R}$ is larger than one, the flow never reverses; this is a situation somewhat similar to the current only case, the flow separates whatever the $\mathrm{K_C}$ value. When $\mathcal{R}$ is smaller than one, the flow reverses periodically; if the $\mathrm{K_C}$ number is sufficiently small, the flow does not separate, even though the current velocity is not nil.

Often the product of $\mathrm{K_C}$ and the $\mathcal{R}$ is also introduced to define the reduced velocity:

$$U_R = \mathrm{K_C}\mathcal{R} = \frac{U_0 T}{D} \tag{98}$$

The direct application of the Morison equation leads to the expression (94) which is also known as the dependent flow Morison formulation. Another possibility to define the drag force is the so called independent flow Morison formulation in which the steady and the unsteady flow contributions to the drag force are separated as follows:

$$F_x = \varrho C_M S a_{f_x} + \frac{1}{2}\varrho C_{D0} D U_0 |U_0| + \frac{1}{2}\varrho C_{D1} D A^2 \omega^2 \sin\omega t\,|\sin\omega t| \tag{99}$$

In this case two independent drag coefficients C_{D0} and C_{D1} are introduced and they need to be adjusted through the fitting with the experimental data.

In principle, the dependent flow Morison formulation (also called relative velocity formulation and given by (88) for the general case) for the drag forces is valid when the amplitude of the sectional motion A is exceeding the sectional characteristic width D i.e. $A/D > 1$. For the lower motion amplitudes, the validity of the formulation depends on the value of the reduced velocity (98). In particular for $U_R < 10$ it is recommended to neglect the velocity of the structure in (88).

3. Other sectional loads

3.1. Lift force

3.1.1 Introduction

The lift force is defined as the force normal to the direction of the flow and normal to the slender body axis. It is due to the non-symmetry of the fluid flow around the section and may occur for several reasons such as:

- unsymmetrical cross section
- unsymmetrical flow (wake effects)
- wall effects
- vortex shedding

3.1.2 Definitions

The lift force on a slender cylindrical structure is expressed in the following form:

$$F_l = \frac{1}{2}\varrho C_l D U |U| \tag{100}$$

where C_l is known as a lift coefficient.

In the case of steady incoming flow the lift force can be of both steady and oscillatory character depending on the position of the separation points. For unsymmetrical section with the separation point fixed in space the steady net lift force occurs. For the cases where the separation point changes in time, even for symmetrical sections, the lift force becomes oscillatory. This oscillatory lift force can induce the Vortex Induced Vibrations (VIV) discussed in [5.2].

3.2. Tangential force

3.2.1 Introduction

When the cylinder is inclined with respect to the incoming flow, tangential force will occur in addition to the normal force. This force is mainly due to skin friction and it is usually rather small except for elongated cylindrical bodies in nearly tangential flow (towing lines, …)

3.2.2 Definitions

Reference is made to Figure 26 and the tangential force component is defined as follows:

$$F_t = \frac{1}{2}\varrho C_t(\alpha) D \mathcal{U}^2 \tag{101}$$

where α is the angle between the axis of the slender body and the velocity vector $\boldsymbol{\mathcal{U}}$ (see Fig. 26.)

It should be noted that the tangential force is related to the total velocity $\mathcal{U}(t)$ which is the common practice. The different formulas have been proposed for $C_t(\alpha)$ and they are usually given in the form:

$$C_t(\alpha) = C_D(m + n\sin\alpha)\cos\alpha \tag{102}$$

where C_D is the drag coefficient in normal direction.

Typical values of the parameters m and n are $m \approx 0.03$ and $n \approx 0.05$.

3.3. Torsion moment

3.3.1 Introduction

Depending on the flow conditions, the non-negligible moment around the axis perpendicular to the cross section (torsion moment) can also occur. This moment can also be subdivided into its inertial and the drag component. A purely potential flow contribution to the inertial component is given by (84).

3.3.2 Viscous torsion moment

The viscous part of the torsion moment occurs mainly due to the unsymmetrical flow conditions. The flow separation occurs at different instants and the different positions along the section, which results in the lift force and the torsional moment.

4. Hydrodynamic coefficients

4.1. General

4.1.1 Introduction

The most important quantities in the hydrodynamic load estimation on slender bodies are the different force coefficients (added mass, drag, lift …). These coefficients are usually obtained by fitting the experimental data for particular flow conditions or, more recently, by the CFD numerical simulations.

4.2. Inline flow

4.2.1 Circular cylinder in steady flow

Typical values of the Reynolds number which are of concern here, are in the range 10^4 to 10^7. There exist a number of experimental studies giving the values of the drag coefficients C_D. Even though there exist significant scatter in between the different results they give the similar tendencies which are schematically shown in Figure 29. Four different regimes are identified: subcritical, critical, supercritical and transcritical. In the subcritical regime ($\mathrm{Re} = 300 \text{ to } 2 \cdot 10^5$) the boundary layer is still laminar up to separation point and the transition to the turbulence occurs in the wake. The C_D takes the value around 1.0 to 1.2. The other extremity ($\mathrm{Re} > 3 \cdot 10^6$) is the transcritical regime where the boundary layer is turbulent from the upstream stagnation point resulting in the delayed separation point and in the lower value of the drag coefficient. In between is a critical regime ($\mathrm{Re} \sim 2 \cdot 10^5$ to $5 \cdot 10^5$) where transition occurs right after the laminar separation, inducing reattachment and a second separation downstream; this means a very narrow wake, hence the very low associated drag coefficients. Finally the intermediate regime in between the critical and transcritical ($\mathrm{Re} \sim 5 \cdot 10^5$ to $3 \cdot 10^6$) is known as supercritical regime. The boundaries between these different regimes are somewhat theoretical and are susceptible to vary, depending on the turbulence level, the rigidity of the experimental set-up, etc.

From Figure 29. it can be seen that the drag coefficient strongly depends on roughness. Roughness is defined as the ratio k/D with D being the cylinder diameter and k a typical dimension of the surface irregularities. For a pipe roughness may result from corrosion (a typical value is then $k \sim 3\,mm$) and/or from marine growth (with much larger k values). The roughness can influence the drag coefficient in many different ways. Among them it decreases the value of the critical Reynolds number at the border between subcritical and critical ranges and induce the reduction of the drag coefficient in the critical regime. At very high roughness coefficient the drag coefficient becomes independent of the Reynolds number.

Figure 29: Drag coefficient for a circular cylinder in steady flow and for different roughness parameters

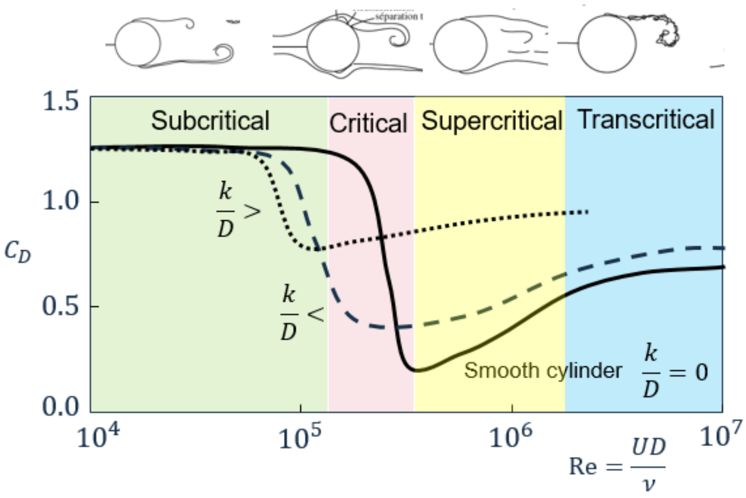

4.2.2 Non circular cylinder in steady flow

A non-circular shape will induce the changes in the flow around the cylinder in particular the position of the separation points. In the case of rectangular section with sharp corners the separation points are imposed at the section corners so that the drag coefficient becomes relatively independent of the Reynolds number as shown in Figure 30 (left). In the case of rectangular section with sharp corners, the drag coefficient depends on the ratio of the side's lengths. Figure 30 (right) shows the C_D for a rectangular cylinder with sharp corners as a function of the aspect ratio b/a with b the length of the side in the flow direction. It can be observed that, in-between the plate and square cases, where $C_D \approx 2$, there is a critical aspect ratio $b/a \approx 0.6$ where the drag coefficient reaches almost 3. From then on there is a monotonous decay of C_D with increasing b/a values.

Similar to the effects of roughness, rounding the section corners results in introducing the transition between the subcritical and supercritical flow regimes as shown in Figure 31.

Figure 30: Drag coefficient for square cylinder with sharp corners.
Left – square cylinder, right – variation of drag coefficient with aspect ratio
(from Molin (2002))

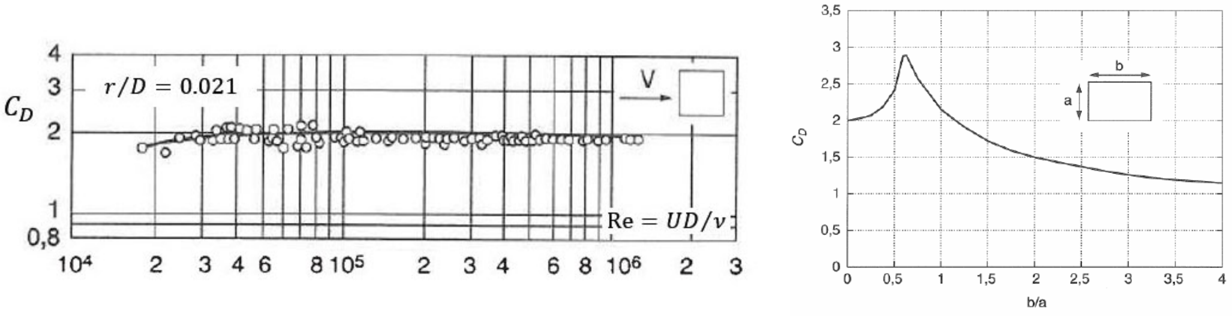

Figure 31: Drag coefficient for rectangular cylinder with rounded corners (from Molin (2002))

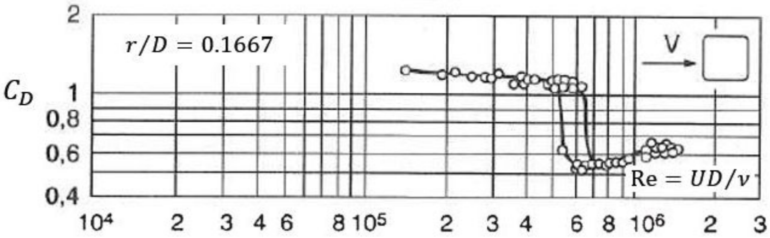

4.2.3 Circular cylinder in inline oscillatory flow

For a smooth cylinder β (or Re) and $\mathrm{K_C}$ are the only two non-dimensional parameters that characterize the flow and thus the loads. When the sectional hydrodynamic coefficients are determined by means of U-tube tests the β parameter remains constant for a given cylinder so that the experimental results are usually given as a function of β and $\mathrm{K_C}$. There have been numerous experiments performed to determine the C_M and C_D values in oscillatory flows. Figure 32 shows values obtained by Sarpkaya through U-tube experiments. Different β values in the figures correspond to different cylinder diameters, from $5\ cm$ up to $16.5\ cm$ (the U-tube cross section being $30 \times 30\ cm$).

Figure 32: Circular cylinder in oscillatory flow. Inertia and drag coefficients vs $\mathrm{K_C}$ for different β
(from Sarpkatya (2010))

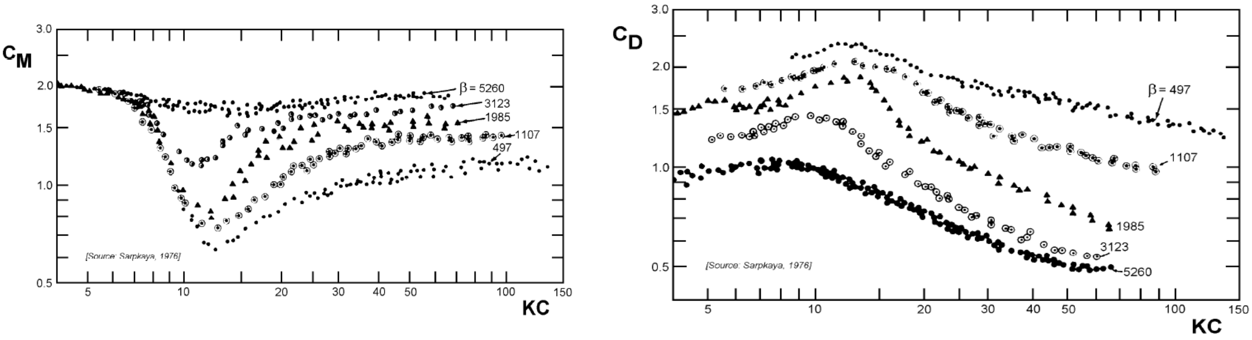

The inertia coefficient C_M for low $\mathrm{K_C}$ values go to potential flow value 2 regardless of the value of β and for large β values, C_M is close to 2 all over the $\mathrm{K_C}$ range.

It is also interesting to compare the results obtained in oscillatory flow with those in steady flow. In Figure 33 the same results as in Figure 32 are presented as a function of the Reynold number for different $\mathrm{K_C}$ values.

It can be seen that the critical zone is less pronounced and shifted to lower Reynolds numbers, alike in the case of a rough cylinder or a smooth cylinder in highly turbulent flow. This is due to the fact that the cylinder encounters its own wake at each flow cycle.

Figure 33: Circular cylinder in oscillatory flow.
Inertia (left) and drag (right) coefficients vs Re for different $\mathrm{K_C}$ (from Sarpkaya (2010))

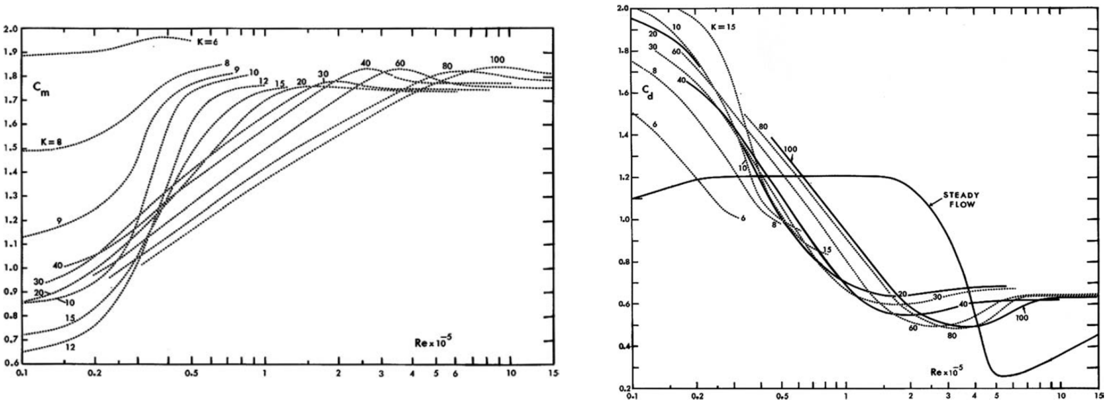

4.3. Practical selection of the drag and inertia coefficients for inline flow

4.3.1 Introduction

In practice, the inertia and the drag coefficients (C_M and C_D) are determined within the idealized experimental conditions and with a limited number of parameters which makes their extrapolation for the general applications in full scale conditions, extremely difficult. Large amount of experimental data has been produced in the past and in many cases quite important scatter in the results from different facilities, can be observed. We refer to Sarpkaya (2010), SNAME (2008) and Summer & Fredsoe (1997) for further details.

4.3.2 Circular cylinders

In practice the tubular structure is of particular interest in the context of jack-up and jacket platforms. These structures are usually operating in postcritical flow regime with relatively large $\mathrm{K_C}$ number which means that the forces will be dominated by the drag component (95). The results at different experimental facilities agree reasonably well for drag coefficient on smooth cylinder ($k/D < 0.0001$) in postcritical flow conditions, giving the approximate value of 0.65. Similarly, for rough cylinders ($k/D > 0.0004$) the suggested value is 1.0 and for the intermediate roughness the following expression is proposed:

$$C_D(k/D) = \begin{cases} 0.65 & ; \quad k/D < 0.0001 \\ 0.65(2.36 + 0.34\log_{10}(k/D)) & ; \quad 0.0001 < k/D < 0.0004 \\ 1.0 & ; \quad 0.0004 < k/D \end{cases} \qquad (103)$$

Regarding the inertia coefficients their values are suggested to be 2.0 for smooth cylinder and 1.8 for rough cylinder. A summary of the recommended values for the inertia and drag coefficients, is given in Table 6.

Table 6 : Recommended hydrodynamic coefficients for circular cylinders

Roughness	C_D	C_M
Smooth ($k/D < 0.0001$)	0.65	2.0
Rough ($k/D > 0.0004$)	1.0	1.8
Intermediate	Eq (103)	2.0

In post-critical conditions, for $\mathrm{K_C}$ numbers lower than say 30-40, the dependency of the drag coefficient on $\mathrm{K_C}$ number should also be taken into account. The following expression is proposed in SNAME (2008):

$$C_D(\mathrm{K_C}, k/D) = \quad C_D(k/D) * \begin{cases} 1.45 & ; \quad \mathrm{K_C} < 10 \\ 2/(\mathrm{K_C} - 5)^{0.2} & ; \quad 10 < \mathrm{K_C} < 37 \\ 1.0 & ; \quad 37 < \mathrm{K_C} \end{cases} \qquad (104)$$

where $C_D(k/D)$ is given by (103).

4.3.3 Drag coefficient for low $\mathrm{K_C}$ values

Even if, at low $\mathrm{K_C}$, the loads are dominated by inertial forces the correct evaluation of the drag forces is very important for the determination of the damping of the slow drift motion of some off shore platforms (semi-submersible platforms, TLPs $\ldots$) where the $\mathrm{K_C}$ lies approximately in between 0 and 5. An approximate expression for the drag coefficient of the cylinder at small $\mathrm{K_C}$ values is:

$$C_D = \frac{3\pi^3}{2\mathrm{K_C}\sqrt{\pi\beta}} \tag{105}$$

This means that C_D is inversely proportional to $\mathrm{K_C}$ which makes the viscous damping force no longer quadratic but linear. The domain of validity of the formula (105) is quite limited and one example is shown in Figure 34 (left).

Semi-submersible platforms and TLPs usually have rectangular pontoons with sharp or chamfered corners. This means that flow always separate regardless of the $\mathrm{K_C}$ value. Typical values of the drag coefficient for square cylinder at low values of $\mathrm{K_C}$ is presented in Figure 34 (right) where significant increase of the drag coefficient, compared to circular cylinder (Figure 34 (left)), can be observed. That is why the pontoons with sharp corners are preferable when one is concerned with damping at low frequency motions of semis or TLPs, even if the mean current loads will increase.

Figure 34: Drag coefficients for low $\mathrm{K_C}$ numbers.
Left – circular cylinder at Stokes parameter $\beta = 1035$ (from Summer & Fredsoe),
Right – square cylinder at β from $2.5 \cdot 10^4$ (triangles) to $7 \cdot 10^4$ (squares) (from Molin 2002)

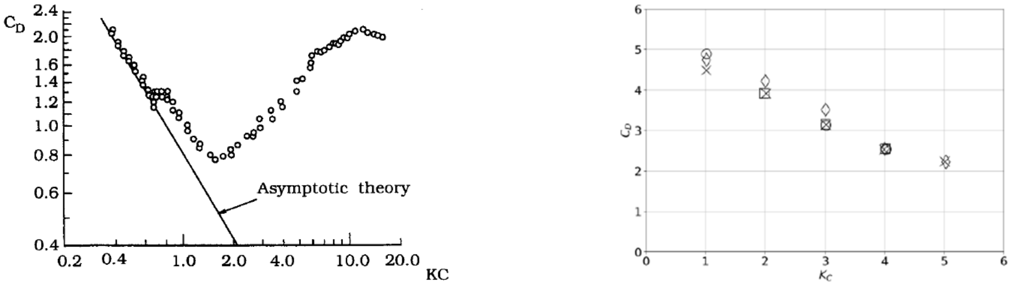

4.4. Perpendicular oscillatory flow

4.4.1 Introduction

The case of the perpendicular oscillatory flow with respect to the steady uniform flow is relevant for the vortex induced vibrations in particular but not only. The representative flow conditions are defined as follows:

$$U = U_0 \quad , \quad v(t) = -A\omega \sin \omega t \tag{106}$$

where U_0 is the current intensity in x direction and A is the amplitude of the oscillatory cylinder motion in y direction with circular frequency ω.

4.4.2 Added mass and drag coefficients

The added mass and drag coefficients are obtained through the fitting of the experimental results to the transverse hydrodynamic load defined by:

$$F_y = -\varrho C_{ay} S\dot{v} - \frac{1}{2}\varrho C_{Dy} D v|v| = \varrho C_{ay} S A\omega^2 \cos \omega t + \frac{1}{2}\varrho C_{Dy} D A^2 \omega^2 \sin \omega t\,|\sin \omega t| \tag{107}$$

In Figure 35 typical experimental results are presented for C_{ay} and C_{Dy} vs the reduced velocity (98) for different ratios A/D.

The Reynolds number was in-between 5000 and 25000, that is the flow was in the subcritical regime. It can be seen that the added mass coefficient, from its reference value 1 at low U_R values, first increases to about 2, then drops down sharply to negative values at $U_R \sim 5$, and remains negative. As for the drag coefficient C_{Dy}, it also takes negative values for some combinations of U_R and A/D, in particular for reduced velocities in-between 5 and 6.

An important effect of the cross-flow motion is that the mean inline force increases, as compared to the fixed cylinder case. An intuitive interpretation is that the effective frontal area increases. Some formulations have been proposed for the increase in the drag coefficient. In the absence of more reliable data, the following expressions can be used for the circular cylinder:

$$C_D(A/D) = C_D(0)[1 + 1.16(W_R - 1)^{0.65}] \quad , \quad W_R = \left(1 + 2\frac{A}{D}\right)\frac{f}{f_0} \tag{108}$$

where f is the oscillation frequency and f_0 is the Strouhal (vortex shedding) frequency.

Figure 35: Circular cylinder oscillating transversally to a current.
Added mass C_{ay} and drag coefficient C_{Dy} vs the reduced velocity U_R, for different ratios A/D
(from Sarpkaya, 1978)

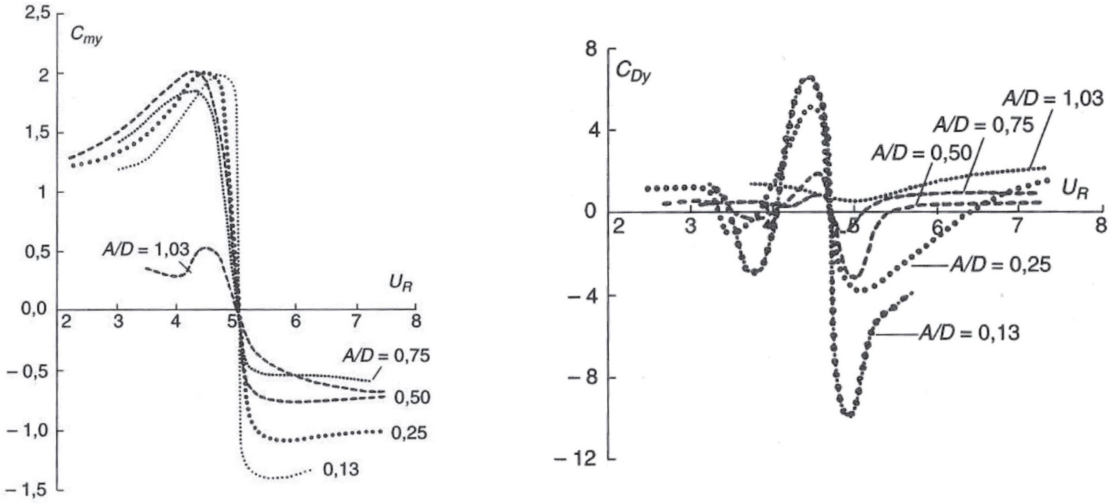

4.5. Lift coefficient

4.5.1 General

The lift coefficient is usually evaluated by fitting the experimental results or alternatively by the CFD numerical simulations. For the constant lift force in steady uniform flow the lift coefficient is defined as the ratio of the lift force divided by $\frac{1}{2}\varrho DLU^2$ with L the length of the weighted part of the cylinder

In the case of an oscillatory lift force the lift coefficient is defined as the amplitude, and sometimes the standard deviation, of the same ratio. A wide scatter is found in the literature and the typical values are presented in Figure 36 where the results of different experiments on circular cylinder, all for short weighted length cylinders, were compiled together.

Figure 36: Lift coefficient compiled (Norberg (2000))

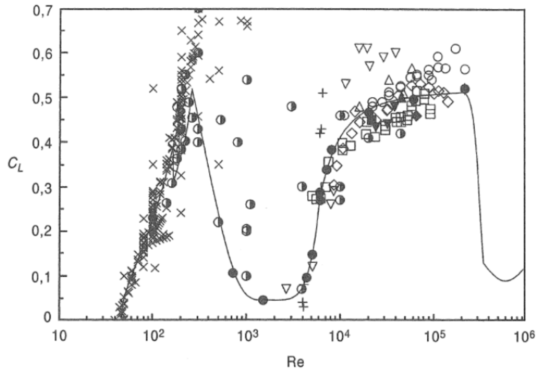

4.6. Vortex shedding

4.6.1 General

In the case of the cylinder in uniform flow a vortex shedding occurs. A relevant non – dimensional number is the Strouhal number (83) where the frequency f_0 is the frequency of vortex shedding. When the vortex shedding frequency is close to the natural frequency of the system resonant response can occur (Vortex Induced Vibrations (VIV), Vortex Indected Motions (VIM), …)

4.6.2 Characteristic flow regimes

The occurrence and the frequency of the vortex shedding is dependent on Reynolds number meaning that the Strouhal number will depend on Reynold number as shown in Figure 37. In the subcritical and transcritical regimes the lift force is quasi sinusoidal and takes place at the frequency such that the Strouhal number is equal to 0.2 in the subcritical regime and somewhat higher in the transcritical case. In the critical and supercritical regimes the lift force is quite erratic with no dominant frequency.

Figure 37: Strouhal number vs Reynolds number

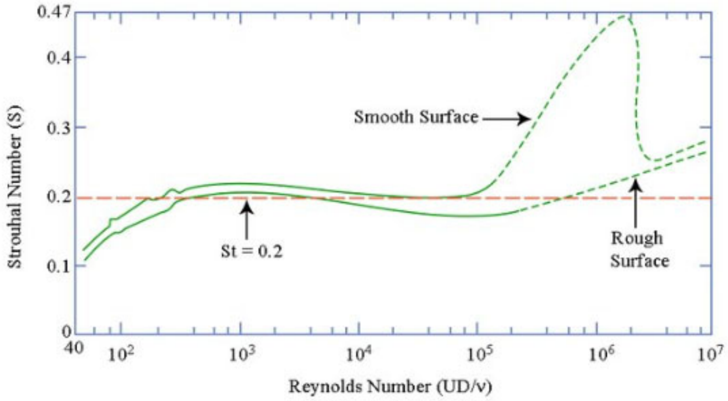

4.6.3 Correlation length

In the context of vortex shedding phenomena the importance of the correlation length is to be considered. The correlation length stands for the length over which the vortex shedding is synchronized. In the subcritical regime the correlation length usually lies in between 2 and 6 cylinder diameters.

4.6.4 Lock in phenomena

In the subcritical regime the Strouhal number is equal to 0.20. A reduced velocity equal to 5 means that the oscillation frequency is equal to the vortex shedding frequency for a fixed cylinder. When the cylinder is undergoing forced motion, the vortex shedding frequency adjusts, over some U_R range around 5, to the oscillation frequency. This is known as lock-in. The intensity of the shed vortices is increased and the phase shift of the lift force, with respect to the imposed motion, varies rapidly and leads to C_{ay} and C_{Dy} varying quickly with U_R. When the ratio A/D increases, the vortex shedding becomes disorganized, leading to the drag coefficient becoming positive beyond some A/D value. That the drag coefficient is negative for some combinations of U_R and A/D suggests that the cylinder sucking in energy from the fluid, unstable behaviors may be observed for an elastically supported cylinder. The phenomena are known as Vortex Induced Vibrations (VIV).

4.6.5 Non circular sections

Lift forces induced by vortex shedding are observed for most cylinder shapes, even though they have sharp corners. In the case of square cylinders, for instance, the Strouhal number drops to $0.13 - 0.15$, but the lift force is much weaker than in the circular case.

4.7. Physical effects which affect the load coefficients

4.7.1 Wall effects

The presence of a wall (sea bed or any other flat boundaries) significantly influences both the added mass and the drag coefficient. As the cylinder approach a wall both the added mass and drag coefficients increase. The typical modifications are shown in Figure 38.

4.7.2 Effects of large structures

For slender structures operating in the presence of large floating bodies the kinematics which should be used in the different expressions for the forces, need to take into account the modifications of the flow due to the presence of the large bodies. This means in particular that the diffraction/radiation effects should be included when evaluating the inflow conditions along the slender structure.

Figure 38: Influence of a wall on added mass and drag force coefficients for the cylinder in oscillatory flow. Supercritical flow with $K_C > 20$ is of concern for drag coefficient

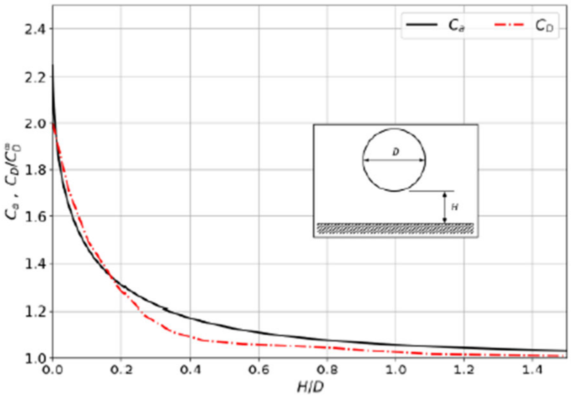

4.7.3 Blockage effects

Cylinders are frequently grouped together, for instance as clusters of risers or tubular elements of jacket frames. Some cylinders may be located in the wakes of upstream cylinders and therefore subjected to currents of reduced velocity. This is known as the shielding effect. The upstream cylinders themselves are subjected to a reduced current, as compared to the case where they would be isolated, by the presence of the neighboring cylinders: this is the blockage effect. Drag loads may then be significantly decreased as a result of blockage and shielding.

4.7.4 Wake effects

In the case of 2 cylinders operating in line (Figure 39), the forces on the downstream cylinders are influenced by the wake. The main influence comes from the incoming speed reduction. At high Reynolds numbers and at some distance from a cylinder, the flow becomes homogenized and the velocity profile takes a Gaussian shape. The following simplified expression for velocity profile in the wake of 2D flow has been proposed by Schlichting (1979):

$$U_d(x,y) = U - 0.95U\sqrt{\frac{C_D D}{x}}\exp\left\{-11.3\frac{y^2}{C_D D x}\right\} \qquad (109)$$

With a C_D value of 1 one gets that the velocity is decreased by 30 % at a distance of 10 diameters (in $y = 0$), so the drag load is decreased by 60 % as compared to an isolated cylinder.

Figure 39: Wake behind the cylinder

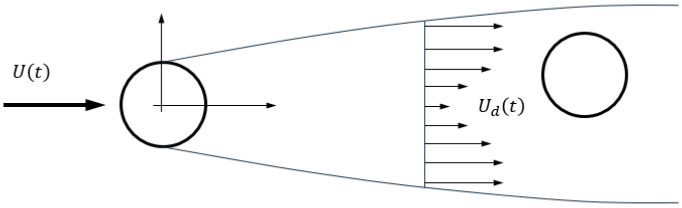

4.7.5 Three dimensional effects

The drag loads are directly related to the velocity increase of the outer flow in the neighborhood of the separation points of the boundary layers. These increases of the speed are higher for plane flows than for "equivalent" three-dimensional geometries. In the circular cylinder case, the potential flow velocity at $\pm 90^o$ from the stagnation point is 2 times the incoming flow velocity. For a sphere it is only 1.5 times. As a consequence, in the subcritical range, the drag coefficient of a sphere is about 0.5, when it is 1.2 for a circular cylinder. In transcritical flow it drops as low as 0.2 Similarly the drag coefficient for a cube is about 1 i.e. half the square cylinder case. It is thus very important to account for these effects when the structure becomes locally 3D.

5. Flow induced responses

5.1. Introduction

5.1.1 General

The slender cylindrical structures operating in steady and/or oscillatory incident flow may experience the dynamic response under some conditions. Typical examples are the flow induced structural vibrations such as:

- Vortex Induced Vibrations (VIV) and Vortex Induced Motions (VIM)
- Wake induced vibrations
- Galloping and flutter

The flow induced vibrations can occur both in the direction transverse or in-line with the flow direction. When VIV and VIM occur, the increase of drag coefficients need to be accounted for.

5.2. Vortex induced vibrations/motions

5.2.1 General

An elastically supported cylinder in a current can naturally oscillate in the cross-flow direction if its natural frequency is close to the vortex shedding frequency. Examples are numerous in offshore, from towing cables to risers but also at larger scale for whole floating bodies such as Spar, semi-submersible or TLP platforms. In the case of cables and risers the wording Vortex Induced Vibrations (VIV) is used and in the case of the floating bodies (Spar, semi, TLP …) the wording Vortex Induced Motion is used. From hydrodynamic point of view the modelling principles are very similar and the difference lies in the modelling of the relevant stiffness which, in the case of cables and risers, is induced by the genuine structural stiffness while in the case of the floating bodies, it is induced by the mooring system.

5.2.2 Mathematical modeling

The simplest mathematical model of the cross flow motion equation is the simple mass-spring dynamic model, from which the natural period of the system can be easily deduced:

$$(M + M_a)\ddot{Y} + B\dot{Y} + KY = F_Y(t) \qquad , \qquad T_n = 2\pi\sqrt{\frac{M + M_a}{K}} \tag{110}$$

where M is the mass of the system, M_a is the added mass (in general might also be influenced by the response), B is the mechanical damping, K is the stiffness of the system and F_Y is the transverse hydrodynamic load.

When the current is turned on, spontaneously, the cylinder undergoes nearly periodic crossflow motion, if the reduced velocity $U_{Rn} = UT_n/D$ is comprised within some interval, typically $[5 - 8]$ in air, but usually much larger in water. VIVs are self-limited phenomena and no matter how small the mechanical damping B can be, the amplitude A of the cross-flow motion hardly exceeds one or one and a half diameter. The reason is that, beyond some A/D value, the vortex shedding process gets disorganized and the drag coefficient becomes positive.

A more sophisticated models for VIV response of 2D cylinder are also available. One of these models which are employed quite often, is based on the use of the Van der Pol oscillator for modelling the nonlinear lift force. The VIV dynamic equation (110) and the Van der Pol oscillator are coupled and solved together in time giving the VIV amplitude (Facchinetti (2004)).

5.2.3 Typical features of the VIV response

One reason why VIVs take place in some U_{Rn} range, and not just at the inverse of the Strouhal number, is that the drag coefficient C_{Dy} is negative over some U_R interval where the vortex shedding frequency locks to the oscillation frequency. Another reason, which is specific to VIVs occurring in water, is that the added mass varies quite a lot with the reduced velocity and amplitude. In air this is of no effect since the added mass is negligible compared to the actual mass, but in water it is appreciable. An important parameter is the mass ratio $m^* = M/(\varrho\pi D^2/4)$ which allows to measure the importance of the mass over the buoyancy. Typical values of the mass ratio for risers are between 1.5 and 2. If one considers that, in air, VIVs take place in the U_R range $[5 - 8]$ and that the added mass coefficient varies from a maximum value of 2 for $U_R \simeq 5$ down to -0.5 at the end of the locking region one deduce that in water VIVs take place in the following U_{Rn} range:

$$5\sqrt{\frac{m^* + 1}{m^* + 2}} \leq U_{Rn} \leq 8\sqrt{\frac{m^* + 1}{m^* - 1/2}} \tag{111}$$

This means that the lock-in region is smaller for low mass ratio (air) and larger for the large mass ratio (water). This can be seen in Figure 40 where typical VIV response is shown in the air and in the water.

Figure 40: Typical VIV response (from Sarpkaya (2010))

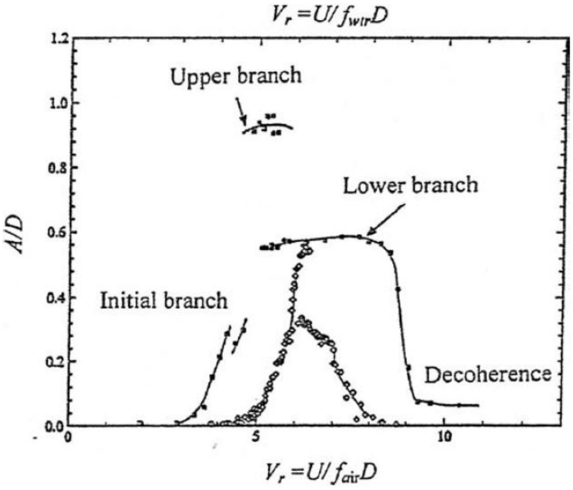

5.2.4 VIV response – 2D case

The amplitude of the VIV response for cylinder in 2D flow can be calculated from the equation (110) provided the values of the added mass, damping and the excitation are available. The excitation force vector is usually expressed as a lift force with the lift coefficient depending both on the characteristics of the incoming flow as well as on the reduced velocity and the amplitude of the response. Experimental data can be used to derive the empirical expressions for the lift coefficient and the motion equation can be solved to give the maximum response. Based on the extensive experimental campaign, in Govardhan & Williamson (2006), the following formula was proposed for maximum amplitude of the VIV response:

$$\left(\frac{A}{D}\right)_{max} = (1 - 1.12\alpha + 0.30\alpha^2)\log_{10}(0.41\mathrm{Re}^{0.36}) \qquad (112)$$

where α is the stability parameter $\alpha = (1 + m^*)\zeta$ with ζ the damping ratio $\zeta = B/\left(2\sqrt{K(M + M_a)}\right)$.

The validity of the 2D approximation depends on the aspect ratio between the cylinder length and its diameter. Indeed, beyond some length, it is known that the eddy shedding is not synchronized all over the cylinder wall. For a fixed cylinder the correlation length is only a few diameters in the subcritical regime and much less in the critical regime.

5.2.5 VIV response - Cables and risers

In the case of elongated cables and risers two new problems arise:

- there is no longer one resonant frequency of the cross flow response, but several, associated with the natural modes of the deformation.
- in the case of risers, the current velocity usually varies from the seafloor up to the free surface. As a result several modes may participate, each mode being excited in some depth region while elsewhere it is damped by drag forces.

The simplest approach which is followed most often in practice is to consider the flow in each strip to be independent and to represent the longitudinal deformation of the line by the modal superposition method:

$$y(z,t) = \sum_{n=1}^{N} A_n(t)Y_n(z) \qquad (113)$$

where $A_n(t)$ denotes the time dependent modal amplitudes and $Y_n(z)$ denotes the space (here only vertical component) dependent mode shapes.

This means that the modal structural analysis of the line is required in preprocessing stage. This also means that the dynamic motion equation is solved for the modal amplitudes $A_n(t)$. The modal excitation forces are evaluated by projecting the individual contributions of each strip onto the mode shapes and by integrating them over the wetted part of the line. Several modes having the frequencies likely to produce the reduced velocity in the lock-in range (111) needs to be considered. It is also important to mention that, due to the fact that the current intensity is varying over the water depth, the different structural modes will be excited at different water depths and all of them needs to be considered with the corresponding excitation vector.

5.2.6 In line Vortex Induced Vibrations

For cylinders in sinusoidal motion in-line with the current, negative drag coefficients are obtained experimentally for certain (low) values of the relative amplitude A/D and of the parameter U_0T/D, with U_0 being the current velocity and T the period of oscillation. This means that the cylinder extracts energy from the fluid and suggests the possible occurrence of instabilities. It follows that, for a cylinder on elastic support, in-line instabilities are likely to appear for the corresponding values of the reduced velocity defined here as U_0/f_nD (f_n being the natural frequency in calm water).

In practice there are two areas of instability (see Figure 41):

- a first zone for reduced velocities between (roughly) 2 and 3, where the vortex shedding remains alternated. The reduced speeds are half of those where cross flow vibrations appear, which makes sense since the frequency of the in-line load is twice the lift frequency.
- a second zone for lower reduced velocities, between 1 and 2, where the vortex shedding is symmetrical

The amplitude of the in-line response is small, typically A/D is less than 0.15. However in-line VIVs concern higher elastic modes than the cross flow VIVs, with the result that the induced bending stresses are comparable.

Figure 41: In-line VIV phenomena (from Molin (2002))

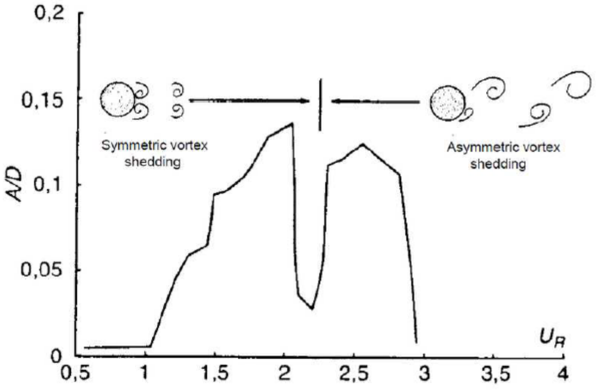

5.2.7 Mitigation of the Vortex Induced Vibrations

Vortex induced vibrations are generally detrimental by the fatigue they cause to the structures. As such, for risers, the stresses due to the higher order modes are the most damaging since, at constant vibration amplitude, the curvatures, and therefore the stresses, are larger and the number of cycles increases with the frequency. The increase in drag can also be detrimental, for instance the mooring loads on a single-column platform (SPAR) can be greatly magnified. The best way to get rid of VIVs is to make sure that the reduced velocities associated with the critical modes of vibration do not take values in the wrong range, between 4 and 10 (or more, in the case of low mass ratios). This can mean adjusting the structural or mooring stiffness's, or the mass distribution. This remedy is hardly applicable to structures like risers which have many modes of vibration. Another way is to increase energy dissipation, by playing either with the structural damping, or with the hydrodynamic damping. For example, flexible risers are reputed to be less prone to VIVs than rigid risers, the friction between the constitutive layers dissipating a large amount of energy. Finally one can try to act at the very source of the problem, by removing or reducing the excitation. This is usually achieved by installing the anti-VIV devices along the cylinder length. Typical practical example are the helical strakes.

5.3. Other flow induced oscillations

5.3.1 Wake induced oscillations

Different types of instabilities may appear in the case of arrays of cylinders, under the action of current. When a cylinder is in the wake of an upstream cylinder, it may vibrate under the action of the vortices shed by the upstream cylinder, when its natural frequency coincides with the shedding frequency. Unstable dynamic responses may also occur at larger values of the reduced velocity, due to the non-uniformity of the time-averaged wake flow. These behaviors are known as Wake Induced Oscillations (WIOs) and are schematically shown in Figure 42. Their modelling is rather complex.

Figure 42: Typical trajectory of the leeward cylinder

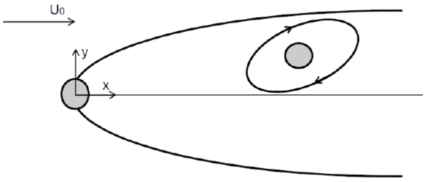

5.3.2 Galloping

Galloping and flutter are another type of instabilities which are not due to alternate vortex shedding. These phenomena that take place at higher values of the reduced velocity well beyond the VIV range. Because of the high reduced velocity they can be efficiently modeled through quasi-steady approaches.

Galloping is due to wake instability which produces the transverse force in the direction opposite to intuition. Only one degree of freedom is involved. Reference configuration and typical transverse force coefficient C_Y (boddy fitted) for a square cylinder of side b, for different incident angles is shown in Figure 43. For convenience the coordinate system is aligned with the symmetry axis of the cylinder. We can observe a peculiar shape in the range $\alpha = [-15°, 15°]$ with a sign conflicting with intuition: the projections of the force and current velocity on the y_S axis are in opposite directions. This fact might induce the negative total damping for the elastically supported cylinder. The linearization of the dynamic motion equation of the elastically supported cylinder allows to identify the instability conditions by requiring the total damping to be positive. This can be written as:

$$\frac{\partial C_Y}{\partial \alpha}(0) < \frac{4\zeta\omega_0(M + M_a)}{\varrho b U_0} = -4\pi\frac{K_S}{U_R} \tag{114}$$

where ζ is the linear damping ratio, ω_0 the natural frequency, $M + M_a$ the mass plus added mass and K_S is the stability parameter known as Scruton number $K_S = 2\zeta(M + M_a)/(\varrho b^2)$.

Figure 43: Square section in oblique flow conditions and the transverse force coefficient for a square section (from Molin (2002))

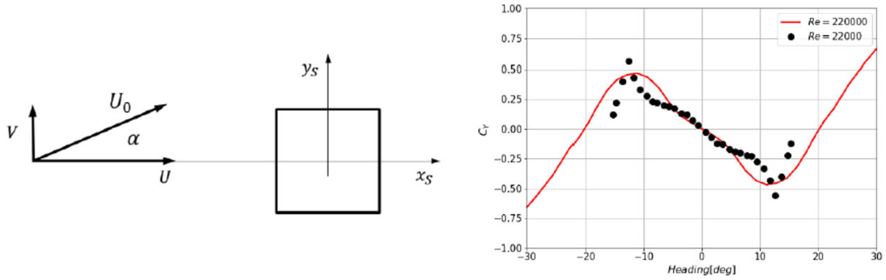

The above condition implies that if $\partial C_Y/\partial\alpha$ is negative meaning that the instability will inevitably occur beyond some U_R value. This is different from VIV problem where the instability is closely linked to the natural frequency of the system. Another difference with the VIV is that the galloping, at least theoretically, is not self bounded. In Figure 44 the typical experimental results of galloping on a square cylinder of side b in current of intensity U_0 are shown.

Most polygonal shapes are susceptible to galloping instabilities. In the case of the circular cylinder there cannot be galloping since the current load is in-line with the flow, meaning that $\partial C_Y/\partial\alpha\,(0)$ is positive. However shapes not so different from circular, like some cross-sections of riser towers, are prone to galloping. Galloping may also affect the rotational (torsional) modes of motion in the multiple risers configurations. Furthermore, when the frequency of the rotational and the translational modes are close to each other the so called flutter instability can occur.

Figure 44: Normalized amplitude of the galloping response vs the reduced velocity $\mathbf{U_R = U_0 T_0/b}$, with $\mathbf{T}$ either the still water value or the actual oscillation period (from Molin et al., 2012)

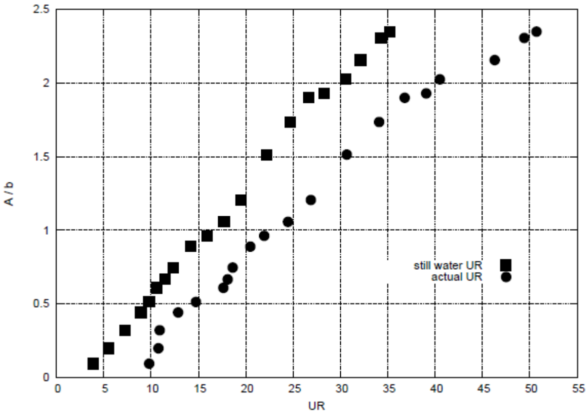

5.3.3 Flutter

Flutter instability is due to mechanical coupling between two degrees of freedom, for instance heave and pitch in the case of foils. It occurs when the two degrees of freedom are coupled through off diagonal terms in the stiffness matrix. For certain combination of the parameters, it can happen that the same natural frequency is associated with both modes of motion (heave and pitch), one of which becomes unstable. In marine engineering this instability should be considered for ship roll stabilization with flaps. It can also be taken advantage of flutter, as a way to extract energy from current, or as a propulsive force. A parent instability is the fishtailing behavior of single point moored ships, under the action of wind or current.

6. Aerodynamic loads on slender bodies

6.1. Introduction

6.1.1 Offshore wind turbines

The energy extraction from wind became a very common way of producing the “green” energy. Both fixed and floating supporting structures are used. Compared to the classical off-shore structures which are used for oil-exploration there is no difference in the modelling of the wave and current loading and the same principles apply. The main difference concerns the aerodynamic loading on the wind turbine, which need to be evaluated separately and added to the global loading before solving for equilibrium of the system. There exist different models for evaluation of the aerodynamic loading on the turbine blades, and the most important appear to be the so-called wake models among which the model based on blade element momentum theory is used most often. More advanced wake models based on generalized dynamic wake theory (see Moriarti et.al. (2005)) or even CFD based numerical models are also sometimes employed but not so often.

6.1.2 Aerodynamic loads

The aerodynamic loads on slender bodies are very similar to the hydrodynamic loads: They can be decomposed into a drag force, collinear to the relative wind velocity, and a lift force perpendicular to the drag force. Both the drag and the lift coefficient depend on the angle of incidence. Because the air density is much smaller than the water density, the inertial forces are usually neglected.

$$F_{drag} = \frac{1}{2}\varrho_a C_D D U|U| \tag{115}$$

$$F_{lift} = \frac{1}{2}\varrho_a C_l D U|U| \tag{116}$$

where ϱ_a is the air density, D is the characteristic width, U is the flow velocity and (C_D, C_l) are the drag and lift coefficients.

Non lifting bodies such as the tower of an Offshore Wind Turbine, or tubular topsides or jacket structure, are submitted only to drag loads. Lifting bodies, such as blades, are submitted to drag and lift loads.

6.1.3 Coupling of the local and global flow

Unlike hydrodynamic loads, where the incoming flow is assumed to be uniform and not influenced by the immersed floating body, there is usually a strong coupling between the incoming aerodynamic flow and the wind turbine blades: the velocity and the direction of the incoming flow is largely modified by the presence of the wind turbine. Hence the drag and lift forces cannot be evaluated directly by the equations (115),(116) with the incoming wind velocity. This coupling of the local and global flow can be done using the Blade element Momentum Theory described below.

6.2. Blade element momentum theory

6.2.1 Basic principles

Blade element momentum theory (BEM) is an extension of the global actuator disk theory (or momentum theory) first proposed by Rankine and Froude in 19th century, for ship propeller applications. The BEM theory is usually attributed to Betz (1920) and Glauert (1935) who applied it to airplane propellers. Blade element theory assumes that the blades can be divided into a certain number of small elements which are modelled independently using the simple 2D airfoils whose aerodynamic forces can be calculated from the local flow conditions using the pre-calculated or empirical drag and lift coefficients. The rotor subdivision and the local 2D airfoil model are sketched in Figure 45 where both the local inflow conditions and the corresponding forces on airfoil are shown. The v_{e-ip} and v_{e-op} are the local in plane and out of plane velocities induced by the blade deformations in case when the blades are considered to be deformable.

The velocities in the axial and the tangential directions are defined by introducing the axial and the rotational induction factors a and a':

$$a = \frac{U_\infty - U}{U_\infty} \quad , \quad a' = \frac{\omega}{\Omega} \tag{117}$$

where U_∞ is the incoming flow velocity and Ω is the rotational velocity of the rotor.

Once the local forces evaluated the thrust and torque at each annulus can be evaluated:

$$\begin{aligned} dT &= N_B \frac{1}{2} \varrho V_{total}^2 (C_L \cos\phi + C_D \sin\phi) c dr \\ dQ &= N_B \frac{1}{2} \varrho V_{total}^2 (C_L \sin\phi - C_D \cos\phi) c r dr \end{aligned} \tag{118}$$

where N_B is the number of blades, C_L and C_D are the lift and drag coefficients respectively, and c is the chord of the airfoil.

At the same time the momentum theory is used to calculate the thrust and torque extracted by each rotor annulus which gives:

$$\begin{aligned} dT &= 4\pi r \varrho U_\infty^2 (1-a) a dr \\ dQ &= 4\pi r^3 \varrho U_\infty \Omega (1-a) a' dr \end{aligned} \tag{119}$$

By requiring the equality of (118) and (119) an iterative procedure can be used until the induction factors (a and a') and inflow angles ϕ have converged to their final values.

Figure 45: Subdivision of the rotor (left), the local velocities and flow angles at airfoil (right top) and the corresponding forces (right bottom). (from Moriarti et al. (2005))

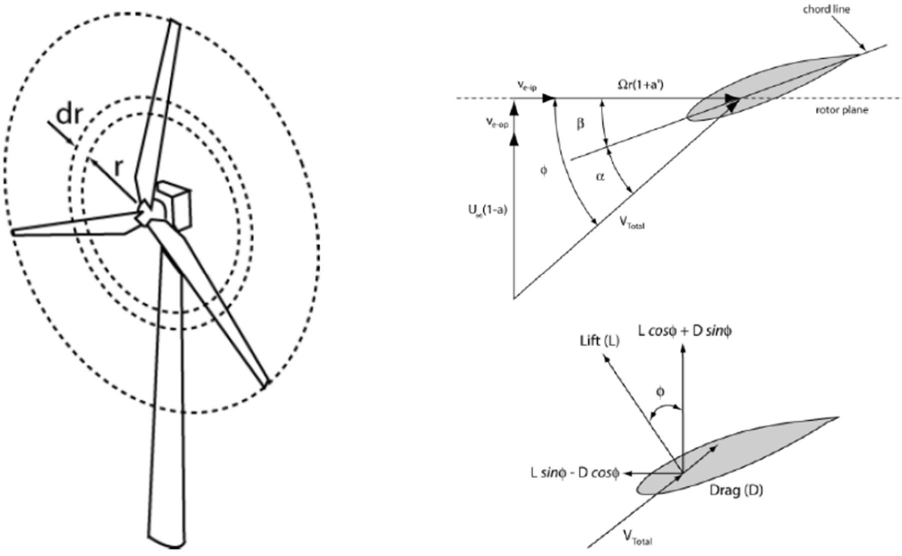

6.2.2 Improved blade element momentum theory

The main advantage of the BEM theory method lies in its relative simplicity and its fairly good approximation of the wind loads in many situations. However the BEM theory has several limitations which can be approximately corrected by some relatively simple means. These corrections include:

- tip and hub loss models to account for vortices shed at these locations
- Glauert correction to account for large induced velocities $(a > 0.4)$
- skewed wake correction to account for the incoming flow deviation from axial direction
- accounting for unsteadiness of the flow and the dynamic wake effects (DBEMT)

With these corrections the BEM theory can be applied to a wider range of practical applications. However, even with the above corrections, the BEMT should be avoided for unsteady or highly skew flows. The so called generalized dynamic wake model (GDW), based on the work of Peters and He (1991) is preferred but its implementation appears to be much more complex.

The most widely used numerical tool based on BEM theory is *Aerodyn* (Moriarti et al. (2005)) which is provided by NREL (National Renewable Energy Laboratory) in open source version. This tool became a kind of standard today and was implemented in most of the current software for the analysis of the wind turbines. All the mentioned options are included in this tool.

7. List of references

[1] Betz A., 1920.: “Das Maximum der theoretisch möglichen Ausnutzung des Windes durch Windmotoren”, Zeitschrift für das gesamte Turbinenwesen, 26.

[2] Facchinetti M.L., de Langre E., Biolley F. 2004.: “Coupling of structure and wake oscillators in vortex-induced vibrations”, Journal of Fluids and Structures, 19.

[3] Glauert, H. 1935.: ”Airplane Propellers.” Aerodynamic Theory (W. F. Durand, ed.), Div. L, Chapter XI. Berlin:Springer Verlag

[4] Govardhan R.N., Williamson C.H.K. 2006.: “Defining the ’modified Griffin plot’ in vortex induced vibration: revealing the effect of Reynolds number using controlled damping”, J. Fluid Mech., 561.

[5] ISO/TR 19905-2, 2012.: “Petroleum and natural gas industries – Site specific assessment of mobile offshore units. Part 2: Jack-ups commentary and detailed sample calculations.”

[6] Keulegan, G.H., Carpenter, L.H., 1958.: “Forces on Cylinders and Plates in an Oscillating Fluid”, Journal of Research of the National Bureau of Standards, Volume 60, No. 5, May 1958

[7] Molin B., 2002.; “Hydrodynamique des structures off shore.”, Editions Technip

[8] Molin B., Remy F., Rippol T., Cinello A., le Hir E., Berhault C., Dassibat C. 2012 “Experimental investigation on the galloping response of square cylinders at high Reynolds numbers”, in Proc. 6th Intl. Conf. on Hydroelasticity in Marine Technology, Tokyo.

[9] Moriarti P.J. & Hansen A.C., 2005.: “AeroDyn theory manual.”, NREL/EL-500-36881

[10] Morison J.R., O’Brien M.P., Johnson J.W. & Schaaf S.A. 1950.: “The force exerted by surface waves on piles”, Petrol. Trans., 189.

[11] Norberg C., 2000.: “Flow around a circular cylinder: aspects of fluctuating lift”, J. Fluids and Structures, 15.

[12] Orcina, 2020; :”Orcaflex – Theory manual”

[13] Peters D.A.; He C.J., 1991.: “Correlation of Measured Induced Velocities with a Finite-State Wake Model.” Journal of American Helicopter Society, July

[14] Sarpkaya T. 1978. “Fluid forces on oscillating cylinders”, J. of Waterway, Port, Coastal and Ocean Division, ASCE, 104, 275-290.

[15] Sarpkaya T., 2010.: “Wave forces on offshore structures”, Cambridge University Press

[16] Schlichting H. 1979.: “Boundary Layer Theory”, New York: McGraw-Hill Book Company.

[17] SNAME, 2008 “Commentaries to Recommended Practice for Site Specific Assessment of Mobile Jack-Up Units”, T&R Bulletin 5-5.

[18] Sumer B.M. & Fredsoe J., 1997.: “Hydrodynamics around cylindrical structures.”, World Scientific, Advanced Series on Ocean Engineering, Vol. 26.

Section 4 Loads on Large Bodies

1. General

1.1. Introduction

1.1.1 Coordinate systems

Different conventions are sometimes used in the literature and the conventions presented here are in line with the Bureau Veritas numerical tools. Reference is made to Figure 46 and three coordinate systems are defined:

(O, X, Y, Z)	Earth fixed coordinate system with the origin at the mean free surface
(G, x', y', z')	Body fixed coordinate system with the origin at the body center of gravity
(o, x, y, z)	Hydrodynamic coordinate system with the origin at the mean free surface and fixed to the instantaneous mean position of the body

The Earth fixed coordinate system is the inertial coordinate system while the other two coordinate systems are not. The instantaneous mean position of the body is moving with the body by slowly varying motion in the horizontal plane (X_o, Y_o, ψ).

Figure 46: Different coordinate systems and the directions of the environmental loads

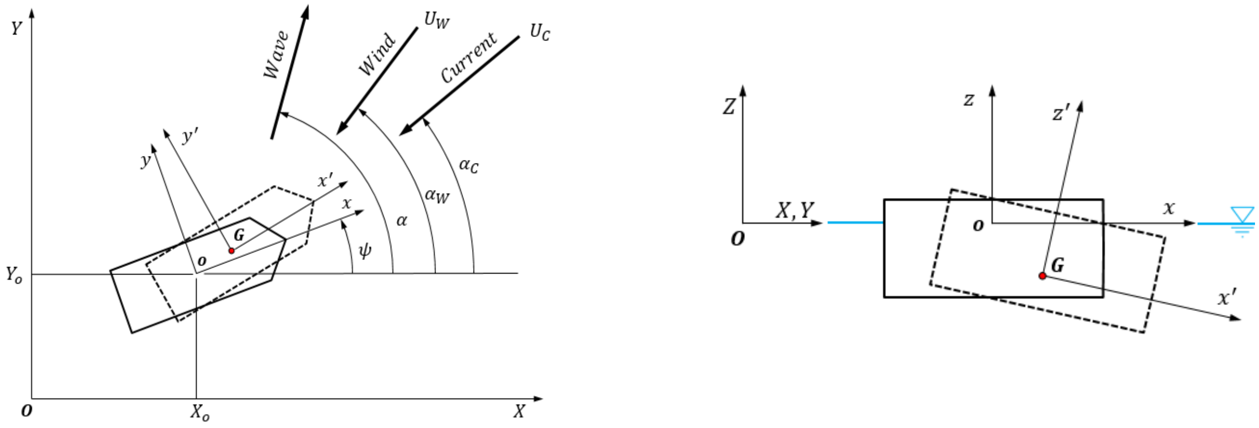

The following definitions are introduced:

ψ	Slowly varying yaw angle (orientation of the hydrodynamic coordinate system vs earth fixed coordinate system
α	Wave incidence relative to Earth fixed coordinate system (going to)
U_C	Current velocity
α_C	Current incidence relative to earth fixed coordinate system (coming from)
U_W	Wind velocity at $10m$ elevation from sea level
α_W	Wind incidence relative to earth fixed coordinate system (coming from)
β	Wave incidence relative to hydrodynamic coordinate system, $\beta = \alpha - \psi$
β_C	Current incidence relative to hydrodynamic coordinate system, $\beta_C = \alpha_C - \psi$
β_W	Wind incidence relative to hydrodynamic coordinate system, $\beta_W = \alpha_W - \psi$

1.2. Classification of the loads

1.2.1 Global and local loads

The external loads consist of localized pressures and frictional forces on one side and the gravity and the inertia loads on the other side. Depending on the physical phenomena the extent of the loading can be of local or global character. In the present context, typical global loads are the seakeeping loads and the typical local loads are the local impact loads (slamming, sloshing, green water …).

1.2.2 Potential flow loads and loads of viscous origin

In the present context of the bodies operating at sea one of the main parts of the loading originates from hydrodynamics. This part of the loading can be accurately evaluated under the potential flow assumptions. This is especially true for the global seakeeping loads but, in some cases, can also be acceptable for the evaluation of the local impact loads, or the inviscid part of the maneuvering loads

There exist loads where the potential flow assumptions are not justified and other effects are more important. Typical examples are the current and wind induced loads where the effects of viscosity and flow separation play dominant role. These loads can be evaluated either by model tests or using CFD numerical models. When using the model tests, due to impossibility to consistently scale all the relevant nondimensional numbers, a special care should always be taken to account for the associated scale effects. The main advantage of potential flow theory is that the resulting numerical models are significantly faster than the equivalent CFD models.

1.2.3 Nonlinear loads and linear loads

Strictly speaking, all the loads contain a certain degree of nonlinearity. However, in some conditions the governing equations can be linearized without significantly affecting the accuracy of the solution. Solving the linear problem being much easier, the linearization is highly appreciated when possible. There exist different aspects of the linearization and the linear potential flow theory assumption represents in itself a particular type of linearization. Within the potential flow models, the linearization is mainly employed to simplify the boundary conditions on the body and at the free surface. The main practical advantage of the linearization lies in the fact that the fluid domain become fixed and the numerical solutions of the Boundary Value Problem (BVP) becomes much easier. When linearizing the problem, it is also common to formulate the BVP at higher orders of approximation (second order, third order …). This is useful for capturing the physical phenomena which happen outside the principal frequencies contained in the sea spectra. In the present context the second order models are particularly useful for the characterization of the low frequency behavior of the moored structures and the high frequency response of “stiff” systems such as the TLP.

1.3. Numerical modelling

1.3.1 Potential flow models

Under the potential flow theory the numerical models are usually based on the Boundary Integral Equation Method (BIEM). The problem reduces to the evaluation of the velocity potential from which all other physical quantities (velocity, pressure, wave elevation …) can be easily deduced. The velocity potential satisfies the relevant Boundary Value Problem (BVP) which is defined by the Laplace equation in the fluid domain and the different conditions at the boundaries of the domain. Green’s theorem is used in order to represent the solution by the appropriate distribution of the singularities over the fluid boundaries only. The practical consequence is that the number of unknowns is significantly reduced which leads to very efficient numerical tools. The BIEM can be applied to linear or nonlinear Boundary Value Problems (BVP) and can be formulated in frequency or time domain. The basics of the BIEM are discussed in Appendix 1.

1.3.2 Viscous flow models

The viscous flow models are based on solving directly the Navier Stokes equations in the fluid domain. The denomination CFD (Computational Fluid Dynamics) is used here to denote the numerical methods other than those based on the potential flow assumptions. The unknown quantities are the flow velocity vector and the scalar hydrodynamic pressure. The numerical approaches consist in discretizing the whole fluid domain and in approximating the different derivatives (time and space) by appropriate numerical techniques. Different numerical techniques can be employed (finite volumes, finite differences, finite elements, particle methods …). Compared to BIEM the resulting number of unknowns is significantly higher which leads to significantly higher hardware and CPU time requirements. That is why the use of CFD methods is limited to the cases where the fluid flow is fundamentally non potential or where the fluid domain boundaries experience very strong variations in space and time. Theoretically the CFD methods are able to treat any type of physical situations, however important numerical problems which affect the stability and the convergence of the solution might occur so that the modelling should be done with greatest care. One of the most important problems, when using CFD for simulation of the wave body interaction, is related to the modelling of the wave generation, propagation and absorption which appears to be extremely complex with CFD, so that the long time simulations (e.g. 3 hours or more) in irregular wave conditions are still in the research stage.

2. Maneuvering loads

2.1. General

2.1.1 Definition

The maneuvering loads are the slowly varying loads acting on the floating body, which are not induced by the waves and do not create the waves. In practice this means that the double body flow assumptions can be adopted which means that the vertical velocity of the fluid at the free surface is equal to zero. The maneuvering loads are induced by the low frequency relative motion of the body with respect to the water and to the wind. These loads can be of either inviscid or viscous origin and are obtained by assuming the fluid domain to be of infinite extent. Even if, in the general case, the maneuvering represents the 3D motion of the body, in this section we restrict ourselves to the horizontal motions in the plane of the free surface. This means that only 3 degrees of freedom are of concern (surge, sway and yaw).

2.2. Hydrodynamic maneuvering loads of inviscid origin

2.2.1 Body forces

The body forces follow from the application of the conservation of momentum, which allows the evaluation of the loads without explicitly calculating the hydrodynamic pressure. In the context of maneuvering, due to the low speed of the vessel and the small current, the double body flow can be assumed and the physical domain, which is initially semi-infinite, is made infinite. The loads are commonly evaluated in the hydrodynamic coordinate system which, in the present case of the horizontal motion without the presence of waves, is identical to the body fixed coordinate system. The following notations are introduced to denote the body velocity relative to current direction and expressed in the hydrodynamic coordinate system:

$$u_R = u - U_C \cos\beta_C \quad , \quad v_R = v - U_C \sin\beta_C \tag{120}$$

where (u, v) denote the slowly varying horizontal velocities of the hydrodynamic coordinate system.

It follows that the amplitude of the relative velocity and the angle between the relative velocity vector and the x axis of the hydrodynamic coordinate system are given by:

$$U_R = \sqrt{u_R^2 + v_R^2} \quad , \quad \beta_R = \tan^{-1}\left(\frac{v_R}{u_R}\right) \tag{121}$$

With these notations, the final expressions for the horizontal forces and the yaw moment, expressed in the hydrodynamic coordinate system, can be written as:

$$\begin{aligned}
F_x &= -a_{11}\dot{u}_R - a_{12}\dot{v}_R - a_{16}\ddot{\psi} + \dot{\psi}\left(a_{21}u_R + a_{22}v_R + a_{26}\dot{\psi}\right) \\
F_y &= -a_{22}\dot{v}_R - a_{21}\dot{u}_R - a_{26}\ddot{\psi} - \dot{\psi}\left(a_{11}u_R + a_{12}v_R + a_{16}\dot{\psi}\right) \\
M_z &= -a_{66}\ddot{\psi} - a_{61}\dot{u}_R - a_{62}\dot{v}_R + \dot{\psi}(a_{16}v_R - a_{26}u_R) - u_R v_R(a_{22} - a_{11}) - (a_{21}u_R^2 - a_{12}v_R^2)
\end{aligned} \tag{122}$$

The quantities a_{ij} denote the components of the added mass matrix (123) and the notation $\dot{u}_R$ is used to represent the time derivative. The above expressions (122) are valid for an arbitrary slowly varying horizontal motion of the body defined by the relative velocity of its center of gravity (u_R, v_R) and by its yaw rotational velocity $\dot{\psi}$ around the center of gravity.

2.2.2 Added mass matrix

The elements of the added mass matrix are defined by:

$$a_{ij} = \varrho \iint_{S_B} \varphi_j n_i \, dS = \varrho \iint_{S_B} \varphi_j \frac{\partial \varphi_i}{\partial n} dS \tag{123}$$

where n_i denotes the generalized normal vector (see Appendix 1) and φ_i are the unitary potentials defined as a solution of the following BVPs (double body flow assumption):

$$\left.\begin{array}{ll}
\Delta\varphi_i = 0 & 0 \geq z \geq -h \\
\dfrac{\partial \varphi_i}{\partial z} = 0 & \text{at free surface } z = 0 \\
\dfrac{\partial \varphi_i}{\partial n} = n_i & \text{body surface } S_B \\
\dfrac{\partial \varphi_i}{\partial z} = 0 & \text{at sea bottom } z = -h \\
\varphi_i \to 0 & \text{at infinity } r \to \infty
\end{array}\right\} \tag{124}$$

We note that the different elements of the added mass matrix are symmetrical $a_{ij} = a_{ji}$.

2.2.3 Linear and quadratic parts of the inviscid maneuvering forces

The above defined forces and moments are fully nonlinear (under the double body flow assumptions); however two relatively distinct parts can be identified. Some terms are proportional to the time derivatives of the local velocity components and they are often called linear terms. Care should be taken in computing these terms: the time derivative of the local velocity component is not equal to the local acceleration. These terms are not proportional to the acceleration! The remaining terms are proportional to the product of two velocity components. They are often called quadratic terms.

2.2.4 Munk moment

The Munk moment is defined as the part of the maneuvering yaw moment M_z which is not zero when the body is placed in a stationary current $\left(\dot{u}_R = \dot{v}_R = \dot{\psi} = \ddot{\psi} = 0\right)$. In the present case this means:

$$M_z = -u_R v_R (a_{22} - a_{11}) - a_{12}(u_R^2 - v_R^2) \tag{125}$$

When $a_{22} > a_{11}$ the Munk moment has a destabilizing effect and tends to orient the body perpendicular to the current.

2.2.5 Lifting forces

When a ship is advancing with a drift angle, the hull acts as a lifting surface and lateral lift loads are induced. If the hull is slender, it can be considered as a low-aspect-ratio lifting surface, and the lifting loads can be expressed by slender body theory as discussed in Newman [1977]. Within the scope of applications of concern here, the lifting loads are usually not considered explicitly but are included in the current induced loads (See 2.3.1).

2.3. Hydrodynamic maneuvering loads of viscous origin

2.3.1 Current induced viscous loads

The current induced loads on large bodies include the combined effects of the friction and the drag. The drag component is usually dominant except for the streamline bodies in head current where the boundary layer remains attached to the body surface. Within the context of maneuvering the horizontal components of the current induced loads, expressed in the hydrodynamic coordinate system, are usually written as:

$$\begin{aligned}
F_{Cx} &= \frac{1}{2}\varrho_w L T C_{Cx}(\beta_R) U_R^2 \\
F_{Cy} &= \frac{1}{2}\varrho_w L T C_{Cy}(\beta_R) U_R^2 \\
M_{Cz} &= \frac{1}{2}\varrho_w L^2 T C_{Cz}(\beta_R) U_R^2
\end{aligned} \tag{126}$$

where:

ϱ_w	Density of water
L	Characteristic wetted length
T	Mean draught
C_{Cx} , C_{Cy} , C_{Cz}	Current drag coefficients

The drag, which depends on the current direction, is evaluated either by model tests or alternatively by CFD simulations. For some classes of floating bodies (VLCCs, LNG-carriers) there exist documented current load coefficients resulting from systematic towing tests in wave tanks (OCIMF (1997)).

When M_{Cz} is evaluated through mode tests (or CFD), by putting the body in a uniform current, both the inviscid and viscous forces are measured (computed) and are included in the current coefficient $C_{Cz}(\beta_C)$. Hence the Munk moment is also included in this coefficient and should be removed from the inviscid forces to avoid being double counted.

2.3.2 Correction of the current induced loads for FPSO's

The formulation (126) in terms of the apparent current velocity does not include possible influence of the yaw velocity i.e. the local apparent velocity along the body. This issue was discussed in Molin & Bureau (1980) where the following correction for the transverse force and the yaw moment, to be added to the previously defined current forces (126), was proposed:

$$\begin{aligned}
F_{Cy}^M &= \frac{1}{2}\varrho_w C_{Mo} \int_L T(x)\left[\mathcal{V}_\perp(x,\dot{\psi})\mathcal{V}(x,\dot{\psi}) - \mathcal{V}_\perp(x,0)\mathcal{V}(x,0)\right]dx \\
M_{Cz}^M &= \frac{1}{2}\varrho_w C_{Mo} \int_L T(x)\left[\mathcal{V}_\perp(x,\dot{\psi})\mathcal{V}(x,\dot{\psi}) - \mathcal{V}_\perp(x,0)\mathcal{V}(x,0)\right]x dx
\end{aligned} \tag{127}$$

where $T(x)$ is the local draught, $\mathcal{V}_\perp$ denotes the local transverse relative velocity and $\mathcal{V}$ denotes the local total relative velocities:

$$\mathcal{V}_\perp(x) = v_R + x\dot{\psi} \quad , \quad \mathcal{V} = \sqrt{u_R^2 + \mathcal{V}_\perp^2} \tag{128}$$

The coefficient C_{Mo} in (127) is given as the percentage of the drag coefficient in y direction $C_{Cy}\left(\frac{\pi}{2}\right)$, and it is specified by the user. In the absence of the more precise estimation, it can be taken between 1.2 and 1.3.

2.3.3 Wind induced loads

Wind loads show much similarity to current loads. The expression for the loads keeps the same form as (126), with the air density instead of the water density and with the different representative surfaces and the drag coefficients. The wind velocity U_{Rw} relative to hydrodynamic coordinate system, and its relative angle β_{RW} , are defined by:

$$u_{Rw} = u - U_W \cos\beta_W \quad , \quad v_{Rw} = v - U_W \sin\beta_W \quad , \quad U_{Rw} = \sqrt{u_{Rw}^2 + v_{Rw}^2} \quad , \quad \beta_{RW} = \tan^{-1}\left(\frac{v_{RW}}{u_{RW}}\right) \tag{129}$$

and we write:

$$\begin{aligned} F_{Wx} &= \frac{1}{2}\varrho_a S_t C_{Wx}(\beta_{RW}) U_{Rw}^2 \\ F_{Wy} &= \frac{1}{2}\varrho_a S_l C_{Wy}(\beta_{RW}) U_{Rw}^2 \\ M_{Wz} &= \frac{1}{2}\varrho_a L S_l C_{Wz}(\beta_{RW}) U_{Rw}^2 \end{aligned} \tag{130}$$

where:

ϱ_a	density of air
L	characteristic length (commonly L_{pp})
S_t	Longitudinal wind area above the waterline
S_l	Transverse wind area above the waterline
C_{Wx} , C_{Wy} , C_{Wz}	Drag coefficients

Compared to the current loads, an important distinction is that, due to boundary layer effects, the mean wind profile is strongly biased over the height of the superstructures whereas, in deep water, the current profile by the free surface is close to vertical. Commonly the wind speed is taken at $10m$ above the sea level. Wind loads are usually assessed through wind tunnel tests or CFD computations. Some reference coefficients are provided by OCIMF for VLCCs and by the Society of International Gas Tanker and Terminal Operators (2007) for LNG-carriers.

Strictly speaking the, so called, Molin's correction (127) should apply to the wind loads too. However, in practice that is not the case and this contribution is usually neglected.

3. Wave loads

3.1. General

3.1.1 Introduction

Wave loading on floating structure is very complex in general. Waves affects the structure both globally (diffraction radiation) and locally (slamming, sloshing, green water …). Local wave induced loads are evaluated almost exclusively in the time domain while the global loads are commonly evaluated in the frequency domain, at least up to second order in wave steepness. As far as the global loading is concerned, the numerical models based on potential flow theory are used most often. With some supplementary assumptions, these models can also account for the non potential flow effects in an approximate way. Typical examples concern the inclusion of the additional damping in the body dynamic motion equation (roll damping …). Another example is the use of the empirical dissipation coefficients to attenuate the free surface flow in resonante conditions (sloshing, moonpool…).

3.1.2 Frequency domain description of wave loads n

The frequency domain description of wave loading helps identifying more explicitly the frequency content of the response which can be very useful in practice. In addition, the frequency domain description, allows for the use of spectral analysis to evaluate the response in irregular seas which is very convenient and much faster than using the direct time domain description.

When formulated in the frequency domain, it is convenient to use complex notation so that, for example, the linear velocity potential and the free surface elevation can be written in the following form:

$$\Phi^{(1)}(\boldsymbol{x},t) = \Re\left\{\varphi^{(1)}(\boldsymbol{x})e^{i\omega t}\right\} \quad , \quad \Xi^{(1)}(\boldsymbol{x},t) = \Re\left\{\eta^{(1)}(\boldsymbol{x})e^{i\omega t}\right\} \tag{131}$$

where $\Phi^{(1)}$ and $\Xi^{(1)}$ are real valued while $\varphi^{(1)}$ and $\eta^{(1)}$ are complex valued.

The irregular incident wave field being composed of many different frequencies it follows that two waves of frequencies ω_i and ω_j will induce the linear contribution at those particular frequencies and the second order contribution at the frequencies: 0 , $2\omega_i$, $2\omega_j$, $\omega_i - \omega_j$ and $\omega_i + \omega_j$. This follows directly from the fact that the second order quantities are induced by the quadratic product of the first order ones:

$$\Re\{Z_1 e^{i\omega_1 t}\}\Re\{Z_2 e^{i\omega_2 t}\} = \frac{1}{2}\Re\{Z_1 Z_2 e^{i(\omega_1+\omega_2)t}\} + \frac{1}{2}\Re\{Z_1 Z_2^* e^{i(\omega_1-\omega_2)t}\} \tag{132}$$

where Z_1 and Z_2 are two arbitrary complex numbers and the superscript star " *" denotes the complex conjugate value.

For a given sea spectra, a linear free surface elevation is given by the expression (61). From (132) it follows that the total frequency content of the typical wave loads, up to 2nd order, can be schematically presented by Figure 47. The linear wave frequency (WF), the second order low frequency (LF) and the second order high frequency (HF) components are clearly identified.

Figure 47: Excitation spectra (S_F) of the first $(S^{(1)})$ and second order difference $(S_-^{(2)})$ and sum $(S_+^{(2)})$ frequency loads together with the sea spectrum (S_η)

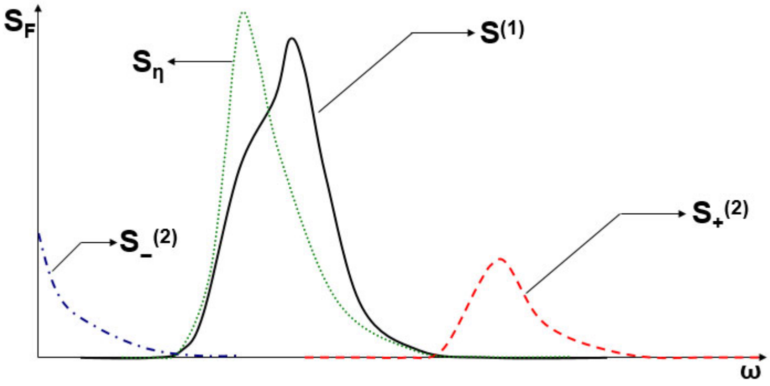

4. Linear wave loads

4.1. General

4.1.1 Definitions

The linear wave loads are the loads whose amplitude is directly proportional to the amplitude of the incoming waves. The basic assumption of the linear model is that the body motions are small and can be considered as a small perturbation around the mean body position. Depending on the type of the body responses which are of concern, the mean body position can vary in time. The typical example is the mooring analysis of the structure where the large low frequency horizontal motions should be combined with the linear wave frequency response. In that case the mean horizontal body position changes in time and this requires the proper update of the phases and the relative wave directions for the linear loads and responses.

4.2. Frequency domain formulation

4.2.1 Introduction

According to the linearization procedure, the frequency of the linear wave loads remains the same as the frequency of the incoming waves. The total linear hydrodynamic loads $\{\boldsymbol{F}^{hd(1)}\}$ are decomposed into the part which is independent of the body motions and the parts which are dependent on the body motions, as follows:

$$\{\boldsymbol{F}^{hd(1)}\} = \{\boldsymbol{F}^{DI(1)}\} + (\omega^2[\,\boldsymbol{A}(\omega)\,] - i\omega[\,\boldsymbol{B}\,(\omega)] - [\,\boldsymbol{C}\,])\{\boldsymbol{\xi}^{(1)}\} \tag{133}$$

where:

$\{\boldsymbol{F}^{DI(1)}\}$	–	Incident and diffraction load vector
$[\,\boldsymbol{A}(\omega)\,]$	–	Hydrodynamic added mass matrix
$[\,\boldsymbol{B}\,(\omega)]$	–	Hydrodynamic damping matrix
$[\,\boldsymbol{C}\,]$	–	Hydrostatic restoring matrix
$\{\boldsymbol{\xi}^{(1)}\}$	–	Vector of linear body motion amplitudes (small perturbation around the mean body position)

It should be noted that the above force decomposition is valid for the freely floating body only and the additional damping and restoring forces might need to be added due to other possible physical effects which are not included in the potential flow diffraction-radiation theory (mooring, roll damping …) (see also Section 5).

4.2.2 Hydrostatic loads

The linear hydrostatic restoring loads result from the variation of the hydrostatic pressure loads and the gravity loads due to body motion in calm water. In the case of single freely floating rigid body, the restoring matrix can be written in the following form:

$$[\boldsymbol{C}] = \varrho g \begin{bmatrix} 0 & 0 & 0 & 0 & 0 & 0 \\ 0 & 0 & 0 & 0 & 0 & 0 \\ 0 & 0 & A_w & A_w y_{AG} & -A_w x_{AG} & 0 \\ 0 & 0 & A_w y_{AG} & I_{11}^{AG} + V z_{BG} & -I_{12}^{AG} & 0 \\ 0 & 0 & -A_w x_{AG} & -I_{21}^{AG} & I_{22}^{AG} + V z_{BG} & 0 \\ 0 & 0 & 0 & 0 & 0 & 0 \end{bmatrix} \tag{134}$$

The A_w denotes the waterplane area, V is the underwater body volume, z_{BG} is the vertical distance between the center of gravity *G* and the center of buoyancy B , and other quantities are defined by the following expressions (S_A denotes the surface of the waterplane):

$$A_w x_{AG} = \iint_{S_A} (x - x_G) dS \quad , \quad A_w y_{AG} = \iint_{S_A} (y - y_G) dS$$

$$I_{11}^{AG} = \iint_{S_A} (y - y_G)^2 dS \quad , \quad I_{22}^{AG} = \iint_{S_A} (x - x_G)^2 dS$$

$$I_{12}^{AG} = I_{21}^{AG} = \iint_{S_A} (x - x_G)(y - y_G) dS$$

where we note that the following notations have been introduced:

$$x_{PQ} = x_P - x_Q \quad , \quad y_{PQ} = y_P - y_Q \quad , \quad z_{PQ} = z_P - z_Q \tag{135}$$

It is common to define the metacentric height for roll and pitch:

$$\overline{GM}^{Roll} = \frac{I_{11}^{AG}}{V} + z_{BG} \quad , \quad \overline{GM}^{Pitch} = \frac{I_{22}^{AG}}{V} + z_{BG} \tag{136}$$

so that the restoring component for roll and pitch take the form:

$$C_{44} = \varrho g V \overline{GM}^{Roll} \quad , \quad C_{55} = \varrho g V \overline{GM}^{Pitch} \tag{137}$$

4.2.3 Decomposition of the velocity potential

In order to be able to write the body motion equation in the form (133) the total velocity potential needs to be decomposed into convenient form. This is done by separating the different terms in the body boundary condition among which some depend on body motion and other do not. The linear wave loads and the BVP are formulated and evaluated in the hydrodynamic coordinate system.

The total linear velocity potential, for rig body, should satisfy the following BVP (see also Appendix 1):

$$\left.\begin{array}{ll} \Delta\varphi^{(1)} = 0 & 0 \geq z \geq -h \\ -\nu\varphi^{(1)} + \dfrac{\partial \varphi^{(1)}}{\partial z} = 0 & z = 0 \\ \dfrac{\partial \varphi^{(1)}}{\partial n} = i\omega \displaystyle\sum_{j=1}^{6} \xi_j^{(1)} n_j & S_B \\ \dfrac{\partial \varphi^{(1)}}{\partial z} = 0 & z = -h \\ \sqrt{k_0 r}\left(\dfrac{\partial \varphi^{(1)}}{\partial r} + i k_0 \varphi^{(1)}\right) \to 0 & r \to \infty \end{array}\right\} \tag{138}$$

where ν represents the infinite depth wave number $\nu = \omega^2/g$, k_0 is the finite depth wavenumberand the mean wetted surface of the body is denoted by S_B. The generalized normal vector n_j is $n_j = \boldsymbol{n}$ for $j = 1,2,3$ and $n_j = (\boldsymbol{r} - \boldsymbol{r}_G) \wedge \boldsymbol{n}$ for

$= 4{,}5{,}6$, where $\boldsymbol{n}$ is the normal vector and $(\boldsymbol{r} - \boldsymbol{r}_G)$ is the vector joining the center of gravity to the point at the body surface (see also Appendix 1 for alternative notations).

Body moves under the action of an incident wave field which is described by the incident velocity potential $\varphi_I^{(1)}$. In order for the body boundary condition to be satisfied, an additional perturbation velocity potential needs to be added to the incident velocity potential. The body boundary condition (138) suggests the following decomposition of the total velocity potential:

$$\varphi^{(1)} = \varphi_I^{(1)} + \varphi_D^{(1)} + i\omega \sum_{j=1}^{6} \xi_j^{(1)} \varphi_{Rj}^{(1)} \tag{139}$$

where $\varphi_D^{(1)}$ is called the diffraction velocity potential and $\varphi_{Rj}^{(1)}$ are called the radiation velocity potentials.

4.2.4 Velocity potential of the incident wave

When expressed in the hydrodynamic coordinate system, the velocity potential of the incident wave can be written as follows:

$$\varphi_I^{(1)}(\boldsymbol{x}) = -\frac{igA}{\omega}\frac{\cosh k_0(z+h)}{\cosh k_0 h} e^{-ik_0(x\cos\beta + y\sin\beta)} e^{-ik_0(X_0\cos\alpha + Y_0\sin\alpha)} \tag{140}$$

where h denotes the water depth, A is the wave amplitude, ω is the wave frequency and β is the wave incidence relative to the hydrodynamic coordinate system respectively and the finite depth wave number k_0 follows as a solution of the dispersion relation:

$$k_0 \tanh k_0 h = \nu \tag{141}$$

The last term in (140) accounts for the change of the phase angle which occurs due to the slowly varying position of the body.

It is convenient to introduce the complex wave amplitude a by rewriting the expression (140) as:

$$\varphi_I^{(1)}(\boldsymbol{x}) = -\frac{iga}{\omega}\frac{\cosh k_0(z+h)}{\cosh k_0 h} \quad , \quad a = Ae^{-ik_0(x\cos\beta + y\sin\beta)} e^{-ik_0(X_0\cos\alpha + Y_0\sin\alpha)} \tag{142}$$

4.2.5 Diffraction velocity potential and the excitation loads

The diffraction velocity potential $\varphi_D^{(1)}$ is calculated by considering the body to be fixed in an incident wave field. The body boundary condition for the velocity potential $\varphi_D^{(1)}$ follows as:

$$\frac{\partial \varphi_D^{(1)}}{\partial n} = -\frac{\partial \varphi_I^{(1)}}{\partial n} \tag{143}$$

Once the diffraction potential calculated, the corresponding excitation force vector $\{\boldsymbol{F}^{DI(1)}\}$ is given by:

$$F_i^{DI(1)} = -i\omega\varrho \iint_{S_B} \left(\varphi_I^{(1)} + \varphi_D^{(1)}\right) n_i dS \tag{144}$$

4.2.6 Radiation velocity potentials and the radiation loads

The radiation velocity potentials $\varphi_{Rj}^{(1)}$ are calculated by considering the body moving with prescribed velocity in an initially calm water. The radiation potentials satisfy the following body boundary conditions:

$$\frac{\partial \varphi_{Rj}^{(1)}}{\partial n} = n_j \tag{145}$$

Once the different radiation potentials calculated, the different elements of the hydrodynamic added mass and damping matrices are evaluated using the following expression:

$$\omega^2 A_{ij} - i\omega B_{ij} = \varrho\omega^2 \iint_{S_B} \varphi_{Rj}^{(1)} n_i dS \tag{146}$$

4.2.7 Numerical evaluation of the velocity potentials

The diffraction and the radiation velocity potentials $\varphi_D^{(1)}$ and $\varphi_{Rj}^{(1)}$ are found as a solution of the dedicated BVP's which are solved using the Boundary Integral Equation Method (BIEM) (see Appendix 1).

4.2.8 Linear wave loads in irregular waves

Since the linear wave loads evolve at the same frequencies as the frequencies contained in the wave spectrum, their time history can be written as follows:

$$F^{(1)}(t) = \Re\left\{\sum_i a_i f^{(1)}(\omega_i, \beta_i) e^{i\omega_i t}\right\}$$

The complex quantity $f^{(1)}(\omega_i, \beta_i)$ represents the linear transfer function also called Response Amplitude Operator (RAO). It follows that, the corresponding spectrum of the first order quantities can be written in the following form:

$$S_{F^{(1)}}(\omega) = \int_{\mathbf{0}}^{\mathbf{2\pi}} S(\omega, \beta) f^{(1)}(\omega, \beta) f^{(1)*}(\omega, \beta) d\beta$$

4.3. Time domain formulation

4.3.1 Introduction

The frequency domain description represents the most efficient tool for the prediction of the linear body response in a particular sea state. Complemented by classical spectral analysis, it can produce the characteristics (significant, maximum …) of the body responses in an extremely efficient way. In the cases where the problem can be linearized there is no need for any other approach than the frequency domain approach. However, there exist many practical situations where the nonlinear effects are significant and cannot be neglected. These nonlinear effects are not necessarily of hydrodynamic origin and can be purely mechanical such as the nonlinear mooring forces, nonlinear damping and others. For those cases it is necessary to perform the simulations in time domain where it is possible to account for any type of the nonlinear physical effects by updating them at each time step. There exist different possibilities to build the time domain simulation model but the most practical one seems to be the hybrid frequency – time domain model initially proposed by Cummins (1962) and elaborated more in details by Ogilvie (1964). Here below, the linear part of the time domain model is described in more details.

4.3.2 Hybrid frequency – time domain model

In the case of fully linear hydrodynamic model, the time and frequency domain responses are strictly equivalent and are linked through the Fourier transform. Similar to frequency domain, the total time domain linear hydrodynamic forces can be decomposed into excitation loads, radiation loads and the hydrostatic restoring loads.

$$\left\{\boldsymbol{F}^{hd(1)}(t)\right\} = \left\{\boldsymbol{F}^{DI(1)}(t)\right\} + \left\{\boldsymbol{F}^{R(1)}(t)\right\} + \left\{\boldsymbol{F}^{HS(1)}(t)\right\} \qquad (147)$$

4.3.3 Excitation loads

The excitation force can be represented as the sum of the individual wave contributions:

$$\left\{\boldsymbol{F}^{DI(1)}(t)\right\} = \Re\left\{\sum_i a_i \boldsymbol{F}^{DI(1)}(\omega_i, \beta_i) e^{i\omega_i t}\right\} \qquad (148)$$

4.3.4 Radiation loads

The radiation loads can be computed in time domain using the following relation:

$$\left\{\boldsymbol{F}^{R(1)}(t)\right\} = -[\,\boldsymbol{A}^{\infty}]\left\{\ddot{\boldsymbol{\xi}}(t)\right\} - \int_0^t [\boldsymbol{K}(t-\tau)]\left\{\dot{\boldsymbol{\xi}}(\tau)\right\} d\tau \qquad (149)$$

where $[\,\boldsymbol{A}^{\infty}]$ is the added mass matrix at infinite frequency. $[\boldsymbol{K}(t)]$ is the matrix of the retardation functions (also called memory functions), which can be obtained from the frequency dependent damping, or added mass, using the following relations:

$$[\boldsymbol{K}(t)] = \frac{2}{\pi}\int_0^{\infty} [\boldsymbol{B}\,(\omega)] \cos\omega t\, d\omega = -\frac{2}{\pi}\int_0^{\infty} ([\boldsymbol{A}(\omega)] - [\boldsymbol{A}^{\infty}])\omega \sin\omega t\, d\omega \qquad (150)$$

In practice, most often, the memory functions are evaluated using the frequency domain hydrodynamic damping. The evaluation of the above integrals should be performed with care and the convergence needs to be ensured by consistently approximating the values of the hydrodynamic damping at high frequencies. One example of the frequency dependent hydrodynamic damping and the corresponding memory function, for heave-heave interaction component, is shown in Figure 48 where the typical decay of the memory function with time can be observed.

For checking the consistency of the frequency domain solution, it is recommended to verify the so called Kramers – Kroning relations (Kotik & Mangulis (1962)) which link the added mass and damping matrices:

$$[\boldsymbol{A}\,(\omega)] - [\boldsymbol{A}^{\infty}\,(\omega)] = \int_0^{\infty} \frac{[\boldsymbol{B}\,(\sigma)]}{\sigma^2 - \omega^2} d\sigma \qquad (151)$$

Figure 48: Frequency dependent hydrodynamic damping component coefficient and the corresponding time dependent memory function for heaving hemisphere

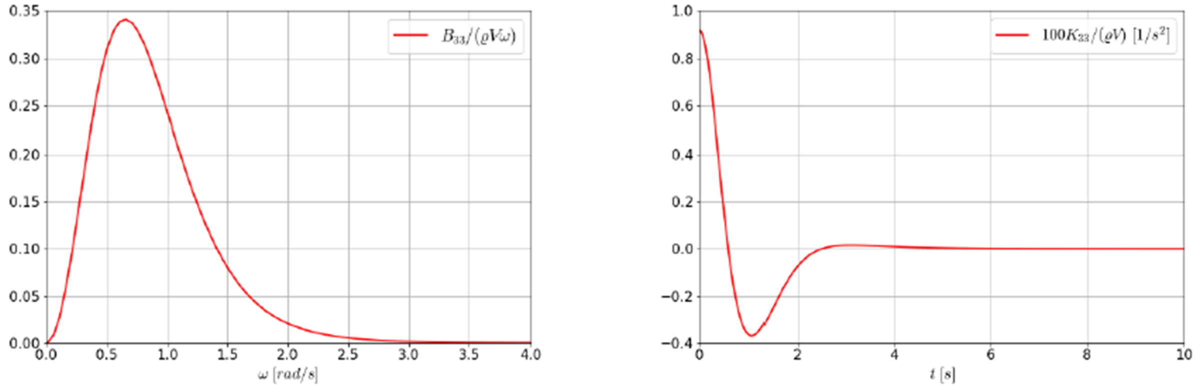

4.3.5 Hydrostatic loads

In the linear case, the hydrostatic force vector can be written in terms of hydrostatic restoring matrix which multiplies the body motion vector:

$$\{\boldsymbol{F}^{HS(1)}(t)\} = -[\,\boldsymbol{C}\,]\{\boldsymbol{\xi}^{(1)}(t)\}$$

4.4. Influence of current

4.4.1 Introduction

The presence of current modifies the floating body loads and responses even for small current intensities. In addition to the current induced viscous drag forces, the presence of current can also significantly modify the wave loads. In principle, the viscous effects and the potential flow effects should be evaluated at the same time because they interact with each other. However, in the case when the current velocity is small compared to the wave induced velocities, it can be assumed that the flow will not detach from the body and still the potential flow theory can be used for evaluation of the wave loads.

4.4.2 Definitions

We refer to Figure 49 and we place ourselves in the hydrodynamic coordinate system.

For simplicity of notations and in order to align with most of the literature on the subject, it is assumed that the body is not drifting but we note that, in the case of the body drifting with small velocity (u, v), the relative velocity U_R and the relative angle β_R (121) should be used instead of U_C and β_C.

Even if the hydrodynamic BVP can be formulated directly in the hydrodynamic coordinate system attached to the body (Figure 49 left), the common practice is to modify the hydrodynamic coordinate system by aligning the direction of the relative current with the horizontal axis of the modified hydrodynamic coordinate system (Figure 49 right). The main reason for that, is the simpler formulation of the BVP and simpler formulation of the corresponding Green's function. This implies that the hydrodynamic mesh should be defined in the modified coordinate system (Figure 49 right) and the hydrodynamic quantities (excitation, added mass, damping, restoring) need to be transferred to the original hydrodynamic coordinate system (Figure 49 left) before solving the motion equation. Whatever the coordinate system in which the hydrodynamic problem is formulated, the encounter frequency at which the body oscillates in waves, is given by:

$$\omega_e = \omega - k_0 U_C \cos(\beta - \beta_C) \qquad (152)$$

where ω is the fundamental wave frequency, U_C is the current intensity and k_0 is the wavenumber.

Figure 49: Reference configuration and rotation of the coordinate system

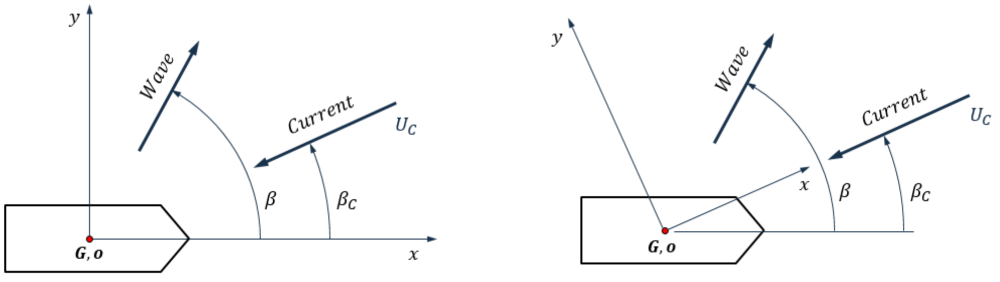

4.4.3 Double body flow

The assumption of small current intensity allows for the steady flow to be approximated by the product of the current intensity U_C and the double body velocity potential $\bar{\phi}$ which is defined by the following BVP (x component of the BVP defined in Section 4. [2.2.2]):

$$\left.\begin{array}{ll} \Delta\bar{\phi} = 0 & 0 \geq z \geq -h \\ \dfrac{\partial\bar{\phi}}{\partial z} = 0 & z = 0 \\ \dfrac{\partial\bar{\phi}}{\partial n} = n_x & S_B \\ \dfrac{\partial\bar{\phi}}{\partial z} = 0 & z = -h \end{array}\right\} \qquad (153)$$

4.4.4 Boundary Value Problem for linear velocity potential

Within the linearization procedure, the double body flow needs to be considered of order $O(1)$ with respect to the wave disturbance. This means that the interaction of the steady (double body) velocity potential and the linear unsteady wave induced velocity potential φ (superscript " $^{(1)}$" is omitted here in order to simplify the notations) should be taken into account. After neglecting the higher order terms with respect to current velocity, the boundary condition at the free surface becomes:

$$-\nu_e\varphi + \frac{\partial\varphi}{\partial z} - 2i\tau\frac{\partial\varphi}{\partial x} + 2i\tau\nabla\bar{\phi}\nabla\varphi - i\tau\varphi\frac{\partial^2\bar{\phi}}{\partial z^2} = 0 \qquad (154)$$

with $\nu_e = \omega_e^2/g$ and $\tau = U_C\omega_e/g$.

The above free surface condition is valid for small values of the parameter τ and for $U_C^2/gL \ll \tau$. This fact fixes some limitations to the use of (154) at small and high frequencies.

The body boundary condition becomes:

$$\frac{\partial\varphi}{\partial n} = i\omega_e\sum_{j=1}^{6}\xi_j\left(n_j + \frac{i\tau}{\nu_e}m_j\right) \qquad (155)$$

where the body motion amplitudes ξ_j are defined in the rotated hydrodynamic coordinate system (x axis aligned with the current direction) and not in the original hydrodynamic coordinate system.

The, so called, m_j terms which occur in (155) , are due to the interaction of the steady flow and the linear body motions, and are given by:

$$\{\boldsymbol{m}\} = \left\{\begin{array}{c} (\{\boldsymbol{n}\}^T\{\nabla\})\{\nabla\bar{\phi} - \boldsymbol{i}\} \\ (\{\boldsymbol{n}\}^T\{\nabla\})[\boldsymbol{u}]\{\nabla\bar{\phi} - \boldsymbol{i}\} \end{array}\right\} \qquad (156)$$

Special care should be given to the evaluation of the m_j terms because of the second order derivatives of the double body velocity potential which occur and which are challenging to evaluate numerically.

The total unsteady velocity potential φ is decomposed into incident, diffracted and radiated parts, in a way similar to the case without current, and the BVP is complemented by the Laplace equation in the fluid, no flow condition at the seabed and the appropriate radiation condition. The BVP can be solved numerically using the BIEM method as described in Appendix 1. Because of the interaction of the steady and the unsteady velocity potentials at the free surface, the numerical procedure requires the meshing of the free surface (see Figure 50). However, the unknowns are distributed over the wetted body part only so that the increase in CPU time is minimized (for details see also Chen & Malenica (1998)).

Figure 50: Hydrodynamic mesh for a typical FPSO in the presence of current

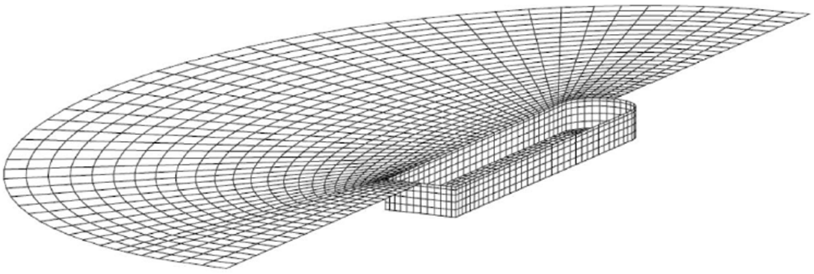

4.4.5 Forces

The presence of current modifies the way in which the hydrodynamic pressure is calculate and the total pressure is given by the following expression:

$$p = -\varrho[gz + i\omega_e\varphi + U_C\nabla(\bar{\phi} - x)\nabla\varphi] \tag{157}$$

The hydrostatic restoring matrix remains the same and the elements of the incident, diffraction and radiation forces are given by:

$$F_i^{DI} = -i\omega_e\varrho\iint_{S_B}\left[(\varphi_I + \varphi_D) - \tau\frac{i}{\nu_e}\nabla(\bar{\phi} - x)\nabla(\varphi_I + \varphi_D)\right]n_i dS \tag{158}$$

$$\omega_e^2 A_{ij} - i\omega_e B_{ij} = \varrho\omega_e^2\iint_{S_B}\left[\varphi_{Rj} - \tau\frac{i}{\nu_e}\nabla(\bar{\phi} - x)\nabla\varphi_{Rj}\right]n_i dS \tag{159}$$

It should be noted that the above defined excitation force and the added mass and damping components are defined with respect to the coordinate system in which the x axis is aligned with the current direction. This means that, before solving the body motion equation, these quantities need to be transferred to the original hydrodynamic coordinate system using the relevant transformation matrices.

4.4.6 Encounter frequency approximation

Some authors propose the so called encounter frequency approximation in order to account for the presence of current. Within this method, the presence of current is accounted for by simply changing the frequency at which the oscillations happen, so that the free surface condition becomes:

$$-\nu_e\varphi + \frac{\partial\varphi}{\partial z} = 0 \tag{160}$$

In this way the solution of the BVP for different velocity potentials can be obtained in exactly the same way as for the case without current which is obviously very convenient from the computational point of view. Different versions of the encounter frequency approximation are proposed in practice and they differ mainly by the way in which the body boundary condition is modified. However none of the proposed methods is consistent from theoretical point of view so that this approach is not recommended.

5. Second order wave loads

5.1. General

5.1.1 Introduction

The second order loads are induced by the quadratic interactions of the first order quantities (see Appendix 1). Their evaluation requires the knowledge of the full first order responses. The amplitude of the second order loads in bichromatic waves is proportional to the product of the incident wave amplitudes.

5.2. Frequency domain formulation

5.2.1 Sum and difference frequency second order quantities in bichromatic waves

When formulated in frequency domain, the second order loads occur at the frequencies equal to the sum and the difference of the corresponding incident wave frequencies. The generic incident wave field to be considered consists of two waves of different amplitudes (A_i, A_j) , different frequencies (ω_i, ω_j) and different directions (β_i, β_j). The corresponding linear free surface elevation of the incident waves is:

$$\Xi_I^{(1)}(t) = \Re\{a_i e^{i\omega_i t} + a_j e^{i\omega_j t}\} \tag{161}$$

where a_i and a_j are the complex amplitudes of the incident wave components (142).

It follows that the arbitrary second order quantity $Q^{(2)}(t)$ can be written as:

$$\begin{aligned} Q^{(2)}(t) = \; & a_i a_i^* q_0^{(2)}(\omega_i, \beta_i) + a_j a_j^* q_0^{(2)}(\omega_j, \beta_j) \\ + \; & \Re\left\{a_i^2 q_+^{(2)}(\omega_i, \omega_i, \beta_i)e^{2i\omega_i t} + a_j^2 q_+^{(2)}(\omega_j, \omega_j, \beta_j)e^{2i\omega_j t}\right\} \\ + \; & 2\Re\left\{a_i a_j q_+^{(2)}(\omega_i, \omega_j, \beta_i, \beta_j)e^{i(\omega_i + \omega_j)t} + a_i a_j^* q_-^{(2)}(\omega_i, \omega_j, \beta_i, \beta_j)e^{i(\omega_i - \omega_j)t}\right\} \end{aligned} \tag{162}$$

where $q_0^{(2)}$ are called the mean second order quadratic transfer function (QTF), and $q_+^{(2)}$ and $q_-^{(2)}$ are called the sum and the difference frequency quadratic transfer functions.

5.2.2 Second order wave loads in irregular waves

In irregular waves, the time history of the second order forces $F^{(2)}(t)$ follows as the sum of all possible bichromatic wave contributions and can formally be written in the following form:

$$F_+^{(2)}(t) = \Re\left\{\sum_i\sum_j a_i a_j f_+^{(2)}(\omega_i,\omega_j,\beta_i,\beta_j)e^{i(\omega_i+\omega_j)t}\right\} \tag{163}$$

$$F_-^{(2)}(t) = \Re\left\{\sum_i\sum_j a_i a_j^* f_-^{(2)}(\omega_i,\omega_j,\beta_i,\beta_j)e^{i(\omega_i-\omega_j)t}\right\} \tag{164}$$

The corresponding spectral responses are:

$$S_{F_+^{(2)}}(\Omega) = 8\int_0^{\Omega/2} d\omega \int_0^{2\pi} d\beta_1 \int_0^{2\pi} d\beta_2\, S(\omega,\beta_1)S(\Omega-\omega,\beta_2)\left\|f_+^{(2)}(\omega,\Omega-\omega,\beta_1,\beta_2)\right\|^2 \tag{165}$$

$$S_{F_-^{(2)}}(\Omega) = 8\int_0^{\infty} d\omega \int_0^{2\pi} d\beta_1 \int_0^{2\pi} d\beta_2\, S(\omega,\beta_1)S(\omega+\Omega,\beta_2)\left\|f_-^{(2)}(\omega,\omega+\Omega,\beta_1,\beta_2)\right\|^2 \tag{166}$$

5.2.3 Decomposition of the second order wave loads

The total second order wave loads $\{\boldsymbol{F}^{hd(2)}(\omega_i \pm \omega_j)\}$ can be formally decomposed in a way similar to the first order loads (133):

$$\{\boldsymbol{F}^{hd(2)}\} = \left[(\omega_i \pm \omega_j)^2[\boldsymbol{A}(\omega_i \pm \omega_j)] - i(\omega_i \pm \omega_j)[\boldsymbol{B}(\omega_i \pm \omega_j)] + [\,\boldsymbol{C}\,]\right]\{\xi^{(2)}\} + \{\boldsymbol{F}^{E(2)}\} \tag{167}$$

The restoring matrix $[\,\boldsymbol{C}\,]$ remains the same as for the first order case, the added mass and damping matrices $[\,\boldsymbol{A}\,]$ and $[\,\boldsymbol{B}\,]$ are also defined in the same way as the first order ones except that the frequency changes to $(\omega_i \pm \omega_j)$ and the second order excitation force $\{\boldsymbol{F}^{E(2)}\}$ regroups all the remaining terms of the second order loads.

5.2.4 Decomposition of the second order velocity potential

The final BVP for the second order diffraction potential $\varphi_D^{(2)}$ is defined by the following set of equations:

$$\left.\begin{array}{ll}
\Delta\varphi_D^{(2)} = 0 & 0 \geq z \geq -h \\
-(\omega_i \pm \omega_j)^2\varphi_D^{(2)} + \dfrac{\partial\varphi_D^{(2)}}{\partial z} = Q_F^{(2)} & z = 0 \\
\dfrac{\partial\varphi_D^{(2)}}{\partial n} = -\dfrac{\partial\varphi_I^{(2)}}{\partial n} + Q_B^{(2)} & S_B \\
\dfrac{\partial\varphi_D^{(2)}}{\partial z} = 0 & z = -h \\
\varphi_D^{(2)} \to 0 & r \to \infty
\end{array}\right\} \tag{168}$$

The BVP for the second order potential differs from that at first order by the non-homogenous term in the free surface condition $Q_F^{(2)}$ and the additional terms in the body boundary condition $Q_B^{(2)}$ (see Appendix 1). Similar to the linear case, the total second order velocity potential is decomposed into the incident, diffracted and radiated parts and the BVP for the radiated parts remains the same as for the linear case except that the frequency changes. All remaining terms in the inhomogeneous free surface boundary condition and in the body boundary condition are included in the boundary conditions for the second order diffraction potential.

5.2.5 Numerical evaluation of the velocity potentials

The above defined BVP's can be solved using the BIEM method as described in Appendix 1. When doing that, special care should be given to the evaluation of the free surface integral which theoretically extends to infinity and is very slowly convergent and highly oscillatory.

5.2.6 Use of Haskind theorem for evaluation of the second order diffraction loads

The second order excitation vector $\{\boldsymbol{F}^{E(2)}\}$ is composed of different parts namely: second order incident wave contribution, contribution of the quadratic products of the first order quantities and the contribution of the second order diffraction potential. The incident wave contribution and the contribution from the quadratic products of the first order quantities can be evaluated relatively straightforwardly, but the evaluation of the second order diffraction potential and the associated excitation load vector $\{\boldsymbol{F}^{D(2)}\}$ requires special attention and represents major difficulty in the resolution of the second order problem. In order to reduce the computational cost, Haskind theorem can be used (e.g. see Molin (2002)). After defining the assisting linear radiation potential ψ_i , satisfying $\partial\psi_i/\partial n = n_i$ on the body, the use of Haskind theorem allows writing the second order diffraction force component as:

$$F_i^{D(2)} = i(\omega_i \pm \omega_j)\varrho\left[\iint_{S_B} \psi_i \left(Q_B^{(2)} - \frac{\partial \varphi_I^{(2)}}{\partial n}\right) dS + \iint_{S_F} \psi_i Q_F^{(2)} dS\right] \qquad (169)$$

Even though the integral over the free surface remains it has to be evaluated only once per each force component, which represents a certain computational advantage. This integral is usually divided in two parts, the first one near the body where the integration is performed directly using the numerical quadrature, and the second part where the integration is performed in semi analytical way using the asymptotic expressions for different quantities (Kim et al (1990), Newman (1991), Chau et al. (1992)). It should also be noted that, for the difference frequency case, the contribution of the free surface integral can be neglected without significant loss of accuracy, as shown in Chen (2004).

5.3. Mean second order loads

5.3.1 Introduction

The mean second order loads, also called drift loads, together with the low frequency second order loads, plays an essential role in practice for the evaluation of the horizontal body motions. Indeed, for unrestrained body, the hydrostatic restoring forces are inexistent for horizontal motions and any constant external load will make the body drifts to infinity. In practice the mooring loads prevent the floating body of drifting and the design of the mooring system is closely related to the magnitude of the drift loading. These mean drift loads can be calculated in different ways and the most common methods are discussed below.

5.3.2 Near-field formulation based on direct pressure integration

The most intuitive way to calculate the mean second order loads is to simply take the time average of the second order loads obtained by direct pressure integration over the body (Appendix 1). The method is called near field method and its main drawback is the relatively poor numerical accuracy especially for the bodies with sharp corners where the potential flow theory has important problems of convergence.

5.3.3 Far-field formulation based on conservation of momentum

Instead of the direct pressure integration, the theorem on conservation of the momentum (linear and angular) can be used for the evaluation of the hydrodynamic loads (Appendix 1). In the case of periodic body motion, the advantage can be taken from the fact that the momentum remains constant from one period to another which means that its time derivative is zero. It follows that the mean forces on the body can be expressed in the form of the integrals over the surfaces surrounding the body. In addition, for the horizontal forces and the moment around the z axis, it can be shown that the contribution from the free surface integral is zero, so that the only remaining integral is the one over the arbitrary control surface surrounding the body and intersecting with the free surface. In practice this control surface is chosen at infinity which leads to so called Maruo & Newman formulation (Maruo (1960), Newman (1967)). The main advantage of this method is its high accuracy which is due to the fact that no local quantities are involved in the expressions. The method is applicable to the loads in horizontal plane only and it cannot be used to evaluate the loads on the individual bodies in multibody configuration.

5.3.4 Middle-field formulation based on Gauss's and Stokes's theorems

Based on application of Gauss' theorem and two variants of Stokes' theorem in a domain limited by a control surface surrounding the body, Chen (2007) developed so called middle-field formulation. This formulation can be applied to obtain not only the global mean drift loads (6 DOF), but also those on any individual body. Furthermore, it can be used to evaluate the low-frequency QTF contributed by the quadratic terms of the first-order wave fields. It has been shown in Chen (2007) that this formulation reduces to Maruo & Newman formulation if the control surface is pushed at infinity. The middle field method appears to be the most practical one and is recommended in practice.

5.3.5 Lagally formulation

It is also worth to mention the formulation, based on the Lagally theorem, which also can be used when the diffraction radiation problem is solved via the integral equation method, based on sources only formulation (see Eq (455)). Within this formulation the drift loads are given in the form of the integrals over the body surface (Ledoux et al. (2006)). For a completely submerged body, the formulation also gives access to the vertical components of the drift torque.

5.3.6 Characteristic features of the mean drift forces

Typical results for the mean drift forces in horizontal plane are shown in Figure 51 for a VLCC ship. In the case of massive structures such as this one, a very good agreement is usually found between experimental and numerical values of the drift force and the quadratic relationship with respect to wave amplitude is well respected. The far field formulation for evaluation of the drift forces indicates that the horizontal components are related to the amplitude of the waves diffracted and radiated by the structure, particularly in the direction opposite to the wave direction. This means that the drift force will approach zero at low frequencies, where the body is almost transparent to the waves, and will approach limiting value at high frequencies where the body acts as a curved wall which totally reflects the waves. The peak which often occurs in the intermediate frequency range is usually related to the resonant response of the body where the radiated waves are maximized. In the case of semis and TLPs a peak usually occurs at a wave length equal to twice the column spacing, where waves diffracted by the back and front columns are in phase. It should also be noted that the drift forces increase as the water depth decreases.

5.3.7 Mean second order wave loads in irregular seas

In an irregular sea state, the mean drift force is obtained by simple summation over all Airy components. By denoting the drift force for the individual wave component by $F_{Dij} = A_{ij}^2 f_D(\omega_i, \beta_j)$, we can write the following expression for the mean drift force F_D in the short crested sea:

$$F_D = \sum_i \sum_j A_{ij}^2 f_D(\omega_i, \beta_j) = 2\int_0^\infty \int_0^{2\pi} S(\omega, \beta) f_D(\omega, \beta) d\beta d\omega \tag{170}$$

Figure 51: Longitudinal drift force in head waves (left) and the transverse drift force (right) in oblique waves for VLCC

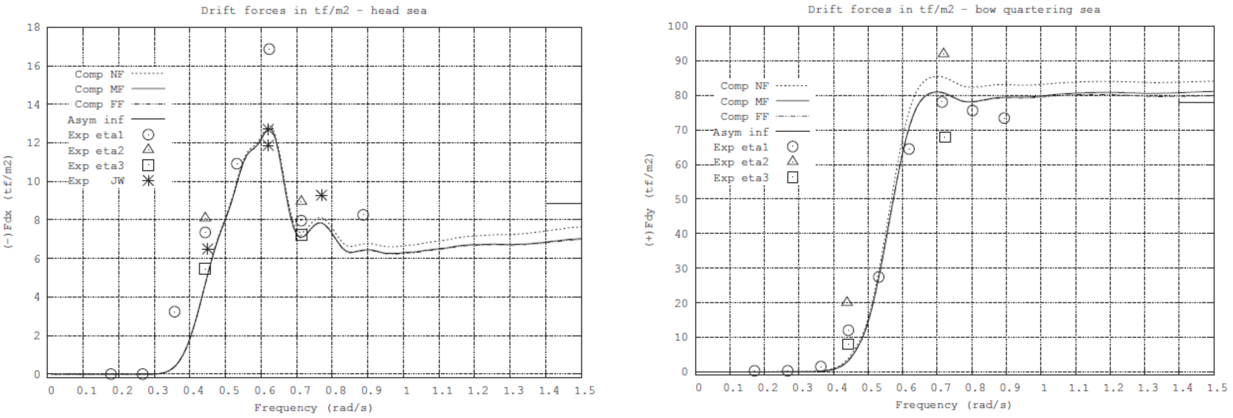

5.3.8 Effect of current and wave drift damping

The presence of current can significantly modify the free surface elevation and consequently the second order loads. The body response in the presence of waves and current is mathematically equivalent to the response of the body advancing with forward speed in waves. An important interpretation, of the influence of forward speed on second order loads, is the introduction of the so called wave drift damping which plays an essential role in the analysis of the low frequency behavior of the moored floating bodies. Usually the slow drift frequency of the moored system is significantly smaller than the wave frequency so that the slow drift velocity can be interpreted as an apparent forward speed. Assuming the situation without current and the body speed in the earth fixed coordinate system $(\dot{X}, \dot{Y})$ to be small, the second order loads can be expanded into Taylor series in terms of the speed and the first term in the series can be interpreted as damping. Only the mean second order forces are considered and we write:

$$\begin{Bmatrix} F_{DX}(\omega, \beta, \dot{X}, \dot{Y}) \\ F_{DY}(\omega, \beta, \dot{X}, \dot{Y}) \end{Bmatrix} = \begin{Bmatrix} F_{DX}(\omega, \beta, 0,0) \\ F_{DY}(\omega, \beta, 0,0) \end{Bmatrix} - \begin{bmatrix} -\dfrac{\partial F_{DX}(\omega, \beta, \dot{X}, \dot{Y})}{\partial \dot{X}} & -\dfrac{\partial F_{DX}(\omega, \beta, \dot{X}, \dot{Y})}{\partial \dot{Y}} \\ -\dfrac{\partial F_{DY}(\omega, \beta, \dot{X}, \dot{Y})}{\partial \dot{X}} & -\dfrac{\partial F_{DY}(\omega, \beta, \dot{X}, \dot{Y})}{\partial \dot{Y}} \end{bmatrix} \begin{Bmatrix} \dot{X} \\ \dot{Y} \end{Bmatrix} \tag{171}$$

where the elements in the matrix are called the wave drift damping.

We also note that, in the slow drift velocities in the earth coordinate system $(\dot{X}, \dot{Y})$ are related to the drift velocities in the body fixed coordinate system (u, v), by the following relations:

$$\dot{X} = u\cos\psi - v\sin\psi \quad , \quad \dot{Y} = u\sin\psi + v\cos\psi \tag{172}$$

Most often the components of the wave drift damping matrix are positive but they can also be negative in some situations such as the case of the multicolumn structures at some frequencies. They can be calculated by numerical differentiation of the second order loads evaluated at two small forward speeds.

5.3.9 Aranha's formula

The direct evaluation of the wave drift damping is very costly and requires the solution of the diffraction radiation problem with current which is significantly more complex than the one without current. That is why some simplified formulations for the evaluation of the wave drift damping were proposed in the literature. One of those formulations which turns out to perform very well, was proposed by Aranha (1994, 1996) (see also Clark et al (1993)). He proposed to express the mean second order force with the presence of current as a function of the mean second order force without current. Using the following notations for the k-th component of the drift force $F_{Dk} = A^2 f_{Dk}$, the Aranha's formula is given by:

$$f_{Dk}(\omega,\beta,U_C,\beta_C) = [1+4\tau\cos\beta_{CW}]f_{Dk}(\omega[1+\tau\cos\beta_{CW}],\beta+2\tau\sin\beta_{CW}\,,0{,}0) \qquad (173)$$

The forward speed parameter τ is defined as the ratio between the current velocity and the wave phase velocity i.e. $\tau = U_C/C_P$ which, for infinite water depth $(C_P = g/\omega)$ gives $\tau = U_C\omega/g$. Finally the relative wave – current angle β_{CW} is given by $\beta_{CW} = \beta_C - \beta$ with β_C and β being the direction of the current and waves respectively (see Figure 46). Even though the wave drift damping could be deduced from the expression (173) the most practical way to implement Aranha's formula in the motion simulation software, is to use directly that expression by replacing the current velocity U_C and its direction β_C by the relative velocity U_R and the relative direction β_R defined by (121).

The original Aranha's formulation for infinite water depth (173) was extended to finite water depth in Malenica et al (1995). The final expression for the finite depth is:

$$f_{Dk}(\omega,\beta,U_C,\beta_C) = \left[1+\frac{\tau}{\gamma}\left(2-\omega\frac{\partial\gamma}{\partial\omega}\right)\cos\beta_{CW}\right]f_{Dk}\left(\omega[1+\tau\cos\beta_{CW}],\beta+\frac{\tau}{\gamma}\sin\beta_{CW}\,,0{,}0\right) \qquad (174)$$

where the forward speed parameter τ is now given by $\tau = U_C/C_P = U_C k_0/\omega$, and γ is the ratio between the group velocity C_G and the phase velocity C_P:

$$\gamma = \frac{C_G}{C_P} = \frac{1}{2}\left(1+\frac{2k_0h}{\sinh 2k_0h}\right) \quad , \quad C_P = \frac{\omega}{k_0} \quad , \quad C_G = \frac{d\omega}{dk_0} \qquad (175)$$

5.4. Low frequency second order loads

5.4.1 Introduction

The low frequency second order loads are the second order loads occurring at the frequency equal to the difference of the individual wave frequencies. They can be evaluated directly as discussed in [5.2] and the resulting loads are usually denoted as the full QTF's. Most diffraction-radiation software nowadays provides the full difference frequency QTFs without the contribution from the free surface integral. However these computations still require extensive CPU effort and different approximations are frequently used.

5.4.2 Newman's approximation

The Newman approximation originates from the proposition made in Newman (1974). The main idea is to take the advantage of the fact that the knowledge of the difference frequency loads is required at relatively low values of $|\omega_i - \omega_j|$ so that it can be assumed that the difference frequency loads can be taken as the zero frequency limit $f_-^{(2)}(\omega_i,\omega_j) = f_D(\omega_i)$ (under the condition of unidirectional waves). Different versions of the Newman approximation were proposed:

$$f_-^{(2)}(\omega_i,\omega_j) = f_D(\omega_i) \qquad \text{Newman (1974)} \qquad (176)$$

$$f_-^{(2)}(\omega_i,\omega_j) = F_D\left(\frac{\omega_i+\omega_j}{2}\right) \qquad \text{Pinkster (1975)} \qquad (177)$$

$$f_-^{(2)}(\omega_i,\omega_j) = \frac{1}{2}(f_D(\omega_i)+f_D(\omega_j)) \qquad \text{Chen (2012)} \qquad (178)$$

$$f_{-k}^{(2)}(\omega_i,\omega_j) = sgn(f_{Dk})\sqrt{|f_{Dk}(\omega_i)f_{Dk}(\omega_j)|} \qquad \text{Molin \& Bureau (1980)} \qquad (179)$$

where the last expression assumes that the mean drift loads for the degree of freedom k keep the same sign when the frequency varies which is indeed true for the surge and sway force components.

Under the above approximations the QTF is real valued and the imaginary part is neglected. Improvements can be made by including the contribution from the incident second-order potential following a Morison type approach, assuming the body to be small with respect to the accompanying long waves. The validity of the Newman's approximation depends on many different parameters (water depth, sea state characteristics, ratio of the natural frequencies and wave frequencies…)

and quite often the results are not accurate enough. That is why the full QTF formulation is recommended in practice, at least at the final design/verification stage

5.4.3 Low frequency wave loads in irregular seas

In principle the expression (164) can be used directly for the evaluation of the second order low frequency loads. When Newman approximation is used, the expression can be further simplified and for the BV formulation (178) we can write:

$$F_{-k}^{(2)}(t) = \Re\left\{\left[\sum_i a_i^* f_{Dk}(\omega_i,\beta) e^{i\omega_i t}\right]\left[\sum_i a_i e^{i\omega_i t}\right]\right\} \qquad (180)$$

The advantage of this expression is that it consists in the products of two simple summations instead of a double summation, offering reduced CPU cost in time domain simulations.

In frequency domain, the expression (166) can also be used directly. When Newman approximation is used, the corresponding second order spectra for long crested sea becomes:

$$S_{F_{-k}^{(2)}}(\Omega) = 8\int_0^\infty S(\omega)S(\omega+\Omega)F_{Dk}(\omega,\beta)f_{Dk}(\omega+\Omega,\beta)\,d\omega \qquad (181)$$

and the one for the short crested sea:

$$S_{F_{-k}^{(2)}}(\Omega) = 8\int_0^\infty d\omega \int_0^{2\pi} d\beta_1 \int_0^{2\pi} d\beta_2\, S(\omega,\beta_1)S(\omega+\Omega,\beta_2)F_{Dk}(\omega,\beta_1)F_{Dk}(\omega+\Omega,\beta_2) \qquad (182)$$

5.4.4 Effect of current and wave drift damping in irregular seas

In the case when the Newman approximation's is used, the inclusion of the effects of current and the wave drift damping, is relatively straightforward and the expression for the zero speed drift force in (178) should be replaced by the drift forces with current (173) or (174).

In the case of the full difference frequency QTF, the direct expression for the second order difference frequency loads at zero relative current is given by (164). The extension to the case with non-zero relative current was proposed in Sclavounos (1997) and the final expression for the finite water depth is:

$$\boldsymbol{F}_{-}^{(2)}(t) = \Re\left\{\sum_i\sum_j a_i a_j^* \boldsymbol{f}_{-}^{(2)}(\omega_i,\omega_j,\beta_i,\beta_j,U_R,\beta_{Ri},\beta_{Rj}) e^{i(\omega_i-\omega_j)t}\right\} \qquad (183)$$

with:

$$\begin{aligned} f_{k-}^{(2)} = {} & \left[1+\frac{\tau_i}{\gamma_i}\left(1-\frac{1}{2}\omega_i\frac{\partial\gamma_i}{\partial\omega_i}\right)c_{\beta_i}+\frac{\tau_j}{\gamma_j}\left(1-\frac{1}{2}\omega_j\frac{\partial\gamma_j}{\partial\omega_j}\right)c_{\beta_j}\right] \\ & f_{k-}^{(2)}\left[\omega_i(1+\tau_i c_{\beta_i}),\omega_j\left(1+\tau_j c_{\beta_j}\right),\beta_i+\frac{\tau_i}{\gamma_i}s_{\beta_i},\beta_j+\frac{\tau_j}{\gamma_j}s_{\beta_j},0{,}0{,}0\right] \end{aligned} \qquad (184)$$

where:

$$c_{\beta_i} = \cos(\beta_{Ri}-\beta_i) \quad , \quad s_{\beta_i} = \sin(\beta_{Ri}-\beta_i) \quad , \quad \tau_i = \frac{U_R}{C_P} \qquad (185)$$

In case of the infinite water depth the expression reduces to:

$$f_{k-}^{(2)} = \left[1+2\tau_i c_{\beta_i}+2\tau_j c_{\beta_j}\right] f_{k-}^{(2)}\left[\omega_i(1+\tau_i c_{\beta_i}),\omega_j\left(1+\tau_j c_{\beta_j}\right),\beta_i+2\tau_i s_{\beta_i},\beta_j+2\tau_j s_{\beta_j},0{,}0{,}0\right] \qquad (186)$$

It has to be noted that the expressions (184) and (186) were derived by simple (intuitive) extrapolation of the expressions for Newman approximation so that their domain of validity is unclear.

5.5. High frequency second order loads

5.5.1 Introduction

High frequency second order loads represent an important source of excitation for the resonant response of the structures whose natural periods fall outside (from upper side) the dominant wave frequency range of the sea state. The phenomena is denoted as springing and typical examples are the tensioned buoyant platforms like TLPs which might experience the high frequency response in vertical modes of motion, and the very large floating structures (VLFS) which might experience structural vibrations.

5.5.2 High frequency wave loads in irregular seas

For high frequency second order wave loads in irregular seas there is no other way to evaluate them than using the expressions (163) directly.

6. Other hydrodynamic loads

6.1. General

6.1.1 Introduction

The hydrodynamic loads discussed in the previous sections cover the main part of the hydrodynamic loads which are needed for seakeeping and global performance analyses of the floating structures (see Sections 5 and 6). Depending on the particular application, other type of loads needs sometimes to be considered and some of these loads are discussed in the next sections.

6.2. Higher order diffraction loads

6.2.1 Introduction

The first and the second order wave loads represent the most dominant contribution to wave loading but, in some cases, they are not sufficient to accurately describe the nonlinear nature of the loading especially in large waves. For those situations the models higher than second order or even fully nonlinear are required. Interest in these loads is historically associated with the TLP and some GBS platforms in North Sea but more recently the masts of the offshore wind turbines renewed the attention on those strongly nonlinear effects.

6.2.2 Ringing phenomena

Model tests on TLP platforms and the GBS in North Sea design sea state conditions (peak period around 15 seconds) revealed the high frequency fluctuating loads at frequencies 4 to 5 times larger than the wave frequencies. This suggests that the nonlinearities higher than second order needs to be accounted for. The phenomena was baptized ringing. An example of the ringing phenomena is shown in Figure 52 where the time traces of the wave elevation and the bending moment on bottom mounted vertical circular cylinder in steep waves are presented. The high frequency content of the loads is clearly visible.

The observations suggest that the phenomena happens in very steep waves but there is no evidence of wave breaking nor impacting. At the same time the K_C number is sufficiently low and the Stokes parameter β is sufficiently high to ensure that flow remains attached i.e. the viscous effects are of no importance. All this suggests that the loads are induced by the higher order diffraction effects.

More recently the ringing phenomena received renewed attention in relation with the design of the fixed offshore wind turbine. In many cases the offshore wind turbines are supported by simple cylindrical structure with the diameter usually smaller than $10\ m$. Because of the smaller diameter the flow is likely to separate in large waves. This is reported as the "secondary load cycle" and is visible in the experiments (Kristiansen & Faltinsen (2017), Bachynsky et al (2017), Bredmose (2013)) but it cannot be predicted by the potential flow theory (Grue (2002), Riise et al. (2018)). In order to properly assess these problems, the model tests and CFD seem to be the only way.

Figure 52: Ringing phenomena. (from Scolan (1997))

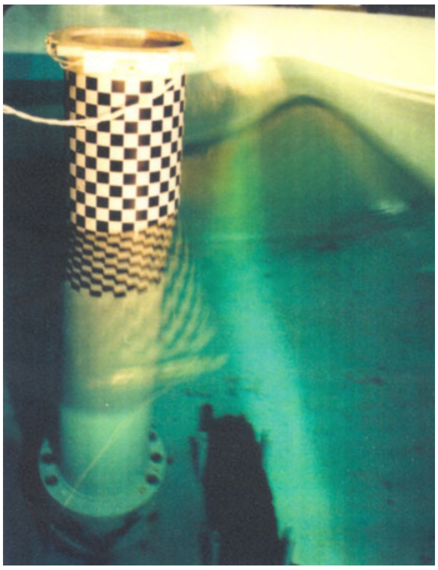

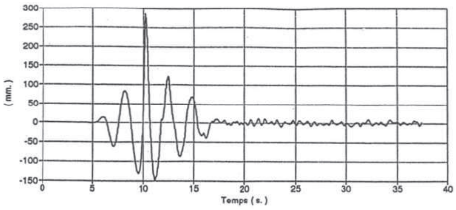

Wave elevation

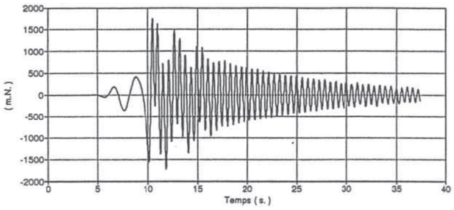

Bending moment at the bottom

6.2.3 Simplified potential flow models for higher order diffraction loads

The potential flow models can be hardly extended above the third order (Malenica & Molin (1995)) so that the complex fully nonlinear models need to be used. Unfortunately up to today the fully nonlinear potential flow models were able to handle simple cylindrical geometries only (Ferrant (1998, 1999)) and their extension to practical geometries was not reported. Several simplified models based on potential flow assumptions were proposed, among which the Rainey's model and the, so called FNV, models are used most widely.

The Rainey's equations [Rainey (1989, 1995)] represent an extension of the inertia component in the Morison equation. The derivation of the equations is based on the energy arguments and the free surface effects are ignored i.e. there are no radiated nor diffracted waves. The equations apply to slender bodies in unbounded fluid. When compared to the original Morison equation, the difference is that the higher order terms are included in the description of the incident wave field. The theory is valid for arbitrary cross section and for the circular cylinder of diameter D, the sectional forces are given by:

$$F_x = \varrho S\left\{2\dot{U} - \dot{u} + 2UU_X + 2VU_Y + 2WU_Z + (U-u)W_Z - 2q(W-w)\right\} \tag{187}$$

$$F_y = \varrho S\left\{2\dot{V} - \dot{v} + 2UV_X + 2VV_Y + 2WV_Z + (V-v)W_Z - 2p(W-w)\right\} \tag{188}$$

where the terms $U_{X,Y,Z}, V_{X,Y,Z}, W_Z$ represent the spatial derivatives of the incoming flow velocities.

The FNV method was first proposed in Faltinsen, Newman and Vinje (1995) for the infinite water depth case and in (Kristiansen & Faltinsen (2017) for the finite water depth case. Contrary to Rainey's approach, which is based on energy arguments, the FNV method uses the direct pressure integration to calculate the loads. Up to the loads proportional to the square of the wave amplitude, the FNV and the Rainey's results are fully equivalent but starts to differ at higher orders. It has been shown in Kristiansen & Faltinsen (2017) that the domain of validity of the FNV method, in terms of the amplitude of the loads up to third order, covers the practical ranges of the wave steepnesses in long regular waves. The domain of validity decreases for shorter waves because the diffraction effects were not taken into account fully consistently. One of the main advantages of the Rainey's and the FNV methods is the possibility to apply them in irregular seas.

6.3. Relative wave elevation, air gap and freeboard exceedance

6.3.1 Introduction

The parts of the body close to the mean waterline can experience important additional hydrodynamic loads induced by the large body motions and the extreme waves. The additional load effects concern mainly the redistribution of the local hydrodynamic pressure close to the waterline, and the occurrence of the hydrodynamic impacts when the initially dry structure suddenly becomes wet (slamming, green water, underdeck impact …). The sections below discuss the identification of the impact conditions (the relative position and the relative velocity before impact) which are used as input for the evaluation of the impact loads by the dedicated numerical models.

6.3.2 Definitions

Reference is made to Figure 53 where the following definitions are introduced:

h_0	Initial vertical position of the point P_0 attached to the body
Ξ	Local free surface elevation at the instantaneous horizontal position of the point P
ζ_v	Vertical displacement of the point P_0 attached to the body

Figure 53: Instantaneous position of the body in waves

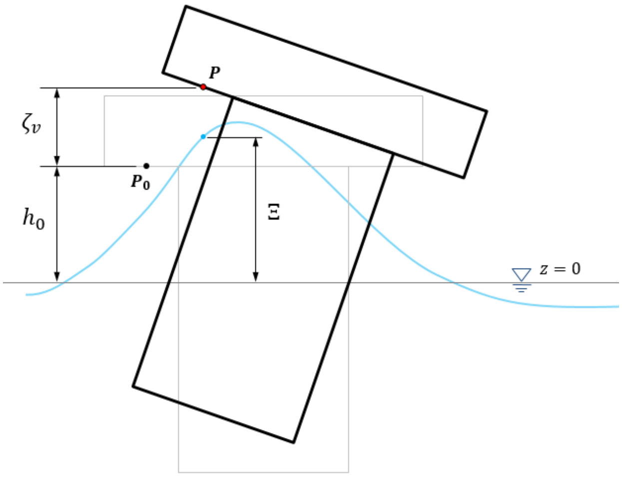

6.3.3 Relative wave elevation

The local relative wave elevation $\Xi^R(t)$ is defined by the following expression:

$$\Xi^R = \Xi - \zeta_v \tag{189}$$

In principle, all the quantities in (189) are to be considered fully nonlinear. The nonlinear displacement of the point attached to the body is given by the expression (347) in Appendix 1, and its vertical component defines ζ_v in (189). At the same time, the free surface elevation Ξ includes both the incident and the perturbed parts (diffracted and radiated).

The following parameters might have significant influence on the relative wave elevation and needs to be taken into account:

- Presence of current

  Even small current can significantly influence the local wave elevation close to the body. The linear part of these effects can be evaluated using the wave-current interaction seakeeping model presented in [4.4].
- Interactions between the columns of the multicolumn structures (TLP, Semi – submersible …)

  In the case of multicolumn structures, important amplifications of the wave elevation might occur in the space between the columns. This is due to the wave interactions between the columns and both the linear and the second order type of interactions matters and should be taken into account.
- Set down effect for TLP platform

  Due to the particular design of the TLP mean off-set of the platform will induce the set down effects which automatically increase the relative wave elevation.
- Local run-up effects

  The local run-up may significantly influence the wave elevation close to the vertical body surface. The physical characteristics of the run-up (height, volume of the fluid involved, jet kinematics …) are difficult to evaluate numerically because the phenomena is highly nonlinear and depends significantly on the wave steepness and on the local geometry. Model tests and CFD simulations might help in evaluating these effects.

6.3.4 Air gap

The instantaneous air gap $a(t)$ is defined as the instantaneous vertical distance between the sea water and the dry part of the body above it (typically deck structure) and is given by:

$$a(t) = h_0 - \Xi^R(t) = h_0 - \Xi(t) + \zeta_v(t) \tag{190}$$

This means that the impact on the deck occurs when the air gap becomes negative.

6.3.5 Freeboard exceedance

When the local relative wave elevation exceeds the freeboard of the floating body, the water will penetrate onto the deck and can potentially induce the severe damages to the superstructures and to the equipment located at the decks. This phenomena is known as the green water phenomena. The same principles as those for air-gap are used to define the freeboard exceedance $f(t)$ which is given by:

$$f(t) = \Xi^R(t) - h_0 = \Xi(t) - \zeta_v(t) - h_0 \tag{191}$$

This means that the green water will occur when the freeboard exceedance $f(t)$ becomes positive.

6.3.6 Third order effects on relative wave elevation

In the case of large floating structures with significant vertical freeboard, important amplifications of the wave elevation can occur when the body is exposed to beam or near - beam incident waves. These amplifications of the relative wave elevation can additionally increase the risk of green water occurrence. Since the amplifications happen at the fundamental wave frequency and cannot be captured by the linear theory, the third-order wave-wave interaction model was proposed by Molin (2005). Within this model the third order interaction theory, between the incoming wave and the wave system reflected by the body, is used to evaluate the modification of the incident wave amplitude locally. The coupling with the classical linear diffraction code is possible through an iterative procedure.

Typical effects are shown in Figure 54 where the diffraction of the oblique incident waves by the fixed barges in side by side configuration (Zhao et al. (2019)) is considered. Clearly, the linear model largely underestimate the relative wave elevation.

Figure 54: Experimental setup (left) and the summary of the RAO's for the wave elevation (from Ouled Housseine (2020))

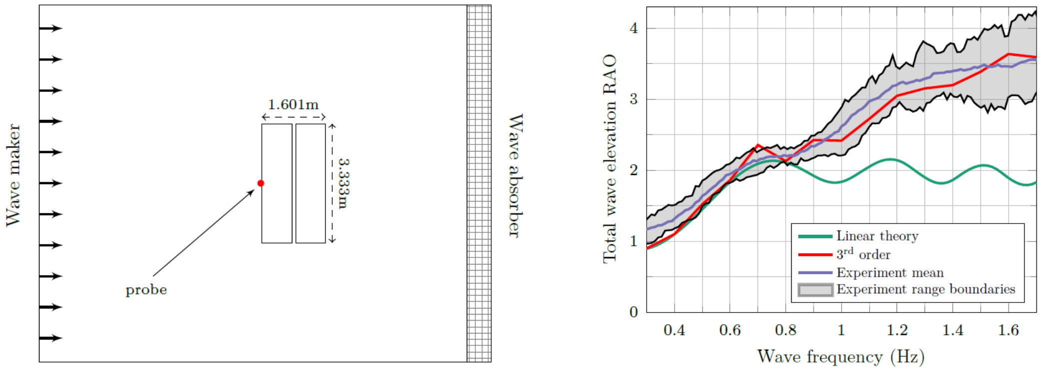

6.4. Nonlinear Froude Krylov and hydrostatic loads

6.4.1 Introduction

One of the main drawbacks of the linear theory is its impossibility to properly account for the pressure distribution close to the body waterline. This is due to the fact that the linear hydrodynamic model includes the mean wetted surface of the body only, which results in unphysical predictions of the pressure close to the waterline. In particular the zero pressure occurs below the wave crest and the negative pressure above the wave trough which is not physical and requires correction. The pressure distribution close to the waterline can be corrected by introducing the various nonlinear effects which are neglected in the linear model. Solution of the fully nonlinear wave body interaction problem being extremely complex, usually the different effects are included independently by accounting for what is believed to be the most dominant contribution. Among the different nonlinear effects, the contribution of the incident wave pressure and the instantaneous hydrostatic pressure appear to be one of the most important ones. In practice two effects are considered together and are known as the Froude – Krylov and nonlinear hydrostatic correction. The way of formulating this part of the loads is not unique and the most common description is given in the following section.

6.4.2 Nonlinear hydrostatic pressure

Once the instantaneous position of the body is known, accounting for the nonlinear hydrostatic pressure is relatively straightforward since the hydrostatic pressure P^{hs} follows directly from the Bernoulli's equation (see Appendix 1). It is common to express the hydrostatic pressure in meters of water height and denote it by $\tilde{P}^{hs}$ which leads to the following expression:

$$\tilde{P}^{hs}(t) = \frac{P^{hs}(t)}{\varrho g} = -z(t) \tag{192}$$

where $z(t)$ is the instantaneous vertical position of the point in the earth fixed coordinate system.

This expression is valid for any point in the fluid domain, otherwise the hydrostatic pressure is zero as shown in the left part of the Figure 55.

6.4.3 Froude Krylov pressure

The part of the wave loads induced by the undisturbed pressure in the incident wave is called Froude – Krylov load and this load is nonlinear by nature. When using the linear model for the incident wave, the corresponding weakly nonlinear pressure distribution $\tilde{P}^{fk}$ is shown in the middle part of Figure 55, and is defined by:

$$\tilde{P}^{fk}(t) = \begin{cases} 0 & \text{for} \quad z(t) > \Xi_I(t) \\ \tilde{P}_I^0(t) & \text{for} \quad 0 < z(t) < \Xi_I(t) \\ \tilde{P}_I^z(t) & \text{for} \quad z(t) < Min[\Xi_I(t); 0] \end{cases} \tag{193}$$

where the notation $\tilde{P}_I^z(t) = \tilde{P}_I^z(x,y,z,t)$ was used to denote the dynamic pressure of the incident wave.

It follows that, for the linear incident wave model, which is of concern here, the incident wave elevation $\Xi_I(t)$ is given by:

$$\Xi_I(t) = \tilde{P}_I^z(x,y,0,t) = \tilde{P}_I^0(t) \tag{194}$$

Figure 55: Froude Krylov and nonlinear hydrostatic pressure distribution for the positive (top) and the negative (bottom) incident wave elevation. (Left –hydrostatics, Middle – Froude Krylov, Right – total)

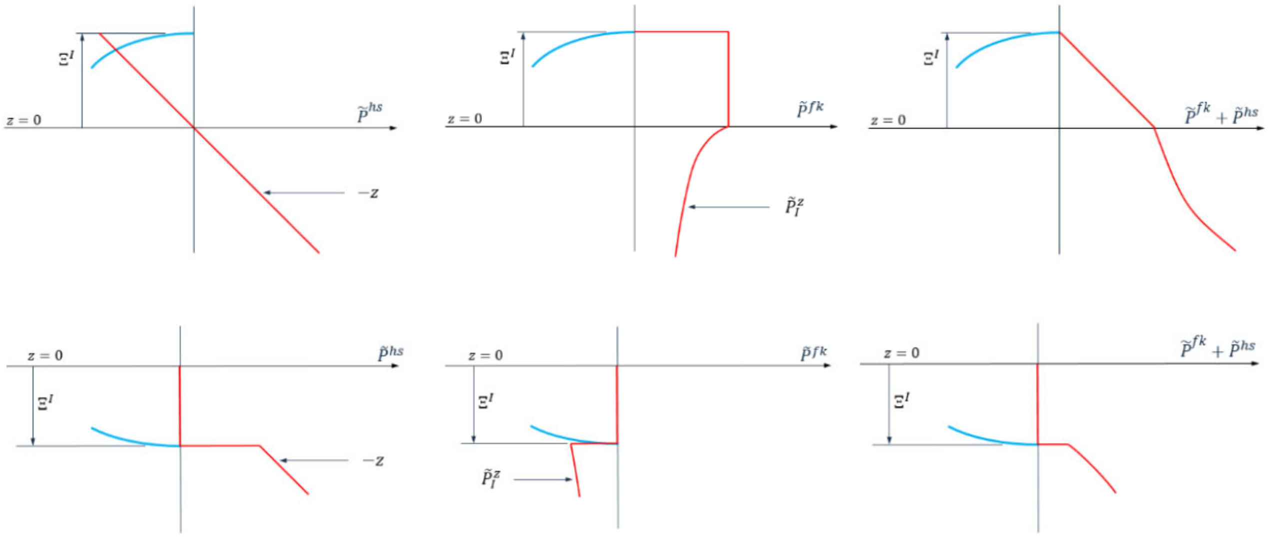

The direct summation of the Froude Krylov and the nonlinear hydrostatic pressures gives:

$$\tilde{P}^{fk\_hs}(t) = \tilde{P}^{fk}(t) + \tilde{P}^{hs}(t) = \begin{cases} 0 & \text{for} \quad z(t) > \Xi_I(t) \\ \tilde{P}_I^0(t) - z(t) & \text{for} \quad 0 < z(t) < \Xi_I(t) \\ \tilde{P}_I^z(t) - z(t) & \text{for} \quad z(t) < Min[\Xi_I(t); 0] \end{cases} \qquad (195)$$

The pressure distribution is shown on the right part of Figure 56 where it can be observed that the pressure is discontinuous for the negative incident wave elevation. This happens because:

$$\tilde{P}_I^z(t) - z(t) \neq 0 \quad \text{for} \quad z(t) = \Xi_I(t) \qquad (196)$$

In order to remove the discontinuity an additional correction is usually introduced. The final pressure distribution is denoted by $\tilde{P}_{cor}^{fk\_hs}$ and is given by:

$$\tilde{P}_{corr}^{fk\_hs}(t) = \begin{cases} 0 & \text{for} \quad 0 < \Xi_I(t) < z(t) \\ \tilde{P}_I^0(t) - z(t) & \text{for} \quad 0 < z(t) < \Xi_I(t) \\ Max[\tilde{P}_I^z(t) - z(t); 0] & \text{for} \quad z(t) < 0 \end{cases} \qquad (197)$$

For the positive wave elevation the pressure distribution remains the same i.e. $\tilde{P}_{corr}^{fk\_hs}(t) = \tilde{P}^{fk\_hs}(t)$ and for the negative wave elevation the distribution $\tilde{P}_{corr}^{fk\_hs}$ is shown in Figure 56. It can be observed that this distribution violates the linear free surface boundary condition and the total pressure is no more equal to zero at $z(t) = \Xi_I(t)$. This fact cannot be avoided within the present model because not all the nonlinearities were taken into account when the incident pressure distribution was corrected.

Figure 56: Continuous Froude Krylov and hydrostatic pressure distribution for the negative incident wave elevation

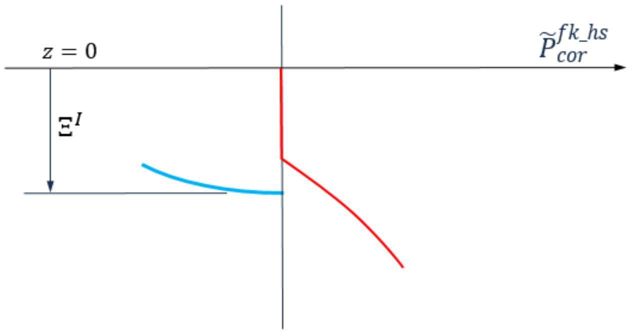

6.4.4 Diffraction – radiation pressure

Within the weakly nonlinear wave body interaction model the diffraction-radiation pressure components need also to be accounted for in order to calculate the total hydrodynamic pressure. In practice these pressure components are taken in a linear sense only i.e. without any nonlinear correction, and they are applied over the mean surface of the body at its instantaneous position. Due to the fact that the diffraction-radiation pressure is taken as linear, the negative pressure can occur locally close to the waterline, and that in spite of the fact that the Froude Krylov pressure was corrected as discussed in [6.4.3].

6.5. Intermittent wetting

6.5.1 Introduction

This issue is mainly relevant for the local fatigue loading of the side shell structural details close to the waterline where the linear theory is not accurate enough and needs to be corrected. The basic principles of the intermittent wetting correction are similar to those discussed in [6.4] in the context of the Froude Krylov and the nonlinear hydrostatic loads. The main difference is that the wave elevation also includes the linear diffraction and radiation parts. At the same time the body motions are assumed to be linear which allows formulating the loads by simple reconstruction of the frequency domain data without any time domain simulations.

6.5.2 Pressure correction close to waterline

The problem is formulated with respect to the initial coordinate system at rest.

The total linear hydrodynamic pressure $\tilde{P}(\boldsymbol{x}, t)$, in meters of water height, is given by:

$$\tilde{P}(\boldsymbol{x}_0, t) = \frac{AP(\boldsymbol{x}_0, t)}{\varrho g} = \Re\left\{-\frac{i\omega A}{g}\varphi(\boldsymbol{x}_0)e^{i\omega t}\right\} - \Re\{A\zeta_v(\boldsymbol{x}_0)e^{i\omega t}\} - z_0 \qquad (198)$$

where $\varphi(x)$ is the total linear velocity potential (incident, diffracted and radiated) and $\zeta_v(x)$ is the RAO of the vertical displacement for the considered point and z_0 is the initial vertical position of the point.

By adopting the notation $\tilde{P}^z(t) = \tilde{P}(x_0, y_0, z_0, t)$, the relative wave elevation $\Xi^R(t)$ is given by:

$$\Xi^R(t) = \tilde{p}(x_0, y_0, 0, t) = \tilde{p}^0(t) \qquad (199)$$

The rest of the procedure follows closely the steps from [6.4] with the important difference that the wave elevation now includes the incident, diffracted and radiated components. With the present notations the pressure distribution without the discontinuity is given by:

$$\tilde{P} = \begin{cases} 0 & \text{for} \quad 0 < \Xi^R < z_0 \\ \tilde{p}^0 - z_0 & \text{for} \quad 0 < z_0 < \Xi^R \\ Max(\tilde{p}^z - z_0; 0) & \text{for} \quad z_0 < 0 \end{cases} \qquad (200)$$

6.5.3 Pressure range

The procedure for evaluation of the fatigue damage of the structural details requires the knowledge of the local pressure range, denoted here by $\Delta\tilde{P}$. The pressure range represents the difference between the maximum and the minimum pressure which occurs during one loading cycle. The direct application of the above expressions for the pressure correction leads to the pressure range shown in Figure 57 where the purely linear pressure range is also presented for comparisons.

Figure 57: Linear and nonlinear pressure ranges

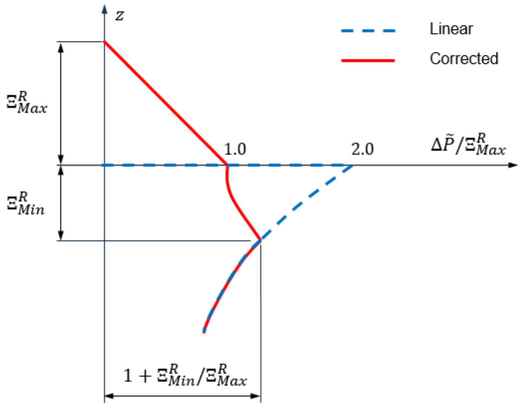

The notations Ξ^R_{Max} and Ξ^R_{Min} are used to denote the maximum and the minimum relative wave elevation over one loading cycle. It can be observed that the maximum relative wave elevation is equal to the linear relative wave elevation but the minimum relative wave elevation is different because of the procedure used for the suppression of the jump in the pressure distribution.

The way in which the intermittent wetting correction is used for fatigue life prediction, of the structural details close to the waterline, can be found in NI611, Sec 11, [3.9].

6.6. Sloshing in tanks

6.6.1 Introduction

There exist many practical situations where some compartments of the floating body are filled with liquid. When the tank is completely full it behaves as a solid body under the translation but behaves differently under the rotation. In the case of partially filled tank, due to the presence of the free surface, the sloshing motion will occur and induce the additional hydrodynamic loads at the tank walls. As a results the global behavior of the floating unit can also be significantly affected and the mutual influence of seakeeping and sloshing need to be accounted for.

Sloshing is in general highly nonlinear hydrodynamic phenomena especially when the body motions contain significant energy in the vicinity of the highest sloshing natural period. For that reason, the tank design should avoid, as much as possible, having the sloshing natural frequencies close to the natural frequencies of the floating body motions. In some cases these situations cannot be avoided and it is common to restrict the filling levels in the tank to a certain limits for some operating conditions.

When violent sloshing motion occurs the hydrodynamic loading inside the tank can be very large and needs to be considered in the design of the cargo containment system and the associated hull structure. The hydrodynamic loading inside a tank can be classified either as impulsive impact loading or non-impulsive dynamic loading. The non-impulsive dynamic loads have dominant time variations on the time scale of the sloshing period of motion, while the impulsive impact loads occur with the time variations of the order of milliseconds. When evaluating the structural response, the complexity of the hydro-structure interaction models, which needs to be applied, greatly depends on the type of loading. This point is further discussed in Section 7, [4.3], and an overview of the currently applied methods and methodologies for, sloshing related, hydro-structure interaction simulations in the LNG tanks of membrane type, is given in Malenica et al. (2017).

An excellent overview of all the practical problems related to sloshing is given in Faltinsen & Timoka (2009).

6.6.2 Global linearized sloshing model

Even though sloshing motion is highly nonlinear phenomena in general, the linearized potential flow theory can in many practical cases adequately describe sloshing effects. This is true for the determination of the sloshing natural frequencies as well as for the evaluation of the coupled response of the floating body with partially filled tanks. Indeed, the experience shows that the main effects of sloshing on body motion are due to the change of the hydrostatic stiffness and to the liquid inertia effect (added mass), which can be evaluated fairly well using the linearized potential flow theory.

Reference is made to Figure 58, the linear potential flow assumption are made and the problem is formulated in frequency domain.

Figure 58: Sloshing in a moving tank

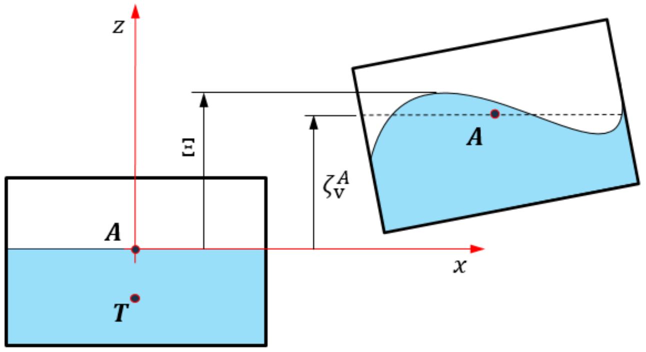

The sloshing hydrodynamic problem is formulated with respect to the coordinate system (A, x, y, z) and the motion of the tank is defined with respect to the reference point $\boldsymbol{T}$. The total hydrodynamic loads in the tank $\{\boldsymbol{F}^{T(1)}\}$ are decomposed as follows:

$$\{\boldsymbol{F}^{T(1)}\} = (\omega^2[\,\boldsymbol{A}^T(\omega)\,] - [\,\boldsymbol{C}^T\,])\{\boldsymbol{\xi}^{T(1)}\} \tag{201}$$

where:

$[\,\boldsymbol{A}^T(\omega)\,]$	–	Hydrodynamic added mass matrix
$[\,\boldsymbol{C}^T\,]$	–	Hydrostatic restoring matrix
$\{\boldsymbol{\xi}^{T(1)}\}$	–	Vector of the tank motion amplitudes

We note the absence of the hydrodynamic damping which does not exist within the closed domain and under the potential flow assumptions. However in order to prevent unphysical behavior at resonant frequencies, an artificial damping can be added to the solution as discussed in Appendix 1.

When evaluating the loads induced by the hydrostatic part of the pressure, the fact that the liquid inside the tank is moving together with the tank and that the free surface inside the tank remains horizontal, should be taken into account. The final expression for the hydrostatic restoring matrix becomes:

$$[\,\boldsymbol{C}^T\,] = -\varrho_L g \begin{bmatrix} 0 & 0 & 0 & 0 & 0 & 0 \\ 0 & 0 & 0 & 0 & 0 & 0 \\ 0 & 0 & 0 & 0 & 0 & 0 \\ 0 & 0 & 0 & I_{11}^{AA} & -I_{12}^{AA} & 0 \\ 0 & 0 & 0 & -I_{21}^{AA} & I_{22}^{AA} & 0 \\ 0 & 0 & 0 & 0 & 0 & 0 \end{bmatrix} \tag{202}$$

Where ϱ_L is the density of liquid and I_{ij}^{AA} denote the free surface moments of inertia with respect to the center of the tank waterplane area (S_{A^T} denotes the free surface of the tank)

$$I_{11}^{AA} = \iint_{S_{A^T}} (y - y_A)^2 dS \ , \qquad I_{22}^{AA} = \iint_{S_{A^T}} (x - x_A)^2 dS \ , \qquad I_{12}^{AA} = I_{21}^{AA} = \iint_{S_{A^T}} (x - x_A)(y - y_A) dS \tag{203}$$

This hydrostatic restoring matrix is negative which leads to the reduction of the global hydrostatic restoring of the body. In particular the metacentric heights of the floating body are reduced as follows (V^T denotes the volume of the liquid inside the tank):

$$\overline{GM}^{Roll} = \frac{I_{11}^{AG}}{V} - \frac{I_{11}^{AA}}{V^T} + z_{BG} \quad , \quad \overline{GM}^{Pitch} = \frac{I_{22}^{AG}}{V} - \frac{I_{22}^{AA}}{V^T} + z_{BG} \qquad (204)$$

In the case when several tanks are present, the total reduction of the metacentric height is equal to the sum of each individual tank contribution. For ship like bodies, mainly the roll motion is significantly affected because the metacentric height in pitch is naturally very high and the reduction due to the tanks is relatively small.

When considering the pure hydrodynamic part of the sloshing problem, the free surface condition should take into account the fact that the free surface is moving also due to the overall motion of the tank (Figure 58). By denoting the corresponding velocity potential by $\varphi^T(\boldsymbol{x})$, the final expression for the free surface condition becomes:

$$-\nu\varphi^T + \frac{\partial \varphi^T}{\partial z} = -i\omega\zeta_{\mathrm{v}}^A \qquad (205)$$

The quantity ζ_{v}^A denotes the vertical displacement of the center of the waterplane area due to the motion of the tank with respect to the reference point $\boldsymbol{T}$:

$$\zeta_{\mathrm{v}}^A = \xi_{T3} + \xi_4^T(y_A - y_T) - \xi_5^T(x_A - x_T) \qquad (206)$$

where ξ_3^T denotes the tank heave motion and ξ_4^T and ξ_5^T the roll and pitch motions respectively.

By adopting the similar formalism as for the seakeeping problem, the total sloshing potential is decomposed into 6 radiation potentials with the corresponding body boundary conditions:

$$\varphi^T = -i\omega \sum_{j=1}^{6} \xi_{Tj}\varphi_{Rj}^T \quad , \quad \frac{\partial \varphi_{Rj}^T}{\partial n} = n_j^T \qquad (207)$$

All the radiation potentials satisfy the homogeneous free surface condition except for heave, roll and pitch. For these potentials the particular solution should be added to the homogeneous one. However, by choosing the reference point to be on the same vertical line as the center of the waterline, only the heave radiation problem remains with inhomogeneous free surface condition, and for this potential the total solution (homogeneous + particular) can be found by inspection as:

$$\varphi_{R3}^T = z \qquad (208)$$

The solution of the homogeneous BVP's for other radiation potentials can be easily found using the same BIE method as for the seakeeping problem (see Appendix 1). Once the velocity potentials evaluated, the hydrodynamic pressure is calculated and integrated over the tank surface to give the corresponding forces. Since the potential flow theory is used and the tank is closed, the total force will be real valued and only the added mass effects will occur. We write:

$$\omega^2 A_{ij}^T = \varrho_L \omega^2 \iint_{S_T} \varphi_{Rj}^T n_i^T \, dS \qquad (209)$$

The dynamic inertia component of the liquid action in the tank is completely described by the above defined added mass matrix $[\,\boldsymbol{A}^T(\omega)\,]$. This means that, in the case of coupling with the overall floating body behavior, the genuine mass of the liquid should be excluded from the total mass matrix of the coupled system (see also Section 5, [0]).

6.7. Hydrodynamic impact loads

6.7.1 Introduction

There exist many situations in offshore and marine operations where the hydrodynamic impacts occur: slamming, sloshing, green water, wave impact, free-fall life boats, underdeck impact …

Figure 59: Practical hydrodynamic impact situations
(from left to right: sloshing, slamming, green water, ditching)

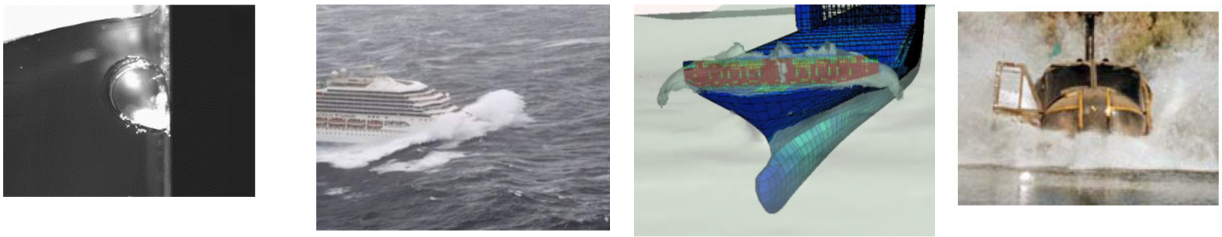

All these phenomena have in common a fast water entry, communicating to the fluid particles accelerations much larger than gravity, of very short duration, and very high pressures localized in time and space. From modelling point of view, the body impacting the water or water hitting the body are fully equivalent and only the relative geometry and the relative velocities matters. This means that the same numerical models are applicable to different types of impact provided that the relative geometry of the impact is properly interpreted. During the impact it is reasonable to assume potential flow and neglect the viscosity. Due to the violent deformations of the free surface and the presence of the jets, even within the potential flow assumptions, the modelling of the hydrodynamic impact is very complex especially in 3 dimensions. That is why the simplified 2D models are usually employed.

6.7.2 Simplified impact models

There exist different simplified impact models, among which the following ones are used most often:

1. Von Karman model
2. Wagner model
3. Generalized Von Karman model (GVKM)
4. Generalized Wagner model (GWM)
5. Modified Logvinovich model (MLM)

All these models are derived within the potential flow assumptions and by neglecting the gravity in the free surface condition, which is justified by the fact that, during the impact, the fluid accelerations are much higher than gravity. Basic aspects of the above models were discussed by Korobkin (2005) in the context of the analytical modelling.

6.7.3 Original Von Karman and Wagner model

Reference is made to Figure 60 where the corresponding BVP's are defined. Both the Von Karman and the Wagner models use the linearized body boundary condition i.e. the body geometry is projected onto the initial mean free surface. The difference between two models comes from the fact that Von Karman model assumes the wetted part of the body to be the geometrical intersection of the instantaneous position of the body and the undisturbed free surface while within the Wagner model the wetted part of the body is unknown. This assumption represents the fundamental difference between two models. For a given value of $c(t)$ the analytical solution can be found for the velocity potential:

$$\varphi(x,0,t) = -V(t)\sqrt{c^2(t)-x^2} \tag{210}$$

The vertical impact force is obtained either using the direct integration of the pressure over the wetted part of the body or using the principle of conservation of momentum. The final result is:

$$F_z(t) = \rho\frac{\pi}{2}\frac{d}{dt}[c^2(t)V(t)] = \rho\pi\left(c\dot{c}V + \frac{1}{2}c^2\dot{V}\right) \tag{211}$$

Within the Von Karman approach the position of the contact point depends on the penetration depth only and is easily found as the intersection of the body with the flat free surface. Within the Wagner approach, the evaluation of the position of the contact point represent the major difficulty and the solution is usually presented in the form of the so called Wagner condition which can be written in the following form:

$$\int_0^{\pi/2} f[c(t)\sin\theta]d\theta = \frac{\pi}{2}h(t) \tag{212}$$

where $z = f(x)$ is the equation of the body geometry.

In the case of the wedge (with deadrise angle γ) and the cylinder (of radius R) we have:

Von Karman $$c(t) = \frac{h(t)}{\tan\gamma} \quad , \quad c(t) = \sqrt{2Rh(t)} \tag{213}$$

Wagner $$c(t) = \frac{\pi}{2}\frac{h(t)}{\tan\gamma} \quad , \quad c(t) = 2\sqrt{Rh(t)} \tag{214}$$

The corresponding forces follow from (211) in the form:

Von Karman $$F_z(t) = \rho\pi\frac{h}{\tan^2\gamma}\left(\dot{h}^2 + \frac{1}{2}h\ddot{h}\right) \quad , \quad F_z(t) = \rho\pi R\left(\dot{h}^2 + h\ddot{h}\right) \tag{215}$$

Wagner $$F_z(t) = \rho\frac{\pi^3}{4}\frac{h}{\tan^2\gamma}\left(\dot{h}^2 + \frac{1}{2}h\ddot{h}\right) \quad , \quad F_z(t) = 2\rho\pi R\left(\dot{h}^2 + h\ddot{h}\right) \tag{216}$$

where the notation $V(t) = \dot{h}(t)$ was used.

It follows that, when Von Karman approach is used, the vertical force is underestimated by factor $\pi^2/4$ in the case of the wedge, and by factor 2 in the case of cylinder.

Figure 60: BVP's for the original Von Karman, Wagner and Modified Logvinovich impact models

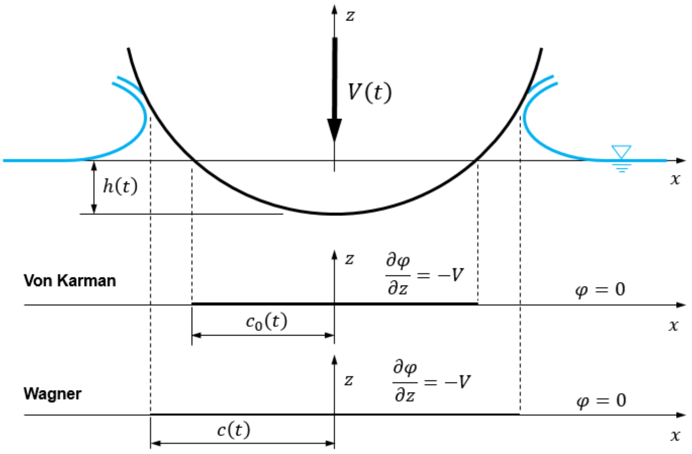

6.7.4 Pressure distribution

One of the drawbacks of the Wagner model is that it gives the infinite pressure at the contact points but the pressure remains integrable so that the hydrodynamic force have finite values. A composite solution can be obtained close to the contact point using the method of matched asymptotic expansions (Cointe & Armand (1987), Zhao & Faltinsen (1993)).The method consist in matching asymptotically the global Wagner solution to the local jet solution close to the contact point. The thickness of the jet $\delta(t)$, the velocity in the jet $V_j(t)$ (assumed to be constant) and the maximum pressure $p_{max}(t)$ (occurring at $x = c(t)$), are obtained as:

$$\delta = \frac{\pi}{8}\frac{c}{\dot{c}^2}V^2 \quad , \quad V_j = 2\dot{c} \quad , \quad p_{max} = \frac{1}{2}\rho\dot{c}^2 \qquad (217)$$

The pressure distribution close to contact point can also be obtained in the form (Zhao & Faltinsen (1993)):

$$p = \rho V\frac{c\dot{c}}{\sqrt{c^2 - x^2}} - \rho V\frac{c\dot{c}}{\sqrt{2c(c - x)}} + 2\rho\dot{c}^2\frac{\sqrt{\tau}}{\left(1 + \sqrt{\tau}\right)^2} \qquad 1 \le \tau \le \infty \qquad (218)$$

$$p = 2\rho\dot{c}^2\frac{\sqrt{\tau}}{\left(1 + \sqrt{\tau}\right)^2} \qquad 0 \le \tau \le 1 \qquad (219)$$

The variable τ and the coordinate x are linked by the following relation

$$x = c + \frac{\delta}{\pi}\left(-\ln\tau - 4\sqrt{\tau} - \tau + 5\right) \qquad (220)$$

which means that $x = \infty$ for $\tau = 0$, $x = c$ for $\tau = 1$ and $x = -\infty$ for $\tau = \infty$.

The comparisons of the original (cut at the maximum theoretical value) and the composite Wagner pressure distributions for wedge impacting the calm water with constant velocity ($13\ m/s$) are presented in Figure 61. The maximum pressure is kept constant ($13\ bars$) for all conditions and 3 different deadrise angles: $\gamma = 5, 10$ and 15. It can be observed that, even if the maximum impact pressure is the same, the corresponding pressure distribution is significantly different and the corresponding pressure coefficients are also very different. This feature of the hydrodynamic impact should be always kept in mind when applying the impact pressures for structural analysis and when interpreting the experimental results.

Figure 61: Impact pressure and pressure coefficient for wedge impact and for different combinations of impact velocity (constant) and deadrise angles. The maximum pressure is kept the same for the left Figure (13 bars) and the velocity is kept constant ($13\ m/s$)

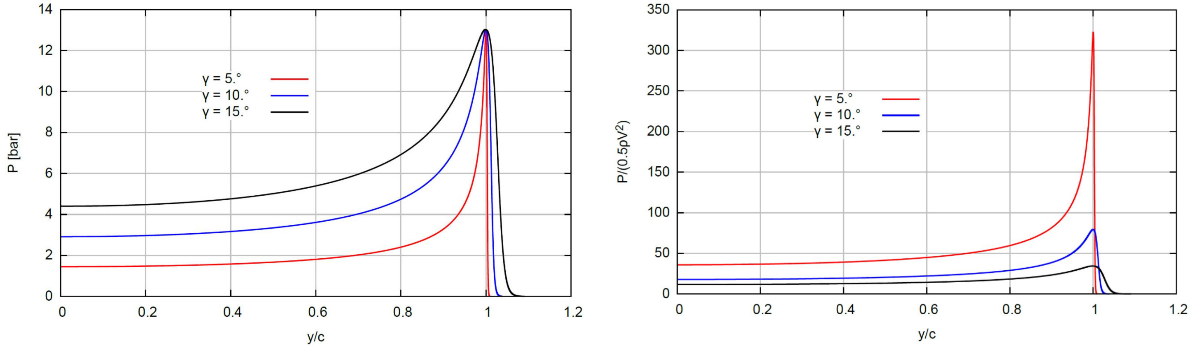

6.7.5 Generalized Von Karman and Wagner models

Reference is made to Figure 62. The main difference between the original and generalized Von Karman and Wagner models lies in the fact that the body boundary condition is applied at the exact wetted position of the body. At the same time the free surface conditions $(\varphi = 0)$ is applied on the horizontal line at the contact points. In the case of GVKM the contact points are found as the geometrical intersection of the body and the initial free surface, and in the case of GWM it is calculated using the numerical variant of the Wagner condition. Furthermore, the nonlinear Bernoulli equation is used to calculate the pressure but the negative pressure is disregarded as discussed by Zhao et al (1996).

Figure 62: BVP's for generalized Von Karman and Wagner impact models

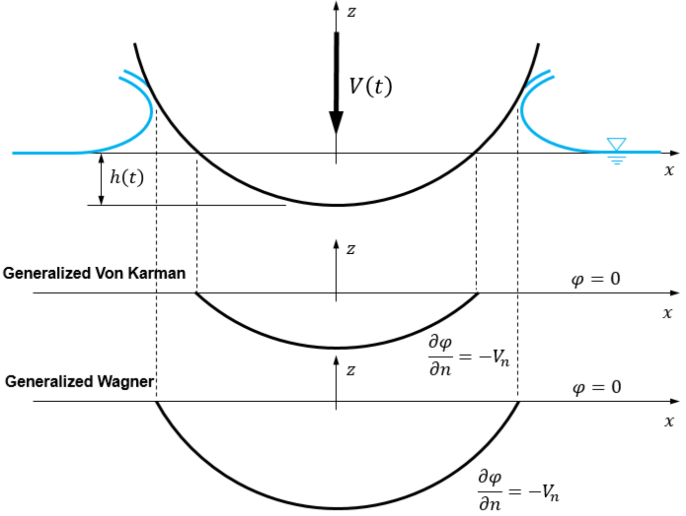

6.7.6 Modified Logvinovich Model

The Modified Logvinovich Model (MLM), first introduced by Korobkin (2005) is an interesting weakly nonlinear model whose assumptions lies somewhere in between the original Wagner and the generalized Wagner models. If the Wagner solution is considered to be the first order solution of the nonlinear impact problem, the MLM can be classified as the approximate second order solution. In that respect the Taylor series expansion is used to write the velocity potential ϕ at the body as a function of the Wagner velocity potential:

$$\phi(x,t) = \varphi(x,0,t) + \dot{h}(t)[f(x) - h(t)] \tag{221}$$

where the body boundary condition $(\varphi_y = -\dot{h})$ was used.

At the same time the nonlinear Bernoulli's equation for pressure, with gravity neglected, is developed up to second order and the following expression is obtained (Korobkin (2005)):

$$p = -\rho \dot{h}^2 \left[\frac{\dot{c}}{\dot{h}} \frac{c}{\sqrt{c^2 - x^2}} - \frac{1}{2} \frac{1}{1 + f_x^2} \left(\frac{c^2}{c^2 - x^2} + f_x^2 \right) + \frac{\ddot{h}}{\dot{h}^2} \left(\sqrt{c^2 - x^2} + f(x) - h(t) \right) \right] \tag{222}$$

From (222), the original Wagner solution is recovered be keeping the first term in brackets only. The main advantage of the MLM, when compared to GWM, lies in its simplicity and incomparably lower CPU time requirements. The disadvantage lies in the fact that the pressure is not provided with sufficient accuracy within MLM model. However, predictions of the total hydrodynamic force by the MLM is surprisingly good compared with GWM for quite general geometries as shown in Figure 63.

Figure 63: Vertical force (right) on typical ship section (left) during vertical impact

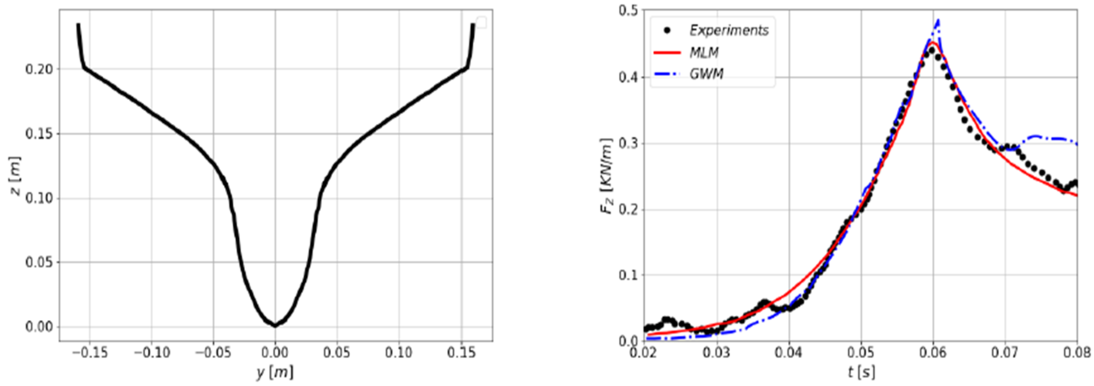

6.7.7 Asymmetric impact

The asymmetric impact conditions can be induced by many different sources: the asymmetric section, oblique impact velocity, presence of the roll motion and others. In principle, all the above described slamming models can be adapted for asymmetric impact conditions, but the technical difficulties increase especially regarding the determination of the contact points but not only. Some of those models are discussed in Korobkin & Malenica (2005) and De Lauzon et al (2015).

6.7.8 Effects of compressibility

Wagner impact model is made under the assumptions of the incompressible fluid flow. Strictly speaking the assumption of incompressibility is not valid at the very beginning of impact when the body touch the fluid or when the body impacts the fluid at zero angle (flat impact). For those conditions the acoustic effects become important and need to be taken into account. The duration of the impact stage when compressibility matters is very short and depends on the Mach number which is defined as $M = V/c_s$ where V denotes the impact speed and c_s the speed of sound in the fluid. The speed of sound for water is approximately 1500 m/s and the impact speed is generally of the order of few meters per second so that the Mach number is very small (this is not the case for aerated fluid where speed of sound drops rapidly depending on aeration). Under the assumptions of the low Mach number the acoustic theory of water impact can be formulated to describe the local flow characteristics. It follows in particular that the maximum pressure during this phase is limited by (ρ denotes the fluid density):

$$p_{max} = \rho c_s V \qquad (223)$$

From practical point of view when calculating the structural response due to impact loading, the effects of compressibility are usually ignored and the structure is assumed to be already wetted at the beginning of the simulations. More discussions on main features of compressible impact can be found in Korobkin (1996,1997).

6.7.9 Water exit

In many applications, e.g. whipping calculations, due to the oscillatory nature of the body motions, both the water entry and the water exit stages are important and should be considered.

The (negative) loads which occur during the water exit can be of the same order as the loads during the entry stage but, in general, last longer (Korobkin (2013)). The simplest mathematical model of water exit is based on the von Karman approach where the wetted part of the body is determined as the part of the body surface below the mean water level. The hydrodynamic force is computed without account for the variation of the added mass in time. This approach describes well the magnitude of the force but under predicts its duration. A more advanced approach is proposed by Korobkin et al. (2014) in where the flat-disc approximation was used for bodies with small deadrise angles and large accelerations of the body motion. A comparisons of the proposed model with CFD results is shown in Figure 64.

Figure 64: The non-dimensional hydrodynamic force acting on the wedge during the entry and exit stages as a function of the non-dimensional time. (From Korobkin et al. (2014)

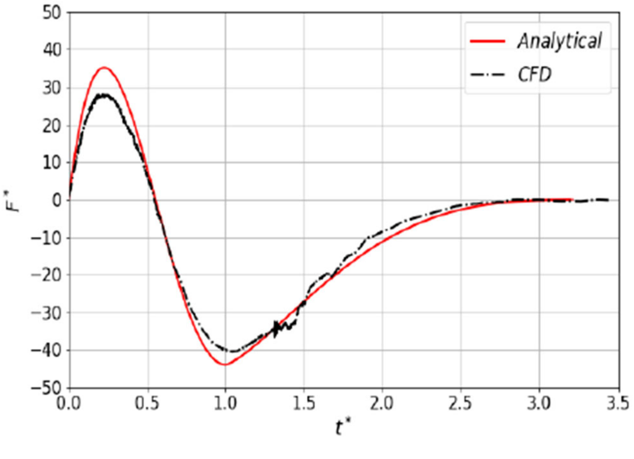

6.7.10 Three dimensional effects

As far as the 3D slamming methods are concerned the evaluation methods are less developed. The main reason is the difficulty in the determination of the instantaneous wetted part of the body which, in 3D case reduces to the evaluation of the closed contact line in space. The exact analytical Wagner solution exist for very simple geometries only, such as axisymmetric cone or elliptic paraboloid. (Scolan & Korobkin (2001), Faltinsen & Chezhian (2004)). Due to its simplicity the Von Karman model is of interest but this model underestimates the impact loading in a way similar to the 2D case. As an indication, in the case of constant impact velocity U the vertical forces for the axisymmetric wedge and the sphere are given by the following expressions:

Von Karman $$F_z(t) = 4\rho \tan^{-3}\gamma\, U^4 t^2 \quad , \quad F_z(t) = 2^{5/2}\rho R^{3/2} U^{5/2} t^{1/2} \qquad (224)$$

Wagner $$F_z(t) = 4\left(\frac{4}{\pi}\right)^3 \rho \tan^{-3}\gamma\, U^4 t^2 \quad , \quad F_z(t) \simeq 6\sqrt{3}\rho R^{3/2} U^{5/2} t^{1/2} \qquad (225)$$

which gives an approximate ratio of 2 between the two approaches.

6.7.11 Strip approach for water impact

Due to the complexity of the 3D impact models, the 2D strip approach is often employed. Within this approach the part of the body, which is likely to experience slamming loads, is subdivided into a certain number of strips which are considered independently (see also Section 7, [3.3.2]).

A rough idea of the error introduce by this approach, can be seen from Figure 65 where the 3D analytical Wagner results are compared to 2D Wagner strip approach for the elliptic paraboloid. The x coordinate represent the ratio between the small and large ellipsoid axes, and the y coordinate represents the ratio between the corresponding forces. When the ratio a/b goes to 0 the conditions approach the infinite 2D parabola and when the ratio a/b approaches unity, the case of sphere is recovered. It can be seen that the 3D effects are very significant and cannot be ignored in practice. The purely numerical CFD modelling remain a promising alternative and is used more and more in practice in spite of large CPU time.

Figure 65: Comparisons of full 3D and 2D strip approach for impact of elliptic paraboloid (from Scolan & Korobkin (2001)

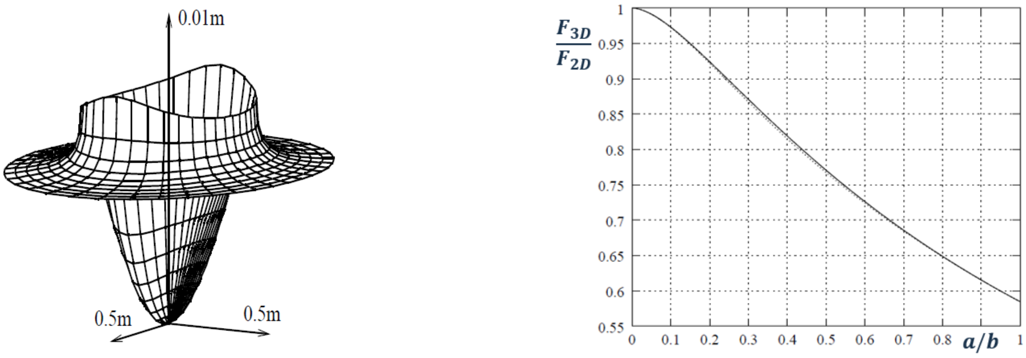

6.8. Perforated structures

6.8.1 Introduction

Perforated structures are used in many practical applications related to offshore installations: perforated breakwaters, vertical screens in the tanks, protection covers, heave plates, fish nets … The openings may be circular, rectangular or just horizontal or vertical slots (see Figure 66).

Figure 66: Perforated structures (from Molin (2002))

(a) Breakwater

(b) Subsea protection cover

(c) Motion stabilizer

6.8.2 Numerical modelling

It turns out that the overall performances are not much affected by the type of openings provided that the porosity, or open-area ratio is the same. This open area ratio (denoted here by) is defined as the area of the openings divided by the total area. Most of the theoretical models dealing with this issue assumes the flow separation through the openings which implies that the total drag load will locally occur and will be proportional to the square of the relative velocity. The additional fundamental assumption is that the velocity and the pressure drop are continuous along the wall, meaning that the perforated wall is idealized as a porous structure. It follows that the pressure drop Δp is related to the normal relative velocity $\boldsymbol{v}_r$ by the following expression (Molin (2002)):

$$\Delta p = \frac{1-\tau}{2\mu\tau^2}\varrho\boldsymbol{v}_r|\boldsymbol{v}_r| \tag{226}$$

The coefficient μ denotes the discharge coefficient which depends on the shape of the openings and, for constant velocity, or very large Keulegan Carpenter number with oscillatory velocity, the typical values of discharge coefficient are $\mu \simeq 0.5$ for sharp openings and $\mu \simeq 1.0$ for rounded ones. Finally, the assumption of very large number of the openings is usually employed which allows for neglecting the local inertial effects close to the perforations. With all these assumptions, the potential flow theory can be applied by simply changing the boundary condition at the body. This boundary condition (226) being non-linear it follows that an iterative procedure needs to be applied when solving the boundary value problem. This also means that approximating the body boundary condition by the linear expression is not acceptable in the present context.

6.8.3 Effects of perforations

The effects of perforations is best illustrated on the associated added mass and damping coefficients. Interesting experiments on perforated three dimensional cylinders are reported by Molin & Legras (1990) where an open ended octagonal cylinder (see Figure 66c) was oscillated in relatively deep water. The experimental results for the added mass and damping coefficients are compared with the numerical ones in Figure 67. As the amplitude increases from zero, the added mass coefficient steadily increases up to its asymptotic value of 2, which corresponds to the case of a solid cylinder full of water. In the low amplitude range the damping coefficient dominates the added mass coefficient, until the two curves cross each other. The crossing corresponds to the maximum value of the damping coefficient, which is equal to one, half the solid case added mass coefficient. This feature has been observed for all geometries, in two and three dimensions (in infinite fluid i.e. without a free surface): the maximum value of the damping coefficient is always half the solid added mass coefficient and the two curves always intersect at that point. It has also to be noted that the end effects should be added to the infinite fluid solution in order to account for the flow separation at the edges of the body (curve denoted: with drag correction in Figure 67). As it can be seen, the proposed mathematical model based on relatively simple potential flow assumptions with the correction of the boundary conditions shows to be reasonably accurate.

Figure 67: Effect of perforations on the added mass and the damping coefficients for the perforated vertical octagonal cylinder in deep water (from Molin (2002))

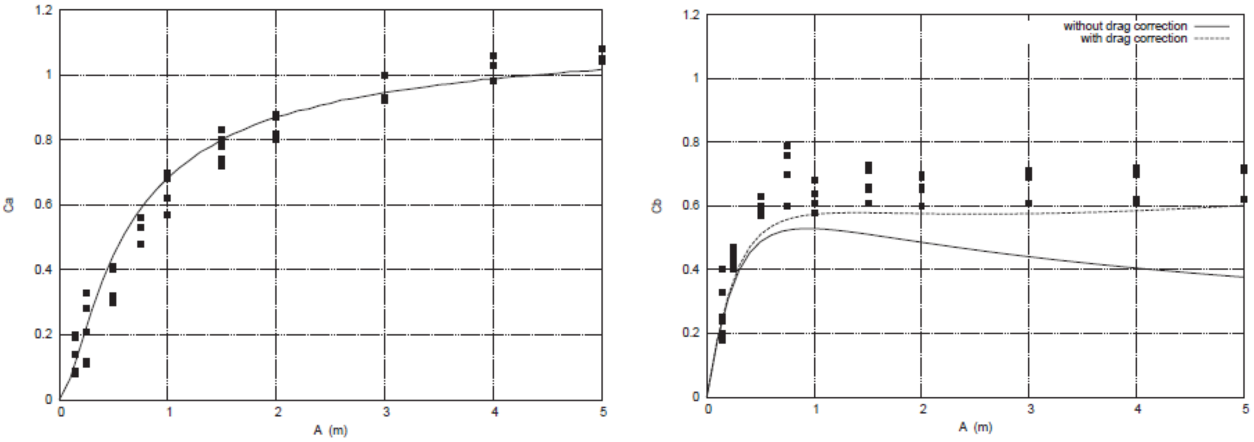

6.9. Gaps and moonpools

6.9.1 Introduction

Whenever there exist a closed volume (even partially) of fluid exposed to the influence of the external forces, there exist the possibility of the resonant behavior of the fluid. This means that, not only the fully closed volumes such as the tanks carrying liquid, but also the partially closed volumes such as the moonpools (vertical openings from deck to keel through the hull) and the narrow gaps between the rigid surfaces (ships in side by side condition, ships close to quay …), can experience similar resonant type of behavior. In practice it is important to have access to the natural frequencies of these resonant modes.

6.9.2 Piston mode in moonpools

In addition to the classical sloshing modes, the resonant modes in the moonpools includes an additional mode known as the piston, or pumping mode, where the entrapped water heaves up and down more or less like a solid body. The theoretical background for the evaluation of the piston like resonance was given in (Molin (2001)). With the assumption of the infinite water depth and the vertical walls of the moonpool, it was shown that the piston mode natural frequency can be approximated by assuming the water entrapped in the moonpool to be "frozen". The natural frequency is obtained as:

$$\omega_0 \simeq \sqrt{\frac{g}{d + b f_0(b/l)}} \tag{227}$$

where d is the draft, and b and l are the width and length of the moonpool and the function f_0 is given by the following expression:

$$f_0(x) = \frac{1}{\pi}\left[\sinh^{-1}\frac{1}{x} + \frac{1}{x}\sinh^{-1}x + \frac{1}{3}\left(x + \frac{1}{x^2}\right) - \frac{1}{3}\left(1 + \frac{1}{x^2}\right)\sqrt{1 + x^2}\right] \tag{228}$$

The quantity $\varrho l b^2 f_0(b/l)$ represents the zero frequency limit of the heave added mass of a flat plate, of length l and breadth b, at the free surface. The function f_0 is presented in Figure 68.

For a circular moonpool of radius a, the natural frequency of the piston mode is given by:

$$\omega_0 \simeq \sqrt{\frac{g}{d + 8a/(3\pi)}} \tag{229}$$

For the moonpool with the cross section slightly varying over the depth, the natural frequency of the piston mode is given by:

$$\omega_0 \simeq \sqrt{\frac{g}{\int_{-d'}^{0} \frac{S(0)}{S(z)} dz}} \tag{230}$$

where $S(z)$ is the area of the cross section and d' is the effective draft given by $d' = d + b f_0(b/l)$ for rectangular shape and $d' = d + 8a/(3\pi)$ for the circular shape.

Figure 68: Function $f_0(b/l)$

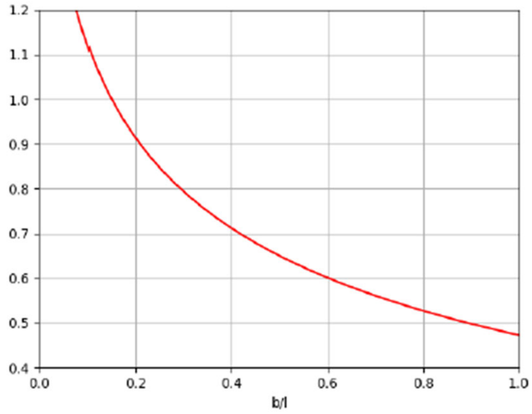

6.9.3 Sloshing modes in moonpools

In addition to the piston mode, the sloshing type modes also occur and can have significant effects for relatively large moonpool openings. For very deep moonpools the sloshing natural frequencies approach those for very deep tank. When the draft decreases the natural frequencies increase from their infinite draft values which is due to the flow taking place below the hull. The approximate formula for the sloshing natural frequencies of the rectangular moonpool with finite draft are given by Molin (2001):

$$\omega_n^2 \simeq g\lambda_n \frac{1 + J_{Nn}(\lambda_n b)\tanh\lambda_n d}{J_{Nn}(\lambda_n b) + \tanh\lambda_n d} \tag{231}$$

where $\lambda_n = n\pi/l$ and the function J_{Nn} is given by:

$$J_{Nn}(\lambda_n b) = \frac{2}{n\pi^2 x}\left\{\int_0^1 \frac{x^2}{u^2\sqrt{u^2 + x^2}}\left[1 + (u - 1)\cos(n\pi u) - \frac{\sin(n\pi u)}{n\pi}\right] du + \frac{1}{\sin\theta_0} - 1\right\} \tag{232}$$

with $x = b/l$ and $\tan\theta_0 = 1/x$.

The function $J_{Nn}(\lambda_n b)$ is shown in Figure 69 for the different values of n.

Figure 69: Functions $J_{Nn}(\lambda_n b)$ and $J_{Dn}(\lambda_n b)$

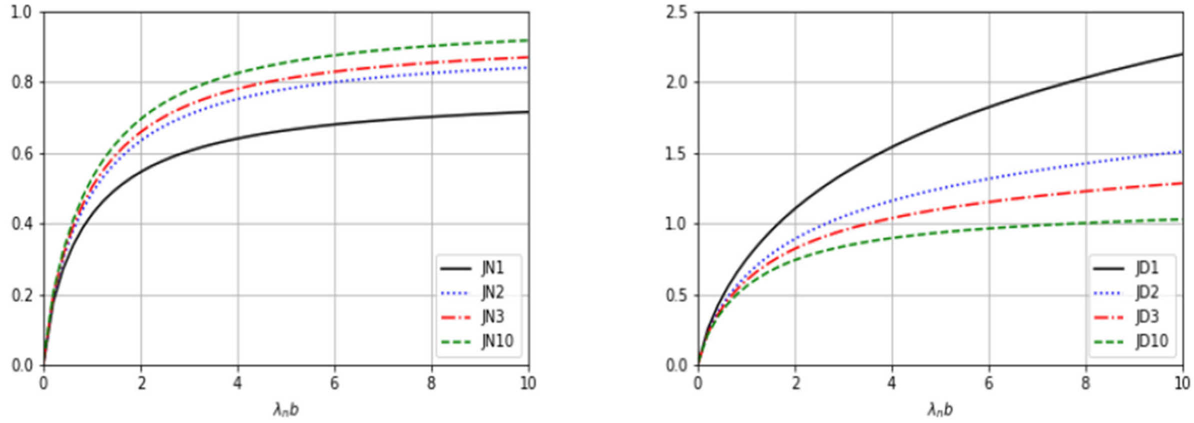

6.9.4 Sloshing modes in gaps

Gaps can be seen as the open moonpools. The expression for the resonant frequencies keeps the same form as for the moonpools (231) with the function with the following expression for J_{Nn} replaced by J_{Dn} which are given by (see Molin et al. (2009)):

$$J_{Dn}(\lambda_n b) = \frac{2}{n\pi^2 x}\left\{\int_0^1 \frac{x^2}{u^2\sqrt{u^2+x^2}}\left[1+2u+(u-1)\cos(n\pi u)-\frac{3\sin(n\pi u)}{n\pi}\right]du - \frac{1}{\sin\theta_0}+1+2x\ln\frac{1+\cos\theta_0}{1-\cos\theta_0}\right\} \tag{233}$$

The function $J_{Dn}(\lambda_n b)$ is shown in Figure 69 for different values of n.

6.9.5 Damping of moonpool and gap resonances

Similar to the sloshing motion in the closed tank, the unrealistically large RAO's of the free surface motion occur close to the resonant frequency. The same comments as those given for sloshing (see Section 5, [2.4.2]) apply here, and the numerical method to take into account the energy dissipation is the same provided that the dissipation coefficients are adapted accordingly.

7. List of references

[1] Aranha J A P, 1994.: “A formula for wave drift damping in the drift of a floating body.”, J. Fluid Mech. 275.

[2] Aranha J.A.P., 1996.: “Second-order horizontal steady forces and moment on a floating body with small forward speed”, J. Fluid Mechanics, 313.

[3] Bachynski E.E., Kristiansen T. & Thys M., 2017.: “Experimental and numerical investigations of monopile ringing in irregular finite-depth water waves.”, Applied Ocean Research, 68.

[4] Bredmose H., Slabiak P., Sahlberg-Nielsen L. & Schlutter F., 2013.: “Dynamic excitation of monopoles by steep and breaking waves. Experimental and numerical study.”, 32nd International Conference on Ocean, Offshore and Arctic Engineering (OMAE2013 – 10948)

[5] Chau F.P. & Eatock Taylor R., 1992.: “Second order wave diffraction by a vertical cylinder.”, J. Fluid Mech., 240.

[6] Chen X.B., 2004.: “Hydrodynamics in Offshore and Naval Applications – Part 1.”, 6th Int. Conference on Hydrodynamics, Perth, Australia

[7] Chen X.B., 2007.: “Middle-field formulation for the computation of wave-drift loads”, J Eng Math (59) 61-82.

[8] Chen X.B., Monroy Ch. & De Hauteclocque G., 2012.: “Taylor development of second order wave loads.”, 10th Int. Conf. on Hydrodynamics, St. Petersburg, Russia

[9] Clark P.J., Malenica S. & Molin B., 1993.: “An heuristic approach to wave drift damping”, Applied Ocean Research, Vol. 15.

[10] Cointe R. & Armand J-L. 1987 “Hydrodynamic impact analysis of a cylinder”, J. Offshore Mech. Arct. Eng, Vol. 109(3), 237-243.

[11] Cummins W.E., 1962.: ”The impulse response function and the ship motions.”, Schiffsctechnik, Vol. 47,

[12] De Lauzon J., Grgic M., Derbanne Q. & Malenica S., 2015.: “Improved generalized Wagner model for slamming.”, 7th Int. Conference on Hydroelasticity, Split, Croatia

[13] Faltinsen O.M. & Chezhian M., 2004.: “A generalized Wagner method for three-dimensional slamming.”, 19th IWWWFB, Cortona, Italy

[14] Faltinsen O.M., Newman J.N. & Vinje T. 1995.: “Nonlinear wave loads on a slender vertical cylinder”, J. Fluid Mechanics, 289.

[15] Ferrant P. 1998.: “Fully non linear interactions of long-crested wave packets with a three dimensional body”, Proc. 22nd ONR Symposium on Naval Hydrodynamics, Washington D.C.

[16] Ferrant P., Malenica S. & Molin B. 1999.: “Nonlinear wave loads and runup on a vertical cylinder, Chapter 3 in Advances in Fluid Mechanics”, Nonlinear Water Wave Interaction, WIT Press.

[17] Grue J., 2002.: “On four highly nonlinear phenomena in wave theory and marine hydrodynamics”, Applied Ocean Res., 24.

[18] Kim S., Sclavounos P.D. & Nielsen F.G., 1997.: “Slow drift response of moored platforms.”, In Proc. of 8th Intl. Conf. Behaviour of Offshore Structures (BOSS’97)

[19] Kim, M.-H. & Yue, D. K. P. 1990.: ‘The complete second-order diffraction solution for an axisymmetric body Part 2. Bichromatic incident waves and body motions,’ J. Fluid Mech., 211.

[20] Korobkin A.A., 2005.: ”Analytical models of water impact.”, Euro. J. Applied Mathematics, Vol. 16, pp. 1-18.

[21] Korobkin, A., Malenica, S., 2005. : “Modified Logvinovich model for hydrodynamic loads on asymmetric contours entering water.”, 20th IWWWFB, Longyearbyen, Norway

[22] Korobkin, A.A., 1996. “Water impact problems in ship hydrodynamics.” Advances in marine hydrodynamics. Ed. Ohkusu M., Southampton: Computational Mechanics Publications

[23] Korobkin, A.A., 1997.; “Asymptotic theory of liquid–solid impact.”, Philosophical Transactions of the Royal Society of London. Series A: Mathematical, Physical and Engineering Sciences, 355(1724)

[24] Korobkin, A.A., 2013. “A linearized model of water exit.” Journal of Fluid Mechanics, 737.

[25] Korobkin A., Khabakhpasheva T, Malenica S. & Kim Y., 2014.: “*A comparison study of water impact and water exit models*”, International Journal of Naval Architecture and Ocean Engineering, Vol. 6, No. 4

[26] Kotik J. & Mangulis V., 1962.: “On the Kramers-Kronig relations for ship motions.”, Int. Shipbuilding Progress. Vol.9

[27] Kristiansen T. & Faltinsen O.M. 2017.: “Higher harmonic wave loads on a vertical cylinder in finite water depth”, J. Fluid Mech., 833.

[28] Ledoux A., Molin B., Delhommeau G. & Remy F. 2006 “A Lagally formulation of the wave drift force”, in Proc. 21st Int. Workshop Water Waves & Floating Bodies, Loughborough.

[29] Malenica S. & Molin B., 1995. : “Third harmonic wave diffraction by a vertical cylinder.” Journal of Fluid Mechanics, vol. 302, pp. 203-229.

[30] Malenica S., Clark P.J. & Molin B., 1995.: “Wave and current forces on a vertical cylinder free to surge and sway.”, Applied Ocean Research, Vol. 17.

[31] Malenica S., De Hauteclocque G., Ten I. & Choi Y.M., 2018.: ”Second order hydroelastic model of floating units.”, 8th Int. Conf. on Hydroelasticity in Marine Technology, Seoul, South Korea

[32] Malenica S., Zalar M. & Chen X.B., 2003.: “Dynamic coupling of seakeeping and sloshing.”, 13th ISOPE Conf., Honolulu, USA

[33] Malenica S., Diebold L., Kwon S.H. & Cho D.S., 2017:” Sloshing assessment of the LNG floating units with membrane type containment system. Where we are?”, Marine Structures

[34] Maruo H. 1960. “The drift of a body floating on waves.”, J. Ship Res.,4, 1-10.

[35] Molin B. & Bureau G. 1980.: “A simulation model for the dynamic behavior of tankers moored to single point moorings”, in Proc. International Symposium on Ocean Engineering Ship Han-dling, SSPA, Gothenburg.

[36] Molin B. & Hairault J.-P., 1983.: “On second-order motion and vertical drift forces for three dimensional bodies in regular waves”, in Proc. Int. Workshop on Ship and Platform Motions, Berkeley.

[37] Molin B. & Legras J-L. 1990.: “Hydrodynamic modelling of the Roseau tower stabilizer, Proc. 9th Int. Conf. on Offshore Mechanics and Arctic Engineering (OMAE)

[38] Molin B. 2001.: “On the piston and sloshing modes in moonpools”, J. Fluid Mech., 430.

[39] Molin B., 1979.: “Second-order diffraction loads upon three-dimensional bodies”, Appl. Ocean Res., 1, 197-202.

[40] Molin B., Remy F., Camhi A. & Ledoux A. 2009.: “Experimental and numerical study of the gap resonances in between two rectangular barges”, in Proc. 13th Congress of Intl. Maritime Assoc. of Mediterranean (IMAM), Istanbul

[41] Molin B., Remy F., Kimmoun O. and Jamois E., 2005. “The role of tertiary wave interactions in wave-body problems.”, J. Fluid Mech, Vol.528.

[42] Newman J.N., 1967.: “The drift force and moment on ships in waves.”, J. Ship Res., 11, 51-60.

[43] Newman J.N., 1974.: “Second-order, slowly-varying forces on vessels in irregular waves”, Proc. Intl Symp. Dyn. Marine Vehicle & Struc. in Waves, Mech. Engng. Pub., London, 193-97.

[44] Newman J.N., 1991. :”WAMIT V3.1S – Second order module – Theoretical background.”, MIT

[45] Ogilvie T.F., 1964.: ”Recent progress toward the understanding and prediction of ship motions.”, 5th Symposium on Naval Hydrodynamics.

[46] Ogilvie, T. F. 1983.: “Second-order hydrodynamic effects on ocean platforms,” in Proc. Int. Workshop on Ship and Platform Motions, Berkeley.

[47] Oil Companies International Marine Forum – OCIMF, 1977.: “Prediction of wind and current loads on VLCCs”, Witherby & Co. Ed.

[48] Ouled Housseine C., Molin B. & Zhao W., 2020.: “Third order wave run-up in diffraction radiation problems.”, 35th International Workshop on Water Waves and Floating Bodies, Seoul, Korea.

[49] Pinkster J.A., 1975.: Low frequency phenomena associated with vessels moored at sea”, Society Petroleum Engineers Journal, December, 487-494.

[50] Rainey R.C.T. 1989.: “A new equation for wave loads on offshore structures, J. Fluid Mechanics, 204.

[51] Rainey R.C.T. 1995. “Slender-body expressions for the wave load on offshore structures”, Proc. R. Soc. Lond. A, 450.

[52] Riise B., Grue, Jensen A. & Johannesen T.B., 2018.: “A note on the secondary load cycle for a monopile in irregular deep water waves”, Journal of Fluid Mechanics, Vol. 849

[53] Sclavounos P.D., 1994.: “Slow drift oscillation of compliant floating platforms.”, In Proc. of 7th Intl. Conf. Behaviour of Offshore Structures (BOSS’94)

[54] Scolan Y.M. & Korobkin A.A., 2001.: “Three-dimensional theory of water impact. Part 1. Inverse Wagner problem.”, J. Fluid Mech. Vol. 440

[55] Scolan Y.-M., le Boulluec M., Chen X.B., Deleuil G., Ferrant P., Malenica S., Molin B., 1997 “Some results from numerical and experimental investigations on the high frequency responses of offshore structures”, in Proc. 8th Int. Conference on the Behaviour of Offshore Structures, BOSS, Delft.

[56] Society of International Gas Tanker & Terminal Operators Ltd. – SIGTTO, 2007.: “Prediction of wind loads on large liquefied gas carriers.”

[57] Zhao R. & Faltinsen O.M. 1993 “Water entry of two-dimensional bodies”, J. Fluid Mechanics, Vol. 246, 593-612.

[58] Zhao R., Faltinsen O.M. & Aarsnes J.V., 1996.: ”Water entry of arbitrary two dimensional sections with and without flow separation.”, 21st Symp. on Naval Hydrodynamics, Trondheim, Norway.

[59] Zhao W., Taylor P.H., Wolgamot H.A. and Eatock Taylor R., 2019.: “Amplification of random wave run-up on the front face of a box driven by tertiary wave interactions.”, J. Fluid Mech, Vol.869.

Section 5 Seakeeping response

1. General

1.1. Introduction

1.1.1 Definition

The denomination seakeeping response is used here to denote the floating body motions induced by the wave component of the hydrodynamic loading. The wind and the current loading are neglected and the maximum motion amplitudes of the body do not exceed its dimensions. This excludes the large slowly varying motions which are considered separately in Section 6.

1.1.2 Dynamic equilibrium of the floating body

Floating body is exposed to the external loads which are counterbalanced by the body inertial loads at each time instant. The general situation is schematically shown in Figure 70 where the different external loads are introduced:

$m\boldsymbol{a}$	Inertia loads
$m\boldsymbol{g}$	Gravity loads
$\boldsymbol{F}_H$	Hydrodynamic loads
$\boldsymbol{F}_W$	Wind loads
$\boldsymbol{F}_R$	Punctual external loads
$\boldsymbol{F}_\sigma$	Internal deformation induced loads

Figure 70: Loads on flexible floating body

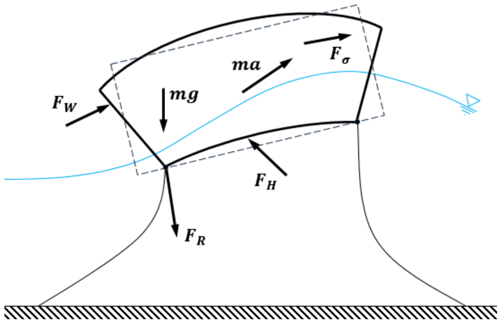

When considering the body to be composed of N_m interconnected particles of individual masses m_i, the equilibrium equation for each individual particle can be formally written as:

$$m_i \boldsymbol{a}_i = m_i \boldsymbol{g} + \boldsymbol{F}_{Hi} + \boldsymbol{F}_{Ri} + \boldsymbol{F}_{\sigma i} + \boldsymbol{F}_{Wi} \quad , \quad i = 1, N_m \tag{234}$$

When the body is supposed to move according to a certain rules (rigid body motion, flexible body motion, multibody configurations …) the equation (234) simplifies accordingly.

1.2. Rigid body dynamics

1.2.1 General

When applied to the freely floating rigid body, the equilibrium equation (234) reduces to 6 dimensional equation for the acceleration of the center of gravity $\{\ddot{\boldsymbol{R}}_G\}$ and the instantaneous rotational acceleration $\{\dot{\boldsymbol{\Omega}}\}$. The final equilibrium equation is recalled below (see also Appendix 1):

$$\begin{aligned} [\boldsymbol{m}]\{\ddot{\boldsymbol{R}}_G\} &= \{\boldsymbol{F}\} \\ [\boldsymbol{I}_{\theta\theta}]\{\dot{\boldsymbol{\Omega}}\} &= \{\boldsymbol{M}\} - [\boldsymbol{\Omega}][\boldsymbol{I}_{\theta\theta}]\{\boldsymbol{\Omega}\} \end{aligned} \tag{235}$$

where $[\boldsymbol{m}]$ is the body mass matrix and $[\boldsymbol{I}_{\theta\theta}]$ is the rotational inertia matrix.

The external force vector $\{\boldsymbol{F}\}$ and the moment $\{\boldsymbol{M}\}$ result from the summation of all the external loads except the deformation loads because the motion of the rigid body, by definition, does not introduce any structural deformations. The system of equations (235) represents the fully nonlinear motion equation which is hard to solve mainly due to the difficulties related to the evaluation of the external loads.

1.2.2 Linearization

Due to the difficulties related to the consistent resolution of the fully nonlinear motion equation, the problem is usually linearized by assuming the body motions to be small. One of the consequences of the linearization is that the rotational velocity $\{\boldsymbol{\Omega}\}$ become the time derivative of the angle of rotation $\{\dot{\boldsymbol{\theta}}\}$ and the quadratic inertia term $[\boldsymbol{\Omega}][\boldsymbol{I_{\theta\theta}}]\{\boldsymbol{\Omega}\}$ in (235) disappears. The linear motion equation becomes:

$$\begin{aligned}[\boldsymbol{m}]\{\ddot{\boldsymbol{R}}_G\} &= \{\boldsymbol{F}\}\\ [\boldsymbol{I_{\theta\theta}}]\{\dot{\boldsymbol{\theta}}\} &= \{\boldsymbol{M}\}\end{aligned} \qquad (236)$$

1.3. Generalized modal description of the linear body dynamics

1.3.1 General

The dynamic systems excited by external loading include various more or less complex configurations with single or several rigid or flexible floating bodies interacting with each other, in freely floating or moored conditions. When linearized, the dynamics of the system can be represented in the form of the space dependent generalized modes of motion/deformation with the corresponding time dependent amplitudes. In this way the instantaneous position $\{\boldsymbol{r}\}$ of the point attached to the body can be written as (see also Appendix 1):

$$\{\boldsymbol{r}(\boldsymbol{r}_0,t)\} = \{\boldsymbol{r}_0\} + [\boldsymbol{\mathcal{h}}(\boldsymbol{r}_0)]\{\boldsymbol{\xi}(t)\} \qquad (237)$$

where $\{\boldsymbol{r}_0\}$ denotes the position of the point at rest and $[\boldsymbol{\mathcal{h}}]\{\boldsymbol{\xi}\}$ is its displacement.

The matrix $[\boldsymbol{\mathcal{h}}(\boldsymbol{r}_0)]$ contains the space dependent generalized modes of motion and $\{\boldsymbol{\xi}(t)\}$ is the vector of the time dependent modal amplitudes. The linear motion equation of the system can be written as:

$$[\boldsymbol{\mathcal{M}}]\{\ddot{\boldsymbol{\xi}}\} = \{\boldsymbol{\mathcal{F}}\} \qquad (238)$$

with:

$$[\boldsymbol{\mathcal{M}}] = \iiint_{\forall_B} [\boldsymbol{\mathcal{h}}]^T[\boldsymbol{\mathcal{h}}]dm \quad , \quad \{\boldsymbol{\mathcal{F}}\} = \sum_{j=1}^{N} [\boldsymbol{\mathcal{h}}]^T\{\boldsymbol{F}_j\} \qquad (239)$$

where $\{\boldsymbol{F}_j\}$ represents the sum of all the external load vectors from Figure 70.

The dynamic equation (238) represent a very convenient way to describe the linear body dynamics for very general configurations. The main difficulty consist in properly choosing the matrix $[\boldsymbol{\mathcal{h}}]$ of the acceptable modes of motion. These modes can be of both the rigid and the flexible type which allows introducing the internal deformation loads $\boldsymbol{F}_\sigma$ within the same formalism. This means that the linear hydroelastic type of simulations is also covered by (238).

1.3.2 Single flexible floating body

In the case of the single flexible body, which occurs most often in practice, the vector of the modal amplitudes can be written as:

$$\{\boldsymbol{\xi}\}^T = \{X_G \quad Y_G \quad Z_G \quad \theta_x \quad \theta_y \quad \theta_z \quad \chi_{f1} \quad \chi_{f2} \quad \cdots\} \qquad (240)$$

where (X_G, Y_G, Z_G) denotes the translation of the center of gravity (surge, sway and heave), $(\theta_x, \theta_x, \theta_x)$ denotes the rotations angles (roll, pitch and yaw) and χ_{fi} denotes the amplitudes of the flexible modes.

2. Linear response in frequency domain

2.1. Introduction

2.1.1 Frequency domain formulation

The most computationally efficient formulation of the linear seakeeping problem is the frequency domain formulation. Combined with the linear spectral analysis, the frequency domain formulation allows for almost instantaneous evaluation of the body response at any return period. The basics of the frequency domain formulation were discussed in Section 4, in the context of the wave loads and here below the corresponding body responses are considered.

2.2. Single floating body

2.2.1 General

The key element in the frequency domain analysis are the linear transfer functions usually called the Response Amplitude Operators (RAO's). The RAO is defined as the linear response of the system to the wave of unit amplitude with particular wave frequency ω and the wave incidence β. In practice the notion RAO is used to describe any physical quantity of interest such as: body motions, local pressure, internal loads, wave elevation, local acceleration … Due to the assumptions of linearity, the response of the system to any particular time history of the excitation is found as a linear combination of the RAO's.

2.2.2 Generalized body motions

The RAO's of the generalized body motions are found as a solution of the linear motion equation (238). In the simplest case of purely wave induced loads, the total external loading is decomposed into the part which is independent of the response (pure excitation) and the part which depends on the response (see Section 4, [3]). The final motion equation becomes:

$$\left[-\omega^2([\boldsymbol{\mathcal{M}}]+[\,\boldsymbol{A}\,]+[\,\boldsymbol{A}_A\,])+i\omega([\,\boldsymbol{B}\,]+[\,\boldsymbol{B}_A\,])+[\,\boldsymbol{C}\,]+[\,\boldsymbol{C}_A\,]+[\,\boldsymbol{k}\,]\right]\{\boldsymbol{\xi}\}=\{\boldsymbol{\mathcal{F}}^{DI}\} \tag{241}$$

where:

$[\boldsymbol{\mathcal{M}}]$	Inertia matrix
$[\,\boldsymbol{A}\,]$	Hydrodynamic added mass matrix of potential flow origin (frequency dependent)
$[\,\boldsymbol{A}_A\,]$	Additional external mass matrix (not used very often but possible in principle)
$[\,\boldsymbol{B}\,]$	Hydrodynamic damping matrix of potential flow origin (frequency dependent)
$[\,\boldsymbol{B}_A\,]$	Additional linear(ized) damping matrix (viscous flow effects, structural damping …)
$[\,\boldsymbol{C}\,]$	Hydrostatic restoring matrix
$[\,\boldsymbol{C}_A\,]$	Additional restoring matrix (mooring …)
$[\,\boldsymbol{k}\,]$	Structural modal stiffness matrix (zero for rigid body modes)
$\{\boldsymbol{\xi}\}$	Amplitude of the response (240), also called the RAO
$\{\boldsymbol{\mathcal{F}}^{DI}\}$	Linear wave excitation vector

In the most general case, the number of the degrees of freedom is equal to $6+N_f$ with N_f denoting the number of the flexible modes. The excitation vector $\{\boldsymbol{\mathcal{F}}^{DI}\}$ and the response vector $\{\boldsymbol{\xi}\}$ are complex quantities and all the other quantities are real valued. The solution of the motion equation gives the amplitudes $\{\boldsymbol{\xi}\}$ of the different modes i.e. the RAO's of the body motions/deformations.

2.2.3 Hydrostatic restoring

Within the generalized modal approach, hydrostatic restoring matrix requires particular attention and several expressions were proposed in the literature. The formulation which is recommended here is the one from Malenica et al. (2020), which is also summarized in Appendix 1, [2.4.6]. Other popular formulations are: Newman (1994), Riggs (2009) and Senjanovic et al. (2012). Note that, for typical floating structures, the structural modal stiffness is much larger than the hydrostatic restoring, so that the response of flexible structural modes will not be much affected by the type of formulation which is used for the hydrostatic restoring stiffness.

2.2.4 Hydrodynamic loads

Within the generalized modal formalism described in Appendix 1, [2.4], the body boundary conditions for the diffracted and radiated velocity potentials become:

$$\frac{\partial\varphi_D}{\partial n}=-\frac{\partial\varphi_I}{\partial n} \quad , \quad \frac{\partial\varphi_{Rj}}{\partial n}=\{\boldsymbol{h}_j\}^T\{\boldsymbol{n}\} \tag{242}$$

where $\{\boldsymbol{h}_j\}$ denotes the mode shape vector.

It follows that the corresponding excitation force and the hydrodynamic added mass and damping matrices are given by:

$$F_i^{DI}=-i\omega\varrho\iint_{S_B}(\varphi_I+\varphi_D)\{\boldsymbol{h}_i\}^T\{\boldsymbol{n}\}dS \quad , \quad \omega^2A_{ij}-i\omega B_{ij}=\varrho\omega^2\iint_{S_B}\varphi_{Rj}\{\boldsymbol{h}_i\}^T\{\boldsymbol{n}\}dS \tag{243}$$

These expressions are valid both for rigid and flexible modes of motion as well as for any type of predefined motion.

2.2.5 Natural frequencies and the natural modes

One of the most important characteristics of the dynamic systems are their natural frequencies and the corresponding natural modes. They are obtained as a solution of the eigenvalue problem associated with the equation (241) which, after neglecting the damping, can be written in the form:

$$\{[\,\boldsymbol{C}\,]+[\,\boldsymbol{C}_A\,]+[\,\boldsymbol{k}\,]-\omega^2\,([\boldsymbol{\mathcal{M}}]+[\,\boldsymbol{A}\,])\}\{\boldsymbol{\xi}\}=\{0\} \tag{244}$$

It should be noted that, due to the fact that the added mass matrix depends on the frequency, the solution of the eigenvalue problem (244) should be found by iterations. In practice an error of 20% on the added mass induces an error of about 5% on the natural frequencies.

In most of the practical cases the $6+N_f$ natural frequencies and natural modes can be extracted. Due to the coupling effects, each natural mode becomes a combination of several degrees of freedom. However, usually the modes of motion are dominated by one particular mode and that is why we usually talk about the natural modes for 3 translations (surge, sway and heave) the 3 rotations (roll, pitch and yaw) and the N_f flexible natural modes.

Due to the fact that the added mass depends on frequency, it may happen that more than $6+N_f$ natural frequencies exist. Typical example are the situations where the additional hydrodynamic resonance, of the system which is coupled with the body motions (sloshing, moonpool …), can occur. In those cases, the iterative procedure which is used for solving the eigenvalue problem (244) can lead to multiple solutions. In Figure 71, the typical results for the roll dominated motion of the classical floating body is shown for the case with and without including the sloshing motion in the tanks:

In the case of the freely floating body, due to the absence of the restoring in the horizontal modes of motion (surge, sway and yaw) the natural frequencies associated with those modes become zero. Even if the presence of the mooring increase the stiffness in those modes, the natural frequencies still remain very low because, in practice the mooring stiffness is relatively low compared to the body inertia. That is why, for the typical off-shore floating systems (FPSO, Semi-submersibles…) the natural periods in the horizontal motions are of the order of few minutes while the natural periods in vertical modes are usually of the order of tenth seconds. On the other side, the stiffness of the flexible modes is dominated by the structural stiffness, which is very large in practice, so that the natural periods of the flexible modes are very low and of the order of second. However, in some particular cases, such as the very large floating structures (VLFS), the natural periods of the flexible modes can be larger and closer to the typical wave periods. Larger the structure larger the natural periods.

Figure 71: Roll resonant frequencies without (left) and with (right) the liquid in the tanks. The intersection of the eigenfrequencies ω_0 of (244) with the straight line $\omega = \omega_0$ gives the true natural frequencies (blue symbols).

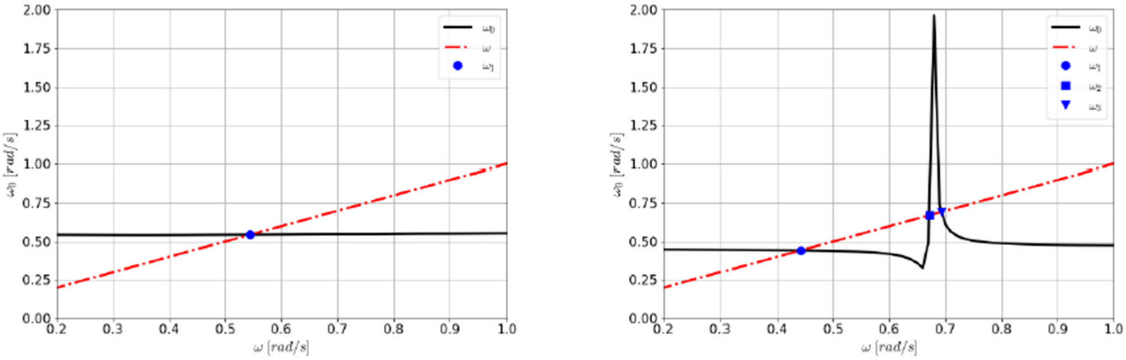

2.3. Multibody interactions

2.3.1 Introduction

When several floating bodies operates in vicinity of each other, the hydrodynamic interaction effects need to be taken into account. Typical multibody configurations occur during the offloading operations in tandem or side by side conditions (Figure 72). The multibody interaction problem can be solved in many different ways and two of them are presented in the following sections.

Figure 72: Typical multibody configurations (left – tandem, right – side by side)

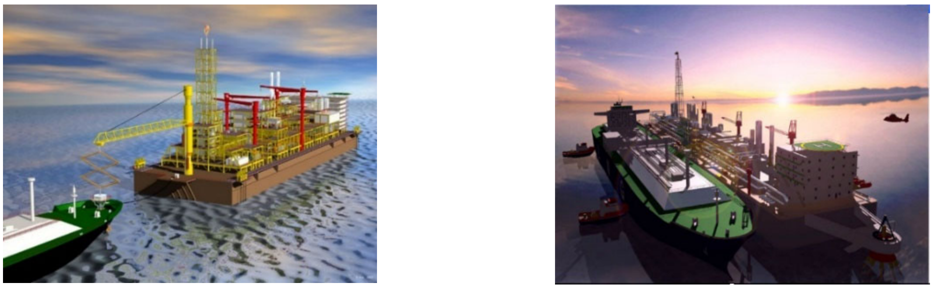

2.3.2 Classical approach to multibody problem

The direct approach consists in considering each body separately by keeping the other bodies fixed (e.g. Chen (2004). The resulting coupled motion equation for M disconnected rigid bodies becomes:

$$\sum_{m=1}^{M}\sum_{j=1}^{6}\left[-\omega^2\left(\delta_{nm}M_{kj}^{nm}+A_{kj}^{nm}\right)+i\omega B_{kj}^{nm}+\delta_{nm}C_{kj}^{nm}\right]\xi_j^m=F_k^{DIn} \quad , \quad n=1,\dots M \quad , \quad k=1,\dots 6 \tag{245}$$

where δ_{nm} denotes the Kronecker symbol ($\delta_{nm}=1$ for $n=m$, zero otherwise).

The hydrodynamic interaction between the bodies is accounted for in the hydrodynamic added mass and the damping coefficients A_{kj}^{nm} and B_{kj}^{nm} , and in the excitation force F_k^{DIn}. These quantities are evaluated by integrating the corresponding velocity potentials over the wetted surfaces of each body. There exist in total $1+6M$ velocity potentials to be evaluated namely one diffraction φ_D and $6M$ radiation velocity potentials φ_{Rj}^k. The corresponding body boundary conditions are:

$$\frac{\partial\varphi_D}{\partial n}=-\frac{\partial\varphi_I}{\partial n} \quad , \quad \frac{\partial\varphi_{Rj}^k}{\partial n}=\begin{cases}n_j^m & k=m\\ 0 & k\neq m\end{cases} \tag{246}$$

The excitation force and the hydrodynamic coefficients are given by:

$$F_k^{DIn}=i\omega\varrho\iint_{S_{B_n}}(\varphi_I+\varphi_D)n_k^n dS \quad , \quad \omega^2A_{kj}^{nm}+i\omega B_{kj}^{nm}=\varrho\omega^2\iint_{S_{B_n}}\varphi_{Rj}^m n_k^n dS \tag{247}$$

The possible physical connections between the bodies can be taken into account through the method of Lagrange multipliers which basically consists in adding the additional constraint equations which fix the motions dependencies. This results in the additional unknowns (connection forces) which should be added to the system of equations (245).

2.3.3 Generalized modal approach to multibody problem

Within the generalized modal approach, the multibody problem is formulated as the problem of single body with additional degrees of freedom (e.g. Newman (1994), Malenica et al (2005)). The overall motion is described by $6M$ generalized modes $\{\boldsymbol{h}_j\}$ and the choice of these modes represents the critical point in the analysis. Due to the assumptions of the linearity, the generalized modes can be defined in many different ways provided that they are linearly independent and are able to represent any particular motion of each body independently. One of the possibilities to do that, is to first consider the generalized body to move as a single rigid body and then define the motion of each, but one, individual body relative to the generalized body as the additional mode of motion. Whatever the choice of the generalized modes, the resulting system of equation keeps the form (241) where the number of degrees of freedom is equal to $6M$. The construction of the BVP's for the diffraction and the radiation velocity potentials, as well as the evaluation of the corresponding hydrodynamic loads becomes straightforward (Section 5. [2.2.3]) where it should be noted that the wetted surface S_B in (249) represents the total wetted surface of the "generalized single body" i.e. the sum of all the individual wetted surfaces $S_B=\sum_{i=1}^{M}S_{B_i}$.

Compared to the classical approach (See [2.3.2]) the generalized modal approach appears to be simpler for the implementation in the existing numerical codes and leads to the smaller system of equations of motions when there exist the connections between the bodies. In the classical approach, each possible connection between the bodies increase the number of unknowns by one while, in the generalized modal approach, the number of degrees of freedom decreases by one. The advantage of the classical approach might be in the fact that the connection forces are part of the solution while, in the generalized modal approach, they must be evaluated in the post processing stage. However, due to the larger order of magnitude of the connection forces relative to the body motions, the conditioning of the linear system, in the classical approach, might become an issue.

2.3.4 Typical effects of the hydrodynamic interactions

To illustrate the effects of the multibody interactions, in Figure 73 the example from Chen (2004) is chosen. The numerical results obtained using the potential flow solver Hydrostar are compared with the experimental results from Kashiwagi et al (2004). The numerical model includes the artificial damping zone between the bodies which is used to reduce the unphysical behavior close to some wave frequencies (see also Appendix 1). The difference between the numerical results for the relative wave elevation between the bodies, with and without the presence of the rectangular barge, show the importance of the hydrodynamic interactions. At the same time, it can be observed that the numerical simulations capture the response fairly accurately.

The multibody interactions can also impact the motion characteristics. The floating body on the weather side or with a smaller size is affected more in most cases. A typical example is that the berth of an accommodation vessel is placed side-by-side with an offshore floating unit, a telescopic offshore gangway is deployed for the crew transfer. The motion of the accommodation vessel can be significantly affected (see Figure 74) with fluctuation behavior depending on wave periods due to multibody interaction (Huang et al (2018)).

Figure 73: Rectangular barge and Wigley hull in waves and drift forces on Wigley hull

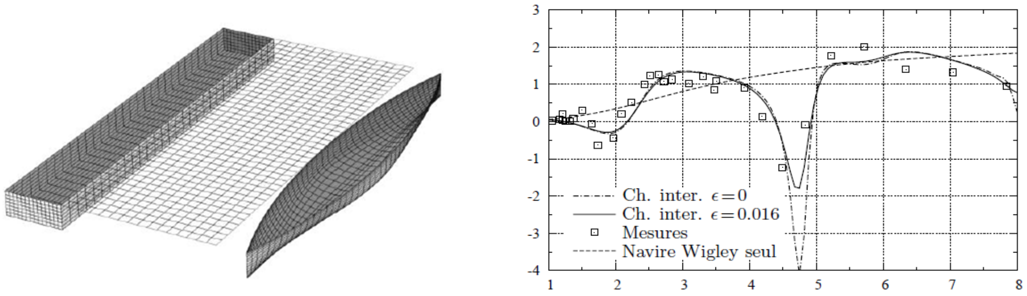

Figure 74: Motion RAO of an accommodation vessel along the side of a FPSO (from Huang et al. (2018))

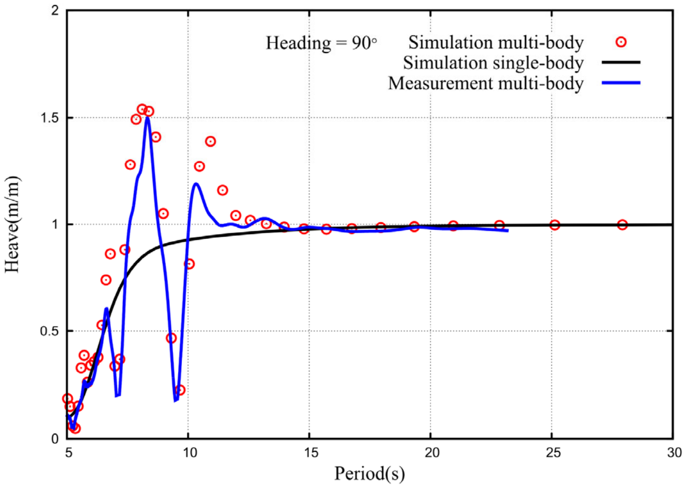

2.4. Effect of internal liquids

2.4.1 Introduction

In practice, there exists many situations where the floating bodies operate with the tanks partially filled with liquid. Typical examples are the bodies with the liquid cargo (oil, LNG …) or the bodies in ballast conditions. Depending on the number of tanks, on their dimensions and filling levels, the dynamics of sloshing can significantly influence the overall dynamical behavior of the body. From physical point of view the problem reduces to the interaction of two dynamic systems (floating body and internal liquid). In many practical cases, it is acceptable to consider the linear aspects of the sloshing only, in which case the coupling of the seakeeping and sloshing can be performed in frequency domain. There exist different methods of coupling which were proposed in the literature (Molin et al (2002), Malenica et al (2003), Newman (2005) …) and here below the method implemented in the diffraction radiation numerical code Hydrostar is presented (Malenica et al (2003)).

2.4.2 Coupling of linear seakeeping and sloshing

Reference is made to Figure 75 where the generic configuration is shown. The loads induced by the linear sloshing motion inside the tank were discussed in Section 4, [6.6] where the total contribution is decomposed into the hydrostatic and the hydrodynamic parts (201).

In order to write the coupled motion equation, the tank added mass matrix and the restoring matrix need to be transferred to the global coordinate system fixed at the overall body center of gravity $\boldsymbol{G}$. Once this done, the coupled seakeeping sloshing dynamic equation of motion can be written as:

$$\{-\omega^2\left([\boldsymbol{\mathcal{M}}]+[\boldsymbol{A}]+[\boldsymbol{A}_T]+[\boldsymbol{A}_{TG}]\right)+i\omega[\boldsymbol{B}]+[\boldsymbol{C}]+[\boldsymbol{C}_T]\}\{\boldsymbol{\xi}\}=\{\boldsymbol{F}^{DI}\} \qquad (248)$$

where the transfer component of the tank added mass matrix $[\boldsymbol{A}_{TG}]$ is given by:

$$[\boldsymbol{A}_{TG}]=\begin{bmatrix} 0 & -[\boldsymbol{r}_{TG}][\boldsymbol{A}_T^{11}] \\ [\boldsymbol{r}_{TG}][\boldsymbol{A}_T^{11}] & [\boldsymbol{r}_{TG}][\boldsymbol{A}_T^{12}]-[\boldsymbol{A}_T^{21}][\boldsymbol{r}_{TG}]-[\boldsymbol{r}_{TG}][\boldsymbol{A}_T^{11}][\boldsymbol{r}_{TG}] \end{bmatrix} \qquad (249)$$

with $\{\boldsymbol{r}_{TG}\}=\{\boldsymbol{r}_T\}-\{\boldsymbol{r}_G\}$ and the different 3×3 sub matrices $\left[\boldsymbol{A}_T^{ij}\right]$ follows from the decomposition of the total 6×6 matrix $[\boldsymbol{A}_T]$:

$$[\boldsymbol{A}_T] = \begin{bmatrix} [\boldsymbol{A}_T^{11}] & [\boldsymbol{A}_T^{12}] \\ [\boldsymbol{A}_T^{21}] & [\boldsymbol{A}_T^{22}] \end{bmatrix} \tag{250}$$

The dynamic inertia component of the liquid action in the tank is completely described by the above defined added mass matrix $[\,\boldsymbol{A}_T(\omega)\,]$ and that is why the genuine mass of the liquid should be excluded from the body mass matrix $[\boldsymbol{\mathcal{M}}]$ in (248). The sloshing action modifies both the restoring and the inertia of the floating body and it is very important to account for both effects simultaneously. For typical ship like bodies the most strongly affected motion is the roll motion because the associated modifications of the restoring and the added mass are the largest.

Within the linearized potential flow theory the unrealistically large RAO's of the free surface motion occur close to the sloshing resonant frequency. This is because the damping associated with the wave radiation does not exist (closed volume) and the most the energy dissipation comes from viscous effects at the tank walls and the dissipation taking place at the free surface due to the breaking wavelike behavior. Within the BIEM numerical method the over prediction of the sloshing motion, can be tackled by adding the dissipation terms in the body and the free surface boundary conditions as discussed in Appendix 1.

Figure 75: Generic configuration for seakeeping – sloshing coupling

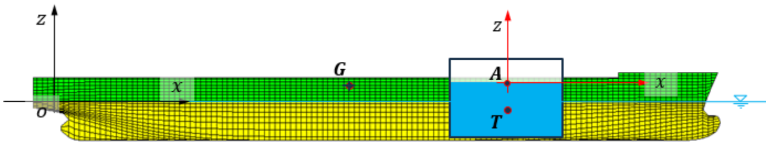

2.4.3 Typical effects of sloshing on body motions

A typical example of the influence of sloshing on floating body dynamics is shown in Figure 76 where the experimental and the numerical results are compared for a ship with two partially filled tanks. The good comparisons of the numerical and experimental results can be observed proving the efficiency of the numerical approach which was described above.

Figure 76: Floating body with liquid in tanks and the roll motion RAO (from Chen (2004))

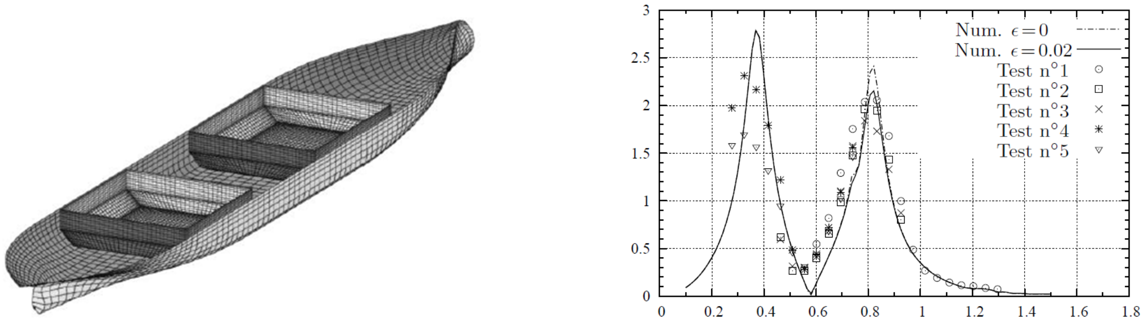

2.5. Effects of current

2.5.1 Introduction

Floating offshore structures operate often in the presence of current or are experiencing the slow drift motion. From mathematical modelling point of view, the two situations are equivalent and the solution of the diffraction radiation problem in the presence of relative current was presented in Section 4, [4.4]. The final hydrodynamic loading being decomposed in the same way, as in the case without the current, the body motion equation remains the same as (241) provided that the encounter frequency ω_e should be used instead of the fundamental wave frequency ω.

2.5.2 Typical effects of current on linear floating body response

The relative current velocity being rather small in practice (few m/s) the linear body motions are not significantly affected. However locally, due to the interaction of the steady and the unsteady fluid flow, important amplification of the relative wave elevation can occur. One typical example is shown in Figure 77 for a generic FPSO in head waves with the current being collinear with the direction of wave propagation. The direct consequence of the modifications of the relative wave elevation are the significant changes in the second order loads which directly depend on the instantaneous wetted part of the body.

Figure 77: Relative wave elevation on a typical FPSO in head waves in the presence of current

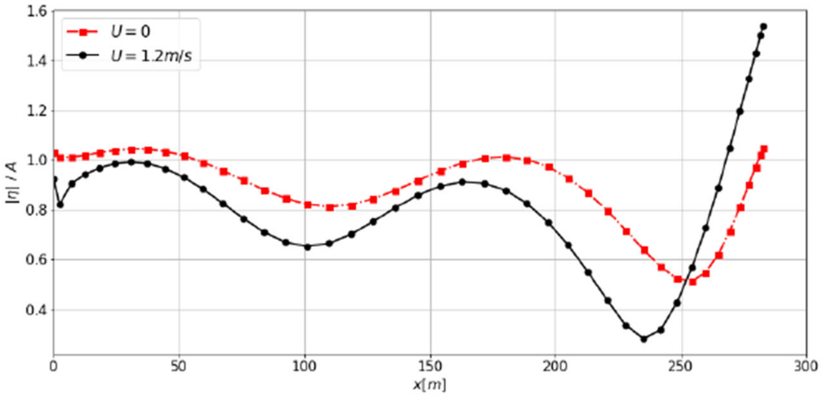

2.6. Lifting operations

2.6.1 Introduction

There exist many practical situations where the floating installation vessel performs the lifting operations of sometimes very heavy weights placed at various positions along the body (Figure 78). Depending on the operating conditions, the seakeeping behavior of the floating body can be significantly affected by the dynamics of the lifting weight.

Figure 78: Lifting operations

2.6.2 Mathematical model

The dynamics of the lifting weight is usually considered using the simple pendulum model. Reference is made to Figure 79 where the basic notations are introduced and where, for the sake of simplicity, the pendulum mass is supposed to be concentrated in a point.

Figure 79: Floating body with attached pendulum

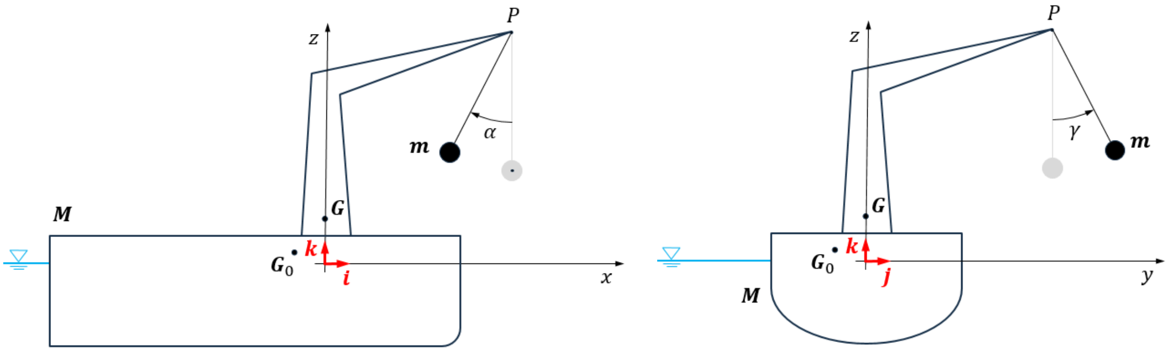

Coupling of the body and the pendulum motion can be performed in different ways. The most intuitive, direct approach consists in considering the multibody interaction problem with constraint equations used to describe the nature of the motion dependences (Malenica et al. (2005)). Even though this approach is theoretically consistent, the implementation into the numerical codes is not straightforward and that is why the generalized modal approach is preferred. As usually, within the generalized modal approach, the critical point is the definition of the generalized modes of motion $\{\boldsymbol{h}_i\}$. An efficient choice is to first consider the "generalized body" with the lifting weight rigidly attached to it, which provides the 6 rigid body modes of motion of the generalized body. The 2 remaining modes of motion are defined as the local pendulum rotations (α, γ) relative to the generalized rigid body. This leads to the modal decomposition presented in Table 1, where $\{\boldsymbol{r}\}$ denotes the position vector of the point attached to the body, relative to body fixed coordinate system (x, y, z) and $\{\boldsymbol{r}_P\}$ denotes the position vector of the attachment point of the pendulum (Figure 79).

Table 1: Generalized mode shapes for floating body with the attached pendulum

i	ξ_i	$\{\boldsymbol{h}_i\}$	
		$\boldsymbol{M}$	$\boldsymbol{m}$
1	X_G	$\{\boldsymbol{i}\}$	$\{\boldsymbol{i}\}$
2	Y_G	$\{\boldsymbol{j}\}$	$\{\boldsymbol{j}\}$
3	Z_G	$\{\boldsymbol{k}\}$	$\{\boldsymbol{k}\}$
4	θ_x	$[\boldsymbol{i}]\{\boldsymbol{r}\}$	$[\boldsymbol{i}]\{\boldsymbol{r}\}$
5	θ_y	$[\boldsymbol{j}]\{\boldsymbol{r}\}$	$[\boldsymbol{j}]\{\boldsymbol{r}\}$
6	θ_z	$[\boldsymbol{k}]\{\boldsymbol{r}\}$	$[\boldsymbol{k}]\{\boldsymbol{r}\}$
7	α	0	$[\boldsymbol{j}](\{\boldsymbol{r}\} - \{\boldsymbol{r}_P\})$
8	γ	0	$[\boldsymbol{i}](\{\boldsymbol{r}\} - \{\boldsymbol{r}_P\})$

Once the generalized modes defined, the straightforward procedure (see [2.3.3]) leads to the coupled motion equation (241). The advantage of the generalized modal approach lies in the fact that it is easily extendable to any type of lifting configurations (several cranes, several lifting ropes per crane …).

2.6.3 Typical effects of the pendulum on linear floating body response

The typical effect of the pendulum on the linear floating body motions is shown in Figure 80 where the classical multibody and the generalized modal approaches are also compared with perfect agreement.

It can be observed that the effects of the pendulum dynamics is somehow similar to the effects of sloshing and leads to two distinct peaks for the roll motion response. This could be intuited from the fact that, in both cases, we are dealing with the coupling of the two dynamic system where the second system (sloshing and/or pendulum) intervene by the modification of the mass and the stiffness properties of the body.

Figure 80: Sway (left) and roll (right) motion of the floating body with attached pendulum

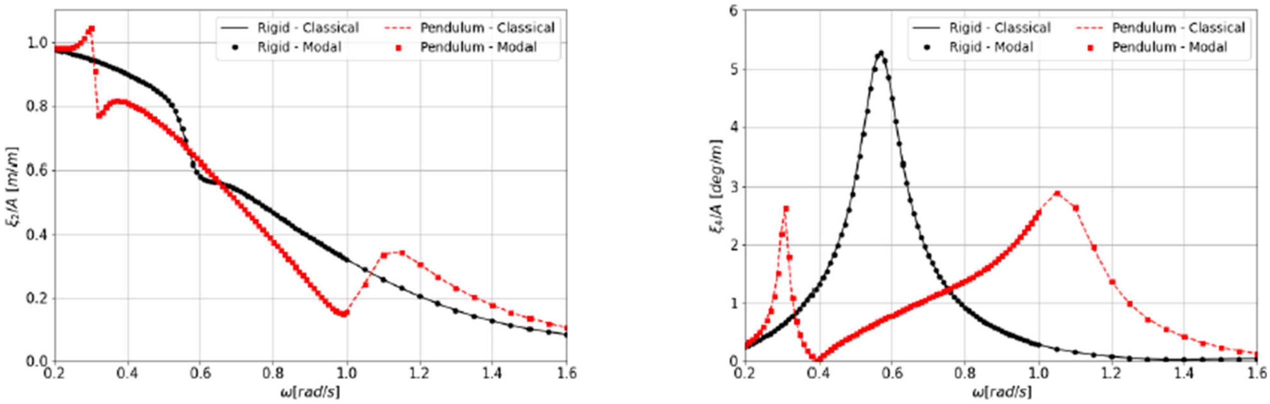

2.7. Accounting for the viscous effects in the linear model

2.7.1 Basic principles

One of the drawbacks of the potential flow theory is the impossibility to account for the viscous flow effects. In general, the viscous effects induce the loads of complex nonlinear nature, but in many cases these effects can be reasonably well modeled by the simplified quadratic velocity force model:

$$F_V = B_Q V|V| \tag{251}$$

In the case where the relevant velocity V in (251) is the velocity of the response, the effect of the viscous forces is naturally interpreted as the damping force and the coefficient B_Q is called the quadratic damping coefficient.

For better understanding of the linearization principles, it is convenient to consider the single degree of freedom oscillating system with the quadratic force included:

$$M\ddot{X} + B_Q\dot{X}|\dot{X}| + KX = F(t) \tag{252}$$

In order to calculate the response in frequency domain, it is necessary to linearize the viscous force. This is usually done by defining an equivalent linear damping coefficient B_L in such a way that the same energy dissipation is ensured.

2.7.2 Harmonic excitation

Since the linearized response is looked for, the excitation force and the body response are assumed in the well-known form:

$$F(t) = \Re\{F_0(\omega)e^{i\omega t}\} \quad , \quad X(t) = \Re\{X_0(\omega)e^{i\omega t}\} \tag{253}$$

After equating the energy, which is dissipated over one sinusoidal cycle of amplitude X_0, for the quadratic and the linear damping, the linearized damping coefficient B_L follows as:

$$B_L = \frac{8}{3\pi}B_Q|X_0|\omega \tag{254}$$

and the linearized motion equation becomes:

$$\left[-\omega^2 M + i\omega^2\frac{8}{3\pi}B_Q|X_0| + K\right]X_0(\omega) = F_0(\omega) \tag{255}$$

This equation should be solved by iteration until the convergence on X_0 is reached.

The floating body response induced by the regular incident waves is the typical example of harmonic excitation and the linearization method is usually denoted as the regular wave linearization. The most important drawback of the method is that is valid for harmonic excitation only i.e. for the regular waves.

2.7.3 Random excitation

Stochastic procedure starts by assuming the response to follow a known probability density distribution which is usually chosen to be represented by the Gaussian law. After equating the mean dissipated energy for the quadratic and the linearized damping, the linearized damping coefficient B_L follows as:

$$B_L = \sqrt{\frac{8}{\pi}}\sigma_{\dot{X}_0}B_Q \tag{256}$$

where $\sigma_{\dot{X}_0}$ is the standard deviation of the response velocity:

$$\sigma_{\dot{X}_0}^2 = \int_0^\infty \omega^2[X_0(\omega)]^2 S(\omega)d\omega \tag{257}$$

The motion equation at each frequency becomes:

$$\left[-\omega^2 M + i\omega\sqrt{\frac{8}{\pi}}\sigma_{\dot{X}_0}B_Q + K\right]X_0(\omega) = F_0(\omega) \tag{258}$$

Similar to the case of the harmonic excitation, the motion equation needs to be solved through iterations until the convergence on $\sigma_{\dot{X}_0}$ is reached. The body response to the particular sea spectra is the typical example where this type of linearization is used. The procedure is usually denoted as the irregular wave linearization and sometimes also the stochastic linearization. It should be noted that the RAO's become sea state dependent.

2.7.4 Damped roll motion

One typical example, where the viscous effects play an important role, is the roll motion of the ship like floating body. In the case of roll motion, the linear wave induced damping is usually very low so that the roll response of the ship will become extremely large around the resonant frequency, if only the potential flow effects are accounted for. In practice the flow separation, hull friction and other nonlinear effects induce the damping loads which are commonly assumed to be proportional to the square of the roll velocity. The corresponding quadratic damping coefficient is evaluated either experimentally (decay tests or forced oscillations), or by the empirical approaches (Ikeda et al (1978), Himeno (1981)), or more recently by CFD simulations. Typical experimental results from the decay tests in calm water for an FPSO, are shown in Figure 81 where the results are also compared with the empirical method of Ikeda & Himeno (1978,1981).

It can be observed that the quadratic approximation is fairly good and that the empirical formula gives the results reasonably close to the experimental ones. It can also be observed that both the experimental and the empirical results approach the finite positive value when the amplitude goes to zero. This value represents the linear damping, which is contributed mainly, but not only, by the potential flow wave effects. This linear part of the damping should also be included in the motion equations (255) and (258).

Figure 81: Roll damping coefficient.
Left - Decay time signal, Right - Comparison with Ikeda-Himeno method

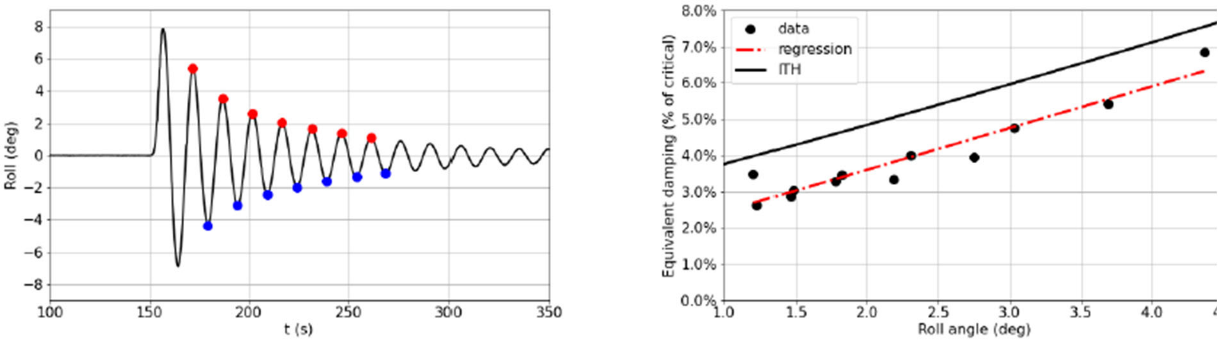

The determination of the quadratic damping coefficient using the decay tests in calm water is common practice in the industry. This method has some drawbacks because the viscous effects are very sensitive to the local features of the flow which can be significantly affected by the wave kinematics (incident, diffraction & radiation). These effects are not present during the decay tests in calm water, and that is why it is sometimes necessary to correct the quadratic damping coefficient in order to account for the wave effects. As an example, in Figure 82 the RAO for the roll motion of the FPSO from Figure 81, are presented for 2 cases: the first one where the damping coefficient from decay tests is used and the second one where this coefficient was multiplied by a corrective factor. It can be observed that the use of the damping from the decay tests in calm water significantly exaggerate the roll response in this particular case. How to choose the corrective factor, which multiplies the damping from calm water experiments, is not clear and it depends on the body shape, loading conditions and the sea state.

Figure 82: RAO of roll motion with the quadratic damping coefficient from decay test in calm water and with the modified damping coefficient. (from Orozco et al.(2002))

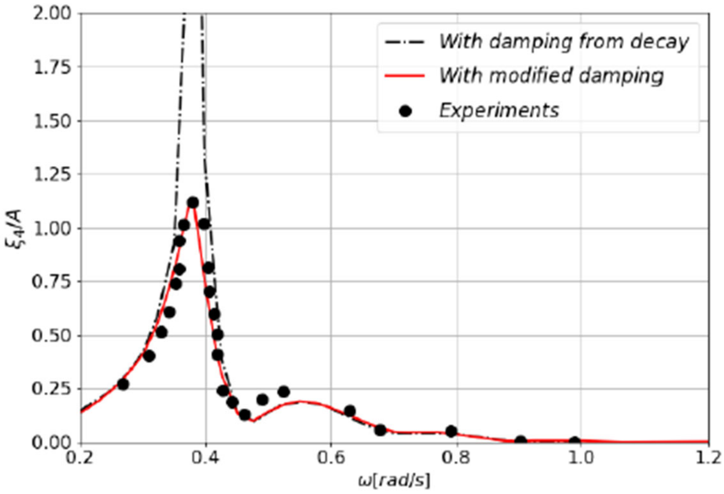

2.7.5 Hybrid seakeeping model with local Morison loading

There exist many floating bodies composed of both relatively large structural parts as well as slender parts (Semi-submersible platforms, FOWT …). Since the slender structural elements will hardly induce any wave effects, they are usually excluded from the diffraction radiation panel model. Their contribution to the loads and the overall equilibrium of the body is usually included in the post processing stage through the application of the Morison equation. The so called mixed, or hybrid, seakeeping model is introduced (Leblanc et al (1993), Sireta et al (2010)). In this model, only the large wetted parts of the body are panelized and used in the construction of the BVP for the velocity potentials. Typical example is shown in Figure 83 where both the hydrodynamic and the structural models are presented.

Figure 83: Hybrid hydrodynamic model (left) and the structural 3DFE model of the semi-submersible platform (right)

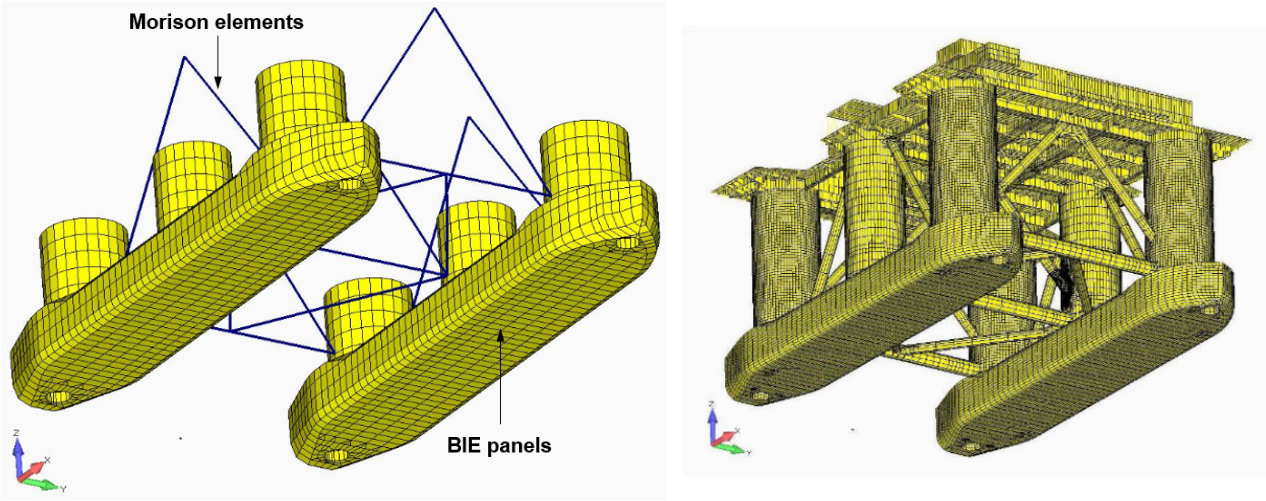

The overall procedure for evaluating the coupled motions starts by solving the hydrodynamic diffraction – radiation problem on large parts of the body using the classical BIE method. This allows calculating the basic hydrodynamic quantities (added mass, damping and wave excitation forces), and also for evaluating the associated flow kinematics (velocity and acceleration) at the different points along the slender elements. The effects of the flow in the direction of the slender body's axis are neglected and the sectional Morison loads are applied in the sectional plane normal to the axis. This requires the projection of the velocities and the accelerations in the plane of the section before evaluating the loads.

When calculating the Morison loads, it is important to note that the relative local flow features should include both the incident and the diffracted/radiated contributions. The total Morison loading $\{\boldsymbol{\mathcal{F}}_M\}$ is obtained by summing up the individual sectional contributions. When the body motion equation is solved in time domain the procedure for the inclusion of the Morison loads into the motion equation is straightforward and the Morison loads are added at each time step. However, in the case when the motion equation is solved in frequency domain, the nonlinear components of the Morison loads need to be linearized according to the procedure discussed in [2.7.2] and [2.7.3]. After linearization the final Morison loading can be decomposed in the following form:

$$\{\boldsymbol{\mathcal{F}}_M\} = \{\boldsymbol{\mathcal{F}}_M^E\} + \omega^2[\,\boldsymbol{A}_M\,]\{\boldsymbol{\xi}\} - i\omega[\,\boldsymbol{B}_M\,]\{\boldsymbol{\xi}\} \qquad (259)$$

where $\{\boldsymbol{\xi}\}$ denotes the body motion and:

$\{\boldsymbol{\mathcal{F}}_M^E\}$	Morison excitation force independent of body motions
$[\,\boldsymbol{A}_M\,]$	Morison added mass matrix
$[\,\boldsymbol{B}_M\,]$	Morison damping matrix

These loads are added to the motion equation (241) from which the body motion is calculated. The details about the implementation into the linear seakeeping code, for different linearization procedures, can be found in Ouled Housseine (2014, 2015). The importance of taking the full fluid flow (incident, diffracted and radiated) when calculating the Morison loads, is illustrated in Figure 84 where the results for the Morison forces in vertical direction, for the total and the incident only flow, are compared for the floating offshore wind turbine. It should however be noted that the influence of the diffracted/radiated wave field on the Morison loads, for the typical offshore oil-platforms (semi-submersibles, FPSO's …) is usually not very important and can be neglected.

Figure 84: Vertical force on slender body parts of the FOWT, for the case when the total, and incident only fluid flow, are included in the calculation of the Morison loads. (from Ouled Housseine (2014))

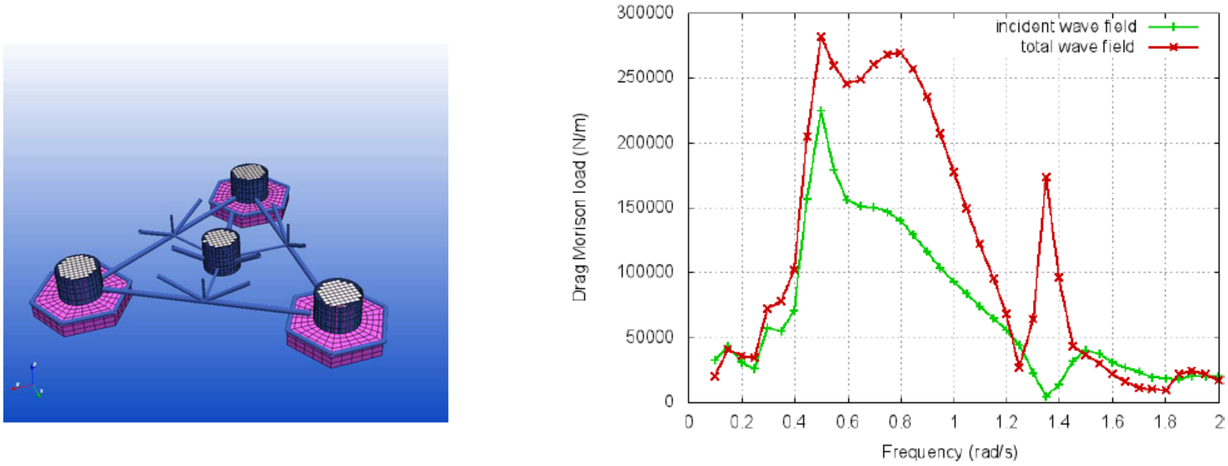

3. Second order response in frequency domain

3.1. Introduction

3.1.1 General

The second order loads are mainly used to evaluate the floating body behavior at the resonant frequencies of the system which fall outside of the common wave spectra. These resonant frequencies can occur either at the frequencies lower or higher than the wave frequencies. In the low frequency regime, the typical examples are the horizontal motions of the moored large bodies and the roll motion of the bodies with low natural frequencies, while in the high frequency range the typical example is the high frequency response of the TLP platform due to tendons, or the high frequency vibration of the hull structure.

3.2. Second order response

3.2.1 Motion equation

In the cases where the nonlinear external loads which occur at the same time as the wave loads (mooring loads, wind and current loads …) can be linearized, the second order body response can be evaluated in frequency domain. The motion equation follows directly from (364), after including the second order hydrodynamic loads (see Appendix 1, [2.4]):

$$\left((\omega_i \pm \omega_j)^2\left([\boldsymbol{\mathcal{M}}] + \left[\boldsymbol{A}(\omega_i \pm \omega_j)\right]\right) - i(\omega_i \pm \omega_j)\left[\boldsymbol{B}(\omega_i \pm \omega_j)\right] + [\boldsymbol{C}]\right)\left\{\boldsymbol{\xi}^{(2)}\right\} = \left\{\boldsymbol{F}^{E(2)}\right\} \qquad (260)$$

3.2.2 Second order low frequency horizontal motion of moored platforms

Even though it is highly recommended to use the time domain simulations to analyze the slowly varying horizontal motion of the moored systems, the frequency domain simulations can, in principle, also be used. The validity of the frequency domain simulation results depends on the importance of the nonlinear effects of the mooring lines restoring forces. In general, the frequency domain simulations are used in the screening phase only, where the accuracy of the results is not of utmost importance.

3.2.3 Second order high frequency springing of TLP

The natural periods of the TLP platform, in vertical modes of motion (heave, pitch, roll), are usually in the range of 2 to 4 seconds. Consequently the sea states with peak periods from 4 to 8 seconds might be responsible for high frequency response also called springing, through their second order contribution to the loading. The numerical evaluation of the high frequency second order loads strictly follows the procedure described in 5. The contribution from the second order diffraction potential represented through the slowly convergent free surface integral is significant and needs to be properly accounted for all the frequency pairs (ω_i, ω_j). Efficiency of the numerical approach proposed in Chen et al. (1995), is demonstrated in Figure 85 where the comparisons of the numerical and the experimental results for the vertical forces on Snorre TLP platform are presented.

Figure 85: Mesh of the Snorre TLP (left) and the second-order vertical forces (right). (from Chen (2004))

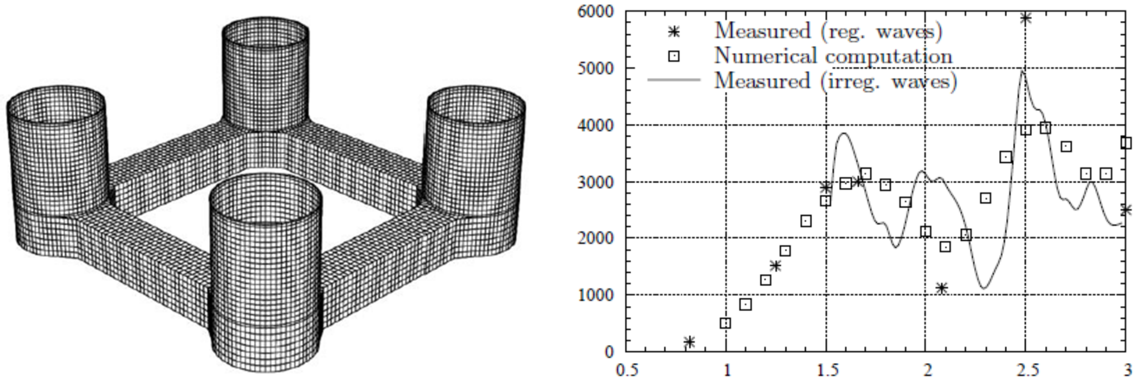

3.2.4 Second order low frequency roll motion of FPSO

The natural periods of the typical FPSO are often close to 30 seconds or even more, where the wave energy of the incident wave is negligible, however significant roll motion might occur in reality as discussed in Rezende et al. (2013). The second order difference frequency theory is usually employed to capture the roll excitation at those natural periods. The numerical evaluation of the second order loads follows the procedure described in Section 4, [5]. Contrary to the sum frequency second order loads, the contribution from the second order diffraction potential is not significant so that the evaluation of the slowly convergent free surface integral can be avoided, which highly simplifies the computations.

4. Response in time domain

4.1. Introduction

4.1.1 General

The linear and the second order approaches in frequency domain are possible only if the nonlinearities in the loading are relatively small. There exist many practical situations where that is not the case and the nonlinear effects are large. The types of the nonlinearities which are of concern are not only related to the wave loading but also to other phenomena such as the nonlinear mooring forces, large body motions, viscous effects … For those cases the time domain simulations remain the only practical way for efficient evaluation of the response. The time domain analysis is based on the direct integration of the equations of motion in time, which makes possible the inclusion of the nonlinearities at each time step. As far as the hydrodynamic part of the problem is concerned, the time domain simulations can be performed in many different ways among which the hybrid frequency-time domain model (Cummins (1962), Ogilvie (1964)) appears to be the most practical (see also Section 4, [4.3]).

4.2. Hybrid frequency – time domain model

4.2.1 Linear response

The representation of the linear hydrodynamic forces in time domain was discussed in Section 4, [4.3]. The pure excitation forces can be directly summed up for each wave component while the frequency dependence of the added mass and damping results in the convolution integral over the retardation functions which takes into account the memory of the flow. The linear motion equation can be written as:

$$([\boldsymbol{\mathcal{M}}] + [\boldsymbol{A}^{\infty}] + [\boldsymbol{A}_A])\{\ddot{\boldsymbol{\xi}}\} + [\boldsymbol{B}_A]\{\dot{\boldsymbol{\xi}}\} + \int_0^t [\boldsymbol{K}(t-\tau)]\{\dot{\boldsymbol{\xi}}(\tau)\}d\tau + ([\boldsymbol{C}] + [\boldsymbol{C}_A])\{\boldsymbol{\xi}\} = \{\boldsymbol{F}^{DI}\} \tag{261}$$

where the different elements were defined in Section 4, [4.3].

In the purely linear case the motion equation in frequency domain (241) and the motion equation in time domain (261) are completely equivalent and lead to the exactly the same results. This is demonstrated in Figure 86 where the pitch motion of a rectangular barge in regular and irregular waves is shown. The results of the response reconstructed from the frequency domain data, and the results obtained by the time domain simulations are compared. The agreement between the two classes of results is excellent after the initial transient which is due to the arbitrary initial conditions which need to be prescribed in the time domain simulations.

Figure 86: Comparisons of the frequency and time domain results in regular (left) and irregular (right) waves.

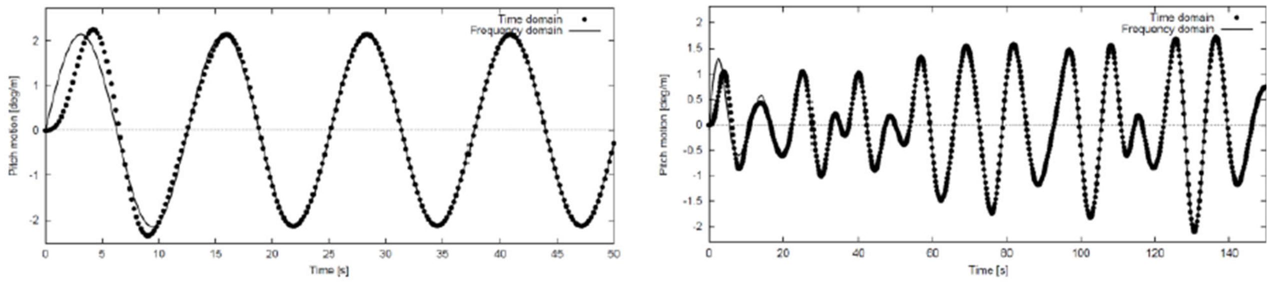

4.2.2 Linear hydrodynamic model with nonlinear mooring loads

Both the frequency (241) and the time domain (261) linear motion equations are valid under the assumption of the small body motions. The advantage of the time domain formulation is that it allows for consistent inclusion of the nonlinear effects other than the hydrodynamic ones (nonlinear mooring, nonlinear damping …). One of such examples are the boats moored by the synthetic ropes which naturally have the nonlinear character because they support the tension loads only. In Figure 87, one example of the simulations is presented and the nonlinear character of the response can be clearly observed in the asymmetric features of the surge response as well as in the tension in the synthetic mooring line which can be positive only.

Figure 87: Boat moored close to the quay by synthetic mooring lines at the stern and the catenary lines at the bow (left), the surge response (middle) and the tension in one of synthetic lines (right).

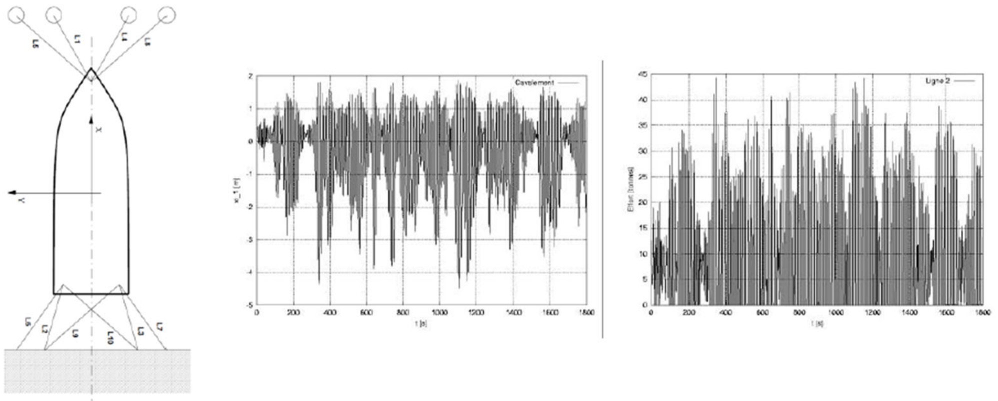

4.2.3 Nonlinear response

The basic idea behind the hybrid approach, is that the linear part of the hydrodynamic loading will be evaluated using the computationally efficient frequency domain analysis, and the complex nonlinear terms will be added in time domain at each time step. When calculating the nonlinear response, the dynamic motion equation is solved in fully nonlinear sense (see Appendix 1) and in particular the arbitrarily large body motions are accounted for. At the same time all the external loads, except the diffraction and the radiation loads, are assumed to be nonlinear. This means that the total gravity loading and the instantaneous hydrostatic pressure loads need also to be included in the external loading. As a consequence the linear hydrostatic restoring matrix disappears from the nonlinear motion equation. Furthermore, since the rigid body motions are assumed arbitrarily large, the instantaneous position of the body needs to be expressed by the general transformation matrix as discussed in Appendix 1. In the most common case of the single rigid body, it follows that the motion equation, written in terms of the (nonlinear) state variables i.e. the translation of the center of gravity $\{\boldsymbol{R_G}\}$ and the $\{\boldsymbol{\theta}\}$ (Euler angles), can be formally written in the following form:

$$\begin{bmatrix}[\boldsymbol{m}] & [0]\\ [0] & [\boldsymbol{I}_{\theta\theta}][\boldsymbol{G}]\end{bmatrix}\begin{Bmatrix}\{\ddot{\boldsymbol{R}}_G\}\\ \{\ddot{\boldsymbol{\theta}}\}\end{Bmatrix} = \{\boldsymbol{F}^{DR}(t)\} + \{\boldsymbol{Q}(t)\} - \begin{Bmatrix}\{\boldsymbol{0}\}\\ [\boldsymbol{I}_{\theta\theta}][\dot{\boldsymbol{G}}]\{\dot{\boldsymbol{\theta}}\} + [\Omega][\boldsymbol{I}_{\theta\theta}]\{\Omega\}\end{Bmatrix} \qquad (262)$$

The notation $\{\boldsymbol{F}^{DR}(t)\}$ was used to denote the linear diffraction and the radiation loads:

$$\{\boldsymbol{F}^{DR}(t)\} = [\,\boldsymbol{A}^{\infty}]\{\ddot{\boldsymbol{\xi}}(t)\} + \int_0^t [\boldsymbol{K}(t-\tau)]\{\dot{\boldsymbol{\xi}}(\tau)\}d\tau + \{\boldsymbol{F}^{D}(t)\} \qquad (263)$$

where $\{\boldsymbol{F}^{D}(t)\}$ denotes the linear loads induced by the diffraction pressure only.

The so called Froude Krylov loads, which are induced by the incident wave pressure, are included in the nonlinear force vector $\{\boldsymbol{Q}(t)\}$ together with the instantaneous hydrostatic pressure loads and gravity loads (see Section 4, [6.4]). The equation (262) is obviously not fully consistent because the linear and the nonlinear loads are “mixed” within the same dynamic equation. In particular the linear diffraction radiation loads $\{\boldsymbol{F}^{DR}\}$ are evaluated with respect to the mean body position while, in the nonlinear motion equation (262), they are applied at the instantaneous body position which can be significantly different from the mean position. How to apply these linear loads in the nonlinear model is one of the major concerns and it should be handled with greatest care knowing that there is no fully consistent way to do it (see also Section 6).

4.2.4 Nonlinear rigid body response in large waves

One of the important applications, where the nonlinear time domain model is particularly useful, is the evaluation of the sectional loads (bending moment…) in the ship exposed to large waves. For instance, when using the linear model the maximum wave induced vertical bending moment in hogging (body at wave crest) and sagging (body at wave trough) remain the same which is not very realistic especially in large waves. Depending on the ship type and the wave amplitude, the difference between the hogging and sagging vertical bending moment can be very large. The main contribution to this effect comes from the Froude Krylov and the nonlinear hydrostatic loading which can vary significantly close to the ship bow and the stern. This contribution can be captured fairly accurately by the nonlinear seakeeping model summarized in the motion equation (262), where the Froude Krylov and the nonlinear hydrostatic loads are calculated using the procedure described in Section 4, [6.3]. In Figure 88, the time history of the vertical bending moment, of a typical FPSO exposed to response conditioned wave (see NI638) is presented. The difference between the hogging and sagging bending moment is clearly visible.

Figure 88: Time history of the linear and nonlinear vertical bending moment (right) on typical FPSO (left) exposed to the response conditioned equivalent design wave

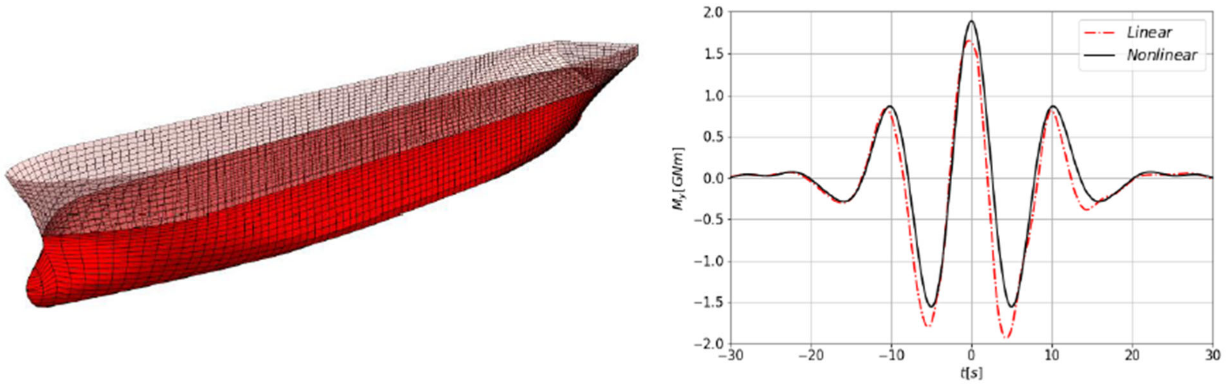

4.2.5 Time integration procedures

In most of the cases, the nonlinear motion equation (262) can be integrated in time using the classical time integration schemes with constant time step, such as the Runge Kutta 4th order scheme. When coupled with the external independent software, for the evaluation of some nonlinear loads, the time stepping procedure needs to be carefully adapted.

In order to minimize the influence of the initial conditions (initial position and velocity) it is useful to apply the loads progressively using the dedicated ramp function. The effect of using the ramp function is illustrated in Figure 89 where the beneficial effects can be appreciated.

Figure 89: Beneficial effects of the ramp function for removal of the horizontal drift

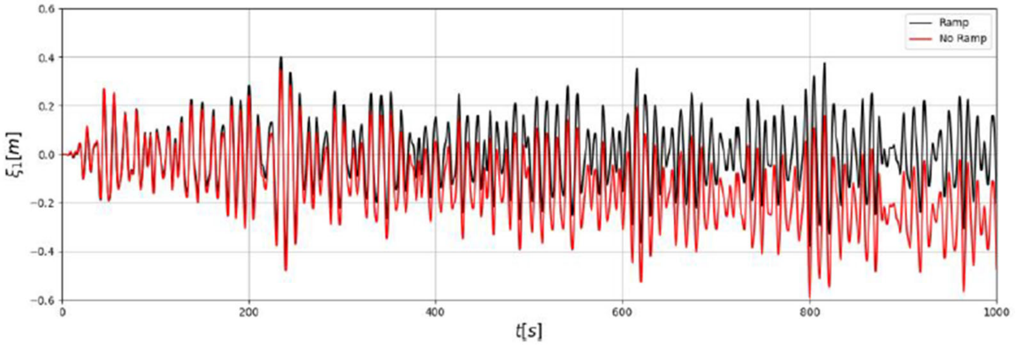

4.2.6 Constraining the horizontal modes of motion

For a freely floating body, the nonlinear wave loads will include a significant component in the horizontal modes of motion (surge, sway and yaw). The hydrostatic stiffness being zero, or close to zero, in those modes the body will drift during the simulations as shown in Figure 89. In reality the wave induced forces in horizontal modes of motion, will be counterbalanced by other loads (maneuvering, thrusters, propulsion, rudder …) so that the body will maintain stable position, and keep the steady course in the case of ship advancing with forward speed. Proper modelling of these effects is not an easy matter so that the simplified solutions are usually employed. Among the different methods which are used in practice, imposing the horizontal modes of motion during the simulations appears to be the most practical method. The exact values of the horizontal motions which have to be imposed, can be chosen in many different ways but using the pre-calculated linear motions appears to be reasonable choice. The motions can be imposed using the method of Lagrange multipliers. This leads to the increase of the degrees of freedom of the motion equation (262) by three additional unknowns, which are the amplitudes of the horizontal forces and moment which are needed to impose the prescribed horizontal motions. In order to be able to apply these additional loads on the FE model, for the purpose of calculating the structural response, the forces and moments need to be distributed over the wetted surface of the body. This can be done by assuming the uniform distribution of the nodal forces over the whole wetted surface.

5. List of references

[1] Chen X.B. & Malenica S. 1998. : “Interaction effects of the local steady flow on wave diffraction radiation at small forward speed.”, International Journal of Offshore and Polar Engineering (IJOPE)

[2] Chen X.B., Molin B. & Petitjean F., 1995.: “Numerical evaluation of the springing loads on Tension Leg Platforms.”, Marine Structures, Vol. 8.

[3] Himeno Y.: “Prediction of Ship Roll Damping - State of the art.”, Report of University of Michigan, 1981.

[4] Huang W., Li B.B., Chen X.B., et al, 2018: "Numerical and experimental studies on dynamic gangway response between monohull flotel and FPSO in non-parallel side-by-side configuration.", Ocean Engineering, Vol. 149: 341-57.

[5] Ikeda Y., Himeno Y. & Tanaka N.: ”A Prediction Method for Ship Roll Damping”, Report of University of Osaka, 1978.

[6] Kashiwagi M., Endo K. & Yamaguchi H., 2004.: “Wave drift forces and moments on two ships arranged side by side in waves”, Journal of Ocean Engineering, 32.

[7] Leblanc L., Petitjean F., Le Roy F. & Chen X.B. 1993.: ”A mixed panel stick hydrodynamic model applied to fatigue life assessment of semi-submersibles.”, Proceedings of OMAE Conf., Glasgow, Scotland

[8] Malenica S., Orozco J.M. & Chen X.B., 2005.: “Some aspects of multibody interactions in seakeeping.”, 15th ISOPE Conf., Seoul, Korea

[9] Malenica S., Orozco J.M. & Chen X.B., 2005.: “Some aspects of seakeeping of the floating body with attached pendulum.”, 11th IMAM Conf., Lisboa, Portugal.

[10] Malenica S., & Bigot F., 2020. : “On the generalized motions/deformations of the floating bodies.”, 35th IWWWFB, Virtual Workshop, Seoul, S.Korea

[11] Molin B., Remy F., Rigaud S., de Jouette C. 2002.: “LNG-FPSO’s: frequency domain, coupled analysis of support and liquid cargo motions”, Proc. IMAM Conference.

[12] Newman J.N. 1994.: “Wave effects on deformable bodies,” Applied Ocean Res., 16.

[13] Newman, J.N., 2005.: “Wave effects on vessels with internal tanks,” 20th Workshop on Water Waves and. Floating Bodies, Spitsbergen, Norway, 2005

[14] Orozco J.M., Malenica S. & Raposo C.V., 2002.: “A pratical procedure for the evaluation of the roll motions of FPSO's including the non-potential damping”, Offshore Technology Conference, Houston, USA

[15] Ouled Housseine C., 2014., “Utilisation de la formule de Morison pour le calcul de tenue à la mer. ”, Internship report, Ecole Centrale de Nantes – Bureau Veritas.

[16] Ouled Housseine C., Monroy Ch. & Bigot F., 2015.: “A new linearization method for vectorial Morison equation.”, 30th IWWWFB, Bristol, UK.

[17] Rezende F., Oliveira A.C., Chen X.B. & Menezes F., 2013.: “A comparison of different approximations for computation of second order roll motions for a FLNG.”, 32nd OMAE Conference

[18] Riggs H.R., 2009. : "The hydrostatic stiffness of flexible floating structure for linear hydroelasticity", Journal of Offshore Mechanics and Arctic Engineering, Vol 131.

[19] Sireta F.X., Malenica S, Bigot F., Derbanne Q., Chen X.B. & Bonniol V., 2010.: “An efficient hydro structure interface for mixed panel-stick hydrodynamic model.”, ISOPE, Beijing, China

[20] Senjanovic I., Vladimir N. & Tomic M., 2012. : "Formulation of consistent restoring stiffness in ship hydroelastic analysis", J. Eng. math, Vol.72, pp. 141-157.

Section 6 Global performance analysis

1. General

1.1. Introduction

1.1.1 Applications

Very complex configurations related to marine operations may occur in practice. Typical examples are schematically shown in Figure 1. Accounting for the interaction between the floater and the subsea equipment (mooring, risers, umbilicals …) can become critical for the evaluation of the body motion, especially in deep waters which can exceed $2000\ m$ in practice.

1.1.2 Definitions

The denomination Global Performance Analysis stands for the evaluation of the overall behavior of the floating systems (floater and underwater equipment) under the action of the environment (wind, waves and current). Due to the presence of the various physical phenomena at the same time, the numerical modelling is a very challenging task. Strictly speaking, the fully nonlinear time domain model of the body dynamics should be used where the value of each load component should be evaluated at each time step. Within the current state of the art this is not practically possible and the different simplifications are usually employed.

1.1.3 Mooring system

Mooring equipment is an essential component of the floating system. It prevents the floating bodies to drift away and keep them under the required design limits. For that purpose, the mooring lines should be able to resist the tension forces induced by the body motions during the lifetime operations. There exist different mooring lines configurations and the most common ones are presented in Figure 90.

Figure 90: Mooring lines configurations

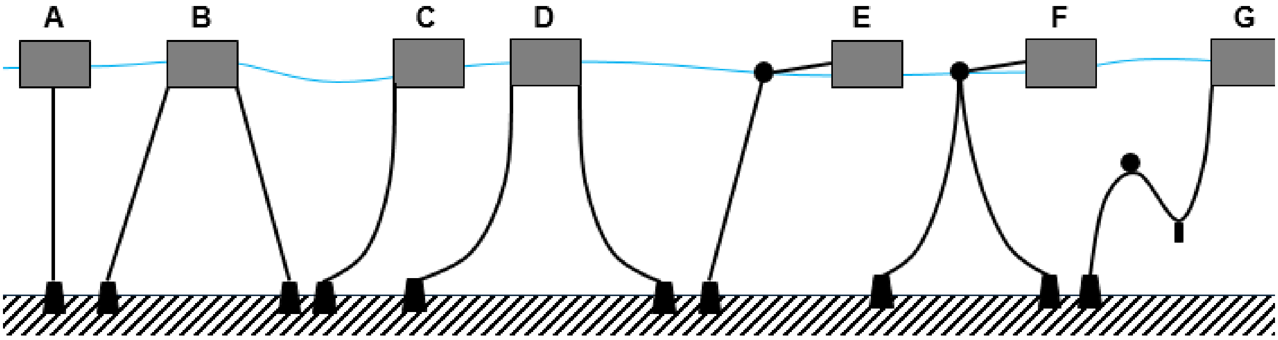

A – Taut, B – Taut spread, C – Catenary, D – Multi catenary,
E – Single Anchor leg Mooring (SALM), F – Catenary Anchor Leg Mooring (CALM), G – Lazy S.

The number and the disposition of the mooring lines for a particular project are chosen with respect to the purpose of the floating system (storage, production, drilling …) and with respect to the onsite environment.

For a typical FPSO, two types of mooring systems are usually employed: spread and single point (turret) mooring system (see Figure 91). A spread moored system keeps the floater in fixed orientation and vessel is more sensitive to global environment intensity and direction. This makes the vessel susceptible to waves incident at large relative wave angles, increasing the probability for substantial vessel motions, especially roll. The turret moored systems orient the vessel to the prevailing environment direction which allows its use in harsh, multi-directional environments with minimized loads and vessel motions. When spread mooring is used, the offloading operations are performed in side by side configuration, while for single point mooring the offloading is performed in tandem configuration (see Figure 72)

Figure 91: Spread (left) and single point (right) mooring configuration of a typical FPSO

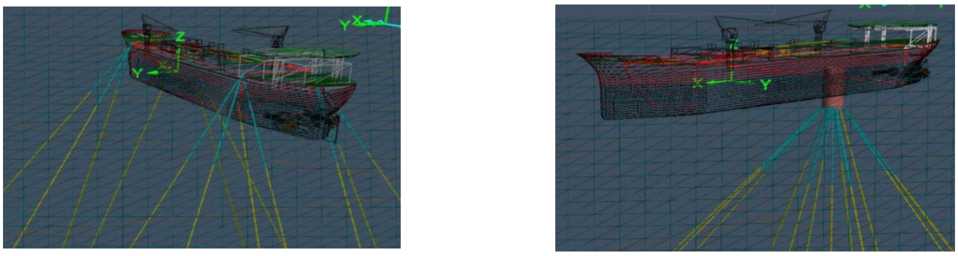

1.1.4 Typical features of the response(s)

Whatever the mooring line configuration, the resulting stiffness in horizontal modes of motion remains usually very low relative to the mass of the floater. This results in very large natural periods (order of minutes) for the body motions in horizontal plane (surge, sway and yaw). At the same time, the natural periods of the motions in vertical plane (heave, roll and pitch) are much lower (order of 10 seconds). Consequently the horizontal motions are also much larger (order of $100\ m$) while the vertical motions are usually much lower and do not exceed the body dimensions (usually below $10m$). In Table 7 the typical natural periods of the rigid body motions for different type of floating units are presented (DDF = Deep Draft Floater):

Table 7 :Typical natural periods of floating units

	FPSO	DDF	TLP	Semi	Spar
Surge	> 100	> 100	> 100	> 100	> 100
Sway	> 100	> 100	> 100	> 100	> 100
Heave	$5 - 12$	$20 - 30$	< 5	$20 - 50$	$25 - 30$
Roll	$5 - 30$	$40 - 90$	< 5	$30 - 60$	$50 - 90$
Pitch	$5 - 12$	$40 - 90$	< 5	$30 - 60$	$50 - 90$
Yaw	> 100	> 100	> 100	> 100	> 100

As it can be seen, a common characteristic of all units are the low natural periods in horizontal plane (surge, sway, yaw) which are of the order of minutes. The natural periods in vertical plane (heave, roll, pitch) varies much from one unit to another. The typical overall response of the floating unit includes the different components which can be formally decomposed as follows:

- Static offset due to mean environmental loads (wind, wave, current)
- Response taking place at the wave frequencies (WF)
- Slow drift or low frequency (LF) response induced by the nonlinear wave loads and the time varying wind and current loads
- High frequency (HF) response for the floaters with high natural frequencies (TLP…)
- Vortex induced motion (VIM) induced by vortex shedding around the columns (TLP, Spar …)

The different response components (except the one related to VIM) are shown in Figure 92 where the time history of the tension in the tendon of the TLP is schematically presented.

Figure 92: Different response components for the tension in the tendon of TLP

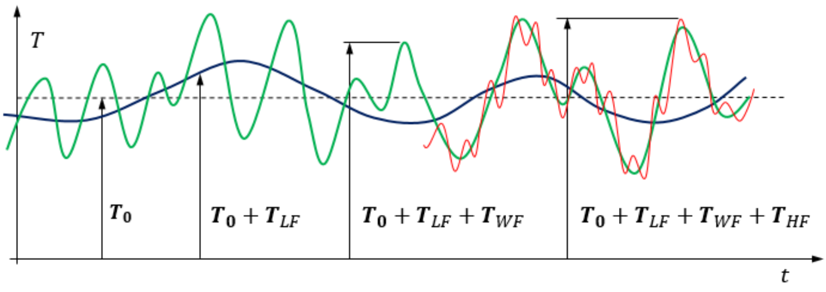

2. Modelling of the lines

2.1. General

2.1.1 Applications

The denomination “lines” is used to denote all the slender elements connecting the floaters between them and connecting them to the sea bed. As discussed in Section 3, the word slender means that the cross-section is small relative to the flow characteristics so that the flow will not be modified by the presence of the slender structures. The following line types are of concern here:

- Mooring lines
- Flexible risers
- Tensioned risers
- Metallic catenary risers
- TLP tendons
- Loading hoses
- Umbilicals
- Towing lines
- Power cables

All those slender elements are modelled using the same theoretical principles which are discussed in the following sections.

2.1.2 External loads on the lines

The main load effects on slender elements are:

- gravity
- buoyancy
- hydrodynamic loads (wave and current)

The inclusion of the gravity and the buoyancy loading is rather straightforward and, thanks to the assumptions of the slenderness, the hydrodynamic loading can be evaluated using the Morison equation (see Section 3, [2.1]).

Some other effects, which can potentially be important in practice (internal flow, contact and friction forces, snap and snatch transient loads, slamming …), are supposed to have minor influence on the body motions and are not discussed explicitly here. These effects need to be considered on case by case basis.

2.2. Numerical modelling

2.2.1 Introduction

The mathematical model of the line dynamics should include all the relevant components of the structural response i.e. tension, bending and torsion and should properly account for the connections with the floater (joints) and the sea floor (anchor, or contact with sea floor). In Figure 93 a general issues important for the line modelling are schematically illustrated.

Figure 93: Large displacements and local deformations of the line. (from Buckham (2003))

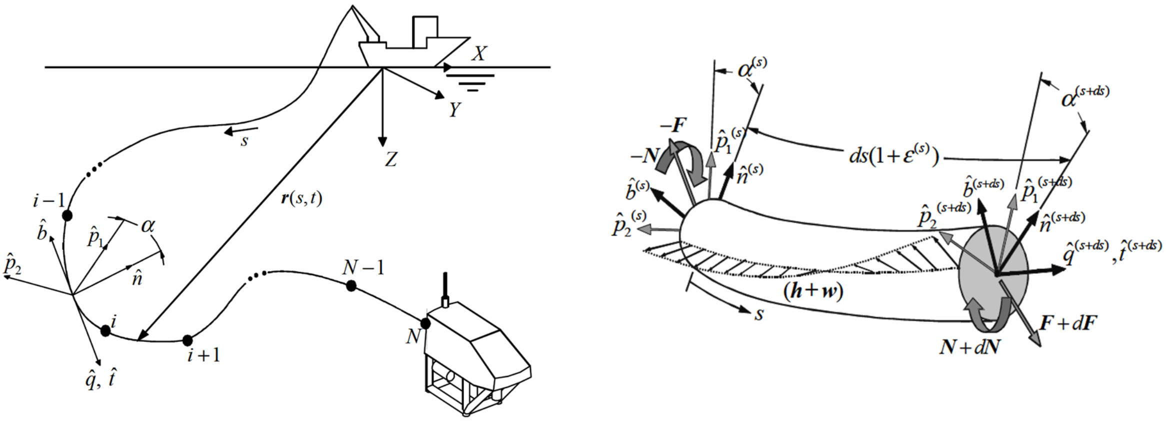

The consistent model of the lines should allow for the large displacements of the line but the structural deformations can still be linearized at each instantaneous position. The comprehensive theoretical description of the mathematical model can be found in Garret (1982), Nordgren (1974), Leonard & Nath (1981) Gerstmayr et al (2013), Buckham (2003) and many others. The complexity of the theoretical models depends on the type of the structural deformations which are accounted for (tension, bending, torsion and their couplings) and on the line geometrical properties (uniform or varying along the line). Once the theoretical model of the line chosen, different numerical techniques can be employed for its solution and the following ones are used most often:

- Finite difference method (FDM)
- Lumped mass method (LMM)
- Finite element method (FEM)

Each numerical techniques has its own advantages and drawbacks with respect to the accuracy, complexity of implementation and the CPU time. Basic features of each method are discussed below.

2.2.2 Finite difference method

The good point of the FDM lies in its relative ease of implementation since it is based on the direct discretization of the constitutive partial differential equations which describe the dynamic system (e.g. Chatjigeorgiou & Mavrakos (1999), Gobat & Grosenbaugh(2006)). However, the FDM appears to not be employed very often in practice because it shows some difficulties when it needs to be adapted for complex line configurations. At the same time, the FDM seems to be quite sensitive to the changes of some numerical parameters, and it also requires very large number of nodes in order to achieve the reasonable accuracy. The LMM and FEM are much more practical and are used more often in practice.

2.2.3 Lumped mass method

Due to its simplicity, the lumped mass model is very attractive. The model consist in assuming the line to be composed of a finite number of discrete mass elements connected by the massless elements which account for the mechanical stiffness and damping. The basic principles of the LMM are depicted in Figure 94 for the simplest case of the 3DOF formulation for the nodal unknowns.

Figure 94: Lumped mass model of the lines (3DOF per node). (from Hall & Goupee (2015))

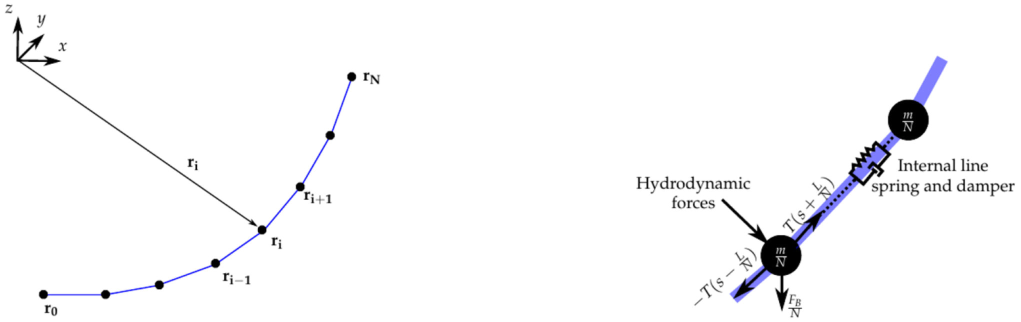

Due to the representation of the masses by discrete set of points the resulting mass matrix is diagonal and does not need inversion during the solution process. At the same time, the numerical implementation of the LMM appears to be rather simple for arbitrary line configurations, and that is why LMM has received much attention in practice. With some modifications the LMM can also be used to model the line bending as well as the torsion. This can be done either by modifying the 3DOF formulation or by introducing the higher order LMM where the 6DOF per node are introduced. For the purpose of global performance analyses, the LMM method is applicable for most of the practical configurations.

2.2.4 Finite element method

The FEM represent the most modern type of the numerical approach which is able to consistently account for all the physical aspects of the line dynamic problem. Highly efficient interpolation functions can be used for representing the distribution of the physical quantities along each finite element leading to extremely accurate solution of the problem (see Figure 95).

**Figure 95: Absolute nodal coordinate finite element formulation of the line dynamics.
Left – finite element representation, Right – complex deformation of single finite element.
(from Shabana & Yakoub (2001))**

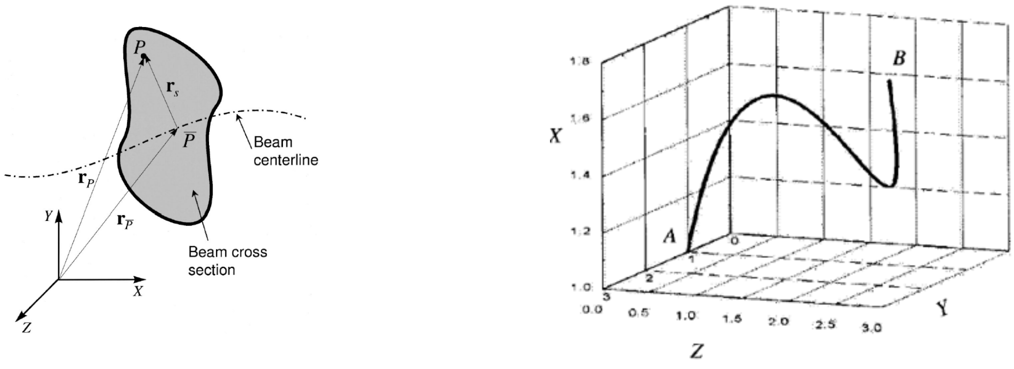

When compared to FDM and/or LMM, the accuracy of the FEM is much better and fewer number of the finite elements is required for the same accuracy. The main disadvantage of the FEM is the complexity of the implementation.

2.3. Simplified line models

2.3.1 General

In the context of the global performance analysis of the moored floating systems, the modelling of the lines presents one of the major difficulties both with respect to the CPU time requirements and with respect to the complexity of the line modelling and coupling. When the motions of the floater are of main concern, the modelling of the lines can be simplified. Two rather distinct aspects of the simplifications can be identified:

- Line dynamics (fully dynamic, simplified dynamic, quasi static or static)
- Structural modelling aspects (tension, bending, torsion, couplings …)

Each time a particular simplification is employed it needs to be clearly justified. In particular, when the structural response of the risers is of concern, no simplifications can be justified on the structural modelling side and the complex structural models including both the bending and the torsional effects need to be employed. However, in the case of mooring lines in particular, different simplifications are possible and they are discussed below.

2.3.2 Simplified modelling of the line dynamics

Modelling the dynamics of the lines means accounting for the genuine line inertia, added inertia, damping and excitation effects along the line. When the full dynamic model of the line is used, the inclusion of these effects is rather straightforward and the Morison loading can be applied along the line at each time step. For some applications (e.g. LF horizontal motion of the floating systems), the dynamic modelling of the lines can be simplified and ultimately reduced to the constant mass and damping matrices to be included directly in the body motion equation. For that purpose the dynamic part of the forces at the fairleads are summed up, linearized and presented in the form of the global inertia and damping loads with respect to the center of gravity:

$$\{\boldsymbol{\mathcal{F}}_L\} = \sum_i \{\boldsymbol{F}_L\}_i = -[\,\boldsymbol{A}_L\,]\{\ddot{\boldsymbol{\xi}}\} - [\,\boldsymbol{B}_L\,]\{\dot{\boldsymbol{\xi}}\} \qquad (264)$$

The inertia $[\,\boldsymbol{A}_L\,]$ and damping $[\,\boldsymbol{B}_L\,]$ matrices can be either pre-calculated using the more sophisticated numerical models or can be deduced from the experiments. Once evaluated the added mass and damping matrices are added directly to the left hand side of the body motion equation. The obvious advantage of this simplified approach is its simplicity (once the inertia and damping matrices evaluated) but the use of this approach need to be done with care and the justifications are to be provided on case by case basis. This approach is not recommended at the final design stage.

2.3.3 Simplified structural modelling of the line: String model

Most often, the main influence of the lines on the body motions consist in the restoring effects from the mooring lines and in the damping effects from all type of lines (mooring, risers …). In some particular cases such as the roll motion, risers can also contribute to the overall restoring. Due to the structural characteristics of the mooring lines, the bending and torsional effects can be safely neglected. This allows using the relatively simple string model i.e. the model accounting for the tension effects in the line only. In that case, in place of the complex FEM models, the simplest 3DOF LMM numerical approach is suitable with good accuracy and reasonable CPU time. The string model is used very often in practice for modelling of any type of mooring lines (chain, cable, synthetic rope …) either within the dynamic or static assumptions.

2.3.4 Static string model: Catenary equation

In the case when the dynamic effects (both the genuine inertia of the line and the Morison loading) can be completely neglected, the original string model can be further simplified and the analytical solution, known under the name of catenary solution, can be used. Consequence of neglecting the dynamic effects is that the equilibrium position of the line becomes 2D i.e. all the elements of the line are located in the same plane. Typical catenary configuration is shown in Figure 96 – left.

In this particular case the dependency of the horizontal force at fairlead T_H on its horizontal displacement X is given analytically by the following nonlinear relation (see Figure 96 – right):

$$X = l - h\left(1 + 2\frac{T_H}{wh}\right)^{\frac{1}{2}} + \frac{T_H}{w}\cosh^{-1}\left(1 + \frac{wh}{T_H}\right) \qquad (265)$$

where w is the weight per unit length of the line in water.

It follows that the vertical force T_z at the fairlead, suspended length l_S and the horizontal scope x (length on plan view from fairlead to touchdown point) are given by:

$$T_z = wl_S \quad , \quad l_S = \frac{T_H}{w}\sinh\frac{wx}{T_H} \quad , \quad x = \frac{T_H}{w}\cosh^{-1}\left(\frac{wh}{T_H} + 1\right) \qquad (266)$$

Figure 96: Catenary mooring line configuration (left) and the displacement tension curve (right)

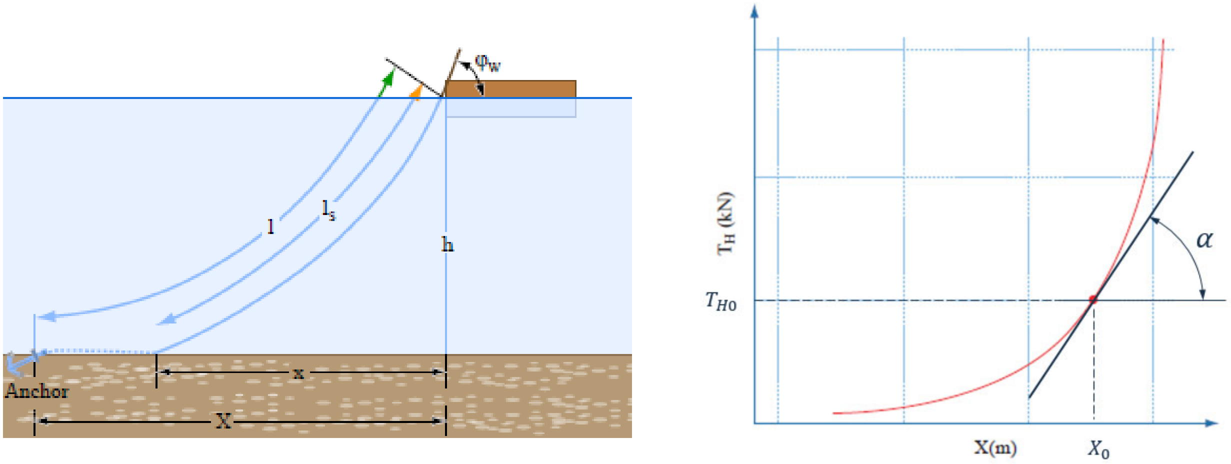

When the floater's motions are large, the nonlinearities of the mooring forces needs to be accounted for and the equation (265) should be used at each time step. However, when the floater's motions are small the linearized solution can be applied around the mean horizontal displacement X_0. In the case from Figure 96 the linearization procedure results in the following expression for the total tension and the restoring coefficient C_{11} :

$$T_H = \quad T_{H0} + C_{11}(X - X_0)$$

$$C_{11} = \quad \tan\alpha = \frac{dT_H}{dX} = w\left[\frac{-2}{\left(1 + 2\frac{T_{H0}}{wh}\right)^{\frac{1}{2}}} + \cosh^{-1}\left(1 + \frac{wh}{T_{H0}}\right)\right]^{-1} \qquad (267)$$

After summing up the contributions from all the mooring lines, the restoring matrix can be defined after transferring the line forces from the fairlead to the center of gravity. Once evaluated, the restoring matrix can be used directly in the body motion equation.

The above theoretical model of the catenary line is derived by assuming that the line is not elastic but the effects of elasticity can also be included in the model (e.g. Chakrabarti (2005)). In addition, the frictional effects of the part of the mooring line, which is lying at the sea floor, can also be accounted for. Finally, we note that the catenary equation can also be used by segments. This means that the total mooring line is decomposed into several catenary components which are connected together by requiring the continuity of the solution at the junction points (Bureau Veritas (2015)).

For more complex line configurations the simple analytical solution might not exist and, for those cases, the displacement – tension curve can be pre-calculated in the form of the look-up table which is subsequently used in the time domain analysis. The typical examples are the hawsers and the complex multiline configurations.

3. Modelling of coupled system

3.1. General

3.1.1 Introduction

The interaction/coupling between the lines and the floaters is one of the key issues in the global performance analysis. From physical point of view the two dynamical systems (floater and lines) are always coupled in some way and, following the definitions from Section 7, [1], this coupling can be classified as 2 way coupling. This is true whatever the model of the lines because in all cases the floater and the lines influence each other at each time step. This notion of mechanical coupling should not be confused with the analyses methods which are sometimes classified as either de-coupled or coupled methods, where the wording de-coupled is employed to describe the fact that effects of the line dynamics (stiffness, mass, damping …) can be pre-calculated prior to the analysis of the floater behavior.

3.2. Simulation models

3.2.1 Introduction

Different possibilities for modelling of the global behavior of the moored floating systems are presented in Table 8.

The decomposition is made according to the use of the combined frequency and time domain simulation models, as discussed in Section 4 and Section 5.

Table 8 : Different technical issues and the simulation models for Global Performance Analysis
(WF : Wave Frequency, LF : Low Frequency)

Lines		Floater				
		Linear (WF)		Nonlinear		
				LF + WF		Unified
		Frequency Domain	Time Domain	Frequency Domain	Time Domain	Time Domain
Linear	Static	X		X	X	X
	Dynamic	X		X	X	X
Nonlinear	Static		X		X	X
	Dynamic		X		X	X

3.2.2 Static equilibrium

The static offset defines the mean position of the body under the mean environmental loads (wave, current and wind). When the wave spectrum and the normalized drift force are known the mean wave loads are obtained using the equation (170) from Section 4. The current and wind loads are evaluated using the expressions given in Section 5 by putting the body velocity to zero. The presence of current will also modify the drift force and this can be accounted for by the Aranha's formula (see Section 4, [5.3.9]). The equilibrium position is found by equating the mooring line connection forces to the external loads. This can be done either through an iterative procedure or by using the transient time domain simulations.

3.2.3 Frequency domain simulation models

When possible, the frequency domain analysis is preferred because of its computational efficiency. The frequency domain analysis is possible only if the hydrodynamic loading allows for the frequency domain formulation which is the case for the 1st and the 2nd order hydrodynamic problems (see Section 4). In addition to that, all the mechanical components of the dynamic system (mass, damping and stiffness) also need to be linearized. In practice this is reasonably true for the 1st order (linear) seakeeping analysis only. However, the second order analysis in frequency domain can sometimes also be acceptable. The typical case is the HF springing response of TLP platform and, sometimes, for the LF slow drift response of the moored systems. It should be noted however, that the LF mooring simulations in frequency domain, are reliable only if the linearization of the mooring stiffness can be justified, which is not often the case (see Section 5). That is why, the LF analysis in frequency domain is usually acceptable in the screening phase only, where the accuracy is not of utmost importance. For all other purposes, the time domain LF analysis is recommended.

3.2.4 Time domain simulation models

The nonlinear motion equation of the floater remains the time domain motion equation (262) where the external loading vector $\{\boldsymbol{Q}(t)\}$ includes the connecting loads from the lines together with all other load components. The motion equation is integrated in time by updating the connecting loads at each time step. When solving the nonlinear body-line interactions two different strategies are usually employed:

- LF – WF decomposition
- Unified formulation

Whatever the method, which is used for the global performance analysis, the line modeling is usually simplified in some way. These simplifications are acceptable in practice, because the main concern of the global performance analyses are the body motions for which the details of the lines structural response usually have minor influence. That is also why the relatively simple LMM of the lines is acceptable. When the detailed structural response of the lines is of interest, a more detailed structural modelling of the lines is required. This part of the analysis is usually performed in post processing phase where the motions at the top of the line are imposed using the results of the global performance analysis. This two-step procedure represent a very efficient method which keeps the accuracy and the CPU time acceptable. Knowing that, in practice, a large number of very long time domain simulations is required in the design process, having the reduced simulation time is of great utility.

3.3. LF – WF decomposition

3.3.1 Assumptions

For the typical floating bodies employed in offshore industry (FPSO, Semi-submersible, TLP, DDF …), the following assumptions can be made:

- The WF and LF components of the response can be de-coupled and solved separately
- The RAO's of the WF response are pre-calculated in the frequency domain together with the second order wave excitation forces which are used as input to the LF response analysis
- The LF response analysis in time domain is performed in the horizontal plane only (3 DOF: surge, sway and yaw)

- The WF response is computed from the pre-calculated RAO's and from the LF motions
- The total response is obtained in the post processing stage by combining the WF and the LF contributions

The critical assumption is that the WF and LF responses can be de-coupled and solved separately. This can be justified by the fact that the LF motions take place at the frequencies much lower than the wave frequencies. In that case the slow-drift velocity can be considered as a steady over a few wave periods and it can be assumed that the corresponding first and second order responses are the same as if the velocity was constant in time. In practice the slow drift velocity is small so that the first order response is little affected, however the second order slow drift excitation change significantly and should be accounted for. The way in which this should be taken into account is discussed in Section 4 where the fully consistent method was presented together with the simplified formulation based on Aranha's formula.

3.3.2 Wave frequency response

The RAO's of the WF motions is calculated using the linear seakeeping model in frequency domain (Section 5). The influence of the mooring system is taken into account through the linear restoring matrix which is evaluated at the mean static position. However, in many cases the restoring stiffness from the mooring lines can also be ignored when evaluating the wave frequency motions. This is because, for the vertical motions (heave, pitch and roll) the mooring contribution to the total restoring is negligible when compared to the hydrostatic restoring, and for the horizontal motions (surge, sway and yaw) the excitation happens far from the resonance and the motion is dominated by the body inertia.

3.3.3 Low frequency response

The low frequency response (also called slow drift motion) takes place at the natural frequencies of the coupled system which is composed of the floating body and its mooring lines. Most often, the LF motions in horizontal direction are of concern only and the motion equation is formulated with 3 degrees of freedom only. Referring to Figure 46, the 3 degrees of freedom are the horizontal displacement of the hydrodynamic coordinate system $(X_o,\ Y_o)$ and its rotation angle ψ with respect to the vertical axis of the earth fixed coordinate system. Assuming the origin of the hydrodynamic coordinate system to be located at the body's center of gravity, the motion equation in the inertial coordinate system can be written as:

$$[\boldsymbol{\mathcal{M}}]\{\ddot{\mathbf{X}}\} = \sum_i \{\boldsymbol{F}_{LF}\}_i \qquad (268)$$

where:

$$\{\mathbf{X}\} = \begin{Bmatrix} X_o \\ Y_o \\ \psi \end{Bmatrix} \quad , \quad [\boldsymbol{\mathcal{M}}] = \begin{bmatrix} m & 0 & 0 \\ 0 & m & 0 \\ 0 & 0 & I_{\psi\psi} \end{bmatrix} \qquad (269)$$

The vectors $\{\boldsymbol{F}_{LF}\}_i$ in (268) represent all sources of the LF loading: wind, current, QTF's, maneuvering loads, mooring and risers loads, different damping loads…

Usually the equation (268) is rewritten with reference to hydrodynamic coordinate system. Assuming the origin of the hydrodynamic coordinate system to be located at the horizontal position of the body center of gravity, the well-known maneuvering equations follows in the form (Triantafyllou & Hover (2003)):

$$\begin{aligned} m(\dot{u} - v\dot{\psi}) &= \sum_i \{F_{LFx}\}_i \\ m(\dot{v} + u\dot{\psi}) &= \sum_i \{F_{LFy}\}_i \\ I_{\psi\psi}\ddot{\psi} &= \sum_i \{M_{LFz}\}_i \end{aligned} \qquad (270)$$

where (u, v) denote the LF horizontal velocities of the body with reference to hydrodynamic coordinate system.

In practice, when solving the above equations, the inertia component of the maneuvering loads (122) is included in the left part of the equation (270) in the form of the product of the zero frequency added mass matrix and the vector $\{\dot{u}, \dot{v}, \ddot{\psi}\}^T$ (see Bureau Veritas (2015)).

3.3.4 Total response

The total response is evaluated in post-processing phase by summing up the LF and the WF contributions. For that purpose, the RAO's of the WF response are used to evaluate the instantaneous WF response at each time step of the LF simulations by taking into account the instantaneous mean position and direction of the body. By doing this, the time domain signals have consistent phasing between the contributions which are induced by the different wave components.

3.3.5 Damping of the LF motions

The LF motion being of resonant character, the evaluation of the damping is fundamental for correct evaluation of the response. The essential role of the damping can be easily understood by considering the single degree of freedom (X) with the associated mass M, the added mass M_a, the linearized stiffness (K) and the linearized damping (B) coefficients. After assuming that the motion takes place in a small neighborhood of the natural frequency $\Omega_0 = \sqrt{K/(M+M_a)}$, the variance of the response, for a given sea state, can be approximately by:

$$\sigma_X^2 \cong \frac{\pi S_{\underline{F}^{(2)}}(\Omega_0)}{2B(M+M_a)\Omega_0^2} \tag{271}$$

where $S_{\underline{F}^{(2)}}(\Omega_0)$ is the difference frequency second order excitation spectrum discussed in Section 4, [5.4].

It follows that, even though the second-order loads are small in magnitude, the amplitude of the low frequency motion can be large when the natural frequency and the damping are low. That is precisely what happen in practice for most of the moored floating systems. While, in the linear WF regime, the radiation damping plays the major role in mitigating resonance, in the LF regime the low frequencies radiation damping is negligible and other energy dissipation processes come into play. The main damping components have been identified as:

- wave drift damping due to the variation of the slow drift forces with velocity
- viscous forces on hull due to friction and flow separation
- drag forces on mooring lines and risers
- friction of the mooring lines on the sea floor
- variation of wind loads with the slow drift velocity of the structure

where the first three components are usually dominant.

When the loading on slender elements is evaluated in time domain at each time step, the inclusion of the damping effects becomes straightforward because all the external forces, including those which induces the damping effects, are updated at each time step. The critical point is the choice of the drag coefficients on the slender structures and the type of the formulation for the Morison loads i.e. independent or dependent (see Section 3). In practice the independent Morison formulation is recommended for the columns and pontoons of the column stabilized units (Semi-submersible, DDF, TLP …) while the dependent Morison formulation is recommended for the mooring lines and risers.

The LF damping contributions can also be linearized, in which case the final linear damping matrix becomes sea state dependent. More detailed discussions about the linearization of the three main components of the LF damping (wave drift damping, viscous hull damping and mooring line damping) can be found in Molin (1994). It has been shown in particular that, after linearization, the mooring line damping coefficient has the linear dependence on the wave height. The wave drift damping being the second order quantity it has the quadratic dependence on wave height. The dependence of the viscous hull damping on wave height depends on the particular flow conditions which dictates the relative importance of the hull frictional forces and the drag forces. For the streamline bodies moving in the streamline direction (turret moored FPSO) the friction is usually dominant while for the bodies with sharp edges (Semi-submersibles, TLP, DDF, barges, spread moored FPSO's …) the drag contribution becomes important and is often dominant. As an example, in Figure 97 the different damping contributions are presented as a function of the significant wave height, for the case of the turret moored FPSO.

Figure 97: Different slow drift damping components as a function of the wave height for a turret moored FPSO (from Molin (1994)).

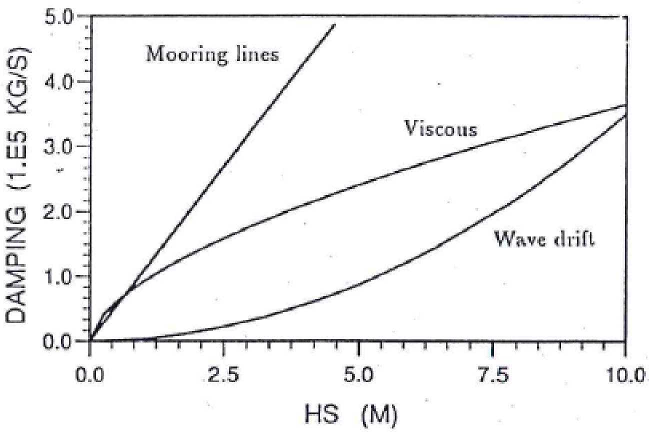

3.4. Unified formulation

3.4.1 Applications

The LF – WF decomposition is justified in the cases when the natural periods of the floating system can be clearly separated into WF and LF components. For many practical applications this is the case but not always. For some floating systems (Spars, FOWT…), the natural periods of the vertical and the horizontal motions are of the same order of magnitude so that the LF – WF decomposition cannot be used and all modes of motions need to be evaluated at the same time. In some other cases, regardless of the natural periods of the system, the body motions at the wave frequencies are so large that the linear theory is not valid anymore and the nonlinear wave loads, other than the second order ones, need to be accounted for. The corresponding theoretical approach, which allows to model these kind of situations, is known under the name “unified formulation” and is discussed below.

3.4.2 Motion equation

The unified formulation is based on directly solving the nonlinear body motion equation (262) which is rewritten here in the following form:

$$\begin{bmatrix} [\boldsymbol{m}] & [0] \\ [0] & [\boldsymbol{I_{\theta\theta}}][\boldsymbol{G}] \end{bmatrix} \begin{Bmatrix} \{\ddot{\boldsymbol{R}}_{\boldsymbol{G}}\} \\ \{\ddot{\boldsymbol{\theta}}\} \end{Bmatrix} = \sum_i \{\boldsymbol{F}\}_i - \begin{Bmatrix} \{\boldsymbol{0}\} \\ [\boldsymbol{I_{\theta\theta}}][\dot{\boldsymbol{G}}]\{\dot{\boldsymbol{\theta}}\} + [\boldsymbol{\Omega}][\boldsymbol{I_{\theta\theta}}]\{\boldsymbol{\Omega}\} \end{Bmatrix} \qquad (272)$$

where $\{\boldsymbol{F}\}_i$ denotes all the external forces acting on the body (gravity, wave induced pressure, friction, line forces …).

3.4.3 Numerical implementation

Integrating the nonlinear body motion equation (262) in time does not represent major difficulties once the instantaneous external loads are available. In the present context, where the external loads are evaluated using the models described in Section 3 and Section 4, there exist several practical reasons why the external loads cannot be formulated fully consistently. The main sources of inconsistencies in calculating the load vector in (262), are related to the assumptions which were made when evaluating the wave loading. The wave loading was formulated by first defining its linear contribution and by adding the different weakly nonlinear contributions in the second step. Because the linear theory is valid under the assumptions of the small waves and small body motions, any nonlinear extrapolation of the linear model is approximate and implies the extrapolation errors.

Among the weakly nonlinear contributions which are of concern here, the second order loads (QTF’s) and the nonlinear Froude Krylov loads are used most often. The main technical problem associated with this, is that these two weakly nonlinear contributions are overlapping with each other. Indeed the Froude-Krylov loading includes the part of the second order loads which is already included in QTF’s. This double counting of the wave loads need to be avoided but this can never be done fully consistently. In practice the second order terms, contained in the Froude Krylov loading, are removed from the QTF loads. When doing this, some errors are inevitably introduced because the QTF’s were evaluated using the pre-calculated linear motions. Another method which is sometimes employed, consists in completely neglecting the QTF loads and assuming that the Froude Krylov loading represents the dominant contribution to the nonlinear wave loads. Which method will be used in practice depends on the application and the choice of the applied method needs to be justified on case by case basis.

Another technical problem, which arise when the body motion equation is evaluated using the unified formulation, is related to the evaluation of the maneuvering and the second order QTF loads. These loads are associated with the slow drift horizontal motions only which means that the high frequency wave component of the body motions needs to be removed prior to the evaluation of these loads. In practice this is done by filtering the total motion signal during the simulations. Different filtering techniques exists but none of them is perfect and their efficiency will depend on the application case. In practice the Butterworth filter is used most often.

3.4.4 Simple verification of the numerical model based on unified formulation

By definition, the unified formulation covers the limiting cases of the linear body response in small waves as well as the weakly nonlinear case where the LF – WF decomposition is justified. The linear time domain model was discussed and validated in Section 5, and in Figure 98 the comparison of the unified formulation and the LF – WF decomposition approach is presented for surge motion of a typical FPSO in head waves. Only the 1st and 2nd order wave loads were included and it can be observed that the LF motion obtained using the LF – WF decomposition model coincide with the filtered LF response obtained using the unified formulation.

Figure 98: Surge motion of an FPSO exposed to head waves, by LF – WF decomposition and by unified formulation. (Top – LF signal, Bottom – total signal)

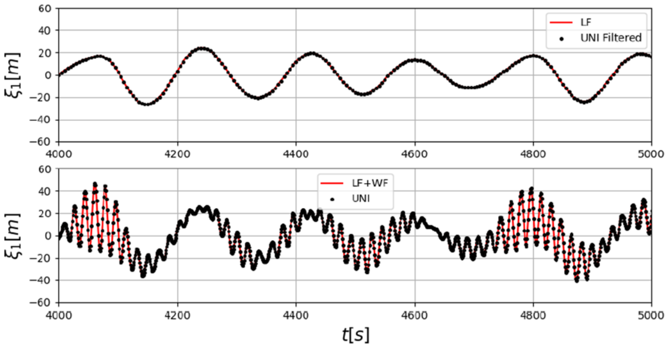

4. List of references

[1] Buckham, B.J., 2003.: “Dynamics modelling of low-tension tethers for submerged remotely operated vehicles.” PhD Thesis, University of Victoria, British Columbia, Canada.

[2] Bureau Veritas, 2015.: “ARIANE 8 – Theoretical Manual”

[3] Chatjigeorgiou I.K. & Mavrakos S.A., 1999.: “Comparison of numerical methods for predicting the dynamic behaviour of mooring lines.”, 9th ISOPE Conference.

[4] Garret D.L., 1982.: “Dynamic analysis of slender rods.”, Journal of Energy Resources Technology, Vol. 104.

[5] Gerstmayr, J. and Shabana, A.A., 2006.: “Analysis of thin beams and cables using the absolute nodal co-ordinate formulation.”, Nonlinear Dynamics, Vol. 45.

[6] Gobat. J.I. & Grosenbaugh M.A., 2006.: “Time domain numerical simulation of ocean cable structures.”, Ocean Engineering, Vol. 33.

[7] Hall M. and Goupee A., 2015.: “Validation of a lumped-mass mooring line model with DeepCwind semisubmersible model test data.” Ocean Engineering, Vol. 104.

[8] Leonard, J.W. and Nath, J.H., 1981.: “Comparison of finite element and lumped parameter methods for oceanic cables.”, Engineering structures, Vol 3.

[9] Masciola M., Jonkman J. & Robertson A., 2014 : ”Extending the capabilities of the mooring analysis program : A survey of dynamic mooring line theories for integration into FAST.”, 33rd OMAE Conference, San Francisco, USA.

[10] Molin B., 1994.: “Second order hydrodynamics applied to moored structures – A state of the art survey.”, Ship Technology Research, Vol. 41.

[11] Nordgren R.P., 1974.: “On computation of the motion of elastic rods.”, Journal of Applied Mechanics, Vol. 41.

[12] Shabana A.A. & Yakoub R.Y., 2001.: “Three dimensional absolute nodal coordinate formulation for beam elements: Theory.”, Journal of Mechanical Design, Vol. 123.

[13] Triantafyllou M.S & Hover F.S., 2003.: “Maneuvering and control of marine vehicles.”, MIT

Section 7 Structural response

1. General

1.1. Introduction

1.1.1 Applications

The practical procedure for ship structural design involves the verification of two main structural failure modes namely the yielding and buckling in extreme conditions and the cracks initiated by fatigue. These two failure modes are fundamentally different and the methodologies for their assessment are also different even if many common points exist (see NI638). The final goal of the extreme event analysis is to predict, for each structural member, the single most likely worst event during the lifetime, while the goal of the fatigue analysis is to analyze the entire life of the structure, by counting all the combinations of the stress ranges and the corresponding occurrences. The design methodologies for both failure modes require efficient hydro-structure interaction tools for the evaluation of the structural response under a variety of deterministic loading conditions.

1.1.2 Direct calculation procedure

Within the direct calculation approach, which is of concern here, the basic idea to evaluate the structural resistance is rather simple: the structural response of the floating body is calculated for the entire lifetime and the identification of the extreme events and fatigue life are determined directly. Since fully consistent non-linear hydro-structure tools are not practically feasible within the current state of the art, approximate solutions are usually introduced. In this Section, the different deterministic numerical models which are commonly applied for these purposes, are described. Most of the time the structural response is assumed to be linear while the body motions and loads can be linear or nonlinear. However, the nonlinear structural response can also be considered for some particular applications such as the nonlinear contact problems (independent LNG tanks), ultimate strength simulations, buckling … Unless explicitly stated, only the linear structural response is discussed here.

1.1.3 Frequency and time domain approaches

Similar to any other response of the floating body, the structural response can be evaluated either in frequency or in time domain. Frequency domain is preferred but, unfortunately, it is practically applicable to the case of linear wave loading only.

1.2. Structural responses

1.2.1 Introduction

The structural response means the stress distribution in the structural elements. The method used for the evaluation of the stresses, which is considered here, is the 3D finite element method (3DFEM).

1.2.2 Evaluation of the structural stresses

The stresses in the structure are the consequence of the structural deformations. This means in particular, that the purely rigid body motions do not induce any stresses in the structure. The structure deforms under the action of the external loading which originates from the hydro structure interactions. This loading can be purely static (body in calm water) or time varying (body in waves), as discussed in Section 3, Section 4, Section 5 and Section 6. Within the linear approach for evaluation of the structural response, the loading is always applied at the mean configuration of the structure i.e. on the initial finite element model which is built relative to the undeformed configuration. In principle, and regardless of the loading and the type of the hydro-structure interactions, the linear structural stresses can be evaluated using two main approaches: the direct approach and the modal approach. The direct approach means evaluating the structural stresses directly by solving the finite element problem at each time step, or for each frequency when the frequency domain approach is used. The modal approach evaluates the modal basis first (usually dry structural natural modes but other modal functions can also be used) and the final solution is represented as the sum of the different modal contributions. In practice the direct approach is used to evaluate the quasi-static structural response and the modal approach is used to evaluate the dynamic amplification of the modes which are likely to be amplified by the loading (usually only few of them). The total response is obtained by summing up the quasi static and the dynamic contributions.

1.2.3 Types of the structural response

Strictly speaking, the structural response can be classified into two main categories:

- Static structural response

- Dynamic structural response

Denoting the structural response by a vector $\{\boldsymbol{\xi}_s(t)\}$, which represents either the response at the level of finite elements or at the level of structural natural modes, the following equilibrium equations are valid for the two types of responses respectively:

$$[\boldsymbol{k}(t)]\{\boldsymbol{\xi}_s(t)\} = \{\boldsymbol{F}_s(t)\} \tag{273}$$

$$[\boldsymbol{m}(t)]\{\ddot{\boldsymbol{\xi}}_s(t)\} + [\boldsymbol{b}(t)]\{\dot{\boldsymbol{\xi}}_s(t)\} + [\boldsymbol{k}(t)]\{\boldsymbol{\xi}_s(t)\} = \{\boldsymbol{F}_s(t)\} \tag{274}$$

The matrices $[\boldsymbol{m}]$, $[\boldsymbol{b}]$ and $[\boldsymbol{k}]$ denote the structural mass, damping and stiffness matrices respectively, and they can potentially depend on time. In the case they are time independent the structural response becomes linear. The excitation force $\{\boldsymbol{F}_s(t)\}$ represents any type of the external loading (gravity, pressure, inertia …) projected on the structural degrees of freedom. The confusion which sometimes occurs, in the context of the floating bodies, is related to the fact that both the static and the dynamic structural responses are induced by the time varying (i.e. dynamic) environmental loading. However, only the dynamic structural response is able to describe the structural vibrations.

1.3. Hydro structure interactions

1.3.1 Introduction

Here we define the different types of the hydro structure interaction models which are of concern in this document. The discussions remain valid both for the global structural response (whole structure) as well as for the local structural responses under localized loading (e.g. slamming, sloshing, green water…).

1.3.2 General

In order to separate the structural response from the rigid body response, the following notations are introduced for the associated unknowns:

$\xi_r(t)$ 6 rigid body motions
$\xi_s(t)$ Structural response (body deformations)

In the most general case, the dynamic equations that govern the rigid body and the elastic structural responses, can be formally written in the following form:

$$\begin{aligned} [\boldsymbol{M}]\{\ddot{\boldsymbol{\xi}}_r(t)\} &= \{\boldsymbol{F}_r(t, \ddot{\boldsymbol{\xi}}_r, \dot{\boldsymbol{\xi}}_r, \boldsymbol{\xi}_r, \ddot{\boldsymbol{\xi}}_s, \dot{\boldsymbol{\xi}}_s, \boldsymbol{\xi}_s)\} \\ [\boldsymbol{m}(t)]\{\ddot{\boldsymbol{\xi}}_s(t)\} + [\boldsymbol{b}(t)]\{\dot{\boldsymbol{\xi}}_s(t)\} + [\boldsymbol{k}(t)]\{\boldsymbol{\xi}_s(t)\} &= \{\boldsymbol{F}_s(t, \ddot{\boldsymbol{\xi}}_s, \dot{\boldsymbol{\xi}}_s, \boldsymbol{\xi}_s, \ddot{\boldsymbol{\xi}}_r, \dot{\boldsymbol{\xi}}_r, \boldsymbol{\xi}_r)\} \end{aligned} \tag{275}$$

where $[\boldsymbol{M}]$ is the rigid body inertia matrix (assumed constant), $\{\boldsymbol{F}_r\}$ is the external loading projected onto rigid body modes of motion and $\{\boldsymbol{F}_s\}$ is the external loading projected onto the body deformation degrees of freedom.

The different approximations of the system of equations (275), which are used most often in practice, are summarized in Table 9 and will be detailed in the following paragraphs.

Table 9 : Different types of hydro structure interactions

Structural response	Body response	
	Calm water	Waves
Static	S (Static)	QS (Quasi static)
Dynamic	-	DD (Dry dynamic) and HE (Hydro-elastic / wet dynamic)

1.3.3 Dynamic amplification factor (DAF)

The nature of the loading and its relation to the structural properties, determines the type of the hydro-structure interaction method which is the most appropriate. In frequency domain, the critical parameter is the ratio between the excitation period and the structural natural period, which characterizes the risk of resonance. In the case of the transient response to impulsive loading the critical parameter is the ratio between the characteristic time of the loading (rise time, decay time …) and the structural natural period. In Figure 99 the typical examples of the dynamic responses are shown in the form of the dynamic amplification factor (DAF) which is defined as the ratio between the dynamic and the quasi static response. It can be clearly seen that the DAF varies significantly depending on the ratio of the duration of the loading and the natural period of the system T_0. For the cases where the DAF is close to unity (large loading periods in frequency domain, or large rise time in time domain) the quasi static approach can be safely used, otherwise the fully coupled dynamic modelling should be employed. Damping is of course also critical parameter, and it is usually very low in the context of structural dynamics, so that the significant amplification of the response can happen over wide range of frequencies close to the resonance.

Figure 99: Dynamic amplification (left – harmonic response to excitation with period T, right – transient response to triangular loading of duration T)

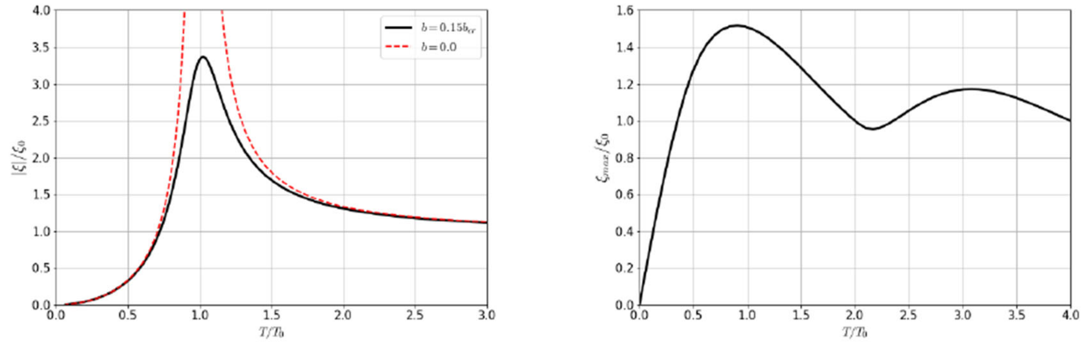

For most of the typical offshore structures, the structural natural frequencies are relatively high compared to the wave frequencies. That is why most often, for the linear and the weakly nonlinear wave loading, the quasi static approach for the evaluation of the structural response can be safely used. The exceptions are the VLFS whose natural frequencies are usually much lower. For the conditions where the external loading is impulsive, the dynamic contribution might become important even if the structural natural frequencies are very high (see Figure 99). These conditions should be considered on case by case basis.

1.4. Static structural response

1.4.1 Body in calm water

F or the body in calm water conditions the external loading is constant in time and composed of the gravity and the hydrostatic pressure. From interaction perspective, the body is generally considered as rigid i.e. the influence of the body deformations on the external loading is neglected. The equilibrium equations are:

$$\begin{aligned} \{\mathbf{0}\} &= \{\boldsymbol{F}_r(\boldsymbol{\xi}_r)\} \\ [\boldsymbol{k}]\{\boldsymbol{\xi}_s\} &= \{\boldsymbol{F}_s(\boldsymbol{\xi}_r)\} \end{aligned} \qquad (276)$$

There exist practical cases where some nonlinear effects might need to be included when calculating the static structural response. Typical example concerns the evaluation of the static structural response in calm water while assuming that the body deformations are large and thus significantly modify the hydrostatic pressure distribution. When doing that, the structural response is usually considered to remain linear i.e. the matrix $[\boldsymbol{k}]$ is kept constant. The equilibrium equations are:

$$\begin{aligned} \{\mathbf{0}\} &= \{\boldsymbol{F}_r(\boldsymbol{\xi}_r, \boldsymbol{\xi}_s)\} \\ [\boldsymbol{k}]\{\boldsymbol{\xi}_s\} &= \{\boldsymbol{F}_s(\boldsymbol{\xi}_r, \boldsymbol{\xi}_s)\} \end{aligned} \qquad (277)$$

1.4.2 Body in waves

In this case, although the loading is time varying, the structural dynamic response is completely neglected. This means that the structural mass and the structural damping matrix are assumed to be zero in (274). Assuming the structural response to be linear the equilibrium equations are:

$$\begin{aligned} [\boldsymbol{M}]\{\ddot{\boldsymbol{\xi}}_r(t)\} &= \{\boldsymbol{F}_r(t, \ddot{\boldsymbol{\xi}}_r, \dot{\boldsymbol{\xi}}_r, \boldsymbol{\xi}_r)\} \\ [\boldsymbol{k}]\{\boldsymbol{\xi}_s(t)\} &= \{\boldsymbol{F}_s(t, \ddot{\boldsymbol{\xi}}_r, \dot{\boldsymbol{\xi}}_r, \boldsymbol{\xi}_r)\} \end{aligned} \qquad (278)$$

Because the external loading is time dependent, the static structural response is usually called quasi-static. In addition to the gravity and the hydrostatic pressure, the loading vector in (278) includes the rigid body inertia and the associated hydrodynamic pressure components (incident, diffracted and radiated).

1.5. Dynamic structural response

1.5.1 Introduction

The dynamic structural response accounts for the structural vibrations when evaluating the stresses. In practice, two types of approaches to calculate the dynamic structural response are usually employed. In the first approach, only the genuine structural dynamic components (structural mass, structural damping and structural stiffness) are accounted for and the hydrodynamic effects associated with the structural dynamics are neglected. In the second approach the hydrodynamic effects associated with the structural dynamics are included and this approach is usually called hydro-elastic approach. The advantage of the first approach, which can be classified as the dry dynamic approach, is that the coupling of the hydrodynamic and structural simulations becomes relatively simple. However, this model should be used with care since it ignores, among other quantities an added mass effect which can modify the dynamic behavior of the system significantly.

1.5.2 Dry dynamic structural response

Under the assumptions that the hydrodynamic loading is not affected by the structural dynamics, and by assuming the linear structural response, the equilibrium equations become:

$$\begin{aligned} [\boldsymbol{M}]\{\ddot{\xi}_r(t)\} &= \{\boldsymbol{F}_r(t, \ddot{\xi}_r, \dot{\xi}_r, \xi_r)\} \\ [\boldsymbol{m}]\{\ddot{\xi}_s(t)\} + [\boldsymbol{b}]\{\dot{\xi}_s(t)\} + [\boldsymbol{k}]\{\xi_s(t)\} &= \{\boldsymbol{F}_s(t, \ddot{\xi}_r, \dot{\xi}_r, \xi_r)\} \end{aligned} \tag{279}$$

As it can be observed, the external loading remains the same as in the quasi static case (278) and the only difference is that the structural model is dynamic. It is important to note that the dynamic characteristics of the structure are related to the dry structure i.e. they are assumed to not be affected by the fluid and they include the structural mass, structural damping and the structural stiffness only. The dry dynamic model is relevant for the fluids with low density such as air, where the effects of the added mass are negligible.

1.5.3 Hydro-elastic structural response

For the bodies surrounded by the fluid, any displacement of the wetted part of the body will modify the external loading in some way. In the case of the dynamic structural response, the hydrodynamic pressure is modified by the structural vibrations. This means, in particular, that the effect of the added mass can become important and should be accounted for when evaluating the dynamic response. The governing system of the coupled equations becomes:

$$\begin{aligned} [\boldsymbol{M}]\{\ddot{\xi}_r(t)\} &= \{\boldsymbol{F}_r(t, \ddot{\xi}_r, \dot{\xi}_r, \xi_r, \ddot{\xi}_s, \dot{\xi}_s, \xi_s)\} \\ [\boldsymbol{m}]\{\ddot{\xi}_s(t)\} + [\boldsymbol{b}]\{\dot{\xi}_s(t)\} + [\boldsymbol{k}]\{\xi_s(t)\} &= \{\boldsymbol{F}_s(t, \ddot{\xi}_r, \dot{\xi}_r, \xi_r, \ddot{\xi}_s, \dot{\xi}_s, \xi_s)\} \end{aligned} \tag{280}$$

The modal approach, which was briefly discussed in [1.2.2], is usually employed to solve this system of equations. The main difference between the dry dynamic structural model and the hydro-elastic structural model is that the natural frequencies of the system, which are one of the most important quantities in any dynamic analysis, change due to the added mass effects.

1.6. Coupling aspects

1.6.1 Mechanical coupling

The mechanical coupling is defined in relation to the physical quantities which are exchanged between the systems while seeking for their respective responses. From physical point of view, the responses of the two systems (rigid body motion and the structural deformations) are always coupled i.e. at least one of the systems influences the other. In order to distinguish between the different coupling methods, here we introduce the denomination 1-way and 2-way coupling models which are defined as follows:

– 2-way	System 1 influences system 2 and system 2 influences system 1
– 1-way	System 1 influences system 2 but system 2 does not influence system 1

When referring to [1.3.2] and in particular Table 9, the different types of the hydro structure interactions are classified in Table 10.

Table 10 : Mechanical coupling aspects

Structural response	Mechanical coupling	
	1 Way	2 Way
Static	S (Static) and QS (Quasi static)	-
Dynamic	DD (Dry dynamic)	HE (Hydro-elastic)

While the 1 way coupling method is self-understandable, the 2 way coupling method requires some clarifications regarding the practical method used for the evaluation of the structural stresses. For details we refer to [3.2.3].

1.6.2 Numerical procedures

When solving a particular hydro-structure interaction problem, the different numerical procedures can be employed. These procedure can also be classified into different categories and the following wording is usually employed:

"… decoupling, weak coupling, loose coupling, full coupling, tight coupling …"

The clear definition of each of these terms is often unclear and it is very important to not confuse these aspects of coupling with the mechanical aspects of coupling discussed in [1.6.1].

1.7. Hydro-structure interactions in offshore applications

1.7.1 Introduction

In the present context, the structural loading is originated by the different environmental loads (wind, wave and current) which were discussed in Section 4 and Section 5. In this Section the structural response of the body is of main concern, and the response of the underwater equipment (mooring, risers, umbilical…) is not addressed. At the same time, only the wave induced loads are discussed in detail. The descriptions are in line with the ideas summarized by Malenica & Derbanne (2014) which were implemented into the numerical software HOMER (Malenica et al (2013)).

1.7.2 Hydro structural issues

The different hydro-structural issues are summarized in Table 11. The hydrodynamic loading is classified into three different categories: linear, weakly nonlinear and strongly nonlinear (see also Section 4). The linear hydrodynamic loading means the classical linear diffraction radiation loads. The weakly non-linear loading means the non-impulsive part of the wave loading which is usually covered through the different variants of the Froude Krylov approximation (see Section 4, [6.4]) combined with the large body motions. The strongly nonlinear loading includes all other types of the nonlinear loads and in particular the transitory impulsive loading such as slamming, green-water, underwater explosion…

Table 11 : Different hydro-structural issues (*H* – Hydrodynamics, *S* – Structure).

S	H		
	Linear	Weakly nonlinear	Strongly nonlinear
Static	X	X	X
Dynamic	X	X	X

1.8. Internal loads

1.8.1 Introduction

The concept of the internal loads is very helpful for better understanding the structural response especially for ship like bodies (FPSO, FSO …). The internal loads (also called sectional loads) are defined for a section which delimitate the body in two distinct parts as shown in Figure 100. They are defined as the loads exerted by one part of the structure on the other part which results in one force vector $\{\boldsymbol{F}_I'\}$ and one moment vector $\{\boldsymbol{M}_I'\}$. Internal loads are usually expressed in the body fixed coordinate system and they named as: the axial force (F_{Ix}'), the horizontal and the vertical shear force $\left(F_{Iy}', F_{Iz}'\right)$, the torsional moment M_{Ix}' and the vertical and the horizontal bending moments $\left(M_{Iy}', M_{Iz}'\right)$. A very important feature of the internal loads is that they do not require the complete solution of the structural response in terms of stresses. In practice, the internal loads are most often obtained as the sum of all the loads (pressure, inertia, mooring, ...) acting on the part of the body up to the section in consideration (see [1.8.2]). Since the floating body is at equilibrium at each time instant, it follows that the same results (with opposite sign) for the internal loads are obtained by summing up the loads from either side of the section. It should also be noted that the definition of the internal loads remain the same whatever the loading conditions: calm water, linear wave in frequency domain, nonlinear wave in time domain … The only difference is that different load components are involved.

Figure 100: Internal loads

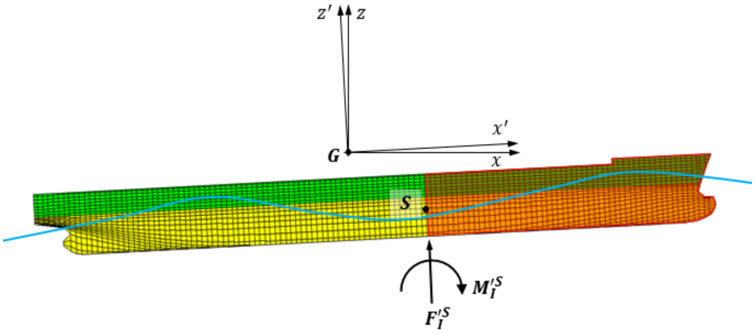

It has to be noted that the above discussions on the internal loads are valid only when the section in consideration is separating the body in two distinct sections. When this is not the case the evaluation of the internal loads in particular structural elements (pontoons of semi-submersible, columns of the jacket structures, hulls of the multihull vessels …) requires the evaluation of the structural response.

1.8.2 Internal loads by integration of the loads acting on the body

When evaluated by the integration of the loads, the internal loads (forces $\{\boldsymbol{F}'_I\}$ and moments $\{\boldsymbol{M}'_I\}$), for rigid body moving in waves, can be written in the following form:

$$\{\boldsymbol{F}'_I\} = \{\boldsymbol{F}'_S\} - [\boldsymbol{m}_S]\{\ddot{\boldsymbol{r}}'_G\} \quad , \quad \{\boldsymbol{M}'_I\} = \{\boldsymbol{M}'_S\} - [\boldsymbol{\Omega}'][\boldsymbol{I}'_{\theta\theta S}]\{\boldsymbol{\Omega}'\} - [\boldsymbol{I}'_{\theta\theta S}]\{\dot{\boldsymbol{\Omega}}'\} \tag{281}$$

The inertial properties $[\boldsymbol{m}_S]$ and $[\boldsymbol{I}'_{\theta\theta S}]$ in (281) are defined by:

$$[\boldsymbol{m}_S] = \iiint_{\forall_S} [\mathbf{I}]dm \quad , \quad [\boldsymbol{I}'_{\theta\theta S}] = \iiint_{\forall_S} [\boldsymbol{u}']^T[\boldsymbol{u}']dm \tag{282}$$

with $\forall_S$ denoting the part of the body between the section and the end of the body (fore or aft).

The external forces and moments are the sum of the gravity contribution and the pressure contribution and are defined as follows:

$$\begin{aligned} \{\boldsymbol{F}'_S\} = & \quad \{\boldsymbol{F}'^{g}_S\} + \{\boldsymbol{F}'^{h}_S\} = -m_S g[\boldsymbol{A}]^T\{\boldsymbol{k}\} + \iint_{S_{bS}} P\{\boldsymbol{n}'\}dS \\ \{\boldsymbol{M}'_S\} = & \quad \{\boldsymbol{M}'^{g}_S\} + \{\boldsymbol{M}'^{h}_S\} = -g\iiint_{\forall_S} [\boldsymbol{u}'][\boldsymbol{A}]^T\{\boldsymbol{k}\}dm + \iint_{S_{bS}} P[\boldsymbol{u}']\{\boldsymbol{n}'\}dS \end{aligned} \tag{283}$$

where S_{bS} denotes the part of the body wetted surface between the section and the end of the body.

It should be noted that the expressions (283) define the internal forces and moments with respect to the body center of gravity $\{\boldsymbol{r}_G\}$. In order to express them with respect to the local point at the section (e.g. neutral axis) they need to be modified as follows:

$$\{\boldsymbol{F}'^{S}_I\} = \{\boldsymbol{F}'_I\} \quad , \quad \{\boldsymbol{M}'^{S}_I\} = \{\boldsymbol{M}'_I\} + [\boldsymbol{u}'_S]\{\boldsymbol{F}'_I\} \tag{284}$$

where $\{\boldsymbol{F}'^{S}_I\}$ and $\{\boldsymbol{M}'^{S}_I\}$ are the internal loads expressed at the point $\boldsymbol{S}$ defined by the position vector $\{\boldsymbol{u}'_S\}$.

1.8.3 Internal loads by integration of the structural stresses

From the structural point of view, the sectional loads are in balance with the stresses in the structural elements along the section in consideration. This means that the same result for the internal loads can be obtained by integrating the structural stresses over the section in consideration. This can be written as:

$$\{\boldsymbol{F}'^{S}_I\} = \iint_{A_S} [\boldsymbol{\sigma}]\{\boldsymbol{n}'\}\,dA \quad , \quad \{\boldsymbol{M}'^{S}_I\} = \iint_{A_S} [\boldsymbol{u}' - \boldsymbol{u}'_S][\boldsymbol{\sigma}]\{\boldsymbol{n}'\}\,dA \quad , \quad [\boldsymbol{\sigma}] = \begin{bmatrix} \sigma_{xx} & \sigma_{yx} & \sigma_{zx} \\ \sigma_{xy} & \sigma_{yy} & \sigma_{yz} \\ \sigma_{xz} & \sigma_{yz} & \sigma_{zz} \end{bmatrix} \tag{285}$$

where $[\boldsymbol{\sigma}]$ is the stress tensor and $\{\boldsymbol{n}'\}$ is the vector normal to the sectional surface A_S.

In the case when $\{\boldsymbol{n}'\}$ coincides with one of the coordinate axis the expressions significantly simplify. This type of the evaluation of the internal loads is mainly employed for verification purposes.

1.8.4 Typical distribution of the internal loads for an FPSO

Typical distribution of the internal loads along the body, is shown in Figure 101 and 102 where the results for the vertical bending moment M'_{Iy} and the vertical shear force F'_{Iz} are presented for a typical FPSO.

It can be observed that both the vertical bending moment and the shear forces vanishes at the fore and the aft end of the body, which proves the correct balancing of the global inertia and the pressure loads. Another useful check of the correctness of the internal loads' evaluation is the comparisons of the loads obtained by fore and aft integration procedures. Finally verifying the consistency between the sectional loads and the stress level in a few points of the section represents a useful check.

1.8.5 Internal loads for flexible bodies

The internal loads are defined in a same way for both the quasi static and the dynamic structural responses provided that the total pressure and inertia, i.e. due to both the rigid body motions and the flexible body deformations, are taken into account when integrating them over the part of the structure. Therefore, in the case of the dynamic response, it is necessary to calculate the structural response (amplitudes of the flexible modes) because the inertia and the associated hydrodynamic pressures in equation (281) should take into account the contribution from the flexible modes too. The calculation of the associated stresses is still not required and the method based on the integration of the loads can be used (see [1.8.2]).

Figure 101: Longitudinal distribution of the vertical bending moment (left) and the vertical shear force (right) along the FPSO in calm water conditions

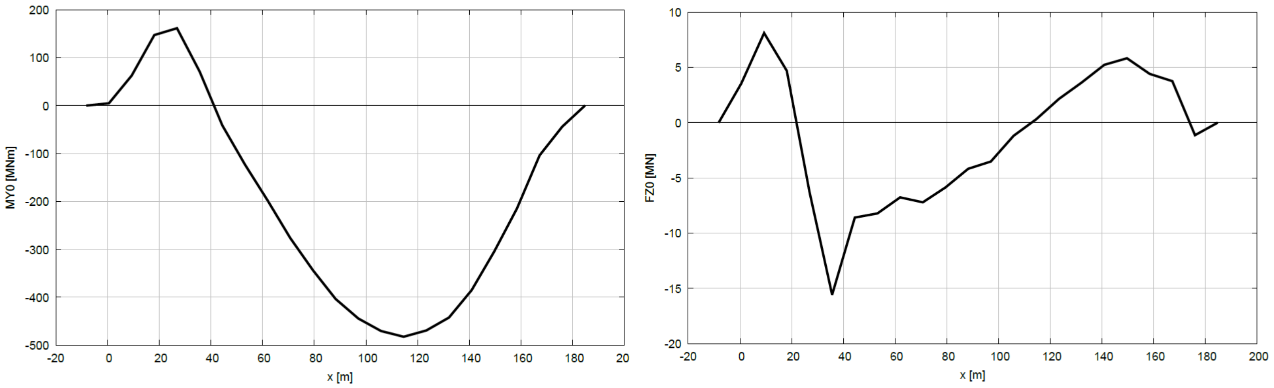

Figure 102: Longitudinal distribution of the amplitude of the linear vertical bending moment (left) and the linear vertical shear force (right) along the FPSO in head waves

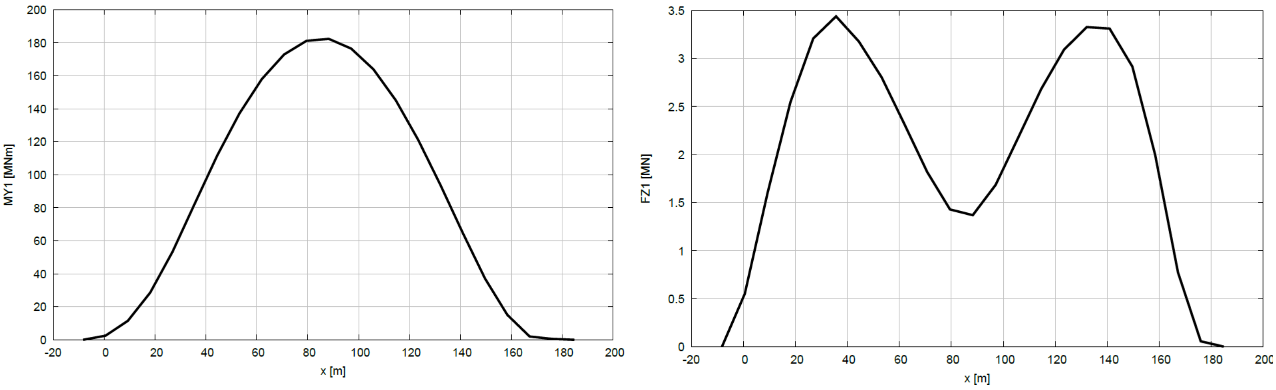

2. Quasi-static hydro-structure interactions

2.1. Introduction

2.1.1 General

The quasi static structural response is the one where the effects of the structural vibrations are neglected. This allows to perform the hydrodynamic and the structural calculations separately. The procedure consists of two independent steps. In the first step, the rigid body motions are evaluated (see Section 5), and in the second step, the hydrodynamic pressure is applied to the structural model together with the rigid body inertia loads and any other loads if existing (mooring …). The structural response is considered linear and is evaluated using the classical 3DFEM solvers. These principles are valid both for the linear and weakly nonlinear wave loading as well as for the formulations in the frequency and in the time domain.

2.2. Static response in calm water

2.2.1 Introduction

Purely static structural response is relevant for the evaluation of the stresses in the structure in calm water conditions. In addition to the local structural response, due to still water pressure and weight, the global response of the structure comes from the fact that the distribution of the ship weight and the buoyancy are different along the body. This difference induces the internal loads along the body (see Figure 101) and important stresses in the structural elements can occur.

2.2.2 Numerical modeling

The evaluation of the structural response of the floating body in calm water conditions is relatively straightforward. The FE model is simply loaded by the gravity loads on all the mass elements, and by the hydrostatic pressure loads at the wetted finite elements. The structural response is commonly assumed to be linear and is obtained directly using the static FE solver (see [1.4.1]). In the cases when the body deformation can be significant, it might be necessary to take the variation of the hydrostatic pressure into account (see [1.4.1]).

2.3. Quasi static structural response to linear wave loading

2.3.1 Introduction

The linear quasi static hydro-structure analysis represents the first and the essential step in the analysis of the structural resistance of offshore structures. The problem is usually formulated in frequency domain because that is much more computationally efficient (see Section 5). The key technical issue appears to be the consistency between the loads (both inertia and pressure) considered in the hydrodynamic model and in the structural model. The inaccurate load transfer will result in the unbalanced loading case, which means that the rigid body inertia will not be in equilibrium with the external pressure loading. The resulting misbalance will be "transferred" to some unphysical reaction forces in the artificial supports, which are required in the quasi static FE analysis of freely floating structures. While the consistency of mass properties can be easily achieved (typically by using the structural model mass properties in the hydrodynamic model), the consistent transfer of the pressure from the hydrodynamic panel model to the FEM model is more difficult and is described into more details here.

2.3.2 Hydrodynamic and structural meshes

In practice, the hydrodynamic and the structural meshes can be very different because they are made according to completely different philosophies (see Figure 103). The hydrodynamic mesh is built with the main requirement to accurately represent the wetted part of the body only, without any consideration for the structural design of the body. On the other hand the structural FE mesh is built with the main requirement to accurately represent the structure without any specific consideration for the character of the fluid flow. Typical hydrodynamic and structural meshes are shown in Figure 103. At the same time, the representation of the solution over two meshes is also very different: constant pressure over the hydrodynamic panels and polynomial distribution of the deformations in the finite elements. All this means that the pressure integration over the hydrodynamic mesh will lead to different result than the integration over the structural mesh. This makes the pressure transfer and the balancing of the load cases to be critical and nontrivial task.

Figure 103: The (linear) hydrodynamic (blue) and the structural meshes (orange) of the floating body

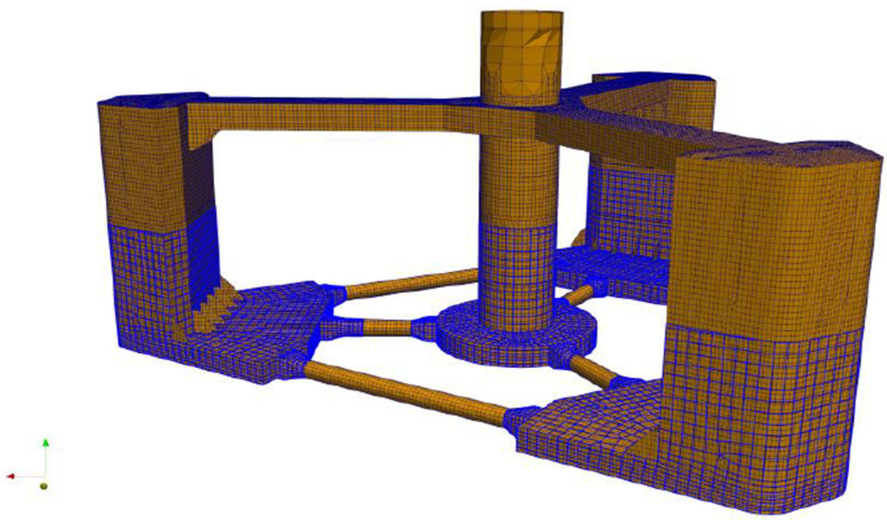

2.3.3 Hydrostatic pressure and gravity

The application of the hydrostatic pressure loading on the FE structural model is a bit specific and sometimes misinterpreted in the literature. The confusion comes from the fact that the linear hydrodynamic problem is formulated in the earth fixed coordinate system while the structural calculations are usually performed in the body fixed coordinate system. When evaluating the external loads, the following two important facts should be kept in mind (see also Appendix 1):

- The gravity loading is constant in the earth fixed coordinate system and varies in the body fixed coordinate system
- The normal vector on the body is constant in the body fixed coordinate system and varies in the earth fixed coordinate system

Due to the assumptions of linearity, the hydrostatic restoring matrix which is composed of the gravity and the hydrostatic pressure contributions, will be the same when formulated in the earth fixed or in the body fixed coordinate system. This is due to the fact that the body weight equals the buoyancy in the calm water conditions. However, even if the global effects of the gravity and the pressure loading are equivalent, their formulation differs from one coordinate system to another. The structural problem being formulated in the body fixed coordinate system the local loading needs to be expressed with respect to that system. This means that the following local hydrostatic pressure and the local gravity loading, should be applied on the FE structural model:

$$p^{hs} = -\varrho g[\xi_3 + \xi_4(y - y_G) - \xi_5(x - x_G)] \quad , \quad \{\boldsymbol{f}^g\} = -mg[\boldsymbol{\theta}]\{\boldsymbol{k}\} \tag{286}$$

2.3.4 Hydrodynamic pressure

The total velocity potential and the corresponding hydrodynamic pressure are decomposed into incident, diffracted and 6 radiated components:

$$\varphi = \varphi_I + \varphi_D i\omega \sum_{j=1}^{6} \xi_j \varphi_{Rj} \qquad , \qquad p^{hd} = i\omega\varrho\varphi = p_I + p_D + i\omega \sum_{j=1}^{6} \xi_j p_{Rj} \tag{287}$$

The potential is calculated numerically using the Boundary Integral Equation technique in which the mean wetted body surface is discretized into a certain number of panels over which the unknowns are assumed to be distributed according to a prescribed rule (most often constant). Within the source-only singularity distribution method, the final velocity potential is written in the following form:

$$\varphi(\boldsymbol{x}) = \iint_{S_B} \sigma(\boldsymbol{\xi}) G(\boldsymbol{x}; \boldsymbol{\xi}) dS \tag{288}$$

where $\sigma(\boldsymbol{\xi})$ stands for the source strength and $G(\boldsymbol{x}; \boldsymbol{\xi})$ is the Green's function (see Appendix 1).

2.3.5 Application of the pressure loading on the FE model

Within the linear theory, the pressure is to be applied on the mean wetted part of the body. As discussed in Section 4, the total pressure action is represented in terms of the added mass, damping and restoring matrices and the excitation vector. When the integration is performed over the hydrodynamic mesh, the motion equation (241) from Section 5, [2] is obtained and its solution gives the motion amplitudes $\{\boldsymbol{\xi}\}$. When the pressure is applied on the FE mesh, which is different from the hydrodynamic mesh (see discussions in [2.3.2] and Figure 103), the resulting total pressure action on the body will be different, meaning that the total external loading on FE model will not be in equilibrium with the inertia loading induced by the body motions $\{\boldsymbol{\xi}\}$. This misbalance is additionally increased by the errors introduced by the 3D interpolation (used most often in practice) of the pressure from the hydrodynamic mesh to the structural mesh. That is the reason why the more efficient method, based on the following three principles, is recommended:

1. Recalculation of the pressure at the structural points (instead of interpolation)
2. Separate transfer of the different pressure components, and evaluation of the hydrodynamic coefficients (added mass, damping, hydrostatic restoring & excitation) by integration over the structural FE mesh.
3. Solution of the motion equation using the above calculated hydrodynamic coefficients together with the inertia properties of the FE model.

The first point is possible thanks to the property of the BIE method which allows for the recalculation of the velocity potential at any point in the fluid as shown by Eqn. (288). The application of the pressure on the structural FE model can be performed either by directly providing the pressure on each wetted finite element or by providing the nodal loading (nodal forces and moments). In the case when the pressure is provided, the FE solver evaluates the nodal loading using its internal procedure which can vary from one FE solver to another. In order to make the coupling procedure general, it is more convenient to provide the pressure loads in terms of the nodal loading. The nodal loading can be pre-calculated outside of the FE solver, using the classical Gauss integration principles and by assuming the most typical FE shape functions. When doing this special attentions should be paid to the loading of the partially wetted finite elements. Such a situation occurs close to the free surface both in calm water and in wave conditions. For those elements it is recommended to increase the number of Gauss points in order to make the pressure integration accurate.

The total forces and moments on the body are obtained by simple summation of the nodal contributions. The corresponding hydrodynamic quantities can be easily deduced, and the body motion equation can be rewritten in the following form:

$$\left[-\omega^2([\boldsymbol{\mathcal{M}}] + [\,\boldsymbol{A}\,]^S) + i\omega([\,\boldsymbol{B}\,]^S + [\,\boldsymbol{B}_A\,]) + [\,\boldsymbol{C}\,]^S + [\,\boldsymbol{C}_A\,] + [\,\boldsymbol{k}\,]\right]\{\boldsymbol{\xi}\}^S = \{\boldsymbol{\mathcal{F}}^{DI}\}^S \tag{289}$$

where the superscript " ^{S} " is used to denote that the quantity was obtained by the integration over the structural FE mesh.

The solution of the motion equation (289) gives the body motion amplitudes $\{\boldsymbol{\xi}\}^S$ which are not the same as those obtained when the pressure loads are integrated over the hydrodynamic mesh. However, the difference should remain small if the two meshes (hydrodynamic and structural) are close to each other. One of the main advantages of the proposed coupling method lies in the fact that the body motions obtained from (289) will automatically lead to the perfect balance of the inertia and the pressure loads, because all the coefficients in the motion equation (289) are calculated by the integration over the FE mesh and the global inertia matrix is also provided by the FE model.

Another important advantage of the method is the fact that the interpolation of the pressure from the hydrodynamic mesh to the structural mesh is avoided since the hydrodynamic pressure on finite elements is recalculated using (288).

2.3.6 Final loading of the finite element model

The final loading of the FE model is composed of three parts:

$-\omega^2 m_i \boldsymbol{\xi}_i$ – Rigid body inertia

$p^{hd} + p^{hs}$ – Pressure

$-m_i g[\boldsymbol{\theta}]\{\boldsymbol{k}\}$ – Gravity

The pressure loading needs to be applied on each wetted finite element and the inertia and gravity loading to be applied on each finite element with non-zero mass.

It should also be noted that, within the linear frequency domain approach, the amplitude of the structural response is a complex quantity, and the load cases need to be created for both the real and the imaginary parts of the loading.

2.3.7 Boundary conditions

Static analysis by the finite element method assumes that the model cannot move as a rigid body (strain free). Consequently, it is not possible to perform conventional finite element quasi static analysis on unconstrained structures. The practical procedure consists in adding some artificial supports, to the FEM model, in order to constrain the six rigid body motions without constraining the elastic deformations. The problem arises when the model is not fully balanced because this unbalanced loading will induce non-zero reaction forces at the artificial supports. Depending on the choice of the supports these reaction forces can be more or less important. It is therefore recommended to constrain the translational degrees of freedom only and that on nodes chosen as far from each other as practically possible. The reaction forces at the artificial supports depend also on the source of the unbalanced loading, and they may alter the computed structural response, both globally and especially locally in the vicinity of the artificial supports. The artificial supports therefore need to be located at sturdy parts of the structure, and out of the area of interest (see Figure 104 - left).

2.3.8 Inertia relief method

Very often, in the commercial FEM packages, the so called inertia relief method is introduced. This method allows for getting the reaction forces zero even if the loading is not balanced. The basic idea is to correct the rigid body accelerations in order to get null reaction forces. This is of course always possible. However this method is obviously inconsistent since it does not correct the balancing error at its source, but just spreads the error over the whole ship through additional inertia which normally should not exist. When the inertia relief method is used, the correction of the acceleration needs to be monitored in order to evaluate the accuracy of the pressure transfer.

2.3.9 Boundary conditions for perfectly balanced model

In the case of the method described in 2.3.5, the choice of the artificial supports becomes arbitrary because the loading is perfectly balanced before being applied to the FE model. In order to illustrate how arbitrary the choice of the additional boundary conditions could be, in Figure 104, the stress distribution in the FE model obtained with two fundamentally different types of the boundary conditions, is presented.

The first set of boundary conditions (Figure 104 - left) is the classical one where three additional supports, far from each other, are set each blocking two translational motions. The second set of the boundary conditions (Figure 104 – right) is made of one single clamped support at the foremost node of the bulb which means that the three translations and three rotations are constrained. The results in terms of stresses are numerically identical. The apparent difference in the absolute displacements is due to the fact that the displacements are expressed relatively to the boundary condition, meaning that the difference between the two sets of displacements is a rigid body motion. Since the rigid body motions are strain free, they do not contribute to the final stress distribution. This example is shown for demonstration purposes only and the first set of the boundary conditions is recommended in practice.

**Figure 104: Different choices of the artificial supports.
Left – three nodes constraining two translations each (arrows indicate the constrained motion),
Right – one clamped node at the foremost position of the structure (double arrows indicate that both translations and rotations are constrained).**

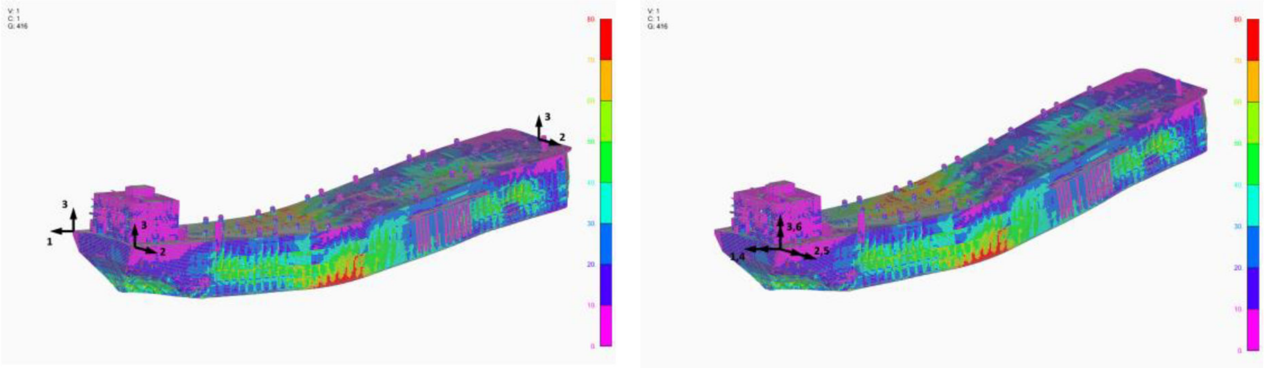

2.4. Quasi static structural response to nonlinear wave loading

2.4.1 Introduction

The most widely employed weakly nonlinear wave loading model accounts for large body motions, the nonlinear Froude Krylov and the nonlinear hydrostatic loading (see Section 4, [6.4]). The body motion equation is formulated in the time domain along the lines described in Section 5, [4]. In this section, the construction of the load cases for the quasi static structural FE analysis is described.

2.4.2 Coupling principles

Within the quasi static approach for the structural response, the final loading of the FE model is still composed of three main components: rigid body inertia, pressure and gravity. However, when compared to the linear case the technical difficulties are more important. The relevant body motion equation is Eqn. (262) from Section 5.

The first technical difficulty is related to the fact that the instantaneous wetted surface of the floating body changes in time so that the wetted finite elements need to be identified at each time step (see Figure 105). Most often in practice, the incident wave elevation is taken into account only and the changes of the wetted part induced by the diffracted and the radiated waves are neglected. This assumption shows to be reasonable in long waves but can be questionable in short waves where the diffraction-radiation effects are usually more pronounced.

Another important technical difficulty is related to the evaluation of the instantaneous pressure induced by the radiation component of the hydrodynamic pressure. When solving the body motion equation in time domain, the radiation effects are taken into account through the convolution integral with the memory functions associated with the global effects of the radiation pressure. According to the Cummins method (Cummins (1962)) the same principles remain valid at the level of the local pressure, which means that the convolution integral needs to be associated with each Gauss point of the FE model. This leads to significant increase in CPU time and in the memory storage requirements. Fortunately, this type of simulations is usually required for very short time period (design waves of less than one minute duration) so that this approach is still acceptable.

Figure 105: Instantaneous wetted part of the structure for weakly nonlinear wave model

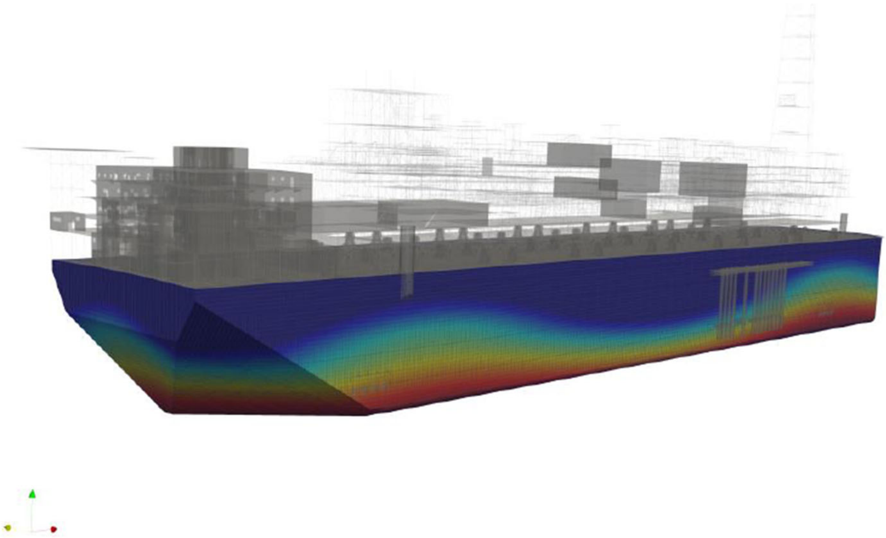

3. Dynamic hydro-structure interactions

3.1. Introduction

3.1.1 General

The dynamic hydro-structure interaction model accounts for the structural vibrations which add up on top of the quasi static structural response. In some cases, the evaluation of the dynamic response requires the 2-way hydro-elastic coupling of the hydrodynamic and the structural models. As far as the global structural response is concerned, two main physical phenomena occur in practice: springing and whipping. The springing phenomena has a resonant character while the whipping has a transient character. In reality, the two phenomena are usually combined and the clear separation between them is not always possible.

3.1.2 Springing

Springing represents the permanent wave induced vibrations of the body. A typical springing signal is shown in Figure 106.

Due to its resonant character, the importance of the springing response is driven by the frequency content of the excitation and by the amount of damping. This means that the bodies which have their structural natural frequencies much higher than the excitation frequencies will not experience significant springing response and the DAF will be close to unity (see Figure 99). However, knowing that the dynamic amplification of the response happens not only at the resonant frequency but also around it, the springing response might need to be evaluated even if the natural frequency is outside of the range of the excitation frequencies (see Figure 109).

The springing response under the linear wave loading can be evaluated in frequency domain, otherwise time domain simulations are needed.

Figure 106: Typical springing event

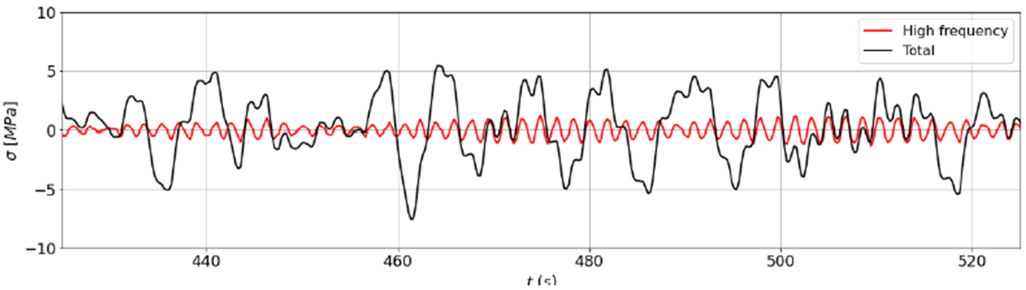

3.1.3 Whipping

Whipping represents the transient body vibrations induced by the impulsive wave loading such as slamming. A typical whipping event is shown in Figure 107.

Figure 107: Typical whipping event. Stress at midship of ULCS

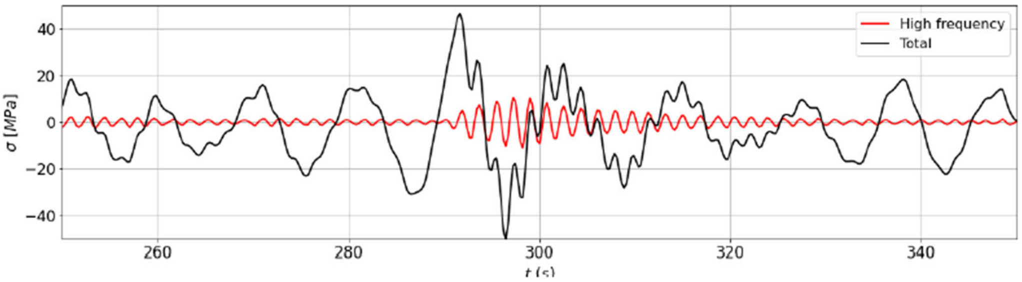

Contrary to springing, whipping is mainly driven by the nature of the impulsive loading which is independent of the structural natural frequencies. This means that any floating body can be potentially affected if the ratio of the impulsive loading duration and the natural period is critical (see Figure 99). The whipping response requires the time domain modelling.

3.1.4 Modelling principles

There exist different methods to perform the hydro-elastic analysis, and the method used here is based on the generalized modal approach (see Appendix 1). Within this approach the total body motions are represented as the sum of the 6 rigid body modes and a certain number (N_f) of the structural dry natural modes. In practice, only a limited number (5 to 10) of flexible modes are likely to experience a significant amplification of their response. This is because the higher modes are associated with much larger natural frequencies and also because the decay of those modes is usually faster. However, this does not mean that the contribution of the higher modes to the structural stresses is negligible, but this should be accounted for in a quasi-static manner.

3.2. Dynamic structural response to linear wave loading

3.2.1 Structural modelling

Due to the fact that only few first structural modes need to be accounted for, it is acceptable to simplify the structural model which is used for the dry modal analysis. In that respect, for the FPSO type of the floating bodies, the non-uniform beam model based on Timoshenko theory is usually acceptable (see Senjanovic et al. (2014)). The main advantage of the beam model is its simplicity and easy coupling with the hydrodynamic model. However, the full 3D FEM is always preferred.

3.2.2 Hydro-elastic coupling

The coupled linear hydro-elastic motion equation in frequency domain is given by (241). According to the generalized modal approach (Section 5 [2.2]) the structural modal deformation needs to be transferred from the structural model onto the hydrodynamic model. In the case of the simplified beam model this task can be done relatively easily and the transfer is almost analytical (see Senjanovic et al (2014)). In the case when the 3DFEM structural model is used, the situation is much more complex and there is no other choice than the 3D interpolation in space (see Malenica & Tuitman (2008)). Typical result of this interpolation is shown in Figure 108.

Figure 108: Transfer of the modal displacements from the structural FE mesh to the hydrodynamic BIE mesh

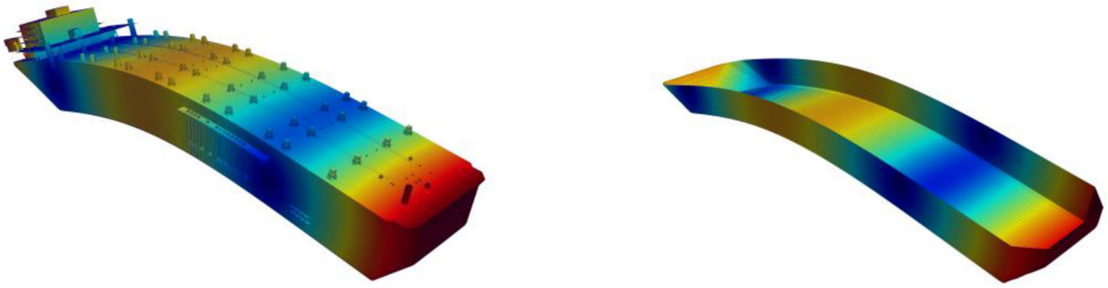

Once the mode shapes are transferred from the structural model to the hydrodynamic model, the body boundary condition for the radiation velocity potential of the flexible modes can be enforced (see Section 5, [2.2.3]) and the corresponding BVP formulated and solved by the classical BIEM (see Appendix 2). After that, all the different hydrodynamic quantities (added mass, damping, restoring and excitation) can be evaluated, and the dynamic motion equation (241) can be solved to give the amplitudes of the different modes of motion (rigid and flexible).

3.2.3 Evaluation of the stresses

Due to the fact that only a few flexible modes were used in the hydro-elastic analysis, the structural stresses cannot be obtained by simply summing up the different modal contributions, because the contribution to the stresses from the higher structural modes will not be accounted for. As already discussed, the higher structural modes contribute in a quasi static manner and their contribution can be very important even if their DAF is equal to unity. In order to properly separate the dynamic and the quasi static contribution to the stresses, the results of the quasi-static structural analysis (see [2.3]) needs to be combined with the results of the hydro-elastic analysis. In that respect, the total response is schematically decomposed, by rewriting the motion equation (289), in the following form (see Malenica & Tuitman (2008)):

$$\left(\begin{bmatrix}[\boldsymbol{RR}] & [\boldsymbol{RE}]\\ [\boldsymbol{ER}] & [\boldsymbol{EE}]\end{bmatrix}+\begin{bmatrix}[0] & [0]\\ [0] & [\boldsymbol{k}]\end{bmatrix}\right)\begin{Bmatrix}\boldsymbol{\xi}^R\\ \boldsymbol{\xi}^E\end{Bmatrix}=\begin{Bmatrix}\boldsymbol{F}^R\\ \boldsymbol{F}^E\end{Bmatrix} \qquad (290)$$

where $\boldsymbol{R}$ stands for the rigid body parts of the different matrices (except the structural stiffness matrix $[\boldsymbol{k}]$), $\boldsymbol{E}$ for the elastic ones and $[\boldsymbol{k}]$ is the modal structural stiffness matrix.

The total response amplitudes (rigid and elastic) are separated into their quasi static (ξ_0) and the dynamic (ξ_d) parts:

$$\boldsymbol{\xi}^R=\boldsymbol{\xi}_0^R+\boldsymbol{\xi}_d^R \quad , \quad \boldsymbol{\xi}^E=\boldsymbol{\xi}_0^E+\boldsymbol{\xi}_d^E \qquad (291)$$

By definition, the quasi static part of the response is given by the following equations:

$$\begin{aligned}[\boldsymbol{RR}]\{\boldsymbol{\xi}_0^R\} &= \{\boldsymbol{F}^R\}\\ [\boldsymbol{k}]\{\boldsymbol{\xi}_0^E\} &= \{\boldsymbol{F}^E\}-[\boldsymbol{ER}]\{\boldsymbol{\xi}_0^R\}\end{aligned} \qquad (292)$$

After inserting (291) and (292) into (290), the following linear system of equations for the dynamic parts is obtained:

$$\left(\begin{bmatrix}[\boldsymbol{RR}] & [\boldsymbol{RE}]\\ [\boldsymbol{ER}] & [\boldsymbol{EE}]\end{bmatrix}+\begin{bmatrix}[0] & [0]\\ [0] & [\boldsymbol{k}]\end{bmatrix}\right)\begin{Bmatrix}\boldsymbol{\xi}_d^R\\ \boldsymbol{\xi}_d^E\end{Bmatrix}=-\begin{Bmatrix}[\boldsymbol{RE}]\boldsymbol{\xi}_0^R\\ [\boldsymbol{EE}]\boldsymbol{\xi}_0^E\end{Bmatrix} \qquad (293)$$

Once the modal amplitude are evaluated, the total (quasi static + dynamic) stress $\Sigma(\boldsymbol{r},\omega)$ is calculated using the following expression:

$$\Sigma(\boldsymbol{r},\omega)=\sigma_0(\boldsymbol{r})+\sum_{i=1}^{N_f}\xi_{d_i}^E(\omega)\sigma_i(\boldsymbol{r}) \qquad (294)$$

where σ_0 is the quasi static stress, and σ_i is the stress associated with the deformation of the *i*-th mode.

The quasi static stress component σ_0 is found using the method described in [2] which avoids the convergence problems associated with the modal expansion method.

3.2.4 Typical springing response

In Figure 109 one typical example of springing response (in terms of stress RAO) obtained using the numerical model described in [3.2.3], is presented. It can be observed in particular, that the dynamic part (springing) of the response contributes to the stresses, not only close to the structural resonant frequency, but also for the frequencies well below. This suggests that the hydro-elastic effects might be important even for relatively stiff structures.

Figure 109: Typical stress RAO due to springing phenomena

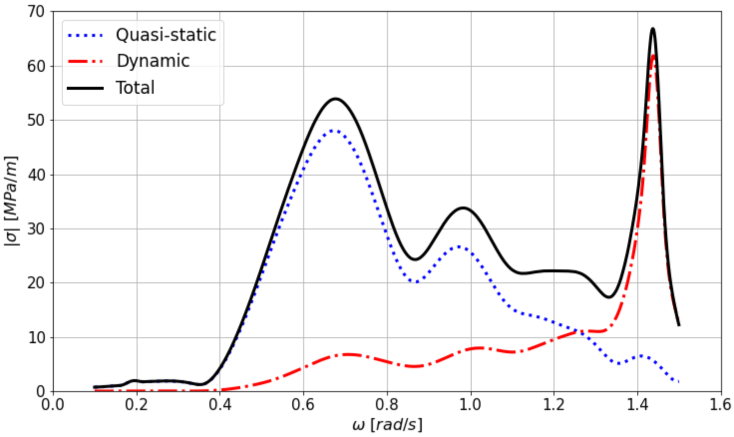

3.3. Dynamic structural response to nonlinear wave loading

3.3.1 Introduction

The global floating body vibrations can also be induced by the nonlinear wave effects. These nonlinear effects can be of non-impulsive and impulsive nature. The structural response remains linear and it is usually denoted as nonlinear springing in the case of non-impulsive excitation and as whipping in the case of impulsive excitation. The limit between nonlinear springing and whipping remains unclear. In principle the weakly nonlinear wave model based on Froude Krylov approximation includes some part of the higher order wave loads too and could potentially induce the nonlinear springing response. However, usually the nonlinear springing response occurs in the lower sea states where the diffraction effect are important so that the Froude Krylov approximation might not be very appropriate. In those cases, more sophisticated nonlinear hydrodynamic models are necessary. In that respect, the second order hydrodynamic model represents an interesting possibility, as discussed in Malenica et al (2018).

3.3.2 Slamming induced whipping

Slamming represents one of the main sources of the whipping excitation. The hydrodynamic modeling of slamming is extremely complex and still no fully satisfactory numerical slamming model exists in three dimensions. However, the 2D modeling of slamming is well mastered today and that is why the 2D models are usually employed within the strip theory approach.

The strip theory approach means that the part of the body, which is likely to experience the slamming loading, is subdivided into a certain number (N_S) of strips (Figure 110), and the slamming loading is evaluated at each strip independently using a dedicated 2D slamming model. The 2D slamming model (typically GWM or MLM) provides the pressure along the strip at each time step. This pressure is then interpolated onto the Gauss points of the FE model and the associated loading is included in the external loading vector of the dynamic motion equation together with other nonlinear load components

3.3.3 Impact conditions

The correct determination of the impact conditions, i.e. the relative geometry and the relative velocity of the strips, represents one of the most critical steps in whipping simulation models. The local impact velocity is defined as the difference between the body velocity and the fluid velocity at the particular point along the structure. According to the potential flow theory, the relative velocity in the normal direction, of the body surface, should be zero at each time instant and at every point on the section. There exist many technical reasons why this condition cannot be applied fully consistently in practice. The main reason is that the 2D strip theory is applied and, at the same time the 2D slamming models assume the impact on calm water.

In practice the numerical approach is used and the relative motion of the section is averaged over three representative calculation points. The relative displacement is defined as the distance between the calculation points and the intersection with the surface of the waves, and this intersection is found using a numerical iteration scheme. The relative velocity is found by differentiation in time. Because the 2D slamming calculation methods can only handle the motions of rigid sections, a single velocity vector is calculated by averaging the values at three points. More details can be found in Tuitman (2010).

Figure 110: Subdivision of the aft part of the body for slamming calculations

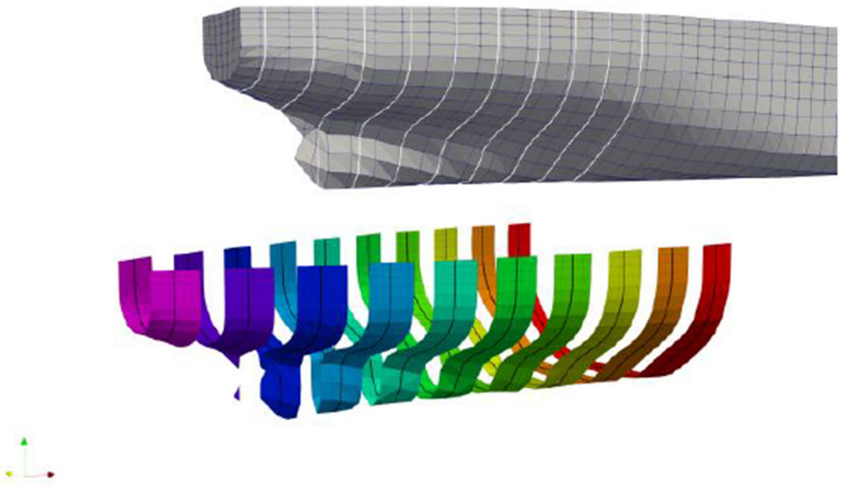

3.3.4 Typical whipping response

One example of the typical whipping response in terms of the vertical bending moment at midship section of an FPSO is presented in Figure 111.

Figure 111: Typical whipping event

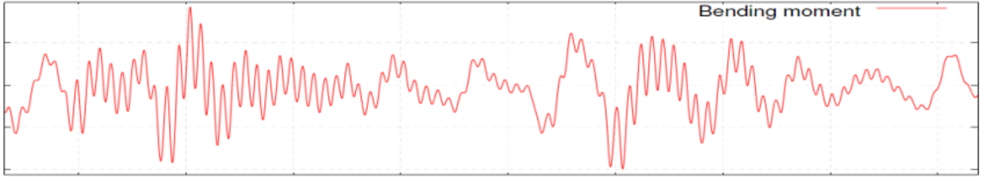

The transient high frequency oscillations, which are mainly due to the vibrational response of the first structural natural wet mode, on top of the quasi static wave frequency oscillations are clearly visible indicating that they cannot be ignored.

4. Local hydro structure interactions

4.1. General

4.1.1 Introduction

Very often in practice, a more refined local structural model needs to be employed. This usually happens either because the loading has a very local character (different impact loads such as slamming, green water, sloshing impacts …) or because we are interested in the detailed stress distribution close to the structural points which are critical from the fatigue point of view. Whatever the purpose of the analysis, the local structural model needs to account for the remaining part of the structure, at least approximately. The most consistent way to do this would be to locally refine the global FE model in which case the influence of the remaining part of the structure would be accounted for automatically. However, this is usually not done because, in many cases the global FE model is not available, but also including the refined local model into the global model leads to a significant increase of the number of unknowns and consequently the CPU time can become prohibitive. That is why, for the purpose of fatigue calculations the so called top-down analysis is employed, while for the local impact problems the local finite element model, with the adapted boundary conditions, is used.

4.2. Top down analysis

4.2.1 General

The top down procedure consists in two main steps:

1. Solving the global coarse mesh FEM problem
2. Imposing the displacements of the coarse FEM at the boundaries of the local fine mesh

When imposing the coarse mesh displacements on the boundaries of the fine mesh, the external loading (pressure and inertia) should also be imposed on the finite elements of the fine mesh. Typical situation is shown in Figure 112.

Note that, instead of imposing the nodal displacements it is also possible to impose the stresses or nodal forces/moments.

Figure 112: Typical local fine mesh FE model embedded in the coarse FE model and the boundary nodes of the fine mesh model

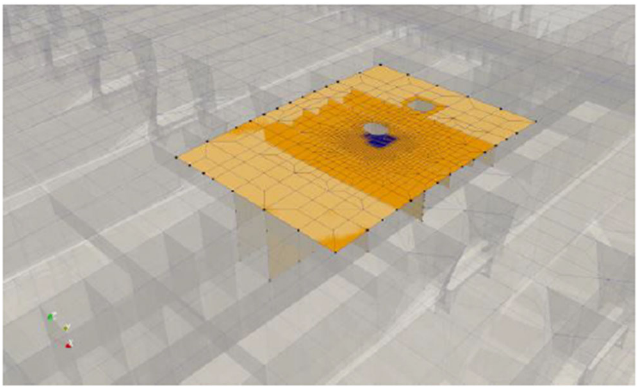

4.2.2 Static structural response

In the case of static structural response, the procedure is rather straightforward and closely follows the overall methodology for the evaluation of the quasi static response, presented in [2]. The local pressure, at the wetted Gauss points of the fine FE mesh, can be calculated using the same principles as those used for the coarse mesh, and at the same time the inertia and gravity loads can also be applied in a classical way. Once the pressure and the inertia loading are evaluated, the displacements at the boundary nodes are imposed and the local FE problem is solved.

4.2.3 Dynamic structural response

In the case of the dynamic response the situation is slightly more complicated because the inertia and the pressure loads need to include both the rigid body and the flexible body parts. This requires the additional interpolation of the flexible mode shapes on the refined FE mesh. For details we refer to Sireta et al (2012).

4.3. Local structural response to impact loads

4.3.1 General

The hydrodynamic impacts occur in many situations of practical interest: slamming, sloshing, green water and many others. The difficulties related to the evaluation of the impact loads were discussed in Section 4, [6.7]. Among the models based on potential flow theory, the strip theory approach with the Generalized Wagner Model for 2D impact represents the state of the art. On the other hand, the CFD methods are in principle able to consider the problem more consistently but they require much larger computational resources. The current tendencies are to use the potential flow methods in the screening phase, and to apply the CFD methods for the final check.

4.3.2 Local structural model for impact loading

The hydrodynamic impact pressure has a local extent so that the FE structural model can be reasonably limited to the part of the body which is affected. When doing that, the boundary conditions at the ends of the FE model need to be chosen in order to not affect the local structural behavior in a significant manner. The practical procedure is to progressively increase the finite elements model size from the zone of interest to the primary structural members (bulkheads, decks …) and to impose the clamped boundary conditions at the boundary nodes. More sophisticated methods where the boundary nodes are constrained with certain pre-calculated stiffness are also possible but used less often due to the difficulties to identify the proper stiffness coefficients. The same structural model is used regardless of the method which is applied for the evaluation of the hydrodynamic loading (CFD or potential flow). The FE model should be fine enough to properly capture the spatial variations of the impact pressure, which can be very sharp in general. It should also be fine enough to properly capture the local structural response of the structure of interest. The choice of the most appropriate type of the hydro-structure interaction model (static or dynamic) for particular impact conditions is driven by the ratio of the impact duration (rise time) and the structural natural periods of the structure (see also [1.3.3]). In many cases the simple quasi static structural model can be used but not always.

4.3.3 Quasi static response to impact loads

When the quasi static approach for the structural response is assumed, the coupling procedure remains the same as the one used for the global structural response (See [2]). The difference is that the pressure interpolation procedure needs to be employed because, within the 2D strip theory approach and the CFD approach, it is not possible to recalculate the pressure at arbitrary points in the fluid. Quasi static approach for evaluating the structural response under impact loading, should be used with care because extremely high impact pressures might occur for some conditions. If applied directly on the structure within the quasi-static approach, these pressures would induce severe structural failure. For those cases the hydro-elastic model is recommended.

4.3.4 Importance of hydro-elasticity during impact

In reality the extreme impact pressures are associated with very short duration and small spatial extent so that their effects on the structural response should be evaluated by considering the structural dynamics. Furthermore, due to the presence of the fluid the fully consistent hydro-structure interaction model is the 2-way hydro-elastic model. The basic principles of coupling remain the same as those used for the global hydro-elastic analysis and the modal approach can also be used. The main difficulties are associated with the evaluation of the hydrodynamic impact pressures for which only approximate numerical models exist.

Water entry of a hull with wedge-shaped cross sections was analyzed in Faltinsen (2000). In order to account for the 3D effects of the structural response, the orthotropic plate theory was used for structural modeling but the 2D strip approach was used for the modelling of the hydrodynamic forces within the Wagner's impact theory. Systematic studies on the importance of hydro-elasticity were conducted and it was concluded that, as far as the local structural response is concerned, slamming must always be analyzed as a combination of the hydrodynamics and the structural mechanics. In particular the definition of the equivalent quasi-static design pressures in this context is purely artificial. This is particularly true for almost flat impact conditions where the local pressures can locally reach very extreme values of short duration. However, for the conditions with larger impact angle, the pressure distribution is smoother and the quasi static approach can be employed.

Similar study was performed in Malenica et al. (2021) on an idealized beam. The semi-analytical and the numerical (CFD) results were compared in different interaction regimes and it was shown that, in spite of relatively poor comparisons of the maximum peak pressures, the agreement between the semi-analytical and the numerical results was very good in terms of the structural response. The results are summarized in Figure 113.

Figure 113: Water entry of wedge-shaped elastic cross section and corresponding dynamic amplification factor (taken from Malenica et. al (2021))

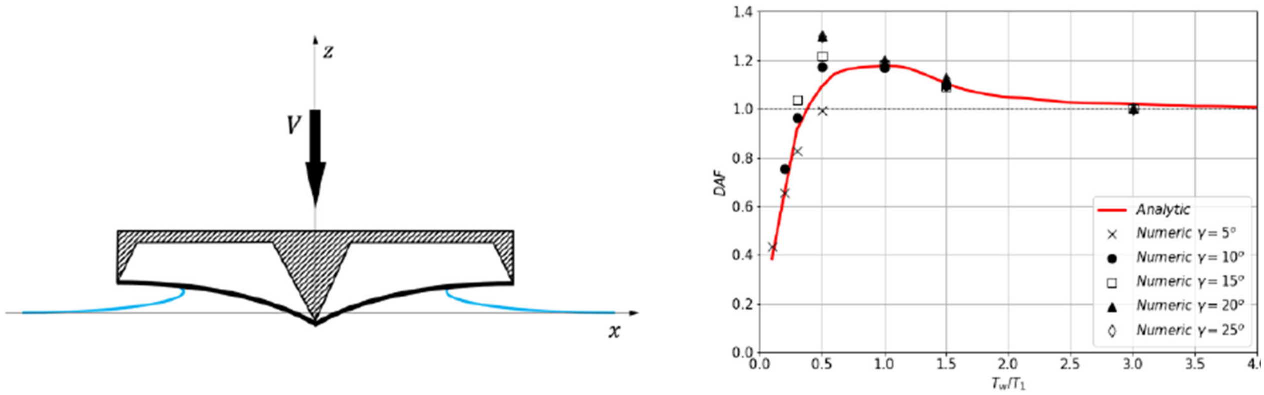

5. Some particular issues

5.1. Introduction

5.1.1 General

In offshore engineering there exist many practical situations where the adaptations/simplifications of either the hydrodynamic and/or the structural models are needed. On the hydrodynamic side, the typical example is the inclusion of the additional damping (e.g. for roll …), or accounting for the Morison loading. On the structural side, the typical example concerns the use of the partial structural models.

5.2. Accounting for global effects

5.2.1 Additional damping

When using the potential flow assumptions for the evaluation of the seakeeping behavior of the floating body, it is sometimes necessary to introduce some additional damping for some modes of motion. In practice the roll motion is of main concern because the associated wave induced damping is very low. Within the potential flow theory, the other sources of damping (friction, flow separation …) cannot be taken into account rationally and the common practice is to introduce the additional damping directly in the motion equation. This is usually done by prescribing the global linear and quadratic damping coefficients (see Section 5, [2.7.4]). When the motion equation is linearized, the total damping can be expressed in the form of the percentage of the critical damping. In the context of calculating the structural response, the technical issue is to apply this damping in the form of the local loading on the finite element model. This local loading is not expected to have a significant influence on the local structural response, but it is necessary in order to maintain the consistency between the motion equation terms and the loading on the FEM model, thus the correct balancing of the later. Since the local distribution of the damping forces is not known, the approximate methods are usually employed. The simplest approach is to assume that the damping occurs at certain nodes of the finite element, usually at the position of the bilge keel or at sharp corners (see Figure 114).

Figure 114: Redistribution of the roll damping loads on the FE model

The distribution of the forces can be assumed in many different ways, but the simplest approach is to assume that the local force $\boldsymbol{F}_i$ is proportional to the local body velocity induced by the mode of motion in consideration. In the case of roll this gives:

$$\{\boldsymbol{F}_i\} = C^v \dot{\xi}_4 [\boldsymbol{i}]\{\boldsymbol{u}_{Pi}\} \tag{295}$$

where $\{\boldsymbol{u}_{Pi}\}$ is the position vector of the point i relative to the body fixed coordinate system located at the body center of gravity $\{\boldsymbol{u}_{Pi}\} = \{\boldsymbol{r}_{Pi}\} - \{\boldsymbol{r}_G\}$, C^v is the “local damping coefficient”, and we recall that the notation $[\boldsymbol{i}]\{\boldsymbol{u}_{Pi}\}$ is used to denote the vector product.

The value of the local damping coefficient C^v is determined by equating the total damping moment with the sum of all the individual local contributions.

$$C^v = \frac{B_{44}}{\sum_{i=1}^{N_i} |\boldsymbol{r}_{Pi}|^2} \tag{296}$$

This procedure leads to exactly the same global roll damping loading, which was initially defined in the form of the percentage of the critical damping, but it also introduces some loading on the other modes of motion (e.g. sway & yaw) because the forces (295) are applied locally at the nodes of FE model. From practical point of view this does not represent the problem since the motion equation is solved after collecting all the individual loads on the whole FE model, so that the resulting structural load cases will also be perfectly balanced. We refer to Sireta et al (2009) for details.

5.2.2 Morison loading

As discussed in Section 5, [2.7.5], in some cases the BIE method is used in combination with the Morison loading model. Typical examples are the semi-submersible platforms and FOWT. For those cases, the transfer of the diffraction-radiation pressures remains exactly the same as described in [2.3.5] but the application of the Morison loading requires a few additional clarifications.

The Morison loading is given in an integrated sense, in the form of the overall force over a particular section, and there is no pressure distribution associated with this load. On the structural modelling side, two cases usually occur in practice, as shown in Figure 115.

Figure 115: Structural modelling of the slender elements. Left – beam, right – 3D shell.

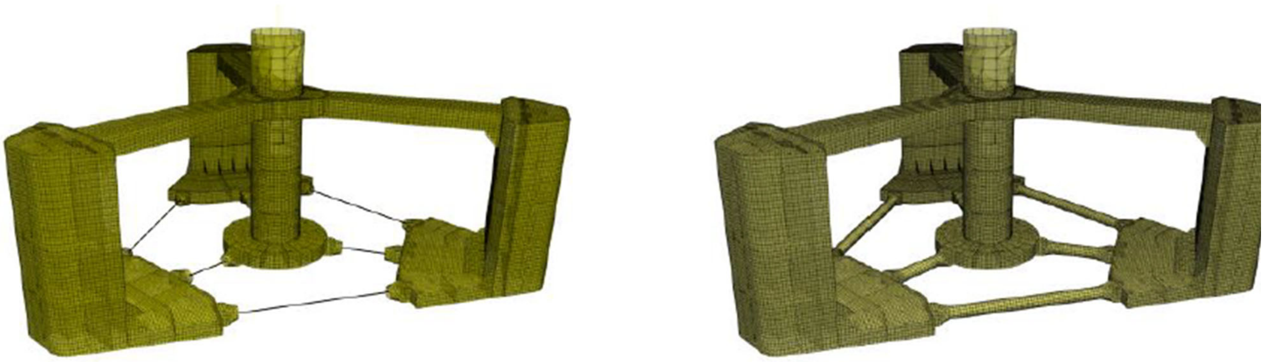

In the first case the part of the structure where the Morison loading is applied, is modeled using 1D beam elements and in the second case 3D shell elements are used. The application of the Morison loading in the first case is straightforward since the FE model directly accepts the loading in the form of nodal forces. In the case when the 3D shell elements are used, the Morison loading needs to be redistributed over the shell elements. The easiest way to do this is to define some massless finite elements connecting the center of the section with the associated FE nodes. The Morison force is applied at the center of the section and the FE solver automatically redistributes it over the nodes of the shell finite elements. When doing this care should be taken to not introduce some additional stiffness into the overall system so that specific finite elements need to be used (e.g. RBE3 elements in Nastran). We refer to Sireta et al (2010) for details.

5.3. Partial structural models

5.3.1 Introduction

Partial structural models can sometimes be used for the structural analysis of a limited part of the structure. The main advantage of using the partial structural modelling is the significant reduction of the modelling time for the 3D FEM structural model.

5.3.2 Three cargo hold model

The typical example of the partial structural models is the, so called, 3 cargo hold model (Figure 116 left) which is commonly accepted by the Class Societies, within the design verification process, for ships and ship-like offshore units (FPSO …). When using the 3 cargo hold model, it is assumed that the boundary conditions at the fore and the aft ends of the FE model, do not influence the response in the middle part of the structure, and consequently the response in the middle part of the structure is analyzed only.

5.3.3 Hybrid beam – 3D FE model

Another example, where the partial structural modelling can be useful, concerns the case when some part of the structure is modelled using the classical 3D finite elements, while the rest of the structure is modelled using the simple beam elements (Figure 116 right). The goal of the analysis is to account for the influence of the global body dynamics on the local structural response. The issue about the boundary conditions remains the same and the local FE model should be large enough, in order for the boundary conditions to not influence the local response significantly.

Figure 116: Partial structural models.
Left – 3 cargo hold model, right – partial FEM model of the flare tower foundation of the FPSO

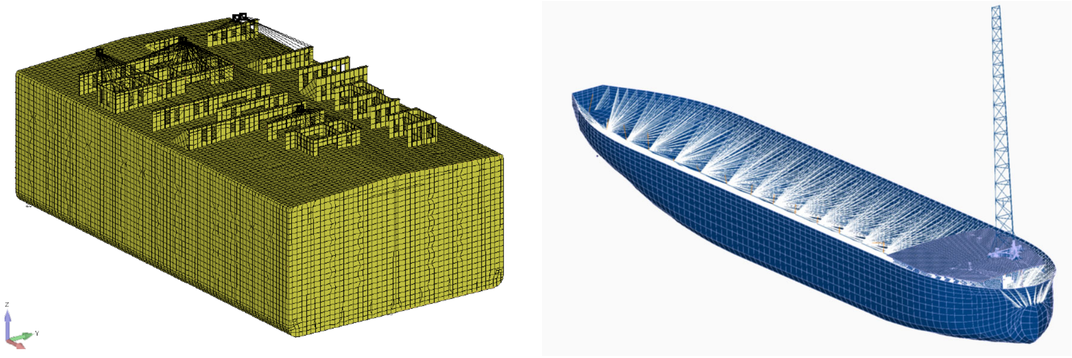

5.3.4 Load transfer for the partial structural models

Whatever the structural model which is used (full or partial), the hydrodynamic loading should be applied fully consistently over the entire wetted surface of the body. This point is critical for the balancing of the loading cases. In order to apply the hydrodynamic and the inertia loading on the whole body, the easiest way is to use massless plate elements, to model the missing portion of the wetted part of the body, and to connect them to the partial structural model using suitable finite elements.

In the case of the 3 cargo hold model one additional structural node is usually created, at the center of gravity of the missing part of the structure and is connected to the massless plate elements (extracted from the hydrodynamic mesh) and to the end of the 3D FEM model, using rigid elements such as Nastran RBE2. The mass properties, of the missing part of structure, are applied at this additional structural node using a mass matrix element. The hydrodynamic pressure loads are applied on the massless plate elements, for the missing part, and on the structural finite elements for the modelled part (see Figure 117). All this basically means that a kind of hybrid full 3D structural model is used which automatically leads to the correct balancing of the structural load cases.

Figure 117: Three cargo hold structural model (left), the hydrodynamic model (top right) and the integration mesh (bottom right)

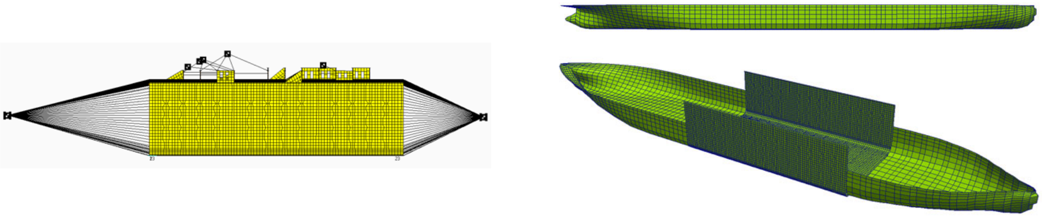

In the case of the hybrid beam – 3D FE model (Figure 116 right) a similar approach is followed and the missing structure is modelled using the non-uniform Timoshenko beam elements, to which the massless panels (extracted from the hydrodynamic mesh) are connected by some dedicated finite elements. The Timoshenko beam model is built in classical way, using the sectional properties of the body, and the mass of the body is redistributed over the associated beam elements. In this way the main effects of the global ship vibrations are included in the structural analysis. The rest of the procedure to calculate the structural response remains the same because a hybrid 3D FE model was constructed.

For details we refer to Sireta et al. (2009) and Benhamou et al. (2019).

6. List of references

[1] Benhamou A., Shimazaki J. & Bontemps F., 2019.: “Influence of whipping on the structural response of the flare tower foundations of a typical spread moored FPSO.”, Offhore Technology Conference, Rio de Janeiro, Brazil.

[2] Faltinsen O.M., 1999. : “Water entry of a wedge by hydroelastic orthotropic plate theory.” J Ship Res 43:180–193

[3] Faltinsen O.M., 2000. “Hydroelastic slamming.” J Mar Sci Technol Vol. 5.

[4] Malenica S. & Derbanne Q., 2014.: “Hydro-structural issues in the design of ULCS” International Journal of Naval Architecture and Ocean Engineering, Vol. 6, No. 4

[5] Malenica S. & Tuitman J., 2008.: “3DFEM – 3DBEM model for springing and whipping analyses of ships.”, RINA Conf. on Design and Operation of Container Vessels, London UK.

[6] Malenica S., De Hauteclocque G., Ten I. & Choi Y.M., 2018.: ”Second order hydroelastic model of floating units.”, 8th Int. Conf. on Hydroelasticity in Marine Technology.

[7] Malenica S., Derbanne Q., Sireta F.X., Bigot F., Tiphine E., De-Hauteclocque G. & Chen X.B., 2013.: “HOMER – Integrated hydro-structure interactions tool for naval and offshore applications”, International Conference on Computer Applications in Shipbuilding, Busan, South Korea.

[8] Malenica S., Gatin I., Seng S., Jagite G., Diebold L., Khabakhpasheva T. & Korobkin A.A., 2021. “Some aspects of the local hydro-structure interactions during hydrodynamic impacts”, 23rd Numerical Towing Tank Symposium (NUTTS), Duisburg, Germany.

[9] Senjanovic I., Vladimir N., Tomic M., Hadzic N. & Malenica S., 2014.: “Global hydroelastic analysis of ULCS by improved beam structural model”, International Journal of Naval Architecture and Ocean Engineering, Vol. 6, No. 4

[10] Sireta F.X., Derbanne Q., Bigot F. , Malenica S. & Baudin E., 2012.: “Hydroelastic response of a ship structural detail to seakeeping loads using a top-down scheme”, 31st OMAE Conference, Rio de Janeiro, Brazil

[11] Sireta F.X., Malenica S, Bigot F., Derbanne Q., Chen X.B. & Bonniol V., 2010. : “An efficient hydro structure interface for mixed panel-stick hydrodynamic model.”, ISOPE, Beijing, China

[12] Sireta F.X., Malenica S., Chen X.B. & Marchal N. 2009 : “Consistent hydro structure interface for partial structural model.”, In Proceedings of Deep water Offshore Specialty Symposium, Harbin, China

[13] Tuitman J., 2010.: “Hydro-elastic response of ship structures to slamming induced whipping”, PhD Thesis, Delft University of Technology.

Section 8 Use of CFD

1. Computational fluid dynamics – CFD

1.1 Introduction

1.1.1 General

CFD stands for Computational Fluid Dynamics. Even though, strictly speaking, this include all types of numerical methods used to solve different problems related to fluid dynamics, most often CFD is used to denote the numerical modelling based on either the RANS (Reynolds averaged Navier-Stokes) or the Navier-Stokes (NS) equations. This means that the potential flow methods which were discussed throughout the present document are significantly different and therefore excluded from being called a CFD method.

The CFD methods commonly solve the flow equations on a discretized field which, in principle, includes the whole fluid domain. In the case when the fluid domain extends to infinity, the discretized field is limited to appropriate size with the far-field domain boundaries replaced by special numerical treatments which are designed to satisfy the expected flow conditions at the infinity up to a certain degree of accuracy. Optionally, the flow conditions at the far-field boundaries are computed using a coupled approach where the flow field at the exterior to the discretized domain is computed with other model which can account more naturally for the expected flow conditions at the infinity.

For a long time, the use of CFD was restricted to applications that do not involve waves. These are e.g. the evaluation of the wind and current loads. Introducing waves into the CFD domains appears to be one of the major technical barriers which pose a strong demand on computational resources. The presence of the free surface at the interface between the liquid and the air introduces important physics which are very challenging to model appropriately. Some models may capture very well the overall volume representation of both liquid and air but have difficulties to evaluate exactly the instantaneous position of the free surface. Vice versa, other models may provide a very sharp representation of the free surface but have difficulties to preserve the overall fluid volume within the computational domain.

1.1.2 Applications

One of the major drawbacks of the CFD methods is the large CPU time and heavy hardware requirements (hundreds or thousands of processors). Knowing that the design procedures in the off-shore industry, require very long simulations for a large number of environmental conditions, the CFD methods cannot be used solely within all stages of the design methodology. The current practice is to use the CFD method selectively in a combination with the potential flow theory. Such a practice is denoted here as unified methodology. The basic idea is to use the potential flow model to identify the critical design conditions and to use the CFD method to simulate these design conditions selectively. Most often, the critical design conditions are deduced statistically in the form of the equivalent design waves (see NI 638) with limited duration and usually less than a minute. CFD simulations which may include complex hydro-structure interactions for such a short period are feasible and cost a reasonable CPU time on a limited number of processors. The simulations concern both the global body behavior as well as some local phenomena like slamming, green water, underdeck impact and many others. The unified methodology is illustrated in Figure 118 where 3 main steps of the overall procedure are shown:

1. Determination of the lifetime operational profile of the unit
2. Determination of the representative design conditions (equivalent design waves)
3. Evaluation of the response

The first step is defined by the design requirements. The second step is carried out using the models based on the potential flow theory and the third step is performed using the CFD method coupled with a structural FEM.

Other important applications of the CFD method in off-shore engineering are the pre-calculation of certain hydrodynamic coefficients (e.g. drag coefficients, roll damping, etc.) which are subsequently used in the potential flow based seakeeping models (see Chapters 5 and 6).

Finally, problems which involve sloshing motion in tanks carrying liquid, in particular the LNG tanks, require special attention due to the highly nonlinear nature of the flow. Here, the CFD simulations remains practically the only choice in addition to the small-scale measurements which suffers from important scale effects. It is generally accepted that the CFD method can correctly reproduce the overall forces on the tank. However, when it comes to the evaluation of the local pressures during the sloshing impacts, the numerical evaluation of the local pressures remains very challenging to verify, validate and carry out consistently. These challenges include the possible compressibility effects which are expected to exist in the LNG tanks (see Malenica et al. (2017)).

Figure 118: Unified methodology

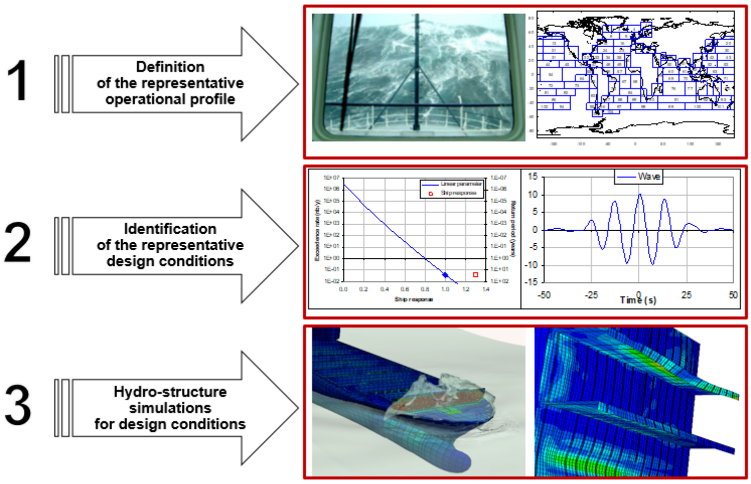

2. Numerical approaches

2.1 Introduction

2.1.1 General

Different numerical methods for solving the Navier-Stokes equations were proposed in the past. Two main categories of approaches are usually distinguished.

The first category, which is employed most often, is based on meshing the fluid domain into a certain number of cells in which the solution is assumed in a simple form (constant, linear…) so that the Navier-Stokes equations can be approximated using the discrete values at the cell centers and the cell nodes. Several sub-categories of mesh-based CFD methods exist among which the following ones are used most often: the finite element method (FEM), the finite differences method (FDM) and the finite volume method (FVM). Even though the classical finite element method (FEM), which is the dominating method for structural analyses, could be also applied for CFD simulations, it happens that the use of FEM in CFD has not received much attention except for some dedicated applications. The FDM and FVM are far more popular. The FDM evaluates the equations at mesh nodes. Any derivatives are approximated discretely at the nodes using finite differences. Such a procedure, usually, requires the mesh nodes to be structured which eventually is limiting its use to cases with simple geometries. The FVM, in comparison, works more naturally on an unstructured mesh which allows complex cases to be meshed more easily. The FVM integrates the equations and evaluates the solution in the form of average values over the cells. Approximations to the integral of e.g. derivative or convective terms are constructed from these cell averages. The FVM is popular due to its versatility and because the solution can be made fully conservative. Most commercial general-purpose CFD software, e.g. StarCCM+, Fluent, Isis-CFD, are based on FVM and open source alternatives exist in particular OpenFOAM (Weller et al. (1998)) which has gained popularity rapidly.

The second category which is termed mesh-less CFD includes methods in which the flow solution is approximated over a set of arbitrarily distributed points in space without any structural nor topological connectivity in between. For example, the Smoothed Particle Hydrodynamic method (SPH) divides the fluid domain into a set of discrete moving points referred to as particles. These particles are allowed to interact only within a predefined spatial region defined by an analytical function known as a kernel function. The flow quantities are then approximated by a weighted sum of the relevant properties (such as mass, momentum and energy) of all particles within the range of the kernel. The kernel function is a free parameter and can be either a globally supported kernel e.g. the Gaussian function or a compactly supported kernel such as a quintic spline. The elimination of the mesh allows simulations of problems which include complex boundary dynamics such as the free surface flows. The drawbacks of the meshless methods are related to the numerical difficulties in evaluating the localized dynamic pressures, to the introduction of waves in the domain, and to account for the floating body dynamics. In addition, the CPU time is also an issue so that these methods are used less often in offshore hydrodynamics. For review we refer to Shadloo et al. (2016).

Among the different numerical approaches in CFD, the method based on the FVM approach appears to be most used and most accessible today. The basics of the FVM are briefly discussed below.

2.1.2 Numerical errors

Numerical methods suffer from all sorts of numerical errors and this is due to the discretization of the continuous form of the conservative flow equations. Whatever the numerical method the errors will exist and need to be controlled. Different types of errors occur and they can be roughly classified into the following three types (Ferziger & Peric (2002)):

- *Modeling errors*: the difference between the actual flow and the mathematical model

- *Discretization errors*: the difference between the exact solution of the conservation equations and the numerical solution of the algebraic system of equations after discretization
- *Iteration and round off errors*: the difference between the iterative and exact solutions of the algebraic system of equations

Modeling errors depend on the assumptions made when deriving the conservative equations for the fluid flow. In the present context, this is mainly related to the modelling of the two-phase flow, to the modelling of the turbulence, and to the modelling of the boundary conditions, where the different mathematical models can be employed. The discretization errors comprise the mesh quality, the way in which the equations are discretized both in terms of interpolation as well as in terms of the order of approximations (first, second, higher). The iteration and the round-off errors are easier to control but the resulting CPU time critically depends on the required accuracy.

To evaluate the modelling errors, the discretization and iteration errors need to be controlled first i.e. the chosen mathematical model needs to converge numerically. In that respect checking the convergence of the particular numerical scheme needs always to be performed. When doing that different procedures for estimating the convergence rate and the associated uncertainties are proposed in the literature (ITTC (2017), Eca & Hoekstra (2014), Celik (2008), Xing & Stern (2010) and others, see Moctar et al (2021) for review)

There exist many solution schemes and the choice of the most appropriate ones is not an easy task and is often driven by the users experience and some empirical rules. The ultimate goal of any numerical simulation is to obtain the desired accuracy with the lowest CPU time or maximum accuracy with the available resources.

2.2 Finite volume method

2.2.1 Introduction

The FVM is the numerical method that discretizes the governing equations by a certain number of small control volumes over which a certain distribution of the unknown physical quantities is assumed. The method allows the use of the unstructured grid which is very useful in practice and allows easy modelling of a wide range of complex geometries. The FVM is naturally conservative as long as surface integrals are the same for cells sharing the boundary. The disadvantage of FVM, compared to FDM, is that procedures of order higher than second are more difficult to develop in 3D.

2.2.2 Navier Stokes equations

The Navier Stokes equations are usually defined as a combination of two conservative laws: mass and momentum. In the most general case of compressible viscous fluid flow, the integral form of the two conservative laws is given by:

mass

$$\frac{\partial}{\partial t}\iiint_V \varrho dV + \iint_S \varrho\boldsymbol{v}\cdot\boldsymbol{n}dS = 0 \tag{297}$$

momentum

$$\frac{\partial}{\partial t}\iiint_V \varrho\boldsymbol{v}dV + \iint_S \varrho(\boldsymbol{v}\boldsymbol{v}^T)\cdot\boldsymbol{n}dS = \iint_S \mathbf{T}\boldsymbol{n}dS + \iiint_V \varrho\boldsymbol{g}dV \tag{298}$$

where V denotes the control volume and S denotes the surface which surrounds the control volume, ϱ is the fluid density, $\boldsymbol{v}$ is the fluid velocity $\boldsymbol{g}$ is the gravity acceleration vector and $\mathbf{T}$ is the stress tensor. For Newtonian fluids, which are of concern here, the stress tensor is a linear function of the velocity gradient and is usually written in the following form:

$$\mathbf{T} = -\left(p + \frac{2}{3}\mu\nabla\cdot\boldsymbol{v}\right)\mathbf{I} + \mu[\nabla\boldsymbol{v} + (\nabla\boldsymbol{v})^T] \tag{299}$$

where $\mathbf{I}$ denotes the unit tensor, p is the pressure and μ is the dynamic viscosity.

The equations (297) and (298) form a closed system of equations to compute fluid velocity and pressure. Several simplifications can be introduced in the Navier Stokes equation when the features of the fluid flow allow it. In particular when the density remains constant in space and in time ($\varrho = const$) the incompressible Navier Stokes equations are obtained. If the viscous effects are neglected ($\mu = 0$) the so called Euler equations are obtained and finally if the flow is assumed to be irrotational ($\nabla\wedge\boldsymbol{v} = 0$) the potential flow regime is described.

In the present document, only the incompressible flow is of concern. One of the problems with the incompressible flow is that the explicit equation for the pressure does not exist and, in addition to the momentum Navier Stokes equation (297) the only remaining equation is the continuity equation (298) which does not contain the pressure. However, the continuity equation can be combined with the momentum equation to give an additional equation for pressure:

$$\nabla^2 p = \nabla\cdot\left[-\varrho\frac{\partial\boldsymbol{v}}{\partial t} - \varrho\nabla\cdot(\boldsymbol{v}\boldsymbol{v}^T) + \mu\nabla\cdot(\nabla\boldsymbol{v}) + \varrho\boldsymbol{g}\right] \tag{300}$$

This equation is of the so-called Poisson type and can be discretized using the same principles as those used for the momentum equation.

2.2.3 Reynolds averaged Navier Stokes equations

In the case when turbulence matters, the direct solution of the Navier Stokes equations become prohibitive because of the extremely small space and time scales that should be used. Instead the Reynolds averaged approaches for turbulence are employed. In this approach the total solution $\boldsymbol{v}(\boldsymbol{x},t)$ is decomposed into the averaged part $\bar{\boldsymbol{v}}(\boldsymbol{x},t)$ which is slowly varying and the highly oscillatory part $\boldsymbol{v}'(\boldsymbol{x},t)$ which has zero mean value:

$$\boldsymbol{v}(\boldsymbol{x},t) = \bar{\boldsymbol{v}}(\boldsymbol{x},t) + \boldsymbol{v}'(\boldsymbol{x},t) \qquad (301)$$

This decomposition is then re-introduced into original Navier Stokes equations and the properties of averaging operation are exploited to give the following conservative equations:

mass $$\frac{\partial}{\partial t}\iiint_V \varrho dV + \iint_S \varrho\bar{\boldsymbol{v}}\cdot\boldsymbol{n}dS = 0 \qquad (302)$$

momentum $$\frac{\partial}{\partial t}\iiint_V \varrho\bar{\boldsymbol{v}}dV + \iint_S \varrho(\bar{\boldsymbol{v}}\bar{\boldsymbol{v}}^T)\cdot\boldsymbol{n}dS = \iint_S \left(\mathbf{T} - \varrho\overline{\boldsymbol{v}'\boldsymbol{v}'^T}\right)\cdot\boldsymbol{n}dS + \iiint_V \varrho\boldsymbol{g}dV \qquad (303)$$

The term $-\varrho\iint_S \overline{\boldsymbol{v}'\boldsymbol{v}'}\boldsymbol{n}dS$ is called Reynolds stress tensor and the set of equations (302)(303) are called the Reynolds Averaged Navier Stokes Equations (RANS). To be able to solve the RANS equations the additional assumptions on Reynolds stress tensor are needed. The procedure consist in expressing the Reynolds stress tensor as a function of the averaged flow quantities. Many different turbulence models were proposed in the literature and the most widely used models for marine applications are the $k-\epsilon$ model and the $k-\omega\, SST$. Details about these models can be found in the classical textbooks on fluid mechanics (e.g. Wilcox (1993), Pope (2000)). It should be understood "*that the complexity of turbulence makes it unlikely that any single Reynolds-averaged model will be able to represent all turbulent flows, so turbulence models should be regarded as engineering approximations rather than scientific laws*" (Ferziger & Peric (2002))

2.2.4 Discretization of the Navier Stokes equations

The FVM uses the integral form of the conservation equations as its starting point. The fluid domain is subdivided into a finite number of cells which can be of general polyhedral type as shown in Figure 119. The unknowns are the velocity and pressure values at each cell center. The conservation equations are applied to each cell and the interpolation is used to express the unknowns at the cell surfaces in terms of their value at the cell center. The volume and surface integrals are approximated by dedicated quadrature formulae and the equilibrium equations for each control volume are written as a function of the nodal values (cell centers) of the neighboring cells. The final system of equations for the unknown quantities is obtained by combining the algebraic equations for each cell.

When describing the different numerical schemes, either in space or in time, it is common to introduce the notion of the "order of accuracy". The first order of accuracy means that the variable in consideration is a function of its local (instantaneous) value only, while the higher order of accuracy means that the variable is approximated through the interpolation between the neighboring values (in space or in time). In that respect, use of the linear interpolation results in the second order accuracy.

Figure 119: Polyhedral control volume (cell)

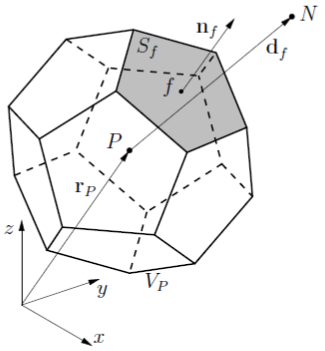

2.2.5 Time marching schemes

All the time integration schemes can be derived from the Taylor series expansion at a given time instant. For a time-dependent variable $\phi(t)$ the Taylor series expansion about the time instant t_n is given by:

$$\phi(t+\Delta t) = \phi(t_{n+1}) = \phi(t_n) + \Delta t\left(\frac{\partial\phi}{\partial t}\right)_{t=t_n} + O[(\Delta t)^2] \qquad (304)$$

The different time integration schemes are classified with respect to the evaluation of the time derivative $(\partial\phi/\partial t)_{t=t_n}$. In practice the following schemes are used most often ($f[\quad]$ means "function of"):

Euler forward (explicit) $$\left(\frac{\partial\phi}{\partial t}\right)_{t=t_n} = f[t_n, \phi(t_n)] \quad (305)$$

Euler backward (implicit) $$\left(\frac{\partial\phi}{\partial t}\right)_{t=t_n} = f[t_{n+1}, \phi(t_{n+1})] \quad (306)$$

Crank-Nicolson (implicit) $$\left(\frac{\partial\phi}{\partial t}\right)_{t=t_n} = \frac{1}{2}\{f[t_n, \phi(t_n)] + f[t_{n+1}, \phi(t_{n+1})]\} \quad (307)$$

The main difference between the explicit and implicit time integration schemes is that the implicit integration schemes require iterations within each time step while the explicit schemes do not. The Euler backward implicit scheme is first-order accurate and the Crank Nicolson scheme is second-order accurate. Other second-order schemes are also proposed in the literature.

2.2.6 Courant number and stability of the time integration schemes

The time step is related to the spatial discretization through the Courant number, also called Courant-Friedrichs-Lewy number (CFL). This number represents the ratio of the distance travelled by the disturbance within the time step and the characteristic mesh size. By noting the characteristic flow velocity by v_R and the characteristic mesh size by Δx_R the Courant number is defined as:

$$CFL = \frac{v_R \Delta t}{\Delta x_R} \quad (308)$$

For the flows dominated by convection, which is the case most often here, the explicit methods are stable only if $CFL < 1$. However, many implicit methods are stable for much larger time step. That is why the implicit time integration schemes are recommended for typical marine applications even if they require iterations within the time step.

In practice, the different time integration schemes can be combined within single simulations. In particular, due to its robustness and despite its poor accuracy, the first order Euler backward scheme can be used at the beginning of the simulations to initialize the fluid flow and the more accurate second order scheme (Crank Nicolson or others) can be used afterwards.

2.2.7 Pressure velocity coupling and solution algorithms

Once the Navier Stokes equations have been discretized, the unknown pressure and velocity values at cell centers can be found using the different numerical procedures. Due to the nonlinear character of the Navier Stokes equations the iterative procedure is needed to reach the convergence. Most often the projection method (see Ferziger & Peric (2002)) is used. This method consists of two main steps:

1. Predictor step: Momentum equation (298) is solved using the rough estimate of the pressure field from the previous time step/iteration. The resulting velocities do not satisfy the continuity equation.
2. Corrector step: The pressure is evaluated by solving the Poisson equation (300) and the velocities are updated. The updated velocities satisfy the continuity equation.

Those two steps are repeated until convergence is reached. The iterative procedure is known as outer iteration loop. Several variants of the projection method were proposed in the past and the most popular seems to be the SIMPLE (Semi-Implicit Method for Pressure-Linked Equations) and PISO scheme (Pressure Implicit Splitting of Operators, Issa (1986)). Within this scheme an additional iteration loop (inner loop) is introduced when solving the Poisson equation to improve the convergence.

2.2.8 Handling of the free surface

Handling of the free surface represents one of the major technical issues for any type of numerical method. The corresponding approaches can be subdivided into free surface tracking and free surface capturing methods which are fundamentally different.

The free surface tracking methods treat the free surface as a sharp interface whose motion is followed in time. Within this method the mesh must be fitted to the free surface and advance in time using the kinematic and dynamic free surface condition. The single phase model is then sufficient since the air part does not need to be modelled. The interface tracking method performs well only for the relatively mild free surface deformations. Once the free surface overturns or breaks into droplets the numerical difficulties dramatically increase and in many cases the method cannot be applied. Violent free surface deformations happening often in marine applications the free surface tracking methods are usually avoided and the free surface capturing methods are preferred.

The free surface capturing methods do not define the free surface as a sharp boundary but they compute the fraction of each near-interface cell that is partially filled. Within this method the computation is performed on a fixed grid and both the water and air need to be modelled. Two main classes of interface capturing methods are used most often: the volume of fraction method (VOF) and the level set method.

2.2.8.1 VOF

Within the VOF method an additional transport equation for the volume fraction, usually denoted by α, is deduced from the continuity equation:

$$\frac{\partial \alpha}{\partial t} + \nabla \cdot (\alpha \boldsymbol{v}) = 0 \qquad (309)$$

The volume fraction α has the value 1 if the cell is filled with water, the value of 0 if it is filled with air and the value between 0 and 1 for partially filled cells. The VOF method allows maintaining accurate mass conservation at all times. Due to the way in which the distribution of the phase liquid fraction is represented, the exact location of the free surface cannot be determined easily and sharply. The main difficulties lie in the solution algorithms to the above transport equation which must avoid excessive smearing of the interface and at the same time respects the physical boundedness criteria for the phase faction value to remain accurately between 0 and 1.

There are two classes of numerical schemes designed particularly for solving the alpha equation: the geometric VOF schemes, and the algebraic VOF schemes. Examples of the geometric VOF schemes include e.g. PLIC (Piecewise Linear Interface Construction, Youngs (1982)) and *isoAdvector* (Roenby et al (2016)) and for the algebraic VOF there are e.g. flux-corrected transport (FCT Zalesak (1979)), MULES (Multidimensional Universal Limiter with Explicit Solution, Weller (2008)) and its variants, and HRIC (High-Resolution Interface Capturing, Muzaferija & Peric (1999)). The algebraic schemes are usually preferred in practice because of their robustness.

2.2.8.2 Level set

Another class of the interface-capturing methods is based on the level-set formulation, introduced by Osher and Sethian (1988). Within this method, the free surface is defined as a point in the fluid where the level set function $\psi(\boldsymbol{x},t)$ takes the zero value $\psi = 0$. Other values of the level set function are of no significance and the function ψ can be chosen in many different ways. The simplest choice is the signed distance i.e. its value is the distance from the nearest point on the free surface and its sign is positive on one side and negative on another. Once chosen, the level set function is allowed to evolve as a solution of the following transport equation:

$$\frac{\partial \psi}{\partial t} + \nabla \cdot (\psi \boldsymbol{v}) = 0 \qquad (310)$$

However, the properties of ψ requires different numerical algorithms. Commonly, with the level-set method it is hard (but not impossible) to achieve a sufficiently accurate mass conservation and maintain its true distance function property. The latter issue may require a frequent re-initialization of ψ to remove numerical distortion and to keep it as the valid shortest distance field to the free surface.

Many different level-set methods have been proposed in the past and some of them introduce additional manipulations in order to satisfy the mass conservation as closely as possible. One of the most popular methods was proposed in Sun & Beckermann (2007) and reused in Vukcevic et al (2016) where the authors introduce an additional parameter W which defines the width of the interface zone over which a smooth transition of the flow properties (phase field) is assumed. It turns out that the transport equation for level set function has to be modified as follows:

$$\frac{\partial \psi}{\partial t} + \nabla \cdot (\psi \boldsymbol{v}) = b\left[\nabla^2 \psi + \frac{\sqrt{2}}{W}(1 - |\nabla\psi|)^2 \tanh\left(\frac{\psi}{W\sqrt{2}}\right) - |\nabla\psi| \nabla \cdot \left(\frac{\nabla\psi}{|\nabla\psi|}\right)\right] \qquad (311)$$

where b is a numerical parameter which control the smoothening of the interface and the accuracy of the mass conservation. This parameter needs to be chosen on case by case basis.

The issues of maintaining a reasonable mass conservation in the level-set method has been an important motivation factor to introduce a hybrid method which combines the benefit of both the VOF and the level-set methods (Sussman & Puckett 2000). One obvious drawback of the hybrid methods is the additional CPU requirements posed by the fact that the solutions of both the VOF and the LS equations are needed at each time step.

2.2.9 Wave generation

The wave generation and wave absorption represent one of the major issue for the CFD methods. Most often the waves are generated at the inlet boundaries and left to propagate numerically through the domain toward the outlet boundaries where they are absorbed in some way. The wave generation at the inlet boundaries can be done either by directly modelling the physical wave maker or by modifying the flow conditions at the boundaries or in a selected region.

When modelling the wave maker, the computational domain is modified either by re-meshing or by deforming the existing mesh according to the instantaneous position of wave-inlet boundaries. The limitations of this model are the same as those of the physical model basins i.e. the determination of the proper time signal of the wave-maker motions and the local nonlinear effects at the interface of the wave maker and the fluid.

Generation of waves through the modification of the boundary condition at the inlet boundaries is also used quite often in practice. Within this method the waves are generated by prescribing wave kinematic at fixed wave-inlet boundaries. This method is popular due to its versatility which allows for introducing a wide range of theoretical wave models, from the simplest linear unidirectional waves to the fully nonlinear irregular multidirectional waves of HOS type.

The momentum source method is another method which generates the waves by local disturbance of the flow. Within these methods the momentum source excitation is introduced within a selected region. The properties of the source terms are derived from the underlying theoretical wave model.

When generating the incident waves, important numerical difficulties occur when trying to propagate the waves along the fluid domain without affecting their target properties (amplitude, length, frequency …). In many cases the wave properties in space and time are affected by all sort of numerical errors which makes difficult to accurately achieve the target values (amplitude, length, frequency …) especially for very steep waves. In order to circumvent this drawback, another class of methods called SWENSE (Spectral Wave Explicit Navier-Stokes Equations) was proposed (Ferrant (2006), Vukcevic et al (2016), Li et al. (2021). The SWENSE method decomposes the total problem into an incident wave part and a complementary part. Only the latter part is solved by the CFD solver, while the incident wave solution is provided by nonlinear wave propagation models based on spectral representation such as stream function method for regular waves or HOS for arbitrary irregular waves. Although the SWENSE method removes the problems related to wave propagation some other numerical issues occur as in Li et al. (2021) so that the method is not yet sufficiently mature to be used in practice.

2.2.10 Wave absorption

Both the incident waves and the waves which occur during the wave-body interactions need to be properly conveyed out of the fluid domain during the simulation, otherwise the solution in the domain of interest might be polluted by reflections from the boundaries. Different numerical strategies can be used to remove these reflections at least partially. Most often a specific damping/relaxation zones are defined where the solution is damped out using some numerical procedures. One of the popular methods uses explicit relaxation schemes which blend the computed solution with target solution in relaxation zones (Jacobsen et al. (2012), Seng (2012)). The explicit relaxation scheme uses a weight function that varies between 0 and 1 in the relaxation zone. After solving the governing equations, the computed solution is relaxed with target solution as (χ stands for any physical quantity in consideration i.e. velocity, volume fraction…):

$$\chi = (1 - w)\chi + w\chi_{ref} \tag{312}$$

where χ is the computed solution, χ_{ref} is the reference or target solution and w is the weight function.

The reference solution can be either the incident wave solution in the case of wave body interactions, simply zero in the case of free body motion. It can also be the far-field potential flow solution for the perturbed flow as proposed in Choi (2019) but no significant improvement as compared to zero was found.

The weight function w can be any smooth function going from 0 to 1 at the blending zone boundaries, and the following function is used most often:

$$w(\xi) = \frac{e^{\xi^{3.5}} - 1}{e - 1} \tag{313}$$

where ξ is the directional non-dimensional representation of the position vector in the blending zone, i.e. $\xi = 1$ at the outer most boundaries where the quantity χ is expected to be exactly the target quantity χ_{ref} and $\xi = 0$ at the inner boundaries where the relaxation zone is connected to the computational domain. The blending zones are illustrated in Figure 120 for the case of incident wave propagation. Different variants of the relaxation methods using the blending zones were proposed in the past and some of them use the explicit integration scheme.

Figure 120: Inlet and outlet relaxation zones

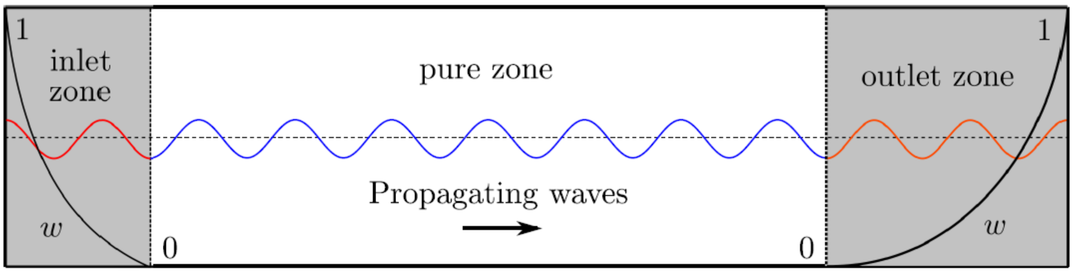

As an alternative to relaxation in the blending zones, a different wave damping technique based on an adjustment of momentum source were also proposed. Within pre-defined zones an additional momentum source $\boldsymbol{q}$ is added to the momentum equations (Peric & Abdel-Maksoud (2018)):

$$\boldsymbol{q} = \gamma w(\xi)(\chi - \chi_{ref}) \tag{314}$$

where $w(\xi)$ is a function similar to the blending function (312) and γ is an additional parameter to be adjusted on case-by-case basis to minimize the wave reflections.

2.2.11 Body dynamics

When using the CFD methods for solving the fluid flow the fully nonlinear body motion equation is usually employed. This means that the equations (352) and (358) from Appendix 1 remain valid for rigid and flexible body respectively. These equations need to be solved at each time step and integrated in time together with the flow solution. The main problem related to the body motion is associated with the handling of the mesh during the simulations. Most often the mesh morphing approach is used. Within this approach, at each time step, the CFD mesh remains fitted to the body but is deformed locally close to the body. This means that the cells keep their normal connectivity properties which simplifies the adaptation of the solution algorithms. One example of the mesh morphing procedure is shown in Figure 121. In the case when the body motions/deformations are large morphing technique becomes complex and should be combined with the re-meshing at selected time steps.

Figure 121: Mesh morphing

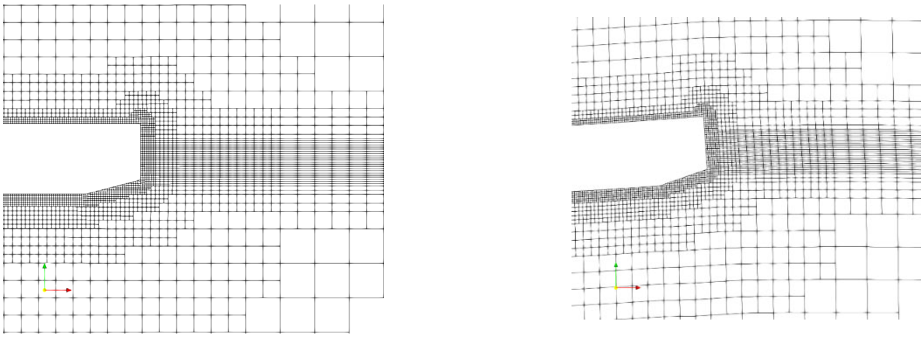

Another numerical approaches can also be used to handle the mesh during the simulations. Among them the overset mesh, sliding mesh and immersed boundaries approaches are used most often.

The overset mesh approach uses the body fitted mesh close to the body and allow it to move together with the body over the background mesh. The method requires complex interpolation algorithms at each time step. This approach is used very often when the different bodies or parts of the body can move independently (rudder, propeller …) of each other

The sliding mesh method is based on the principle that the different parts of the mesh might slide with respect to each other over the common interface. The method also requires the interpolation procedure but only over the interface. The typical examples where the sliding mesh can be used is the modelling of the propeller or the modelling of the bodies passing close to each other along the prescribed path.

The immersed boundary approach accounts for the solid boundaries on a mesh that is not necessarily fitted to the body. The main technical issue is to enforce the solid body boundary conditions sufficiently accurately. The approach is to add momentum sources to the proximity cells such that the solution algorithms yield a flow field which satisfies the solid boundary conditions to its best approximation. Determining the momentum sources in a selected cells and making them evolve in time is very complex task which unavoidably introduce the additional numerical errors. The advantages of the immersed boundary approach is that it can accommodate a complex motion of single or multiple bodies on a static fluid domain mesh.

2.2.12 Numerical parameters

As discussed in [2.1.2] all numerical models of the NS equations suffer from numerical errors and the accuracy of the simulations strongly depends first on the choice of the mathematical model and then on the choice of the different numerical parameters (spatial and temporal schemes, time step control, parameters related to PISO and SIMPLE algorithms …). Once the mathematical model and the associated numerical schemes have been chosen, the quality of the mesh and the size of the time step remain the only two parameters that matters, and both the CPU time and the accuracy critically depend on them. The final objective of adjusting the CFD mesh and the different numerical parameters is to ensure a reasonable balance between efficiency, stability and accuracy. This is not a trivial task and it is impossible to give universal recipes for a general CFD simulation and here we concentrate on the simulations of ship motions in waves.

One of the most critical aspects of the meshing strategy is the choice of the size of the computational domain which cannot be too large such that the total cell count is too high for the available computational power. In general, it is important to have a sufficient size of the computational domain such that the flow characteristics and other perturbations introduced by the presence of the body do not interfere artificially with the truncated boundaries of the domain. In that respect the size of the blending zones is also critical since these zones usually require at least one wave length to function properly.

A general rule of thumb applied to topologically static meshes is that cells shall be distributed reasonably according to the variation of velocity and pressure in the field. The local mesh density also depends on the geometrical features e.g. sharp corners or a locally smooth surface but with a strong curvature. These sharp corners often cause discontinuities in the flow field (e.g. free surface separation, vortex shedding, etc.). At the same time local physics, e.g. viscous boundary layer, may require a careful cell arrangement to avoid artificial perturbations due to mesh size. The viscous boundary layers are formed on wall surfaces, relatively thin in thickness and yet need layers of prismatic cells to capture the strong gradients of the velocity field. Depending on the applied turbulence model, the computed viscous shear stress may not be accurate enough without these prismatic-layer cells.

For all the above reasons it is particularly useful to have an even rough idea of the flow that will be produced. In the case of wave body interactions this can be estimated from the potential flow considerations. In that respect for the ship advancing in calm water, or in waves, very important general properties of the generated wave systems can be found in terms of the direction of propagation, wave lengths and frequencies. As an example we mention the case of the ship advancing in waves of frequency ω with speed U, where the speed parameter $\tau = U\omega_e/g$ together with the Froude number $Fr = U/\sqrt{gL}$ completely defines the basic properties of the generated waves. In particular for $\tau < 0.25$ both the waves propagating upstream and downstream will coexist while for $\tau > 0.25$ only the downstream waves will exist. At the same time, the angle of the divergent waves propagating downstream can also be defined, so that the meshing strategy can be adapted to those flow features.

As for the shape of the domain, it is usually not judged to be a critical issue, and most often a simple three-dimensional box is chosen. This allows for a uniform definition of the truncated open boundaries and the associated blending zones.

Figure 122: Typical mesh distribution for a ship simulations in waves.
Left – global mesh, Right – mesh refinements.

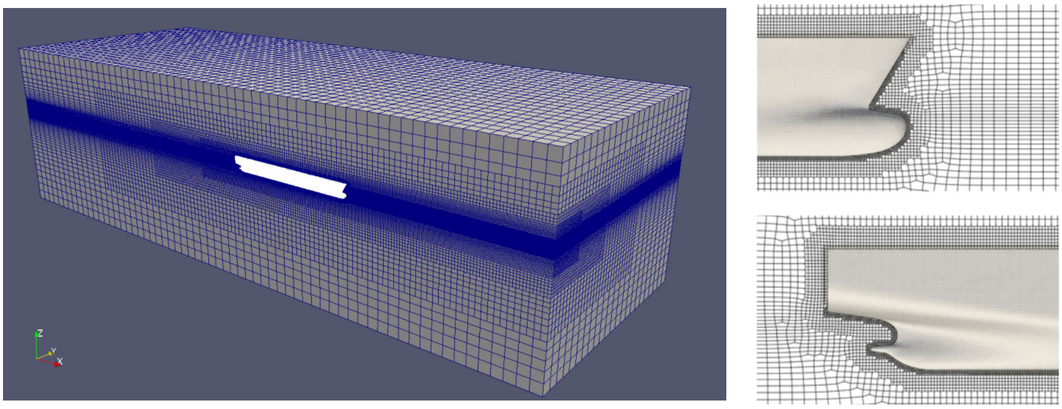

2.2.13 Hydro structure interactions

The hydro structure interaction models based on using the CFD solver for fluid part follows the similar principles as those used for the potential flow. However there exist some differences.

In the case of quasi static hydro structure interactions, the main difference is due to the fact that the pressure cannot be re-calculated at any point in the fluid, as it was the case with the potential flow theory but need to be interpolated from the CFD mesh to structural FE mesh. Efficient interpolation procedure exist but all of them introduce small interpolation error which needs to be corrected before solving the structural FE problem. This is usually done using the inertia relief method i.e. the misbalance of the loads and the acceleration is adjusted by slightly modifying body accelerations.

In the case of hydroelastic hydro-structure interactions both the direct and modal coupling approaches can be used, the modal approach being preferred. Due to the particularities of the CFD approach, in which the CFD mesh is deformed during the simulations an additional interpolation procedure is required to transfer the modal deformations from the FE mesh to CFD mesh. This interpolation procedure is required at each time step but important part of work can be done in pre-processing phase. Fact that the mesh is moving at each time step and the fact that the total hydrodynamic loads are applied on the body, makes the extraction of the added mass part and the evaluation of the wet natural frequencies more complex and additional manipulations are necessary.

3. List of references

[1] Celik I.B., Ghia U., Roache P.J., Freitas C.J., Coleman, H. & Raad P.E., 2008.: “Procedure for estimation and reporting of uncertainty due to discretization in CFD applications,” Int J Fluids Eng, Vol. 130.

[2] Choi Y.M., 2019.: “Two-way Coupling between Potential and Viscous Flows for a Marine Application.”, PhD Thesis, Ecole Centrale de Nantes.

[3] Eca L. & Hoekstra M., 2014.: “A procedure for the estimation of the numerical uncertainty of CFD calculations based on grid refinement studies.”, J. Comput. Phys. Vol. 262.

[4] El Moctar B.O., Schelin T.E. & Soding H., 2021.: “Numerical methods for seakeeping problems.”, Springer

[5] Ferrant P., 2006.: “Modelisation en hydrodynamique a surface libre.”, HDR Thesis, Ecole Centrale de Nantes

[6] Ferziger J.H. & Peric M., 2002.: “Computational methods for fluid dynamics.”, Springer

[7] Issa R., 1986.: “Solution of the implicitly discretized fluid flow equations by operator splitting.”, J.Comput. Phys. Vol. 62.

[8] ITTC, 2017.: “Uncertainty analysis in CFD-verification and validation methodology and procedures.”, ITTC Recommended Procedures and Guidelines 7.5-03-01-01

[9] Jacobsen N. G., Fuhrman, D. R., & Fredsoe, J.. 2012.: “A Wave Generation Toolbox for the Open-Source CFD Library: OpenFOAM.”, International Journal for Numerical Methods in Fluids, Vol. 70.

[10] Li Z., Bouscasse B., Ducrozet G., Gentaz L., Le Touze D. & Ferrant P., 2021.: “Spectral Wave Explicit Navier Stokes Equations for wave-structure interactions using two phase Computational Fluid Dynamics solvers”, Ocean Engineering

[11] Malenica S., Diebold L., Kwon S.H. & Cho D.S., 2017:” Sloshing assessment of the LNG floating units with membrane type containment system. Where we are?”, Marine Structures

[12] Muzaferija, S. & Peric, M., 1999.: “Computation of free-surface flows using interface-tracking and interface-capturing methods.”, In Nonlinear water wave interaction. Computational Mechanics Publication.

[13] Osher, S. & Sethian, J.A., 1988.: “Fronts propagating with curvature-dependent speed: algorithms based on Hamilton-Jacobi formulations.”, J. Comput. Phys., Vol.79

[14] Pope S., 2000.: “Turbulent Flows”, Cambridge University Press

[15] R. Peric, & Abdel-Maksoud M., 2018. “Analytical prediction of reflection coefficients for wave absorbing layers in flow simulations of regular free-surface waves.”, Ocean Eng. Vol. 147.

[16] Roenby J., Bredmose H. & Jasak H., 2016.: “A computational method for sharp interface advection,” Royal Society Open Science, Vol. 3.

[17] Seng S., 2013.: “Slamming and whipping analysis of ships.”, PhD Thesis, Technical University of Denmark.

[18] Seng S., Jensen J.J. & Malenica S. 2014.: “Global hydroelastic model for springing and whipping based on a free-surface CFD code (OpenFOAM)”, International Journal of Naval Architecture and Ocean Engineering, Vol. 6, No. 4

[19] Shadloo.M.S, Le Touze D. & Oger G., 2016.: “Smoothed Particle Hydrodynamics Method for Fluid Flows, Towards Industrial Applications- Motivations, Current state, and Challenges”, Computers & Fluids, Vol. 136.

[20] Sussman M. & Puckett E., 2000.: “A coupled level set and volume-of-fluid method for computing 3D and axisymmetric incompressible two-phase flows.”, Journal of Computational Physics, Vol. 162.

[21] Sun Y. & Beckermann C., 2007.: “Sharp interface tracking using the phase field equation.”, J. Comput. Phys., Vol. 220.

[22] Vukcevic V., Jasak H. & Malenica S., 2016.: “Decomposition Model for Naval Hydrodynamic Applications, Part I: Computational Method”, Ocean Engineering, Vol. 121

[23] Weller H.G., 2008.: “A new approach to VOF-based interface capturing methods for incompressible and compressible flow.”, Technical report TR/HGW, OpenCFD Ltd.

[24] Weller H.G., Tabor G., Jasak H. & Fureby C., 1998.: “A tensorial approach to computational continuum mechanics using object oriented techniques.”, Computers in Physics, Vol. 12.

[25] Wilcox D. C., 1993.: “Turbulence Modeling for CFD.”, DCW Industries.

[26] Xing T. & Stern F., 2010.: “Factors of safety for Richardson extrapolation.” J. Fluids Eng. Vol. 132.

[27] Youngs D. L., 1982.: “Time-dependent multi-material flow with large fluid distortion.”, Numerical Methods for Fluid Dynamics

[28] Zalesak S.T., 1979.: “Fully multidimensional flux-corrected transport algorithms for fluids.”, J. Comput. Phys. Vol. 31.

Section 9 Model testing

1. General

1.1. Introduction

1.1.1 When & why model tests?

There exist many practical reasons to perform the model testing and the following ones appear to be the most important:

- Study of the global behavior of the novel floating system
- Validation of the numerical tools
- Determination / checking of certain physical parameters to be used in the numerical simulation model (wind and current load coefficients, added mass and drag component of local forces …)
- Ultimate design check
- Commercial promotion

The last two points indicates the reluctance of the industry people who, very often, have the tendency to prefer to rely on model testing rather than on the numerical tools. However most often the numerical tools and the model tests are used in combination with each other which allows to take the best part of two types of approaches. This is especially true for ultra-deep water projects where it is not possible anymore to build the model at a reasonable scale in the existing testing facilities. In those cases, separate model tests must be performed on different system components and their results assembled within a numerical model. Alternatively a numerical model can be directly connected to the model tests, for instance to input the reactive loads from the mooring lines or the wind loads on wind turbines. This technique is known under the name “real time hybrid model testing “ or “software in the loop” and is used commonly for model testing of the floating wind turbines where the wind loads on the turbine cannot be accurately modelled due to the effects of scaling.

It should be noted that in some cases, model tests lead to the discovery of new phenomena which are not predicted by the existing theories and many of the new theories were developed only after a phenomenon was discovered during a model observation. Moreover, there has hardly been a model test where the experimenters not learnt something new, no matter how trivial the tests were.

1.2. Modelling principles

1.2.1 Froude scaling

The basic idea of model testing is to use the scaled model of the real structure and expose it to the scaled environmental conditions. The subscript “ $_M$” is used to denote the quantities at model scale and the subscript “ $_R$” the quantities at real (full) scale and the scale factor (denoted here by λ) is defined as:

$$\lambda = \frac{L_M}{L_R} \tag{315}$$

where L denotes the length related quantity.

It follows directly that the areas (S) scale by λ^2 and the volumes (V) by λ^3 :

$$S_M = \lambda^2 S_R \quad , \quad V_M = \lambda^3 V_R \tag{316}$$

When dealing with tests in gravity waves, the wave length is scaled by the same scale factor λ and the scaling of time is deduced from the dispersion relation as:

$$t_M = \sqrt{\lambda} t_R \tag{317}$$

from which it follows that the velocities v and the accelerations γ are related by:

$$v_M = \sqrt{\lambda} v_R \quad , \quad \gamma_M = \gamma_R \tag{318}$$

This scaling law is known as Froude scaling law and should be used whenever the gravity wave effects are of main concern. From the equality of the accelerations at both scales (318), it follows that the ratio between the fluid inertia loads and the gravity loads remains the same. The square root of this ratio is called the Froude number and is denoted by Fr. Knowing that the inertia loads are proportional to $\varrho U^2 L^2$ and the gravity loads to $\varrho g L^3$ this gives:

$$Fr = \frac{U}{\sqrt{gL}} = \frac{U_R}{\sqrt{gL_R}} = \frac{U_M}{\sqrt{gL_M}} \tag{319}$$

The summary of the scaling factors, when Froude scaling is applied, for some physical quantities are presented in Table 12. The density ratio μ which is the ratio between the density of fresh water and the density of sea water is introduced in order to account for the fact that the most common wave basins are operating with fresh water.

Table 12 : Scaling factor (ratio between the quantity value at model scale and its value at full scale) when Froude scaling is applied. (μ – density ratio; fresh water/sea water)

Length	$[m]$	λ
Time	$[s]$	$\sqrt{\lambda}$
Velocity	$[m/s]$	$\sqrt{\lambda}$
Acceleration	$[m/s^2]$	1
Angular acceleration	$[rad/s^2]$	$1/\lambda$
Frequency	$[1/s]$	$1/\sqrt{\lambda}$
Angular frequency	$[rad/s]$	$1/\sqrt{\lambda}$
Mass	$[kg]$	$\mu\lambda^3$
Pressure	$[N/m^2]$	$\mu\lambda$
Force	$[N]$	$\mu\lambda^3$
Moment	$[Nm]$	$\mu\lambda^4$

1.2.2 Scale effects

Froude scaling law is just one of the possible scaling laws and it ensures that the same ratio of the inertial and the gravity loads, at model and full scale, is respected. In reality there exist many other types of loads which are dominated by other physical effects (viscosity, compressibility …) and these loads cannot be scaled using the scaling factors from Table 12. The most important physical effects which are not properly accounted for, with Froude scaling, are those associated with the viscosity. The loads which are induced by viscous effects are scaling with respect to the Reynolds number:

$$\mathrm{Re} = \frac{UL}{\nu} \tag{320}$$

where ν is the kinematic viscosity.

The kinematic viscosity ν being about the same for fresh and sea water it follows that the Reynolds numbers at model scale and the full scale are related by:

$$\mathrm{Re}_M = \lambda^{3/2}\mathrm{Re}_F \tag{321}$$

The scale of typical model tests based on using the Froude scaling, being of the order of $\lambda = 1{:}50$, this means that it is practically impossible to keep the Froude and Reynolds number the same at model scale and at full scale. Consequently the difference between the Reynolds numbers at model and full scale can change the flow regimes (laminar, transient, turbulent …) and the resulting loads can be completely unrealistic if they are Froude scaled. In many cases the flow over the large flat surfaces, which is turbulent in reality, becomes laminar at model scale. This can be partially corrected by initiating the turbulence artificially at model scale through the modification of the rugosity at some places along the model such as the bow part of the ship. Similarly, for the slender tubular structures, the flow regimes (attached, separated …) depends critically on the Reynolds, Keulegan Carpenter and Strouhal numbers, so that the drag and lift forces are biased.

There exists many other practical situations where other scaling effects might become important. Typical example are the model tests in which the air is entrapped by the fluid such as the problem of air cushion supported floating bodies or the impact problems related to sloshing, slamming, green water … In those cases the compressibility of the air matters and, since the atmospheric pressure is not scaled, the pressure loads in the air pocket are biased.

1.2.3 Choosing the scale

The model testing for offshore applications is most commonly performed at scales between $1{:}30$ and $1{:}90$. The choice of the scale depends on many different considerations which are often contradicting each other.

The first important consideration concerns the capabilities of the wave generation system of the experimental facility. Maximum wave height which can be generated in the wave basin rarely exceeds 80 centimeters and the associated wave periods are 2 to 3 seconds. As an example, the wave height which occurs in North Sea is about 30 meters with the peak periods between 15 and 18 seconds, which leads to the scale λ around $1{:}40$.

Another important factor is the water depth. Most of the ocean wave basins have the depth less than 10 meters with an occasional deeper pit with very local extent. In many cases, due to the large water depth in reality and the horizontal extent of the mooring and riser system the proper geometric scaling is not possible so that the approximate hybrid modelling of the mooring lines and risers is necessary.

One additional consideration concerns the size of the model relative to the dimensions of the basin: too large model might lead to spurious effects of wave reflections; too small scale might lead to inaccuracies in the measurements and in the adjustment of the wave parameters.

The issues related to handling and lifting of the scaled model can also become critical parameter when choosing the scale. This is particularly important when identifying the inertia of the model?

Finally, some particular scale values may have to be avoided because they lead to the coincidence of a natural frequencies of the system with the characteristic sloshing frequencies of the basin. For example, if the natural period of the moored floating system is 3 minutes at full scale and the natural period of the first longitudinal sloshing mode of the basin is equal to 25 seconds, then the scale $1{:}\,50$ should be avoided.

1.2.4 Scaling of hydroelasticity

For some applications it is important to consistently scale the elastic properties of the model. Typical practical examples are: springing and whipping, hydroelastic impact, VIV and others. In those cases, and assuming that the Froude scaling is adopted, it is necessary to ensure that the scaled structural natural frequencies obeys to (see Table 12):

$$\omega_M = \omega_F / \sqrt{\lambda} \tag{322}$$

The natural frequencies of the dry structure depend on the structural properties and on the mass distribution, and can be of various types (bending, torsion, coupled …). Most often the bending is of concern and the simple uniform beam model is used at model scale. In that case the bending stiffness of the beam EI (E being the Young modulus and I being the second moment of area of the beam cross-section) needs to be adjusted. Knowing that the natural frequencies of the beam behave as:

$$\omega \sim \sqrt{\frac{EI}{mL^4}} \tag{323}$$

where m is the mass per unit length and L is the model length, it follows that the bending stiffness should be scaled as:

$$(EI)_M = \lambda^5 (EI)_F \tag{324}$$

2. Modelling of the environment

2.1. Wave generation and absorption

2.1.1 Types of wavemakers

Waves are generated by disturbing the fluid flow locally using the mechanical device, the wavemaker. Different types of wavemakers exist and some of them are shown in Figure 123.

The most common type is the flap wavemaker (Figure 123-a) where the flap articulated at its base (not necessarily at the tank floor), is set in rotation by a hydraulic jack. In order to minimize the driving force, the optimal wavemaker should move according to the profile of the horizontal wave particle motion i.e. $\cosh k_0(z+h)\,/\,\sinh k_0 h$. This leads to the double flap concept where the second flap is embarked on top of the first one (Figure 123-b). The piston type wavemaker operates at the similar principle but only the horizontal motion of the piston is allowed. Both the dry (Figure 123-c) and the wet (Figure 123-d) piston types of wavemakers are employed in practice. There exist also other types of wavemakers, for instance the wedge (Figure 123-e) in forced vertical motion, which has the advantage of minimizing the space occupied; or just a horizontal float (Figure 123-f) in forced horizontal motion, such as at BGO-FIRST (La Seyne/France), offering the advantage of combined current generation.

Figure 123: Most common types of wavemakers

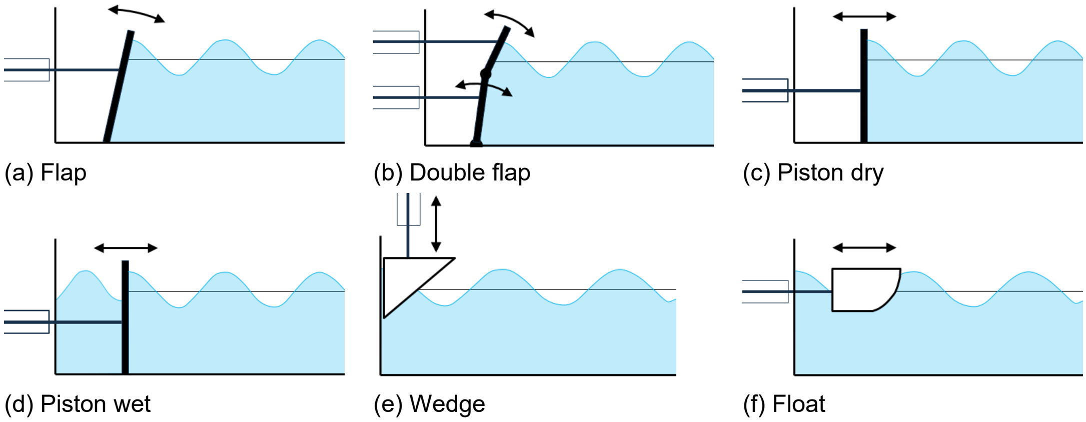
(a) Flap
(b) Double flap
(c) Piston dry
(d) Piston wet
(e) Wedge
(f) Float

2.1.2 Snake wavemakers

Most of offshore wave basins are equipped with multiple flap wave makers called snake wavemakers, often along two adjacent sides but sometimes also along the complete extent of the tank walls (Figure 124). The snake wavemakers are able to produce almost any type of waves including the multidirectional seas and the three dimensional focusing waves. Another advantage of the snake wavemakers is that the mean wave direction can be varied without having to rotate the model and its moorings.

Figure 124: Snake wavemaker in National Maritime Research Institute – NMRI (Tokyo - Japan)

2.1.3 Efficiency of wave making

The efficiency of a wavemaker can be measured by the transfer function which relates the amplitude of the generated waves (A) to the motion amplitude of the wavemaker (X_0). Within the linear assumptions, the following expressions are obtained for the piston and flap wavemaker respectively (Molin (2002)):

$$\frac{A}{X_0} = \frac{4\sinh^2 k_0 h}{2k_0 h + \sinh 2k_0 h} \quad , \quad \frac{A}{X_0} = \frac{4\sinh k_0 h\,(k_0 h \sinh k_0 h - \cosh k_0 h + 1)}{k_0 h(2k_0 h + \sinh 2k_0 h)} \qquad (325)$$

where the amplitude of the wavemaker is taken at the level of free surface.

In Figure 125, the two transfer functions (325) are plotted vs $k_0 h$ and it can be seen that the piston wavemaker is more efficient than the flap, particularly in shallow water. However, the piston wavemaker requires the larger driving force because larger mass of water is set into motion.

The wave heights which can be generated depend on the stroke and the power of the wavemaker and are also limited by wave breaking which occurs at large steepnesses. In Figure 125, the maximum waves which can be obtained in the SINTEF Ocean basin for 3 different water depths are shown.

Figure 125: Transfer function of the piston and flap wavemakers (left) and maximum wave heights in the Ocean Basin of SINTEF Ocean, for 3 water depths (from Molin (2002))

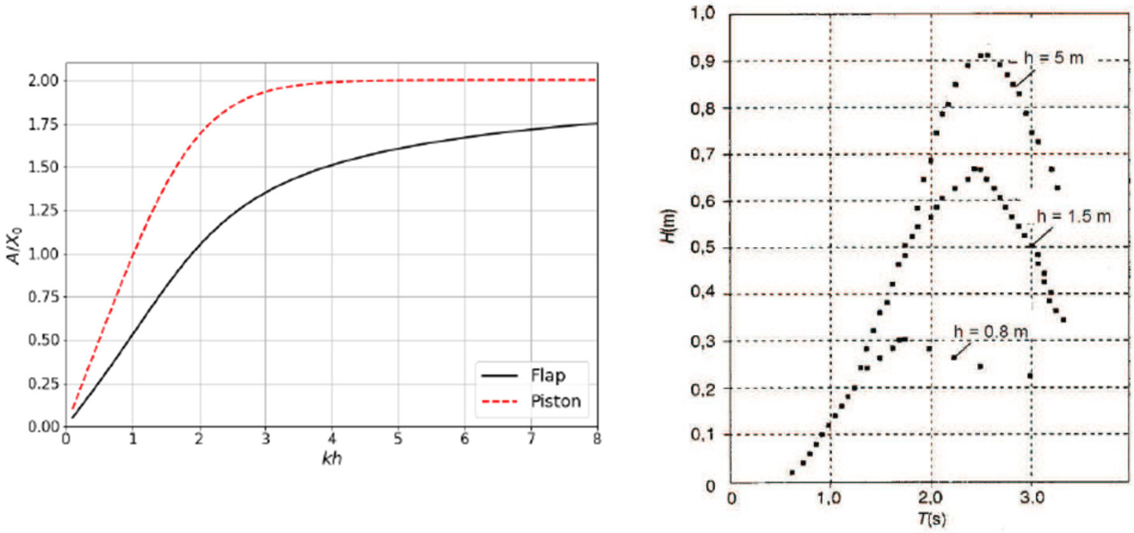

2.1.4 Wave absorption

The waves which are generated by the wavemakers needs to be absorbed at the opposite side otherwise the wave reflection will quickly pollute the measurement results. The most common wave absorber is just a beach (Figure 126): as the water depth decreases the waves overturn and break, most of their energy is then dissipated through turbulent mixing and viscous effects.

When they are well-shaped, and sufficiently long, beaches are very efficient, ensuring reflection coefficients of less than 5 or 10% over a wide range of wave periods. Their efficiency may be improved by taking advantage of some other mechanisms of energy dissipation, for instance with some added roughness, or porosity.

Figure 126: Absorbing beach (left – SINTEF Ocean, right – IFREMER)

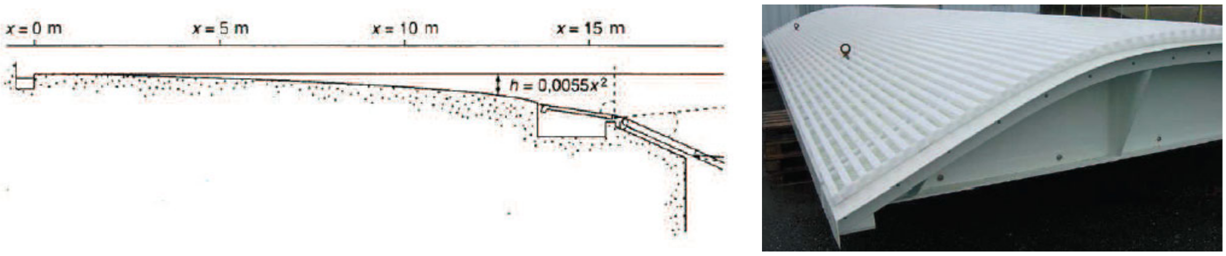

An alternative to the beach absorber is the progressive wave absorber (Figure 126), which consists in a succession of vertical perforated screens of decreasing porosity toward the end wall. Such wave absorbers can be found at the Multidirectional Wave Basin of NRC at St-John's, Canada, at OTRC in Texas, and at CCOB in Santander. An advantage over the parabolic beach is that they are relatively insensitive to the water depth. A variant is a horizontal, or quasi-horizontal, perforated plate, slightly immersed (Molin (2001). This system may offer appreciable advantages when current is to be combined with waves.

Figure 127: Wave attenuation with the progressive wave absorber (from Molin (2002))

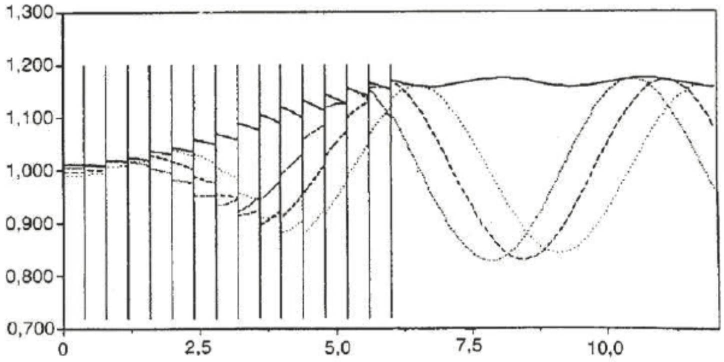

Finally there exist dynamic absorbers where the absorber is just a wave paddle whose motion is driven to absorb the incoming waves. Some information is then required to identify the incoming waves: the free surface elevation needs to be measured some short distance from the paddle; another option is to incorporate pressure or force sensors.

2.1.5 Reflection coefficient

Model basins usually qualify their beaches through dedicated tests, in regular waves, that provide the reflection coefficient C_R, defined as the ratio of the amplitude of the reflected wave A_R to the amplitude of the incident wave A_I (sometimes also defined as the ratio of the square of the amplitudes in order to relate it to the associated wave energy). The reflection coefficient can be obtained via various methods, the simplest one being using just two wave gauges. When the free surface elevation is taken to be

$$\eta(x,t) = A_I \cos(k_0 x + \omega t) + C_R A_I \cos(k_0 x - \omega t + \vartheta) \qquad (326)$$

the local amplitude of the free surface motion is:

$$A(x) = A_I \sqrt{1 + C_R^2 + 2C_R \cos(2k_0 x + \vartheta)} \simeq A_I[1 + C_R \cos(2k_0 x + \vartheta)] \qquad (327)$$

When η is measured in two points of adequate separation (ideally a quarter wave length), the reflection coefficient is obtained.

In towing tanks the beach performance can be visually estimated (during calibration tests of regular waves) by looking at the separation contour between the wet and dry parts of the longitudinal walls: if it is a straight line, the reflection coefficient is nil.

Strictly speaking the reflection coefficients depend both on the wave period and on the wave steepness. It is rare that model basins give complete information on their reflection coefficients (the dependence on steepness is often missing).

Strictly speaking the reflection coefficients depend both on the wave period and on the wave steepness. It is rare that model basins give complete information on their reflection coefficients (the dependence on steepness is often missing).

2.2. Parasitic phenomena related to wave generation

2.2.1 Introduction

All sort of the different physical phenomena related to wave generation, propagation and absorption can significantly influence the accuracy of the measurements and the measuring signals should be carefully analyzed. For instance, when performing the model tests in regular waves, when looking at the records of the different sensors, it often looks as if a steady state is never achieved: one can see transients, long-lasting modulations, beating effects, superimposed low or high frequency components, etc.

2.2.2 Proximity of the wavemaker

Whatever the wavemaker, the local evanescent waves are generated together with the propagative wave component. These waves decay exponentially with the distance from the wavemaker. It is generally considered that the contribution of the evanescent modes is negligible at the distance equal to twice the water depth.

2.2.3 Modulation of the wave front

Once the wavemaker motion is initialized the wave front propagates at group velocity and it takes many waves before the wave amplitude stabilize. Some modulation occurs in the first waves far from the wavemaker. This is visible from Figure 128 where the wave envelope and the instantaneous wave shape at different time instant during the process of regular wave generation is presented. The nonlinearities of the free surface tend to increase the modulation and the wave breaking can occur at the wave front for steep waves.

Figure 128: Transient waves and their envelopes for different time instants during the process of wave generation (from Chen et al. (2019))

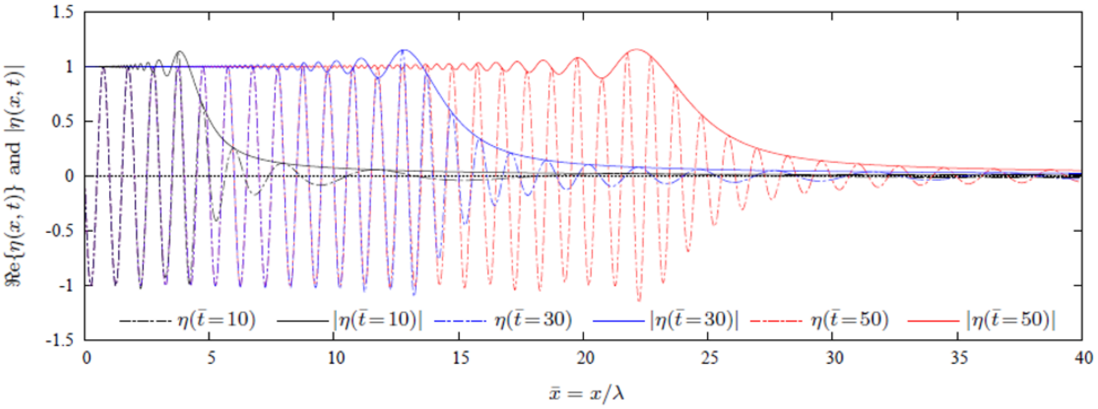

2.2.4 Benjamin Feir instability

The regular gravity waves are naturally unstable and, for the wave of steepness less than 0.1, one of the main instability mechanism is the Benjamin Feir instability. This instability can be explained by studying the third order free surface nonlinearities using the Schrodinger equation which predicts a series of modulations and demodulations leading to occurrence of the parasitic wave components which grow exponentially with the distance from the wave maker. When the wave steepness is moderate, the Benjamin Feir instability usually does not occur but for higher steepness's it quickly leads to wave breaking which disorganize the wave system. The Benjamin-Feir instability usually is not a problem in ocean basins where the model is stationary at a relatively short distance from the wavemaker.

2.2.5 Return current

It has been shown in Section 2, [2.3.3] that mass transport take place in waves and, in the absence of current generation, the mass transport is cancelled by a return current. The depth averaged velocity of the return current U_R is given by:

$$U_R = -\frac{1}{2}\frac{A^2\omega}{h}\coth k_0 h \tag{328}$$

This return current is far from negligible, particularly at shallow depth. Taking for instance a wave amplitude A equal to $30cm$, a wave period of $2s$, and a depth of $2m$, the return current velocity is $7cm/s$ that is 1 knot at a scale of $1:50$!

2.2.6 Free harmonics

The second order theory of wavemaker interaction with the water predicts the occurrence of the second order free wave components in addition to second order locked wave component. As a result parasitic wave is generated with the frequency 2ω and wave number k_2 given by the dispersion relation:

$$(2\omega)^2 = gk_2\tanh(k_2 h) \tag{329}$$

This implies that, away from the wavemaker the free surface elevation up to second order is given by:

$$\eta(x,t) = A\cos(k_0x+\omega t) + C_Lk_0A^2\cos(2k_0x+2\omega t) + C_Fk_0A^2\cos(k_2x+2\omega t+\vartheta) \tag{330}$$

At large depth, the locked wave coefficient C_L approaches the value of 0.5. The free wave coefficient C_F depends on the type of wavemaker and can be evaluated numerically for a given wavemaker motion (Sulisz & Hudspeth (1993), Schaffer (1996)). It appears that the ratio C_L/C_F is usually between 0.5 and 1.0.

2.2.7 Natural modes

Due to the presence of the physical boundaries, the water in the tank can experience resonant dynamic behavior at some particular frequencies: sloshing natural frequencies. For a tank of length L, width B and water depth h, the velocity potential of the sloshing natural modes are given by:

$$\Phi_{mn}(x,y,z,t) = \frac{g\mathrm{A}_{mn}}{\omega_{mn}}\frac{\cosh\nu_{mn}(z+h)}{\cosh\nu_{mn}h}\cos\lambda_m x\cos\mu_n y\sin(\omega_m t+\vartheta) \tag{331}$$

where m and n are the integer numbers, $\lambda_m = m\pi/L$, $\mu_n = n\pi/B$, $\nu_{mn}^2 = \lambda_m^2 + \mu_n^2$ and the resonant frequencies are given by:

$$\omega_{mn}^2 = g\nu_{mn}\tanh\nu_{mn}h \tag{332}$$

Typically the natural periods of the longitudinal modes are very high and beyond the range of wave periods but possibly coinciding with the large natural periods of the slow-drift responses. The natural periods of the transverse modes are more likely to fall within the wave period range.

The natural modes of the tank are excited during the transient phases, for instance when the wavemaker is started or stopped, and in the time span when the wave front travels from the wavemaker to the beach. Being weakly damped these modes last throughout the tests and beyond. It is customary to wait for quite some time, typically several dozens of minutes, in between two tests, for the basin to go back to calm.

2.2.8 Seiching

The first longitudinal sloshing modes of the tank are also named seiching modes because of their large period. It was shown by Molin (2001) that the second order effects are the main driver for the generation of these modes. This has been confirmed by detailed comparisons with the experiments in the ECN (Ecole Centrale de Nantes - France) tank, and also with a second-order numerical wave tank developed by Stassen (1999) (see also Molin et al., 1999). In Molin (2001) it is proposed, and confirmed experimentally, that the seiching generation can be annihilated by an additional motion of the wavemaker at the seiching frequency, when the wavemaker is activated and when it is stopped. Dynamic absorbers can also efficiently reduce the persistence of seiching after the tests.

2.2.9 Reflections and side wall effects

With the model is placed in the tank, the waves which are diffracted and radiated by the model will travel back to the wavemaker and be re-reflected back to the model, unless the wavemaker has an absorption function. The time taken for the roundtrip to the wavemaker is twice the distance divided by the group velocity. When the model is too close to the wavemaker the exploitable time window may be very short.

The diffracted and radiated waves travelling back to the wavemaker are only part of the wave system which can exist in the tank. In the general case the longitudinal and transverse wave system can coexist as indicated by (331). When the wave number is such that the wave frequency coincides or nearly coincides with one of the natural frequencies of the transverse modes, the standing wave system between the side walls can occur. This will seriously bias the emitted wave field and affect the extraction of the hydrodynamic coefficients in particular the radiation damping and the drift forces. As an illustration, in Figure 129 the experimental results are compared to the theoretical ones with and without the account for the side wall effects. A simple conclusion is that, when doing the regular wave tests, the wave frequencies which coincide with the natural frequencies of the transverse sloshing modes should be avoided, if that is possible. Otherwise the numerical tools needs to be considered when interpreting the experimental results. Influence of the tank walls on the experimental results are also discussed in Zhao et al. (1988).

Figure 129: Heave RAO (left) and the horizontal drift force (right) for the hemisphere of radius $0.3m$ in a middle of the $5m$ wide tank (zero speed). Full line – open ocean theory, dotted line – wave tank theory (with side walls), markers – experimental results. (from Chen (1994))

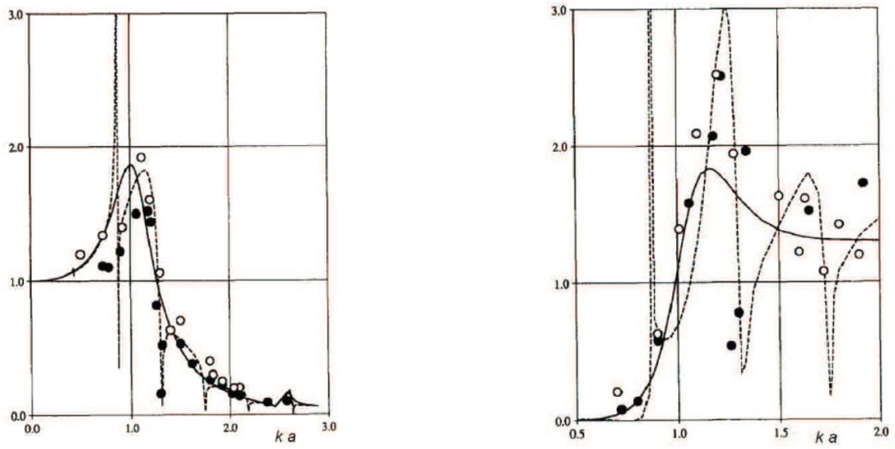

2.3. Wave generation techniques

2.3.1 Introduction

Before running the tests with the model, it is customary to perform the calibration tests in order to achieve the specified wave conditions at the location where the model will be installed. These time signals of the wavemaker motion are then used with the model installed.

2.3.2 Regular waves

Regular waves are usually generated by a simple harmonic motion of the wavemaker, with linear ramps at the beginning and at the end of the input signal. The amplitude of motion of the wavemaker is the target wave amplitude divided by the transfer function of the wavemaker. This transfer function may be known from linear theory such as (325), or from past experience of the basin. It can also be updated during the calibration tests through an iterative procedure as usually done for the irregular waves.

2.3.3 Irregular waves

The irregular seastate is usually defined by its spectrum (see Section 2, [2.6.2]) which needs to be reproduced at a specific location in the basin. The most widely used method for the discretization of the wave spectrum is to construct the wavemaker signal $X(t)$ as a sum of sinusoidal components:

$$X(t) = \sum_i X_i \cos(\omega_i t + \varphi_i) \tag{333}$$

where X_i is the amplitude, ω_i is the frequency and φ_i is the phase (randomly chosen) of each component.

At the same time, the wave spectrum is represented by the similar sum of the regular wave components with the same frequencies ω_i so that, knowing the wavemaker transfer function, the amplitudes X_i of the wavemaker motion signal (333) are easily deduced. Since the wavemaker transfer function may be sensitive to diverse nonlinearities, and the wave spectrum may evolve somewhat on its way to the target location, the usual procedure is to build up the wavemaker signal through iterations, where the transfer functions are reconstructed at each iteration. The iterative procedure is stopped (usually after one or two iterations) when the target and achieved seastates are considered sufficiently close; the H_S and T_P values, together with the spectral shape, being the most critical parameters. In order to avoid the repeatability of the wavemaker signal the wave frequency can be randomly chosen within each frequency interval (see also Section 2, [2.8]).

2.3.4 Wave packets

It is possible to run the wavemaker to produce, at the target location, a single wave, or a wave group, of specified shape. This can be useful for many practical reasons:

- For a particular choice of the phases φ_i in (333) with nearly equal amplitudes X_i it is possible to obtain the RAO of the system in a single run of short duration.
- Waves of much higher amplitude and steepness can be generated than can be achieved when running the wavemaker to produce regular waves.

- Short duration of tests minimize the spurious effects such as reflections from the beach and side-walls.
- It is possible to reproduce a prescribed time record of the wave elevation e.g. from full scale measurements. This is particularly useful for the deterministic generation of the waves from full scale measurements and for the generation of the Response Conditioned Design Waves (see NI638).

According to linear theory, if the transfer function between wavemaker motion and free surface elevation is known, a simple inversion and a convolution in time enable one to derive the wavemaker motion from the desired wave profile. In practice, particularly if the distance from wavemaker to target location is long, nonlinear effects will come into play and several adjustments may become necessary.

2.4. Generation of current

2.4.1 Introduction

Some testing facilities allows the generation of current. There exist 3 possibilities to do that:

- towing
- global circulation of the water in the tank
- local current generation

2.4.2 Towing

Towing offers the advantage that the current velocity is known (opposite to the towing velocity), steady in time and in space and with zero turbulence intensity. However no other current profile than constant over the depth can be achieved. A major drawback is that, if there are catenary mooring lines, or other links to the seafloor (risers, tendons), the end points need to be towed as well. The test duration is limited by the useable length of the tank, over which the wave conditions are stationary.

2.4.3 Global circulation

Several offshore tanks provide current generation, with a pumping system that sets the whole water mass into motion. Maximum attainable velocities depend on the water height and the velocities are typically a few decimeters per second (a few knots at full scale following Froude scaling). Difficulties are to ensure a uniform flow over the width of the tank, and to control the vertical profile. Other issues are how to combine wave generation and current injection at one end, wave absorption and current suction at the other end. The current injection is necessarily located below the wavemakers, which makes it difficult to achieve a vertical profile with the maximum velocity at the free surface, as most often required.

2.4.4 Local generation

Local generation, through an assembly of pipes and injection nozzles, can be found in some facilities, for instance the OTRC wave basin at Texas A&M University. Issues are the time and space variabilities of the current generated, the perturbations caused to the wave flow, etc.

2.4.5 Wave current interactions

When the waves and current need to be generated at the same time, additional care should be given to the interpretation of the results. Most often the same wave spectrum is specified with and without current. When current is simulated by towing, keeping the wavemaker signal unchanged produces the same waves, but the encounter frequencies vary with the towing velocity. If the encounter frequencies need to be kept the same, as many wave calibrations are necessary as specified current velocities. When current is generated by global circulation, keeping the wavemaker signal unchanged conserves the frequencies, but the wave lengths are increased and the wave heights are decreased (with the current flowing in the same direction as the waves).

2.5. Modelling of wind

2.5.1 Introduction

There are two ways to model the effects of wind: generate the wind directly or reproduce artificially the wind loads.

2.5.2 Wind generation

To generate wind over an ocean basin a cluster of fans is often utilized. As for current, there are many difficulties associated with achieving a flow field that is horizontally uniform, steady and has the correct shear, with controlling the turbulence level, etc. In many instances the fan signal is adjusted, not to produce the specified wind velocity, but to produce the expected mean loads, previously determined by tests in a wind tunnel or by CFD.

2.5.3 Modelling of wind effects

An alternative method is to generate the wind loads artificially. For a long time ship mooring tests have been performed with two fans on the deck, at the aft and bow, giving the proper wind loads in surge, sway and yaw, as determined from wind tunnel tests. This technique has gained renewed interest with offshore wind turbines. At a typical scale of $1{:}50$ an 8

MW wind turbine has a diameter of about 4 m: generating an adequate wind field, over such a wide area, with fans, is virtually impossible. Moreover using embarked rotors (or dynamic cables) has the advantage that the wind load signal can easily be varied in time, simulating gusts which fans fail to do. To correct for the support velocity (in the case of floating wind turbines), the software in the loop technique is now routinely used. The tests may even be coupled with real time calculations of the wind loads. Another advantage is that scale issues, due to the bias in Reynolds number, are eliminated.

3. Critical aspects of testing

3.1. Sensors

3.1.1 Introduction

A large variety of sensor is needed in order to produce the results which can be exploited in a most suitable and the most accurate way. Among them the wave elevation sensors, motion sensors, pressure and force sensors are usually the most important.

3.1.2 Free surface elevation

For measurements of the free surface elevation the wave gauges are employed most often. The wave gauges can be of resistive or capacitive type and they consist in thin tensioned vertical wires running through the free surface. Resistive wave gauges consist in two parallel wires and what is measured is the electric conductivity of the water medium in between the wires, which is directly proportional to their wetted lengths. In the case of capacitive gauges, there is only one wire which, with the surrounding fluid, acts as a capacitor with its capacity proportional to its wetted length. The sensitivities of the resistive and capacitive wave gauges are very good: free surface variations less than one millimetre can be detected. Resistive and capacitive gauges need to be regularly calibrated, ideally on a daily basis, at the beginning and at the end of the tests.

Other techniques for measurements of the free surface elevation also exist nowadays such as the ones based on laser technology or 3D image processing.

3.1.3 Motion measurements

All model basins nowadays use optical techniques to measure the motion of the models. Qualisys system is used most widely and it consists in a set of cameras which tracks the positions in space of passive targets (with Qualisys small white spheres) placed on the models. Other systems use infra-red light and pulsating active targets. Some can operate under water. The resolution of these systems is very good, less than one millimetre when the distance from target to cameras is not excessive. Their acquisition rate is up to several hundred Hertz.

3.1.4 Pressure sensors

The pressure sensors are used most often for measuring the impact loads (slamming, sloshing, green water …). Impact pressures are not easy to measure since they are very much localized in time and space. The area of the sensor should be as small as possible and the acquisition rate must be very high, larger than 20 kHz. Moreover pressure gauges are sensitive to thermal effects, which can result in unrealistic negative values. Different types of pressure sensors are used in practice; piezoelectric, piezoresistive, capacitive, strain gauge based … Typical dimensions of the pressure sensors are of the order of few millimetres and the sampling frequency goes up to 50 KHz. Interpretation of the impact pressure measurements should be done with greatest care since large variability i.e. poor repeatability is usually observed. The sensitivity of the measurements of the sloshing impact pressures to the type of sensors was investigated by Ahn et al. (2013), Kim S.Y. et al. (2015), Razzak et al. (2013). Large differences in measuring pressures are obtained using different sensors.

The force panels can also be used to measure the pressure loads. They are usually larger (few centimetres) and the sampling frequencies are lower (usually below 1 kHz). Resulting pressure signal is usually smoother since the extreme peaks are filtered by the size of the sensor area and by the lower natural frequency of the force panel when compared to piezo- type sensors. The force panels are usually employed for milder impact conditions.

3.1.5 Measurement of the flow kinematics

Using the laser non-intrusive techniques it is possible to measure the kinematics of the flow. Two main types of measurements are usually employed Laser Dopler Velocimetry (LDV) and the Particle Imaging Velocimetry (PIV). Both of them require seeding the fluid with small particles, 10 to 100 micrometres in size. In practice the 2D flow configuration only are usually considered. One example of PIV measurements is shown in Figure 130. These types of results are of great use for the validation of the numerical models.

Figure 130: PIV measurements of the overturning wave impact at the wall. (from Kimmoun (2009))

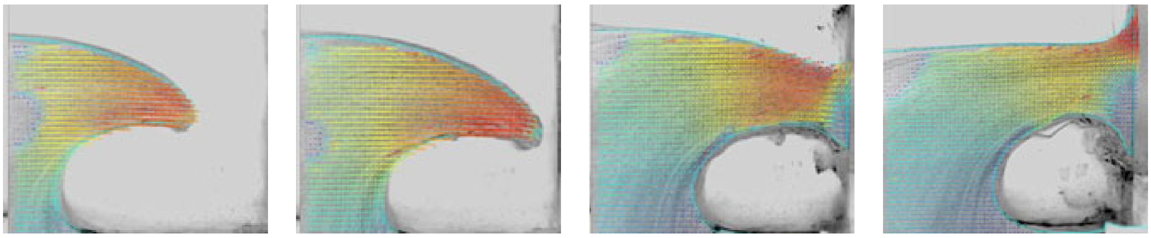

3.2. Exploitation of the measurements

3.2.1 Introduction

The first step in the analysis of the measurements is to identify the exploitable time window i.e the time interval over which the measurements can be considered valid. In regular wave tests a few cycles suffice but the matter is far different in irregular waves where the analysis requires a large number of cycles, to enable the extraction of statistical parameters; the study of slow drift motion in particular requires very long durations. The exploitable time window extends from the time when the transients have died out, or are sufficiently attenuated, until the time when the wave system in the vicinity of the model has become too degraded. These two instants are not always easy to determine objectively, the analyst having for example a tendency to take as unique criterion the regularity of the signal, estimated visually or quantitatively. This criterion is not always reliable: the regularity of the signal does not guarantee the absence of reflections, for example.

3.2.2 Regular wave tests

In regular waves, after an initial transient period, the measured signal becomes more or less periodic at the wave encounter frequency. To this signal is generally superimposed some noise, of various origins, requiring some filtering. When the signal is periodic or very close to periodic, a Fourier analysis can be used to extract the successive harmonics. This analysis can be performed via the following procedure (recommended by ITTC):

1. Separate the time series into wave frequency and low frequency components by filtering
2. Select a portion of the signal with a limited number of regular cycles
3. Determine the average value
4. Subtract the average value from the signal
5. Chose an integer number of oscillations and determine the average period by an up- or down-crossing criterion
6. Fourier analysis on the basis of this period

The determination of the average value of the signal generally requires a greater number of cycles than that required for the harmonic analysis, in particular in the case of residual oscillations at low frequency.

3.2.3 Irregular wave tests

For irregular wave tests the usual procedure starts by the statistical analysis of the time signal. First the average value, the standard deviation and the extreme values of the signal, over the exploitable time interval, are determined. Then the signal is divided into successive cycles, on an up-crossing criterion. After that the number of cycles are deduced together with the average up-crossing period, the number of maxima and minima. These maxima and minima are then presented in the form of histograms, or distribution functions compared to the Rayleigh law or adjusted to a Weibull law.

When the WF and LF parts of the response are clearly separated, which is often the case, it can be useful to first decompose the time signal, by filtering, into a LF and a WF component and to apply the statistical analysis to each component separately. This procedure enables to better identify the contribution of each component to the total signal, but makes the interdependencies disappear.

Spectral densities may be obtained by direct FFT of the time series, or via the determination of the autocorrelation and Fourier transform. The calculations of the moments of orders 0 and 2 give alternative estimates of the standard deviation and of the mean period, that can be checked to agree with the values obtained by the statistical analysis.

Under the assumptions of linearity, the RAO’s of the response can be obtained by taking the square root of the ratio of the response spectrum and the wave spectrum. To check the linearity it is preferable to calculate the cross-spectrum, from the cross-correlation function $E\{\eta_I(t)X(t+\tau)\}$. The modulus of the cross-spectrum divided by the square root of the product: wave spectrum × output spectrum provides the coherence and allows one to check the linearity: if the coherence is equal to 1, the linear relationship is established. In practice, it is considered that linearity holds when the coherence exceeds a certain threshold, for example 0.5 or 0.6. The cross-spectrum divided by the input spectrum then provides the complex transfer function (that is the modulus of the RAO and its phase).

3.2.4 Error analysis

All sort of errors occur during the model testing and the results should always be taken within a certain range of accuracy. The bias errors, such as those related to impossibility to get full similitude for all relevant nondimensional numbers (Froude, Reynolds, Strouhal …), should be clearly identified and differentiated from the errors occurring due to the accuracy of the measurement systems.

3.3. Specification of the tests

3.3.1 Introduction

Defining the test program is not an easy task. From technical point of view, it depends mainly on the type of the platform (fixed or floating) and on the information sought through the tests (results directly usable for the design or for the calibration of a numerical model). On the other side, the cost of the testing is another important factor, often the most limiting. Testing campaign should be planned very carefully and in principle as much time should be spent in the planning of the tests as the actual testing time in the basin. The test goal should remain focused rather than all-inclusive. Often different types of testing should be designed for different goals for the same system and sometimes, the multiple model scales of the system may be needed.

An interesting overview of the model testing philosophy, associated technical issues and the difficulties, in the context of the FPSO type of floaters in deep waters, is presented in Naciri (2010).

3.3.2 Wave calibration tests

The wave conditions are specified in the absence of the model and the correctness of the wave generation needs to be checked first. Adjusting regular waves is usually not very complicated but it is always useful to check for example that they are not too degraded in the test zone and/or that reflections from the beach are small. Simple visual examination of the time traces of the wave elevation is the first thing to check, but it can be also useful to check if the amplitudes of the higher harmonics (at double and triple frequencies) agree with the theoretical values of the Stokes model

The calibration of the irregular waves usually requires some iterations and often the agreement between specified and achieved wave spectra is never perfect. As much as the shape of the spectrum, the distribution of the wave heights, with respect to the theoretical laws, is to be verified.

Verification of wave group spectrum is often done to make sure that the wave realization is not overly conservative at the slow drift natural frequencies

3.3.3 Decay tests

For dynamic systems the free vibration or decay tests are more or less mandatory. The goal is to determine the natural frequencies of the system which are one of the most important parameters of the dynamic systems. The procedure consists in displacing the system from its equilibrium position in one degrees of freedom and releasing it. In the absence of coupling with the other degrees of freedom, the ensuing motion is a simple damped sinusoid from which the natural period can be easily deduced. Furthermore, by assuming the total damping B to be composed of the linear plus quadratic component, i.e. $B = B_L + B_Q|\dot{X}|$ the damping coefficients B_L and B_Q can be derived from the slowly-decreasing amplitude. Indeed, for relatively weak damping, the response appears as a slowly decreasing sinusoid with successive amplitudes X_n. From one cycle n to the following $n+1$ the amplitude ratio is given by:

$$\frac{X_{n+1}}{X_n} = e^{-\left(B_L+\frac{8}{3\pi}B_Q X_n \omega_0\right)\frac{T}{2M}} \simeq 1 - \left(B_L + \frac{8}{3\pi} B_Q X_n \omega_0\right)\frac{T}{2M} \qquad (334)$$

This means that, when plotting $\Delta X_n / X_n$ vs X_n, the experimental points should align on a straight line. From its intercept with the vertical axis the linear damping component B_L is deduced and, from its slope, the quadratic component B_Q. This procedure is routinely applied to roll decay tests of ships and FPSOs, to extract the viscous damping. It should be noted however that the assumption of quadratic damping, even if it performs well in many cases, might not be always justified.

3.3.4 Tests in regular waves

Tests in regular waves are useful for the following reasons:

- to check the RAOs and their sensitivity to the wave amplitude (at a given frequency),
- to obtain the wave drift forces, and compare with the values delivered by a potential flow model; check their sensitivity to increasing wave amplitude,
- to derive the wave drift damping when combined with a decay test

Some tests may also be duplicated with co-flowing or adverse current, which provides, among other information, an alternate access to wave drift damping.

In the cases when the considered system responds dynamically, it makes little sense to assess the design on the basis of tests in regular waves: if the wave frequency coincides with a natural frequency (or a subharmonic) of the system, an exaggerated dynamic response will appear; mean wave drift forces may take unrealistic values, while no slow-drift response will appear in regular waves.

3.3.5 Tests in bichromatic waves

Tests in bichromatic waves are occasionally specified, in order to extract QTFs. An unfortunate feature of bichromatic waves is that they are rather unstable, due to free surface nonlinearities (Lo & Mei (1985)).

3.3.6 Tests in irregular waves

Through the tests in irregular waves the priority is often to reproduce the seastate considered for the design in order to obtain results that are directly usable. This may lead to a very large number of tests since many parameters may have to be varied, for instance:

- the draft of the structure (ballast or fully loaded)
- the seastate, depending on whether one wants to simulate extreme or operational conditions

- for a given seastate, the peak period of the spectrum which is often imprecise and need to be adjusted
- the relative directions and velocities of the wind and current
- the integrity of the mooring system: one or two lines broken for instance
- the integrity of the vessel: intact or one/two compartment flooded i.e. with trim/list.

More and more frequently the main goal of the tests is to validate and calibrate a numerical model, or a suite of numerical models, that have been used for the design. Nowadays computer power is so vast and so cheap that complex numerical models can be run hundreds of times over, to cover all combinations of seastate, loading, mooring integrity, etc. The numerical model is tuned to the model tests (the ”model of the model”), then some parameters may be modified to account for scale effects (some drag coefficients for instance, on the basis of experience or larger scale tests or CFD computations).

3.3.7 Tests in wave groups

The tests in wave groups can be very useful to clarify the effects of non-linearities in various offshore systems. The use of two phase and four phase separation in wave group tests to extract higher harmonics due to nonlinear effects, e.g. double and triple frequency effects isolated in experiments, has been very effective as discussed in Fitzgerald et al. (2014). Specific aspects related to nonlinear effects in wave group generation are discussed in McAllister et al (2018) and Zhao et al (2019).

3.3.8 Forced motion tests

Many testing facilities are now equipped with ”hexapods” (see Figure 131) that can oscillate the models through 6 degrees of freedom. Most common types of application are:

- forced motion tests in still water or in current to derive added mass and damping coefficients
- sloshing model tests

Figure 131: Use of hexapod system. Left – forced motion in water, Right – sloshing model tests.

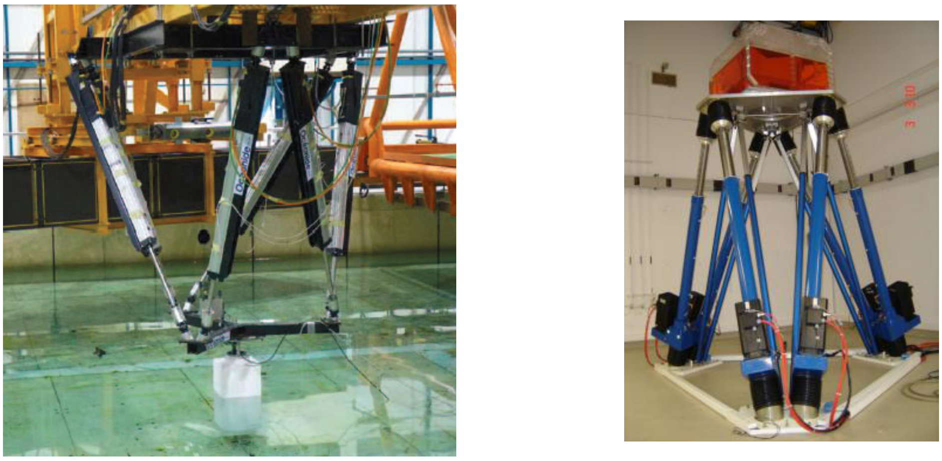

3.3.9 Towing and wind tunnel model tests

The current drag coefficients are commonly obtained using either the wind tunnel tests, towing tests or alternatively by CFD. Although the wind tunnel tests can be naturally recommended for evaluation of the wind drag coefficients, their use for evaluation of the current drag coefficients may suffer from important inaccuracies as discussed in Huang et al. (2016). These inaccuracies are due to the boundary layer effects at the wind tunnel floor, as already indicated in 58Section 4. [2.3.3].

4. List of references

[1] Ahn Y., Kim K.H., Kim S.Y., Lee S.W., Kim Y. & Lee J.H., 2013.: “Experimental study on the effects of pressure sensors and time window in violent sloshing pressure measurement.”, ISOPE, Anchorage, USA.

[2] Chen X-B. 1994.: “On the side wall effects upon bodies of arbitrary geometry in wave tanks.”, Applied Ocean Research, Vol.16.

[3] Chen X.B., Zhao B.B. & Li R.P. 2019.: “Mysterious wavefront uncovered.” 34th IWWWFB, Newcastle, Australia.

[4] Fitzgerald, C.J., Taylor, P.H., Grice, J.R., Eatock Taylor, R. & Zang J., 2014.: “Phase manipulation and the harmonic components of ringing forces on a surface-piercing column.” Proceedings of the Royal Society A, 470:20130847

[5] Huang Z.J., Jang H., Kim J. & Slocum S.T., 2016.: “Current drag from tow and wind tunnel tests of a FLNG hull”, OMAE2016-54493.

[6] Kim S.Y., Kim K.H. & KIM Y., 2015.: “Comparative study on pressure sensors for sloshing experiment.”, Ocean Engineering, Vol. 94

[7] Kimmoun O., Malenica S. & Scolan Y.M., 2009.: “Fluid structure interactions occurring at a flexible wall impacted by a breaking wave.”, Conference ISOPE, Osaka, Japan

[8] Lo E. & Mei C.C., 1985.: “A numerical study of water-wave modulation based on a higher-order nonlinear Schrodinger equation.”, J. Fluid Mechanics, Vol. 150.

[9] McAllister, M. L., Adcock, T. A. A., Taylor, P. H. & Van Den Bremer, T. S. 2018 “The set-down and set-up of directionally spread and crossing surface gravity wave groups.”, Journal of Fluid Mechanics, 835, 131–169

[10] Molin B. 2001.: “Numerical and physical wave tanks. Making them fit.”, Ship Technology Research, Vol. 48.

[11] Molin B., Stassen Y. & Marin S. 1999.: “Etude theorique et experimentale des seiches parasites generees dans les bassins de houle.“, Septiemes Journees de l’Hydrodynamique (in French).

[12] Naciri M. 2009.: “Model Test Philosophy for FPSO’s in Deep Brazilian Waters”. Marine Systems & Ocean Technology, Vol. 5, pp.91-101.

[13] Razzak S., Amaichan J., Damion J.P. & Sarraf C., 2013.: “Dynamic pressure calibration.”, ISOPE, Anchorage, USA.

[14] Schaffer H.A. 1996.: Second-order wave maker theory for irregular waves, Ocean Engineering., Vol. 23.

[15] Stassen Y. 1999.: “Simulation numerique d’un canal a houle bidimensionnel au troisieme ordre d’approximation par une methode integrale“, PhD thesis, Nantes University (in French).

[16] Sulisz W. & Hudspeth R.T. 1993.: “Complete second-order solution for water waves generated in wave flumes.”, J. Fluids & Structures, Vol. 7.

[17] Z hao R., Faltinsen O.M., Krokstad J.R. & Aanesland V., 1988.: “Wave current interaction effects on large volume structures”, Proceedings of Behavior of Offshore Structures (BOSS), Trondheim, Norway.

[18] Z hao, W., Taylor, P.H., Wolgamot, H. & Eatock Taylor, R. (2019) “Amplification of random wave run-up on the front face of a box driven by tertiary wave interactions.” Journal of Fluid Mechanics, 869, 706-725.

Appendix 1 Outline of the theories

1. Body dynamics

1.1. Introduction

1.1.1 General

A clear understanding of the general body dynamics is one of the most important points in the analysis of the floating body behavior in waves. The body dynamics can be introduced in many different ways and there exist a large amount of the excellent textbooks on this subject. The description adopted here follows the book of Shabana (1989).

1.1.2 Notations

The compact matrix notations are introduced where $[\boldsymbol{A}]$ is used to denote the $n \times m$ matrix with the elements $A_{ij}\,,(i = 1, n\,; j = 1, m)$. At the same time, any vector quantity $\boldsymbol{a} = a_x\boldsymbol{i} + a_y\boldsymbol{j} + a_z\boldsymbol{k}$ is written as a single column matrix $\{\boldsymbol{a}\}$. Finally, to each vector quantity, the skew symmetric matrix $[\boldsymbol{a}]$ is associated as follows:

$$\{\boldsymbol{a}\} = \begin{Bmatrix} a_x \\ a_y \\ a_z \end{Bmatrix} \quad , \quad [\boldsymbol{a}] = \begin{bmatrix} 0 & -a_z & a_y \\ a_z & 0 & -a_x \\ -a_y & a_x & 0 \end{bmatrix} \qquad (335)$$

These notations allow writing the scalar and vector product of two vectors $\{\boldsymbol{a}\}$ and $\{\boldsymbol{b}\}$ as:

$$\boldsymbol{a} \cdot \boldsymbol{b} = \{\boldsymbol{a}\}^T\{\boldsymbol{b}\} \quad , \quad \boldsymbol{a} \wedge \boldsymbol{b} = [\boldsymbol{a}]\{\boldsymbol{b}\} \qquad (336)$$

1.2. Kinematics

1.2.1 Coordinate systems

Reference is made to Figure 132 where the two coordinate systems are identified:

(O, X, Y, Z) Earth fixed (inertial) coordinate system with arbitrary origin
(G, x', y', z') Body fixed coordinate system with the origin at the body center of gravity

Figure 132: Rigid (left) and flexible (right) body motion and the different coordinate systems

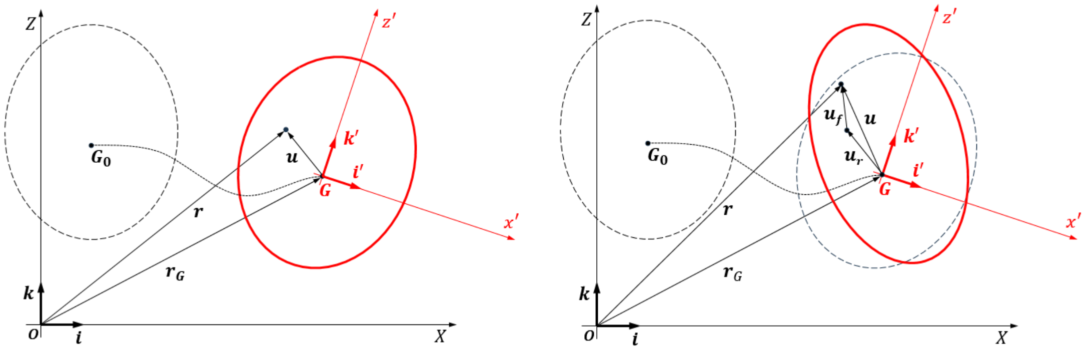

Two sets of coordinates (O, X, Y, Z) and (G, x', y', z') are related to each other through the transformation matrix $[\boldsymbol{A}]$ so that, for any vector quantity $\{\boldsymbol{u}\}$ defined in (O, X, Y, Z) , the following relation is valid:

$$\{\boldsymbol{u}\} = [\boldsymbol{A}]\{\boldsymbol{u}'\} \qquad (337)$$

The transformation matrix $[\boldsymbol{A}]$ is the critical parameter in the analysis of the nonlinear body motion and the instantaneous body rotation velocity vector $\{\boldsymbol{\Omega}'\}$ is related to the transformation matrix by:

$$[\boldsymbol{\Omega}'] = [\boldsymbol{A}]^T[\dot{\boldsymbol{A}}] \qquad (338)$$

1.2.2 Time derivatives of the vector quantities

In order to properly interpret the time derivatives of the vector quantities in the different coordinate systems, the following notations are introduced:

- Time derivative of the vector in the earth fixed coordinate system expressed in the body fixed coordinate system

$$\{\dot{\boldsymbol{a}}\}' = \left\{\frac{d\boldsymbol{a}}{dt}\right\}' = [\boldsymbol{A}]^T\{\dot{\boldsymbol{a}}\} \tag{339}$$

- Time derivative of the vector which was transformed from the earth to body fixed coordinate system

$$\{\dot{\boldsymbol{a}}'\} = \frac{d}{dt}\{\boldsymbol{a}'\} = \frac{d}{dt}([\boldsymbol{A}]^T\{\boldsymbol{a}\}) = [\dot{\boldsymbol{A}}]^T\{\boldsymbol{a}\} + [\boldsymbol{A}]^T\{\dot{\boldsymbol{a}}\} = \{\dot{\boldsymbol{a}}\}' - [\boldsymbol{\Omega}']\{\boldsymbol{a}'\} \tag{340}$$

This means that the time derivative of the transformed vector quantity and the transformation of the time derivative of the same vector quantity should be clearly distinguished:

$$\{\dot{\boldsymbol{a}}\}' \neq \{\dot{\boldsymbol{a}}'\} = \{\dot{\boldsymbol{a}}\}' - [\boldsymbol{\Omega}']\{\boldsymbol{a}'\} \tag{341}$$

1.2.3 Euler angles

There exists many possibilities to describe the instantaneous position and orientation of the body. Most common way is to define it by the instantaneous position of the body center of gravity $\{\boldsymbol{r}_G\}$ and the instantaneous rotations angles of the body fixed coordinate system (Euler angles) $\{\boldsymbol{\theta}\}$:

$$\{\boldsymbol{r}_G\} = \begin{Bmatrix} X_G \\ Y_G \\ Z_G \end{Bmatrix} \quad , \quad \{\boldsymbol{\theta}\} = \begin{Bmatrix} \theta_x \\ \theta_y \\ \theta_z \end{Bmatrix} \tag{342}$$

There are 12 different ways to choose the Euler angles and here we adopt the so called zyx or 321 convention schematically shown in Figure 133.

Figure 133: ***Euler angles.***

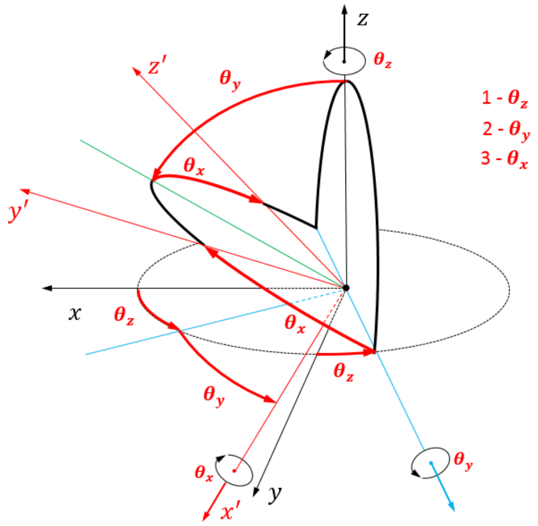

The corresponding transformation matrix $[\boldsymbol{A}]$ from the inertial to body fixed coordinate system becomes:

$$[\boldsymbol{A}] = \begin{bmatrix} \cos\theta_z\cos\theta_y & -\sin\theta_z\cos\theta_x + \cos\theta_z\sin\theta_y\sin\theta_x & \sin\theta_z\sin\theta_x + \cos\theta_z\sin\theta_y\cos\theta_x \\ \sin\theta_z\cos\theta_y & \cos\theta_z\cos\theta_x + \sin\theta_z\sin\theta_y\sin\theta_x & -\cos\theta_z\sin\theta_x + \sin\theta_z\sin\theta_y\cos\theta_x \\ -\sin\theta_y & \cos\theta_y\sin\theta_x & \cos\theta_y\cos\theta_x \end{bmatrix} \tag{343}$$

The following important relation between the instantaneous rotation vector $\{\boldsymbol{\Omega}'\}$ and the time derivatives of the Euler angles can be deduced from (338):

$$\{\boldsymbol{\Omega}'\} = [\mathbf{G}']\{\dot{\boldsymbol{\theta}}\} \quad , \quad [\mathbf{G}'] = \begin{bmatrix} 1 & 0 & -\sin\theta_y \\ 0 & \cos\theta_x & \cos\theta_y\sin\theta_x \\ 0 & -\sin\theta_x & \cos\theta_y\cos\theta_x \end{bmatrix} \tag{344}$$

1.2.4 Rigid body

The rigid body motion is described by the following position, velocity and the acceleration vectors:

$$\begin{aligned} \{\boldsymbol{r}\} &= \{\boldsymbol{r}_G\} + [\boldsymbol{A}]\{\boldsymbol{u}'\} \\ \{\boldsymbol{v}\} &= \{\boldsymbol{v}_G\} + [\boldsymbol{A}][\boldsymbol{\Omega}']\{\boldsymbol{u}'\} \\ \{\boldsymbol{a}\} &= \{\boldsymbol{a}_G\} + [\boldsymbol{A}][\dot{\boldsymbol{\Omega}}']\{\boldsymbol{u}'\} + [\boldsymbol{A}][\boldsymbol{\Omega}'][\boldsymbol{\Omega}']\{\boldsymbol{u}'\} \end{aligned} \tag{345}$$

where $\{\boldsymbol{r}_G\}$, $\{\boldsymbol{v}_G\}$ and $\{\boldsymbol{a}_G\}$ are the position, velocity and acceleration of the center of gravity in the inertial coordinate system and $\{\boldsymbol{\Omega}'\}$ is the instantaneous rotational velocity vector.

1.2.5 Flexible body

The main difference between the rigid and the flexible body kinematics lies in the fact that the distance between the points attached to the body is not constant in time for the flexible body. Reference is made to Figure 132b, and the total displacement of the point attached to the body $\{\boldsymbol{u}\}$ is decomposed into its rigid body part $\{\boldsymbol{u}_r\}$ and the deformation part denoted by $\{\boldsymbol{u}_f\}$:

$$\{\boldsymbol{u}\} = \{\boldsymbol{u}_r\} + \{\boldsymbol{u}_f\} \tag{346}$$

The motion of the flexible body is described by the following position, velocity and acceleration vectors:

$$\begin{aligned} \{\boldsymbol{r}\} &= \{\boldsymbol{r}_G\} + [\boldsymbol{A}]\{\boldsymbol{u}'\} \\ \{\boldsymbol{v}\} &= \{\boldsymbol{v}_G\} + [\boldsymbol{A}][\boldsymbol{\Omega}']\{\boldsymbol{u}'\} + [\boldsymbol{A}]\{\dot{\boldsymbol{u}}'_f\} \\ \{\boldsymbol{a}\} &= \{\boldsymbol{a}_G\} + [\boldsymbol{A}][\boldsymbol{\Omega}'][\boldsymbol{\Omega}']\{\boldsymbol{u}'\} + [\boldsymbol{A}][\dot{\boldsymbol{\Omega}}']\{\boldsymbol{u}'\} + 2[\boldsymbol{A}][\boldsymbol{\Omega}']\{\dot{\boldsymbol{u}}'_f\} + [\boldsymbol{A}]\{\ddot{\boldsymbol{u}}'_f\} \end{aligned} \tag{347}$$

where the facts that $\{\dot{\boldsymbol{u}}'_r\} = \{\boldsymbol{0}\}$ was used.

It should be noted that the instantaneous position of the center of gravity is obtained by considering the rigid body motions only. In order to write the flexible body dynamic motion equation, the body deformations should be represented in a convenient way. In the general case, the body deformation vector $\{\boldsymbol{u}'_f\}$ can be arbitrarily large but here the deformation vector is assumed to be small and is represented as a sum of the N_f modal contributions:

$$\{\boldsymbol{u}'_f(\boldsymbol{u}'_r, t)\} = \sum_{i=1}^{N_f} \chi_{fi}(t)\{\boldsymbol{h}'_{fi}(\boldsymbol{u}'_r)\} = [\boldsymbol{\hbar}'_f]\{\boldsymbol{\chi}_f\} \tag{348}$$

where $\boldsymbol{h}'_{fi} = h'_{fix'}\boldsymbol{i}' + h'_{fiy'}\boldsymbol{j}' + h'_{fiz'}\boldsymbol{k}'$ is the modal displacement expressed relative to the body fixed coordinate system, and:

$$[\boldsymbol{\hbar}'_f] = \begin{bmatrix} h'_{f1x'} & h'_{f2x'} & \cdots & h'_{fN_fx'} \\ h'_{f1y'} & h'_{f2y'} & \cdots & h'_{fN_fy'} \\ h'_{f1z'} & h'_{f2z'} & \cdots & h'_{fN_fz'} \end{bmatrix} \quad , \quad \{\boldsymbol{\chi}_f\}^T = \{\chi_{f1} \quad \chi_{f2} \quad \cdots \quad \chi_{fN_f}\} \tag{349}$$

1.3. Dynamics

1.3.1 Rigid body

The rigid body motion equation, expressed in the inertial coordinate system (O, X, Y, Z), follows from the Newton - Euler law or from the D'Alembert principle of virtual work, in the form:

$$\begin{aligned} [\boldsymbol{m}]\{\ddot{\boldsymbol{r}}_G\} &= \{\boldsymbol{F}\} \\ [\boldsymbol{I}_{\boldsymbol{\theta\theta}}]\{\dot{\boldsymbol{\Omega}}\} &= \{\boldsymbol{M}\} - [\boldsymbol{\Omega}][\boldsymbol{I}_{\boldsymbol{\theta\theta}}]\{\boldsymbol{\Omega}\} \end{aligned} \tag{350}$$

where:

- $[\boldsymbol{m}]$ body mass matrix
- $[\boldsymbol{I}_{\boldsymbol{\theta\theta}}]$ body rotational inertia matrix
- $\{\boldsymbol{F}\}$ instantaneous external force vector
- $\{\boldsymbol{M}\}$ instantaneous external moment vector

The mass and inertia matrices are defined as follows:

$$[\boldsymbol{m}] = \iiint_{\forall_B} [\mathbf{I}]dm \quad , \quad [\boldsymbol{I_{\theta\theta}}] = \iiint_{\forall_B} [\boldsymbol{u}]^T[\boldsymbol{u}]dm \quad , \quad \{\boldsymbol{u}\} = \{\boldsymbol{r}\} - \{\boldsymbol{r_G}\} = \begin{Bmatrix} X - X_G \\ Y - Y_G \\ Z - Z_G \end{Bmatrix} \qquad (351)$$

where $[\mathbf{I}]$ stands for the identity matrix (all terms zero except diagonal equal to 1).

Being defined in the inertial coordinate system, the rotational inertia matrix $[\boldsymbol{I_{\theta\theta}}]$ depends on time and it is more convenient to rewrite the motion equation in the body fixed system (G, x', y', z') where the rotational inertia matrix is time independent:

$$\begin{aligned} [\boldsymbol{m}]\{\ddot{\boldsymbol{r}}_{\boldsymbol{G}}\}' &= \{\boldsymbol{F}'\} \\ [\boldsymbol{I}'_{\theta\theta}]\{\dot{\boldsymbol{\Omega}}\}' &= \{\boldsymbol{M}'\} - [\boldsymbol{\Omega}'][\boldsymbol{I}'_{\theta\theta}]\{\boldsymbol{\Omega}'\} \end{aligned} \qquad (352)$$

with:

$$[\boldsymbol{I}'_{\theta\theta}] = \iiint_{\forall_B} [\boldsymbol{u}']^T[\boldsymbol{u}']dm \qquad (353)$$

The external forces are assumed to act at the discrete points at the body and they are denoted by $\{\boldsymbol{f}_j\}$ in the earth fixed coordinate system and by $\{\boldsymbol{f}'_j\}$ in the body fixed coordinate system. In the case of the freely floating body, there exist two types of the external forces namely the gravity forces and the pressure forces:

$$\{\boldsymbol{f}'_j\} = \left\{\boldsymbol{f}_j^{g'}\right\} + \left\{\boldsymbol{f}_j^{p'}\right\} \qquad (354)$$

The gravity force remains constant in the earth fixed coordinate system and it is possible to write:

$$\left\{\boldsymbol{f}_j^{g}\right\} = -m_j g\{\boldsymbol{k}\} \quad , \quad \left\{\boldsymbol{f}_j^{g'}\right\} = -m_j g[\boldsymbol{A}]^T\{\boldsymbol{k}\} \qquad (355)$$

The discrete pressure forces are obtained by integrating the pressure over the elementary wetted surface:

$$\left\{\boldsymbol{f}_j^{p'}\right\} = P\{\boldsymbol{n}'\}dS_j \qquad (356)$$

where P is the external pressure and $\{\boldsymbol{n}'\}dS_j$ is the oriented element of the wetted surface.

With these notations, the instantaneous rigid body forces and moments become:

$$\{\boldsymbol{F}'\} = \sum_{j=1}^{N} \{\boldsymbol{f}'_j\} \quad , \quad \{\boldsymbol{M}'\} = \sum_{j=1}^{N} [\boldsymbol{u}']\{\boldsymbol{f}'_j\} \qquad (357)$$

1.3.2 Flexible body

The application of the D'Alambert principle of the virtual work leads to the following dynamic motion equation for the flexible floating body (e.g. Shabana (1989)):

$$\begin{bmatrix} [\boldsymbol{m}] & [0] & [\boldsymbol{I}'_{Rf}] \\ [0] & [\boldsymbol{I}'_{\theta\theta}] & [\boldsymbol{I}'_{\theta f}] \\ [\boldsymbol{I}'_{Rf}]^T & [\boldsymbol{I}'_{\theta f}]^T & [\boldsymbol{I}'_{ff}] \end{bmatrix} \begin{Bmatrix} \{\ddot{\boldsymbol{r}}_{\boldsymbol{G}}\}' \\ \{\dot{\boldsymbol{\Omega}}\}' \\ \{\ddot{\boldsymbol{\chi}}_f\} \end{Bmatrix} = \begin{Bmatrix} \{\boldsymbol{F}'\} \\ \{\boldsymbol{M}'\} \\ \{\boldsymbol{F}_f\} - [\boldsymbol{K}]\{\boldsymbol{\chi}_f\} \end{Bmatrix} - \begin{Bmatrix} \{\boldsymbol{Q}'_{vR}\} \\ \{\boldsymbol{Q}'_{v\theta}\} \\ \{\boldsymbol{Q}'_{vf}\} \end{Bmatrix} \qquad (358)$$

The matrix $[\boldsymbol{K}]$ in the above equation, denotes the structural stiffness matrix for the flexible modes, and $\{\boldsymbol{Q}'_{vi}\}$ is the quadratic velocity inertia force vector. This quadratic inertia force vector becomes quite complex in the case of the arbitrary body motions/deformations but, in the case of the rigid body it reduces to:

$$\{\boldsymbol{Q}'_{vR}\} = 0 \quad , \quad \{\boldsymbol{Q}'_{v\theta}\} = [\boldsymbol{\Omega}'][\boldsymbol{I}'_{\theta\theta}]\{\boldsymbol{\Omega}'\} \qquad (359)$$

so that the expressions (352) for the rigid body are recovered.

It should be noted that the body deformations are defined in the body fixed coordinate system and that the motion equation is written in the body fixed coordinate system. This means that the inertia terms related to rigid body motions ($[\boldsymbol{m}]$, $[\boldsymbol{I}'_{\theta\theta}]$) are still given by (351) and (353) and those related to the flexible modes are defined as follows:

$$[\boldsymbol{I}'_{Rf}] = \iiint_{\forall_B} [\boldsymbol{\hbar}'_f]dm \quad , \quad [\boldsymbol{I}'_{\theta f}] = \iiint_{\forall_B} [\boldsymbol{u}'_r]^T[\boldsymbol{\hbar}'_f]dm \quad , \quad [\boldsymbol{I}'_{ff}] = \iiint_{\forall_B} [\boldsymbol{\hbar}'_f]^T[\boldsymbol{\hbar}'_f]dm \qquad (360)$$

where it should be noted that, for the orthogonal deformation modes, the matrix $[\boldsymbol{I}'_{Rf}]$ is zero and $[\boldsymbol{I}'_{ff}]$ is the diagonal matrix.

The external rigid body forces and moments remain defined by (357) and the flexible body modal forces are given by:

$$F_{fi} = \sum_{j=1}^{N} \left\{\tilde{\boldsymbol{h}}'_{fi}\right\}^{T} \left\{\boldsymbol{f}'_{j}\right\} \tag{361}$$

where $\left\{\tilde{\boldsymbol{h}}'_{fi}\right\}$ denotes the instantaneous value of the modal displacement.

1.4. Linearization of the body dynamics

1.4.1 Introduction

Solving the fully nonlinear body motion in waves is very complex and commonly the problem is linearized and solved at different orders of approximation. In practice only the linear and the second order problems are considered. The description which follows is inspired by the work of Ogilvie (1983).

1.4.2 Body motion equations at first and second order

Within the linearization process, all the physical quantities are developed into perturbation series with respect to small parameter ε and we write:

$$\begin{aligned}
\{\boldsymbol{r}_G\} - \{\boldsymbol{r}_{G_0}\} &= \varepsilon\left\{\boldsymbol{R}_G^{(1)}\right\} + \varepsilon^2\left\{\boldsymbol{R}_G^{(2)}\right\} + O(\varepsilon^3) \\
\{\boldsymbol{\Omega}'\} &= \varepsilon\left\{\boldsymbol{\Omega}'^{(1)}\right\} + \varepsilon^2\left\{\boldsymbol{\Omega}'^{(2)}\right\} + O(\varepsilon^3) \\
\{\boldsymbol{\theta}\} &= \varepsilon\left\{\boldsymbol{\theta}^{(1)}\right\} + \varepsilon^2\left\{\boldsymbol{\theta}^{(2)}\right\} + O(\varepsilon^3) \\
\{\boldsymbol{\chi}_f\} &= \varepsilon\left\{\boldsymbol{\chi}_f^{(1)}\right\} + \varepsilon^2\left\{\boldsymbol{\chi}_f^{(2)}\right\} + O(\varepsilon^3) \\
\{\boldsymbol{F}'\} &= \varepsilon\left\{\boldsymbol{F}'^{(1)}\right\} + \varepsilon^2\left\{\boldsymbol{F}'^{(2)}\right\} + O(\varepsilon^3) \\
\{\boldsymbol{M}'\} &= \varepsilon\left\{\boldsymbol{M}'^{(1)}\right\} + \varepsilon^2\left\{\boldsymbol{M}'^{(2)}\right\} + O(\varepsilon^3) \\
\{\boldsymbol{F}_f\} &= \varepsilon\left\{\boldsymbol{F}_f^{(1)}\right\} + \varepsilon^2\left\{\boldsymbol{F}_f^{(2)}\right\} + O(\varepsilon^3)
\end{aligned} \tag{362}$$

These perturbation series are introduced into the fully nonlinear motion equation (358) and the terms at different orders are collected and the following motion equations can be formally written:

$$\begin{bmatrix} [\boldsymbol{m}] & [0] & [0] \\ [0] & [\boldsymbol{I}'_{\theta\theta}] & [\boldsymbol{I}'_{\theta f}] \\ [0] & [\boldsymbol{I}'_{\theta f}]^T & [\boldsymbol{I}'_{ff}] \end{bmatrix} \begin{Bmatrix} \left\{\ddot{\boldsymbol{R}}_G^{(1)}\right\}' \\ \left\{\dot{\boldsymbol{\Omega}}^{(1)}\right\}' \\ \left\{\ddot{\boldsymbol{\chi}}_f^{(1)}\right\} \end{Bmatrix} = \begin{Bmatrix} \left\{\boldsymbol{F}'^{(1)}\right\} \\ \left\{\boldsymbol{M}'^{(1)}\right\} \\ \left\{\boldsymbol{F}_f^{(1)}\right\} - [\boldsymbol{K}]\left\{\boldsymbol{\chi}_f^{(1)}\right\} \end{Bmatrix} \tag{363}$$

$$\begin{bmatrix} [\boldsymbol{m}] & [0] & [0] \\ [0] & [\boldsymbol{I}'_{\theta\theta}] & [\boldsymbol{I}'_{\theta f}] \\ [0] & [\boldsymbol{I}'_{\theta f}]^T & [\boldsymbol{I}'_{ff}] \end{bmatrix} \begin{Bmatrix} \left\{\ddot{\boldsymbol{R}}_G^{(2)}\right\}' \\ \left\{\dot{\boldsymbol{\Omega}}^{(2)}\right\}' \\ \left\{\ddot{\boldsymbol{\chi}}_f^{(2)}\right\} \end{Bmatrix} = \begin{Bmatrix} \left\{\boldsymbol{F}'^{(2)}\right\} \\ \left\{\boldsymbol{M}'^{(2)}\right\} \\ \left\{\boldsymbol{F}_f^{(2)}\right\} - [\boldsymbol{K}]\left\{\boldsymbol{\chi}_f^{(2)}\right\} \end{Bmatrix} + \begin{Bmatrix} \left\{\boldsymbol{Q}'^{(2)}_{vR}\right\} \\ \left\{\boldsymbol{Q}'^{(2)}_{v\theta}\right\} \\ \left\{\boldsymbol{Q}'^{(2)}_{vf}\right\} \end{Bmatrix} \tag{364}$$

The quadratic velocity inertia forces $\left\{\boldsymbol{Q}'^{(2)}_{vi}\right\}$ can be deduced by perturbing their original nonlinear expressions (Shabana (1989)). The final expressions become quite complex and are not recalled here, and we simply note that, for the rigid body case, they are given by replacing $\{\boldsymbol{\Omega}'\}$ by $\left\{\boldsymbol{\Omega}'^{(1)}\right\}$ in (359).

1.4.3 Transformation matrix

Within the linearization procedure, the transformation matrix $[\boldsymbol{A}]$ requires special attention. When using the description in terms of the Euler angles (343), the following expressions are obtained:

$$[\boldsymbol{A}] = [\mathbf{I}] + \varepsilon\left[\boldsymbol{A}^{(1)}\right] + \varepsilon^2\left[\boldsymbol{A}^{(2)}\right] + O(\varepsilon^3) \tag{365}$$

$$\left[\boldsymbol{A}^{(1)}\right] = \left[\boldsymbol{\theta}^{(1)}\right]$$

$$\left[\boldsymbol{A}^{(2)}\right] = \left[\boldsymbol{\theta}^{(2)}\right] - \frac{1}{2}\begin{bmatrix} \theta_z^{(1)^2} + \theta_y^{(1)^2} & -2\theta_y^{(1)}\theta_x^{(1)} & -2\theta_z^{(1)}\theta_x^{(1)} \\ 0 & \theta_z^{(1)^2} + \theta_x^{(1)^2} & -2\theta_z^{(1)}\theta_y^{(1)} \\ 0 & 0 & \theta_y^{(1)^2} + \theta_x^{(1)^2} \end{bmatrix} = \left[\boldsymbol{\theta}^{(2)}\right] - \frac{1}{2}[\boldsymbol{H}]$$

Similarly the conversion matrix $[\mathbf{G}']$ becomes:

$$[\mathbf{G}'] = [\mathbf{I}] + \varepsilon\left[\mathbf{G}'^{(1)}\right] + O(\varepsilon^2) \quad , \quad \left[\mathbf{G}'^{(1)}\right] = \begin{bmatrix} 0 & 0 & -\theta_y^{(1)} \\ 0 & 0 & \theta_x^{(1)} \\ 0 & -\theta_x^{(1)} & 0 \end{bmatrix} \tag{366}$$

It follows that the instantaneous rotation velocity vector and its time derivative become:

$$\left\{\boldsymbol{\Omega}'^{(1)}\right\} = \left\{\dot{\boldsymbol{\theta}}^{(1)}\right\} \quad , \quad \left\{\boldsymbol{\Omega}'^{(2)}\right\} = \left\{\dot{\boldsymbol{\theta}}^{(2)}\right\} + \left[\mathbf{G}'^{(1)}\right]\left\{\dot{\boldsymbol{\theta}}^{(1)}\right\} \tag{367}$$

$$\left\{\dot{\boldsymbol{\Omega}}'^{(1)}\right\} = \left\{\ddot{\boldsymbol{\theta}}^{(1)}\right\} \quad , \quad \left\{\dot{\boldsymbol{\Omega}}'^{(2)}\right\} = \left\{\ddot{\boldsymbol{\theta}}^{(2)}\right\} + \left[\dot{\mathbf{G}}'^{(1)}\right]\left\{\dot{\boldsymbol{\theta}}^{(1)}\right\} + \left[\mathbf{G}'^{(1)}\right]\left\{\ddot{\boldsymbol{\theta}}^{(1)}\right\} \tag{368}$$

When interpreting the time derivatives of the rotational velocity vector in (367) and (368), the relations (341) should be kept in mind.

1.4.4 Generalized description of the linear body dynamics

In the linear case it is convenient to describe the dynamics of the floating flexible body in a more compact form (e.g. see Newman (1994), Tuitman et al. (2012)). For simplicity, the superscript " $^{(1)}$" is omitted and the instantaneous linear position vector $\{\boldsymbol{r}\}$ of on point attached to the body is rewritten as:

$$\{\boldsymbol{r}\} = \left\{\boldsymbol{r}_{G_0}\right\} + \{\boldsymbol{u}_r\} + \{\boldsymbol{R}_G\} + [\boldsymbol{\theta}]\{\boldsymbol{u}'_r\} + \left[\boldsymbol{\hbar}'_f\right]\left\{\boldsymbol{\chi}_f\right\} = \{\boldsymbol{r}_0\} + [\boldsymbol{\hbar}']\{\boldsymbol{\xi}\} \tag{369}$$

where $\{\boldsymbol{r}_0\} = \left\{\boldsymbol{r}_{G_0}\right\} + \{\boldsymbol{u}_r\}$ and the following elements of $[\boldsymbol{\hbar}']$ and $\{\boldsymbol{\xi}\}$:

$\{\boldsymbol{h}'_1\} = \{\boldsymbol{i}'\}$, $\xi_1 = X'_G$

$\{\boldsymbol{h}'_2\} = \{\boldsymbol{j}'\}$, $\xi_2 = Y'_G$

$\{\boldsymbol{h}'_3\} = \{\boldsymbol{k}'\}$, $\xi_3 = Z'_G$

$\{\boldsymbol{h}'_4\} = [\boldsymbol{i}']\{\boldsymbol{u}'_r\}$, $\xi_4 = \theta_x$

$\{\boldsymbol{h}'_5\} = [\boldsymbol{j}']\{\boldsymbol{u}'_r\}$, $\xi_5 = \theta_y$

$\{\boldsymbol{h}'_6\} = [\boldsymbol{k}']\{\boldsymbol{u}'_r\}$, $\xi_6 = \theta_z$

$\{\boldsymbol{h}'_i\} = \left\{\boldsymbol{h}'_{f(i-6)}\right\}$, $\xi_i = \chi_{f(i-6)}$, $i = 7, 6 + N_f$ (370)

The total mode shape matrix $[\boldsymbol{\hbar}']$ becomes:

$$[\boldsymbol{\hbar}'] = \begin{bmatrix} 1 & 0 & 0 & 0 & z' & -y' & h'_{f1x'} & h'_{f2x'} & \dots & h'_{fN_fx'} \\ 0 & 1 & 0 & -z' & 0 & x' & h'_{f1y'} & h'_{f2y'} & \dots & h'_{fN_fy'} \\ 0 & 0 & 1 & y' & -x' & 0 & h'_{f1z'} & h'_{f2z'} & \dots & h'_{fN_fz'} \end{bmatrix} \tag{371}$$

so that the linear motion equation (363) can be simply written as:

$$[\boldsymbol{\mathcal{M}}]\{\ddot{\boldsymbol{\xi}}\} = \{\boldsymbol{\mathcal{F}}\} \tag{372}$$

where:

$$[\boldsymbol{\mathcal{M}}] = \iiint_{\forall_B} [\boldsymbol{\hbar}']^T[\boldsymbol{\hbar}']dm \quad , \quad \{\boldsymbol{\mathcal{F}}\} = \sum_{j=1}^{N} [\boldsymbol{\hbar}']^T\{\boldsymbol{f}'_j\} \tag{373}$$

This generalized formulation of the body dynamics is valid at first order only!

2. Potential flow theory of wave loads

2.1. Introduction

2.1.1 General

Similar to the body dynamics, there exist lot of literature on wave hydrodynamics and its linearization. The description adopted here follows is inspired from Molin & Marion (1985) and Ogilvie (1983) and the description for flexible body is based on Malenica et al. (2018) with some minor corrections.

2.1.2 Hydrodynamic coordinate system

In addition to the two coordinate systems introduced in [1.2], here the additional coordinate system (o, x, y, z), called hydrodynamic coordinate system, is introduced as shown in Figure 134. In the present context, the hydrodynamic coordinate system is the inertial coordinate system which is parallel to the earth fixed coordinate system (O, X, Y, Z) with the difference that its origin is placed at the mean free surface.

Figure 134: Definition of the hydrodynamic coordinate system $(\boldsymbol{o}, \boldsymbol{x}, \boldsymbol{y}, \boldsymbol{z})$

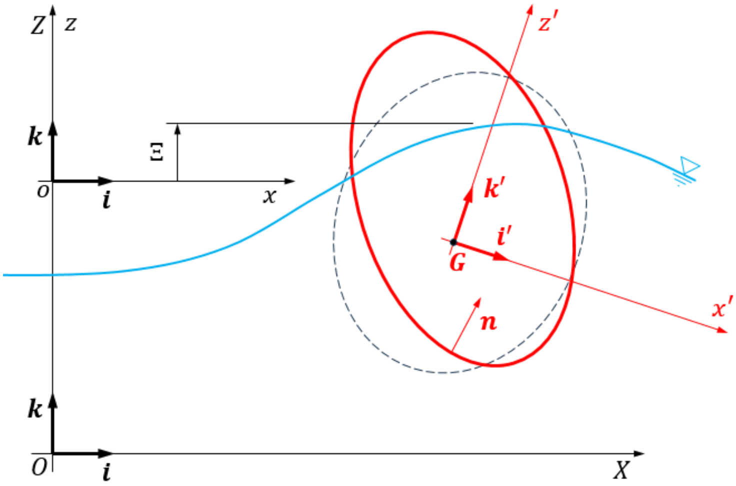

2.2. Fully nonlinear formulation

2.2.1 Governing equations

The fluid flow is described with respect to the hydrodynamic coordinate system (o, x, y, z) defined in Figure 134. Within the potential flow approach, which is of concern here, the fluid velocity vector **V** at any point in the fluid domain and at any time instant can be represented as the gradient of the velocity potential Φ which satisfies the Laplace equation in the domain:

$$\mathbf{V}(\boldsymbol{x}, t) = \nabla\Phi(\boldsymbol{X}, t) \quad , \quad \nabla^2\Phi(\boldsymbol{x}, t) = 0 \tag{374}$$

The total pressure in the fluid is calculated by the Bernoulli equation:

$$P(\boldsymbol{x}, t) = -\varrho\left[\frac{\partial\Phi}{\partial t} + \frac{1}{2}(\nabla\Phi)^2 + gz\right] + P_a + C(t) \tag{375}$$

where $C(t)$ is an arbitrary time dependent constant and P_a is the atmospheric pressure.

Without loss of generality the constant $C(t)$ is taken to be equal to $-P_a$ and the total pressure is usually split in hydrostatic pressure and hydrodynamic pressure parts as follows:

$$P(\boldsymbol{x}, t) = P^{hs}(\boldsymbol{x}, t) + P^{hd}(\boldsymbol{x}, t) \tag{376}$$

with:

$$P^{hs}(\boldsymbol{x}, t) = \quad -\varrho g z$$

$$P^{hd}(\boldsymbol{x}, t) = \quad -\varrho\left[\frac{\partial\Phi}{\partial t} + \frac{1}{2}(\nabla\Phi)^2\right]$$

2.2.2 Boundary conditions

In addition to the Laplace equation, the boundary value problem for the velocity potential requires the definition of the appropriate conditions at the boundaries of the fluid domain. In the present case the boundaries consist of the body surface, the free surface, the sea bed and infinity. At infinity we simply requires that the perturbation part of the velocity potential tends to zero in a manner which ensures the uniqness of the physical solution. The way in which the potential and the velocity tends to zero depends on the particularities of the Boundary Value Problem in consideration.

The conditions at other boundaries are described below

- Kinematic condition at material boundaries

The boundary conditions at the material boundaries are the kinematic conditions and describe the fact that there is no flow passing through the boundary. The mathematical description is:

$$\{\nabla\Phi\}^T\{\boldsymbol{n}\} = \{\boldsymbol{v}\}^T\{\boldsymbol{n}\} \tag{377}$$

where $\{\boldsymbol{v}\}$ is the local velocity of the point attached to the boundary and $\{\boldsymbol{n}\}$ is the local normal vector.

In the particular case of the seabed, the local velocity of the surface is zero while, in the case of the floating body, the local velocity follows from the description of the body motion (see [1.2]).

- Boundary conditions at the free surface

The case of non-overturning free surface is considered so that the instantaneous free surface position $\Xi(x,y,z,t)$ can be described by the following expression:

$$z - \Xi(x,y,t) = 0 \tag{378}$$

The free surface being material surface the kinematic boundary condition (377) applies and this condition can be written in the following form:

$$\left(\frac{\partial}{\partial t} + \nabla\Phi \cdot \nabla\right)[z - \Xi(x,y,t)] = 0 \tag{379}$$

The dynamic condition at the free surface follows from the requirement that the pressure in the fluid and in the air are equal. Knowing that, within the potential flow theory, the pressure is evaluated from the Bernoulli's equation the dynamic free surface condition becomes:

$$\frac{\partial\Phi}{\partial t} + \frac{1}{2}(\nabla\Phi)^2 = -g\Xi \tag{380}$$

Both the dynamic and kinematic free surface conditions are to be applied at the exact position of the free surface $z = \Xi$ which is unknown in advance. Within the potential flow formulation it is also possible to combine the kinematic and the dynamic boundary condition into one single condition, which gives:

$$\frac{\partial^2\Phi}{\partial t^2} + 2\nabla\Phi \cdot \nabla\frac{\partial\Phi}{\partial t} + \frac{1}{2}\nabla\Phi \cdot \nabla(\nabla\Phi)^2 + g\frac{\partial\Phi}{\partial Z} = 0 \tag{381}$$

2.2.3 Pressure loads

The most natural way to evaluate the pressure loads is to perform the direct pressure integration over the wetted body surface. Similar to the pressure decomposition (376), the resulting pressure loads $\{\boldsymbol{\mathcal{F}}^{p}\}$ are naturally decomposed into the hydrostatic loads $\{\boldsymbol{\mathcal{F}}^{hs}\}$ and the hydrodynamic loads $\{\boldsymbol{\mathcal{F}}^{hd}\}$:

$$\{\boldsymbol{\mathcal{F}}^{p}\} = \iint_{S_b} P\{\mathbb{N}\}dS = \{\boldsymbol{\mathcal{F}}^{hs}\} + \{\boldsymbol{\mathcal{F}}^{hd}\} \tag{382}$$

with:

$$\{\boldsymbol{\mathcal{F}}^{hs}\} = \quad -\varrho g \iint_{S_b} z\{\mathbb{N}\}dS$$

$$\{\boldsymbol{\mathcal{F}}^{hd}\} = \quad -\varrho \iint_{S_b} \left[\frac{\partial\Phi}{\partial t} + \frac{1}{2}(\nabla\Phi)^2\right]\{\mathbb{N}\}dS$$

where S_b denotes the instantaneous wetted part of the surface, and the generalized normal vector $\{\mathbb{N}\}$ (399),(433) is used which allows for compact definition of the loads (forces, moments and modal forces).

2.2.4 Conservation of momentum

The correct evaluation of the hydrodynamic loads represents the major problem in the numerical off shore hydrodynamics. The difficulties are related both to the evaluation of the hydrodynamic pressure as well as to the evaluation of the instantaneous wetted surface of the body. In the case of the rigid body, there exist the situations where the evaluation of the hydrodynamic loads can be significantly simplified by the use of the theorem of momentum conservation. This theorem states that the rate of change of the momentum (linear and the angular) in the fluid, is related to the external forces and the fluid flow at its boundaries, by the following expressions:

$$-\varrho\frac{d}{dt}\iiint_V \{\nabla\Phi\}\, dV = \quad \iint_S \left[P\{\boldsymbol{n}\} + \varrho\{\nabla\Phi\}\left(\frac{\partial\Phi}{\partial n} - \{\boldsymbol{v}\}^T\{\boldsymbol{n}\}\right)\right] dS \tag{383}$$

$$-\varrho\frac{d}{dt}\iiint_V [\boldsymbol{r}]\{\nabla\Phi\}\, dV = \quad \iint_S \left[P[\boldsymbol{r}]\{\boldsymbol{n}\} + \varrho[\boldsymbol{r}]\{\nabla\Phi\}\left(\frac{\partial\Phi}{\partial n} - \{\boldsymbol{v}\}^T\{\boldsymbol{n}\}\right)\right] dS \tag{384}$$

where *S* denotes the sum of all the surfaces enclosing the fluid volume *V* and $[\boldsymbol{r}]\{\boldsymbol{n}\}$ denotes the vector product of the position vector $\{\boldsymbol{r}\}$ and the normal vector $\{\boldsymbol{n}\}$.

The principle of momentum conservation can be used in many different contexts such as: the evaluation of the mean drift forces in waves, evaluation of the maneuvering forces, evaluation of the impact forces within the Wagner impact model … In particular, for the body evolving in an infinite fluid, the following expression for the hydrodynamic forces and moments can be deduced in the following form:

$$\{\boldsymbol{F}^{hd}\} = -\varrho \frac{d}{dt} \iint_{S_b} \Phi\{\boldsymbol{n}\}\, dS \quad , \quad \{\boldsymbol{M}^{hd}\} = -\varrho \frac{d}{dt} \iint_{S_b} \Phi[\boldsymbol{r}]\{\boldsymbol{n}\}\, dS \tag{385}$$

With some additional assumptions these expressions are employed for the evaluation of the slowly varying maneuvering forces in horizontal plane (see Section 4, [2]).

2.3. Linearization for rigid body

2.3.1 Basic principles

In general, the linearization procedure consists of two main steps. In the first step the physical quantity $q(\boldsymbol{x}, t)$ is developed in the perturbation series with respect to the small parameter ε and we write:

$$q = \varepsilon q^{(1)} + \varepsilon^2 q^{(2)} + O(\varepsilon^3) \tag{386}$$

At the same time, the change of the computational domain at each time instant is assumed to be small (Figure 135) and the boundary conditions are transferred from their instantaneous position $\{\boldsymbol{r}\}$ to their position at rest $\{\boldsymbol{r}_0\}$ by using the Taylor series expansion:

$$q(\boldsymbol{r}) = q(\boldsymbol{r}_0) + (\{\boldsymbol{r} - \boldsymbol{r}_0\}^T\{\nabla\})q(\boldsymbol{r}_0) + O(\{\boldsymbol{r} - \boldsymbol{r}_0\})^2 \tag{387}$$

where the operator $\{\boldsymbol{a}\}^T\{\nabla\}$ is defined by:

$$\{\boldsymbol{a}\}^T\{\nabla\} = a_x \frac{\partial}{\partial x} + a_y \frac{\partial}{\partial y} + a_z \frac{\partial}{\partial z} \tag{388}$$

Figure 135: Small body motions/deformations

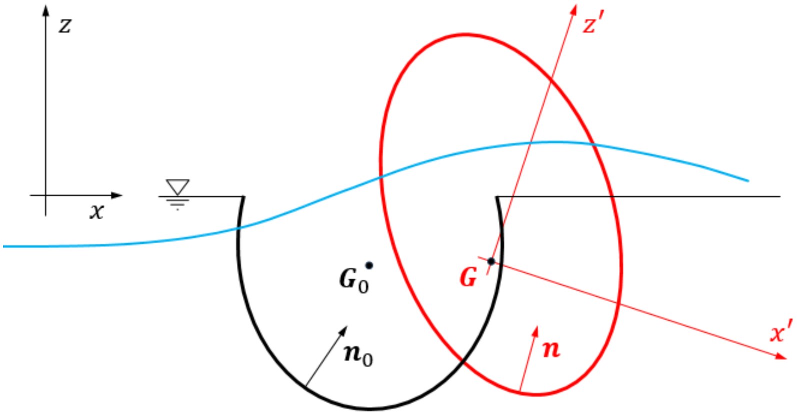

By assuming the displacement vector $\{\boldsymbol{r} - \boldsymbol{r}_0\}$ to be of the same small order ε and after introducing the above developments (386),(387), into the original fully nonlinear problem, the corresponding BVP's at different orders are deduced by collecting the terms of the same order. In practice only the first order $O(\varepsilon)$ and the second order $O(\varepsilon^2)$ are considered.

2.3.2 Boundary Value Problem

The velocity potential Φ is developed into the following perturbation series:

$$\Phi = \varepsilon\Phi^{(1)} + \varepsilon^2\Phi^{(2)} + O(\varepsilon^3) \tag{389}$$

It follows directly that the velocity potential at each order satisfies the Laplace equation while the boundary conditions needs to be carefully derived at different orders. The application of the linearization principles leads to the following expression for the fluid velocity:

$$\{\nabla\Phi\} = \varepsilon\{\nabla\Phi^{(1)}\} + \varepsilon^2\left[\{\nabla\Phi^{(2)}\} + \left(\{\boldsymbol{\delta}^{(1)}\}^T\{\nabla\}\right)\{\nabla\Phi^{(1)}\}\right] + O(\varepsilon^3) \tag{390}$$

where $\{\boldsymbol{\delta}^{(1)}\}^T$ denotes the linear distance between the instantaneous and mean position of the considered point which, in the case of the body boundary, corresponds to the displacement of the point attached to the body surface and, in the case of the free surface boundary, corresponds to the free surface elevation.

- Body boundary condition

The kinematic body boundary condition (377) states that the normal velocity of the body and the normal velocity of the fluid are equal at the boundary. The linearized description of the body motions is presented in [1.4] for both the rigid and the flexible bodies. In the case of rigid body, the corresponding local displacement $\{\boldsymbol{r}\}-\{\boldsymbol{r}_0\}$, the local velocity $\{\boldsymbol{v}\}$ and the normal vector at different orders, can be deduced as follows:

$$\begin{aligned}
\{\boldsymbol{r}\}-\{\boldsymbol{r}_{\boldsymbol{0}}\} &= \quad \{\boldsymbol{r}_G\}-\{\boldsymbol{r}_{G_0}\}+[\boldsymbol{A}]\{\boldsymbol{u}'\}=\varepsilon\{\boldsymbol{R}^{(1)}\}+\varepsilon^2\{\boldsymbol{R}^{(2)}\}+O(\varepsilon^3)\\
\{\boldsymbol{v}\} &= \quad \{\dot{\boldsymbol{r}}_G\}+[\boldsymbol{A}][\boldsymbol{\Omega}']\{\boldsymbol{u}'\}=\varepsilon\{\boldsymbol{v}^{(1)}\}+\varepsilon^2\{\boldsymbol{v}^{(2)}\}+O(\varepsilon^3)\\
\{\boldsymbol{n}\} &= \quad [\boldsymbol{A}]\{\boldsymbol{n}_0\}=\{\boldsymbol{n}_0\}+\varepsilon\{\boldsymbol{n}^{(1)}\}+\varepsilon^2\{\boldsymbol{n}^{(2)}\}+O(\varepsilon^3)
\end{aligned} \tag{391}$$

where:

$$\begin{aligned}
\{\boldsymbol{R}^{(1)}\}&=\{\boldsymbol{R}_G^{(1)}\}+[\boldsymbol{A}^{(1)}]\{\boldsymbol{u}'\} \quad , \quad \{\boldsymbol{R}^{(2)}\}=\{\boldsymbol{R}_G^{(2)}\}+[\boldsymbol{A}^{(2)}]\{\boldsymbol{u}'\}\\
\{\boldsymbol{v}^{(1)}\}&=\{\dot{\boldsymbol{R}}_G^{(1)}\}+[\boldsymbol{\Omega}'^{(1)}]\{\boldsymbol{u}'\} \quad , \quad \{\boldsymbol{v}^{(2)}\}=\{\dot{\boldsymbol{R}}_G^{(2)}\}+\left([\boldsymbol{\Omega}'^{(2)}]+[\boldsymbol{A}^{(1)}][\boldsymbol{\Omega}'^{(1)}]\right)\{\boldsymbol{u}'\}\\
\{\boldsymbol{n}^{(1)}\}&=[\boldsymbol{A}^{(1)}]\{\boldsymbol{n}_0\} \quad , \quad \{\boldsymbol{n}^{(2)}\}=[\boldsymbol{A}^{(2)}]\{\boldsymbol{n}_0\}
\end{aligned} \tag{392}$$

With this in mind, the body boundary conditions at first two orders follows in the form:

$$\{\nabla\Phi^{(1)}\}^T\{\boldsymbol{n}_0\} \quad = \quad \{\boldsymbol{v}^{(1)}\}^T\{\boldsymbol{n}_0\} \tag{393}$$

$$\{\nabla\Phi^{(2)}\}^T\{\boldsymbol{n}_0\} \quad = \quad \left[\{\boldsymbol{v}^{(2)}\}-\left(\{\boldsymbol{R}^{(1)}\}^T\{\nabla\}\right)\{\nabla\Phi^{(1)}\}\right]^T\{\boldsymbol{n}_0\}+\left(\{\boldsymbol{v}^{(1)}\}-\{\nabla\Phi^{(1)}\}\right)^T\{\boldsymbol{n}^{(1)}\} \tag{394}$$

– Free surface boundary condition

The nonlinear free surface condition (381) is developed at different orders by using the same principles. The final expressions for the free surface conditions and the corresponding free surface elevations at first two orders are:

$$O(\varepsilon) \qquad \frac{\partial^2\Phi^{(1)}}{\partial t^2}+g\frac{\partial\Phi^{(1)}}{\partial z} \; = \; 0 \tag{395}$$

$$O(\varepsilon^2) \qquad \frac{\partial^2\Phi^{(2)}}{\partial t^2}+g\frac{\partial\Phi^{(2)}}{\partial z} \; = \; -2\nabla\Phi^{(1)}\nabla\frac{\partial\Phi^{(1)}}{\partial t}+\frac{1}{g}\frac{\partial\Phi^{(1)}}{\partial t}\left[\frac{\partial^3\Phi^{(1)}}{\partial t^2\partial z}+g\frac{\partial^2\Phi^{(1)}}{\partial z^2}\right] \tag{396}$$

$$O(\varepsilon) \qquad \Xi^{(1)} \; = \; -\frac{1}{g}\frac{\partial\Phi^{(1)}}{\partial t} \tag{397}$$

$$O(\varepsilon^2) \qquad \Xi^{(2)} \; = \; -\frac{1}{g}\left[\frac{\partial\Phi^{(2)}}{\partial t}+\frac{1}{2}\left(\nabla\Phi^{(1)}\right)^2-\frac{1}{g}\frac{\partial\Phi^{(1)}}{\partial t}\frac{\partial^2\Phi^{(1)}}{\partial t\partial z}\right] \tag{398}$$

2.3.3 Forces

The external loads and the body motion equation are described relative to the body fixed coordinate system and the following compact notation for the forces and for the normal vectors are introduced:

$$\{\boldsymbol{\mathcal{F}}'\}=\begin{Bmatrix}\{\boldsymbol{F}'\}\\\{\boldsymbol{M}'\}\end{Bmatrix} \quad , \quad \{\mathbb{N}'\}=\begin{Bmatrix}\{\boldsymbol{n}'\}\\ [\boldsymbol{u}']\{\boldsymbol{n}'\}\end{Bmatrix} \tag{399}$$

where it should be noted that, in the case of the rigid body, the generalized normal vector $\{\mathbb{N}'\}$ is constant in the body fixed coordinate system and we have $\{\boldsymbol{n}'\}=\{\boldsymbol{n}_0\}$. Similar to all other physical quantities, the external load vector is developed into perturbation series as follows:

$$\{\boldsymbol{\mathcal{F}}'\}=\{\boldsymbol{\mathcal{F}}'^{(0)}\}+\varepsilon\{\boldsymbol{\mathcal{F}}'^{(1)}\}+\varepsilon^2\{\boldsymbol{\mathcal{F}}'^{(2)}\}+O(\varepsilon^3)$$

In the case of the freely floating body the total external forces $\{\boldsymbol{\mathcal{F}}'\}$ are composed of the gravity forces $\{\boldsymbol{\mathcal{F}}^{g\prime}\}$ and the hydrodynamics pressure forces $\{\boldsymbol{\mathcal{F}}^{h\prime}\}$ and these forces are considered separately below.

2.3.4 Gravity forces

Due to the fact that the motion equation is written with respect to the body center of gravity, the external moment is zero and the gravity force is constant in the earth fixed coordinate system. However, when expressed in the body fixed coordinate system, the gravity force is not constant but depends on the instantaneous orientation of the body as follows:

$$\{\boldsymbol{\mathcal{F}}^g\}=-mg\begin{Bmatrix}\{\boldsymbol{k}\}\\\{\boldsymbol{0}\}\end{Bmatrix} \quad , \quad \{\boldsymbol{\mathcal{F}}^{g\prime}\}=-mg\begin{Bmatrix}[\boldsymbol{A}]^T\{\boldsymbol{k}\}\\\{\boldsymbol{0}\}\end{Bmatrix} \tag{400}$$

After developing the transformation matrix at different orders, the following expressions are obtained:

$$\left\{\boldsymbol{\mathcal{F}}^{g'(0)}\right\} = \quad -mg\begin{Bmatrix}\{\boldsymbol{k}\}\\ \{\boldsymbol{0}\}\end{Bmatrix} \tag{401}$$

$$\left\{\boldsymbol{\mathcal{F}}^{g'(1)}\right\} = \quad -mg\begin{Bmatrix}\left[\boldsymbol{A}^{(1)}\right]^T\{\boldsymbol{k}\}\\ \{\boldsymbol{0}\}\end{Bmatrix} \tag{402}$$

$$\left\{\boldsymbol{\mathcal{F}}^{g'(2)}\right\} = \quad -mg\begin{Bmatrix}\left[\boldsymbol{A}^{(2)}\right]^T\{\boldsymbol{k}\}\\ \{\boldsymbol{0}\}\end{Bmatrix} \tag{403}$$

2.3.5 Pressure induced forces

The surface integral over the instantaneous wetted surface S_b is subdivided into the integral over the mean wetted surface S_B and the integral over the surface δS_B which is the difference between S_b and S_B:

$$\left\{\boldsymbol{\mathcal{F}}^{h'}\right\} = \iint_{S_b} P\{\mathbb{N}'\}dS = \iint_{S_B} P\{\mathbb{N}'\}dS + \iint_{\delta S_B} P\{\mathbb{N}'\}dS \tag{404}$$

The pressure is calculated from the Bernoulli's equation (375) which is developed into different orders.

Following the pressure loads decomposition (382) the different components become:

- Hydrostatic forces

The instantaneous hydrostatic pressure $-\varrho gz$ is found by projecting the instantaneous position vector $\{\boldsymbol{r}\}$ onto the unit vector in vertical direction:

$$z = \{\boldsymbol{r}\}^{\boldsymbol{T}}\{\boldsymbol{k}\} = \{\boldsymbol{r_0}\}^{\boldsymbol{T}}\{\boldsymbol{k}\} + \ \varepsilon\left\{\boldsymbol{R}^{(1)}\right\}^{\boldsymbol{T}}\{\boldsymbol{k}\} + \varepsilon^2\left\{\boldsymbol{R}^{(2)}\right\}^{\boldsymbol{T}}\{\boldsymbol{k}\} = Z^{(0)} + \varepsilon Z^{(1)} + \varepsilon^2 Z^{(2)} \tag{405}$$

After introducing this expression in (404) and collecting the terms of the same order in ε the following expressions up to second order are obtained:

$$\left\{\boldsymbol{\mathcal{F}}^{hs'(0)}\right\} = \quad -\varrho g\iint_{S_B} Z^{(0)}\{\mathbb{N}'\}dS \tag{406}$$

$$\left\{\boldsymbol{\mathcal{F}}^{hs'(1)}\right\} = \quad -\varrho g\iint_{S_B} Z^{(1)}\{\mathbb{N}'\}dS \tag{407}$$

$$\left\{\boldsymbol{\mathcal{F}}^{hs'(2)}\right\} = \quad -\varrho g\iint_{S_B} Z^{(2)}\{\mathbb{N}'\}dS - \frac{1}{2}\varrho g\int_{C_B}\left[\left(\Xi^{(1)}\right)^2 - \left(\mathrm{Z}^{(1)}\right)^2\right]\frac{\{\mathbb{N}'\}}{\cos\gamma}dC \tag{408}$$

where C_B denotes the mean waterline and γ is the angle between the body normal vector and the mean water surface level. This integral results from the integration over the perturbation wetted surface δS_B.

- Hydrodynamic forces

The hydrodynamic force vector $\{\boldsymbol{\mathcal{F}}^{hd'}\}$ follows from the integration of the hydrodynamic pressure which can be re-written in the following form:

$$P^d = -\varrho\frac{\partial\Phi}{\partial t} - \frac{1}{2}\varrho\{\nabla\Phi\}^2 = \varepsilon P^{(1)} + \varepsilon^2 P^{(2)} + O(\varepsilon^3) \tag{409}$$

with:

$$P^{(1)} = \quad -\varrho\frac{\partial\Phi^{(1)}}{\partial t} \tag{410}$$

$$P^{(2)} = \quad -\varrho\frac{\partial\Phi^{(2)}}{\partial t} - \frac{1}{2}\varrho\left\{\nabla\Phi^{(1)}\right\}^2 - \varrho\left(\left\{\boldsymbol{R}^{(1)}\right\}^T\{\nabla\}\right)\frac{\partial\Phi^{(1)}}{\partial t} \tag{411}$$

After performing the integration over the wetted body surface, the following expressions up to second order are obtained:

$$\left\{\boldsymbol{\mathcal{F}}^{hd'(0)}\right\} = \quad 0 \tag{412}$$

$$\left\{\boldsymbol{\mathcal{F}}^{hd'(1)}\right\} = \quad \iint_{S_B} P^{(1)}\{\mathbb{N}'\}dS \tag{413}$$

$$\left\{\boldsymbol{\mathcal{F}}^{hd'(2)}\right\} = \quad \iint_{S_B} P^{(2)}\{\mathbb{N}'\}dS + \varrho g\int_{C_B}\Xi^{(1)}\left(\Xi^{(1)} - Z^{(1)}\right)\frac{\{\mathbb{N}'\}}{\cos\gamma}dC \tag{414}$$

2.4. Linearization for flexible body

2.4.1 Introduction

In the case of flexible body the basic principles of the linearization remain the same and the main additional difficulties are related to the description of the body boundary condition. In order to define the instantaneous body shape, it is convenient to introduce the notion of the deformation gradient $[\mathbf{F}]$, which is defined relative to the coordinate system fixed to the rigid body, as follows:

$$[\mathbf{F}] = [\boldsymbol{I}] + [\nabla \boldsymbol{u}_f'] \quad , \quad [\nabla \boldsymbol{u}_f'] = \begin{bmatrix} \dfrac{\partial u_{fx'}'}{\partial x'} & \dfrac{\partial u_{fx'}'}{\partial y'} & \dfrac{\partial u_{fx'}'}{\partial z'} \\ \dfrac{\partial u_{fy'}'}{\partial x'} & \dfrac{\partial u_{fy'}'}{\partial y'} & \dfrac{\partial u_{fy'}'}{\partial z'} \\ \dfrac{\partial u_{fz'}'}{\partial x'} & \dfrac{\partial u_{fz'}'}{\partial y'} & \dfrac{\partial u_{fz'}'}{\partial z'} \end{bmatrix} \tag{415}$$

It follows that the instantaneous body normal vector can be written as:

$$\{\boldsymbol{n}'\} dS_b = \|\mathbf{F}\| ([\mathbf{F}]^{-1})^{\boldsymbol{T}} \{\boldsymbol{n}_0\} dS_B \tag{416}$$

This expression can be developed up to order $O\left({\boldsymbol{u}_f'}^2\right)$ as:

$$\|\mathbf{F}\| ([\mathbf{F}]^{-1})^{\boldsymbol{T}} = 1 + \nabla \boldsymbol{u}_f' - [\nabla \boldsymbol{u}_f']^T + [\mathbf{Q}]^T + O\left({\boldsymbol{u}_f'}^2\right) \tag{417}$$

where $[\mathbf{Q}]^T$ is given by:

$$[\mathbf{Q}]^T = \left[\left\{ \frac{\partial \boldsymbol{u}_f'}{\partial y'} \wedge \frac{\partial \boldsymbol{u}_f'}{\partial z'} \right\} \quad \left\{ \frac{\partial \boldsymbol{u}_f'}{\partial z'} \wedge \frac{\partial \boldsymbol{u}_f'}{\partial x'} \right\} \quad \left\{ \frac{\partial \boldsymbol{u}_f'}{\partial x'} \wedge \frac{\partial \boldsymbol{u}_f'}{\partial y'} \right\} \right] \tag{418}$$

2.4.2 Boundary conditions

The free surface boundary condition at different orders remains formally the same as in the rigid body case (395),(396) but the body boundary condition needs to be modified in order to account for the velocity induced by the body deformations. The total body motion is composed of the rigid body motion, defined by the translation of the body's center of gravity and by the instantaneous transformation matrix $[\boldsymbol{A}]$, and of the body deformations around the instantaneous position of the rigid body. The local displacement and the local velocities of the point attached to the body are given in [1.2] and the following expressions, up to second order, can be deduced:

$$\{\boldsymbol{r}\} - \{\boldsymbol{r}_0\} = \varepsilon\{\boldsymbol{R}^{(1)}\} + \varepsilon^2\{\boldsymbol{R}^{(2)}\} \quad , \quad \{\boldsymbol{v}\} = \varepsilon\{\boldsymbol{v}^{(1)}\} + \varepsilon^2\{\boldsymbol{v}^{(2)}\} \tag{419}$$

with:

$$\begin{aligned} \{\boldsymbol{R}^{(1)}\} &= \{\boldsymbol{R}_G^{(1)}\} + [\boldsymbol{A}^{(1)}]\{\boldsymbol{u}_r'\} + \{\boldsymbol{u}_f'^{(1)}\} \\ \{\boldsymbol{R}^{(2)}\} &= \{\boldsymbol{R}_G^{(2)}\} + [\boldsymbol{A}^{(2)}]\{\boldsymbol{u}_r'\} + \{\boldsymbol{u}_f'^{(2)}\} + [\boldsymbol{A}^{(1)}]\{\boldsymbol{u}_f'^{(1)}\} \\ \{\boldsymbol{v}^{(1)}\} &= \{\dot{\boldsymbol{R}}_G^{(1)}\} + [\boldsymbol{\Omega}'^{(1)}]\{\boldsymbol{u}_r'\} + \{\dot{\boldsymbol{u}}_f'^{(1)}\} \\ \{\boldsymbol{v}^{(2)}\} &= \{\dot{\boldsymbol{R}}_G^{(2)}\} + [\boldsymbol{\Omega}'^{(2)}]\{\boldsymbol{u}_r'\} + \{\dot{\boldsymbol{u}}_f'^{(2)}\} + [\boldsymbol{\Omega}'^{(1)}]\{\boldsymbol{u}_f'^{(1)}\} + [\boldsymbol{A}^{(1)}]\left([\boldsymbol{\Omega}'^{(1)}]\{\boldsymbol{u}_r'\} + \{\dot{\boldsymbol{u}}_f'^{(1)}\}\right) \end{aligned} \tag{420}$$

At the same time the normal vector can be written as:

$$\{\boldsymbol{n}\} = [\boldsymbol{A}]\{\boldsymbol{n}'\} = [\boldsymbol{A}]\left(1 + \nabla \boldsymbol{u}_f' - [\nabla \boldsymbol{u}_f']^T + [\mathbf{Q}]^T\right)\{\boldsymbol{n}_0\} = \{\boldsymbol{n}_0\} + \varepsilon\{\boldsymbol{n}^{(1)}\} + \varepsilon^2\{\boldsymbol{n}^{(2)}\} \tag{421}$$

with

$$\{\boldsymbol{n}^{(1)}\} = \left(\nabla \boldsymbol{u}_f'^{(1)} - [\nabla \boldsymbol{u}_f'^{(1)}]^T + [\boldsymbol{A}^{(1)}]\right)\{\boldsymbol{n}_0\} \tag{422}$$

$$\{\boldsymbol{n}^{(2)}\} = \left(\nabla \boldsymbol{u}_f'^{(2)} - [\nabla \boldsymbol{u}_f'^{(2)}]^T + [\mathbf{Q}^{(1)}]^T + [\boldsymbol{A}^{(2)}] + [\boldsymbol{A}^{(1)}]\left(\nabla \boldsymbol{u}_f'^{(1)} - [\nabla \boldsymbol{u}_f'^{(1)}]^T\right)\right)\{\boldsymbol{n}_0\} \tag{423}$$

where $[\mathbf{Q}^{(1)}]^T$ is obtained by replacing $\{\boldsymbol{u}_f'\}$ by $\{\boldsymbol{u}_f'^{(1)}\}$ in (418).

The fluid flow velocity being given by the same expression as in the rigid body case, the body boundary condition remains formally the same as (393),(394) provided that the values of $\{\boldsymbol{R}^{(1)}\}$, $\{\boldsymbol{v}^{(1)}\}$, $\{\boldsymbol{v}^{(2)}\}$ and $\{\boldsymbol{n}^{(1)}\}$ are replaced by (420),(422) and (423).

2.4.3 Forces

The modal approach is considered (see [1.2.5]) and the body deformations are described by a certain number of flexible modes. These additional modes of body motions/deformations are defined with respect to the body fixed coordinate system and the modal forces are given by the expression (361). It has to be noted that the modal force is scalar quantity given by the scalar product of the instantaneous local force vector and the instantaneous local modal displacement vector. The scalar product can be performed either in the hydrodynamic coordinate system or in the body fixed coordinate system. Since the additional flexible modes are defined in the body fixed coordinate system it is more convenient to perform the scalar product in this coordinate system. For that purpose, the instantaneous modal displacement vector is developed into Taylor series expansion, in the body fixed coordinate system, as follows:

$$\{\widetilde{\boldsymbol{h}}'_{fi}\} = \left(1 + \{\boldsymbol{u}'_f\}^T\{\nabla\}\right)\{\boldsymbol{h}'_{fi}\} = \{\boldsymbol{h}'_{fi}\} + [\nabla\boldsymbol{h}'_{fi}]\{\boldsymbol{u}'_f\} = \{\boldsymbol{h}'_{fi}\} + \varepsilon\left\{\widetilde{\boldsymbol{h}}'^{(1)}_{fi}\right\} + \varepsilon^2\left\{\widetilde{\boldsymbol{h}}'^{(2)}_{fi}\right\} \tag{424}$$

where the values at first and second orders are given by:

$$\left\{\widetilde{\boldsymbol{h}}'^{(1)}_{fi}\right\} = \quad [\nabla\boldsymbol{h}'_{fi}]\left\{\boldsymbol{u}'^{(1)}_f\right\} \tag{425}$$

$$\left\{\widetilde{\boldsymbol{h}}'^{(2)}_{fi}\right\} = \quad [\nabla\boldsymbol{h}'_{fi}]\left\{\boldsymbol{u}'^{(2)}_f\right\} \tag{426}$$

2.4.4 Gravity forces

After taking into account the fact that the elementary gravity force vector is constant in the hydrodynamic coordinate system, and after accounting for (424), the total gravity induced force vector $\{\boldsymbol{\mathcal{F}}^{g\prime}\}$ can be developed as follows:

$$\{\boldsymbol{\mathcal{F}}^{g\prime}\} = \{\boldsymbol{\mathcal{F}}^{g\prime(0)}\} + \varepsilon\{\boldsymbol{\mathcal{F}}^{g\prime(1)}\} + \varepsilon^2\{\boldsymbol{\mathcal{F}}^{g\prime(2)}\} \tag{427}$$

with:

$$\{\boldsymbol{\mathcal{F}}^{g\prime(0)}\} = \quad -\sum_{j=1}^{N} m_j g \begin{Bmatrix} \{\boldsymbol{k}\} \\ [\boldsymbol{u}'_r]\{\boldsymbol{k}\} \\ \left\{\{\boldsymbol{h}'_{fi}\}^T\{\boldsymbol{k}\}\right\} \end{Bmatrix} \tag{428}$$

$$\{\boldsymbol{\mathcal{F}}^{g\prime(1)}\} = \quad -\sum_{j=1}^{N} m_j g \begin{Bmatrix} [\boldsymbol{A}^{(1)}]\{\boldsymbol{k}\} \\ [\boldsymbol{u}'_r][\boldsymbol{A}^{(1)}]\{\boldsymbol{k}\} + \left[\boldsymbol{u}'^{(1)}_f\right][\boldsymbol{A}^{(1)}]\{\boldsymbol{k}\} \\ \left\{\{\boldsymbol{h}'_{fi}\}^T[\boldsymbol{A}^{(1)}]\{\boldsymbol{k}\} + \left\{\widetilde{\boldsymbol{h}}'^{(1)}_{fi}\right\}^T\{\boldsymbol{k}\}\right\} \end{Bmatrix} \tag{429}$$

$$\{\boldsymbol{\mathcal{F}}^{g\prime(2)}\} = \quad -\sum_{j=1}^{N} m_j g \begin{Bmatrix} [\boldsymbol{A}^{(2)}]\{\boldsymbol{k}\} \\ [\boldsymbol{u}'_r][\boldsymbol{A}^{(2)}]\{\boldsymbol{k}\} + \left[\boldsymbol{u}'^{(1)}_f\right][\boldsymbol{A}^{(1)}]\{\boldsymbol{k}\} + \left[\boldsymbol{u}'^{(2)}_f\right]\{\boldsymbol{k}\} \\ \left\{\{\boldsymbol{h}'_{fi}\}^T[\boldsymbol{A}^{(2)}]\{\boldsymbol{k}\} + \left\{\widetilde{\boldsymbol{h}}'^{(1)}_{fi}\right\}^T[\boldsymbol{A}^{(1)}]\{\boldsymbol{k}\} + \left\{\widetilde{\boldsymbol{h}}'^{(2)}_{fi}\right\}^T\{\boldsymbol{k}\}\right\} \end{Bmatrix} \tag{430}$$

By putting $\{\boldsymbol{u}'_f\} = 0$, the case of the rigid body is recovered. It can also be observed that due to the presence of the flexible body modes the rigid body moment is also modified by the body deformations.

2.4.5 Pressure induced forces

One of the important differences between the rigid and flexible body is the fact that, for the rigid body case, the normal vector remains constant in the body fixed coordinate system i.e. $\{\boldsymbol{n}'\} = \{\boldsymbol{n}_0\}$, while, for the flexible body it does not so that $\{\boldsymbol{n}'\} \neq \{\boldsymbol{n}_0\}$. The modifications of the normal vector were discussed in [2.4] where the corresponding expressions at different orders were given in the hydrodynamic coordinate system (422),(423). The corresponding expressions in the body fixed coordinate system are:

$$\{\boldsymbol{n}'\} = \left(1 + \nabla\boldsymbol{u}'_f - [\nabla\boldsymbol{u}'_f]^T + [\boldsymbol{Q}]^T\right)\{\boldsymbol{n}_0\} = \{\boldsymbol{n}_0\} + \varepsilon\{\boldsymbol{n}'^{(1)}\} + \varepsilon^2\{\boldsymbol{n}'^{(2)}\} \tag{431}$$

with

$$\{\boldsymbol{n}'^{(1)}\} = \quad \left(\nabla\boldsymbol{u}'^{(1)}_f - \left[\nabla\boldsymbol{u}'^{(1)}_f\right]^T\right)\{\boldsymbol{n}_0\}$$

$$\{\boldsymbol{n}'^{(2)}\} = \quad \left(\nabla\boldsymbol{u}'^{(2)}_f - \left[\nabla\boldsymbol{u}'^{(2)}_f\right]^T + [\boldsymbol{Q}^{(1)}]^T\right)\{\boldsymbol{n}_0\} \tag{432}$$

It is convenient to define the following generalized normal vector $\{\mathbb{N}'\}$:

$$\{\mathbb{N}'\} = \left\{ \begin{matrix} \{\boldsymbol{n}'\} \\ [\boldsymbol{u}']\{\boldsymbol{n}'\} \\ \left\{\{\widetilde{\boldsymbol{h}}'_{fi}\}^T\{\boldsymbol{n}'\}\right\} \end{matrix} \right\} = \{\mathbb{N}'^{(0)}\} + \varepsilon\{\mathbb{N}'^{(1)}\} + \varepsilon^2\{\mathbb{N}'^{(2)}\} \tag{433}$$

with:

$$\{\mathbb{N}'^{(0)}\} = \left\{ \begin{matrix} \{\boldsymbol{n}_0\} \\ [\boldsymbol{u}'_r]\{\boldsymbol{n}_0\} \\ \left\{\{\boldsymbol{h}'_{fi}\}^T\{\boldsymbol{n}_0\}\right\} \end{matrix} \right\} \tag{434}$$

$$\{\mathbb{N}'^{(1)}\} = \left\{ \begin{matrix} \{\boldsymbol{n}'^{(1)}\} \\ [\boldsymbol{u}'_r]\{\boldsymbol{n}'^{(1)}\} + \left[\boldsymbol{u}'^{(1)}_f\right]\{\boldsymbol{n}_0\} \\ \left\{\{\boldsymbol{h}'_{fi}\}^T\{\boldsymbol{n}'^{(1)}\} + \left\{\widetilde{\boldsymbol{h}}'^{(1)}_{fi}\right\}^T\{\boldsymbol{n}_0\}\right\} \end{matrix} \right\} \tag{435}$$

$$\{\mathbb{N}'^{(2)}\} = \left\{ \begin{matrix} \{\boldsymbol{n}'^{(2)}\} \\ [\boldsymbol{u}'_r]\{\boldsymbol{n}'^{(2)}\} + \left[\boldsymbol{u}'^{(1)}_f\right]\{\boldsymbol{n}'^{(1)}\} + \left[\boldsymbol{u}'^{(2)}_f\right]\{\boldsymbol{n}_0\} \\ \left\{\{\boldsymbol{h}'_{fi}\}^T\{\boldsymbol{n}'^{(2)}\} + \left\{\widetilde{\boldsymbol{h}}'^{(1)}_{fi}\right\}^T\{\boldsymbol{n}'^{(1)}\} + \left\{\widetilde{\boldsymbol{h}}'^{(2)}_{fi}\right\}^T\{\boldsymbol{n}_0\}\right\} \end{matrix} \right\} \tag{436}$$

The total pressure being given by the Bernoulli equation (375) and the expressions for the pressure at different orders, remain the same as in the rigid body case (405),(409) provided that the local displacements $\{\boldsymbol{R}^{(1)}\}$ and $\{\boldsymbol{R}^{(2)}\}$ includes the body deformations too (420). By keeping the same notations for the pressure components the expressions for the pressure forces on flexible body become:

- Hydrostatic forces

$$\{\boldsymbol{\mathcal{F}}^{hs'(0)}\} = -\varrho g \iint_{S_B} Z^{(0)}\{\mathbb{N}'^{(0)}\}dS \tag{437}$$

$$\{\boldsymbol{\mathcal{F}}^{hs'(1)}\} = -\varrho g \iint_{S_B} (Z^{(1)}\{\mathbb{N}'^{(0)}\} + Z^{(0)}\{\mathbb{N}'^{(1)}\})dS \tag{438}$$

$$\{\boldsymbol{\mathcal{F}}^{hs'(2)}\} = -\varrho g \iint_{S_B} (Z^{(2)}\{\mathbb{N}'^{(0)}\} + Z^{(1)}\{\mathbb{N}'^{(1)}\} + Z^{(0)}\{\mathbb{N}'^{(2)}\})dS \tag{439}$$

$$-\frac{1}{2}\varrho g \int_{C_B} \left[\left(\Xi^{(1)}\right)^2 - \left(\mathrm{Z}^{(1)}\right)^2\right]\frac{\{\mathbb{N}'^{(0)}\}}{\cos\gamma}dC \tag{440}$$

- Hydrodynamic forces

$$\{\boldsymbol{\mathcal{F}}^{hd'(0)}\} = 0 \tag{441}$$

$$\{\boldsymbol{\mathcal{F}}^{hd'(1)}\} = \iint_{S_B} P^{(1)}\{\mathbb{N}'^{(0)}\}dS \tag{442}$$

$$\{\boldsymbol{\mathcal{F}}^{hd'(2)}\} = \iint_{S_B} (P^{(2)}\{\mathbb{N}'^{(0)}\} + P^{(1)}\{\mathbb{N}'^{(1)}\})dS + \varrho g \int_{C_B} \Xi^{(1)}(\Xi^{(1)} - Z^{(1)})\frac{\{\mathbb{N}'\}}{\cos\gamma}dC \tag{443}$$

2.4.6 Wave loads within the generalized modal approach

Within the generalized modal approach for the linear body dynamics (see [1.4.4]) the straightforward application of the linearization procedure leads to the following expressions for the linear wave loads:

$$F^g_{fi} = -\sum_{j=1}^{N_m} m_j g \left(\{\boldsymbol{h}'_i\}^T[\boldsymbol{\theta}] + \{\boldsymbol{u}'_f\}^T[\nabla\boldsymbol{h}'_i]^T\right)\{\boldsymbol{k}\} \tag{444}$$

$$\mathcal{F}^{hs}_i = -\varrho g \iint_{S_B} \left[\zeta_v\{\boldsymbol{h}'_i\}^T + z\left(\{\boldsymbol{h}'_i\}^T\left(\nabla\boldsymbol{u}'_f - [\nabla\boldsymbol{u}'_f]^T\right) + \{\boldsymbol{u}'_f\}^T[\nabla\boldsymbol{h}'_i]^T\right)\right]\{\boldsymbol{n}_0\}dS \tag{445}$$

$$\mathcal{F}^{hd}_i = -\varrho \iint_{S_B} \frac{\partial\Phi}{\partial t}\{\boldsymbol{h}'_i\}^T\{\boldsymbol{n}_0\}dS \tag{446}$$

3. Boundary Integral Equation Methods

3.1. Introduction

There exist a large amount of literature on the application of the BIE Methods to wave body interactions. The description adopted here closely follows the BV in house work initiated by Chen (1988) around the numerical tool HYDROSTAR.

3.1.1 Generic Boundary Value Problem

Reference is made to Figure 136 where the different boundaries of the fluid domain, together with the associated boundary conditions, are presented.

Figure 136: Generic BVP definition

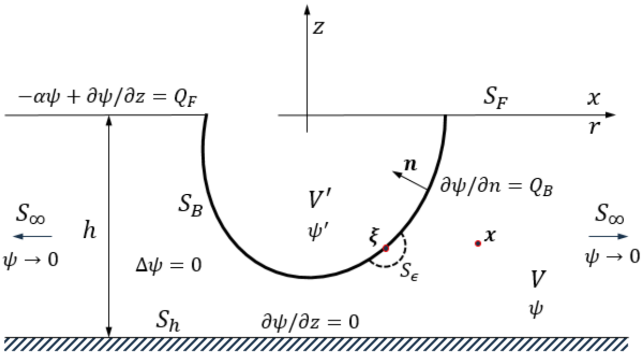

The generic BVP for velocity potential $\psi(\boldsymbol{x})$ is defined by the following set of equations:

$$\left.\begin{array}{ll} \Delta\psi = 0 & 0 \geq z \geq -h \\ -\alpha\psi + \dfrac{\partial\psi}{\partial z} = Q_F & z = 0 \\ \dfrac{\partial\psi}{\partial n} = Q_B & S_B \\ \dfrac{\partial\psi}{\partial z} = 0 & z = -h \\ \psi \to 0 & r \to \infty \end{array}\right\} \tag{447}$$

where Q_F and Q_B are the nonhomogeneous forcing terms at the free surface and the body surface respectively, and α is the parameter associated with the oscillation frequency ($\alpha = \omega^2/g$ in the linear case, $\alpha = 4\omega^2/g$ in the second order case …).

The dispersion relation associated with the free surface condition can be written in the form:

$$\kappa_0 \tanh \kappa_0 h = \alpha \tag{448}$$

The solution of this equation gives the wave number κ_0 which defines the characteristic wave length.

3.2. Boundary Integral Equation Method

3.2.1 Basic principles

The most widely used numerical methods for the resolution of above BVP are based on the Boundary Integral Equations technique (BIE). This method takes the advantage that the velocity potential satisfying the Laplace equation in the fluid allows the use of the Green's identities for representing the potential as a distribution of singularities over boundary surfaces only. The method requires an appropriate choice of Green's functions which can be defined in different ways. For the time-harmonic problem, the Green's function is classically defined as the real part of

$$\mathrm{G}(\boldsymbol{x};\boldsymbol{\xi},\boldsymbol{t}) = \mathrm{Re}\{G(\boldsymbol{x};\boldsymbol{\xi})e^{i\omega t}\}$$

in which the spatial Green's function $G(\boldsymbol{x};\boldsymbol{\xi})$ is usually classified into two main types commonly denoted as the Rankine and the Kelvin Green functions.

3.2.2 Green's function of Rankine type

The Rankine type Green's function is the fundamental solution of Poisson equation in the whole physical space R^3 :

$$\Delta G = \delta(\boldsymbol{x};\boldsymbol{\xi}) \tag{449}$$

where $\delta(\boldsymbol{x};\boldsymbol{\xi})$ denotes the Dirac delta function. Strictly speaking, (3) is a Poisson equation due to the non-zero right hand side.

The simplest solution of (449) is easily found in the form:

$$G(\boldsymbol{x};\boldsymbol{\xi}) = -\frac{1}{4\pi \boldsymbol{r}} \tag{450}$$

where $\boldsymbol{r}$ is the distance between the field point $\boldsymbol{x}$ and the singularity point $\boldsymbol{\xi}$ i.e. $\boldsymbol{r} = |\boldsymbol{x} - \boldsymbol{\xi}|$.

Physically the Green function represents the potential at any point $\boldsymbol{x} = (x, y, z)$ in the fluid due to a source placed at $\boldsymbol{\xi} = (\xi, \eta, \zeta)$. The direct application of the Green's second identity leads to the following representation for the potential at any point in the fluid domain:

$$\psi(\boldsymbol{x}) = \iint_{S_B+S_F+S_h+S_\infty} \left(G(\boldsymbol{x};\boldsymbol{\xi}) \frac{\partial \psi(\boldsymbol{\xi})}{\partial n_\xi} - \psi(\boldsymbol{\xi}) \frac{\partial G(\boldsymbol{x};\boldsymbol{\xi})}{\partial n_\xi} \right) dS_\xi \quad , \quad \boldsymbol{x} \in V \tag{451}$$

The main drawback of the BIE method based on the Rankine type Green's function, is the fact that the surface integrals apply over all boundaries of the fluid domain. In principle the integral over the surface at infinity disappears and, at the same time, the integral over the seabed can be removed by adding an additional (image) source point at $(\xi, \eta, \zeta - 2h)$, but it is not possible to avoid the integral over the free surface! This is rather impractical, not only because the number of unknowns will increase but also because the free surface theoretically extends to infinity and it is necessary to introduce the additional assumptions in order to satisfy the radiation condition. For these reasons, the Kelvin type Green's function is usually preferred.

3.2.3 Green's function of Kelvin type

The Kelvin type Green's function $G(\boldsymbol{x};\boldsymbol{\xi})$ is defined as a solution of the following system of equations:

$$\left.\begin{array}{ll} \Delta G = \delta(\boldsymbol{x};\boldsymbol{\xi}) & 0 \geq z \geq -h \\ -\alpha G + \dfrac{\partial G}{\partial z} = 0 & z = 0 \\ \dfrac{\partial G}{\partial z} = 0 & z = -h \\ \sqrt{\kappa_0 R} \left(\dfrac{\partial G}{\partial R} + i\kappa_0 G \right) \to 0 & R \to \infty \end{array}\right\} \tag{452}$$

where κ_0 is the wave number (141), and R denotes the horizontal distance $R = \sqrt{x^2 + y^2}$.

The Kelvin type Green's function satisfies, in addition to Poisson equation in the fluid, the homogenous boundary conditions at the free surface, no flow condition at the sea bed and the radiation condition at infinity. The Kelvin type Green's function can be found using the Fourier transform technique and written generally in the following form:

$$G(\boldsymbol{x};\boldsymbol{\xi}) = -\frac{1}{4\pi \boldsymbol{r}} + H(\boldsymbol{x};\boldsymbol{\xi}) \tag{453}$$

As can be seen an additional term $H(\boldsymbol{x};\boldsymbol{\xi})$ is added to the fundamental solution (450) in order to satisfy the boundary conditions at the free surface, at the sea bed and at infinity. The consequence is that the surface integrals at the free surface, sea bottom and infinity in (451) disappears and only the surface integral on body surface remains. Two types of the BIE methods based on Kelvin Green function are commonly used, namely the mixed distribution method and the source only distribution method. The mixed distribution method relies on the direct application of the Green second identity, and the final expression for the velocity potential ψ at any point in the fluid is obtained in the form:

$$\psi(\boldsymbol{x}) = -\iint_{S_B} \psi(\boldsymbol{\xi}) \frac{\partial G(\boldsymbol{x};\boldsymbol{\xi})}{\partial n_\xi} dS_\xi + \iint_{S_B} G(\boldsymbol{x};\boldsymbol{\xi}) Q_B(\boldsymbol{\xi}) dS_\xi - \iint_{S_F} G(\boldsymbol{x};\boldsymbol{\xi}) Q_F(\boldsymbol{\xi}) dS_\xi \ , \ \boldsymbol{x} \in V \tag{454}$$

where we note that the symmetry property of the Green's function [$G(\boldsymbol{x};\boldsymbol{\xi}) = G(\boldsymbol{\xi};\boldsymbol{x})$] was used when deriving the above expression.

The unknown on the body (dipole strength) are evaluated from the following BIE which is obtained after carrying out the limiting process for the points at the body surface $\boldsymbol{x} \in S_B$:

$$\frac{1}{2}\psi(\boldsymbol{x}) + \iint_{S_B} \psi(\boldsymbol{\xi})\frac{\partial G(\boldsymbol{x};\boldsymbol{\xi})}{\partial n_\xi} dS_\xi = \iint_{S_B} G(\boldsymbol{x};\boldsymbol{\xi})Q_B(\boldsymbol{\xi})dS_\xi - \iint_{S_F} G(\boldsymbol{x};\boldsymbol{\xi})Q_F(\boldsymbol{\xi})dS_\xi \ , \qquad \boldsymbol{x} \in S_B$$

The source only formulation follows from combining the BIE for the physical (exterior) fluid domain with the BIE for the fictitious interior problem which is possible due to the fact that the Green function satisfies the BVP in the whole domain $z \le 0$. The final expression for the velocity potential ψ is obtained in the form:

$$\psi(\boldsymbol{x}) = \iint_{S_B} \sigma(\boldsymbol{\xi})G(\boldsymbol{x};\boldsymbol{\xi})dS_\xi - \iint_{S_F} G(\boldsymbol{x};\boldsymbol{\xi})Q_F(\boldsymbol{\xi})dS_\xi \quad , \qquad \boldsymbol{x} \in V + V' \qquad (455)$$

and the corresponding BIE for the source strength $\sigma(\boldsymbol{\xi})$ is given in the following form:

$$\frac{1}{2}\sigma(\boldsymbol{x}) + \iint_{S_B} \sigma(\boldsymbol{\xi})\frac{\partial G(\boldsymbol{x};\boldsymbol{\xi})}{\partial n_x} dS_\xi = Q_B(\boldsymbol{x}) + \alpha \iint_{S_F} G(\boldsymbol{x};\boldsymbol{\xi})Q_F(\boldsymbol{\xi})dS_\xi \quad , \qquad \boldsymbol{x} \in S_B \qquad (456)$$

In both cases the BIE is solved by discretization of the body surface into a certain number of panels. Most common approach assumes the constant singularity distribution over the flat panels and the BIE is enforced at the centroids of each panel. Even though the two BIE formulations (mixed and source) are theoretically equivalent, there exist some differences when it comes to the numerical implementation. In particular, to compute the fluid velocity $\nabla\psi$ necessary in solving second-order problems, it is preferred to use the source method because only the first-order derivatives of the Green's function are needed. On the other side the source method has the drawback to not be used for thin bodies, or thin elements of bodies, unless the panels are small compared to the thickness. This might lead to a very large number of panels necessary for modelling of the body surface.

Figure 137: Typical hydrodynamic mesh (left $\mathbf{Q_F = 0}$, right $\mathbf{Q_F \neq 0}$).

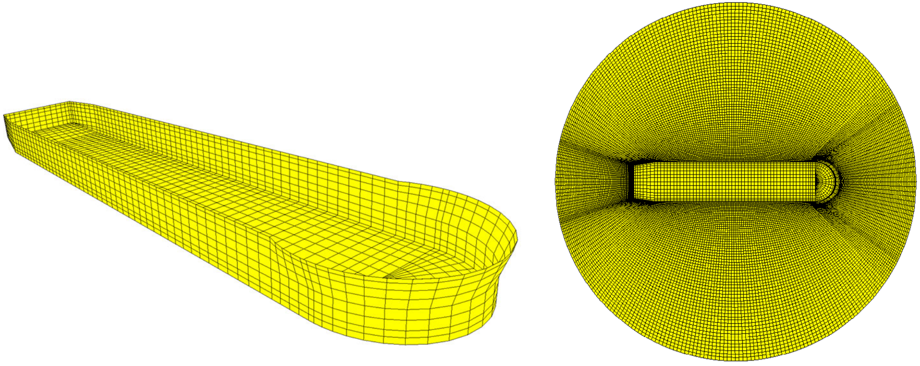

As already indicated, the above defined BVP covers all present needs i.e. both the linear and the second order problems as well as their diffraction and radiation parts. It should be noted that the linear problem is significantly simpler due to the absence of the free surface integral. The complexity of the free surface integration will depend on the behavior of the forcing term $Q_F(x, y)$ which theoretically extends to infinity. In particular, for the second order problem (even at zero forward speed) this integration is extremely complex because of very slow decay and highly oscillatory nature of $Q_F(x, y)$. It is also important to note that, even if we need to discretize the free surface, that is for the integration purposes only and no additional unknowns are added. This means that the unknowns (source and dipoles strength) are distributed at the body only regardless of the fact that Q_F is zero or not. Typical hydrodynamic meshes are shown in Figure 136.

3.2.4 Artificial dissipation

One of the most important drawbacks of the potential flow theory is related to the assumption of ideal fluid and irrotational flow so that the fluid viscosity and its damping effects are neglected. This might lead to unrealistic results especially close to the resonant conditions where large free surface deformations can be expected. It appears to be possible to model the overall effect of the non-potential flow effects by artificially modifying the boundary conditions. The generic case is shown in Figure 138 where, for simplicity, the homogeneous boundary condition at the free surface is considered ($Q_F = 0$). Two different dissipation coefficients can be introduced and they are denoted by ϵ_{FS} at the free surface and by ϵ_B at the body surface.

Using the same Green function as before, in the case of source only formulation, the following representation of the velocity potential can be obtained:

$$\psi(\boldsymbol{x}) = \iint_{S_B+S_F} \sigma(\boldsymbol{\xi})G(\boldsymbol{x};\boldsymbol{\xi})dS_\xi \quad , \qquad \boldsymbol{x} \in V + V' \qquad (457)$$

and the corresponding BIE for the source strength $\sigma(\boldsymbol{\xi})$ are:

$$\frac{1}{2}\sigma(\boldsymbol{x}) + \iint_{S_B+S_F} \sigma(\boldsymbol{\xi})\left[\frac{\partial G(\boldsymbol{x};\boldsymbol{\xi})}{\partial n_x} - i\kappa_0\epsilon_B G(\boldsymbol{x};\boldsymbol{\xi})\right] dS_\xi = Q_B(\boldsymbol{x}) \quad , \qquad \boldsymbol{x} \in S_B \qquad (458)$$

$$\sigma(\boldsymbol{x}) + i\kappa_0\epsilon_{FS}\iint_{S_B+S_F}\sigma(\boldsymbol{\xi})G(\boldsymbol{x};\boldsymbol{\xi})dS_{\xi} = 0 \quad , \quad \boldsymbol{x} \in S_{FS} \tag{459}$$

Figure 138: Modified boundary conditions

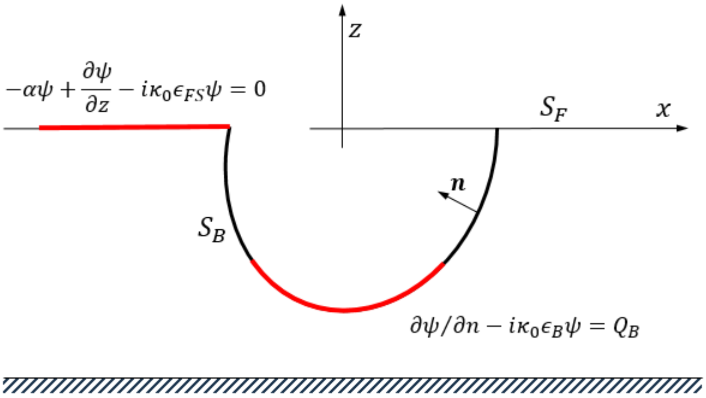

It should be noted that the part of the free surface with the non-zero dissipation coefficient ϵ_{FS} needs to be discretized and the additional unknowns (source strength) should be located on those elements. This means that the size of the linear system will increase. The effects of putting the dissipation at the free surface or at the body is not the same even if both methods damp the response, as it can be seen from Figure 139. The determination of the proper values of the dissipation coefficients remains the main problem within this approach. This can be done by comparing the final results with experimental ones or the ones obtained using the CFD simulations.

Within the numerical codes the dissipation coefficient is usually defined in a different way. As an example, in Hydrostar it is defined as:

$$\epsilon = \frac{\epsilon^*}{2-\epsilon^*} \tag{460}$$

and the typical values of ϵ^* range from 0.05 to 0.1 for ϵ_{FS}^* when used for side by side operations, and from 0.01 to 0.02 for ϵ_B^* when used for sloshing.

Figure 139: Effects of the artificial dissipation on the added mass component A_{22} for the rectangular tank. Left – Dissipation at the free surface, Right – Dissipation at the wall

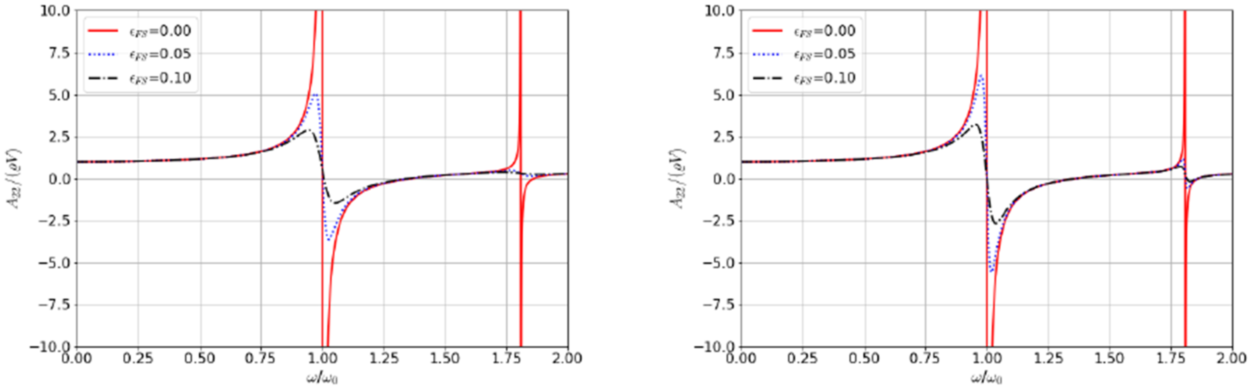

3.2.5 Irregular frequencies

A drawback of the BIE methods based on the Kelvin Green function is the irregular frequencies effect which occurs when the body pierces the free surface. This is a purely numerical problem related to the fact that, when the exterior problem is being solved, the interior problem is solved as well. Within the source formulation continuity of the potential across the body surface is imposed which means that any eigensolution to the interior problem, verifying a homogeneous Dirichlet condition at the body surface ($\psi = 0$), can be added up so that the unicity is lost. The practical consequence is that the matrix of the linear system becomes ill conditioned in the vicinity of the irregular frequencies, which are the eigen frequencies of the interior problem ($\psi = 0$ at the body). Since the mixed singularity distribution method has the same kernel as the source distribution method, it also suffers from the same problem. There exist different methods to remove the problem of the irregular frequencies, and the most intuitive one is based on the redefinition of the interior problem in such a way that the eigensolutions do not exist anymore (see Malenica & Chen (1998)). This is usually done by modifying the free surface boundary condition, in the interior domain, and the common choice is $\partial\psi/\partial z = 0$. In order to enforce this boundary condition, it is necessary to discretize the interior free surface (see Figure 140) and put the additional unknowns on it.

Figure 140: Hydrodynamic mesh for EBIEM and the effects of the irregular frequencies on longitudinal drift force

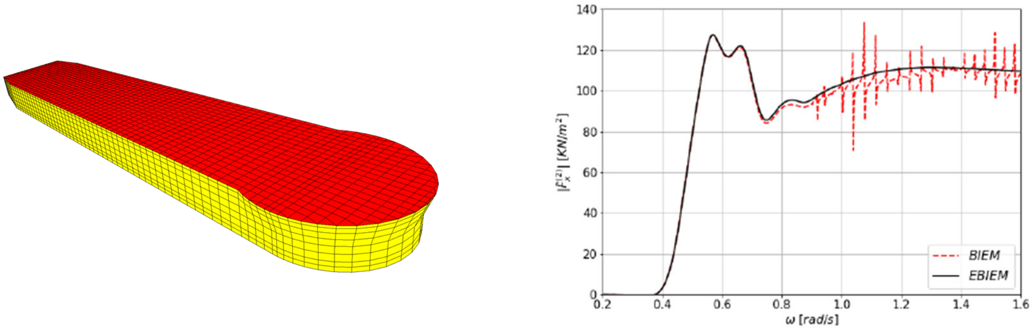

The corresponding extended BIE method (EBIEM) can be obtained straightforwardly using the Green's identities as before. In the case of source formulation, the potential is defined by:

$$\psi(\boldsymbol{x}) = \iint_{S_B+S_F'} \sigma(\boldsymbol{\xi})G(\boldsymbol{x};\boldsymbol{\xi})dS_\xi \quad , \quad z \leq 0 \tag{461}$$

and the corresponding EBIE is:

$$\frac{1}{2}\sigma(\boldsymbol{x}) + \iint_{S_B+S_F'} \sigma(\boldsymbol{\xi})\frac{\partial G(\boldsymbol{x};\boldsymbol{\xi})}{\partial n_x}dS_\xi = Q_B(\boldsymbol{x}) \quad , \quad \boldsymbol{x} \in S_B \tag{462}$$

$$\sigma(\boldsymbol{x}) + \iint_{S_B+S_F'} \sigma(\boldsymbol{\xi})\frac{\partial G(\boldsymbol{x};\boldsymbol{\xi})}{\partial n_x}dS_\xi = 0 \quad , \quad \boldsymbol{x} \in S_F' \tag{463}$$

The main drawback of EBIEM is the increase of the number of unknowns. Typical hydrodynamic mesh for EBIEM is shown in Figure 140, together with the typical effects of the irregular frequencies. Another methods for elimination of the effect of irregular frequencies also exist and among them the one proposed in Ohmatsu (1983) is particularly interesting.

In practice it is useful to know the value of the lowest irregular frequency. A lower bound can be obtained based on the fact that, for any closed geometry surrounding the body, the irregular frequencies are lower than the actual irregular frequencies of the body. For shiplike body, the rectangular box can be taken as a reference The lowest eigenfrequency ω_1 of the rectangular box with the dimensions: L - box length, B - box width and D - box depth, is given by:

$$\omega_1 = \sqrt{\frac{\pi g}{L}}\left[\frac{\sqrt{1+(L/B)^2}}{\tanh\left(\frac{\pi D}{L}\sqrt{1+(L/B)^2}\right)}\right]^{1/2} > 1.77\sqrt{g/L} \tag{464}$$

For the truncated circular cylinder of radius R and depth D, the lowest eigenfrequency is given by:

$$\omega_1 = \sqrt{gk\coth(kD)} > 1.55\sqrt{g/R} \quad , \quad k \rightarrow \; J_0(kR) = 0 \tag{465}$$

with J_0 denoting the Bessel function of the first kind.

3.2.6 Boundary Integral Equation Method with current

Even though the basic principles remain the same, the presence of current introduces some changes. The generic BVP remains the same except for the free surface condition which changes to (see also Section 4, [4.4.4]):

$$\omega_1 = \sqrt{gk\coth(kD)} > 1.55\sqrt{g/R} \tag{466}$$

where $\nu_e = \omega_e^2/g$ and $\tau = U\omega_e/g$, with ω_e denoting the encounter frequency and U the current speed.

The procedure similar to the one used for the case without current, leads to the following BIE for the mixed singularity distribution:

$$\begin{aligned}\frac{1}{2}\psi(\boldsymbol{x}) - \iint_{S_B} \psi(\boldsymbol{\xi})\frac{\partial G(\boldsymbol{x};\boldsymbol{\xi})}{\partial n_\xi}dS_\xi + 2i\tau\int_{C_w} \psi(\boldsymbol{\xi})G(\boldsymbol{x};\boldsymbol{\xi})d\eta \\ = -\iint_{S_B} G(\boldsymbol{x};\boldsymbol{\xi})Q_B(\boldsymbol{\xi})dS_\xi - \iint_{S_F} G(\boldsymbol{x};\boldsymbol{\xi})Q_F(\boldsymbol{\xi})dS_\xi \; , \quad \boldsymbol{x} \in S_B\end{aligned} \tag{467}$$

where C_w denotes the body waterline and we note that, similar to the case without current, the symmetry property of the Green's function [$G(\boldsymbol{x};\boldsymbol{\xi};\tau) = G(\boldsymbol{\xi};\boldsymbol{x};-\tau)$] was used to derive the above expression.

The source formulation leads to the following expression for the velocity potential:

$$\psi(\boldsymbol{x}) = \iint_{S_B} \sigma(\boldsymbol{\xi}) G(\boldsymbol{x};\boldsymbol{\xi}) dS_\xi - \iint_{S_F} G(\boldsymbol{x};\boldsymbol{\xi}) Q_F(\boldsymbol{\xi}) dS_\xi \quad , \quad \boldsymbol{x} \in V + V' \tag{468}$$

and the corresponding BIE for the source strength $\sigma(\boldsymbol{\xi})$ is:

$$\frac{1}{2}\sigma(\boldsymbol{x}) + \iint_{S_B} \sigma(\boldsymbol{\xi}) \frac{\partial G(\boldsymbol{x};\boldsymbol{\xi})}{\partial n_x} dS_\xi = Q_B(\boldsymbol{x}) + \iint_{S_F} \frac{\partial G(\boldsymbol{x};\boldsymbol{\xi})}{\partial n_x} Q_F(\boldsymbol{\xi}) dS_\xi \quad , \quad \boldsymbol{x} \in S_B \tag{469}$$

Compared to the mixed singularity distribution, it can be observed that the integral over the waterline disappears in the source formulation which makes the source formulation more attractive. It can also be noted that the free surface integral which occurs in the BIE's can be evaluated with relatively low CPU cost because the nonhomogeneous term Q_F decays rapidly far from the body so that only limited portion of the free surface needs to be discretized.

The Green's function for the problem with current can be obtained by manipulating the zero current Green's function in the following form (see Noblesse & Chen (1995) or Malenica (1997)):

$$G = e^{-2i\tau\frac{\partial k}{\partial \nu}k(x-\xi)}\left\{G_0 + 2i\tau\left[\frac{\partial^2 G_0}{\partial\nu\partial x} + \frac{\partial k}{\partial \nu}k(x-\xi)G_0\right]\right\} \tag{470}$$

where G_0 denotes the zero current Green's function.

Figure 141: Wave system without (left) and with (right) current.
Upper part – real part of the Green's function,
Lower part – Imaginary part of the Green's function

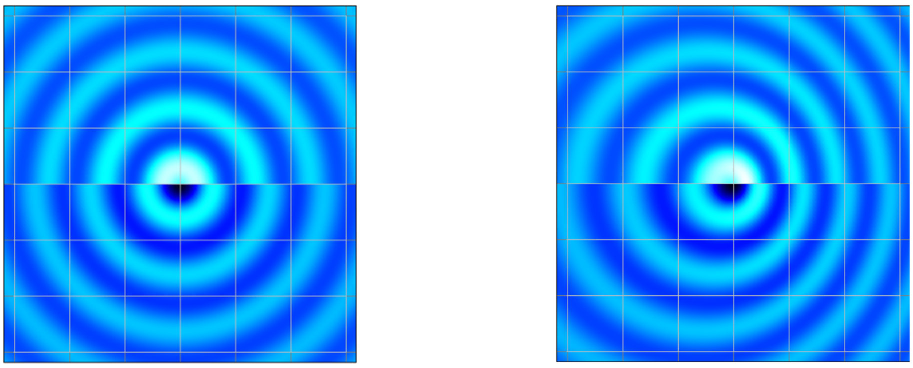

From the above representation of the Green's function (470) a very important feature of the generated wave systems can be deduced. Indeed, knowing that the zero current Green's function produces only the circular (ring) waves at infinity (Figure 141 left) it can be concluded that the presence of current will also produce the ring waves but now shifted in space due to Doppler effect (Figure 141 right). This fact limits the domain of validity of the present approach. Indeed, a more complex wave systems such as the well-known transverse and divergent waves will never be properly represented with this approach. The fundamental reason for that, lies in the fact that the quadratic velocity term in the free surface boundary condition ($U^2\,\partial^2\varphi/\partial x^2$) was neglected. This means that the use of the above approach should be made with care because, not only the parameter τ should be small but also the Froude number $F_n = U^2/gL$ should be smaller than it i.e. $F_n \ll \tau$.

3.3. Numerical evaluation of the Green's function of Kelvin type

3.3.1 Infinite water depth

The Kelvin type Green's function (453) defined by the set (452) of differential equations contains one free-space Rankine type source and the term $H(x;\boldsymbol{\xi},\nu,h)$ satisfying the boundary conditions on the free surface, sea bed and the radiation condition at infinity. In deep water a convenient expression for the Green function is:

$$G(\boldsymbol{x};\boldsymbol{\xi},\nu,h=\infty) = -\frac{1}{4\pi\boldsymbol{r}} - \frac{1}{4\pi\boldsymbol{r}'} - 2\nu G_\infty(Z',R') \; - 2i\pi\nu e^{\nu(z+\zeta)} J_0(\nu R) \tag{471}$$

where:

$$R = \sqrt{(x-\xi)^2 + (y-\eta)^2} \quad , \quad \boldsymbol{r} = \sqrt{R^2 + (z-\zeta)^2} \quad , \quad \boldsymbol{r}' = \sqrt{R^2 + (z+\zeta)^2} \tag{472}$$

The function $G_\infty(Z',R')$ in (471) is given by the following Fourier integral

$$G_\infty(Z',R') = \int_0^\infty \frac{e^{-kZ'}}{k-1} J_0(kR')dk \tag{473}$$

which means that G_∞ is the real function of two variables $Z' = -\nu(z+\zeta)$ and $R' = \nu R$ (Figure 142)

Figure 142: Free-surface term of Kelvin type Green's function in deep-water

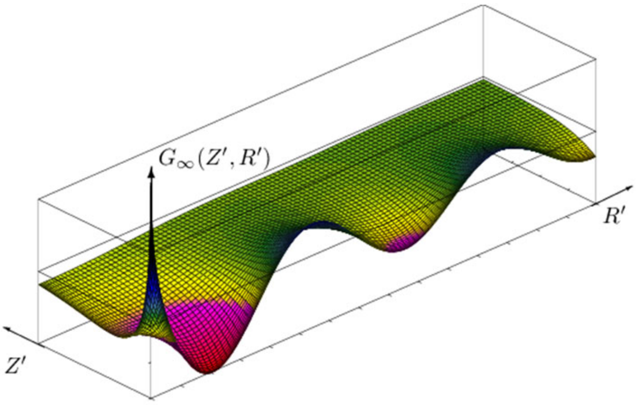

This function can be replaced by various analytical expressions of high accuracy in different zones of (Z',R'). For the purpose of numerical efficiency, the function $G_\infty(Z',R')$ is further decomposed as:

$$G_\infty(Z',R') = \begin{cases} -e^{-Z'}J_0(R')\left[\ln\left(Z'+\sqrt{Z'^2+R'^2}\right) - \ln(2) + \gamma\right] + S(Z',R') & ; \quad 0 \le R' \le 2\,, 0 \le Z' \le 4 \\ -\pi e^{-Z'}\widetilde{H}_0(R') + S(Z',R') & ; \quad \text{elsewhere} \end{cases} \tag{474}$$

where $\gamma = 0.577215$ is the Euler's constant and $\widetilde{H}_0(\cdot)$ is the zero order Struve function.

The function $S(Z',R')$ in (474) is a smoothly varying function and is approximated by Chebychev polynomials for a series of partitions in $Z'$and R'. This leads to an extremely efficient evaluation of the Green function for any combination of parameters (Newman (1992), Chen (1993)).

3.3.2 Finite water depth

In water of finite depth, the so-called John's series formulation (John (1950)) is available and written as:

$$\begin{aligned} G(\boldsymbol{x};\boldsymbol{\xi},\nu,h) = &-\frac{i4\pi\kappa_0}{2\kappa_0 h + \sinh 2\kappa_0 h}\cosh\kappa_0(z+h)\cosh\kappa_0(\zeta+h)H_0(\kappa_0 R) \\ &-\sum_{m=1}^{\infty}\frac{8\kappa_m}{2\kappa_m h + \sin 2\kappa_m h}\cos\kappa_m(z+h)\cos\kappa_m(\zeta+h)K_0(\kappa_m R) \end{aligned} \tag{475}$$

in which κ_0 is determined by (448) and κ_m by $\kappa_m \tan\kappa_m h = -\nu$, while $H_0(\cdot)$ and $K_0(\cdot)$ are the zeroth-order Hankel function of the first kind and the zeroth-order modified Bessel function of the second kind, respectively.

The John's formulation (475) is well suited for numerical computations when $R/h > 1$. However, the series converges slowly for $R/h < 1$, or even diverges when $R/h \to 0$ so that other formulations for $R/h < 1$ are needed. For this purpose, the Green's function is written as

$$G(\boldsymbol{x};\boldsymbol{\xi},\nu,h) = R_n - 2\kappa_0 G_h - \frac{i4\pi\kappa_0}{2\kappa_0 h + \sinh 2\kappa_0 h}\cosh\kappa_0(z+h)\cosh\kappa_0(\zeta+h)J_0(\kappa_0 R) \tag{476}$$

in which R_n is defined by

$$R_n = -\frac{1}{4\pi \boldsymbol{r}} - \frac{1}{4\pi \boldsymbol{r}_1} - \frac{1}{4\pi \boldsymbol{r}_2} - \frac{1}{4\pi \boldsymbol{r}_3} - \frac{1}{4\pi \boldsymbol{r}_4} - \frac{1}{4\pi \boldsymbol{r}_5} \tag{477}$$

with $\boldsymbol{r}_j$ for $j = 1,2,\dots 5$ denote the distances between the field point $\boldsymbol{x}(x,y,z)$ and the mirror source points $\boldsymbol{\xi}_j(\xi,\eta,\zeta_j)$ for $j = 1,2,\dots 5$ with ζ_j given by

$$\zeta_1 = -\zeta = \zeta' \quad , \quad \zeta_2 = -\zeta - 2h \quad , \quad \zeta_3 = \zeta - 2h \quad , \quad \zeta_4 = \zeta + 2h \quad , \quad \zeta_5 = -\zeta - 4h \tag{478}$$

The real part of the free-surface term in (476) is given by

$$G_h(Z_P, Z_M, \bar{R}) = \begin{cases} g_P(Z_P, \bar{R}, H) + G_M(Z_M, \bar{R}, H) + \operatorname{th} H G_\infty(Z', R') & ; \quad 0 \le Z_P < 1 \\ G_M(2 - Z_P, \bar{R}, H) + G_M(Z_M, \bar{R}, H) & ; \quad 1 \le Z_P \le 2 \end{cases} \tag{479}$$

where the following notations are used

$$\bar{R} = R/h \quad , \quad Z_P = |z + \zeta|/h \quad , \quad Z_M = |z - \zeta|/h \quad , \quad H = \kappa_0 h \tag{480}$$

The depth-effect functions $g_P(Z_P, \bar{R}, H)$ and $G_M(Z_M, \bar{R}, H)$ represented by Fourier wavenumber integrals (Chen (1993)) are smooth-varying functions as shown in Figure 143.

Figure 143: Depth-effect functions of the Green's function in water of finite depth

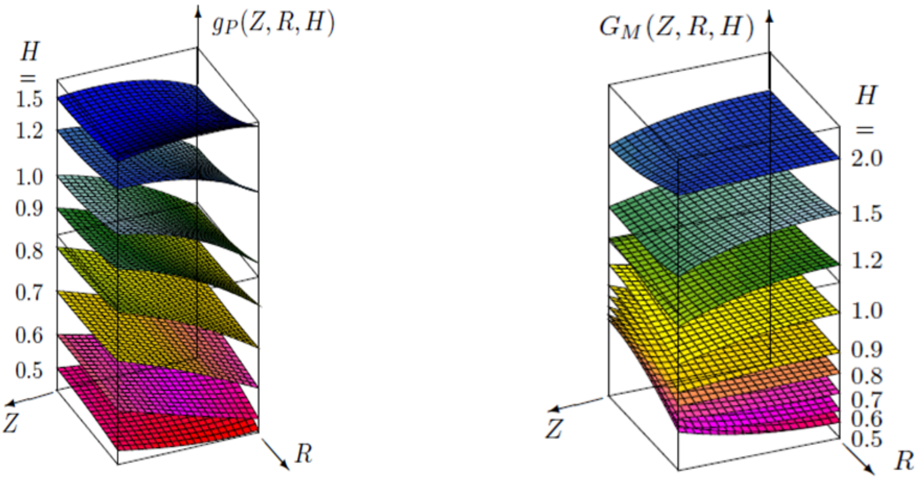

For the purpose of an efficient numerical evaluation, the functions g_P and G_M are finally approximated by Chebychev polynomials of three variables.

The depth-effect functions $g_P(Z, \bar{R}, H)$ and $G_M(Z, \bar{R}, H)$ tends to zero for $H = \kappa_0 h \to \infty$. However, they vary rapidly for $H \to 0$ and an improved formulation is adopted for $0 \le H < 1/2$ as follows:

$$g_P(Z, \bar{R}, H) = -(\ln H)/H + \tilde{g}_P(Z, \bar{R}, H) \quad , \quad G_M(Z, \bar{R}, H) = -(\ln H)/H + \tilde{G}_M(Z, \bar{R}, H) \tag{481}$$

where the functions $\tilde{g}_P(Z, \bar{R}, H)$ and $\tilde{G}_M(Z, \bar{R}, H)$ are also approximated by Chebychev polynomials.

4. List of references

[1] Chen X.B., 1988.: "Etude des reponses du second ordre d'une structure soumise a une houle aleatoire", Ph.D. Thesis, Univ. Nantes, ENSM.

[2] Chen X.B., 1993.: "Evaluation de la fonction de Green du probleme de diffraction/radiation en profondeur d'eau finie - Une nouvelle methode rapide and precise", Proc. 4e Journees de l'Hydrodynamique, Nantes, France.

[3] John F., 1950.: "On the motion of floating bodies II: simple harmonic motions", Comm. Pure and App. Math., Vol. 1.

[4] Lee C.H., 1995.: "WAMIT – Theory manual", MIT

[5] Malenica S. & Chen X.B., 1998: « On the irregular frequencies appearing in wave diffraction-radiation solutions. », International Journal of Offshore and Polar Engineering (IJOPE).

[6] Malenica S., 1997. : "Some aspects of water wave diffraction radiation at small forward speed.", Brodogradnja, Vol. 45, pp. 35-43

[7] Malenica S., Molin B., Remy F. & Senjanovic I., 2003. : "Hydroelastic response of a barge to impulsive and non-impulsive wave loads.", 3rd Int. Conf. On Hydroelasticity, Oxford, UK.

[8] Mei C.C, Stiassnie M. & Yue D.K.P., 2005. : "Theory and applications of ocean surface waves.", Advanced series on ocean engineering, Vol.23, World Scientific

[9] Molin B. & Marion A., 1985.: "Etude au deuxieme ordre du comportement des corps flottants en houle régulière", IFP report 33031.

[10] Newman J.N., 1992.: "The approximation of free-surface Green functions", Wave Asymptotics - Proc. F. Ursell Retirement Meeting, Cambridge University Press.

[11] Newman, J.N., 1994.: "Wave effects on deformable bodies", Applied Ocean Research, Vol. 16, pp.47-59.

[12] Noblesse F. & Chen X.B., 1995.: "Decomposition of free surface effects into wave and near-field components.", Ship Technology Research, Vol. 42.

[13] Ohmatsu S., 1983.: “A new simple method to eliminate the irregular frequencies in the theory of water wave radiation problem”, Ship Res. Inst., 70.

[14] Shabana A.A., 1989.: ”Dynamics of multibody systems”, John Wiley & Sons

[15] Tuitman J.T., Malenica S. & Van ’t Veer R., 2012.: “Generalized modes in time domain seakeeping calculations”, Journal of Ship Research, Vol 56.

Appendix 2 Illustrative Numerical Results

1. Introduction

1.1. General

1.1.1 Comparisons of the numerical and the analytical results

In order to demonstrate the accuracy of the numerical method, the comparisons with the analytical results are very helpful. Here we present two well known cases where the analytical results for the wave loads can be obtained. The first case concerns the freely floating sphere and the second one concerns the bottom mounted fixed circular cylinder.

1.1.2 Numerical results for different floaters

The character of the wave loading on the floating body and the resulting body motions, depend on the underwater body geometry on one side and the inertial properties of the body on the other side. In this Appendix, the characteristic wave loads and the responses, for the most typical floating bodies employed in the offshore industry, are presented. The floaters are listed below:

1. FPSO – Floating Production Storage and Offloading unit
2. Semi-submersible platform
3. TLP – Tension Leg Platform
4. FOWT – Floating Offshore Wind Turbine

The following quantities are presented:

1. Added mass and damping matrices
2. First order excitation forces
3. First order response
4. Second order drift forces in horizontal plane (surge, sway, yaw)
5. Difference frequency second order loads in horizontal plane (Full QTF_-)
6. Sum frequency second order loads in vertical plane for TLP platform

1.2. Conventions

1.2.1 Definitions

Coordinate system and the wave directions are defined following the conventions used in HYDROSTAR and indicated in Figure 144.

Figure 144: Coordinate system and heading definition

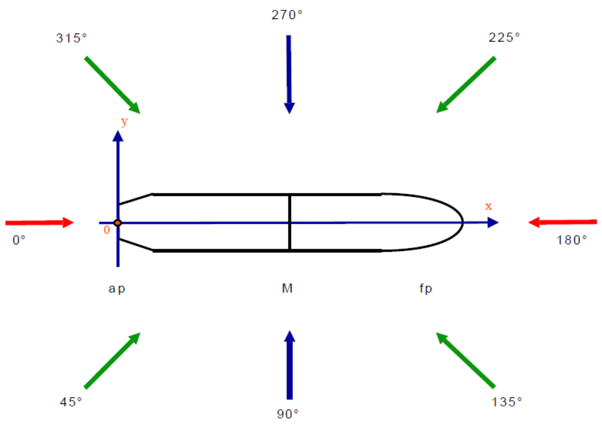

2. Comparisons of the numerical and the analytical results

2.1. General

2.1.1 Overview

When validating the diffraction radiation numerical methods it is important to consider the radiated and the diffracted wave forces independently. For the radiation forces (expressed in terms of the added mass and the damping matrices) the analytical results which are commonly used as a reference are those given for the case of hemisphere (Hulme (1982)), while for the diffraction loads the well-known analytical solution for the wave diffraction by the bottom mounted vertical circular cylinder (McCamy & Fuchs (1954)). Both cases are considered here and, in addition, the comparisons of the local wave elevation for the cylinder case and for few wave frequencies are also included.

2.2. Floating hemisphere

2.2.1 Description of the test case

The radius of the hemisphere is chosen to be 1 meter and the water depth is assumed to be infinite. The hydrodynamic mesh is composed of 1580 panels on half surface and is shown in Figure 172 .

Figure 145: Hydrodynamic mesh of the hemisphere

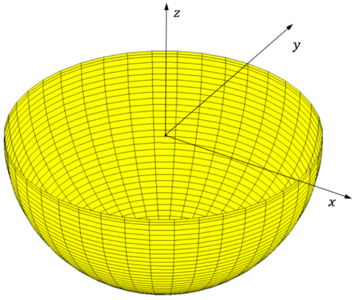

2.2.2 Comparisons

Due to the particularity of the geometry, the hydrodynamic quantities of interest are related to the motion in surge and heave only., The comparisons for the components A_{11} and A_{33} of the hydrodynamic added mass matrix are shown in Figures 146 and the comparisons for the corresponding components B_{11} and B_{33} of the hydrodynamic damping matrix are shown in Figure 147 The agreement between the analytical and the numerical results is excellent which demonstrate the accuracy of the BIE method.

Figure 146: Hydrodynamic added mass components A_{11} and A_{33}

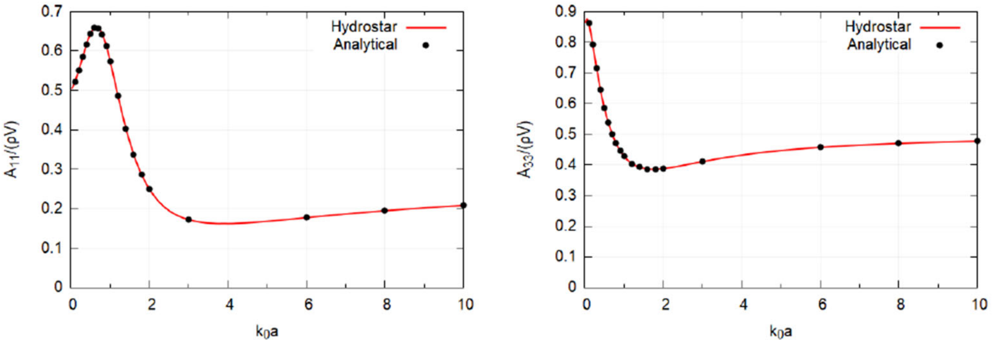

Figure 147: Hydrodynamic damping components B_{11} and B_{33}

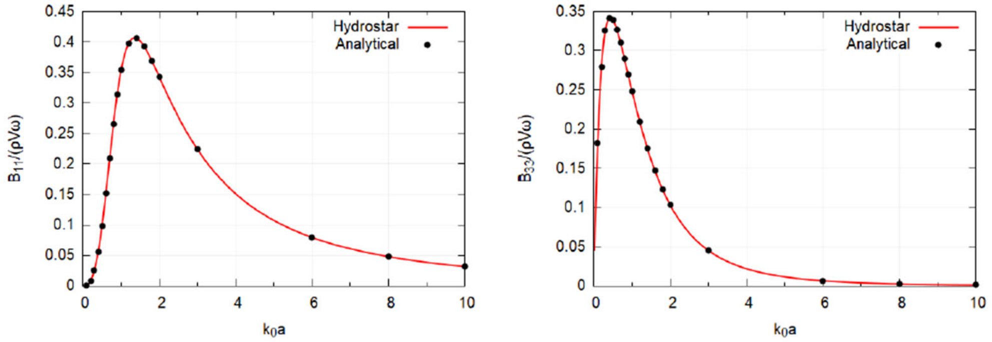

2.3. Vertical circular cylinder fixed to sea bottom

2.3.1 Description of the test case

The details of the considered configuration and the corresponding hydrodynamic mesh are shown in Figure 148. The ratio between cylinder radius and water depth is $h/a = 10$ and the incident wave is propagating in negative x direction.

Figure 148: Configuration and the hydrodynamic mesh (3200 panels on half body)

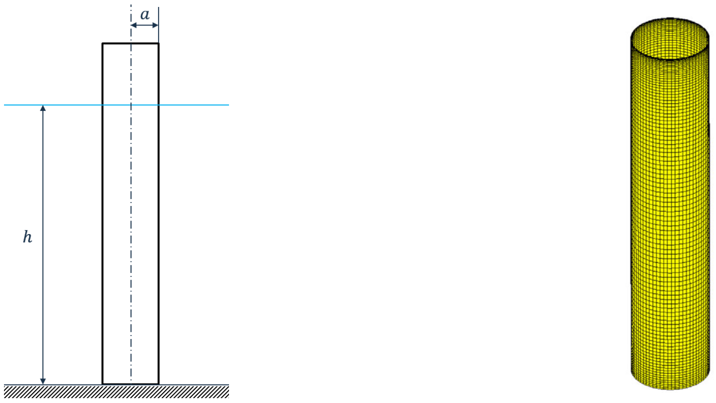

2.3.2 Comparisons

In Figure 149, the amplitude of the first (left) and the mean second order (right) wave forces are shown, and in Figure 150 the wave elevation at waterline is presented for two different wave frequencies.

Figure 149: First order (left) and the second order drift force (right) in longitudinal direction

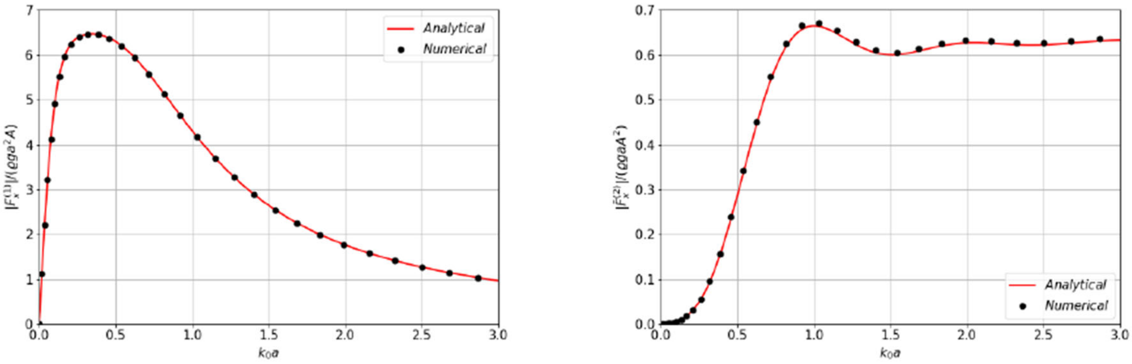

Figure 150: Amplitude of the first order wave elevation around the cylinder at waterline, for two wave frequencies: $\omega = 0.5 rad/s$ (left) and $\omega = 1.0 rad/s$ (right)

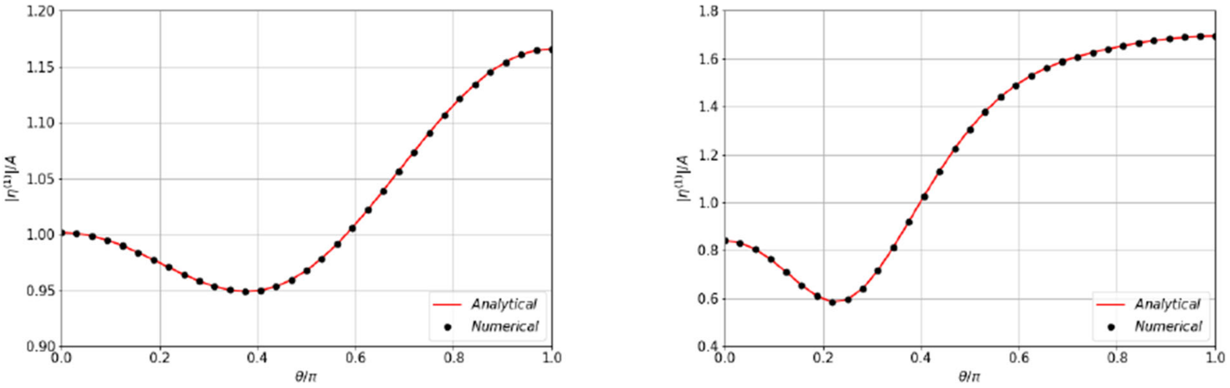

The sum frequency second order results, in monochromatic waves, are compared in Figures 151 and 152. For that purpose the different quantities are decomposed into two parts: the first one is the contribution from the quadratic products of the first order quantities and the second one is the contribution from the second order velocity potential.

For the inline force this means:

$$F_1^{(2)} = -\frac{1}{4}\varrho \iint_{S_B} (\nabla\varphi^{(1)} \cdot \nabla\varphi^{(1)}) n_x dS + \frac{1}{4}\varrho g \int_{C_B} \eta^{(1)}\eta^{(1)}\, n_x dC$$

$$F_2^{(2)} = -2i\omega\varrho \iint_{S_B} \varphi^{(2)} n_x dS$$

$$F^{(2)} = F_1^{(2)} + F_2^{(2)}$$

and for the wave elevation:

$$\eta_1^{(2)} = -\frac{1}{4g}\nabla\varphi^{(1)} \cdot \nabla\varphi^{(1)} - \frac{\nu^2}{2}\varphi^{(1)}\varphi^{(1)}$$

$$\eta_2^{(2)} = -\frac{2i\omega}{g}\varphi^{(2)}$$

$$\eta^{(2)} = \eta_1^{(2)} + \eta_2^{(2)}$$

Figure 151: Real and imaginary parts of the second order forces

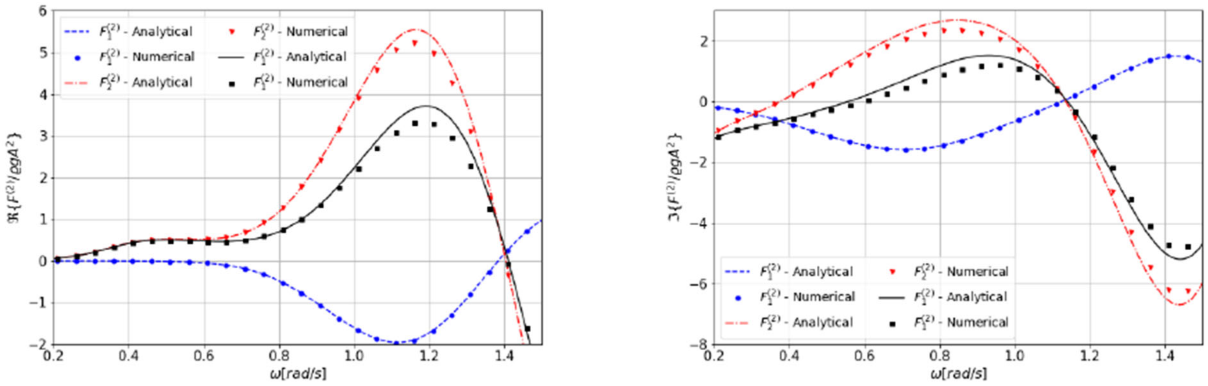

Figure 152: Amplitude of the second order sum frequency wave elevation around the cylinder at waterline for two wave frequencies: $\omega = 0.5 rad/s$ (left) and $\omega = 1.0 rad/s$ (right)

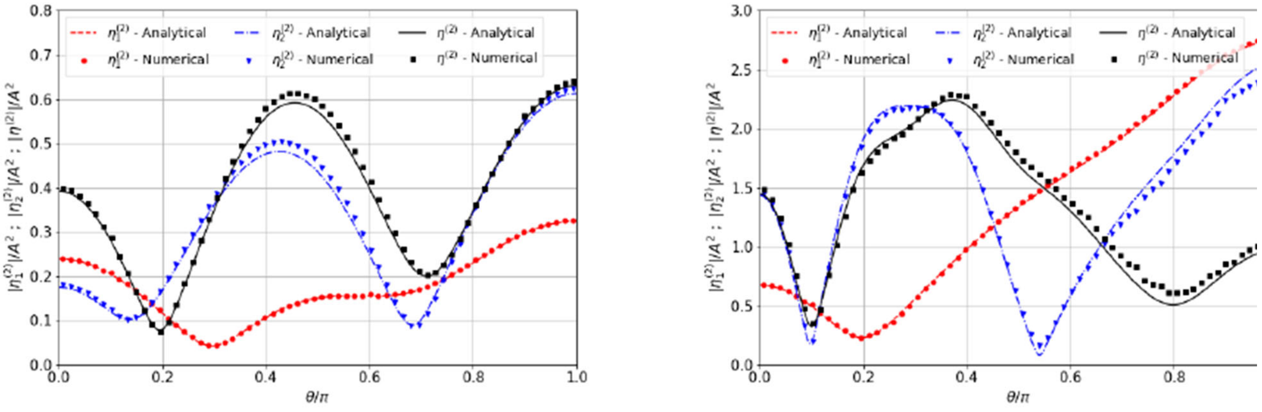

3. FPSO

3.1. Description of the floater

3.1.1 Main dimensions

The main dimensions of the FPSO are given in Table 13.

Table 13 Main dimensions of the FPSO.

L [m]	331.6
B [m]	60.0
T [m]	21.07

3.1.2 Mass properties

FPSO mass properties are given in Table 14.

Table 14 Mass properties of the FPSO

Mass [kg]	3.37E+08
R_{xx} [m]	21.0
R_{yy} [m]	75.695
R_{zz} [m]	78.537
X_{COG} [m]	167.54
Y_{COG} [m]	0.000
Z_{COG} [m]	-4.585

3.1.3 Natural periods

The FPSO is considered freely floating and no stiffness of mooring lines was taken into account. The resulting natural periods are given in Table 15.

Table 15 Natural periods (in seconds) of the FPSO

Surge	-
Sway	-
Heave	12.438
Roll	15.566
Pitch	10.650
Yaw	-

3.1.4 Hydrodynamic model

The hydrodynamic mesh of the FPSO is shown in Figure 153. The mesh is composed of 1728 panels on half wetted surface of the body. The water depth is assumed infinite.

Figure 153: Hydrodynamic mesh of the FPSO

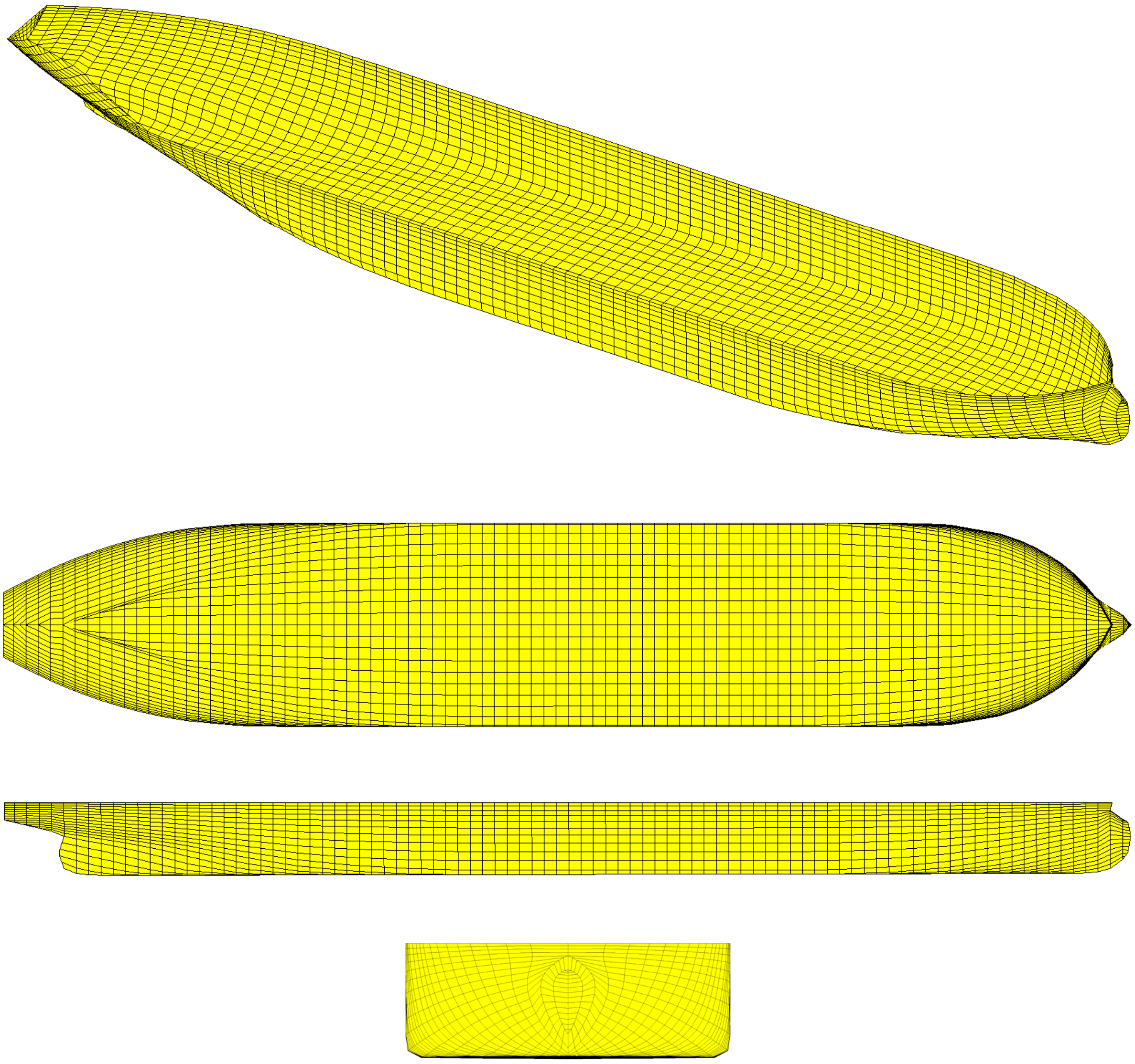

3.2. Results

3.2.1 Hydrodynamic added mass and damping

Figure 154: Diagonal components of the hydrodynamic added mass matrix

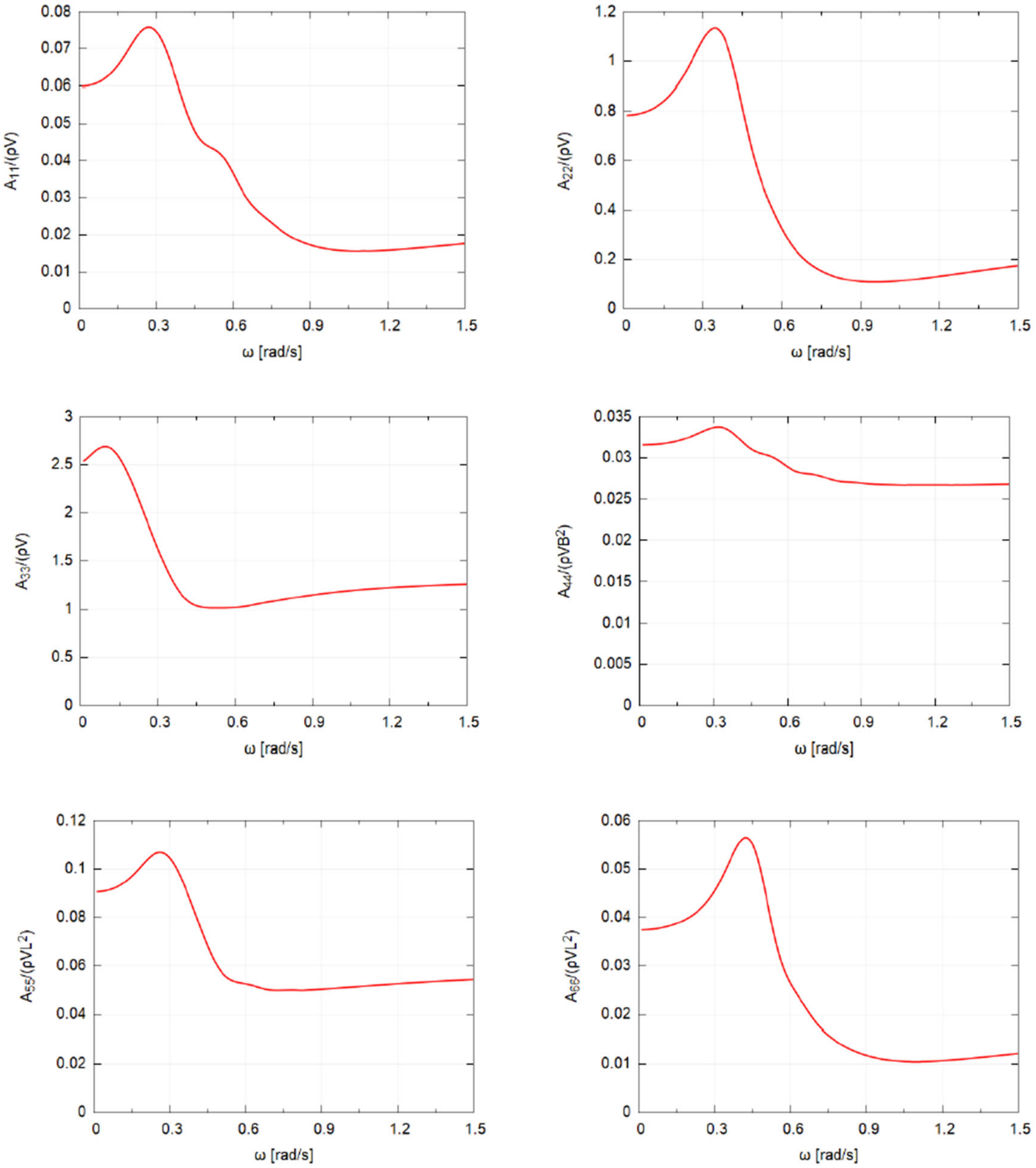

Figure 155: Diagonal components of the hydrodynamic damping matrix

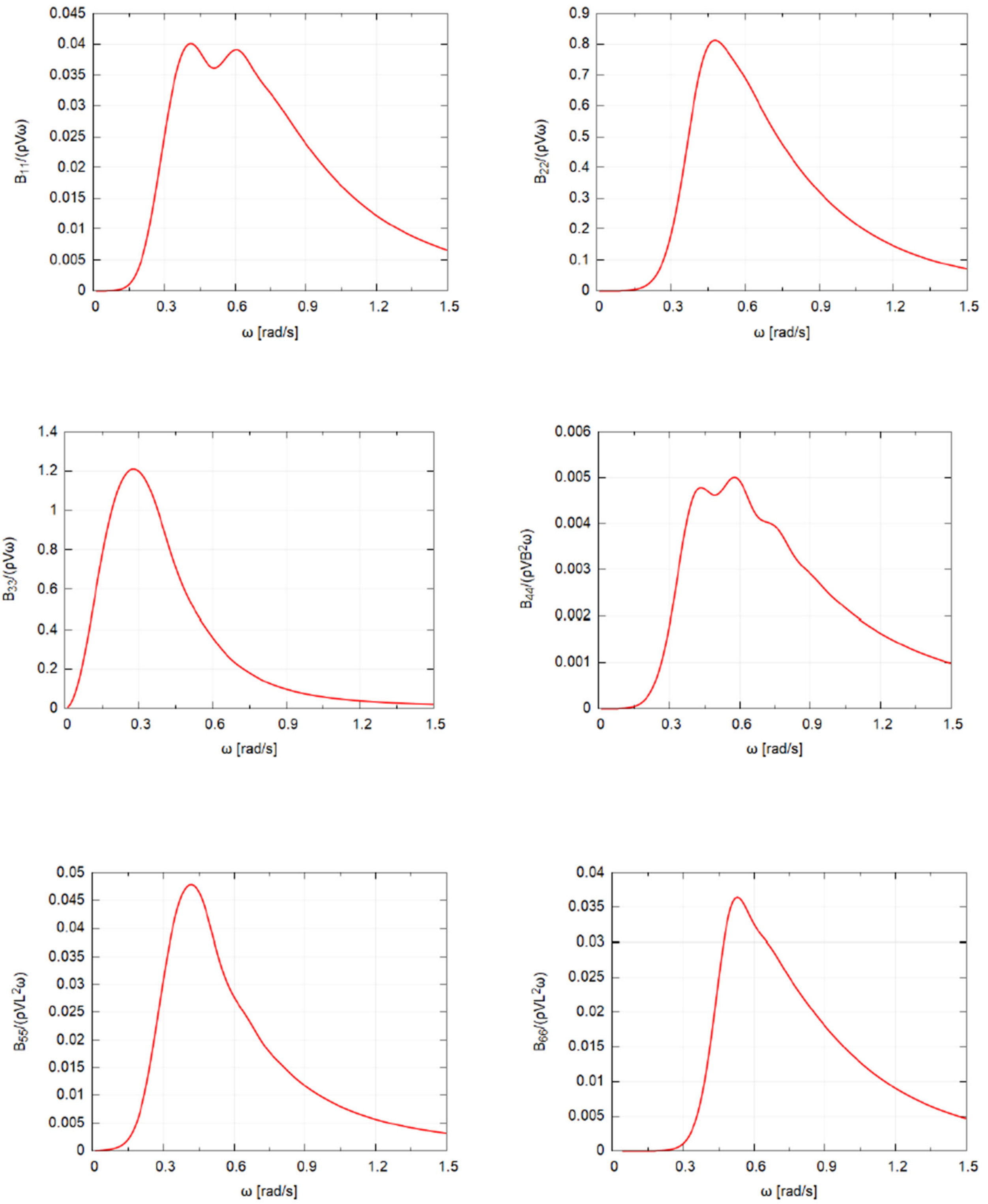

3.2.2 Linear excitation forces

Figure 156: First order excitation forces and moments.

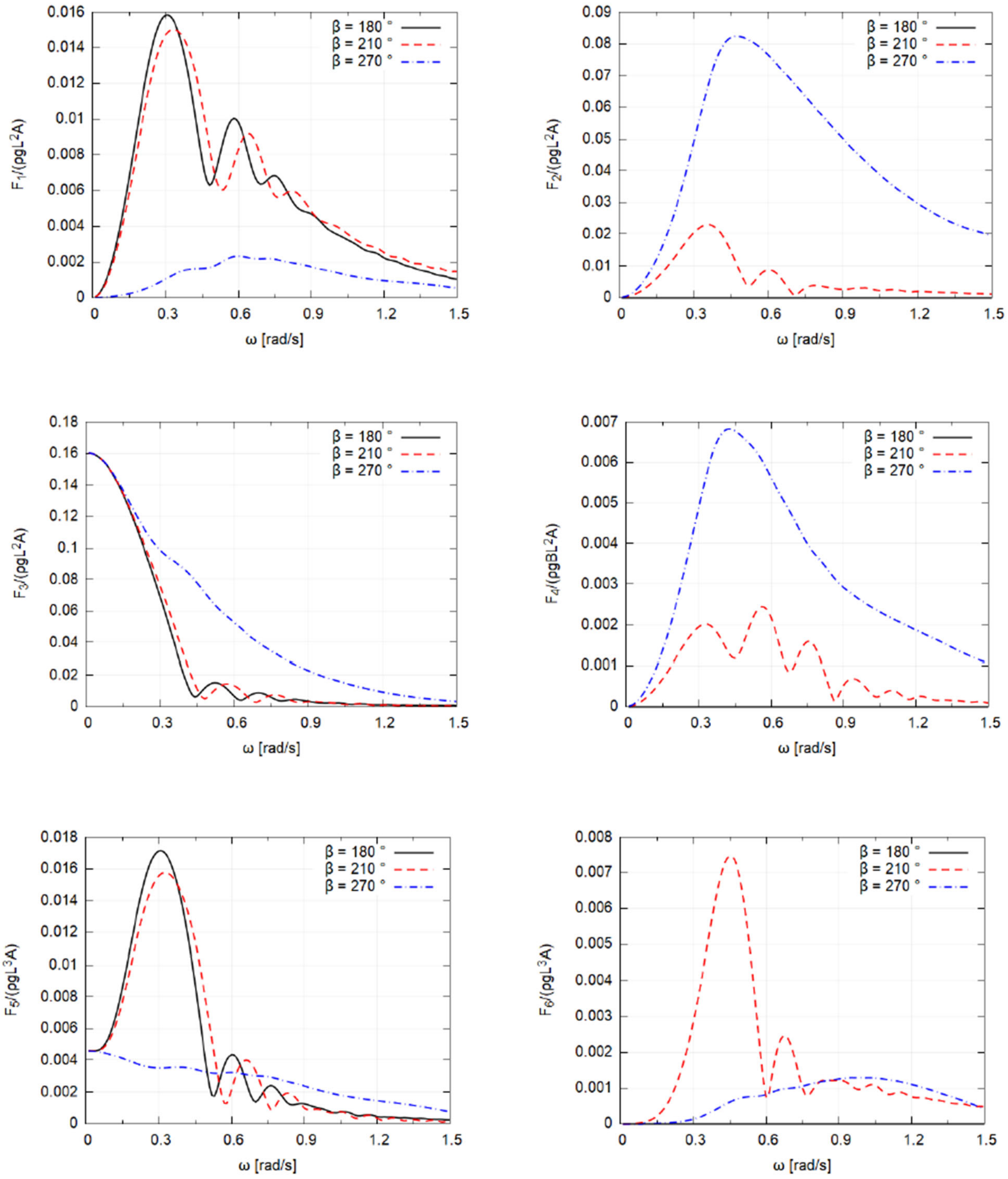

3.2.3 Motion RAO's

Figure 157: Motion's RAO's

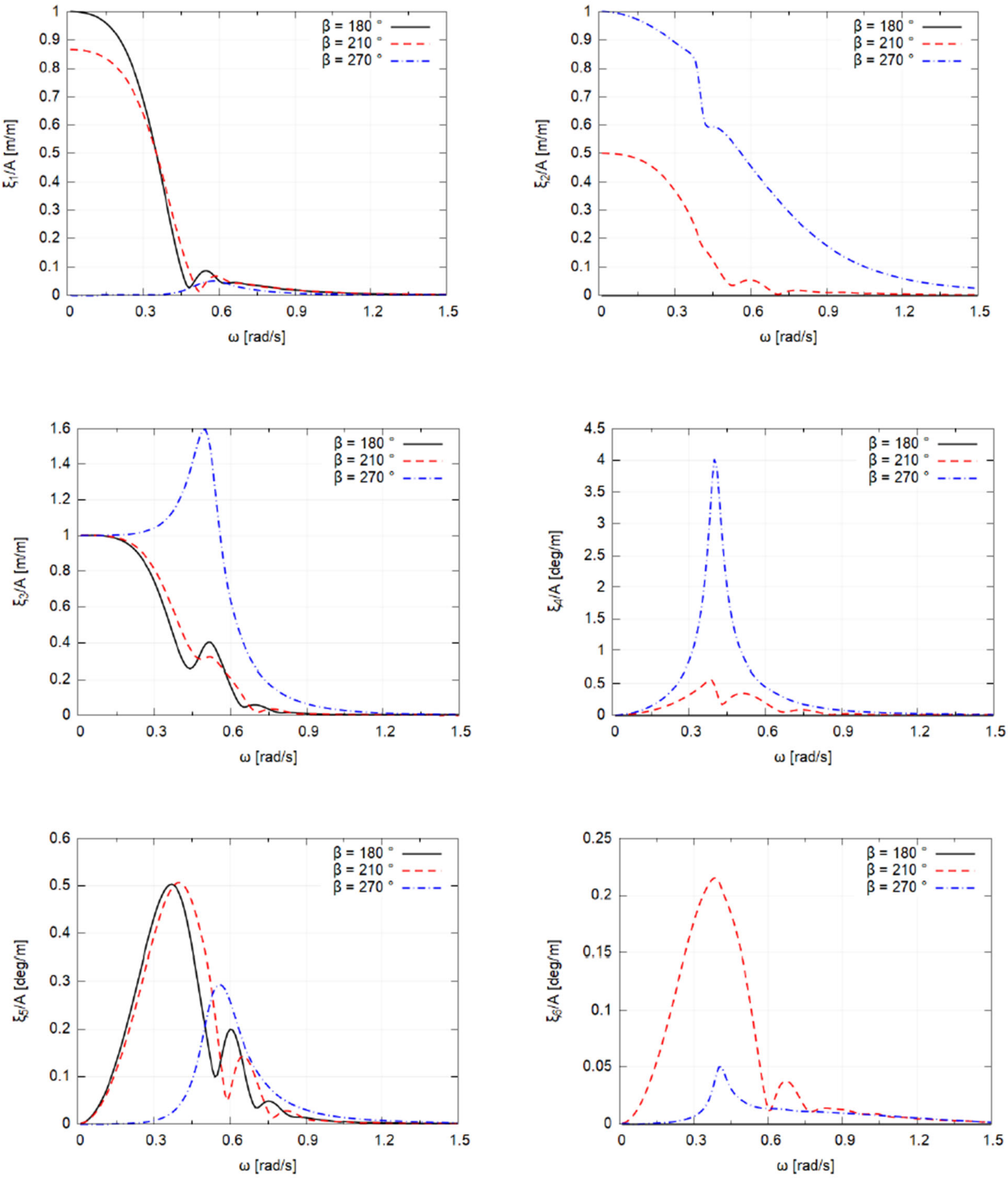

3.2.4 Low frequency second order loads

Figure 158: Mean drift forces and moment, and the QTF_- for $\beta = 210°$, in the horizontal plane

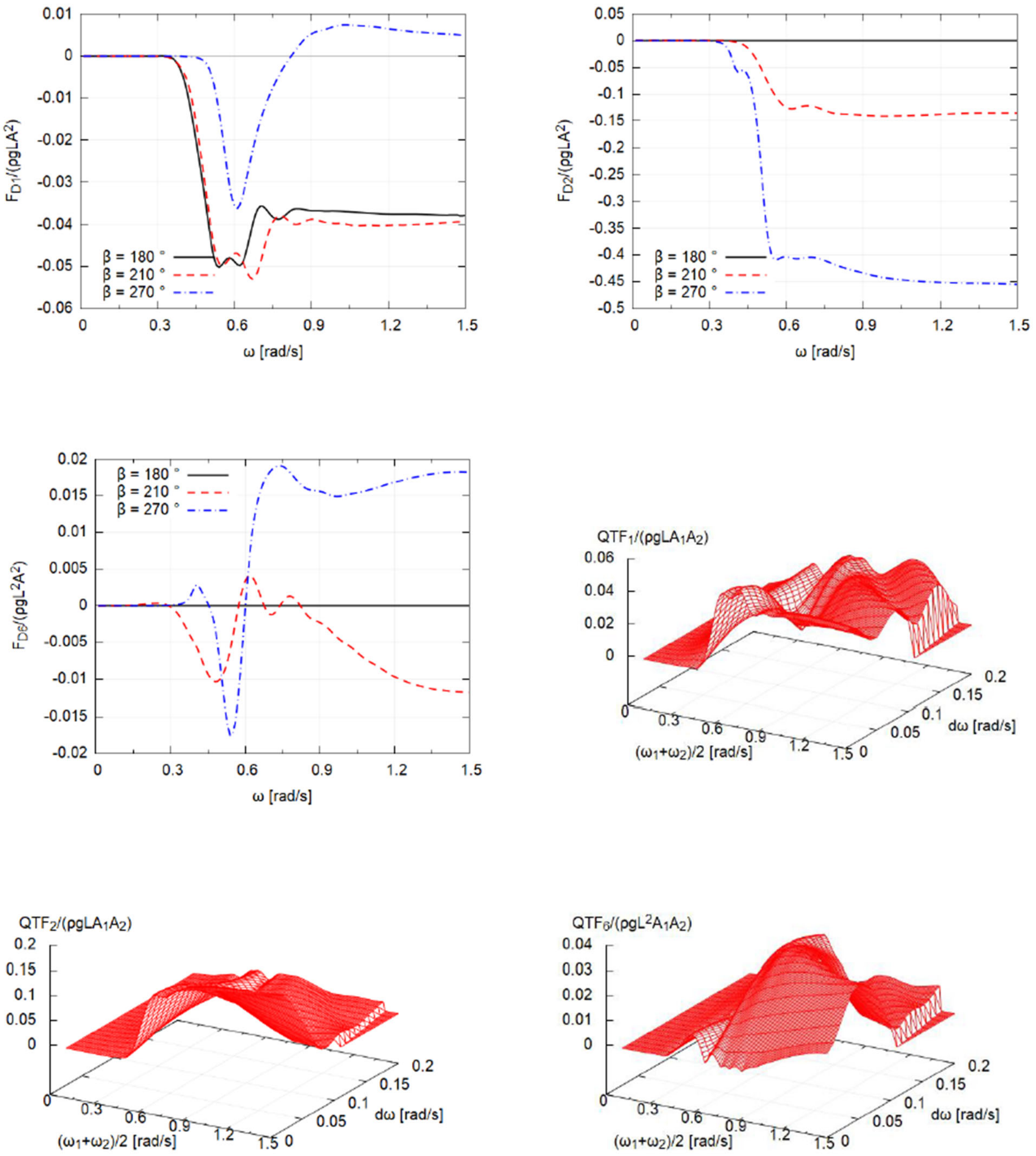

4. Semi-submersible platform

4.1. Description of the floater

4.1.1 Main dimensions

The main dimensions of the semi-submersible platform are given in Table 16.

Table 16 : Main dimensions of the semi-submersible platform

L [m]	82.3	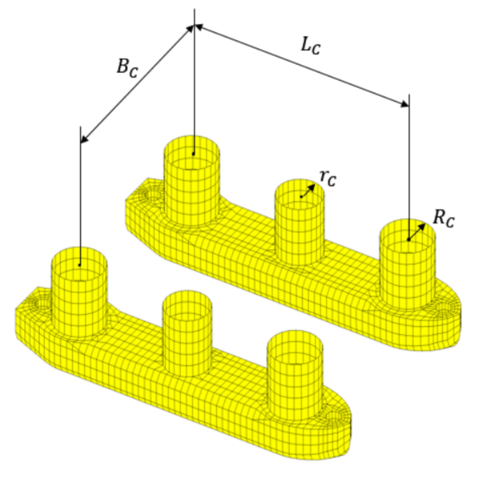
B [m]	61.0	
T [m]	19.8	
R_C [m]	5.30	
r_C [m]	5.25	
B_C [m]	45.5	
L_C [m]	56.4	

4.1.2 Mass properties

The mass properties of the semi-submersible platform are given in Table 17.

Table 17 Mass properties of the semi-submersible platform

Mass [kg]	2.80E+07
R_{xx} [m]	26.3
R_{yy} [m]	27.9
R_{zz} [m]	30.7
X_{COG} [m]	40.7
Y_{COG} [m]	0.0
Z_{COG} [m]	-3.5

4.1.3 Natural periods

The semi-submersible platform is considered freely floating and no stiffness of mooring lines was taken into account. The resulting natural periods are given in Table 18.

Table 18 Natural periods of the semi-submersible platform

Surge	-
Sway	-
Heave	19.091
Roll	39.352
Pitch	35.417
Yaw	-

4.1.4 Hydrodynamic mesh

The hydrodynamic mesh of the semi-submersible platform is shown in Figure 159. The mesh is composed of 1900 panels on half wetted surface of the body. The water depth is assumed to be infinite.

Figure 159: Hydrodynamic mesh of the semi-submersible platform

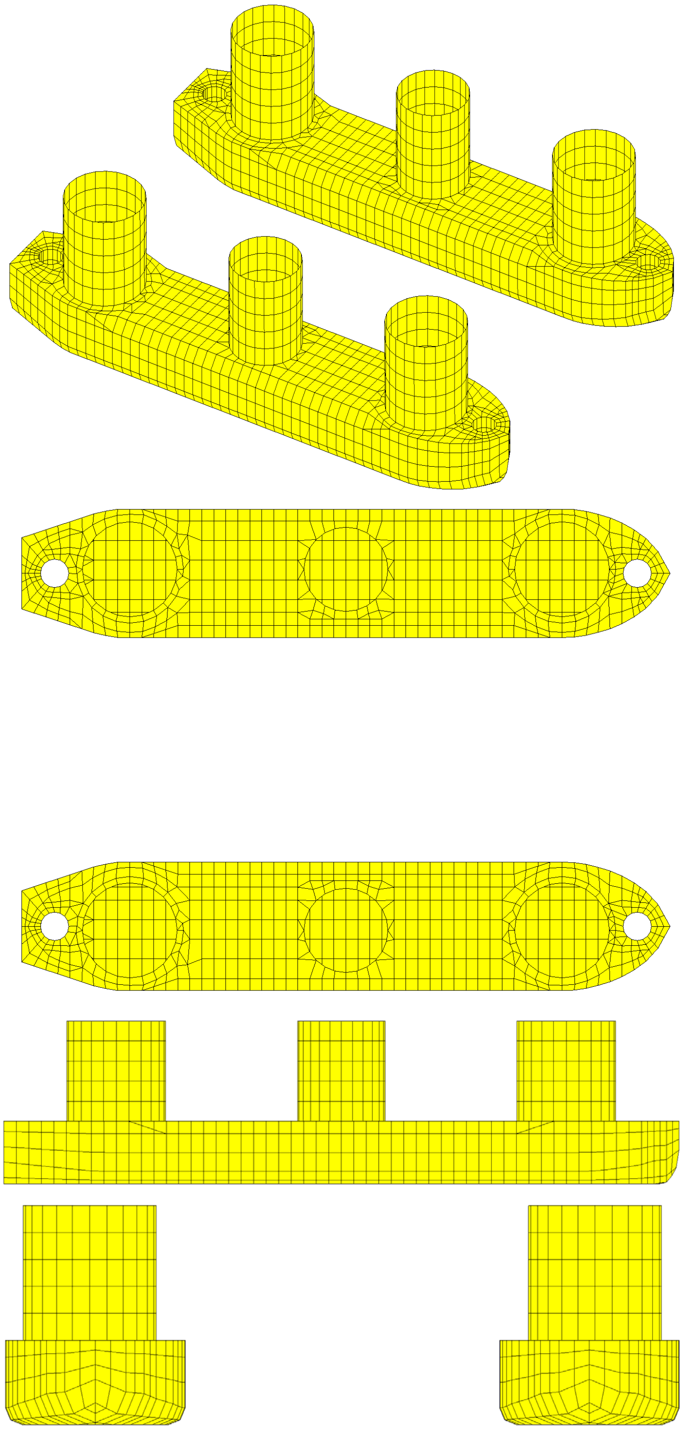

4.2. Results

4.2.1 Hydrodynamic added mass and damping

Figure 160: Diagonal components of the hydrodynamic added mass matrix

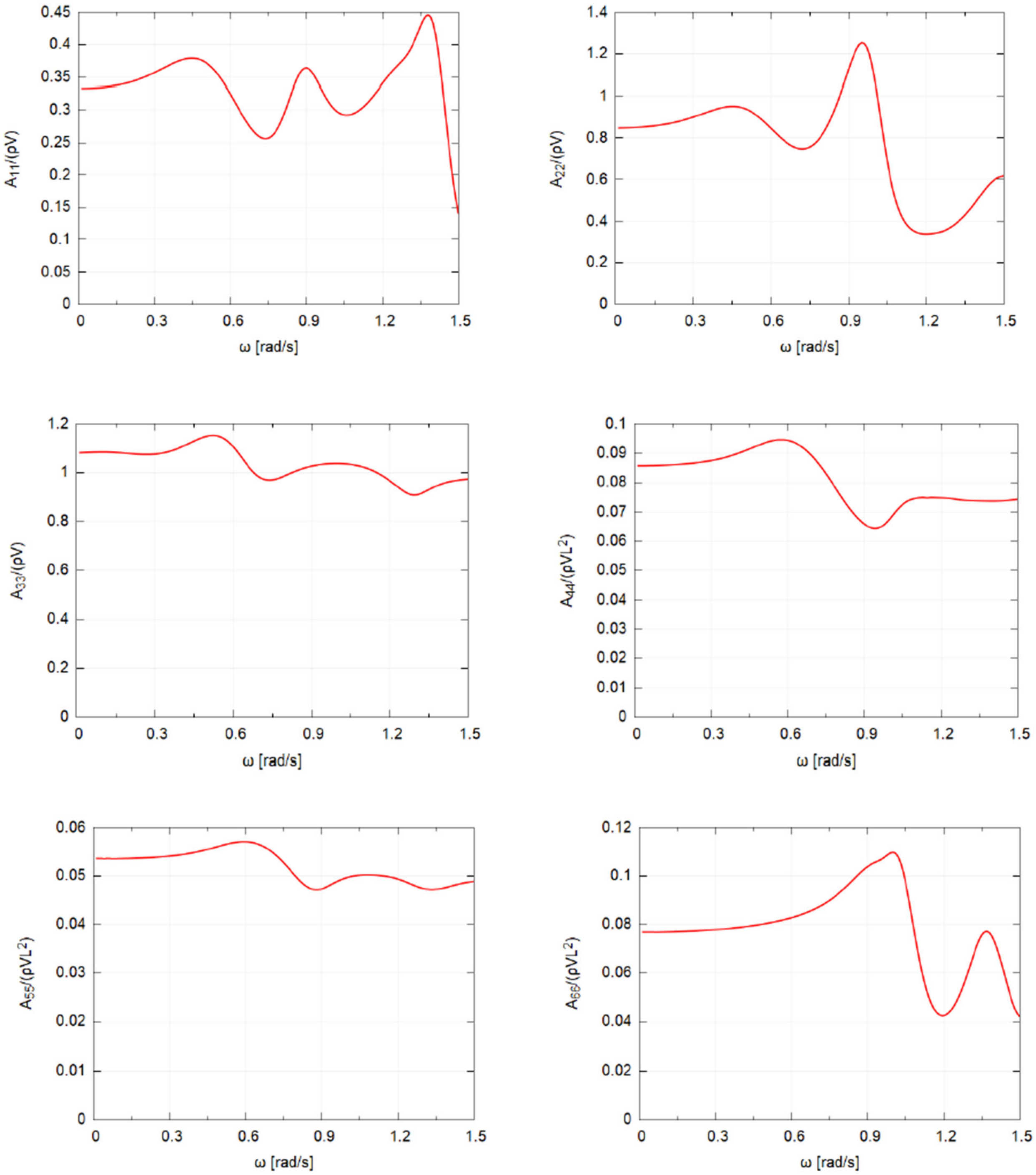

Figure 161: Diagonal components of the hydrodynamic damping matrix

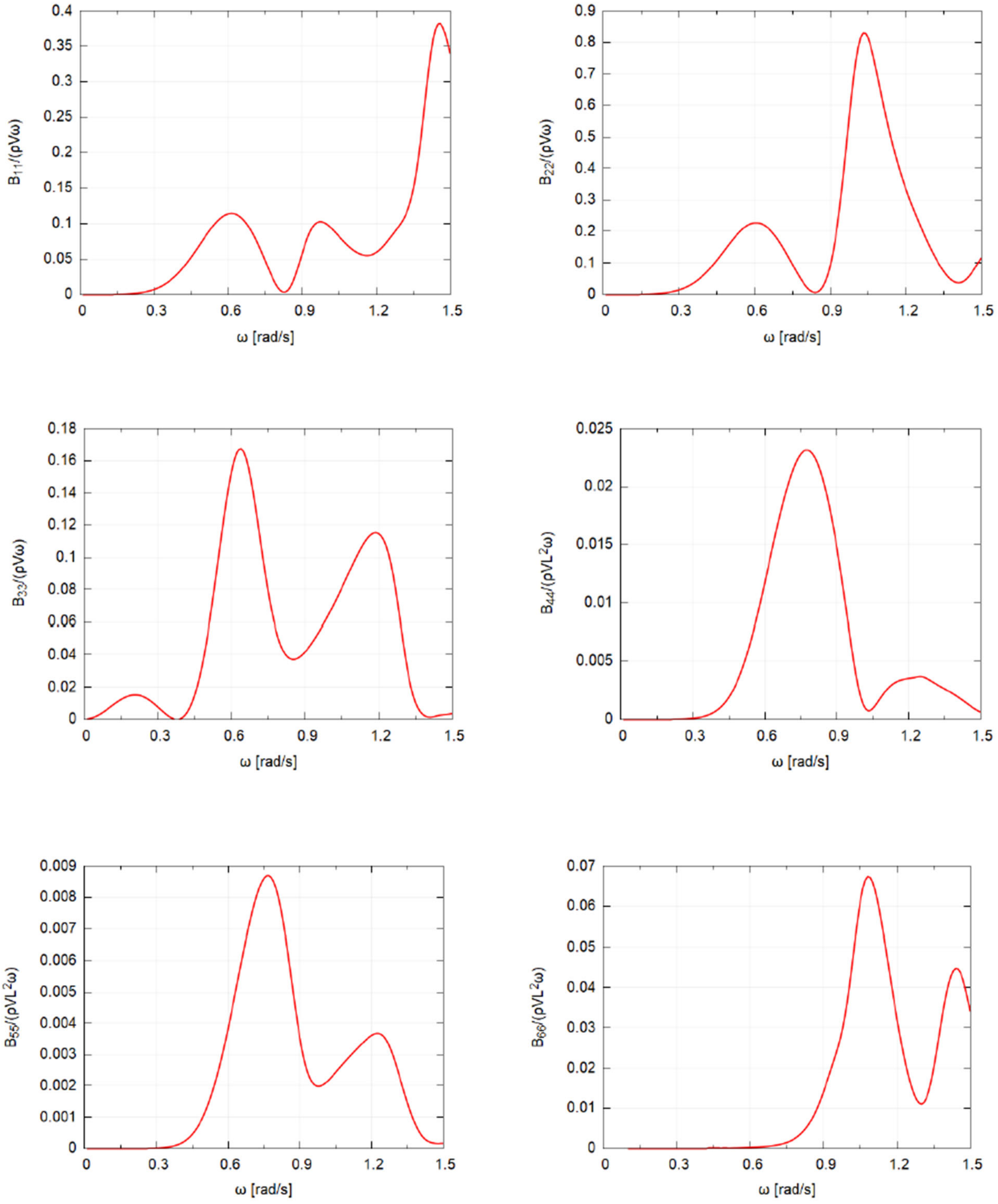

4.2.2 Linear excitation forces

Figure 162: First order excitation forces and moments

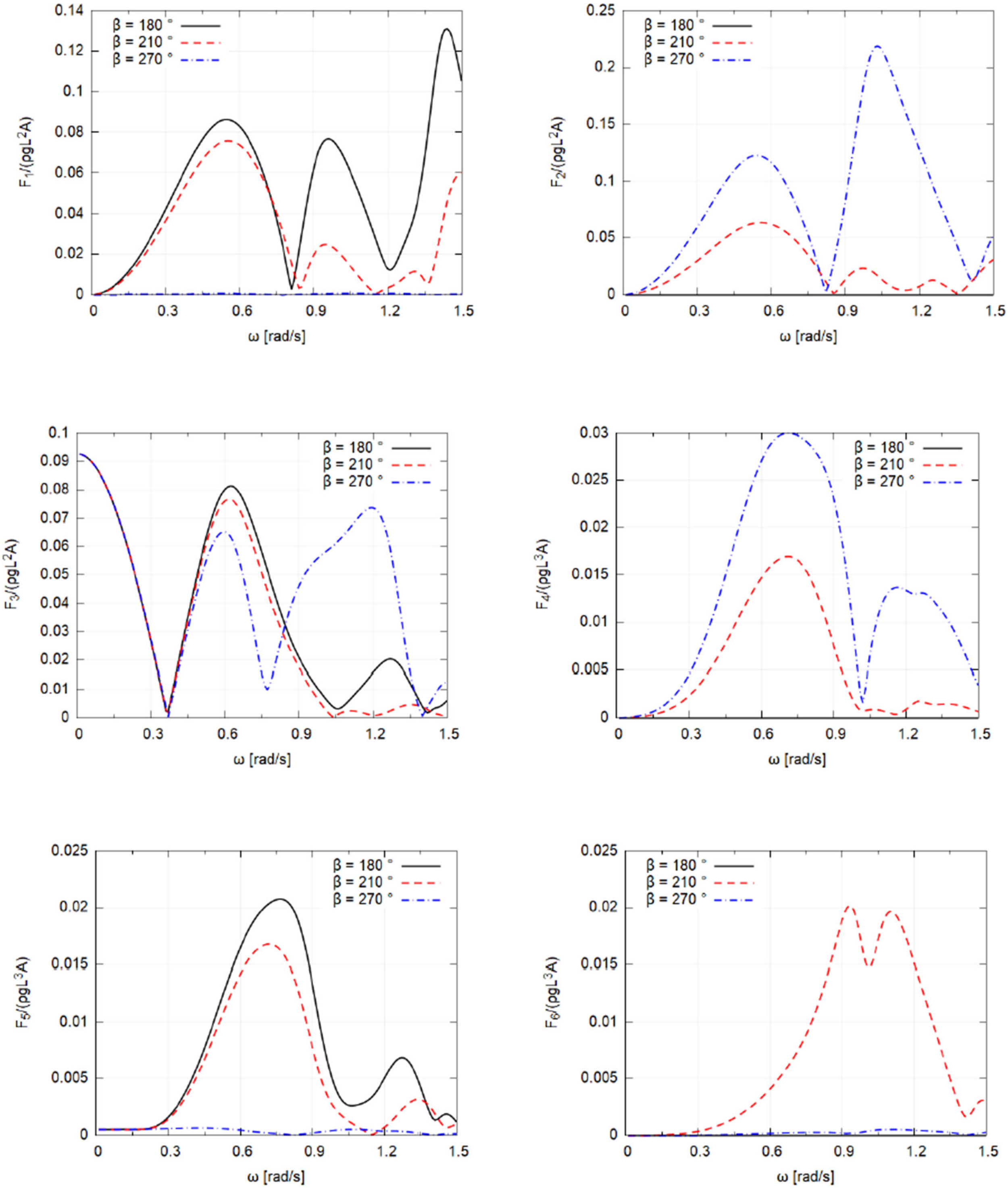

4.2.3 Motion RAO's

Figure 163: Motion's RAO's

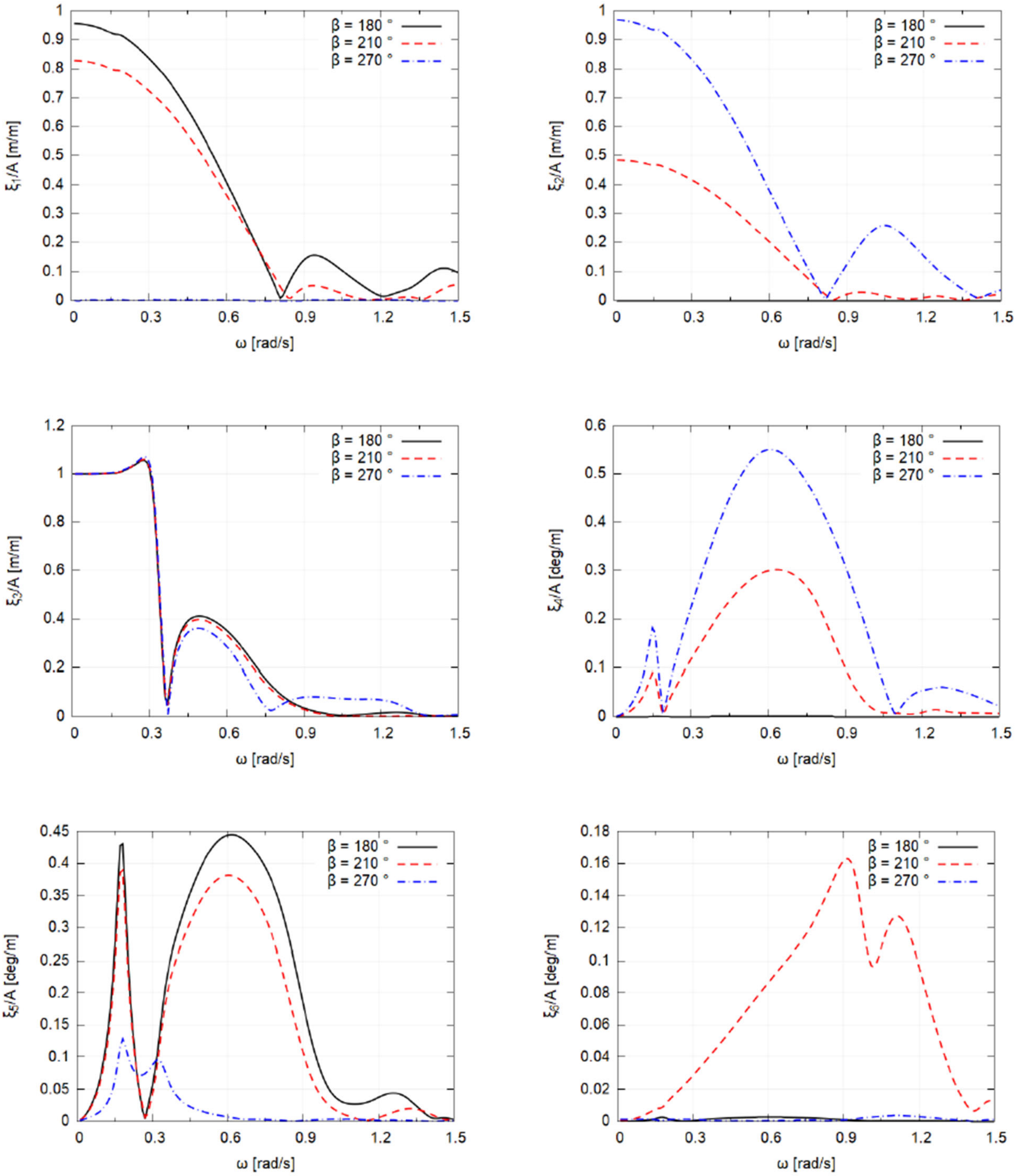

4.2.4 Low frequency second order loads

Figure 164: Mean drift forces and moment, and the QTF_{-} for $\beta = 210°$, in the horizontal plane

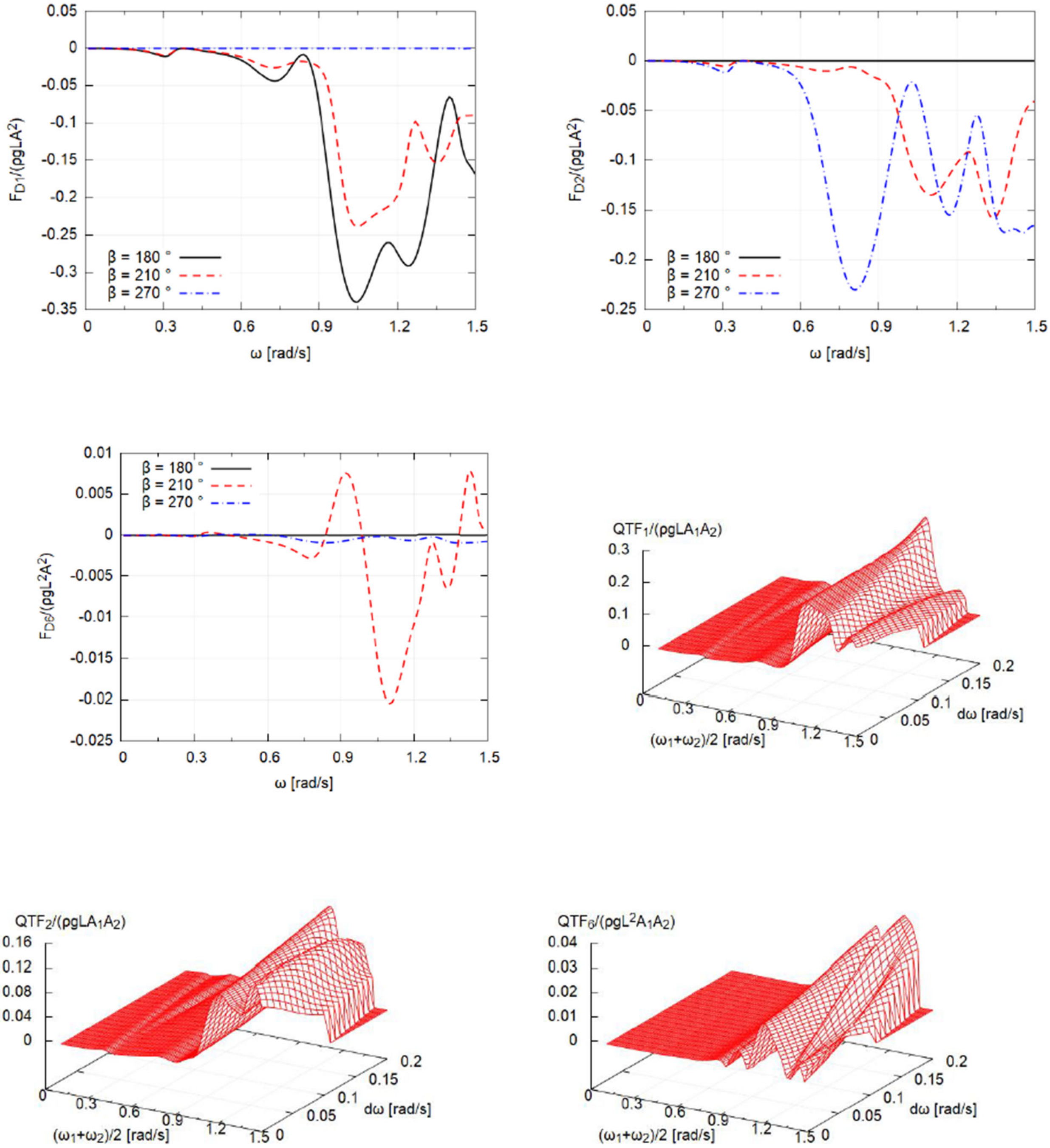

5. TLP

5.1. Description of the floater

5.1.1 Main dimensions

The main dimensions of the TLP are given in Table 19.

Table 19 Main dimensions of the TLP

L_C [m]	47.0	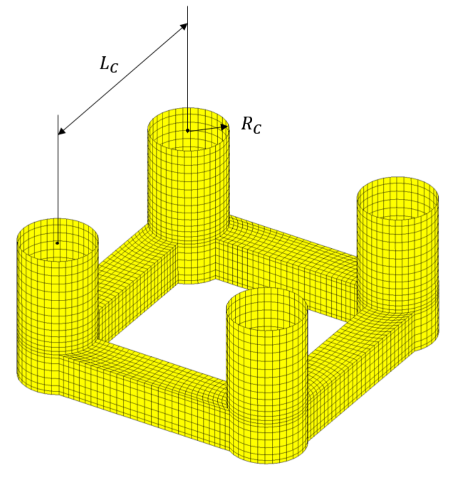
R_C [m]	7.8	
T [m]	30.0	

5.1.2 Mass properties

The mass properties of the TLP are given in Table 20.

Table 20 Mass properties of the TLP

Mass [kg]	2.69E+07
Buoyancy [m^3]	3.32E+04
R_{xx} [m]	31.6
R_{yy} [m]	31.6
R_{zz} [m]	28.0
X_{COG} [m]	0.0
Y_{COG} [m]	0.0
Z_{COG} [m]	-3.35

5.1.3 Natural periods

From mechanical point of view the TLP is considered to be pre-tensioned by 12 tendons (3 at each column). The resulting natural periods are given in Table 21.

Table 21 Natural periods of the TLP

Surge	156.814
Sway	156.814
Heave	3.280
Roll	3.326
Pitch	3.326
Yaw	105.478

5.1.4 Hydrodynamic mesh

The hydrodynamic mesh of the TLP is shown in Figure 165. The mesh is composed of 5016 panels on half wetted surface of the body. The water depth is assumed infinite.

Figure 165: Hydrodynamic mesh of the TLP

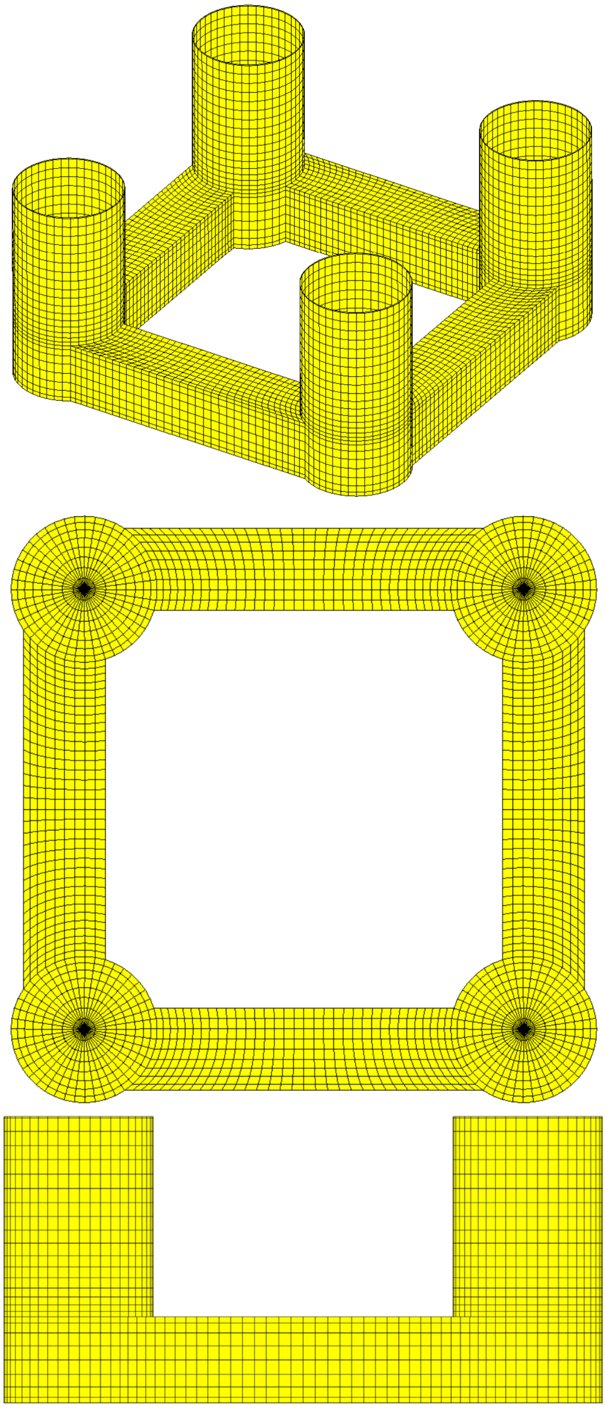

5.2. Results

5.2.1 Hydrodynamic added mass and damping

Figure 166: Diagonal components of the hydrodynamic added mass matrix

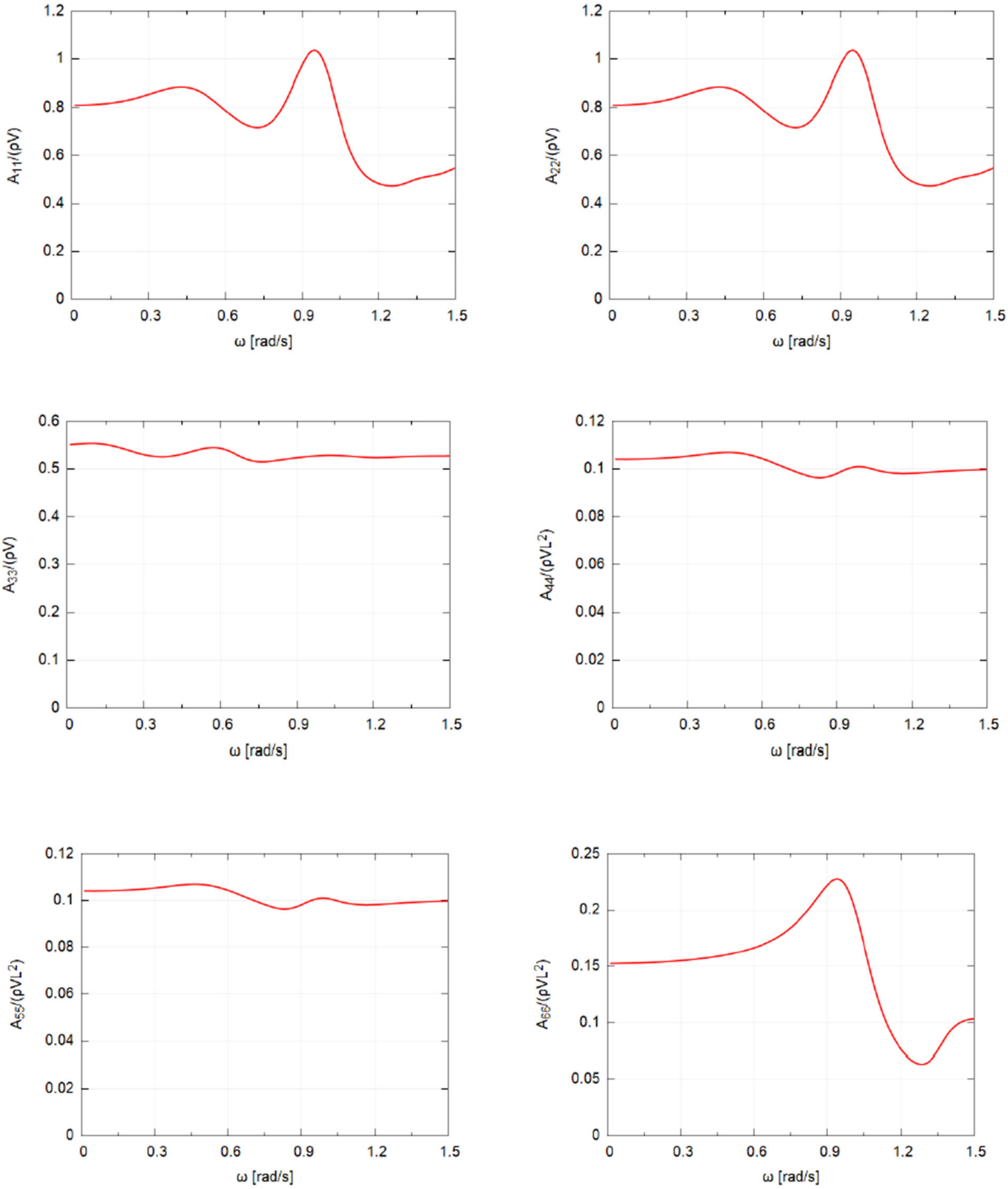

Figure 167: Diagonal components of the hydrodynamic damping matrix

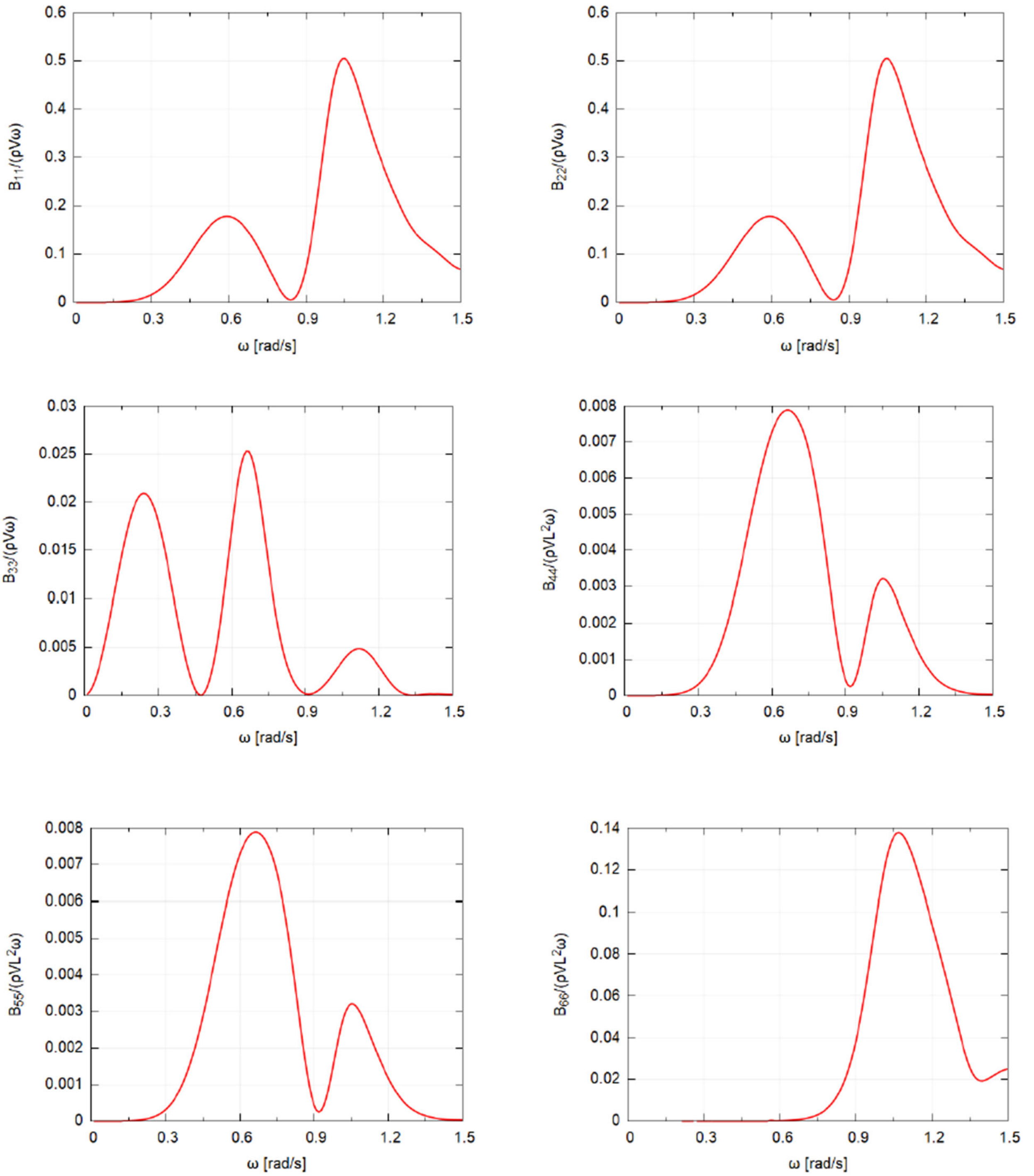

5.2.2 Linear excitation forces

Figure 168: First order excitation forces and moments.

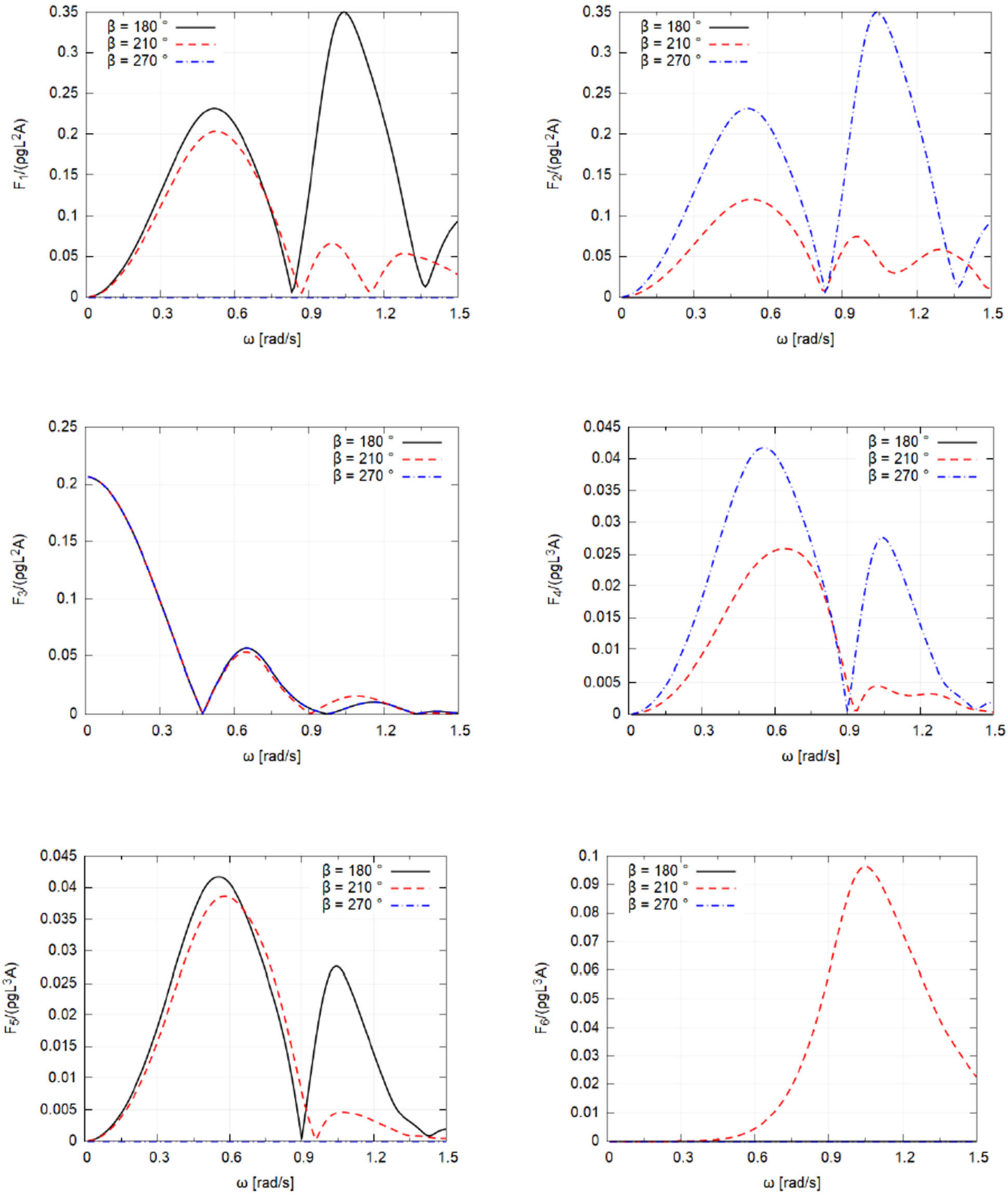

5.2.3 Motion RAO’s

Figure 169: Motion’s RAO’s

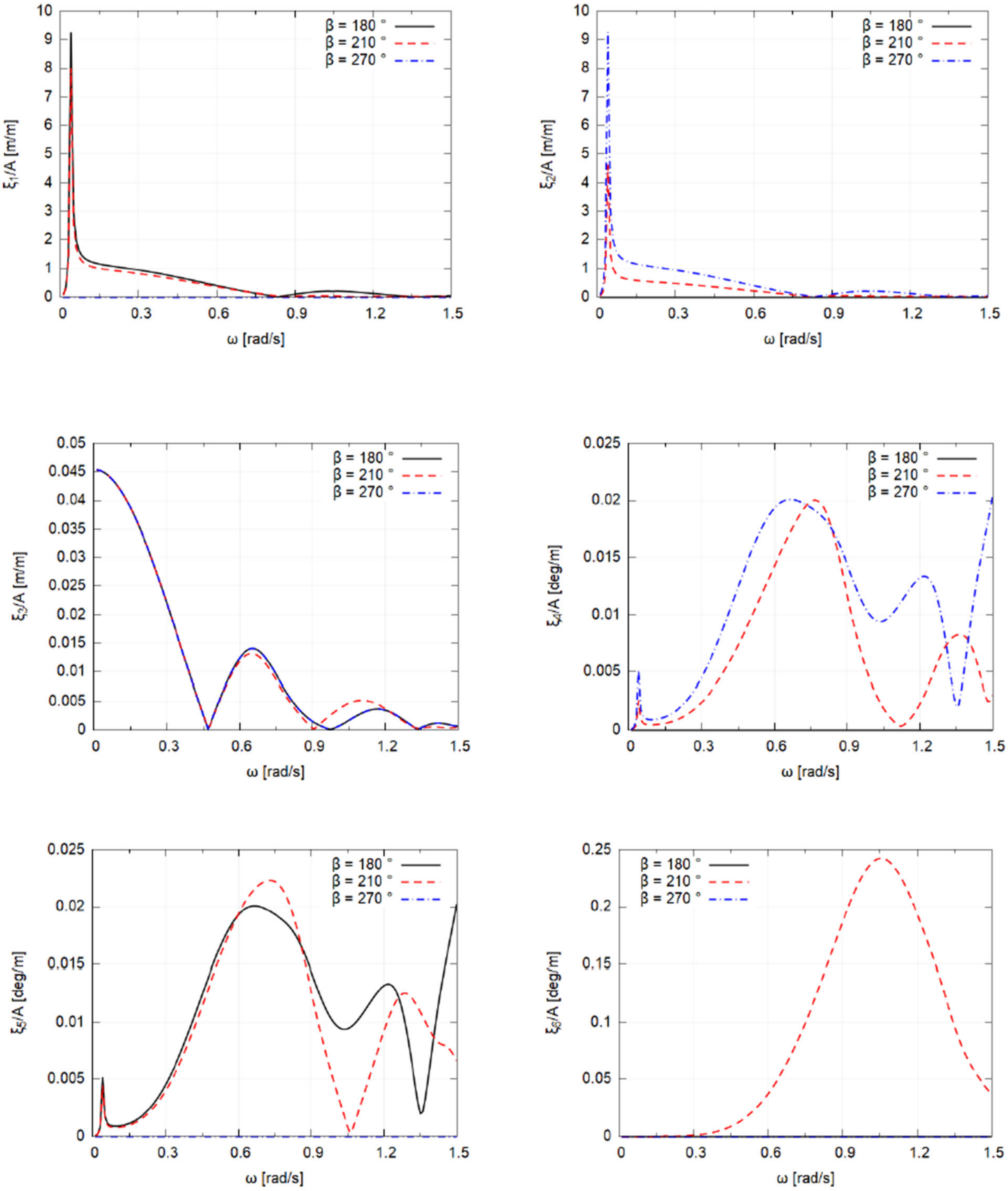

5.2.4 Low frequency second order loads

Figure 170: Mean drift forces and moment, and the QTF_- for $\beta = 210°$, in the horizontal plane

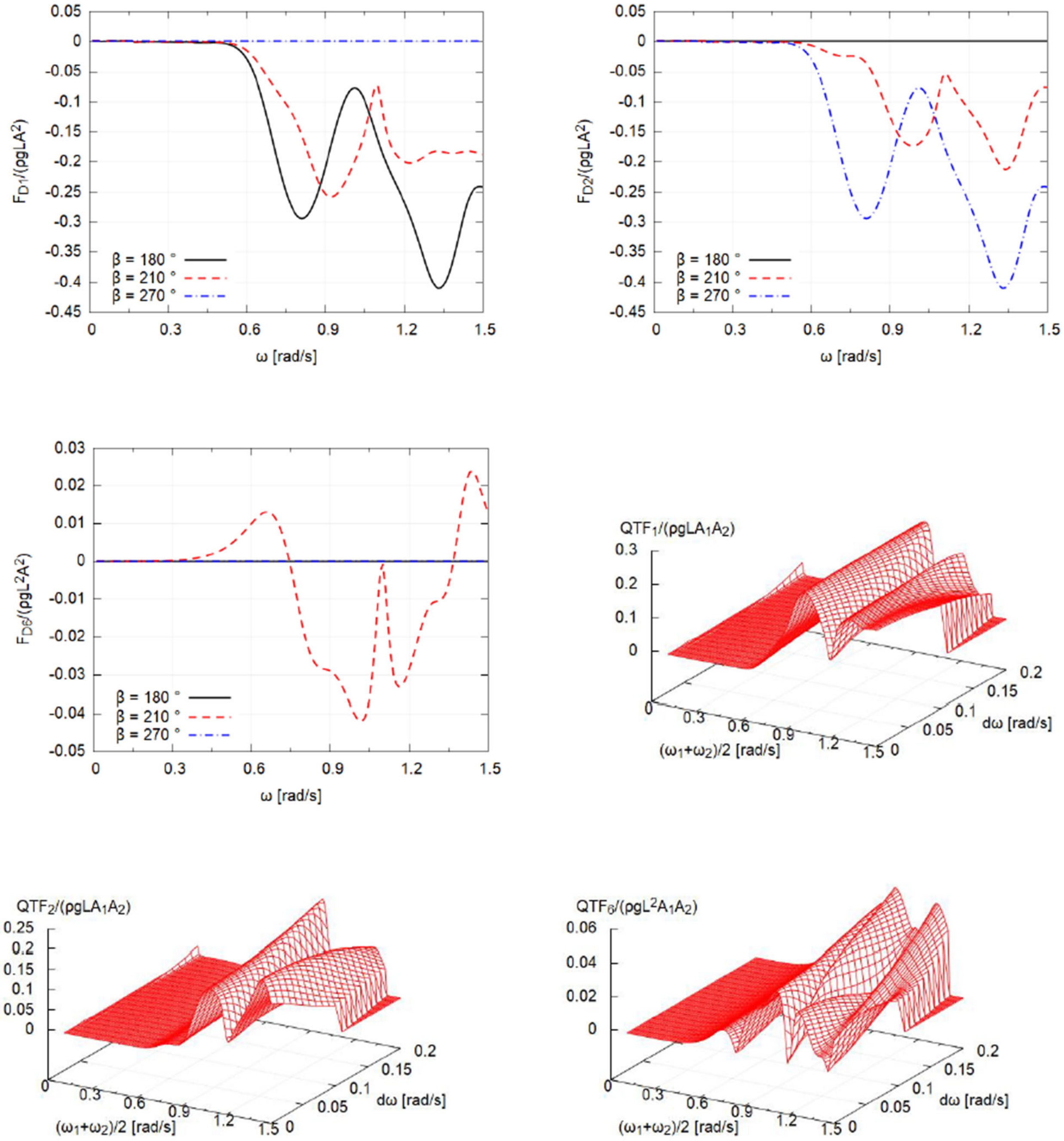

5.2.5 High frequency second order loads

Figure 171: QTF_+ in vertical plane

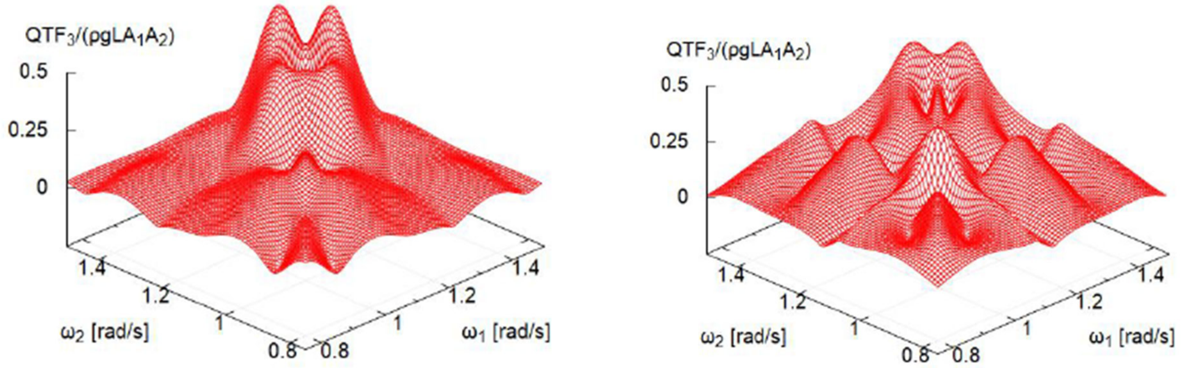

$\beta = 180°$ $\beta = 225°$

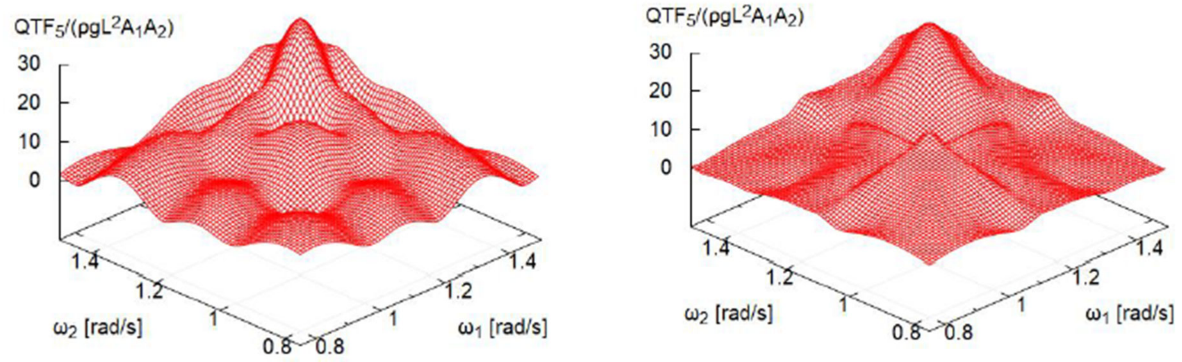

$\beta = 180°$ $\beta = 225°$

.

6. FOWT

6.1. Description of the floater

6.1.1 Main dimensions

The main dimensions of the FOWT are given in Table 22.

Table 22 : Main dimensions of the FOWT

T [m]	9.185	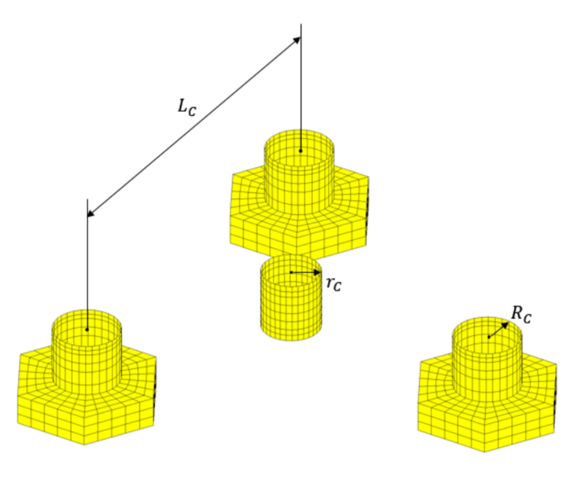
R_C [m]	3.6	
r_C [m]	3.15	
L_C [m]	41.4	

6.1.2 Mass properties

The mass properties of the FOWT are given in Table 23.

Table 23 Mass properties of the FOWT

Mass [kg]	2.67E+06
R_{xx} [m]	22.0
R_{yy} [m]	22.0
R_{zz} [m]	23.0
X_{COG} [m]	0.0
Y_{COG} [m]	0.0
Z_{COG} [m]	1.15

6.1.3 Natural periods

The FOWT is considered moored in water depth of 65 meters. The resulting natural periods are given in Table Figure 74.

Table 24 Natural periods of the FOWT

Surge	43.398
Sway	43.398
Heave	12.028
Roll	22.720
Pitch	22.720
Yaw	118.064

6.1.4 Hydrodynamic mesh

The hydrodynamic mesh of the FOWT is shown in Figure 172.The mesh is composed of 1016 panels on half wetted surface of the body. The water depth is assumed to be 65 meters.

Figure 172: Hydrodynamic mesh.

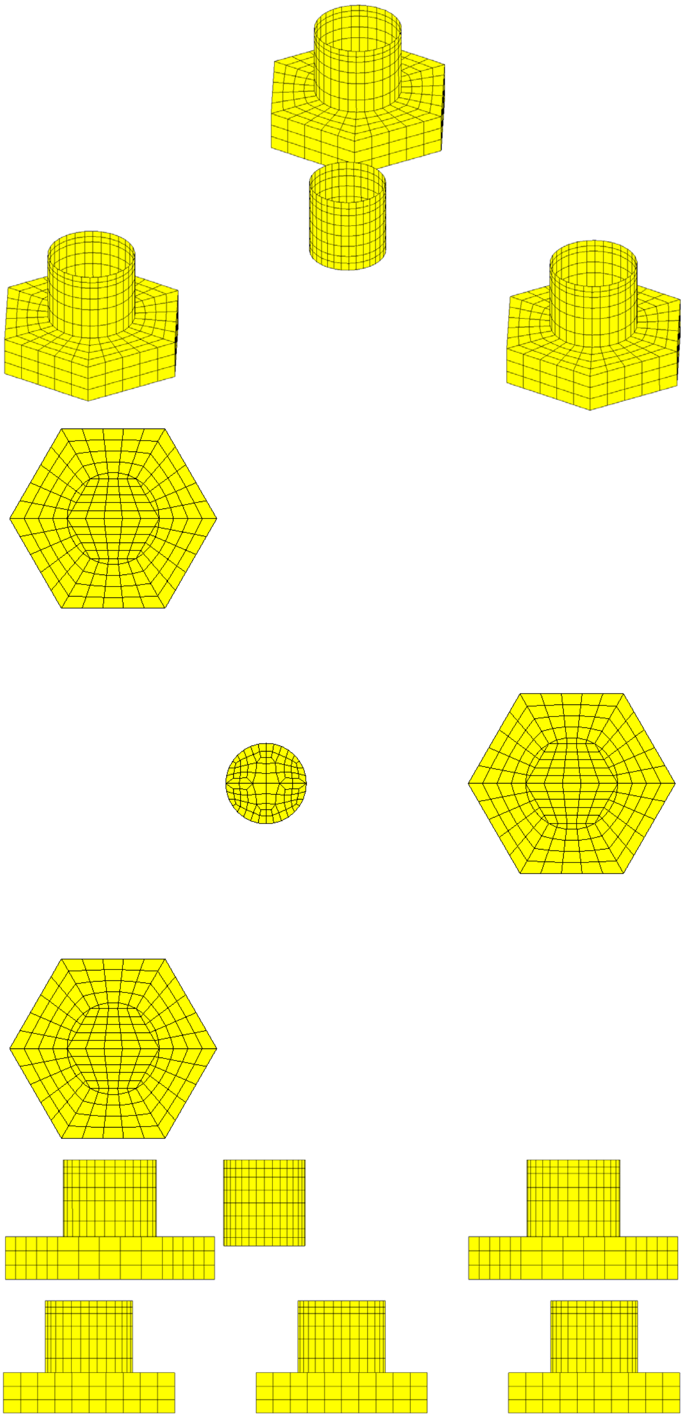

6.2. Results

6.2.1 Hydrodynamic added mass and damping

Figure 173: Diagonal components of the hydrodynamic added mass matrix

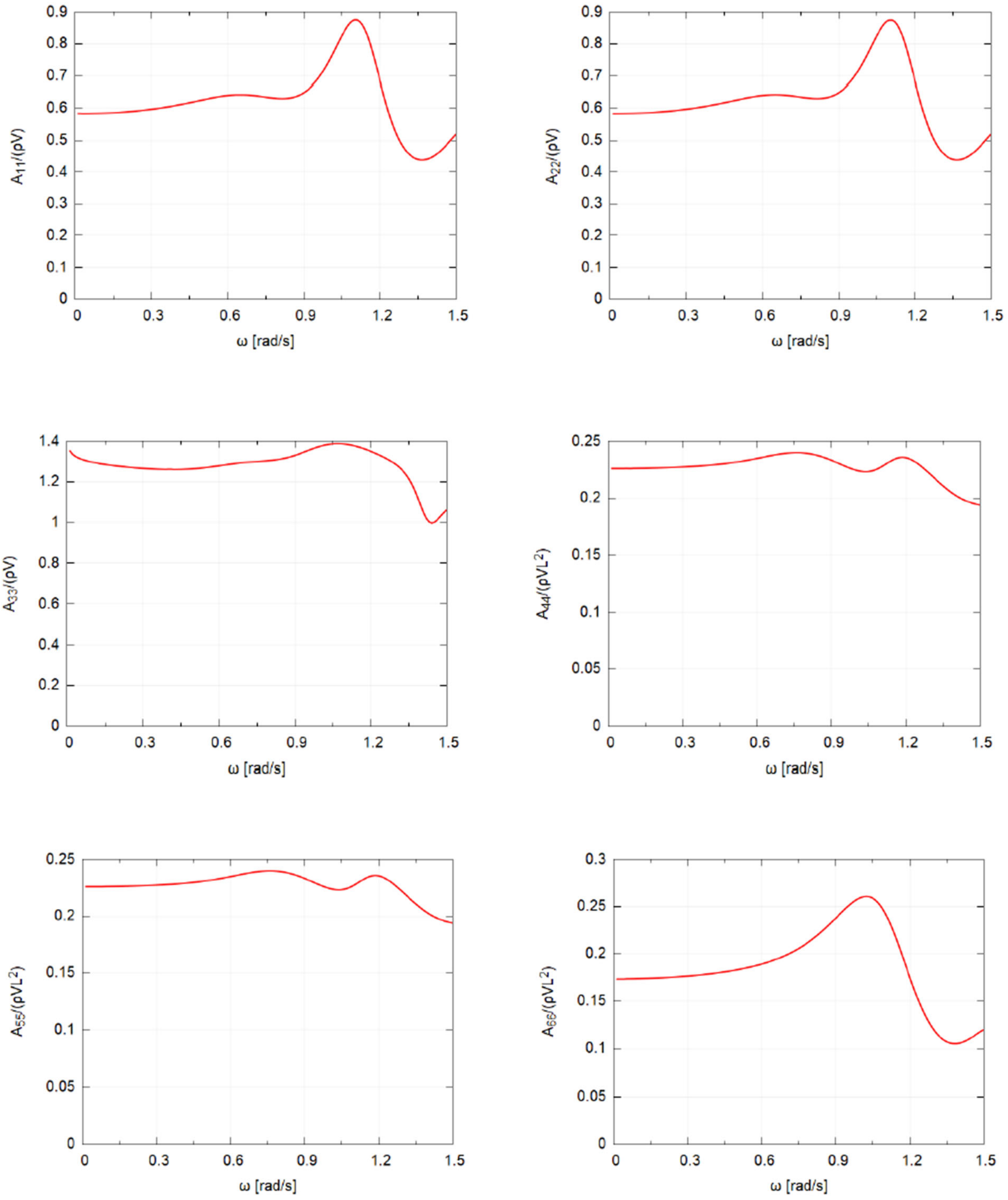

Figure 174: Diagonal components of the hydrodynamic damping matrix

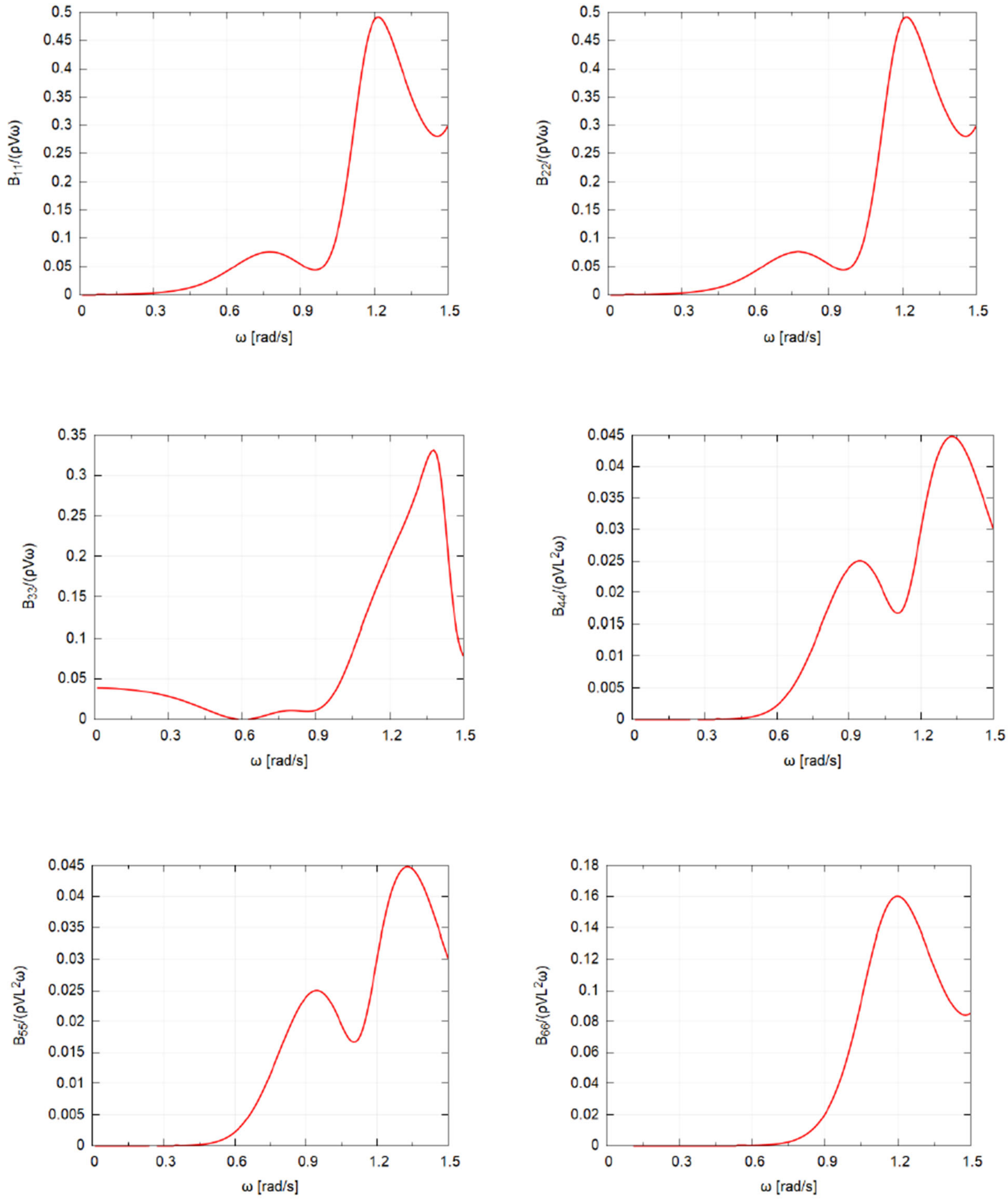

6.2.2 Linear excitation forces

Figure 175: First order excitation forces and moments

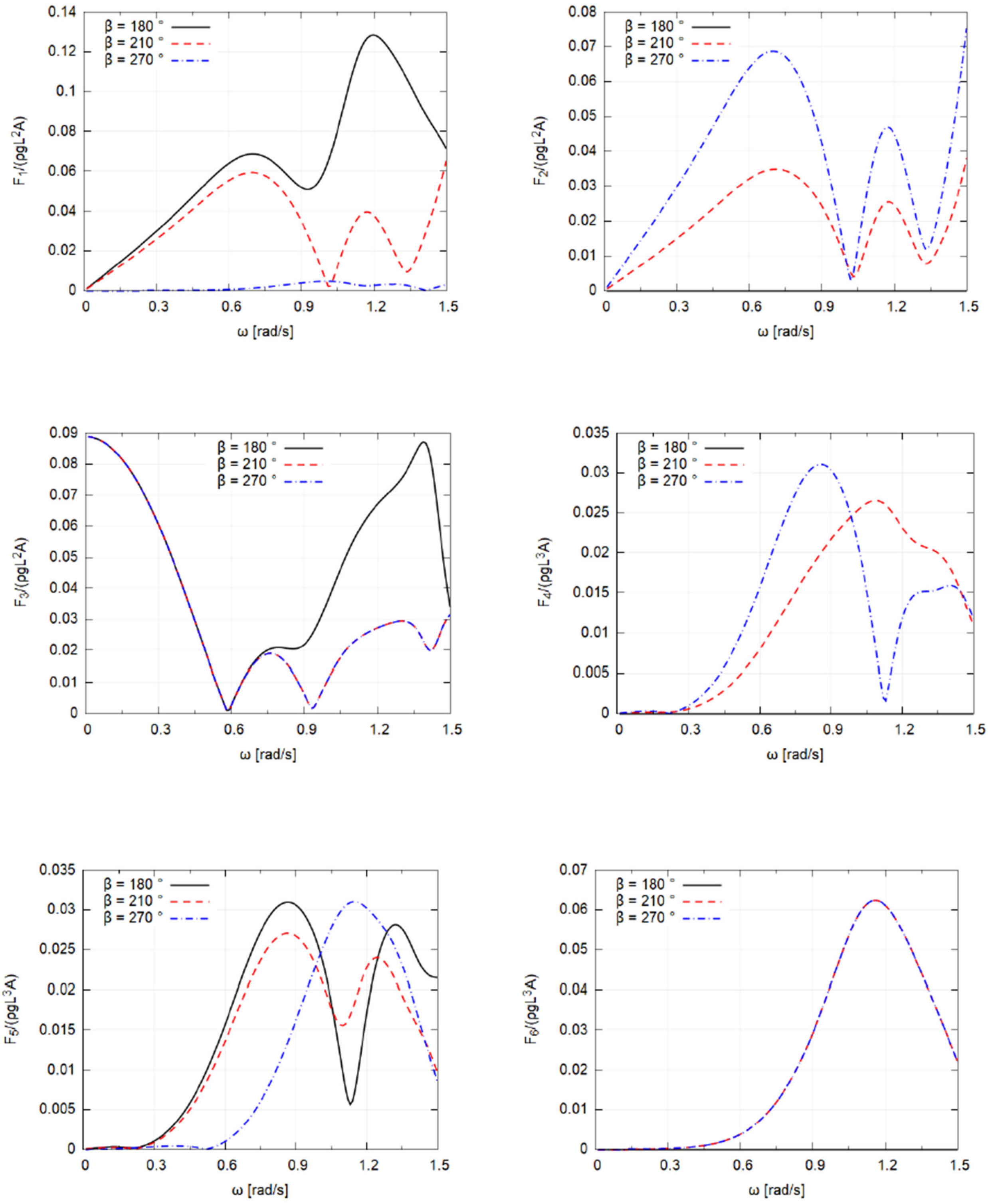

6.2.3 Motion RAO’s

Figure 176: Motion’s RAO’s

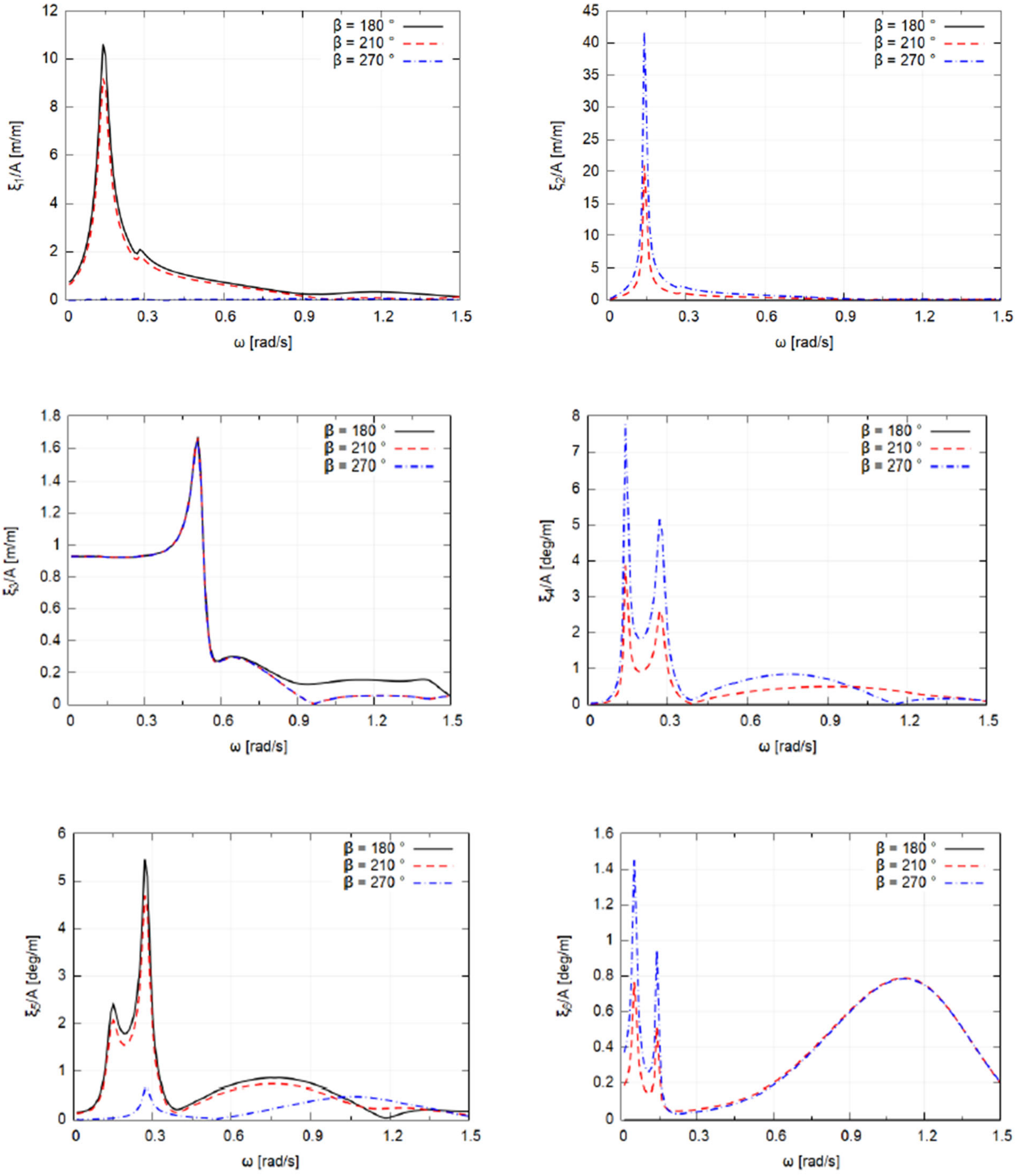

6.2.4 Low frequency second order loads

Figure 177: Mean drift forces and moment, and the QTF_- for $\beta = 210°$, in the horizontal plane

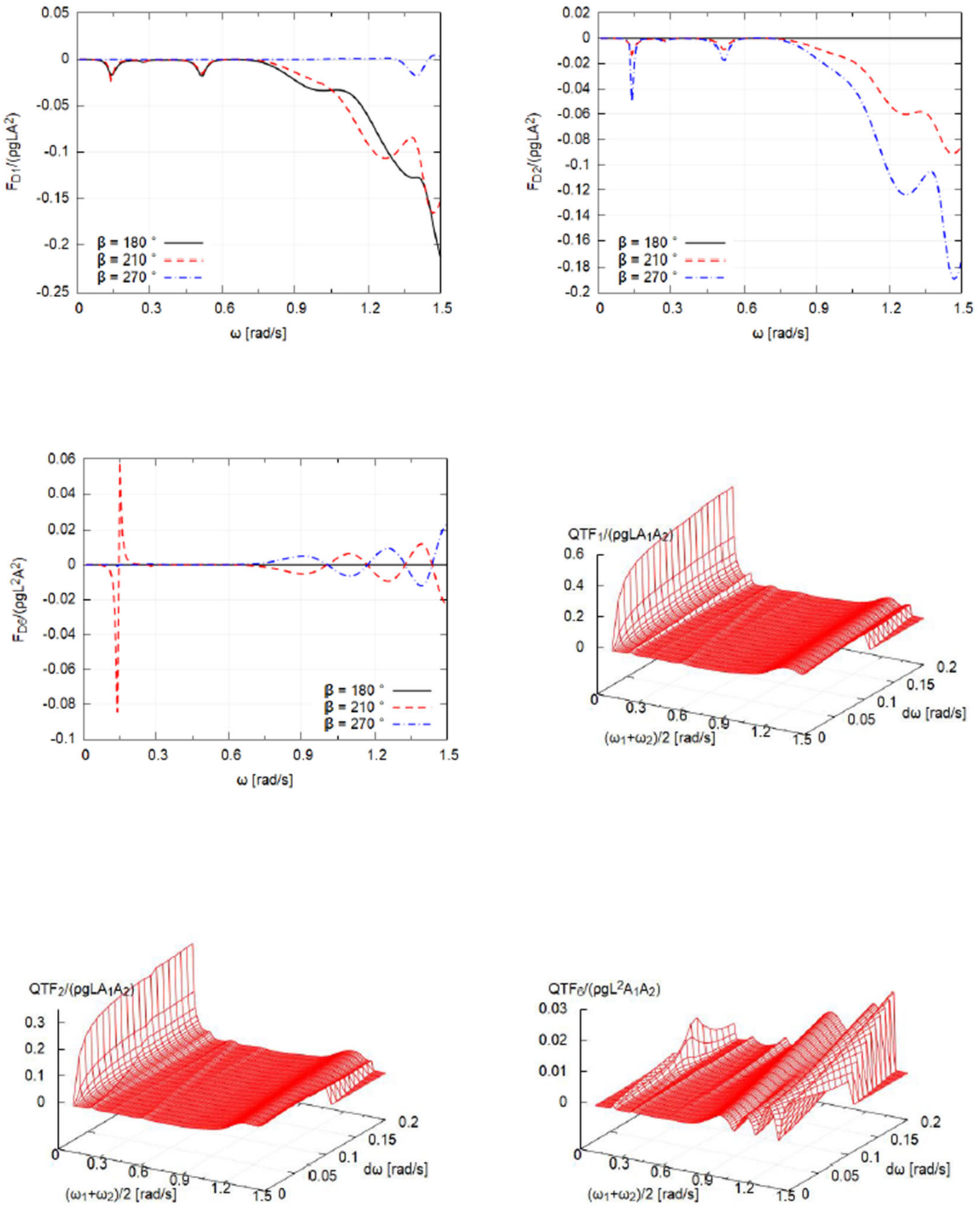

7. List of references

[1] Hulme A., 1982.: ” The wave forces acting on a floating hemisphere undergoing forced periodic oscillations”, Journal of Fluid Mechanics; Vol. 121, pp 443 463

[2] McCamy R.C. & Fuchs R.A., 1954.: “Wave forces on a pile : A diffraction theory”, Tech. Memo. No. 69, U.S. Army Board, Army Corp. of Eng.

[3] Choi Y.M., 2013.: “Second order hydroelastic responses of a vertical circular cylinder in monochromatic waves.”, MSc Thesis, Pusan National University

BUREAU VERITAS MARINE & OFFSHORE

8 cours du triangle
92937 Paris La Défense Cedex - France
+33 (0)1 55 24 70 00

marine-offshore.bureauveritas.com/rules-guidelines

BUREAU
VERITAS

Shaping a World of Trust